HYDRODYNAMICS OF GAS-SOLID TURBULENT FLUIDIZED BEDS

by

Naoko Ellis

B.Sc., The University of Waterloo, 1990
M.E.Sc., The University of Western Ontario, 1993

A THESIS SUBMITTED IN PARTIAL FULFILMENT OF
THE REQUIREMENTS FOR THE DEGREE OF

DOCTOR OF PHILOSOPHY

in

THE FACULTY OF GRADUATE STUDIES

Department of Chemical and Biological Engineering

We accept this thesis as conforming
to the required standard

THE UNIVERSITY OF BRITISH COLUMBIA

February 2003

In presenting this thesis in partial fulfilment of the requirements for an advanced degree at the University of British Columbia, I agree that the Library shall make it freely available for reference and study. I further agree that permission for extensive copying of this thesis for scholarly purposes may be granted by the head of my department or by his or her representatives. It is understood that copying or publication of this thesis for financial gain shall not be allowed without my written permission.

Department of Chemical & Biological Engineering

The University of British Columbia
Vancouver, Canada

Date Feb 21/03

DE-6 (2/88)

ABSTRACT

Many commercial fluidized bed processes (e.g. catalytic and gas-solid reactions, drying) operate in the turbulent fluidization flow regime owing to its excellent gas-solids contacting, favourable heat transfer, and relatively low axial dispersion of gas. The flow characteristics of turbulent fluidized beds, having transient voids and a diffuse bed surface, have not been well defined, and there have been relatively few previous studies on the fundamental hydrodynamics of this industrially important flow regime. In this research project, four different size fluidized beds – 0.11 m, 0.29 m, 0.61 m and 1.56 m in diameter – with Fluid Cracking Catalyst and a commercial catalyst, all involving Geldart Group A particles, have been used to investigate the effect of reactor size, system pressure and temperature on U_c, the superficial gas velocity corresponding to the onset of the turbulent fluidization flow regime, and on the local flow structure for different superficial gas velocities beyond U_c.

The transition velocity, U_c, from the bubbling to the turbulent flow regime was deduced by measuring the pressure fluctuations in the bed using gauge and differential pressure transducers. Results show a different trend of column diameter, D, on U_c between shallow ($H/D < 3$) and deep beds ($H/D \geq 3$). U_c from differential pressure measurements was a stronger function of the height of the pressure cell compared to the effect of radial position for the 1.56 m fluidization column. The transition velocity decreased with increasing system pressure (to 0.4 MPa) confirming findings by earlier investigators. Increasing temperature (to 240°C) led to a decrease in the transition velocity. The amplitude of the differential pressure fluctuations indicated very little change in void size with changing temperature for the range investigated. U_c from differential pressure signals decreased with increasing height above the distributor plate. This implied greater homogeneity at the top of the bed. Spectral analysis of differential pressure signals at different axial positions revealed a shift towards lower frequencies with increasing height. Once the turbulent fluidization flow regime was achieved, the dominant frequency becomes less sensitive to height.

Axial pressure profiles indicated diffuse bed surfaces. The gauge pressure in the freeboard increased with increasing superficial gas velocity due to solids entrainment. The bed expansion depended on the configuration of the solids collection and return system. In systems where the solids circulation rate was not controlled, the characterization of the overall operating conditions in terms of bed

voidage becomes difficult. Increases in both absolute pressure and temperature were found to increase bed voidage, with pressure having a greater influence than temperature.

Local voidages were measured experimentally by means of optical fiber and capacitance probes. The signals indicated continuous probability distribution functions and rapid fluctuations, indicating a breakdown of the discrete-two-phase structure, i.e., discrete dense and dilute phases, a common feature of the bubbling bed flow regime. Cycle times obtained from rescaled range analysis of voidage signals suggested a range of cycle frequencies similar to those detected by the dominant peak from spectral analyses.

A recently established optical velocity probe capable of simultaneously measuring particle velocity and voidage was used to delineate the change in the local two-phase flow structure when the superficial gas velocity was increased beyond U_c. Void velocities deduced from cross-correlation of voidage signals obtained from two identical optical voidage probes were shown to become increasingly sensitive to the threshold value separating the dense and dilute phases. Hence the utility of the two-phase theory in characterizing void dynamics in the turbulent fluidization flow regime became limited. De-noising voidage fluctuation signals using a nonlinear wavelet transform through soft thresholding was shown to be successful in pre-conditioning the signal for cross-correlation of bivariate time series.

This study provides further understanding of the hydrodynamics of the turbulent fluidization flow regime using equipment of substantial size to determine transition velocities and provide hydrodynamic data which are meaningful for industrial-sized fluidized beds.

TABLE OF CONTENTS

HYDRODYNAMICS OF GAS-SOLID TURBULENT FLUIDIZED BEDS i

ABSTRACT ii

TABLE OF CONTENTS iv

LIST OF TABLES xi

LIST OF FIGURES xii

ACKNOWLEDGEMENTS xxv

CHAPTER 1 1

INTRODUCTION 1

1.1 Flow regimes and transitions between regimes 3

1.2 Turbulent fluidization flow regime 4

1.3 Outstanding issues 4

1.4 Research objectives 6

1.5 Thesis layout 7

CHAPTER 2 10

EQUIPMENT AND MACROSCOPIC HYDRODYNAMICS 10

2.1 Introduction 10

2.1.1 Bed expansion 10

2.1.2 Axial voidage profile 10

2.2 Particulate material 11

2.3 Column I: 0.29 m diameter fluidization column 13

2.3.1 Pressure transducers and data acquisition system 13

2.3.2 Bed expansion 17

2.3.3 Bed voidage 17

2.3.4 In-bed inventory of solids 19

2.3.5 Solids circulation rate 23

2.3.6 Axial voidage distribution 23

2.4 Column II: 0.61 m diameter column 23

2.4.1 Pressure balance in circulation loop 27

2.4.2 Expanded bed height 29

2.4.3 Bed density 29

2.5 Column III: 1.56 m diameter fluidization column 29
2.5.1 Traversing arm design and construction 32
2.5.2 Pressure measurements 32
2.5.3 Bed expansion 35
2.5.4 Axial voidage profile 35
2.5.5 Voidage profile 35
2.6 Column IV: 0.11 m diameter column 38
2.6.1 Instrumentation (hot unit) 38
2.6.2 Bed expansion (hot unit) 38
2.6.3 Bed voidage (hot unit) 40
2.7 Conclusions 45
CHAPTER 3 47
REGIME TRANSITION AND SCALE EFFECT 47
3.1 Regime transition 47
3.2 Observation of current knowledge and its gaps 51
3.2.1 Regime transition 51
3.2.2 Scale effect 52
3.3 Experimental approach 52
3.3.1 Pressure measurement method 56
3.3.2 Error analysis 56
3.4 Results 58
3.4.1 Effect of axial probe location and static bed height on U_c 58
3.4.2 Effect of column diameter on U_c 61
3.4.3 Effect of particle properties on U_c 68
3.4.4 Effect of system pressure on U_c 70
3.4.5 Effect of temperature on U_c 75
3.4.6 Combined effects of pressure and temperature on U_c 77
3.4.7 U_c correlation 80
3.5 Conclusions and recommendations 84
CHAPTER 4 86
VOIDAGE MEASUREMENTS 86
4.1 Introduction 86
4.2 Local voidage measurement 86

4.3 Voidage in turbulent fluidized beds 88
4.3.1 Radial voidage distribution 88
4.3.2 Dense phase voidage 91
4.4 Optical probe measuring method principles 92
4.5 Optical voidage probe used in this study 95
4.5.1 Optical probe calibration 97
4.5.2 Experimental calibration of optical voidage probe 98
4.5.3 Glass window 101
4.6 Capacitance probe 104
4.7 Results 109
4.7.1 Optical fiber probe 109
4.7.2 Radial voidage profile 109
4.7.3 Scale effect on radial voidage profile 116
4.7.3.1 Results from 0.61 m diameter fluidization column 120
4.7.3.2 Results from 1.56 m diameter fluidization column 120
4.7.3.3 Scale effect 123
4.7.4 Dense phase voidage 127
4.7.5 Capacitance probe measurements 127
4.8 Conclusions 130
CHAPTER 5 132
VELOCITY MEASUREMENTS 132
5.1 Introduction 132
5.1.1 Void velocity 132
5.1.2 Particle velocity 133
5.2 Optical fiber probe 134
5.3 Data acquisition and analysis 136
5.4 Results 139
5.4.1 Particle velocities in 0.61 m diameter column 139
5.4.2 Effect of superficial gas velocity on particle velocity 144
5.4.3 Particle velocity and voidage 147
5.4.4 Particle velocities in the 0.29 m diameter column 152
5.4.5 Void velocities in the 0.29 m diameter column 152
5.5 Conclusions and recommendations 156

CHAPTER 6 160
SIGNAL ANALYSES AND INTERPRETATION 160
6.1 Introduction 160
6.2 Frequency analysis of pressure fluctuations in fluidized beds 160
6.2.1 Fourier transform 162
6.2.2 Experimental data analysis 162
6.2.3 Crossing frequency 164
6.2.4 Sensitivity of threshold value to crossing frequency 167
6.2.5 Effect of air-feed system 170
6.2.5.1 Experimental investigation of dominant frequency from air-feed system 170
6.3 Cross-correlation function 172
6.3.1 Correlation function coefficient of voidage signal 172
6.4. Autocorrelation 174
6.5 Coherence structure and characterization 176
6.5.1 Coherence function from pressure measurements 184
6.5.2 Coherence function from optical probe voidage measurements 184
6.6. Chaotic analysis 190
6.6.1 Hurst exponents 191
6.6.2 Cycle time and V statistic 191
6.6.3 Results from pressure signals 193
6.6.4 Results from voidage signals 197
6.7 Conclusions 200
CHAPTER 7 203
MULTISCALE RESOLUTION 203
7.1 Introduction 203
7.2 Turbulence – two phase flow 203
7.3 Multiple scales in fluidized beds 205
7.3.1 Kolmogorov scale of turbulence 206
7.3.2 Time scale 206
7.4 Turbulence energy decomposition - phase space 207
7.5 Wavelet analysis 207
7.5.1 Wavelets and turbulence 208
7.6 Analysis method 209

7.6.1 Application of wavelet transform to de-noising signals 209
7.6.1.1 Crude method 209
7.6.1.2 Thresholding 211
7.6.2 Local intermittency measure 211
7.6.2.1 Wavelet analysis applied to particle velocity 214
7.6.2.2 Wavelet analysis applied to voidage fluctuation 221
7.6.3 Qualitative analysis using wavelet 231
7.7 Multiple scales in turbulent fluidized beds 234
7.8 Conclusions 235
CHAPTER 8 237
CONCLUSIONS 237
NOMENCLATURE 242
REFERENCES 250
APPENDIX A 274
COLUMN III: 1.56 M DIAMETER FLUIDIZATION COLUMN 274
A.1 Rig modification 274
A.1.1 Cyclone inlet area 274
A.1.2 Distributor plate and pressure drop 274
A.1.3 Solids storage 274
A.2 Traversing arm design and construction 278
A.3 Commissioning the rig 278
A.4 Pressure measurements 280
A.5 Summary of operating conditions 280
APPENDIX B 284
VELOCITY MEASUREMENT DATA ANALYSES 284
B.1 Cross-correlation 284
B.2 Group number 286
B.3 Elimination criteria 289
B.4 Peak detection 289
B.5 Dense-phase-associated particle velocity 290
B.6 Binary coding 293
B.7 Optical fiber voidage probes 298
B.8 Conclusions with respect to data analysis method 305

APPENDIX C 306
FOURIER AND WAVELET TRANSFORMATIONS 306
C.1 Fourier transform 306
C.2 Wavelet analysis 307
C.2.1 Introduction to wavelet transformation 307
C.2.2 Comparison of wavelet transform to windowed Fourier transform 309
C.2.3 Different types of wavelet transform 312
C.2.3.1 Continuous wavelet transform 312
C.2.3.2 Discrete wavelet transform 312
C.2.4 Details and approximations 313
C.2.5 Thresholding 314
APPENDIX D 319
HYDRODYNAMIC AND CFD MODELLING 319
D.1 Introduction 319
D.2 Primary forces acting on a fluidized particle 319
D.3 Forces acting on solids in gas-solid multiphase flows 320
D.3.1 Drag Forces 321
D.3.2 Particle inertia 322
D.3.3 Electrostatic forces 323
D.3.4 Other forces 324
D.4 Hydrodynamic modelling 324
D.4.1 Discrete particle model 325
D.4.2 Continuum model 326
D.4.3 Kinetic theory of granular flow 327
D.4.4 Restitution coefficient, e 330
D.4.5 Radial distribution function, g_0 331
D.4.6 Solids pressure, P_a 332
D.4.7 Particle shear viscosity, μ_s 334
D.4.8 Solids phase (bulk) viscosity: λ_s 336
D.5 Turbulence in two-phase flow 336
D.5.1 Gas phase turbulence 336
D.5.2 Particle phase turbulence 337

D.6 Turbulent two-phase flow models applied to fluidized beds 337
D.7 Modelling turbulent fluidized beds 338
D.8 Simulation using CFX 339
D.8.1 Computer speed and capacity 340
D.8.2 Computational techniques 340
D.8.3 Geometry and grid generation 340
D.8.4 Boundary and conditions 342
D.8.5 Command file 342
D.8.6 User Fortran 343
D.8.6.1 USRINT 343
D.8.6.2 USRCVG 343
D.8.6.3 USRTRN 343
D.8.6.4 USRBCS 343
D.8.6.5 CVIS 344
D.8.7 Parameters 344
D.8.8 Convergence 345
D.8.9 Typical result 345
D.8.10 Future studies 348
D.9 Conclusions 348

LIST OF TABLES

Table 2.1 Particle properties. 11

Table 2.2 Coefficients for the Modified Richardson-Zaki equation. 21

Table 3.1 Particle properties used in 0.29 m diameter column. 70

Table 3.2 Published exponents for Equation 3.2. 71

Table 4.1 Summary of reported hydrodynamic parameters in turbulent fluidized beds. 89

Table 4.2 Summary of literature data on radial voidage distribution in turbulent fluidized beds. 90

Table 5.1 MATLAB® functions written for data analysis. 137

Table 5.2 Average voidage. D=0.61 m, H_0=2 m, FCC IV. 141

Table 5.3 Moments of particle velocity distributions. D=0.29 m, z=0.78 m, r/R=0.55, FCC I. 154

Table 6.1 Transducer positions for Figure 6.22. 183

Table A.1 Experimental conditions. 283

Table B.1 Effect of threshold determination methods on threshold voidage values. U=0.69 m/s, D=0.61 m, z=0.80 m, r/R=0.09, f=30,147 Hz. 298

Table B.2 Effect of threshold determination methods on voidage value and crossing frequency. D=0.29 m, U=0.69 m/s, r/R=0.70, z=0.78 m, FCC I. 299

Table D.1 Summary of fluid and particle characteristic parameters based on typical FCC used in those parts of this work carried out at UBC. 320

Table D.2 Drag coefficients. 321

Table D.3 Radial distribution functions. 332

Table D.4 Solid phase elastic modulus. 332

Table D.5 Particle shear viscosity expressions in the literature. 335

Table D.6 Grid quality for Aug02-geo02. 342

LIST OF FIGURES

Figure 1.1 Gas-solid fluidization flow regimes. (Adapted from Grace, 1986) 2

Figure 2.1 Particle size distribution of spent FCC particles. 12

Figure 2.2 Progressive change in particle size distribution in 1.56 m diameter fluidization column. FCC II. 12

Figure 2.3 Schematic of 0.29 m diameter, 4.5 m tall fluidization column at UBC. 14

Figure 2.4 Photograph of 0.29 m diameter column with PVC piping for air supply. Wooden enclosure on the top level contains bag filters. 15

Figure 2.5 Schematic of 0.29 m diameter fluidization column depicting axial distances (in m) of ports relative to distributor plate. 16

Figure 2.6 Axial gauge pressure profile for 0.29 m column. H_0=0.51 m. D=0.29 m, FCC I. 18

Figure 2.7 Expanded bed height calculated from gauge pressure profiles in Figure 2.6. D=0.29 m, FCC I. 18

Figure 2.8 Determination of bed pressure drop. U=0.96 m/s, H_0=1.2 m, D=0.29 m, FCC I. 20

Figure 2.9 Time-mean bed voidage vs. U. D=0.29 m, FCC I. 20

Figure 2.10 Time-mean bed voidage vs. superficial gas velocity. Determination of effective terminal velocity, $\mathbf{U}_t^*$, in modified Richardson-Zaki equation. H_0=0.6 m, D=0.29 m, U_c=0.62 m/s ($\bar{\mathbf{z}}$=0.31 m, DP). 21

Figure 2.11 Height of dense bed corresponding to voidage at minimum fluidization vs. superficial gas velocity. D=0.29 m, FCC I. 22

Figure 2.12 Solids circulation flux vs. superficial gas velocity. D=0.29 m, H_0=1.0 m, FCC I. 24

Figure 2.13 Axial voidage profile from time-mean DP measurements. D=0.29 m, H_0=1.1 m, FCC I. 24

Figure 2.14 Schematic diagram of location (in m) of pressure ports in 0.61 m column. 25

Figure 2.15 Location (in mm) of pressure transducers and optical fibre probes for dynamic measurements in 0.61 m diameter fluidization column. 26

Figure 2.16 Distributor plate pressure drop measured in empty column. D=0.61 m. 28

Figure 2.17 Pressure profile for circulation loop for D=0.61 m, H_0=2 m, FCC IV. 28

Figure 2.18 Expanded bed height and height of dense bed corresponding to voidage at ε_{mf} calculated from axial gauge pressure profiles. D=0.61 m, H_0=2 m, U_c=1.12 m/s ($\bar{z}$=1.55 m, DP), FCC IV. 30

Figure 2.19 Time-mean bed density vs. superficial gas velocity for D=0.61 m, H_0=2.0 m, axial location of DP taps: 0.73-1.55 m, FCC IV. U_c at $\bar{z}$=1.55 m from DP fluctuations. 30

Figure 2.20 Location of pressure transducers and traversing probe arms in 1.56 m column. 31

Figure 2.21 Distributor plate pressure drop measured in empty 1.56 m column. 33

Figure 2.22 Frequency spectrum analysis of gauge pressure fluctuations in empty bed. D=1.56 m, U=1.1 m/s, z=0.2 m, r/R=0.9. 33

Figure 2.23 Bed and distributor pressure drop for 1.56 m fluidization column. U=0.43 m/s, H_0=0.9 m, FCC II. 34

Figure 2.24 Schematic diagram of the tip of a traversing probe arm. 34

Figure 2.25 Calculated expanded bed height from time-mean gauge pressure profile. D=1.56 m, FCC II. 36

Figure 2.26 Height of dense bed corresponding to voidage at minimum fluidization vs. superficial gas velocity. U_c deduced from gauge pressure signals. D=1.56 m, FCC II. 36

Figure 2.27 Axial voidage profile from time-mean DP measurements. D=1.56 m, FCC II. 37

Figure 2.28 Voidage calculated from DP method and optical probe signal. D=1.56 m, z=0.85 m, H_0=0.9 m. All sensors positioned at r/R=0.9. U_c ($\bar{z}$=0.84 m, DP)=0.39 m/s, FCC II. 37

Figure 2.29 Schematic diagram of 0.11 m diameter hot unit. All dimensions are in metres. 39

Figure 2.30 Effect of system pressure on expanded bed height at room temperature. D=0.11 m, Catalyst C, H_0=0.7 m. 41

Figure 2.31 Effect of temperature on bed expansion at a system pressure of 0.2 MPa. D=0.11 m, Catalyst C, H_0=0.7 m. 41

Figure 2.32 Effect of system pressure and temperature on time-mean bed voidage deduced from DP signals. D=0.11 m, U=0.40 m/s, Catalyst C. 42

Figure 2.33 Comparison of experimental voidage data with predictions from literature correlations. Catalyst C. Ambient conditions. 43

Figure 2.34 Experimental voidage measurement at 240°C compared to correlation predictions. D=0.11 m, H_0=0.7 m, Catalyst C. 44

Figure 3.1 Definitions of transition velocities U_c and U_k based on standard deviation of pressure fluctuations. Adapted from Yerushalmi and Cankurt (1979). 48

Figure 3.2 Typical standard deviation of pressure fluctuations and bed density measurements. Pressure fluctuation measurement: $\bar{z}$=1.50 m, Δz=0.10 m. Bed density: $\bar{z}$=1.14 m, Δz=0.82 m. D=0.61 m, FCC IV, H=1.67~1.77 m. 54

Figure 3.3 Bed density measurements. $\bar{z}$=1.85 m (z_{lower}=1.55 m, z_{upper}=2.14 m), Δz=0.59 m, D=0.61 m, FCC IV, $\bar{d}$=98 μm. H=1.67~1.77 m.Figure 3.4 Standard deviation of optical fiber voidage probe signal. z=1.55 m, r/R=0.09, D=0.61 m, FCC IV, H=1.67~1.77 m. 54

Figure 3.4 Standard deviation of optical fiber voidage probe signal. z=1.55 m, r/R=0.09, D=0.61 m, FCC IV, H=1.67~1.77 m. 55

Figure 3.5 Typical plot of standard deviation of DP fluctuations vs. U. D=0.29 m, H_0=0.60 m, FCC I. Δz=0.064 m for z=0.18, 0.31, 0.43 m; and Δz=0.13 m for z=0.59 m DP port locations. 59

Figure 3.6 Typical plot of standard deviation of gauge pressure fluctuations vs. U. D=0.29 m, H_0=0.51 m, FCC I. 59

Figure 3.7 Effect of pressure port location on U_c from DP signals. D=0.29 m, FCC I. 60

Figure 3.8 Effect of aspect ratio H/D on U_c from gauge pressure signals. D=0.29 m, FCC I. 62

Figure 3.9 U_c obtained in this study from gauge pressure signals as a function of column diameter. FCC. 64

Figure 3.10 U_c based on gauge pressure fluctuations vs. bed aspect ratio for the three columns investigated in this work together with data from Bi (1994). FCC. 64

Figure 3.11 Comparison of experimental U_c obtained from DP signals to published data for H/D≥3. 66

Figure 3.12 Standard deviation of DP signals and voidage plotted against superficial gas velocity. D=0.29 m, FCC I, H_0=0.51 m, z=0.31 m. 66

Figure 3.13 Plot of U_c vs. corresponding bed voidage, ε_c. FCC. 67

Figure 3.14 Standard deviation of DP signals plotted a s a function of U. D=1.56m, H_0=2 m, FCC II. 67

Figure 3.15 Cumulative distribution of particle size based on mass fraction. 69

Figure 3.16 Comparison of expanded bed height from axial pressure distribution for FCC and Catalyst Cr. D=0.29 m, H_0=0.6 m. 69

Figure 3.17 Effect of particle properties on axial profiles of U_c from DP signals. H_0=0.60 m, D=0.29 m. 71

Figure 3.18 Archimedes number vs. particle Reynolds number based on U_c compared to published correlations based on Equation 3.2 and Table 3.2. D=0.29 m. 72

Figure 3.19 Effect of system pressure on U_c. D=0.11 m, z=0.9 m, H_0=0.7 m, Catalyst C fluidized with N_2. 74

Figure 3.20 Effect of system pressure on U_c. Comparison of this work (D=0.11 m, Catalyst C, fluidizing air: N_2, T=20 °C) to others. 76

Figure 3.21 Effect of temperature on U_c. D=0.11 m, Catalyst C. 78

Figure 3.22 Standard deviation of gauge pressure signals against volumetric gas flow rate. D=0.11 m, Catalyst C, P=0.2 MPa. 78

Figure 3.23 Effect of gas viscosity and system pressure on Q_c, transition based on volumetric flow rate. D=0.11 m, Catalyst C. Subscript T denotes system temperature. 79

Figure 3.24 Comparison of predictions by Equation 3.10 with experimental U_c. Catalyst C. D=0.11 m diameter column, H_0=0.7 m. D=0.29 m diameter column, H_0=0.6 m. 81

Figure 3.25 Comparison of predictions by Equation 3.11 with experimental U_c. Catalyst C. D=0.11 m diameter column, H_0=0.7 m. D=0.29 m diameter column, H_0=0.6 m. 81

Figure 3.26 Comparison of U_c data from this work to literature data for fluidized bed of Geldart Group A particles from gauge pressure signals. 82

Figure 3.27 Comparison of predictions by Equation 3.19 with experimental U_c. FCC. 82

Figure 3.28 Comparison of predictions by Equation 3.18 and 3.19 with experimental U_c from gauge pressure signals. FCC I, D=0.29 m. 83

Figure 4.1 Reflective-type optical fiber probe response curves for various fiber configurations (adapted from Krohn, 1987). 93

Figure 4.2 Probe tip in relation to particle size. Reflective optical fiber probe detecting (a) swarm of particles; and (b) single particles (adapted from Matsuno et al., 1983). 94

Figure 4.3 Optical fiber probe for measuring local particle concentrations: the probe is shown detecting a swarm of particles. 96

Figure 4.4 Schematic of local voidage measurement apparatus and configuration. 96

Figure 4.5 Schematic of optical probe calibration equipment applying "drop-trap" technique. 99

Figure 4.6 Response curve for calibration of optical probe using FCC I without glass window. The line represents the calibration curve of Issangya (1998). 100

Figure 4.7 Response curve for calibration of optical probe using FCC I and coke particles with glass window. 102

Figure 4.8 Response signal of experimental calibration curves for FCC II with glass window in water-solids system.Figure 4.9 Signal obtained from optical probe without glass window.

(Dotted line represents the maximum calibrated value.) D=0.29 m, U=0.15 m/s, z=0.15 m, r/R=0.0, FCC I. 102

Figure 4.9 Signal obtained from optical probe without glass window. (Dotted line represents the maximum calibrated value.) D=0.29 m, U=0.15 m/s, z=0.15 m, r/R=0.0, FCC I. 103

Figure 4.10 Setting the upper intensity in dense bed: (a) without window; (b) with window. 105

Figure 4.11 Signal obtained from optical probe with glass window. (Dotted line represents the maximum calibrated value.) D=0.29 m, U=0.15 m/s, z=0.15 m, r/R=0.0, FCC I. 105

Figure 4.12 Schematic of needle-type capacitance probe. 107

Figure 4.13 Signal response of capacitance probe with FCC II in water-solids suspensions. 107

Figure 4.14 Effect of volumetric solids fraction on the effective relative dielectric permittivity of a water-FCC system. All models assume K_p = 14 and K_h = 80 for FCC and water, respectively, based on Louge and Opie (1990). 108

Figure 4.15 Radial voidage distributions. H_0=0.51 m, D=0.29 m, FCC I. U_c ($\bar{z}$ =0.43 m, DP) = 0.49 ± 0.015 m/s. 111

Figure 4.16 Cross-sectional average voidage from local radial voidage measurements from optical probe. H_0=0.51m, D=0.29 m, FCC I. 112

Figure 4.17 Comparison of cross-sectional average voidage from optical signal to that from DP. H_0=0.51 m, D=0.29 m, z=0.27 m FCC I. 112

Figure 4.18 Radial profile of normalized time-mean average voidage. H_0=1.1 m, D=0.29 m, FCC I, U=0.40 m/s. 114

Figure 4.19 Radial profile of normalized time-mean average voidage. H_0=1.1 m, D=0.29 m, FCC I, U=0.80 m/s, U_c ($\bar{z}$ =0.85 m, DP)=0.73 m/s . 114

Figure 4.20 Radial profile of voidage fluctuation represented by standard deviation of local voidage measured by optical probe. D=0.29 m, H_0=0.8 m, z=0.40 m, U_c=0.75 m, FCC I. 115

Figure 4.21 Probability distribution function of local voidage measured by optical probe. U_c DP ($\bar{z}$ =0.85 m)= 0.727 ± 0.039 m/s, H_0=1.1m, D=0.29 m, r/R=0.0, z=0.40 m, FCC I. 117

Figure 4.22 Probability distribution function of local voidage measured by optical probe. U_c DP ($\bar{z}$ =0.85 m)= 0.727 ± 0.039 m/s, H_0=1.1m, D=0.29 m, r/R=0.0, z=0.78 m, FCC I. 117

Figure 4.23 Contour plot of time-mean local voidage measured by optical probe. D=0.29 m, FCC I, H_0= 1.1 m, U=0.4 m/s. 118

Figure 4.24 Contour plot of time-mean local voidage measured by optical probe. D=0.29 m, FCC I, H_0= 1.1 m, U=0.9 m/s 118

Figure 4.25 Contour plot of time-mean local voidage measured by optical probe. D=0.29 m, FCC I, H_0=1.5 m, U=0.4 m/s 119

Figure 4.26 Contour plot of time-mean local voidage measured by optical probe. D=0.29 m, FCC I, H_0=1.5 m, U=0.9 m/s 119

Figure 4.27 Radial profile of time-mean voidage from optical probe signals. H_0=1.1-1.3m, D=0.61 m, z=0.8 m, FCC III, U_c=0.83 m/s (z=0.8m, DP). 121

Figure 4.28 Radial profile of time-mean voidage from optical probe signals. H_0=2 m, D=0.61 m, z=1.55 m, FCC IV, U_c=1.12 m/s (z=1.5 m, DP). 121

Figure 4.29 Radial profile of time-mean voidage from optical probe signals. H_0=1.7 m, D=0.61 m, U=0.85 m/s, z=0.8 m, FCC III, U_c=0.77m/s (z=0.36 m, DP). 122

Figure 4.30 Radial profile of time-mean voidage from optical probe signals. z=0.84 m, D=1.56 m, H_0=1.2 m, FCC II, U_c (z=0.84 m, DP)=0.39 m/s. 124

Figure 4.31 Probability density of voidage obtained from optical probe signals measured at r/R=0.90 and 0.0. D=1.56 m, H_0=1.2 m, FCC II, z=0.84 m. 124

Figure 4.32 Radial profile of time-mean voidage from optical probe signals. D=1.56 m, z=0.84 m, H_0=2.2 m, U_c (z=0.85 m, DP)=0.53 m/s, FCC II. 125

Figure 4.33 Effect of U on time-mean voidage and DP fluctuation at r/R=0.0. D=1.56 m, z=0.84 m, H_0=2.2 m, U_c (z=0.85 m, DP)=0.53 m/s, FCC II. 125

Figure 4.34 Radial profile of normalized time-mean voidage. Comparison of experimental data to other publications. Particle properties and operating conditions listed in Table 4.2. 126

Figure 4.35 Effect of U/U_c on radial profile of normalized time-mean voidage. FCC. 128

Figure 4.36 Probability density of voidage from optical probe signals. D=0.29 m, z=0.527 m, U=0.78 m/s, FCC I, H_0=0.8m. 129

Figure 4.37 Probability distribution of voidage measured by optical probes. D=0.29 m (FCC I). D=1.56 m (FCC II). 129

Figure 4.38 Probability density of voidage from capacitance and optical probe signals. D=0.61 m, U=0.86 m/s (capacitance); U=0.85 m/s (optical), H_0=2 m, z=1.55 m, FCC III, r/R=0.83. 131

Figure 5.1 Details of optical fiber velocity probe. 135

Figure 5.2 Schematic of optical velocity probe tip showing measurement volume and elimination of 'blind zone' by addition of glass cover. 135

Figure 5.3 Typical optical signal obtained by two identical voidage probes separated by 0.01 m. D=0.29 m, z=0.78 m, U=0.90 m/s, r/R=0.70, H_0=1.5 m, FCC I. 137

Figure 5.4 Schematic of the optical fiber velocity probe system for simultaneous measurement of local solids concentration and particle velocity. 138

Figure 5.5 Axial profile of time-mean voidage determined from differential pressure signals. D=0.61 m, H_0=2 m, FCC IV, U_c (DP at $\bar{z}$ =1.55 m)=1.12 m/s. 140

Figure 5.6 Cumulative void-associated particle velocity profile. D=0.61 m, U=1.56 m/s, z=1.55 m, H_0=2 m, FCC IV. 140

Figure 5.7 Probability distribution of voidage. D=0.61 m, U=0.82 m/s, z=1.55 m, H_0=2 m, FCC IV. 141

Figure 5.8 Radial profile of time-mean void-associated particle velocity (●)and voidage (▲)distributions: (a) U=1.56 m/s; (b) U=0.82 m/s. D=0.61 m, z=1.55 m, H_0=2 m, FCC IV. 142

Figure 5.9 Cumulative void-associated particle velocity occurrence at (a) r/R=0.09 and (b) r/R=0.50. D=0.61 m, H_0=2 m, FCC IV. 143

Figure 5.10 Wall measurements of gauge pressure and standard deviation of pressure fluctuation. D=0.61 m, H_0=2 m, FCC IV. 145

Figure 5.11 Effect of U on average particle velocities. r/R=0.09, D=0.61 m, H_0=2 m, FCC IV, U_c =1.12 m/s (DP at $\bar{z}$ =1.55 m). 145

Figure 5.12 Standard deviation of particle velocities. D=0.61 m, z=1.55 m, r/R=0.09, U_c=1.12 m/s (DP at z=1.55 m), FCC IV. 146

Figure 5.13 Probability distribution of particle velocities for (a) U=0.42 m/s, and (b) U=1.00 m/s at radial positions of 0.94, 0.50, and 0.09. D=0.61 m, z=0.80 m, FCC IV. 148

Figure 5.14 Particle velocity and voidage distribution for U=0.42 m/s at radial positions of 0.94, 0.50, and 0.09. D=0.61 m, z=0.80 m, FCC IV. 149

Figure 5.15 Particle velocity and voidage distribution for U=1.00 m/s at radial positions of 0.94, 0.50, and 0.09. D=0.61 m, z=0.80 m, FCC IV. 150

Figure 5.16 Particle velocity and voidage distribution for U=1.56 m/s at radial positions of 0.94, 0.50, and 0.09. D=0.61 m, z=1.55 m, FCC IV. 151

Figure 5.17 Distribution of particle velocities associated with dense-phase. D=0.29 m, r/R=0.70, z=0.78 m, H_0=1.0 m, FCC I. 153

Figure 5.18 Void velocity distribution for (a) r/R=0.0, and (b) r/R=0.70. D=0.29 m, z=0.78 m, Δz=0.02 m, H_0=1.5 m, FCC I. 155

Figure 5.19 Average void velocity. D=0.29m, z=0.78 m, Δz=0.02 m, H_0=1.5 m, FCC I. 157

Figure 5.20 Radial distribution of average void frequency. D=0.29m, z=0.78 m, Δz=0.02 m, H_0=1.5 m, U_c (z=1.16 m, AP)=0.85 m/s, FCC I. 157

Figure 6.1 Power spectral density functions of pressure fluctuations. U=0.65 m/s, H=1.1 m, r/R=1, FCC I. (n identifies recurrent "natural frequency") 163

Figure 6.2 Effect of expanded bed height on natural frequency from AP signals with comparison to calculated values based on Equation 6.1. D=0.29m, FCC I. 165

Figure 6.3 Effect of superficial gas velocity on major frequency from DP signals. D=0.29 m, H_0=1.1 m, FCC I. 165

Figure 6.4 Variation of dominant frequency, f_{DP}, with superficial gas velocity. D=1.56 m, H_0=2.2 m. 166

Figure 6.5 Strouhal number vs. Froude number correlation for U > U_c, FCC. 166

Figure 6.6 Radial profiles of voidage and crossing frequency. D=0.29 m, H_0=1.1 m, U=0.70 m/s, FCC I. 168

Figure 6.7 Effect of superficial gas velocity and height on crossing frequency. D=0.29 m, H_0=1.1 m, U_c=0.68-0.73 m/s, r/R=0.0, FCC I. 168

Figure 6.8 Radial profiles at different superficial gas velocities of crossing frequency calculated from threshold value of time-mean voidage. D=0.29 m, H_0=1.1 m, z=0.78 m, FCC I. 169

Figure 6.9 Effect of superficial gas velocity on crossing frequency calculated from threshold value of time-mean voidage. D=0.29 m, H_0=1.1 m, z=0.78 m, r/R=0.0, FCC I. 169

Figure 6.10 Fast Fourier Transform of pressure fluctuations: (a) AP at z=0.15 m; (b) DP across grid; (c) AP in windbox. D=0.29 m, H_0=1.5 m, U=0.19 m/s. 171

Figure 6.11 Cross-correlation function of optical voidage probe signals. D=0.29 m, H_0=1.5 m, distance between probes=0.01 m, r/R=0.70, U=0.90 m/s, FCC I. 173

Figure 6.12 Variation of correlation function coefficients with superficial gas velocity. D=0.29 m, H_0=1.5 m, r/R=0.35, U_c=0.75 m/s , H_0=1.5 m, $z_{lower\ probe}$ =0.77 m, FCC I. 173

Figure 6.13 Effect of optical probe separation distance on cross-correlation function coefficient. (a) U=0.40 m/s; (b) U=0.90 m/s. D=0.29 m, H_0=1.5 m, $z_{lower\ probe}$ =0.77 m, FCC I. 175

Figure 6.14 Autocorrelation function of voidage signal. D=0.29 m, U=0.90 m/s, z=0.78 m, r/R=0.0, H_0=1.1 m, FCC I. 177

Figure 6.15 Radial profile of characteristic time of autocorrelation function from voidage measurements. D=0.29 m, U=0.90 m/s, H_0=1.1 m, FCC I. 177

Figure 6.16 Radial profile of time-mean voidage for data presented in Figure 6.15. D=0.29 m, U=0.90 m/s, H_0=1.1 m, FCC I. 178

Figure 6.17 Effect of U on τ_c. r/R=0.0, D=0.29 m, H_0=1.1 m, FCC I. 178

Figure 6.18 Coherence function and standard deviation vs. superficial gas velocity. (Adapted from Cai et al., 1990; D=0.139 m, d_p=280 μm, probe separation distance=0.1 m) 181

Figure 6.19 Incoherent-output power spectral density (defined in Equation 6.10) from gauge pressure fluctuations for two superficial gas velocities. D=0.29 m, z_1=0.21 m, z_2=0.34 m, H_0=1.5 m. 183

Figure 6.20 Typical coherence function. D=0.29 m, U=0.87 m/s, r/R=0.0, z=0.40 and 0.46 m, H_0=1.5 m, FCC I. 185

Figure 6.21 Average coherence function from gauge pressure signals. D=0.29 m, H_0=1.1 m, U_c=0.73 m/s, FCC I.Figure 6.22 Average coherence function from DP signals. D=0.29 m, H_0=1.1 m, ch1 locations, U_c ($\overline{\mathbf{\Delta z}}$ =0.845 m) = 0.727±0.039 m/s, FCC I. 185

Figure 6.22 Average coherence function from DP signals. D=0.29 m, H_0=1.1 m, ch1 locations, U_c ($\overline{\mathbf{\Delta z}}$ =0.845 m) = 0.727±0.039 m/s, FCC I. 186

Figure 6.23 Average coherence function and correlation function coefficient. D=0.29 m, r/R=0.0, U_c=0.75 m/s, probe separation distance=0.063 m, z=0.40 m and 0.463 m, H_0=1.5 m, FCC I. 186

Figure 6.24 Power spectra density of voidage data at U=0.65 m/s. D=0.29 m, r/R=0.0, z=0.46 m, H_0=1.5 m, FCC I. 188

Figure 6.25 Coherence function of voidage data at U=0.65 m/s. D=0.29 m, r/R=0.0, probe separation distance=0.063 m, z=0.40 m and 0.463 m, H_0=1.5 m, FCC I. 188

Figure 6.26 Radial profile of average coherence function. D=0.29 m, Δz=0.01 m, H_0=1.5 m, FCC I. 189

Figure 6.27 Effect of U on average coherence function form voidage measurements. D=0.29 m, z=0.77 m and 0.78 m, distance between probes=0.01 m, H_0=1.5 m, FCC I. 189

Figure 6.28 Variation of the rescaled range with sub-period length for gauge pressure fluctuation. Sampling frequency=500 Hz, sampling duration=200 s, U=0.39 m/s, D=0.29 m, z=0.65 m, H_0=0.97 m, FCC I. 192

Figure 6.29 Variation of the Hurst exponents from DP signals with superficial gas velocity. D=0.29 m, H_0=1.1 m, $\bar{\mathbf{z}}$ =0.59 m, $\mathbf{\Delta z}$ =0.12 m, sampling frequency=100 Hz, sampling duration=100 s. 194

Figure 6.30 Axial profiles of cycle time from (a) DP, and (b) AP signals. D=0.29 m, H_0=1.5 m, r/R=1, FCC I. 196

Figure 6.31 Variation of cycle time with dimensionless height for U > U_c from DP signals. 198

Figure 6.32 Variation of cycle time regularity with dimensionless superficial gas velocity. Axial positions: D=0.29 m (z/H=0.64); D=0.61 m (z/H=0.87); D=1.56 m (z/H=0.62). 198

Figure 6.33 Radial profile of Hurst exponents for U=0.40 and 0.90 m/s. D=0.29 m, z=0.78 m, H_0=1.1 m, FCC I. 199

Figure 6.34 Variation of maximum Hurst exponent from optical voidage probe signals with superficial gas velocity. D=0.29 m, z=0.40 m, U_c=0.75 m/s, r/R=0.0, H_0=1.5 m, FCC I. 201

Figure 6.35 Variation of cycle time with superficial gas velocity for optical voidage probes signals. D=0.29 m, z=0.40 m, r/R=0.0, H_0=1.5 m, U_c=0.75 m/s, FCC I. 201

Figure 7.1 Original and de-noised signals. 210

Figure 7.2 De-noising signal using Daubechies 3 wavelet level 5. 212

Figure 7.3 De-noising signal using Daubechies 3 wavelet level 5 with soft thresholding method. 212

Figure 7.4 Comparison of void velocity distribution between cut-off method (O); and db3 level 5 wavelet transform with soft thresholding (▲) (data of Figure 7.6a). 213

Figure 7.5 Voidage fluctuation captured by optical velocity probe. Sampling frequency, 28,741 Hz, D=0.61 m, U=1.56 m/s, r/R=0.09, z=1.55 m, z=1.55 m, H_0=2 m, FCC IV. 215

Figure 7.6 Particle velocity fluctuation of data from Figure 7.10 based on cross-correlation of 4096 data points, representing 142.5 ms. D=0.61 m, U=1.56 m/s, r/R=0.09, z=1.55 m, H_0=2 m, FCC IV. 215

Figure 7.7 Contour plot of LIM for 6 levels depicting passage of energetic microstructure centred around scale 3. U=0.42 m/s, r/R=0.09, D=0.61 m, z=1.55 m, H_0=2 m, FCC IV. 217

Figure 7.8 Contour plot of LIM for 6 levels depicting passage of energetic microstructure centred at all scales of analysis. U=0.82 m/s, r/R=0.09, D=0.61 m, z=1.55 m, H_0=2 m, FCC IV. 218

Figure 7.9 Contour plot of LIM for 6 levels depicting passage of energetic microstructure mostly at small scales of analysis. U=1.56 m/s, r/R=0.09, D=0.61 m, z=1.55 m, H_0=2 m, FCC IV. 219

Figure 7.10 Effect of superficial gas velocity on probability distribution of LIM at: (a) level 1; and (b) level 6. D=0.61 m, r/R=0.09. z=0.80 m for U=0.42 m/s; z=1.55 m for U=0.82 and 1.56 m/s, H_0=2 m, FCC IV. 220

Figure 7.11 Effect of scale on probability distribution of LIM_j. D=0.61 m, r/R=0.09. z=0.80 m for U=0.42 m/s; z=1.55 m for U=0.82 and 1.56 m/s, H_0=2 m, FCC IV. 222

Figure 7.12 Voidage fluctuation signal from optical velocity probe and probability distribution of LIM at 6 scales. U=0.57 m/s, r/R=0.09, D=0.61 m, z=0.80 m, H_0=2 m, FCC IV. 223

Figure 7.13 Voidage fluctuation signal from optical velocity probe and probability distribution of LIM at 6 scales. U=0.82 m/s, r/R=0.09, D=0.61 m, z=1.55 m, H_0=2 m, FCC IV. 224

Figure 7.14 Voidage fluctuation signal from optical velocity probe and probability distribution of LIM at 6 scales. U=1.56 m/s, r/R=0.09, D=0.61 m, z=1.55 m, H_0=2 m, FCC IV. 225

Figure 7.15 Effect of U on probability distribution of LIM at 6 scales for r/R=0.94. D=0.61 m, z=1.55m, H_0=2 m, FCC IV. 226

Figure 7.16 Comparison of LIM_j of 6 scales for probe in various radial position and phases: (a) r/R=0.94; (b) r/R=0.09, high-density phase; (c) r/R=0.09, low-density phase; (d) r/R=0.09, fluctuating phase. D=0.61 m, U= 1.56 m/s, z=1.55 m, H_0=2 m, FCC IV. 227-230

Figure 7.17 Continuous wavelet transform using Morlet wavelet. (a) U=0.32 m/s; and (b) 1.0 m/s. D=0.29 m, z=0.77 m, r/R=0.0. (lowest scale corresponding to 50 Hz) 232

Figure 7.18 Distribution of energy in the time-frequency plane of voidage signal using continuous wavelet transform with Morlet wavelet during defluidization. D=1.56 m, r/R=0.5, z=0.84 m, H_0=2.0 m, FCC II. 233

Figure A.1 Photograph of the 1.56 m fluidization column standing beside heavy tech building at CSIRO Minerals, Clayton. 275

Figure A.2 Isometric view of cyclones and top of 1.56 m fluidization column. 276

Figure A.3 Schematic diagram showing bubble caps on distributor of 1.56 m diameter fluidization column. 276

Figure A.4 Schematic of bubble cap (in mm) as originally installed. 277

Figure A.5 Photograph taken upward from the plenum chamber of the 64 mm sockets installed to reduce the open area of air inlet and the central bubble cap removed from service. 277

Figure A.6 Photograph of a probe arm socket depicting the interlocking angle mechanism. 279

Figure A.7 Photograph of a traversing probe arm #2 positioned at the centre of an empty 1.56 m diameter column. 279

Figure A.8 Photograph of the scaffold supporting frame and a massive amount of silicone sealant after a welding failure. 281

Figure A.9 Comparison of pressure profile from two data logging systems. Error bars depict maximum error of 10,000 sample size. D=1.56 m/s, U=0.43 m/s, H_0=1.2 m, FCC II. 282

Figure B.1 Logic flow sheet for data cross-correlation and elimination. 285

Figure B.2 (Original) Typical raw signal; (a) One void isolated from Figure 5.6; (b) Binary coding; (c) Cut-off method. D=0.61m, U=0.57 m/s, r/R=0.17, z=0.80 m, f=29,378 Hz. 287

Figure B.3 Comparison of data processing method with respect to fraction of data groups eliminated. Data from Figures 5.6 (a) and (c). 287

Figure B.4 Effect of group number on percentage of data eliminated for void-associated particle velocities. Threshold voidage=0.62, D=0.29 m, U=0.42 m/s, r/R=0.55, z=0.78 m, FCC I. 288

Figure B.5 Effect of group number on average velocity and solid fraction of void-associated particles. D=0.29 m, U=0.42 m/s, r/R=0.55, z=0.78 m, FCC I. 288

Figure B.6 Comparison of void-associated particle velocity distribution between cross-correlation and peak-picking methods. D=0.29 m, U=0.42 m/s, z=0.78 m, r/R=0.55, f=13,357 Hz, FCC I. 291

Figure B.7 Comparison of void-associated particle velocity distribution between cross-correlation and peak-picking methods. U=0.69 m/s, D=0.29 m, z=0.78 m, r/R=0.55, f=12,059 Hz, FCC I. 292

Figure B.8 Comparison of the positive and negative void-associated particle velocity distribution between cross-correlation and peak-picking methods. U=0.69 m/s, D=0.29 m, z=0.78 m, r/R=0.55, f=12,059 Hz, FCC I. 292

Figure B.9 Probability distribution function of local voidage measured by optical velocity probe and determination of threshold value corresponding to boundary between dilute and dense phases. U=0.69 m/s, D=0.29 m, z=0.78 m, r/R=0.55, f=12,059 Hz, FCC I. 294

Figure B.10 Logic flow sheet for binary coding signals. 295

Figure B.11 Voidage signal from two fibers. Broken lines denote the threshold values from Methods (a), (b), (c), and (d). U=0.69 m/s, D=0.29 m, z=0.78 m, r/R=0.55, f=12,059 Hz, FCC I. 297

Figure B.12 Velocity distribution applying Method (d) binary coding. U=0.69 m/s, D=0.61 m, z=0.80 m, r/R=0.09, f=30,147 Hz, FCC IV. 297

Figure B.13 Probability distribution of voidage indicating threshold values from Methods (a), (b), (d), and (e). D=0.29 m, U=0.69 m/s, r/R=0.70, z=0.78 m, FCC I. 300

Figure B.14 Voidage fluctuation measured by optical voidage probe. D=0.29 m, U=0.69 m/s, r/R=0.70, z=0.78 m, FCC I. 300

Figure B.15 Probability distribution of void velocity and its effect of threshold voidage expressed as crossing frequency. D=0.29 m, U=0.69 m/s, z=0.78 m, r/R=0.70, Δz=0.01 m, FCC I. 301

Figure B.16 Voidage signals depicting void velocity evaluation method of Matsuura and Fan (1984). D=0.29 m, U=0.90 m/s, r/R=0.70, z=0.78 m, H_0=1.5 m, FCC I. 303

Figure B.17 Voidage signals processed by cut-off method exemplifying the erratic movement of voids. D=0.29 m, U=0.90 m/s, r/R=0.70, z=0.78 m, H_0=1.5 m, FCC I. 303

Figure B.18 Void velocity with voidage fluctuation. X error bars representing periods of signal considered for cross-correlation. Threshold voidage value=0.704 from Method (a), D=0.29 m, H_0=1.5 m, U=0.69 m/s, r/R=0.70, z=0.78 m, FCC I. 304

Figure B.19 Effect of group number on cumulative void velocity distribution. D=0.29 m, U=0.90 m, r/R=0.70, z=0.78 m, H_0=1.5 m, FCC I. 304

Figure C.1 Typical shapes of (a) sine wave; (b) real part of Morlet wavelet; and (c) Mexican hat wavelet. 308

Figure C.2 Phase space associated with different transforms: (a) Fourier transform, (b) windowed Fourier transform, and (c) wavelet transform. (Adapted from Farge, 1992) 310

Figure C.3 (a) Function f with support $[-2^{J_1}, 2^{J_1})$ piecewise constant on $[k2^{-J_0}, (k+1)2^{-J_0})$. (b) Magnification of a portion of f. On every pair of intervals, f is replaced by its average ($\rightarrow f^1$); the difference between f and f^1 is g^1, a linear combination of Haar wavelets. (Adapted from Daubechies, 1992) 315

Figure C.4 Discrete wavelet decomposition and wavelet tree using Haar wavelets of voidage fluctuation from optical probe. D=0.29 m, U=0.90 m/s, r/R=0.0, H_0=1.1 m, z=0.78 m, FCC I. 316

Figure C.5 Discrete wavelet decomposition of voidage fluctuation from optical probe using Haar wavelet. D=0.29 m, U=0.90 m/s, r/R=0.0, H_0=1.1 m, z=0.78 m. 317

Figure D.1 Modelling geometry for 2D simulation of a turbulent fluidized bed. Green rectangle depicts three solids, i.e., areas, that are set as 3D patch to set static bed height of FCC. The 2D patch highlighted with pink shows the secondary inlet patch to feed solids back in to the column. Top of the column geometry is not shown. 341

Figure D.2 Mass residual of gas phase with iteration. Run # Oct022-m01. 346

Figure D.3 Simulated voidage profile of 2D fluidized bed operated at atmospheric pressure, U=0.5 m/s. Initial bed height 1.0 m. Coefficient of restitution 0.9. Run # Aug02-m01,m02,m04. 347

ACKNOWLEDGEMENTS

The completion of this degree would not have been possible if it were not for those people who truly believed in my potential and provided me with opportunities; who unconditionally supported me in my endeavour; who took the time to let me discover; and who gave me the hugs when I needed them most.

To Prof. John Grace, Prof. Jim Lim and Prof. Xiaotao Bi, who enriched my learning by sharing with me their unremitting wealth of knowledge, invaluable guidance, and tremendous opportunities, I am so deeply indebted. Their unfailing confidence in me gave me the latitude to explore and develop concepts in my research.

Grateful appreciation is expressed to Seng Lim for his professionalism and hospitality while at CSIRO, where the work for scale-up was conducted. Terry Joyce and Ross Close have taught me skills and technical expertise in the operation and construction of the apparatus that I have never learned in school.

Providing enormous assistance through technical support were Peter, Alex, Robert, Horace and Qi. I recognize and appreciate the assistance of the support staff and faculty at the department. Special thanks to Lori and Helsa for their proficiency in keeping me on track.

Financial support from the NSERC, and UBC Graduate Fellowship Fund is also gratefully acknowledged.

Jonathan Taylor, Felix Herrmann, Martin Rhodes, Masayuki Horio and Cedric Briens have allowed me to leap forward into new directions through insightful discussions, sparkling dialogues, and thought-provoking questions. Their knowledge and insights are reflected in this thesis.

For their guidance and support, I acknowledge Profs. Bruce Bowen, Fariborz Taghipour and Ian Gartshore.

I extend my gratitude to Sijin Wen, Lauren Briens, Xuqi Song, Hiroshi Morikawa, Jian Xu, Pierre Constantineau, Alfi Zakhari and Peter Witt for their generosity in sharing their expertise and experiences.

I thank Abba, Gorkem, Ian, and Arturo for making a difference in my life. The constant encouragement from Kim, Eddie, Masato, Kathy, Robyn, Garth, Fumiko and Ikuko was the source of continual energy. Thank-you. You all have been such amazing cheerleaders in my life. In particular, I acknowledge Bob for his generous sense of humour that pulled me out of the tunnel of hopelessness.

Countless numbers of people have supported me throughout the endeavour in so many helpful indirect ways. To Jay, Kelly-Ann, Joy, Gill, Anne, Harriet, Liz, Yuri, Diana, Shigeko, Tom, and Peter, my array of unique mentors, I thank-you.

Enough thanks cannot be said to my family, Pat, Miki, Erica and Alicia, for their love and support through all the many challenging times they were subjected. You have demonstrated how true understanding and patience translated into everyday life, and coped with the absence of a Mom. Thank-you for always braving a smile. I am, as I am sure they are too, looking forward to getting back to a normal family life.

This work is dedicated to Isabelle whose remarkable strength, determination and love carried me this far. She knew all along that some day this task would be completed. I know she is smiling with me now.

While others are not specifically mentioned, their support and assistances have been truly appreciated.

To keep your edge you have to feel insecure…

Gay Laliberté

Founder, Cirque du Soleil

CHAPTER 1

INTRODUCTION

Gas-solid fluidization is a unit operation which brings two phases, one comprised of solid particles, into intimate contact. Fluidized beds have been widely used in industry owing to their excellent gas-solids contacting and favourable heat and mass transfer characteristics. The advantages of high gas throughputs, overcoming the tendency of sticky particles to agglomerate, and more efficient contact between gas and solids, led the way to high-velocity fluidization (Avidan, 1980). The merit of a gas-fluidized bed operated in the turbulent fluidization flow regime was initially discovered through industrial experience, where an increased gas flow rate resulted in a higher efficiency during the Fluid Cracking Catalyst (FCC) regeneration process. In fact, many practical fluidized beds operate beyond the terminal settling velocity of individual particles (Grace, 1992). Presently, commercial fluid bed catalytic reactors such as those used in the production of acrylonitrile and chlorinated hydrocarbons, and FCC regenerators, operate in the turbulent fluidization flow regime with superficial gas velocities ranging between about 0.5 and 0.8 m/s. In many industrial fluidized bed applications where minimizing entrainment and maximizing gas throughput lead to increased reactor performance, the turbulent fluidization flow regime is a viable operating mode.

Turbulent fluidization is commonly characterized by the 'gradual' disappearance of discrete bubbles and voids, with the bed surface no longer clearly defined due to considerable entrainment of the solids into the freeboard. Some of the early photographs showing a flow pattern distinctively different from that of the bubbling flow regime were reported by Matheson et al. (1949) and Zenz and Othmer (1960). Breakdown of large bubbles into smaller transient voids assists in increasing the homogeneity of turbulent fluidized beds. Compared to bubbling beds, turbulent fluidized beds are characterized by: (1) higher gas throughput; (2) improved gas-solids contact; (3) higher gas-to-solid mass and heat transfer rates; and (4) additional conversion in the freeboard (Venderbosch, 1998). Turbulent fluidization also defines a transition regime between the low velocity bubbling bed and highly entraining flow in circulating fluidized beds, as depicted in Figure 1.1. Understanding this flow regime is critical to the design and operation of many fluidized bed processes and applications.

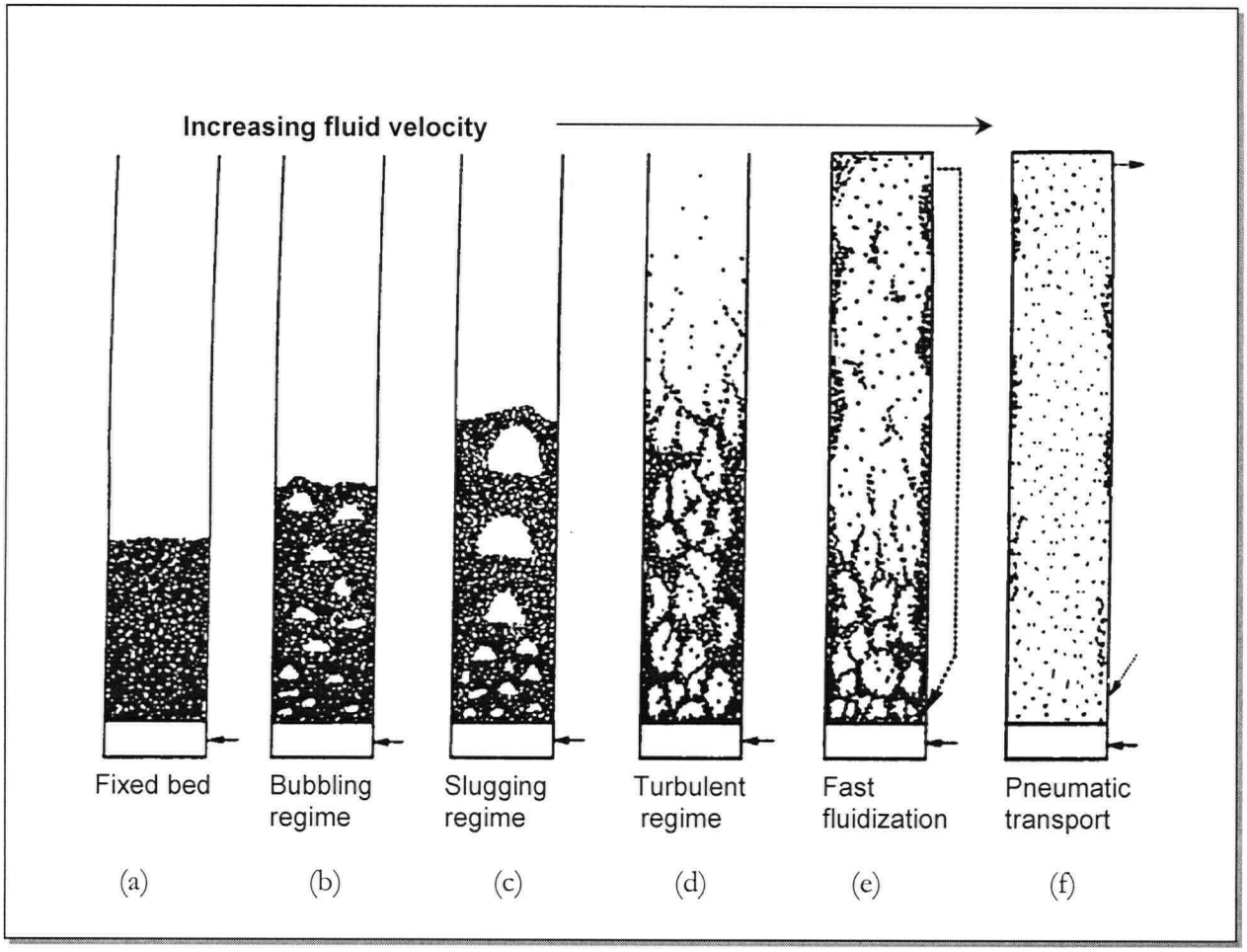

Figure 1.1 Gas-solid fluidization flow regimes. (Adapted from Grace, 1986)

1.1 Flow regimes and transitions between regimes

As fluid enters the bottom of a vessel containing a bed of solids, several flow regimes are observed with increasing fluid throughput. A bed is fluidized when the frictional force between particle and fluid counterbalances the weight of the particles, initially occurring at the minimum fluidization velocity, U_{mf}. Fluid passes through the interstitial space between the fluidizing particles, and expands the bed homogeneously, leading to a 'fluidlike' state of solids. With a further increase in fluid flow, the superficial gas velocity passes through the minimum bubbling velocity, U_{mb}, i.e., the transition between Figure 1.1 (a) and (b), where two distinct phases, the bubble phase and the emulsion phase, are present. The bubbling regime is one of the most studied flow regimes in gas-solid fluidization. Bubble coalescence and break-up take place as fluid flow is increased. Eventually, the bubbles become large enough to occupy a considerable fraction of the cross-section of small diameter columns, with slug flow observed, as shown in Figure 1.1 (c). A further increase in gas flow makes bubbles (slugs) unstable, and bubble splitting becomes dominant. Although the definitions relating to the turbulent fluidization flow regime are controversial (e.g. Rhodes, 1996), the smoothness in fluidization prevailing beyond transition, Figure 1.1 (d), is what is considered as the defining characteristic of the turbulent fluidization flow regime. Bubbles no longer retain their usual spherical-capped shape and character as in the bubbling regime. Instead there are transient voids zig-zagging their way to the surface. The high frequency of void splitting is one of the most significant characteristics of turbulent fluidization. This breakdown not only improves gas-solid contacting, but also increases macromixing. Moreover, the upper surface of the bed becomes increasingly diffuse, with substantial entrainment of solids out of the top. Further increasing the fluid flow and efficient return of entrained solids enables the bed to be operated in the fast fluidization flow regime. In some cases, the lower region of the fast fluidization regime has similar hydrodynamics to those of the turbulent fluidization flow regime; however, the upper region of the bed exhibits a core-annulus structure with strands of solids, a characteristic unique to fast fluidization. Pneumatic conveying represents the upper limit of fluid flow.

Transition velocities are used to help distinguish between different flow regimes; however, they are subjected to confusion and controversy when flow regime characteristics are not clear. Moreover, transitions between the respective regimes are often not sharp.

1.2 Turbulent fluidization flow regime

The term 'turbulent fluidization' has seen its share of controversy mainly due to the subjective observations by many earlier researchers (Johnsson et al., 1992). The dynamics of the fluidized state are governed (Zijerveld et al., 1998) by:

- superficial gas velocity
- size of the facility
- solids holdup
- gas distributor design
- solids properties
- gas properties
- axial solids distribution
- solids mass flux.

In addition, numerous definitions exist for a flow regime between bubbling and fast fluidization. Challenges arise when a particular phenomenon is referred to as a 'turbulent fluidized bed' without reporting on the details of operating conditions and material properties. For instance, Trnka et al. (2000) identified several states of gas-solid fluidized beds, including two for turbulent beds, namely intermediate turbulence and fully turbulent beds, using a three-dimensional space diagram of pressure fluctuations obtained from spectral analysis. Based on Zijerveld et al. (1998), the turbulent fluidization flow regime is divided into an intermediate turbulent bed and a turbulent bed, characterized through chaos analysis of pressure fluctuations. Furthermore, transition to turbulent fluidization has been denoted as type I, a sharp transition as bubble wakes become open, rather than closed, and type II, gradual transition through intermittent slug-like structures (Bi et al., 1995). Although standardization of these definitions is important, the flow characterization pertaining to fluid-particle interactions must be established not only to distinguish between flow regimes, but also to assist in defining transitions.

1.3 Outstanding issues

Until recently, the majority of work on the turbulent fluidization flow regime has dealt with the transitional velocities (Rhodes and Geldart, 1986; Brereton and Grace, 1992; Chehbouni et al., 1994; Bi et al., 1995). To extend and validate current predictions of transition velocities against realistic operating conditions of industrial reactors, knowledge must be extended with respect to the influence of pressure (see Lanneau, 1960; Yang and Chitester, 1988; Cai et al., 1989; Tsukada et al., 1993; Marzocchella and Salatino, 1996; Newton et al., 2001), temperature (see Cai et al., 1989; Foka

et al., 1996; Peeler et al., 1999) and equipment scale (see Cai et al., 1989; Sun and Chen, 1989; Ellis et al., 2001).

Very limited work has been reported on the detailed hydrodynamics and flow structure for units operating in the turbulent fluidization flow regime. Extending the current knowledge of macroscopic hydrodynamics, e.g., obtained by characterizing axial and radial profiles of voidage using local measurements, should clarify the features which contribute to favourable gas-solid contacting. There is enough evidence that 'bubbles' in a traditional bubbling fluidization sense break down (Lanneau, 1960; Rowe and MacGillivary, 1980; Lee and Kim, 1989). Local void size and rise velocity have been investigated in the turbulent fluidization flow regime as analogous to the bubbling regime (Lanneau, 1960; Yamazaki et al., 1991; Lu et al., 1997; Farag et al., 1997a; Taxil et al., 1998). However, Taxil et al. (1998) found little correlation between the void chord length and rise velocity, suggesting breakdown of the two-phase theory, and the limitations in characterizing turbulent fluidized bed hydrodynamics through extension of bubble characteristics studied extensively in the bubbling flow regime. Departure from the familiar terminology of the two-phase theory, i.e., dense and dilute phases, to describe the system in terms of distribution of voidage may be required to fully characterize the hydrodynamics of the turbulent regime.

In turbulent fluidized beds, coalescence and splitting of voids exist as competing mechanisms. Attempts to explain gas-solid interactions based on turbulence characteristics may contribute to our understanding of this complex phenomenon. Van den Akker (1998) highlighted the occurrence of coherent structures in multiphase systems. Coherent structures of the vorticity field giving organized patterns containing most of the energy may be a result of local differences in mixture density. Investigations of factors contributing to energy dissipation, turbulence and chaos are much needed (Hartman et al., 2001). Although challenges exist in obtaining concrete experimental data pertaining to such structures, careful experimentation with numerical modelling may also extend our understanding.

With the advent of increased computational capabilities, computational fluid dynamics (CFD) is emerging as a promising new tool in hydrodynamic modelling. While it is now a standard tool for single-phase flows, it is still at the development stage for multiphase systems, such as fluidized beds. Work is required to make CFD suitable for fluidized bed reactor modelling and scale-up purposes. Two different approaches have been applied in early attempts to apply CFD modelling to gas-solid

fluidized beds: two-fluid models treating fluid and solid phases as interpenetrating continuum phases; and Eulerian/Lagrangian models which treat the fluid phase as a continuum, and the particle phase as Lagrangian, solving Newtonian equations of motion for each particle. Due to computational limitations, the Eulerian/Lagrangian model is normally limited to a number of particles of order 10^7. For small particles, such as typical catalyst particles of diameter 75 μm, it becomes difficult to simulate any meaningful reactor volume. Therefore, the two-fluid model is the preferred choice for simulating macroscopic hydrodynamics. By pursuing fundamental studies of parameter validation, and experimentally validating the hydrodynamics predicted by the two-fluid model, which incorporates coupling terms, CFD can become a significant contributor to reactor modelling and scale-up of industrial fluidized beds.

1.4 Research objectives

The research presented in this thesis addresses some of the issues outlined above. Key objectives are to:

- Conduct experimental investigation on the transition from bubbling to the turbulent fluidization flow regime, and the effect of pressure, temperature and scale on the transition velocity, U_c. Four different fluidization columns of diameter 0.11, 0.29, 0.61, and 1.56 m are used in this study. One of these is a high-temperature unit with pressures ranging from 0.1 to 0.4 MPa absolute pressures and temperatures from 20 to 240°C. The effect of scale on regime transition is investigated with two relatively large columns owned by CSIRO Minerals, Australia. This organization has complementary ongoing research interests, and they have recently embarked upon a research program to study the effect of temperature on the transition velocity of turbulent fluidization (Peeler et al., 1999).
- Obtain local measurements in these fluidization columns using optical fiber probes, measuring both voidage and velocity, and a capacitance probe, measuring voidage. A novel optical velocity probe developed at the Fluidization Research Centre at UBC is applied to measure particle velocity and voidage, and hence particle flux, simultaneously in turbulent fluidized beds of FCC particles. Bivariate local voidage measurements from two identical optical fiber voidage probes are also obtained to investigate the fluid-particle interactions.
- Provide experimental evidence relating to the flow structure of the turbulent fluidized bed using various analysis methods, such as statistical, spectral, wavelet and chaos analyses. Turbulent fluidized beds have been reported to exhibit unique chaotic characteristics (Bai et

al., 1999). Further exploration of various data analysis methods applied to experimental data may broaden understanding of the complexity of the flow dynamics.

- Investigate the effect of particle size distribution on the transition velocity, U_c. However, particles used in this study only pertain to Geldart Group A particles.

1.5 Thesis layout

Chapter 2 summarizes the detailed design of the four fluidization columns used in this work, as well as the macroscopic hydrodynamics obtained from pressure measurements. The time-mean pressure measurements at the wall of a fluidized bed provide information about the overall bed voidage, and estimation of bed expansion. Operating conditions characterized by superficial gas velocity, solids circulation rate, distributor plate pressure drop, and initial bed inventory are described. Details on the design and construction of traversing probe arms used to obtain local measurements inside the largest column (1.56 m diameter) are included. This chapter also summarizes the properties of the particulate materials used in this study.

Chapter 3 focuses on the transition from the bubbling to the turbulent fluidization flow regime. The transition velocity, U_c, is defined as the superficial gas velocity at which the standard deviation of pressure fluctuations reaches a maximum. The effects of initial solids inventory, and location of pressure transducer ports on U_c are reported from the cold model UBC unit. The effect of scale on the transition velocity is determined from measurements obtained in the 0.61 and 1.56 m diameter columns at CSIRO, in comparison to the data obtained at UBC from a 0.29 m diameter column. The effect of particle properties on U_c is reported for two different catalysts having similar densities. Finally, the effect of system pressure and temperature on transition velocity is discussed based on results obtained in the hot unit.

Chapter 4 presents a detailed description of the two identical optical voidage probes used to measure the local voidages in four fluidization columns, and on the capacitance probe used in the two CSIRO columns. The design, calibration and placement of a quartz cover at the tip of the optical voidage probe are discussed. Reported results include radial profiles, probability distributions, standard deviations of local voidages, and the effect of scale on such measurements. Comparison of the optical voidage probe and capacitance probe measurements highlights the difference in the measuring volume of the probes.

In **Chapter 5**, experimental results from the optical fiber velocity probe in the 0.29 and 0.61 m columns are reported. Cross-correlation of signals between the two fibers allowed velocities to be determined in turbulent fluidized beds. The high-speed data acquisition, ~29 kHz, for the particle velocity measurement required conditioning of the data prior to cross-correlation. The effects of different pre-conditioning techniques on the resulting velocity measurements are shown to be substantial. Simultaneous measurements of voidage and particle velocity reveal changes in flow dynamics with superficial gas velocity, and with radial location. An attempt is made to deduce void velocity, simultaneously with particle velocities, highlighting the difference in the physical scale of these measurements, and the requirement for further data conditioning to obtain the velocity of voids, which are themselves of transitory character.

Chapter 6 presents analysis of the pressure and voidage measurements obtained in Chapters 2 through 5, using various statistical, spectral and chaotic analysis methods. Particular focus is placed on methods which help delineate structural changes as the bed undergoes transition to the turbulent fluidization flow regime. Spectral analysis highlights dominant frequencies present in the signals, while rescaled range analysis can deduce cycle times inherent in signal fluctuations. The data are further analyzed with a coherence function, which characterizes the coherence of a pair of signals at a given frequency. The significance of the physical length scale to the scale of interest is emphasized.

In **Chapter 7**, wavelet analysis, a relatively new analysis tool, which finds numerous applications including the interpretation of non-linear data, is employed in an effort to gain physical insight into the gas-solid turbulent fluidized bed. Wavelet analysis allows the decomposition of data into different frequency components, with the positions and scales then resolved as independent variables. This method can deal with the multiple levels of scales present in fluidized beds, namely the macro-, meso- and micro-scales, which affect signals at various temporal and spatial resolutions. Wavelet transformation is also applied to non-linear de-noising to remove high frequency fluctuations resulting from local particle variations in distinguishing void movements for void velocity calculations. Local Intermittency Measure (LIM) applied in turbulence research is extended to search for coherent structures.

Finally, **Chapter 8** provides a summary of experimental findings, interpretations of data analysis, and future perspectives related to advancing the understanding of fluid-particle interactions as well as void and particle dynamics in turbulent fluidized beds.

Appendix A lists further details on the modifications and commissioning of the 1.56 m diameter fluidization column.

Appendix B discusses the analysis methods employed for pre- and post- processing of data in deducing the velocity measurements. Cross-correlation is performed on the raw data as well as on data that had been pre-processed with binary coding and cut-off methods.

Appendix C summarizes the background on the Fourier and wavelet transformations applied in Chapters 6 and 7. Discussions on the continuous and discrete wavelet transformation, and details on the thresholding method are included.

Appendix D reviews forces on solids in gas-solid fluidized beds, including interparticle and fluid-particle interaction terms. CFD simulation was attempted using the two-fluid model to simulate turbulent fluidized bed of FCC particles. However, definitive results were not obtained owing to time constraints.

CHAPTER 2

EQUIPMENT AND MACROSCOPIC HYDRODYNAMICS

2.1 Introduction

Four separate experimental systems were used in this study. Details on particle characteristics, configuration, air supply, operation, challenges encountered in large-scale units, and instrumentation are presented in this chapter and in Appendix A. The macroscopic hydrodynamics obtained through pressure measurements are also summarized as a preface to more localized voidage measurements presented in Chapter 4.

2.1.1 Bed expansion

Due to the fluctuating and diffuse bed surface in turbulent fluidized beds, it is not possible to determine bed expansion solely by visual observation. Commonly, the bed voidage, deduced from the mean pressure drop, is used to characterize the bed expansion. Avidan and Yerushalmi (1982) related changes in slope of the expansion curve, for a 0.15 m diameter column, to regime transitions. However, Geldart and Rhodes (1985), employing a similar Group A powder in their 0.29 m column, observed gradual changes as the transition occurred with no indication of any discernible abrupt variation as a result of entry to the turbulent regime.

A modified Richardson-Zaki equation was applied to both Group A particles (Avidan and Yerushalmi, 1982) and Group B particles (Lee and Kim, 1990) to correlate the average bed voidage with the superficial gas velocity within the turbulent fluidization regime. Avidan (1980) introduced the concept of the effective terminal cluster velocity, U_t^*, such that:

$$\frac{U}{U_t^*} = \varepsilon^n \tag{2.1}$$

It should also be noted that the pressure drop method in obtaining voidage has been criticized (Werther and Wein, 1994) as yielding too high solids fraction values due to the acceleration of solid material in the region close to the distributor.

2.1.2 Axial voidage profile

Axial voidage distributions in turbulent fluidized beds are characterized by a smooth increase of gas volumetric concentration in the freeboard with the voidage remaining at ~0.65 to 0.75 in the bed. In

the turbulent flow regime, the voidage is a strong function of height (Venderbosch, 1998). As the gas velocity increases, the average solids concentration measured by optical fibre probes decreases in the bed. In examining the effect of static bed height on the axial voidage distribution, both Horio et al. (1992a) and Venderbosch (1998) reported that the decrease in hold-up shifted towards higher heights. Although the axial voidage distribution along the column and bed expansion may not uniquely characterize turbulent fluidized beds, they provide vital information in designing fluidized bed reactors operating in the turbulent fluidization flow regime.

2.2 Particulate material

Two different types of solids and several different particle size distributions for each were investigated in this study. The particle properties are tabulated in Table 2.1. Spent FCC particles were donated by Chevron Texaco Corp. in Burnaby, and by a local refinery in Victoria, Australia.

Particle size distributions of FCC samples are shown in Figure 2.1, while those for Catalysts C and Cr are shown in Figure 3.15. In the largest fluidization column, considerable entrainment of fines was observed. This is depicted by the change in particle size distribution, shown in Figure 2.2.

Table 2.1 Particle properties.

Identity	FCC I	FCC II	FCC III	FCC IV
Particle density, kg/m^3	1560	1450	1450	1450
Bulk density, kg/m^3	860	740	820	NA
Mean diameter, μm	78	58	81	98

Identity	Catalyst C	Catalyst Cr
Particle density, kg/m^3	1580	1580
Bulk density, kg/m^3	1093	NA
Mean diameter, μm	41	33

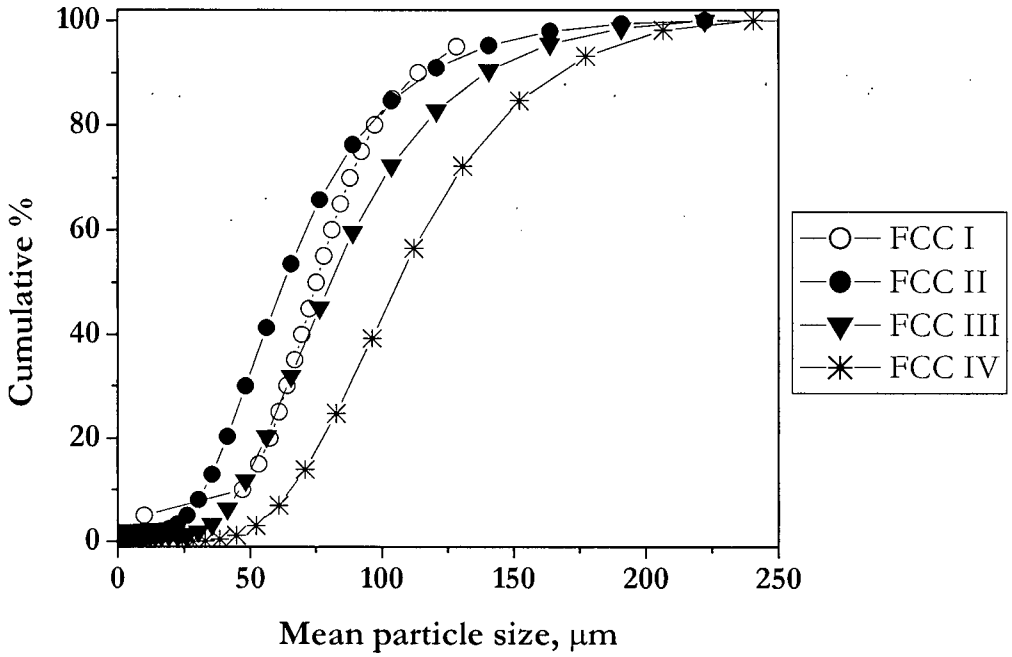

Figure 2.1 Particle size distribution of spent FCC particles.

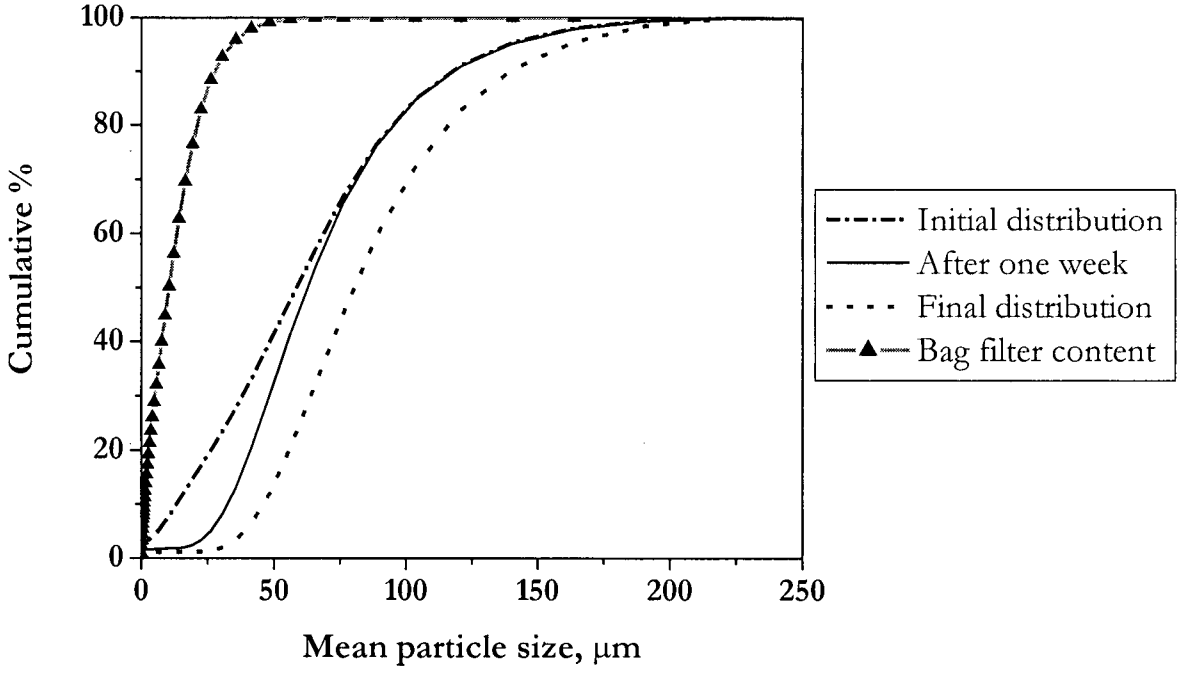

Figure 2.2 Progressive change in particle size distribution in 1.56 m diameter fluidization column. FCC II.

In order to alleviate electrostatic effects in the fluidizing system, the catalysts were mixed with approximately 0.5 weight% of Larostat 519 particles supplied by PPG Industries Inc. In addition, the columns were grounded at multiple points.

2.3 Column I: 0.29 m diameter fluidization column

The 0.29 m diameter, 4.5 m tall Plexiglas vessel is located at the University of British Columbia. It is equipped with 58 sampling ports. The distributor is an aluminium perforated plate containing 98 holes of 5.6 mm diameter arranged in an equilateral triangular configuration with a 32 mm pitch, resulting in an open area ratio of 3.7%. A second supporting distributor with the same number of holes of 64 mm diameter is located below the first plate with a 38 micron stainless screen mesh sandwiched between the two plates to prevent particles from falling into the windbox. The disengaging section at the top of the column, expanded to 0.4 m ID, abruptly converges to a 0.1 m exit duct connected to two external cyclones in series. A schematic diagram of the 0.29 m diameter column appears in Figure 2.3. Solids circulation is not controlled, but rather determined through a pressure balance between the return leg and the column. There are two flapper valves installed in the return leg to prevent gas from escaping up the standpipe.

Fluidizing air is supplied by a Roots blower with a maximum capacity of 425 Nm^3/h @ 69 kPa. As shown in Figure 2.4, fluidizing air is supplied through 0.15 m PVC piping. The air flow rate is controlled by the by-pass line located close to the blower, and calculated from the pressure drop across an orifice plate.

2.3.1 Pressure transducers and data acquisition system

Both steady-state and dynamic pressure measurements were obtained by 20 gauge and differential pressure transducers (OMEGA PX140) positioned at regular intervals along the column, as shown in Figure 2.5. Pressure taps were mounted flush with the wall of the column with 38 μm mesh stainless steel screens glued over the entrance to prevent solids from entering the pressure sensing lines. Modifications were incorporated to prevent clogging of the sampling ports resulting in better accuracy (Werther, 1999). A liquid manometer was used to calibrate the pressure transducers. Their linear response characteristics were incorporated into the calibration equations. Pressure signals were logged into a computer via an A/D converter (DAS08-EXP32).

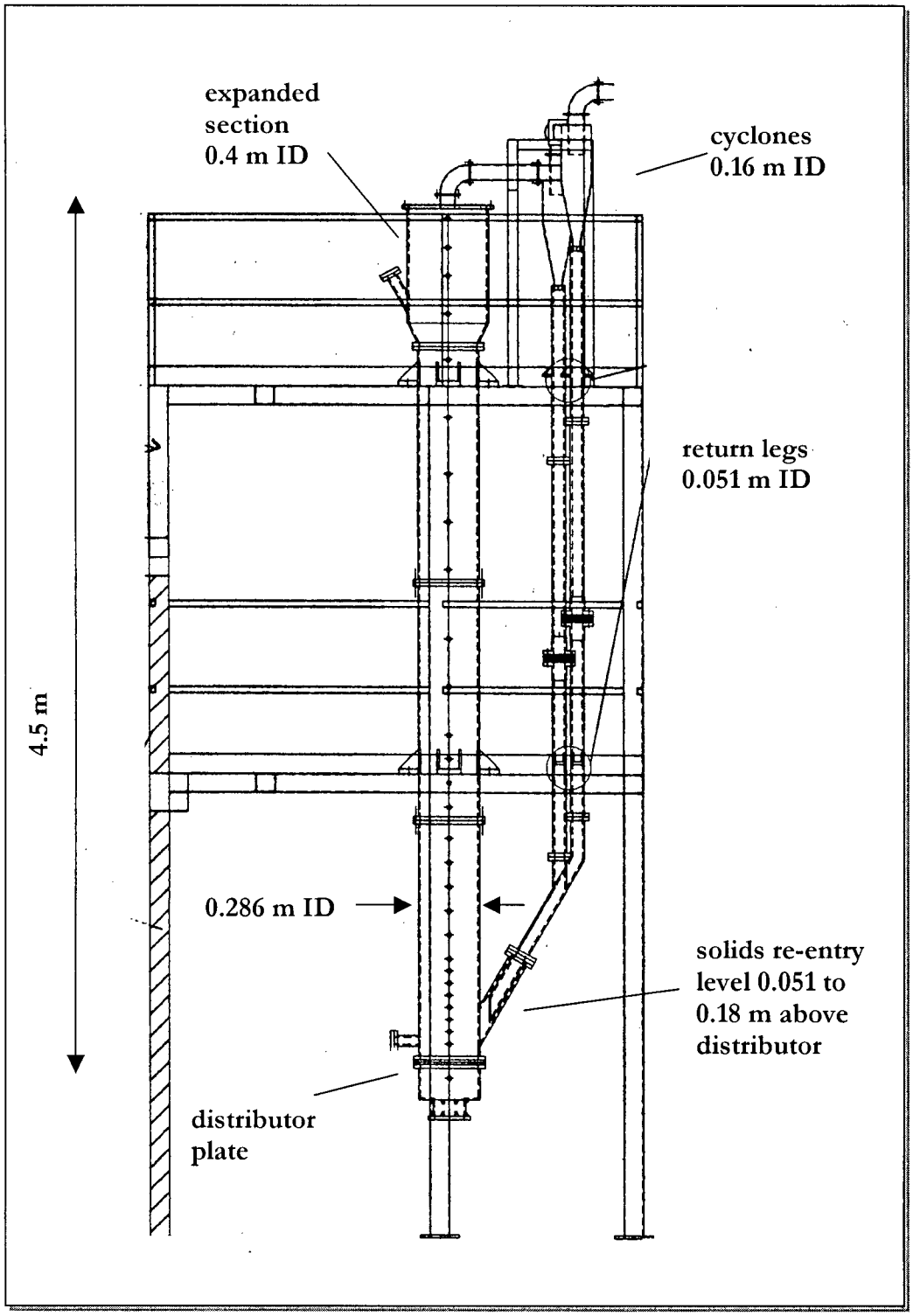

Figure 2.3 Schematic of 0.29 m diameter, 4.5 m tall fluidization column at UBC.

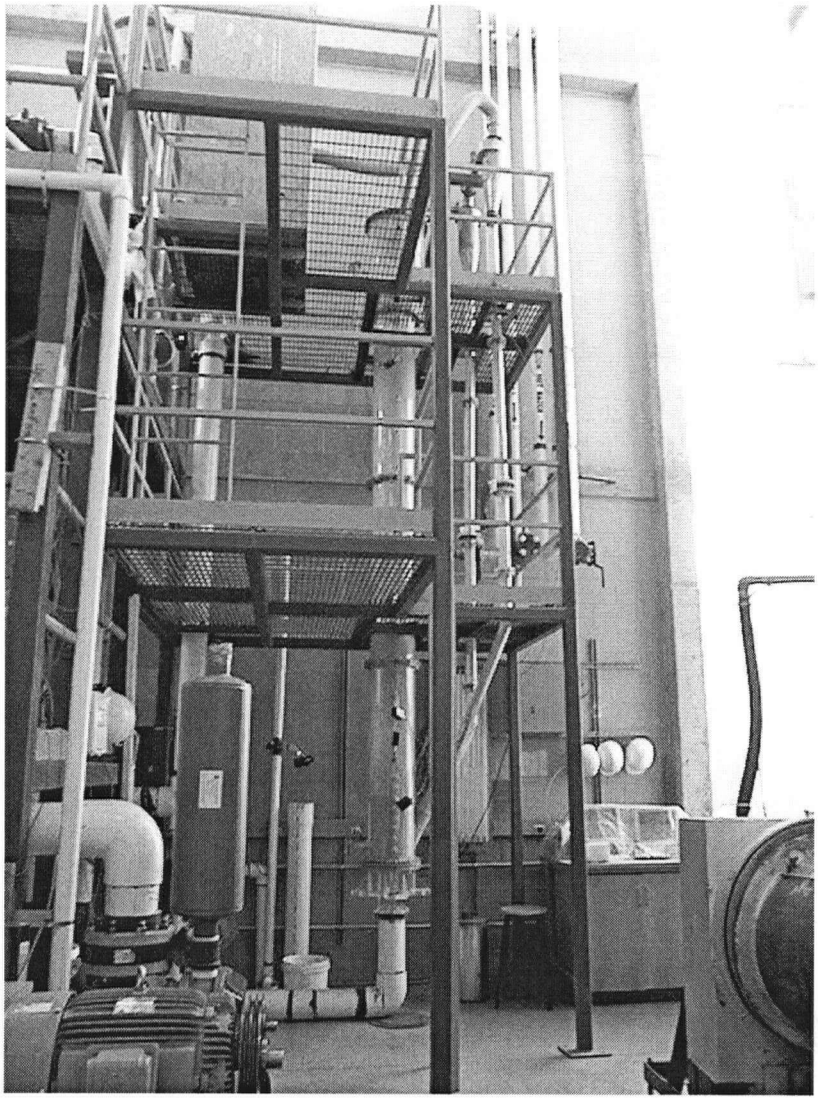

Figure 2.4 Photograph of 0.29 m diameter column with PVC piping for air supply. Wooden enclosure on the top level contains bag filters.

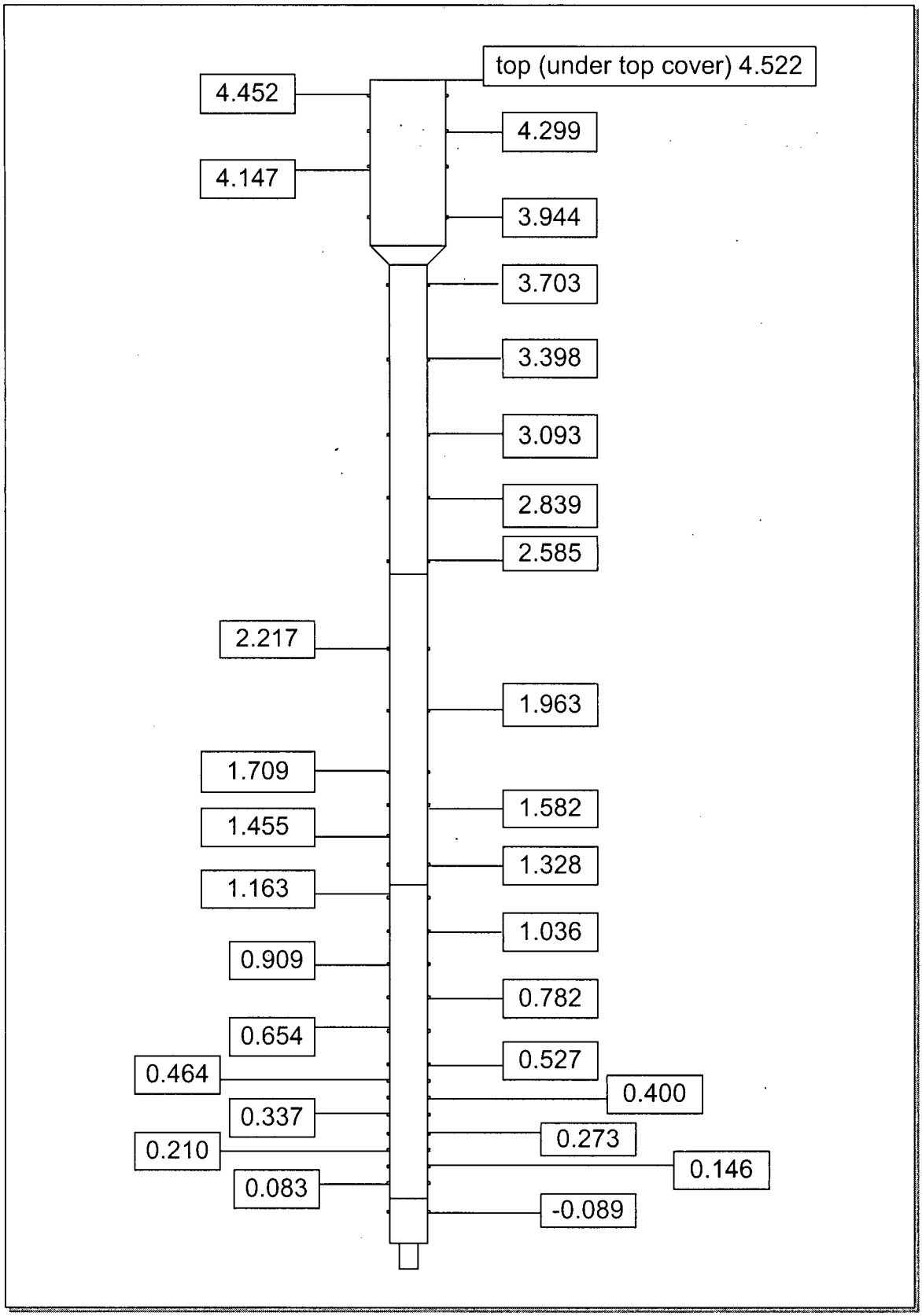

Figure 2.5 Schematic of 0.29 m diameter fluidization column depicting axial distances (in m) of ports relative to distributor plate.

Data acquisition was performed through a program written in Visual Basic and the LABTECH® software, Notebook pro ver. 10.12, for steady-state and dynamic pressure measurements, respectively.

2.3.2 Bed expansion

In many fluidized beds operated in the turbulent fluidization flow regime, solids circulation is not controlled, but it is determined by the superficial gas velocity and by the overall pressure balance within the system. In the 0.29 m diameter column, an increase in the superficial gas velocity resulted in an increase in the overall bed voidage, consequently in bed expansion. Once in the turbulent fluidization flow regime, the bed surface becomes increasingly diffuse, with considerable fluctuations, rendering determination of the bed level by visual observations impossible. The common method used to deduce the expanded bed height is to plot the time-mean gauge pressure (single-point pressure) against the height of the transducer ports, as exemplified in Figure 2.6, where the intercepts of the two slopes correspond to the level of the expanded bed.

The effect of initial static bed height on bed expansion is shown in Figure 2.7. The increases in expanded bed heights with U for the initial static bed heights of 1.5 m and 0.51 m are not observed for H_0=0.80 m. The differences in trend are attributed to the solid return leg, which constrains the entrained solids flow. The sudden expansion at higher U was observed to depend on the overall 'smoothness' of the solids flow, i.e., solids being efficiently returned through the dipleg, which seemed to be affected by the humidity of the air in the laboratory from which fluidizing air was drawn into the blower. In fact, the upper limit of the experiment was set by the capacity of the dipleg solids throughput, and not the blower.

2.3.3 Bed voidage

A momentum balance on a cross-sectional slice of a fluidized bed can be expressed (Gidaspow, 1994) as

$$\frac{d}{dz}\left(\varrho_g \varepsilon \upsilon_g^2 + \varrho_s \varepsilon_s \upsilon_s^2\right) = -\frac{dP}{dz} - \frac{d\sigma}{dz} - g\left(\varrho_g \varepsilon + \varrho_s \varepsilon_s\right) - \frac{4\left(\tau_{wg} + \tau_{ws}\right)}{D} \qquad (2.2)$$

where the terms from the left are: net rate of momentum outflow for gas/solids; fluid pressure gradient; gradient of solids normal stress; gravitational force; and force due to wall shear. For a fully developed flow and ignoring wall shear and solid stress, the momentum balance can be simplified to:

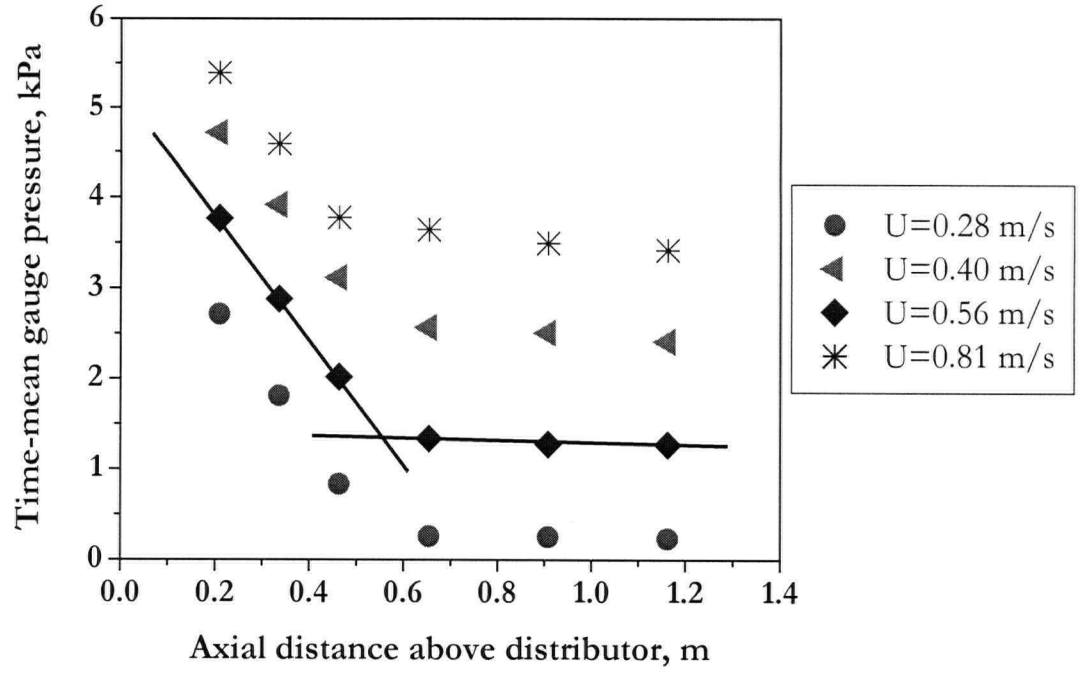

Figure 2.6 Axial gauge pressure profile for 0.29 m column. H_0=0.51 m. D=0.29 m, FCC I.

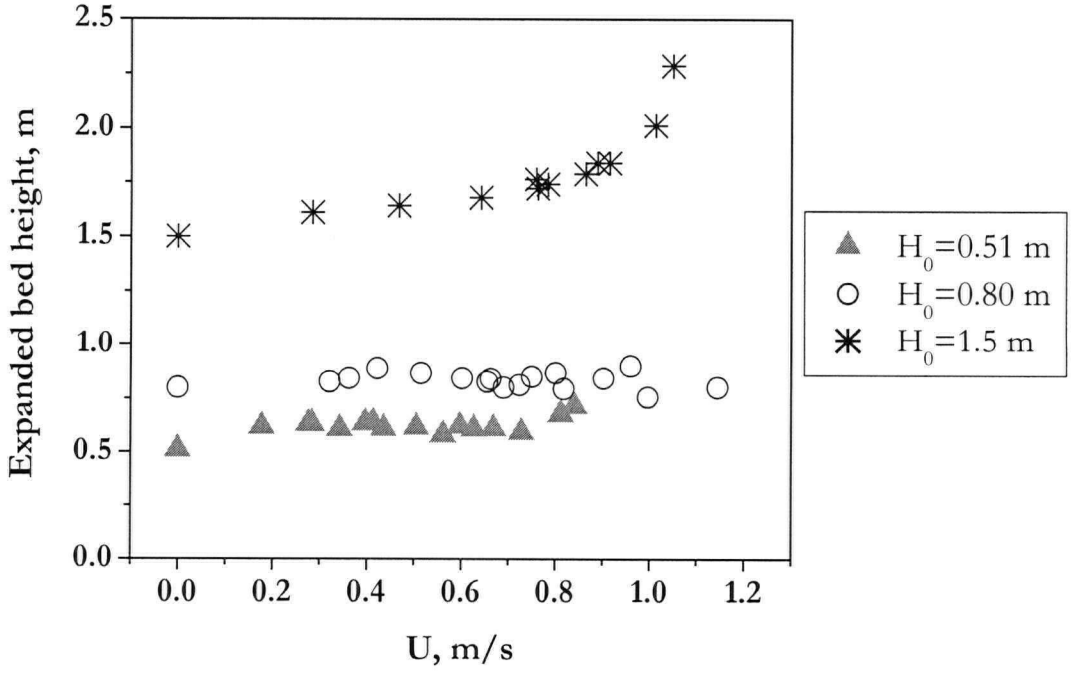

Figure 2.7 Expanded bed height calculated from gauge pressure profiles in Figure 2.6. D=0.29 m, FCC I.

$$-\frac{dP}{dz} \approx g\left(\varrho_g \varepsilon + \varrho_s \varepsilon_s\right) \tag{2.3}$$

From the time-mean gauge pressure profile, a least-squares linear fit can be performed to deduce the slope, i.e., dP/dz. In order to systematically include or exclude pressure data points near the diffuse bed surface, the standard deviation of each data point is compared to the root mean standard error of the curve fit, as shown in Figure 2.8. Since the pressure measurements do not display a common variance, a weighted regression using Reduced Square-Chi of the standard deviation of the pressure fluctuation was performed. As a result, the error imposed on the fitted parameter was minimized.

The time-mean bed voidage for three different initial static bed heights calculated from the above procedure is shown in Figure 2.9. As indicated by arrows in the figure, the trend with increasing bed height changes with $U > U_c$ for H_0=0.51 and 1.5 m. (U_c is defined as the superficial gas velocity at which the standard deviation of pressure fluctuations reaches a maximum, and is described further in Chapter 3). However, this trend is not always consistent, as exemplified by the plot for H_0=0.80 m. This is attributed to the varying in-bed inventory of solids due to increasing entrainment of solids in the freeboard as well as the solids in the return system.

Variations of bed voidage with superficial gas velocity are next analyzed using a modified Richardson-Zaki equation as proposed by Avidan (1980). From a plot of U versus voidage on a logarithmic scale, Avidan (1980) chooses the slope, n, to represent the homogeneity of the fluidized bed. The superficial gas velocity of the extrapolation of slope to ε=1 is said to give the effective terminal cluster velocity, U_t^*, through Equation 2.1 as shown in Figure 2.10. The resulting coefficients are listed in Table 2.2. As H_0 is increased, both exponents are seen to decrease.

2.3.4 In-bed inventory of solids

In order to correct for the solids contained in the freeboard and return loop, the mass of solids remaining in the dense bed (Rhodes and Geldart, 1986) is used, i.e.,

$$M_b = \frac{\Delta P_{bed} A}{g} = HA(1-\varepsilon)\varrho_s \tag{2.4}$$

Figure 2.11 depicts the height of the dense bed corresponding to voidage at minimum fluidization, expressed as $H'=H(1-\varepsilon)/(1-\varepsilon_{mf})$, based on Equation 2.4. The bed height representing the amount of solids remaining in the dense bed, H', indicates a slight decrease approaching U_c, beyond which a

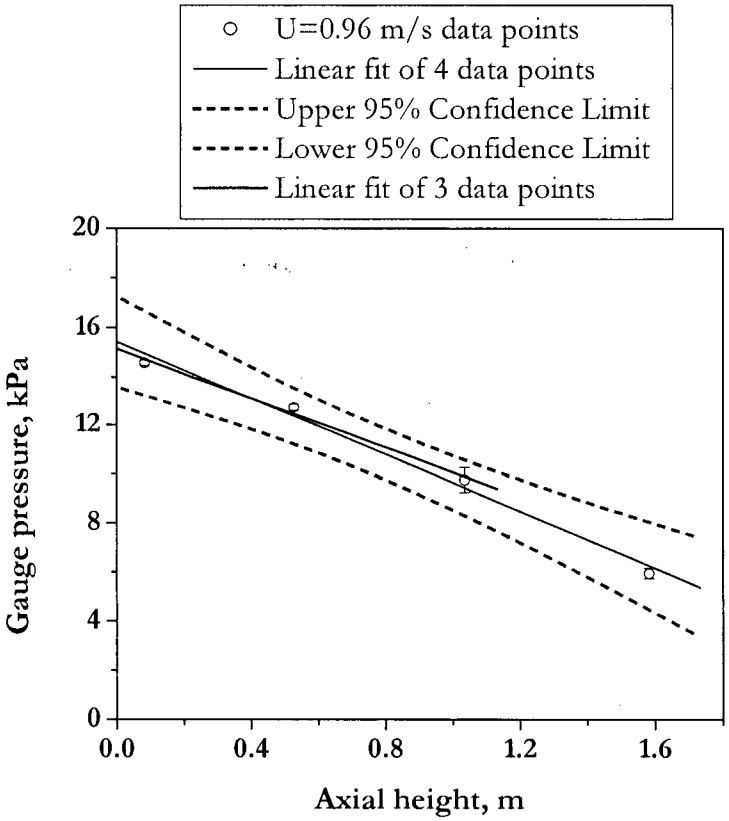

Figure 2.8 Determination of bed pressure drop. U=0.96 m/s, H_0=1.2 m, D=0.29 m, FCC I.

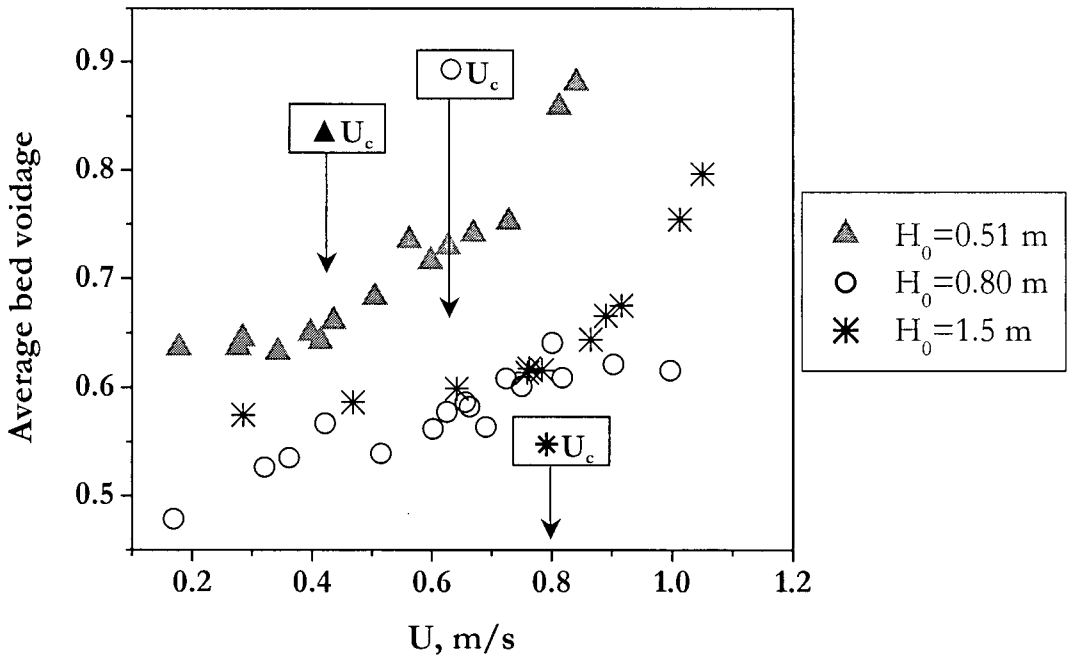

Figure 2.9 Time-mean bed voidage vs. U. D=0.29 m, FCC I.

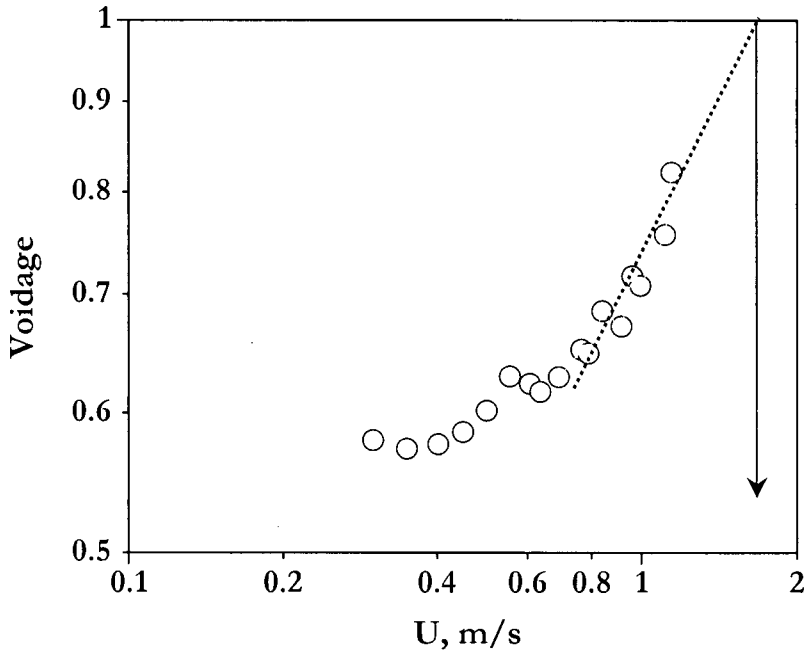

Figure 2.10 Time-mean bed voidage vs. superficial gas velocity. Determination of effective terminal velocity, U_t^*, in modified Richardson-Zaki equation. H_0=0.6 m, D=0.29 m, U_c=0.62 m/s ($\bar{z}$=0.31 m, DP).

Table 2.2 Coefficients for the Modified Richardson-Zaki equation.

H_0, m	U_t^*, m/s	n
0.6	1.76	1.82
1.2	1.23	0.76
1.5	1.16	0.41

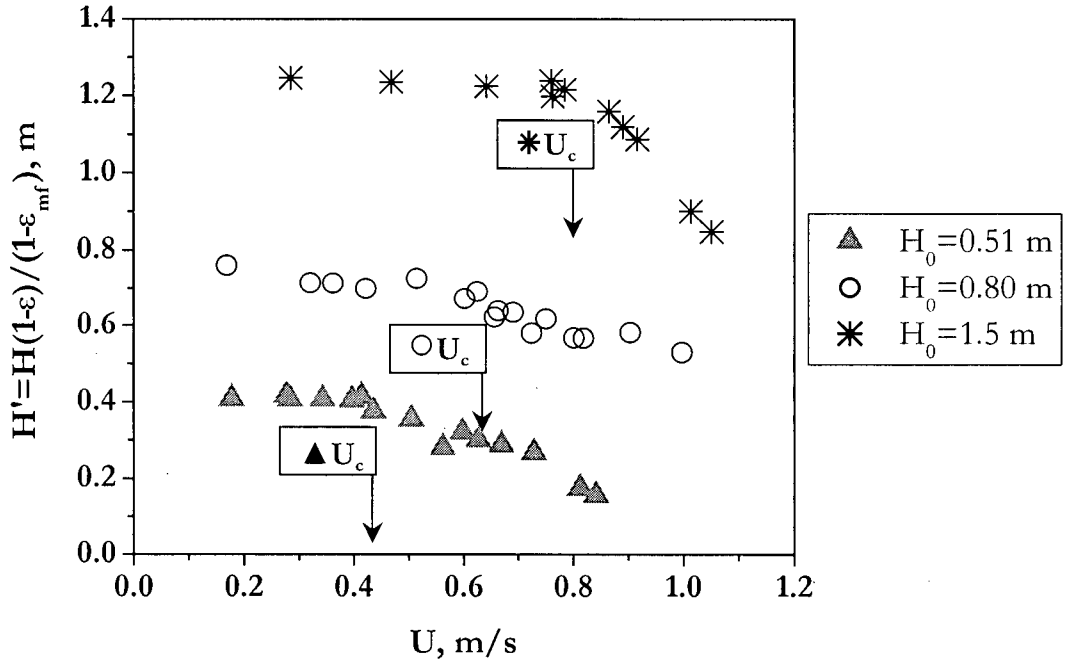

Figure 2.11 Height of dense bed corresponding to voidage at minimum fluidization vs. superficial gas velocity. D=0.29 m, FCC I.

steeper decrease is observed. This implies that the net decrease in solids remaining in the dense bed occurs at $U > U_c$, in agreement with the findings of Rhodes and Geldart (1986).

2.3.5 Solids circulation rate

The solids circulation rate was measured using the flapper valve by estimating the collected solids in the dipleg over a given time interval. Morikawa (1999) and Morikawa et al. (2001) reported an extensive study on entrainment from this column. In Figure 2.12, a typical range of solids circulation rates is given to provide information about the system.

2.3.6 Axial voidage distribution

From the eight differential pressure transducers located along the column, the cross-sectional average voidage is calculated as represented in Figure 2.13. As a result of increased entrainment at higher gas velocities, the average dense bed voidage increases while the freeboard voidage slightly decreases. The time-mean voidage at the axial position closest to the distributor plate possibly reflects the jetting effect. Furthermore, the lower voidage indicated at the lower axial locations for U=0.94 m/s may be due to the influence of solids re-entering the column at axial distances between 0.051 and 0.18 m above the distributor plate. Increasing superficial velocity has been shown to cause the bed surface to become more diffuse.

2.4 Column II: 0.61 m diameter column

The 0.61 m diameter, 9.8 m tall fluidization column is located at CSIRO Minerals, Clayton, Australia. Both perforated plate and bubble cap type distributor plates are available. A single external cyclone of 1.2 m diameter is located at the top to return solids to the fluidization column at an average distance of 0.88 m above the distributor plate via a return leg. The solids circulation rate is controlled by aeration gas via a distributor at the base of the loopseal. As shown in Figure 2.14, the column is fitted with multiple pressure taps to monitor the pressure balance in the circulation loop. Additionally, as shown in Figure 2.15, multiple ports were available to accommodate insertion of optical probes, fast response pressure transducers and capacitance probes.

The 0.61 m fluidized bed column was modified to operate in the turbulent fluidization flow regime with FCC particles. The inlet of a single cyclone of 1.2 m diameter was reduced from 0.146 m^2 to 0.032 m^2 by inserting a 280 mm by 540 mm metal plate to ensure that the inlet velocity of gas was

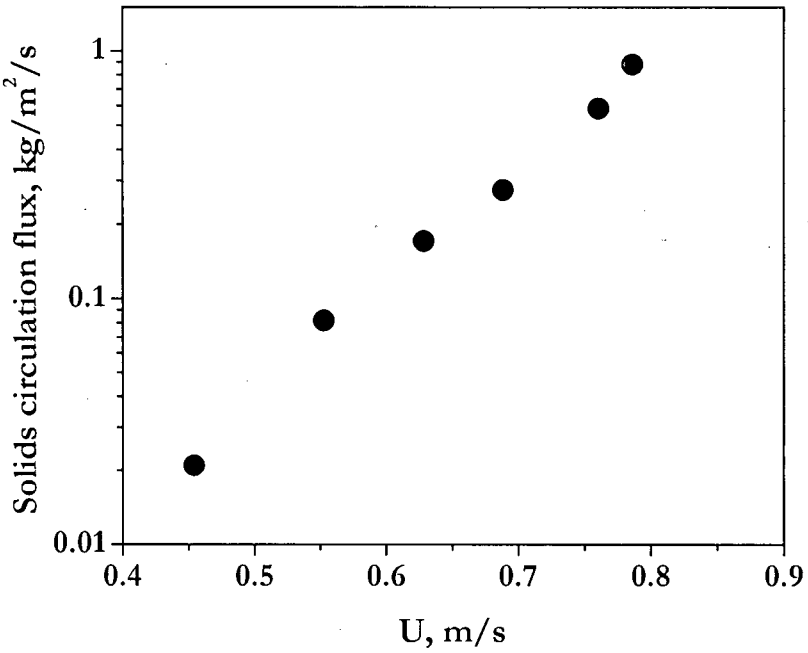

Figure 2.12 Solids circulation flux vs. superficial gas velocity. D=0.29 m, H_0=1.0 m, FCC I.

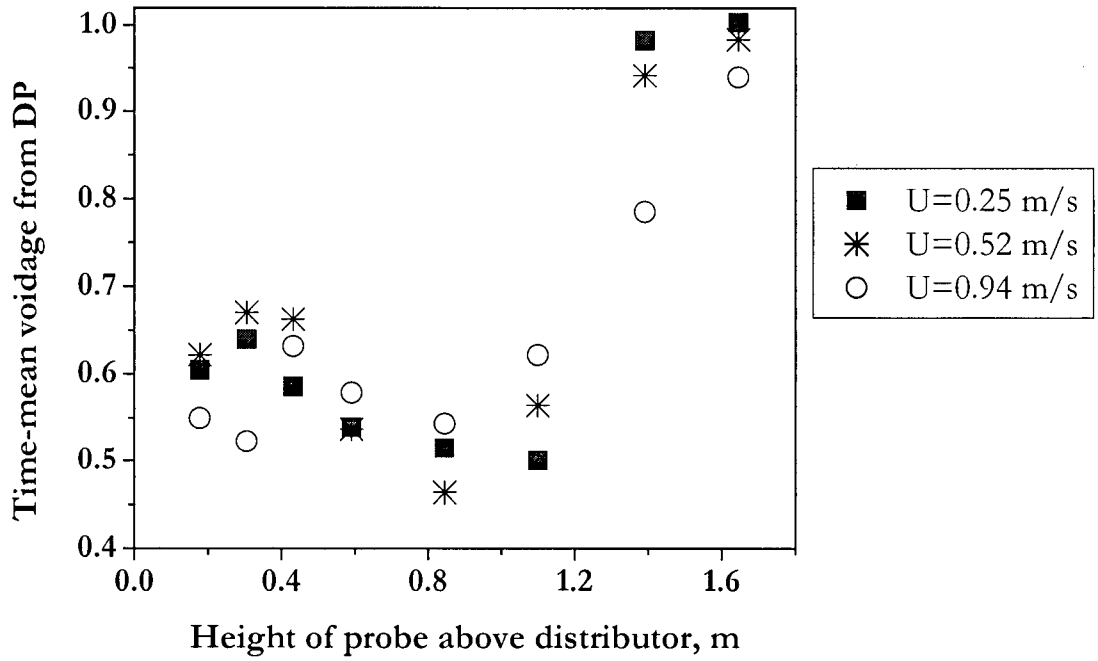

Figure 2.13 Axial voidage profile from time-mean DP measurements. D=0.29 m, H_0=1.1 m, FCC I.

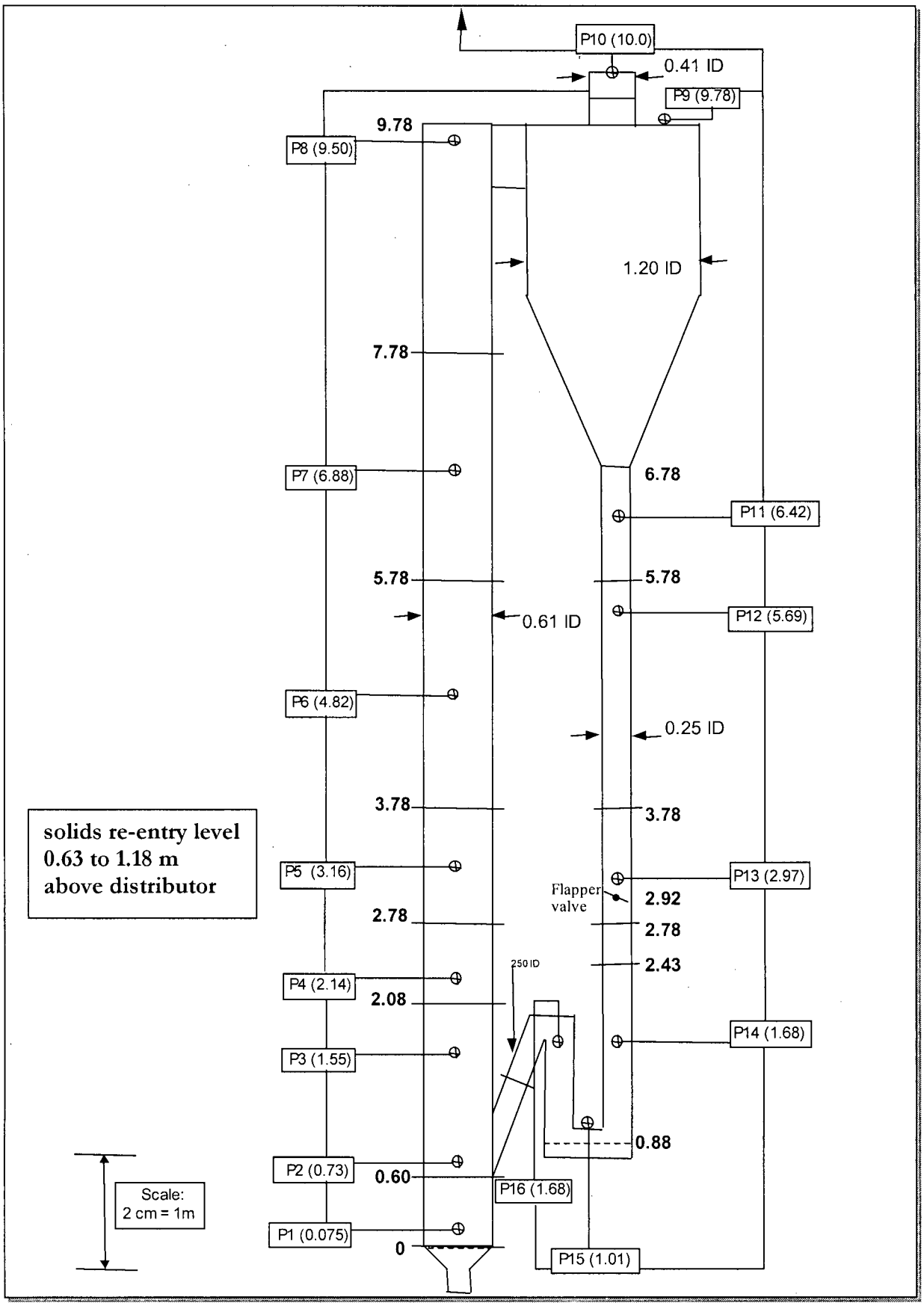

Figure 2.14 Schematic diagram of location (in m) of pressure ports in 0.61 m column.

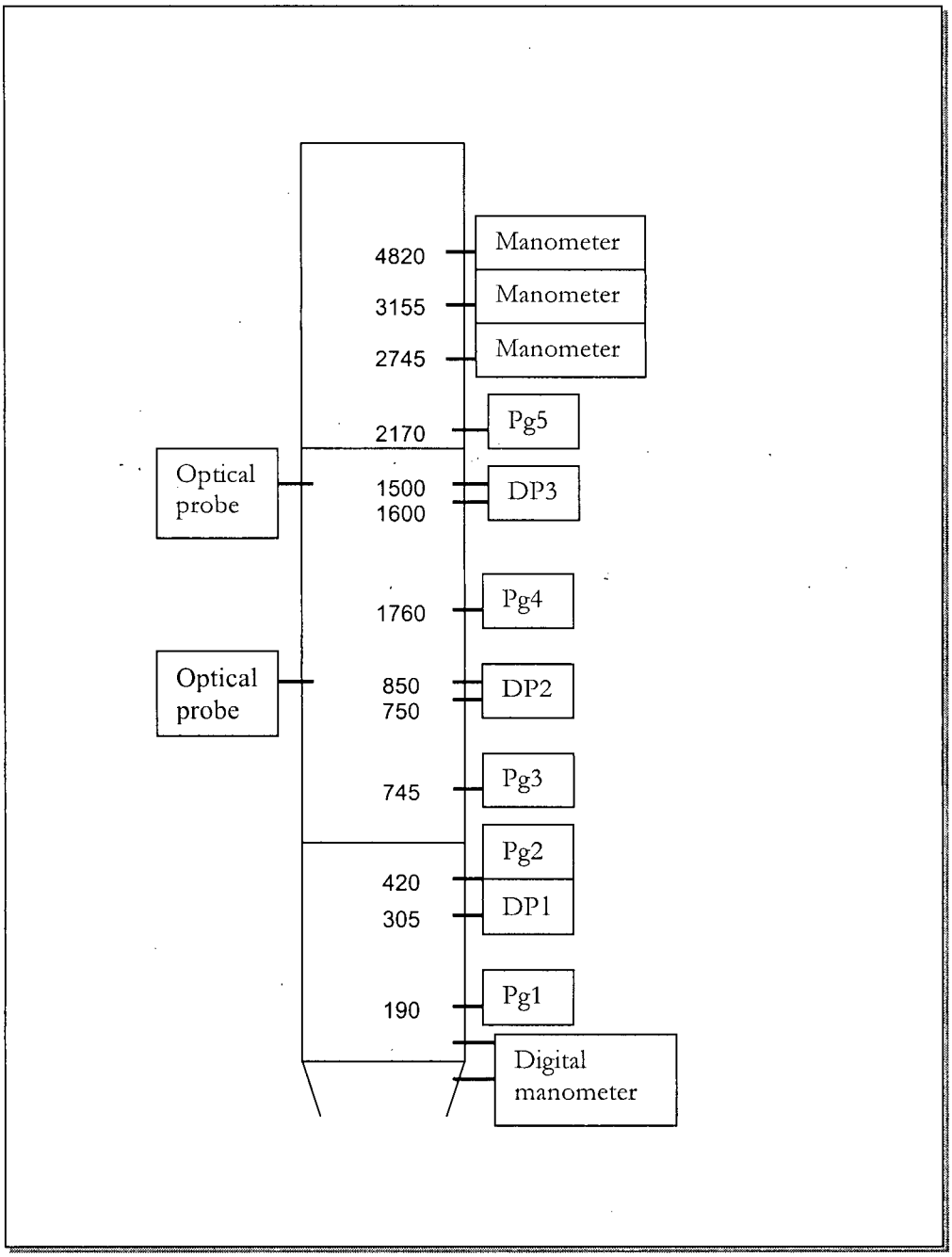

Figure 2.15 Location (in mm) of pressure transducers and optical fibre probes for dynamic measurements in 0.61 m diameter fluidization column.

sufficient to capture entrained particles in an efficient manner. The distributor plate contained 523 holes of 6.4 mm in diameter on a 25.4 mm triangular pitch. The pressure drop across the distributor plate for an empty fluidization column is shown in Figure 2.16. The high pressure drop results from the fabric placed under the distributor to prevent solids from falling into the windbox.

Two Roots blowers with maximum capacities of 30,000 Nm^3/h @ 20 kPa and 10,000 Nm^3/h @ 60 kPa supply the fluidizing air for both the 1.56 m and 0.6 m diameter fluidization columns. The air flow rate is calculated by measuring the gauge and differential pressures and the thermocouple readings across an orifice plate.

Two separate pressure logging systems for dynamic and steady-state pressure measurements were used on the 0.61 m fluidization column. For the steady-state pressure measurements, differential pressure transducers (Sensym 30 mb to 1000 mb; Rosemount 375.65 mb; Taylor 373.65 mb; Honeywell 100 mb) were used. Pressure taps were mounted flush with the wall of the column and fitted with cigarette filters to prevent solids from entering the pressure sensing lines. The data acquisition system was configured to sample at 100 Hz.

For the dynamic measurement system, five SURSENSE™ ultra low pressure sensors from Data Instruments (model DCAL405DN, ± 5 in. H2O F.S.) and five Sensym Signal Conditioned Pressure Transducers (models 142SC01D, 0-1 psid and 142SC05D, 0-5 psid) were calibrated and connected to the pressure taps via 15 mm stainless steel sintered filters. Between the author's two visits (13 month apart) to CSIRO, the particle size distribution of the FCC particles fluidized in the 0.61 m diameter column changed. The two lots are identified as FCC III and IV in Section 2.2.

2.4.1 Pressure balance in circulation loop

Figure 2.17 shows the pressure balance for the bubbling and turbulent fluidization flow regimes in a 0.61 m diameter column circulation loop. At U=0.26 m/s, entrainment of solids was minimal. When U was increased to 1.56 m/s, there was considerable entrainment as reflected by the pressure profile. Efficient return of solids through the cyclone and dipleg is observed with solids accumulating at the loopseal.

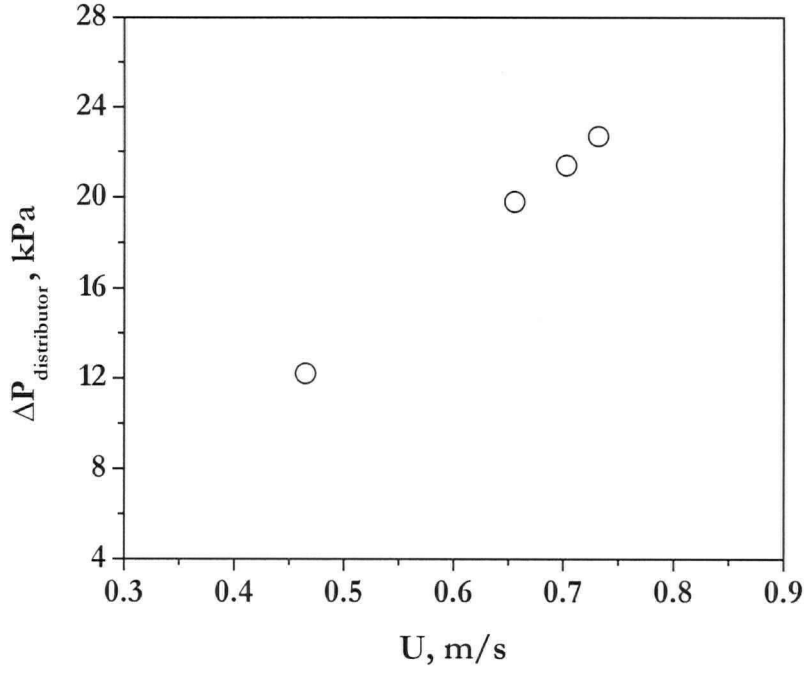

Figure 2.16 Distributor plate pressure drop measured in empty column. D=0.61 m.

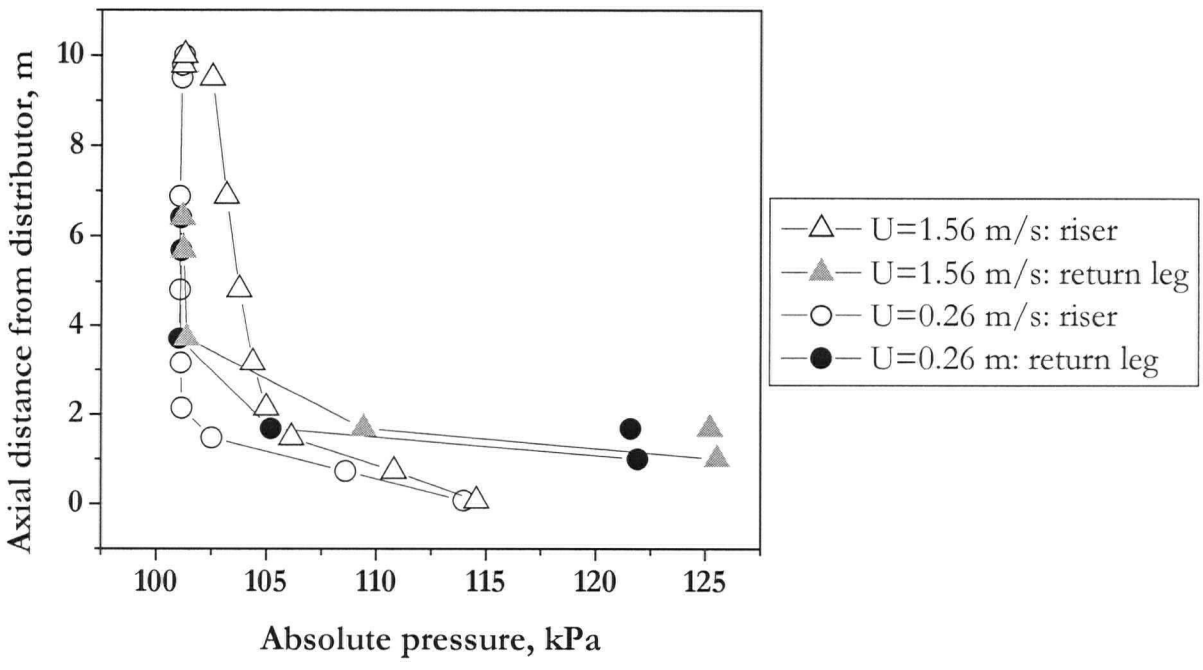

Figure 2.17 Pressure profile for circulation loop for D=0.61 m, H_0=2 m, FCC IV.

2.4.2 Expanded bed height

From the axial pressure profiles, expanded bed height is calculated for each superficial gas velocity as shown in Figure 2.18. The initial FCC static bed height was approximately 2 m. The expanded bed height data reflect the large storage capacity of the loopseal and return leg system. It also shows an initial increase with superficial gas velocity, followed by a slight decrease. As deduced from a DP transducer located between 1.50 and 1.60 m above the distributor plate, U_c=1.12 ± 0.05 m/s. Increasing U results in a decrease in the dense bed height corresponding to the minimum fluidization voidage without a noticeable change in its slope near U_c, as shown in Figure 2.18. This implies that the mass of solids remaining in the dense bed continually decreases with increasing U, and that U_c does not solely correspond to the loss of solids.

2.4.3 Bed density

Variations of the time-mean suspension density with superficial gas velocity are shown in Figure 2.19. Bed densities at $U > U_c$ in the 0.61 m column indicate very efficient return of entrained solids, as the corresponding voidage remains below 0.6 at U=1.56 m/s. This suggests that there are statistically steady suspension densities resulting from pressure balance in the circulation loop at $U > U_c$. This seems contrary to the earlier investigations where the existence of the turbulent fluidization flow regime as an independent regime was questioned, e.g. Rhodes (1996), that the transition is caused by the transfer of solids from the bed to the freeboard with the exposure of the pressure probe to the freeboard.

2.5 Column III: 1.56 m diameter fluidization column

The 1.56 m diameter, 15 m tall cold-model is also located at CSIRO Division of Minerals in Clayton. Fluidizing air is supplied through a 0.95 m air duct, a plenum chamber expanding the diameter to 1.56 m, and a distributor plate consisting of 18 bubble caps. Two external cyclones in parallel at the top of the column separate gas and solids and feed solids back to the column through return legs equipped with flapper valves. Aeration via a distributor at the base of the loopseal controls the solids circulation rate. In order to operate this rig in the turbulent fluidization regime with Geldart Group A solids, the distributor plate and cyclone inlet area were modified. The locations of the pressure transducers and traversing probe arms are shown in Figure 2.20. Further details on the modifications and commissioning of the 1.56 m diameter fluidization column are reported in Appendix A.

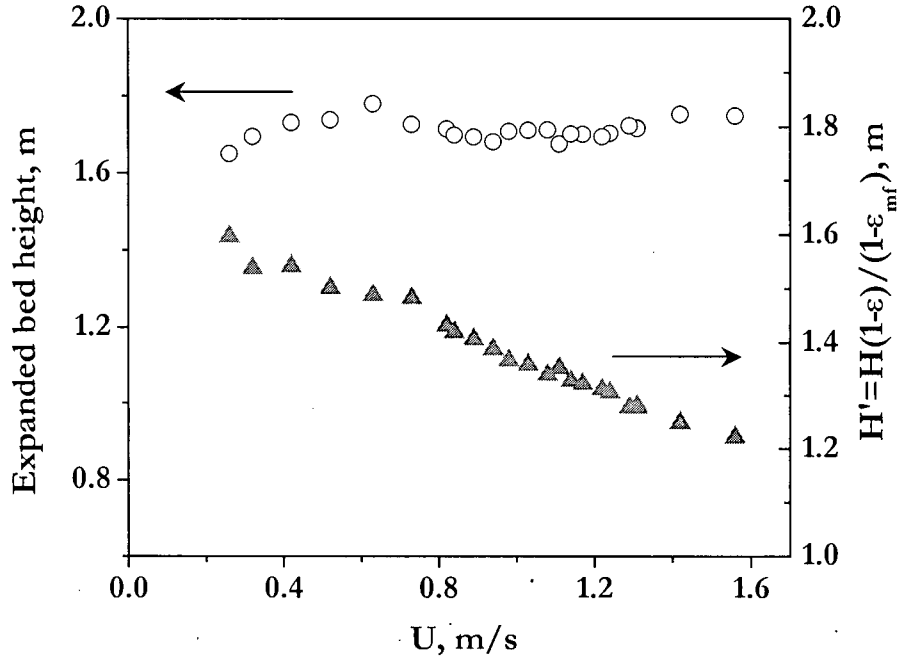

Figure 2.18 Expanded bed height and height of dense bed corresponding to voidage at ε_{mf} calculated from axial gauge pressure profiles. D=0.61 m, H_0=2 m, U_c=1.12 m/s ($\bar{z}$=1.55 m, DP), FCC IV.

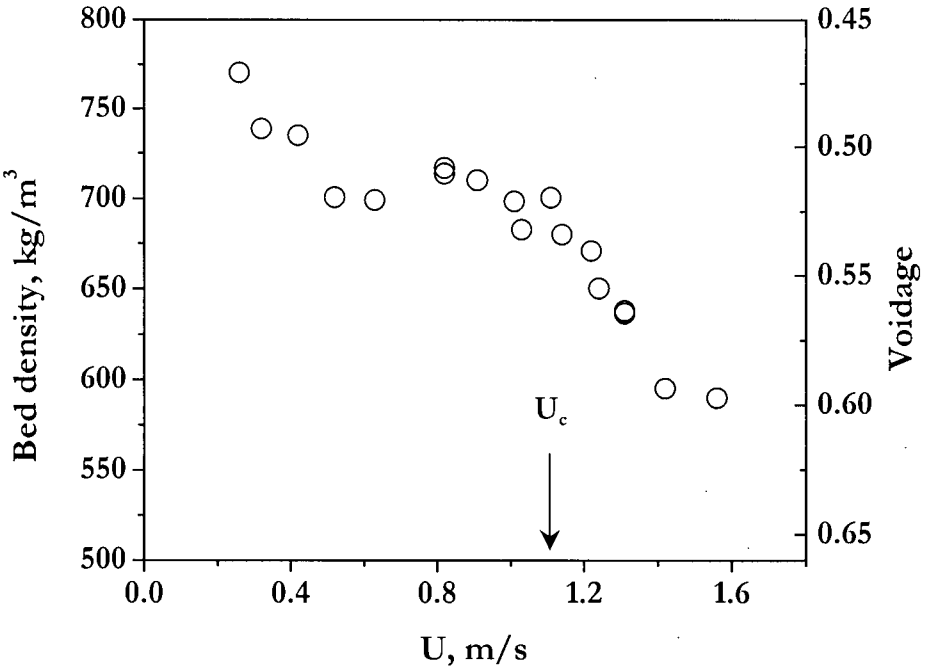

Figure 2.19 Time-mean bed density vs. superficial gas velocity for D=0.61 m, H_0=2.0 m, axial location of DP taps: 0.73-1.55 m, FCC IV. U_c at $\bar{z}$=1.55 m from DP fluctuations.

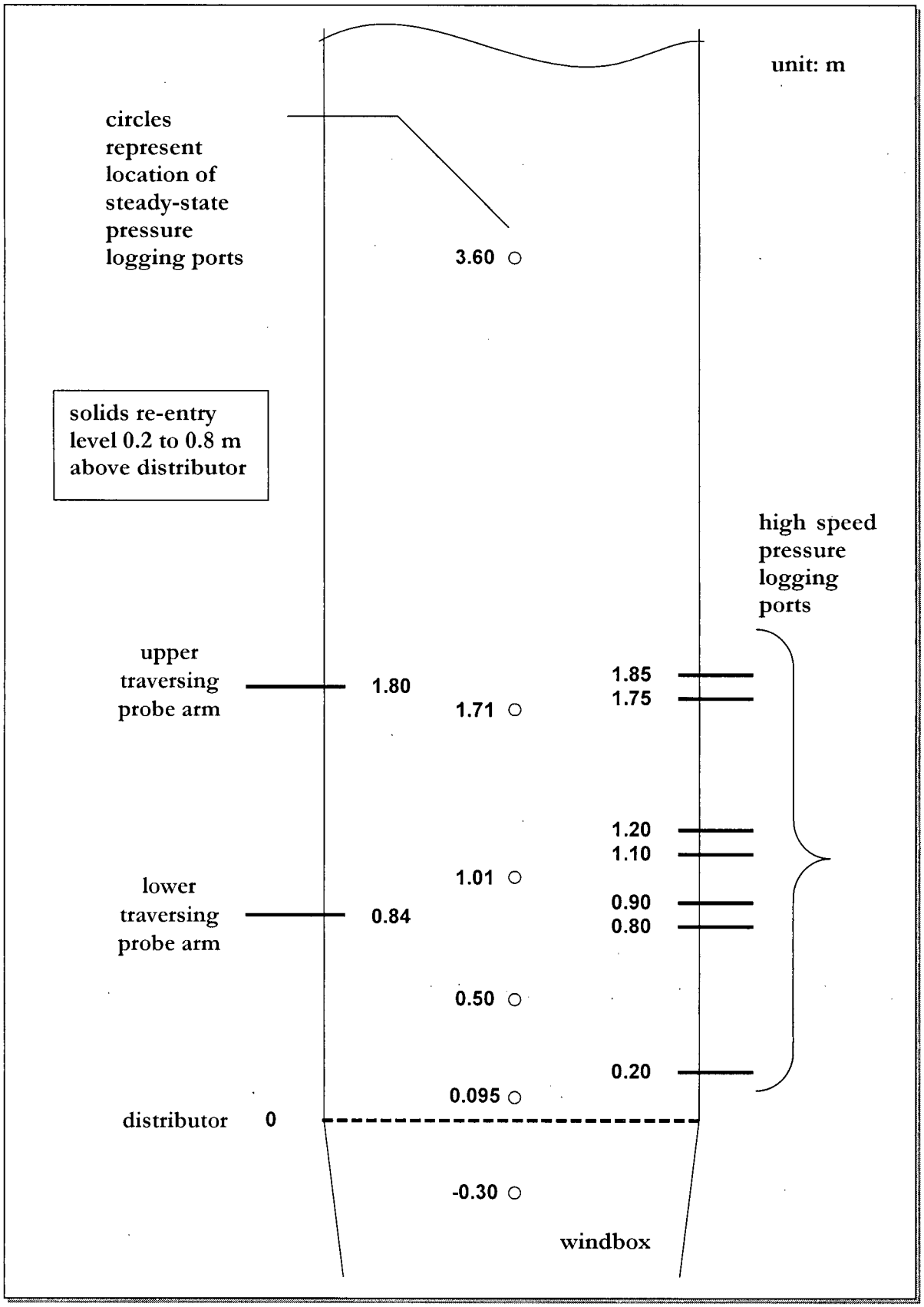

Figure 2.20 Location of pressure transducers and traversing probe arms in 1.56 m column.

The distributor pressure drop was measured in an empty column for an open area ratio of 3%, as shown in Figure 2.21. After installing 5 mm spacers, the final open area ratio was reduced to 2.3% without a significant increase in distributor pressure drop. As shown in Figure 2.22, frequency analysis of the gauge pressure measurements in the 1.56 m diameter fluidization column without any Solids exhibits two small-amplitude wide band peaks. Peaks at these frequencies increased in amplitude with increasing superficial gas velocity, and are attributed to the inherent frequency of the blower, and/or natural frequency of the air supply system.

As indicated in Figure 2.23, the ratio of distributor plate pressure drop to bed pressure drop was experimentally shown to be between 10 and 30% for the range of superficial gas velocities studied, ensuring a uniform distribution of gas; however, no bubble caps were located in the centre of the distributor which likely contributed to a preferential flow of gas towards the wall, as discussed in Chapter 4.

2.5.1 Traversing arm design and construction

In order to measure pressure and voidage simultaneously at various radial positions in the bed, two stainless-steel traversing probe arms were designed and fabricated for a differential pressure transducer and to hold optical and capacitance probes. As shown in Figure 2.24, the probe arm consisted of either an optical probe for probe arm #1 or both the optical and the capacitance probes for probe arm #2, a differential pressure transducer, and two 15 μm sintered filters as pressure ports. The support structure at the end of the probe arm was designed to have minimum interference between different measuring probes, and was made of 64 mm OD stainless steel tube, 60 mm in length. The probe arms, made of 38 mm OD stainless steel tube with a total length of ~850 mm, were inserted into the rig 0.84 m and 1.8 m above the distributor at 90° to each other.

2.5.2 Pressure measurements

Two separate systems for dynamic and steady-state pressure measurements were used on the 1.56 m diameter fluidization column. For the steady-state pressure measurements, differential pressure transducers of XTC Model 341 Series - smart Pressure transmitter from Moore Product (model type: 341DD1S2BN1NN2N, 4-20 mA DC, 10-450" H2O programmable) were programmed to register a maximum of 100 mbar (for 0.4-2 volt). Pressure taps were mounted flush with the wall of the column and were fitted with cigarette filters to prevent solids from entering the pressure sensing lines. The data acquisition system was configured to sample at 1 Hz, and was installed in a portable

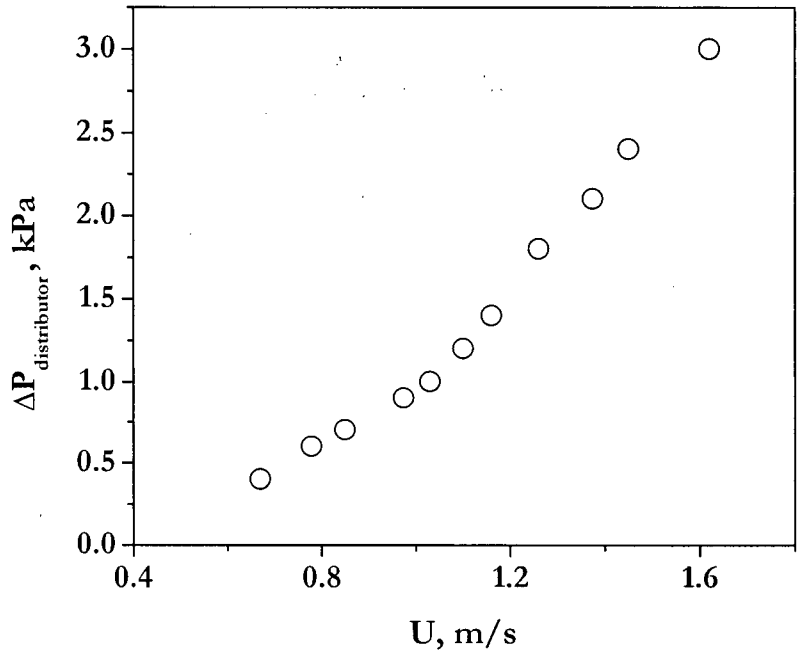

Figure 2.21 Distributor plate pressure drop measured in empty 1.56 m column.

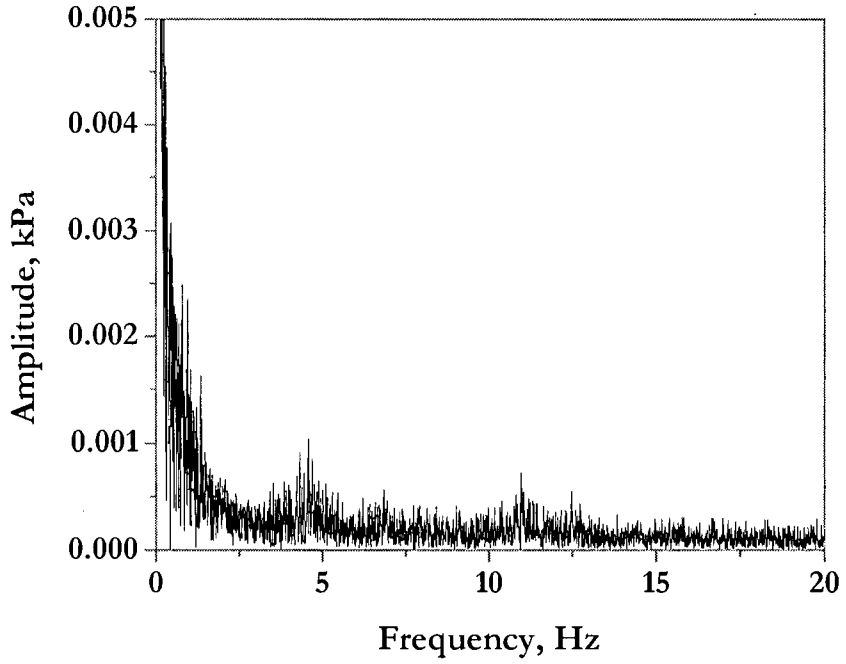

Figure 2.22 Frequency spectrum analysis of gauge pressure fluctuations in empty bed. D=1.56 m, U=1.1 m/s, z=0.2 m, r/R=0.9.

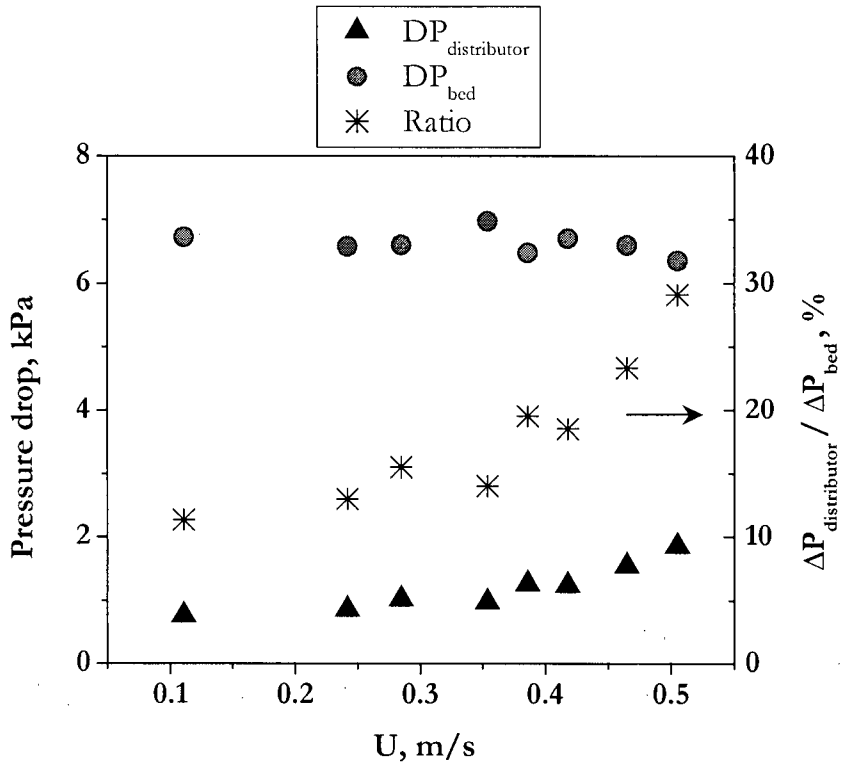

Figure 2.23 Bed and distributor pressure drop for 1.56 m fluidization column. U=0.43 m/s, H_0=0.9 m, FCC II.

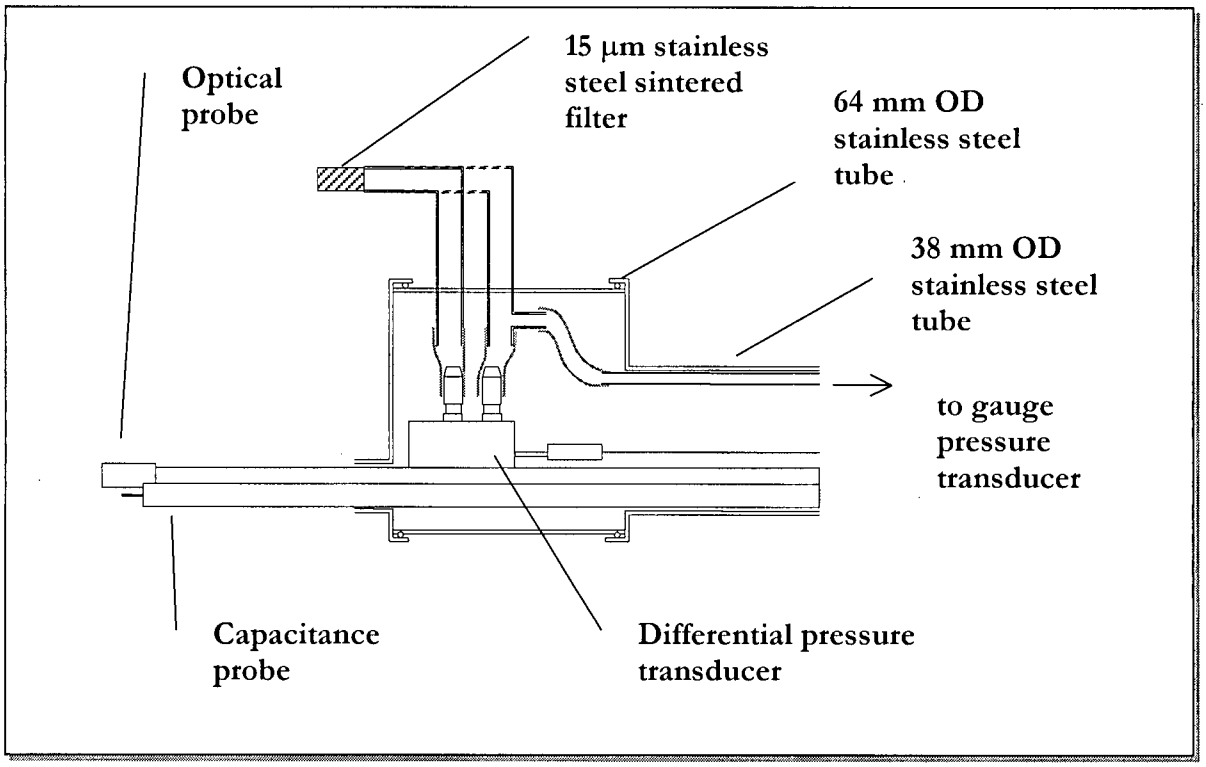

Figure 2.24 Schematic diagram of the tip of a traversing probe arm.

hut located next to the rig. For the dynamic measurement system, five transducers each of 1) SURSENSE™ ultra low pressure sensors from Data Instruments: model no. DCAL405DN (± 5 in. H2O F.S.), and 2) Sensym Signal Conditioned Pressure Transducers: model no. 142SC01D (0-1 psid) and model no. 142SC05D (0-5 psid) were calibrated and connected to the pressure taps via 15 μm stainless steel sintered filters. To minimize reduction in transducer response amplitude, the transducer volume was made as small as possible (~ 6 cm^3), and the transducer-data acquisition card cable length was shortened to reduce noise; therefore, the data acquisition board and the computer were positioned on the platform of the supporting structure of the rig. Pressure fluctuations were recorded by the data acquisition card CIO-DAS08 (Computer Boards, Inc.) with a Pentium™ 233 computer using the data acquisition software LABTECH® Notebook Pro ver. 10.1, sampling at 100 Hz for periods of 100 s.

2.5.3 Bed expansion

The expanded bed height, H, and height representing solids remaining in the bed, H′, both estimated from axial pressure profiles, are shown in Figures 2.25 and 2.26. In both cases there are insignificant change for H_0=0.9 m, compared to H_0=2.2 m where a decreasing trend is observed at $U > U_c$. This may be due to the H_0=0.9 m run not reaching high enough U.

2.5.4 Axial voidage profile

By assuming that the friction and acceleration terms are negligible and assuming identical response times for transducers logged at 1 Hz, voidages can be calculated from the pressure drop measurements. As a result of increased entrainment at higher gas velocity, the average dense bed voidage increases as the freeboard voidage decreases slightly, as shown in Figure 2.27. This profile is dependent on the solids re-circulation rate, which could not be measured.

2.5.5 Voidage profile

The voidages calculated from DP measurements at the wall in Figure 2.28 appear to exhibit a two-stage increase with gas velocity. Voidages calculated from DP signals on the traversing probe arm resulted in consistently higher values until the gas flow exceeded 0.47 m/s; at this point both DP measurements showed similar voidages indicative of increased bed homogeneity at gas velocities beyond U_c. The differences in voidages obtained from these DP measurements may be attributed to the location of the traversing probe arm in relation to the solids injection port from the return leg. The column diameter may significantly affect the entrainment flux, thereby influencing the solids

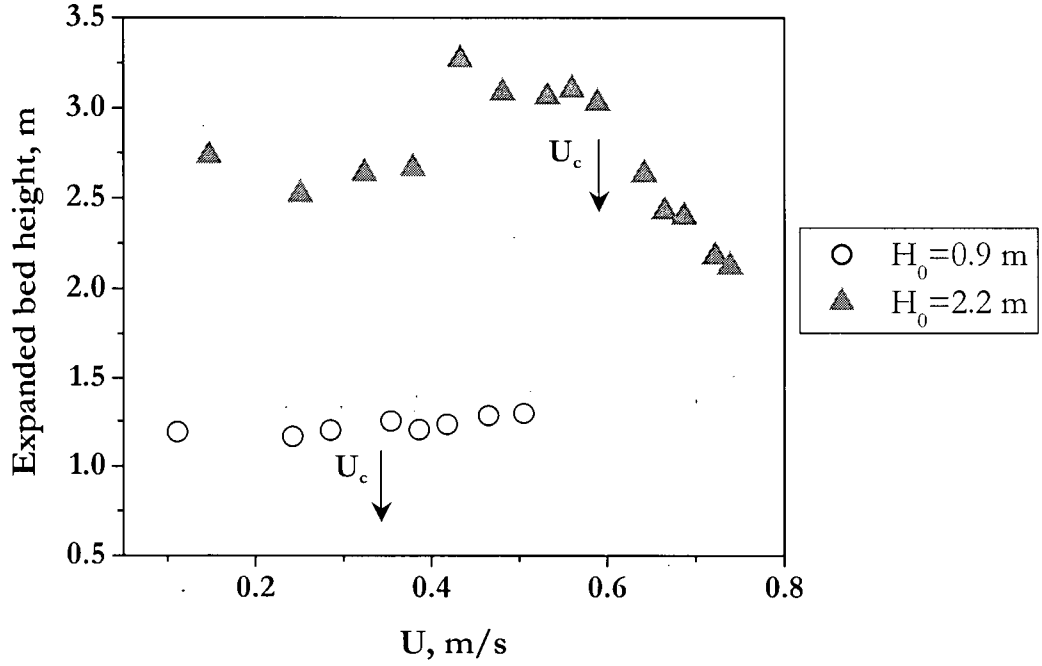

Figure 2.25 Calculated expanded bed height from time-mean gauge pressure profile. D=1.56 m, FCC II.

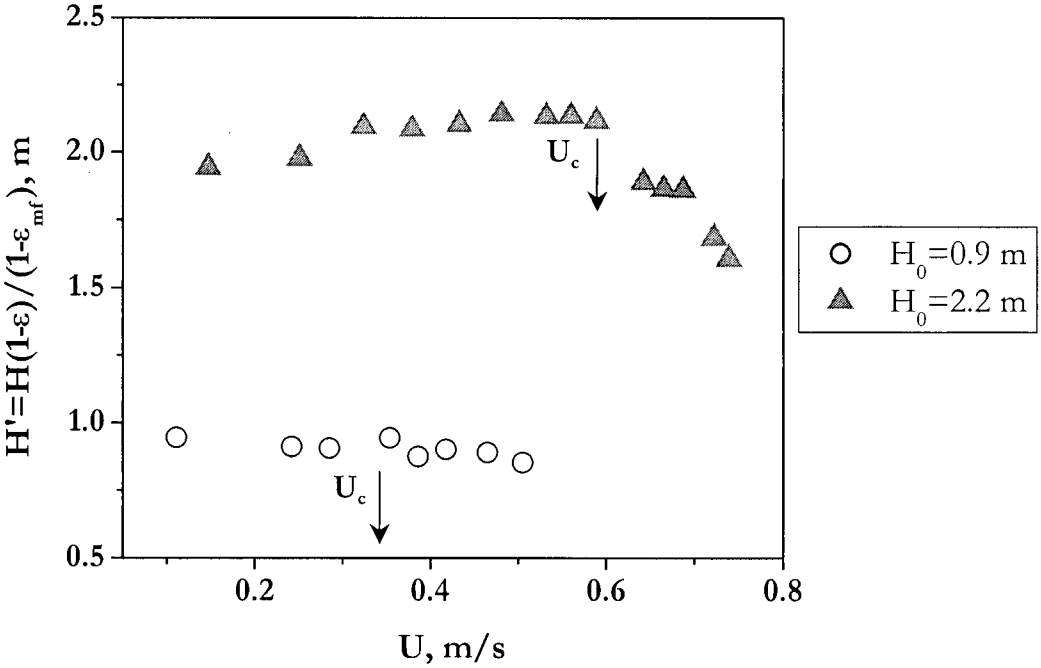

Figure 2.26 Height of dense bed corresponding to voidage at minimum fluidization vs. superficial gas velocity. U_c deduced from gauge pressure signals. D=1.56 m, FCC II.

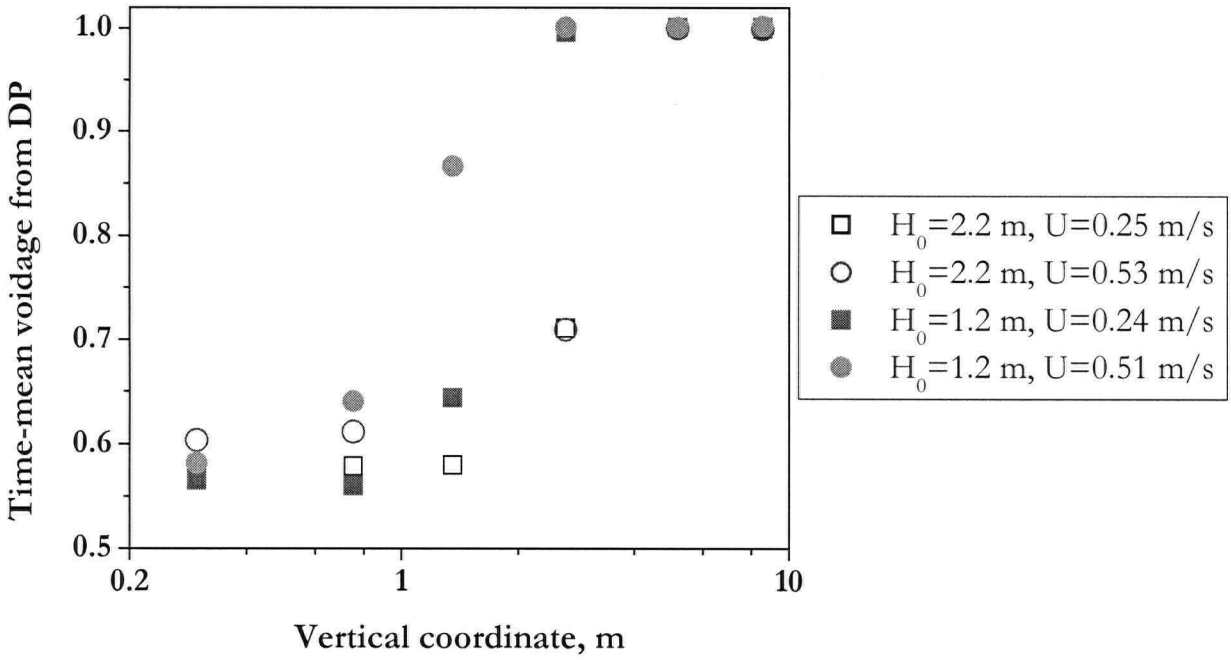

Figure 2.27 Axial voidage profile from time-mean DP measurements. D=1.56 m, FCC II.

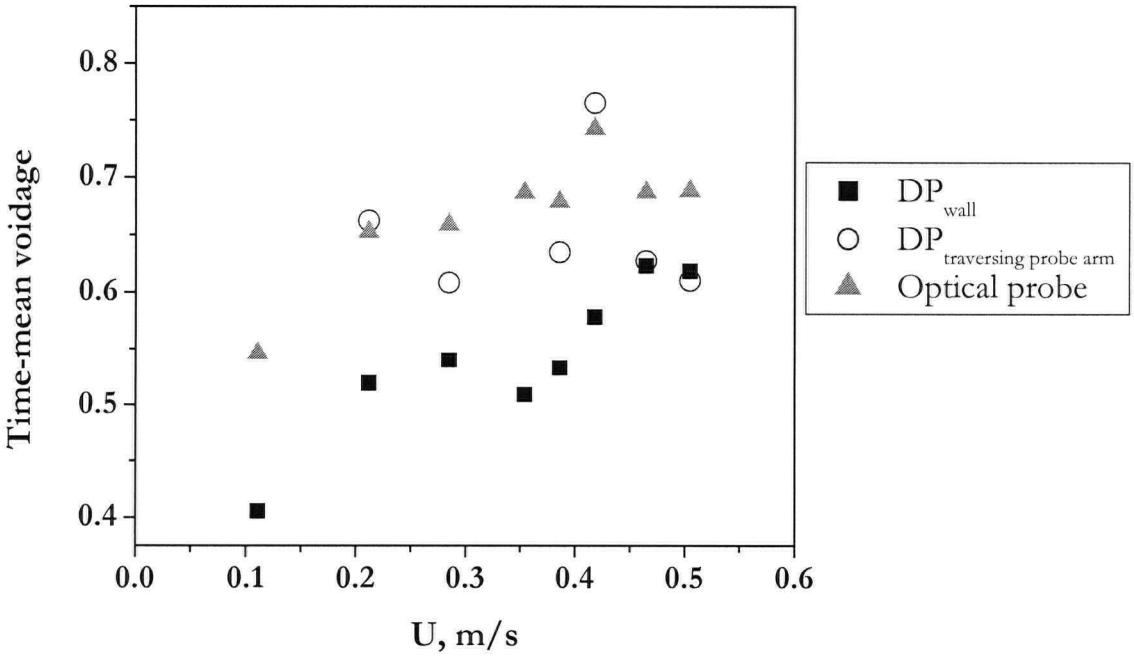

Figure 2.28 Voidage calculated from DP method and optical probe signal. D=1.56 m, z=0.85 m, H_0=0.9 m. All sensors positioned at r/R=0.9. U_c ($\bar{z}$=0.84 m, DP)=0.39 m/s, FCC II.

flow in the region near the return leg. Tasirin and Geldart (1998) reported a decrease in total entrainment rate with increasing column diameter; however, since their largest column size was only 0.152 m, their results may not correctly predict the trend when the column diameter is increased to 1.56 m. Further comparison can be drawn from the dense bed voidages shown in Figure 2.9 (D=0.29 m), Figure 2.19 (D=0.61 m), and Figure 2.28 (D=1.56 m). However, as indicated in Figure 2.9, the bed voidage is influenced by the static bed height. Information on the solids circulation rate, the solids hold-up in the return system, and the in-bed solids inventory must be taken into consideration to compare the effect of scale on bed voidage.

2.6 Column IV: 0.11 m diameter column

A hot model unit study was conducted to investigate the effects of pressure and temperature on the hydrodynamics of turbulent fluidized beds using commercial Catalyst C. The unit, residing at an industrial research facility (contract work), is constructed of stainless steel with a diameter of 106 mm for a height of 2 m above the distributor, with an expansion to a diameter of 212 mm for a further height of 1 m at the top. A schematic is shown in Figure 2.29. A single stage internal cyclone with a return leg OD of 22 mm captures and returns entrained particles. The solids inventory was maintained at 7 kg for all runs. Gas leaving the top of the unit is cooled before being discharged via a filter. A sintered plate is used as the distributor plate with nitrogen as the fluidizing gas. The fluidizing gas is heated to a preset temperature upstream using an electrical heater.

2.6.1 Instrumentation (hot unit)

There are six equally spaced ports on the wall starting 300 mm above the distributor. Nitrogen gas is purged at 0.05 Nm^3/h through a T-junction in order to prevent solids from entering the pressure transducers. Two differential and three gauge pressure transducers are located as shown in Figure 2.29 to measure pressure fluctuations in the hot unit. A Keyence NR-250 data acquisition card acquires data at a rate of 10 Hz for periods of 7 minutes.

2.6.2 Bed expansion (hot unit)

Owing to the limited number of pressure transducers in the hot unit, a second method of analysis was adopted to estimate the expanded bed height. From the time-mean differential pressure drop across a certain interval in the middle of the dense bed, and across another section extending from the lowest pressure tap to a tap in the freeboard, the following equation was used:

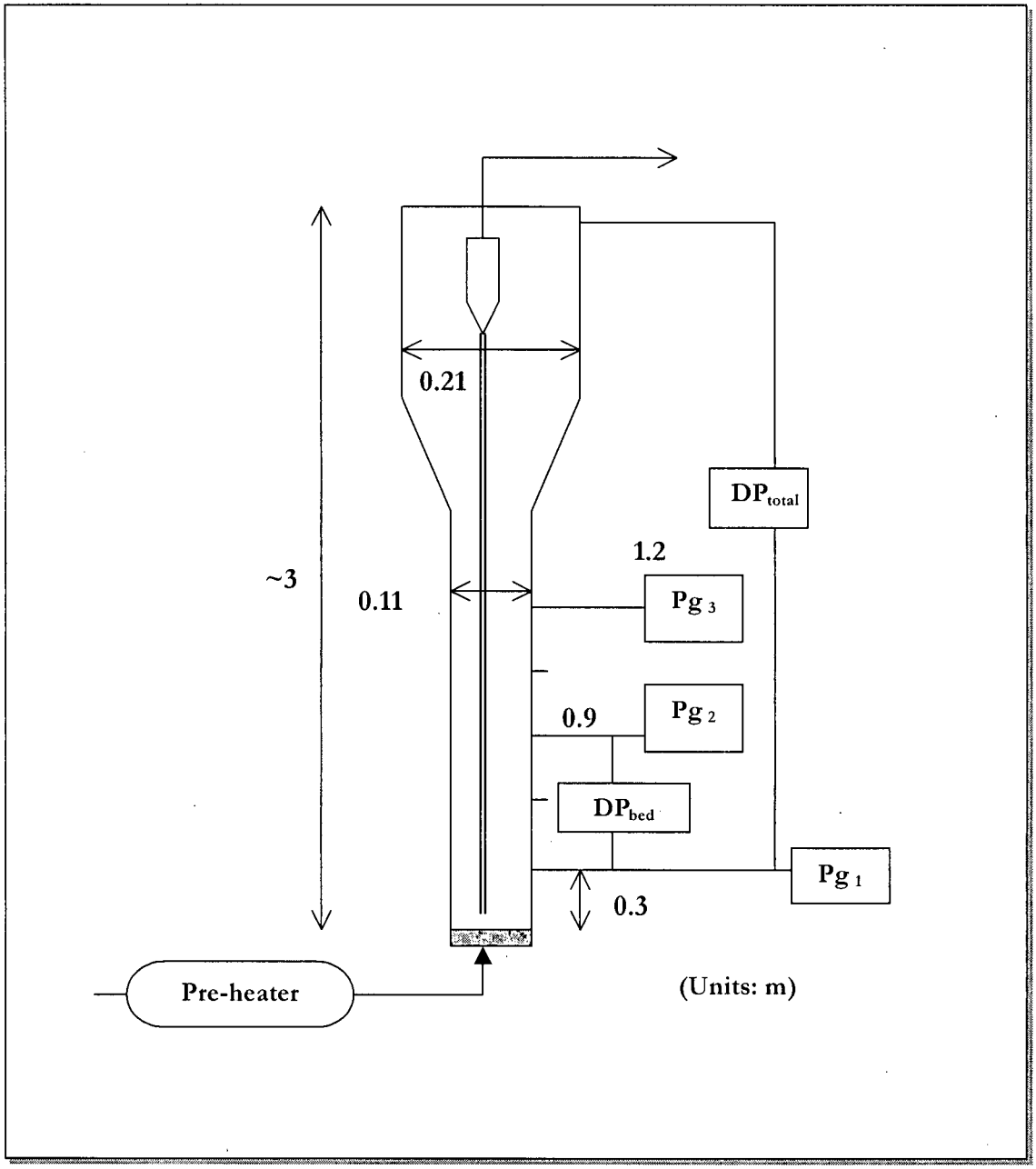

Figure 2.29 Schematic diagram of 0.11 m diameter hot unit. All dimensions are in metres.

$$H = \frac{\Delta P_{total}}{\Delta P_{bed}} \Delta z_{bed} + z_{bottom\ probe} \tag{2.5}$$

Since this method relies on a single pressure drop measurement across the bed, it is much more prone to error than the method based on the gauge pressure measurement profile, as shown in Figure 2.6. However, this is a common method applied in industrial units to estimate the overall bed voidage. Figure 2.30 plots the expanded bed height against superficial gas velocity at room temperature. As the absolute pressure in the vessel increases, the bed expansion ratio increases for the same superficial gas velocity owing to the increase in gas density. Changing the temperature had less effect on the expanded bed height, as indicated in Figure 2.31. The increase in temperature increases the gas viscosity and decreases the gas density. Moreover, the elevated temperatures may affect the role of the hydrodynamic and interparticle forces, as reported for the stability of a fluidized bed at minimum fluidization by Lettieri et al. (2001). Further investigation is required before any conclusions can be drawn.

2.6.3 Bed voidage (hot unit)

The effect of system pressure and temperature on the time-mean bed voidages is presented in Figure 2.32. The results show some increase in voidage with increasing pressure, with voidage being approximately proportional to $P^{0.08}$ for a given superficial gas velocity. With an increase in the absolute pressure of the column, voidage tended to increase with increasing bed temperature as shown in Figure 2.32.

The data are compared with voidage correlations in Figure 2.33. The following voidage correlation by Cai et al. (1989) incorporates a column size effect::

$$\bar{\varepsilon} = \left(0.796 + \frac{8.94 \times 10^{-3}}{D}\right)\left(\frac{Re_p^3}{Ar^2}\right)^{0.0653} \tag{2.6}$$

However, this correlation overpredicts the voidage for both columns, with the trend for column size not consistent with the experimental trend. The empirical correlation of King (1989)

$$\bar{\varepsilon} = \frac{U+1}{U+2} \tag{2.7}$$

gives better predictions. When the difference in gas density due to the effect of pressure and temperature is taken into consideration, the simple correlation of King (1989) underestimated the voidage, as portrayed in Figure 2.34.

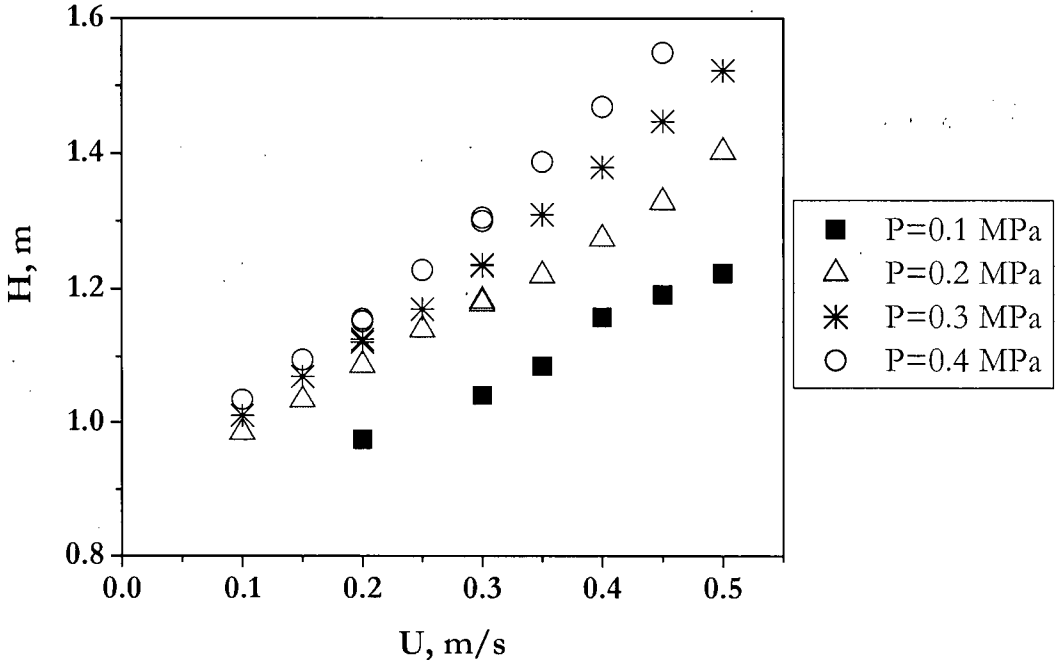

Figure 2.30 Effect of system pressure on expanded bed height at room temperature. D=0.11 m, Catalyst C, H_0=0.7 m.

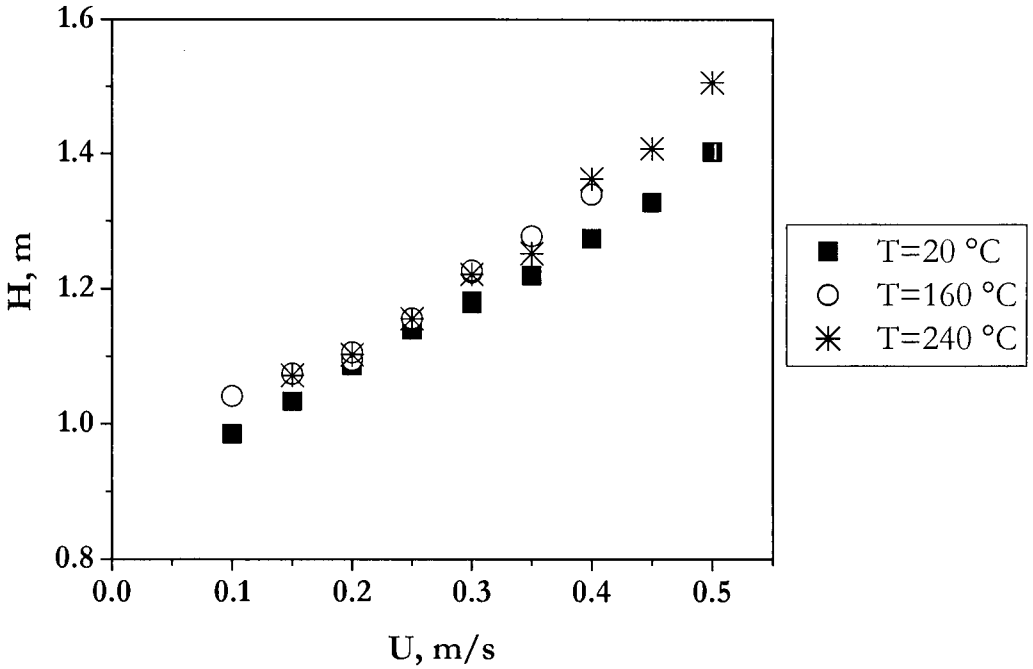

Figure 2.31 Effect of temperature on bed expansion at a system pressure of 0.2 MPa. D=0.11 m, Catalyst C, H_0=0.7 m.

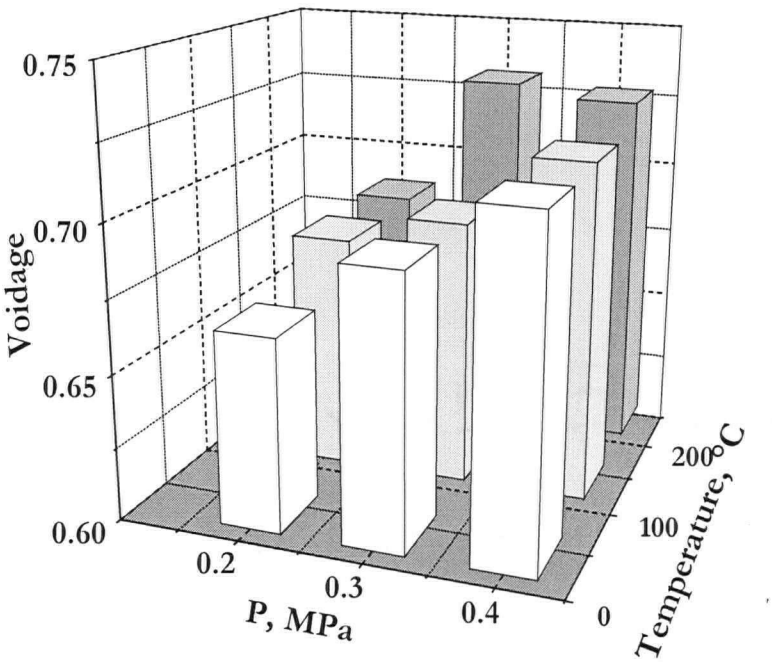

Figure 2.32 Effect of system pressure and temperature on time-mean bed voidage deduced from DP signals. D=0.11 m, U=0.40 m/s, Catalyst C.

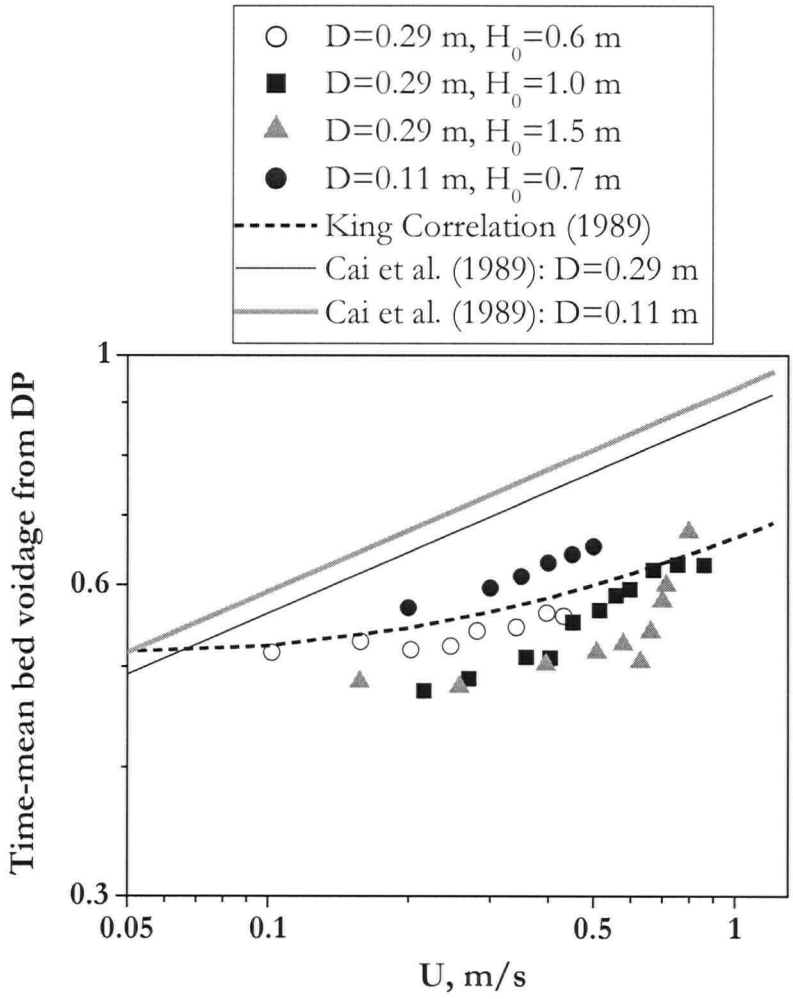

Figure 2.33 Comparison of experimental voidage data with predictions from literature correlations. Catalyst C. Ambient conditions.

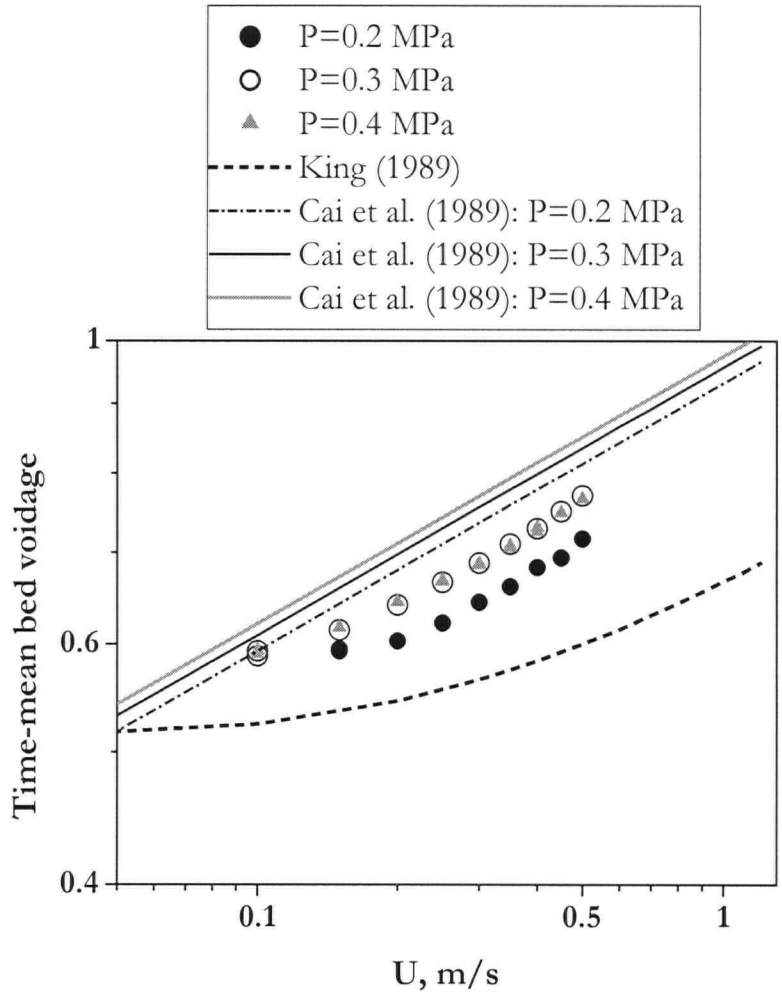

Figure 2.34 Experimental voidage measurement at 240°C compared to correlation predictions. D=0.11 m, H_0=0.7 m, Catalyst C.

2.7 Conclusions

Four different fluidization columns used in this study are described. Macroscopic hydrodynamics were determined based on time-mean pressure measurements. Two different types of catalysts belonging to Geldart Group A were used, with their properties listed in Table 2.1. The operating conditions are summarized in Table A.1 in Appendix A.

- Axial pressure profiles indicated diffuse bed surfaces with higher gauge pressure in the freeboard with increasing superficial gas velocity due to solids entrainment. The solids circulation rate was not controlled for the two smaller diameter columns. For the two larger columns, adjusting the fluidizing air to the loopseal controlled the solids circulation rate, but this rate could not be measured.
- Increasing the initial static bed height changed the bed expansion vs. superficial gas velocity trend. In the 0.29 m diameter fluidization column, flow in the solids return system seemed to affect the overall bed expansion. Occasionally the expanded bed height decreased gradually with increasing U, indicating accumulation of solids in the return leg system. This was only noticed in the 0.29 m unit as the Plexiglas unit allowed visual observations of solids flow, and because of the material of the column, the system was much more susceptible to electrostatic charges which are known to be sensitive to the humidity of the fluidizing air.
- The dense bed height corresponding to voidage at minimum fluidization calculated from the bed pressure drop allowed the characterization of the fluidized bed without the effect of the solids contained in the freeboard and return system in order to isolate the in-bed inventory of the solids. The decrease in the dense bed height corresponded well with the superficial gas velocity at U_c for the 0.29 m diameter fluidization column. However, in the 0.61 m diameter column and in some cases in the 1.56 m diameter column, a gradual decrease in dense bed height was observed without any noticeable change at U_c.
- The modified Richardson-Zaki equation was applied to the bed voidage measurements. However, consistency of the exponents was questionable as the bed voidage was sensitive to the 'smoothness' of operation. Moreover, in a system where the solids circulation rate cannot be controlled, it is difficult to characterize the overall operating conditions. Thus, it was not possible to draw any conclusions.
- Increases in both absolute pressure and temperature caused increases in bed voidage, with pressure having greater influence than temperature. For measurements at ambient pressure and temperature condition, bed voidage was better correlated by the empirical correlation of

King (1989) than other approaches. However, the correlation of Cai et al. (1989) indicated better predictions for increased pressure and temperature, accounted for by the particle Reynolds number and Archimedes number. Further study of the effect of scale is required under high pressure and elevated temperature operating conditions.

CHAPTER 3

REGIME TRANSITION AND SCALE EFFECT

3.1 Regime transition

Regime transition from bubbling to turbulent fluidized flow has been based on visual observation, bed expansion, voidage fluctuations, and pressure fluctuations. A still photograph of FCC particles fluidized in a two-dimensional bed in Zenz and Othmer (1960) shows a breakdown of bubbles at a gas velocity of 0.91 m/s (3 ft/s). A number of reports have been published in the past two decades analyzing definitions of the turbulent fluidized flow regime (see reviews such as Bi et al., 2000; Smolders and Baeyens, 2001). As discussed by Grace (2000), this flow regime has adopted the name 'turbulent' from the chaotic appearance of its voids movement, and is not necessarily based on a sound description of the physics of the phenomenon. Consequently, this regime has been subject to much controversy and there remains no clear definition of its hydrodynamic structure. In gas-solid fluidization, there exists a transitional regime between bubbling and fast fluidization, i.e., between the superficial gas velocity at which a maximum bubble size is attained and the transport velocity at which the dilute phase transport state is reached. The competing mechanisms of increasing homogeneity due to the break-up of bubbles/voids, and increasing heterogeneity owing to the formation of clusters, determines where the transition, U_c, lies.

In investigating the transition from bubbling to turbulent fluidization, Yerushalmi and Cankurt (1979) identified two transition velocities: U_c, the superficial gas velocity at which the pressure fluctuations reach a maximum; and U_k, the velocity at which the pressure fluctuations begin to level off, as depicted in Figure 3.1. One point of controversy is how the 'transition velocity' should be defined. As summarized by Rhodes (1996), early work contributing to the definition of the flow regime was ambiguous owing to the lack of reporting important details, such as the measurement method of U_c, and the solids circulation rate.

Kehoe and Davidson (1970) reported greater homogeneity of the bed through breakdown of distinct bubbles as an important characteristic of the onset of turbulent fluidization. However, Abed (1984) demonstrated that the hydrodynamic structure of the bed in the turbulent regime is radially non-homogeneous.

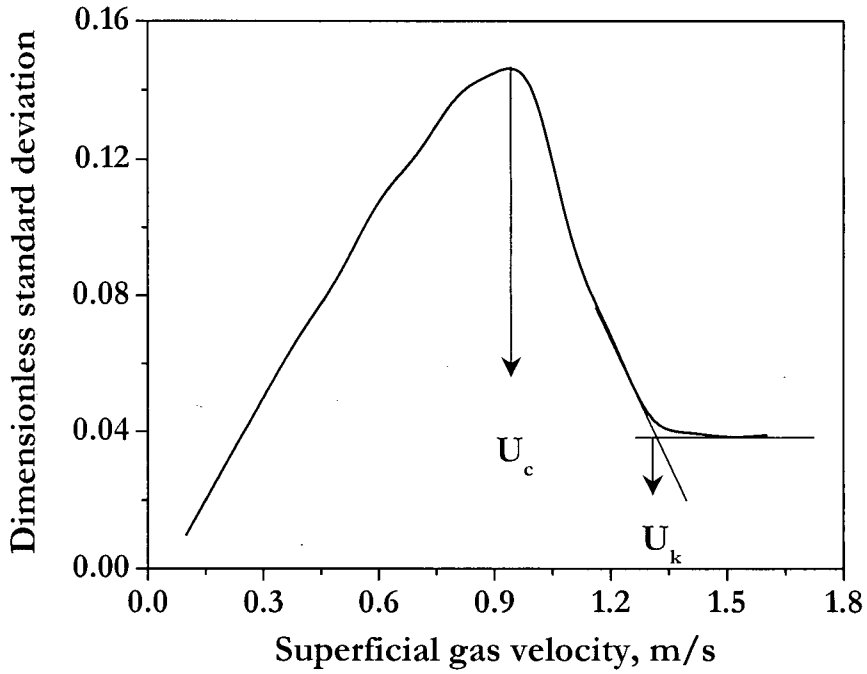

Figure 3.1 Definitions of transition velocities U_c and U_k based on standard deviation of pressure fluctuations. Adapted from Yerushalmi and Cankurt (1979).

The factors contributing to the confusion that exists even today are mainly: 1) lack of details regarding the method by which the regime was identified; and 2) no clear agreement between researchers on what constitutes the turbulent flow regime. Furthermore, the issue of whether U_c or U_k should demarcate the onset of the turbulent flow regime has gained more attention than understanding the hydrodynamic structure of the flow regime once it has been reached. The different schools of thought regarding this transition can be categorized into two classes, as suggested by Sun and Chen (1989): 1) it is related to gas-solid contact characteristics in the fluidized bed; or 2) it is based on the axial expansion and entrainment characteristics of the whole reactor. These two interpretations are discussed further in this chapter; however, the reason for clarifying the definition needs to be addressed first. When designing a gas-solid fluidized bed reactor, one requires a reactor model which is capable of coupling the contact mode and the kinetics (Levenspiel, 2002). The contact mode, i.e., the hydrodynamics, of the fluidized bed dictates key parameters such as phase hold-up, velocity profiles, mixing and residence time distribution. It is critical to know when the transition to the turbulent regime occurs with respect to reactor modelling. The overall reactor model depends on the kinetics and the contact mode, which in turn depend on the velocity, solids circulation rate, and operating conditions, including pressure and temperature. In other words, if the gas velocity is being increased from the bubbling fluidized flow regime, one needs to be able to predict the velocity at which breakdown of the two-phase theory occurs. With this in mind, the following summarizes the reported characteristics and perceived definitions in the area of turbulent fluidization flow regime in the two categories, followed by the author's experimental findings.

The first types of characterization of the turbulent fluidized bed relate to the local contacting characteristics of the bed. The most noticeable change in the bed in going from the bubbling to the turbulent flow regime is the break-up of bubbles. This phenomenon is well documented from local voidage measurements using capacitance and optical fiber probes (Lanneau, 1960; Massimilla, 1973; Lancia et al., 1988). The condition at which bubble splitting becomes prevalent throughout the bed depends on particle properties and operating conditions. The bubble break-up characterized by a decrease in pressure fluctuations is the basis in marking the transition using pressure fluctuation measurements. Sun and Chen (1989) correlated U_c values based on the notion that once a gas velocity has reached the point where maximum bubble size is attained just above the distributor, bubble splitting will be dominant throughout the bed. As summarized by Brereton and Grace (1992), both differential and gauge pressure fluctuations have been analyzed in terms of standard deviation, average fluctuations, peak-to-peak, and r.m.s. about mean, and these can give different

values. Through the statistical analysis of pressure fluctuations plotted against superficial gas velocity, a maximum point, denoted as U_c, is attained, indicating a change in the bed structure. However, it was not until the study of Bi and Grace (1995) that the discrepancies between reported U_c values from pressure fluctuations were analyzed in terms of the effect of measurement methods.

U_c is generally considered to be the superficial velocity at which the onset of the turbulent fluidized flow regime occurs, when distinct bubbles start splitting at high frequency resulting in smaller voids and a decrease in the standard deviation of the pressure fluctuations. Beyond U_c, there is some indication that the fluidized bed can no longer be modelled by simple two-phase models like those applied to bubbling fluidized beds (see Foka et al., 1996).

On the other hand, some researchers have concentrated on the axial solids distribution in interpreting what constitutes a transition. According to Geldart and Rhodes (1985), the transition is due to the two competing mechanisms of increasing bubble size and bed depth, and decreasing bed height because of greater entrainment of particles as the gas velocity is increased. U_k has been interpreted (Yerushalmi and Cankurt, 1979) as the gas velocity corresponding to the onset of the turbulent flow regime where solids rearrange into distinct clusters, with strong interaction between the dense and lean phases. Moreover, U_k obtained from the pressure fluctuations is generally taken as the gas velocity at which the pressure fluctuations reach a plateau. The analysis of Geldart and Rhodes (1985) suggested that U_k is, in fact, the gas velocity at which the bed surface falls below the top differential pressure tap used to indicate the bed surface. Regardless of whether or not the pressure tap is submerged in the bed, the increase in gas velocity results in a decrease in the time-mean differential pressure as a result of the expansion of the bed. The transition velocity, U_k, is reported to be dependent on the solids return efficiency (i.e., cyclone efficiency), measurement technique, measurement location, and particle properties. For a system with an efficient solids return system, U_k is not reached until a much higher gas velocity (Geldart and Rhodes, 1985). Thus, it has been criticized as having no physical meaning and as only an experimental artefact due to the use of a differential pressure transducer (Chehbouni et al., 1994).

Horio et al. (1992a) examined the inflection point of $dz/d\varepsilon$ to confirm the finding of Yerushalmi and Cankurt (1979) that the transport velocity, U_{tr}, is the transition gas velocity between turbulent and fast fluidization. By analyzing the local voidage measured by optical probes, they concluded that

the clusters in the turbulent regime were not completely suspended by the gas. Schnitzlein and Weinstein (1988) suggested that the levelling-off of pressure fluctuations coincided well with the levelling-off of the bed voidage. Some researchers (see Bi and Fan, 1992) have supported U_k as the onset of transport. In that case, the range between U_c and U_{tr} ($\sim U_k$) should constitute the turbulent fluidization flow regime. Note that this second method of interpretation is based on the time-averaged distribution of solids, which neglects the complex dynamic behaviour of the fluidized bed (Zijerveld et al., 1998).

Some questions that arise from a mechanistic understanding of the phenomena relate to:

- physical meaning of U_k;
- significance of clusters;
- competing mechanisms of increase in expanded bed height from increased gas flow vs. decrease in bed inventory due to significant entrainment.

The change in local and macroscopic structures of the bed in passing through the turbulent regime can be viewed as starting from U_c, with a gradual transition from the continuous phase being a dense phase containing dispersed voids to the continuous phase being the gas phase with dispersed solid clusters. This transitional regime, called the turbulent fluidization flow regime, exhibits unique hydrodynamic features resulting in significant advantages when fluidized beds operating in this mode are used as reactors.

3.2 Observation of current knowledge and its gaps

Pressure fluctuations in fluidized beds depend on particle properties, bed geometry, flow conditions, pressure and temperature conditions (M'chirgui et al., 1997). Numerous studies have used pressure fluctuations to indicate the quality and/or flow regime of fluidization (e.g. Bai et al., 1996; Schouten and van den Bleek, 1998; Xu et al., 1998). From an industrial point of view, the use of simple pressure measurements in the reactor to determine the fluidization quality or regime is convenient and attractive.

3.2.1 Regime transition

Transition from the bubbling to the turbulent regime has been commonly characterized by the transitional velocity, U_c, defined as the velocity at which the standard deviation of pressure fluctuations, obtained with either single or double probes measuring either gauge or differential

pressure, reaches a maximum as the superficial gas velocity is increased. However, due to the effect of the measurement method on U_c, it has been difficult to compare reported values in a standardized manner as pointed out by Brereton and Grace (1992) and Bi and Grace (1995). Pressure fluctuations in fluidized beds are considered to originate from multiple physical phenomena such as bed oscillations and the formation/rise/eruption of voids (Bi et al., 1995). Gauge pressure measurements from a single probe reflect more global phenomena in the bed as opposed to the more localized phenomena measured by the dual (differential pressure) probes. By using closely spaced dual probes, higher frequency pressure waves reflecting the void behaviour resulting from their formation, coalescence, eruption or rising may be studied. In the latter measurements, a decreasing standard deviation of the differential pressure fluctuations denotes a more homogeneous bed. According to this interpretation, $U_{c,}$ indicates where the bed starts to become more homogeneous as the gas velocity increases.

However, considerable scatter in data has been reported, making it difficult to predict the transition velocity with confidence for a given geometry, operating conditions and solids characteristics. Moreover, reported transition velocities are column- and solids-specific.

3.2.2 Scale effect

Although they are utilized in a number of industrial processes, there are only a few reported studies of scale-up effects in turbulent fluidized beds. In the bubbling flow regime, conversion tends to decrease due to inefficient gas-solid contacting from increased void size when the column diameter is increased. In order to alleviate this problem, Edwards and Avidan (1986) ensured bubble suppression by increasing the proportions of fine catalyst particles. Monitoring the local void behaviour while increasing the column diameter should provide invaluable insight into how units can be scaled up without loss of conversion or yield. The effect of column diameter on U_c provides a convenient benchmark for designing new reactors. Cai (1989) reported, after using Geldart A and B particles in columns of diameter 0.05, 0.14, 0.28 and 0.48 m, that U_c was unchanged with increasing column diameter beyond a certain scale. Further hydrodynamic investigation of this trend may clarify the relationship between homogeneity of the bed and U_c.

3.3 Experimental approach

For the remainder of this chapter, the transition velocity, U_c, refers to the superficial gas velocity at which the maximum standard deviation of pressure fluctuations is attained. Reference to local

voidage fluctuations is made where deemed necessary. However, in view of the interest in establishing a general correlation for U_c and its applicability to industrial operating conditions, pressure fluctuations are the main focus. The standard deviation is calculated according to:

$$\sigma = \sqrt{\frac{n\sum x^2 - (\sum x)^2}{n(n-1)}} \tag{3.1}$$

where x is the instantaneous value and n the number of determinations. For all experimental measurements pertaining to the determination of transition velocity through pressure fluctuations, a sampling frequency of 100 Hz and a sampling duration of 100 s were used for consistency. An FFT analysis of the pressure signals revealed that most peaks observed were within 10 Hz. Thus, a sampling frequency of 100 Hz was considered sufficient. Sampling durations of 100 s and 200 s were compared and these indicated at most a 1.9 % difference in the standard deviation of pressure fluctuation for steady-state operations. Thus, the sampling frequency and duration were considered acceptable.

Note that the standard deviation of pressure fluctuation shown in Figure 3.2 indicates a rather broad maximum, i.e., a transition which was not at all sharp. This was especially so in larger diameter columns. The error involved in deducing the maximum point, indicative of U_c, through curve fitting is investigated in Section 3.3.2, while alternative ways of deducing U_c are examined in Chapter 6.

The study conducted in this work pertains to bubbling fluidized beds and the transition to the turbulent flow regime. As exemplified in Figure 3.2, bed density reaches a plateau before steadily deceasing at $U \approx 1$ m/s. The standard deviation from differential pressure (DP) signals within the bed indicates a gradual transition. Moreover, when the bed density from a DP cell with one port located above the expanded bed height is plotted against U, Figure 3.3, it shows a sudden drop at around U=0.8 m/s, followed by a plateau. The physical meaning of this drop is related more to the location of the bed surface rather than to any change in bed dynamics. When the local voidage fluctuation is plotted, as shown in Figure 3.4, the change occurs around U=1.1 m/s. This demonstrates that different definitions of the transition velocity can result in values for this parameter.

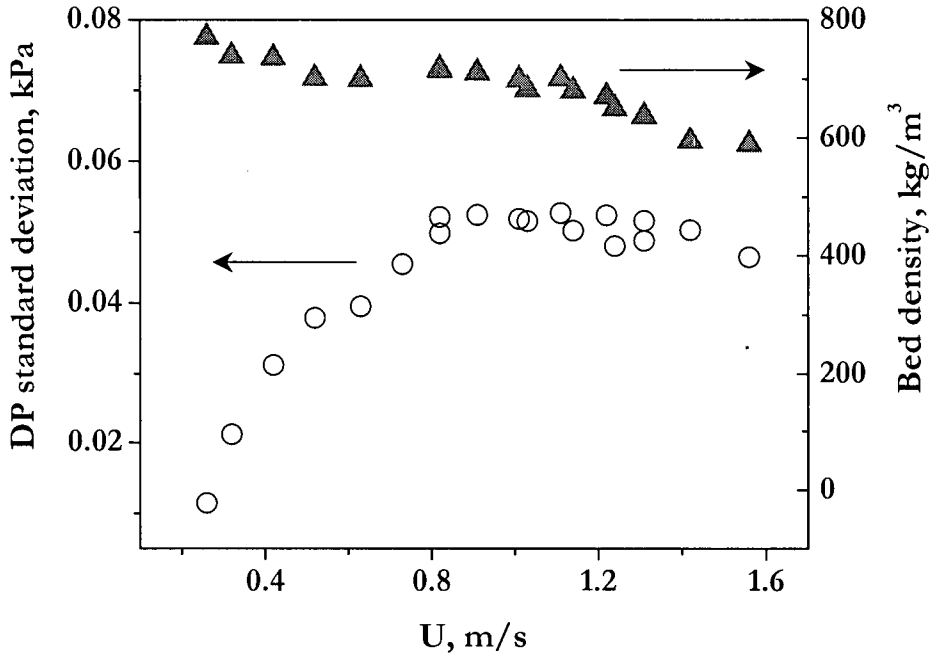

Figure 3.2 Typical standard deviation of pressure fluctuations and bed density measurements. Pressure fluctuation measurement: $\bar{z}$ =1.50 m, Δz =0.10 m. Bed density: $\bar{z}$ =1.14 m, Δz =0.82 m. D=0.61 m, FCC IV, H=1.67~1.77 m.

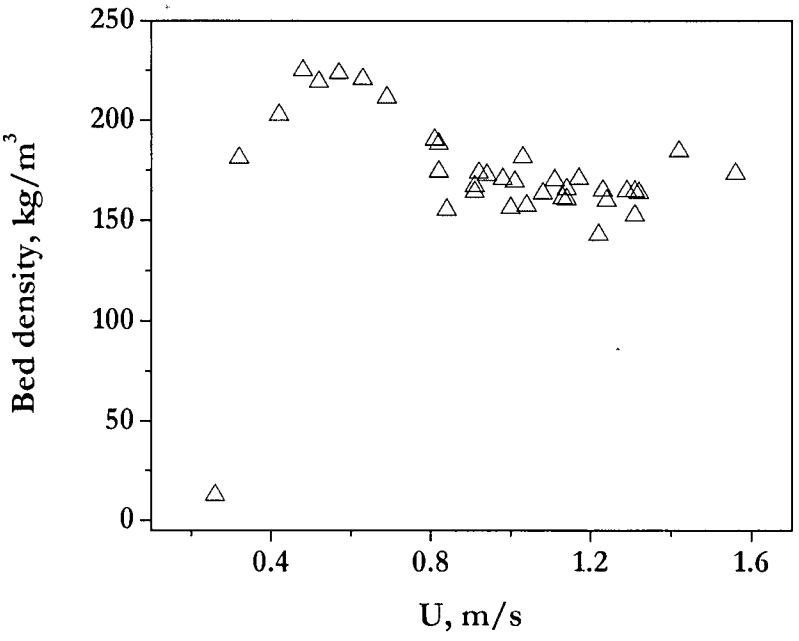

Figure 3.3 Bed density measurements. $\bar{z}$ =1.85 m (z_{lower}=1.55 m, z_{upper}=2.14 m), Δz =0.59 m, D=0.61 m, FCC IV, $\bar{d}$ =98 μm. H=1.67~1.77 m.

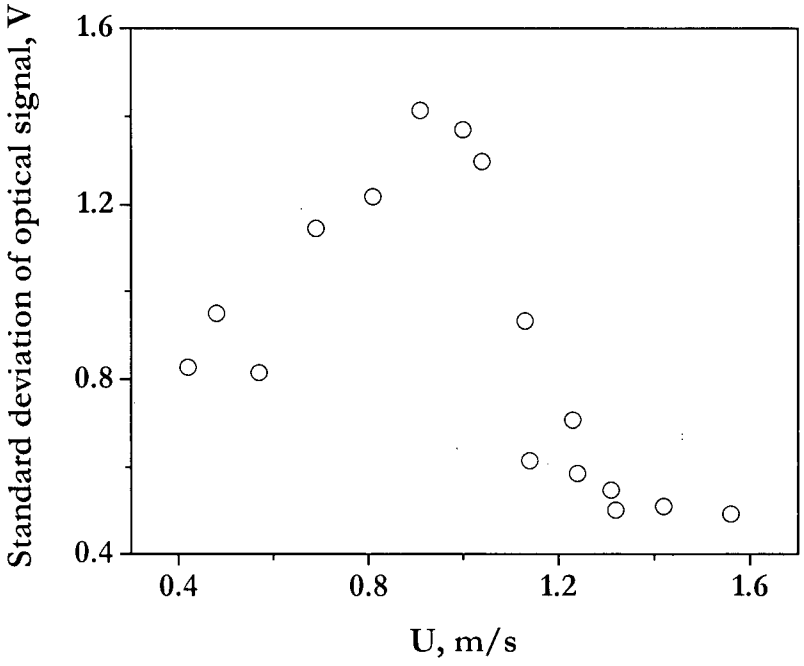

Figure 3.4 Standard deviation of optical fiber voidage probe signal. z=1.55 m, r/R=0.09, D=0.61 m, FCC IV, H=1.67~1.77 m.

3.3.1 Pressure measurement method

To date, most predictive correlations are of the general form:

$$Re_c = \frac{\varrho_g U_c d_p}{\mu_g} = a\, Ar^b \tag{3.2}$$

where

$$Ar = \frac{\varrho_g (\varrho_p - \varrho_g) g\, d_p^3}{\mu_g^2} \tag{3.3}$$

Fitted values of a and b have been tabulated by Horio (1997). Correlations of this form suggest that U_c is solely influenced by the gas and particle properties, with pressure and temperature also entering through their influence on gas properties.

As summarized by Bi et al. (2000), the factors that affect U_c include:

- probe location
- type of transducer
- particle size distribution
- solids circulation rate
- pressure probe resistance
- DP pressure port spacing
- static bed height
- column diameter
- particle characteristics
- operating conditions (pressure and temperature)
- internals (e.g. baffles)

A number of these have been examined (Bi and Grace, 1995). In this chapter, a further study is conducted to determine the role of other factors such as probe location, static bed height and column diameter.

3.3.2 Error analysis

As shown in Figure 3.2, the plot of standard deviation of pressure fluctuations vs. superficial gas velocity does not necessarily produce sharp peaks which can be identified unambiguously as U_c. U_c was determined through a second-order polynomial curve fitting of the data, followed by solving for the maximum. The confidence level from a purely statistical point of view was examined to obtain

error bars on the curve fit of data. This procedure was recommended by the UBC Statistical Consulting and Research Laboratory (SCARL file #01-01-004).

For the number of superficial gas velocity data, I, let y_i be the value of the standard deviation of the pressure fluctuation corresponding to the i^{th} gas velocity x_i. Through the quadratic polynomial regression model, the regression parameters are estimated from the data, and expressed as:

$$\hat{y} = \hat{\beta}_0 + \hat{\beta}_1 x + \hat{\beta}_2 x^2 \tag{3.4}$$

The value of x which maximizes $\hat{y}$ is obtained by differentiating equation (3.4) with respect to x and setting the result to 0, giving

$$x_{max} = -\frac{\hat{\beta}_1}{2\hat{\beta}_2} \tag{3.5}$$

Through the *Delta* method, an approximation of the variance of x_{max} is expressed as:

$$\hat{var}(x_{max}) = \left(\frac{1}{4}\right)\left(\frac{\hat{\beta}_1}{\hat{\beta}_2}\right)^2 \left(\frac{var(\hat{\beta}_1)}{\hat{\beta}_1^2} - \frac{2\,cov(\hat{\beta}_1, \hat{\beta}_2)}{\hat{\beta}_1 \hat{\beta}_2} + \frac{var(\hat{\beta}_2)}{\hat{\beta}_2^2}\right) \tag{3.6}$$

The statistical software JMPIN ver. 4.0.3 from SAS Institute was used to perform the regression and to estimate the parameters. Covariance was calculated from:

$$cov(\hat{\beta}_1, \hat{\beta}_2) = corr(\hat{\beta}_1, \hat{\beta}_2) * s.e.(\hat{\beta}_1) s.e.(\hat{\beta}_2) \tag{3.7}$$

The statistic

$$z = \frac{x_{max}}{\sqrt{\hat{var}(x_{max})}} \tag{3.8}$$

has an approximately standard normal distribution. Hence the approximate confidence interval for x_{max} can be expressed as:

$$(x_{max} - z_{\alpha/2}\sqrt{\hat{var}(x_{max})},\ x_{max} + z_{\alpha/2}\sqrt{\hat{var}(x_{max})}) \tag{3.9}$$

Through this statistical method, the 95% confidence interval for the example in Figure 3.2 was calculated to be (1.07 m/s, 1.17 m/s). From Figure 3.4, it is clear that this range coincides well with the superficial gas velocity at which the local voidage fluctuation drops precipitously.

The error associated with curve fitting was approximately 4 to 7%. Those results with errors greater than 10 % of the predicted U_c suggested standard deviation curves too broad to determine maxima, and thus were discarded.

Van Ommen et al. (1999) considered factors affecting the accuracy of probe-transducer systems in gas-solid fluidized beds, and provided guidelines with respect to probe diameter and length for minimum distortion of pressure signals. For the frequencies of interest, they recommended that the probe diameter be between 2 and 5 mm, and transducer volumes be 2500 mm^3 or less. Care was taken in this study to minimize the transducer volume and probe length. The majority of transducers used in the UBC column had a tube diameter of 3.2 mm and length of about 0.1 m (equivalent to a transducer volume of ~810 mm^3), except for the transducers connected to the freeboard, which had lengths of around 0.3 m. The maximum volume encountered in this study was for a gauge pressure (AP) cell mounted at the end of a traversing probe arm at CSIRO in order to obtain pressure measurements at the centre of the 1.56 m diameter column. The calculated volume in this case was approximately 6700 mm^3.

Wire mesh and sintered filters were used at UBC and CSIRO, respectively, at the tip of the pressure probe to prevent FCC particles from entering the transducers. These filters inevitably caused some dampening of the pressure signals. It was assumed that the signal frequencies were linearly filtered, and thus had no affect on the location of the maximum standard deviation with respect to superficial gas velocity.

Fluctuations of the fluidizing air flow, supplied by the Roots blower at UBC, as a result of the blower performance and temperature variations in the feed line were estimated to cause pressure fluctuations between 0.5 to 3.6 % of the mean.

3.4 Results

3.4.1 Effect of axial probe location and static bed height on U_c

The effect of the axial probe location on U_c in the 0.29 m diameter column is depicted in Figures 3.5 and 3.6 for DP and AP, respectively. As indicated, U_c deduced from DP is quite sensitive to the axial position of the probe, as opposed to those from AP, which show very similar maxima. The difference in U_c obtained from differential vs. gauge pressure measurements is due to their reflecting local and global phenomena in the bed, respectively, as noted above. The trend confirms the findings of Bi and Grace (1995), and is extended in Figure 3.7, illustrating the effect of probe location as well as static bed height.

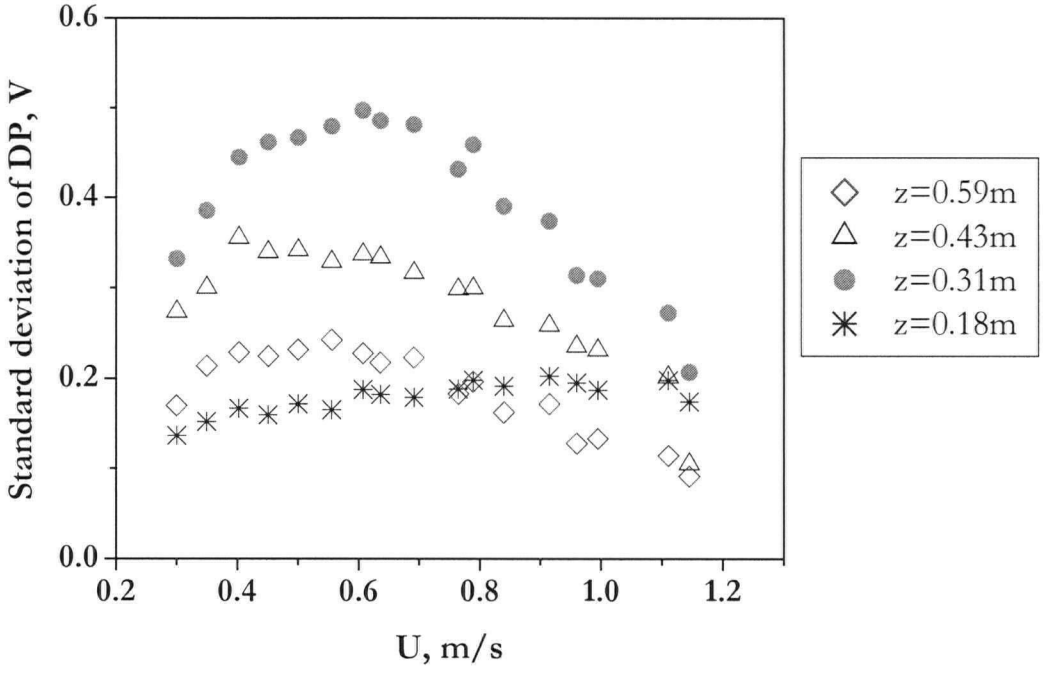

Figure 3.5 Typical plot of standard deviation of DP fluctuations vs. U. D=0.29 m, H_0=0.60 m, FCC I. Δz=0.064 m for z=0.18, 0.31, 0.43 m; and Δz=0.13 m for z=0.59 m DP port locations.

Figure 3.6 Typical plot of standard deviation of gauge pressure fluctuations vs. U. D=0.29

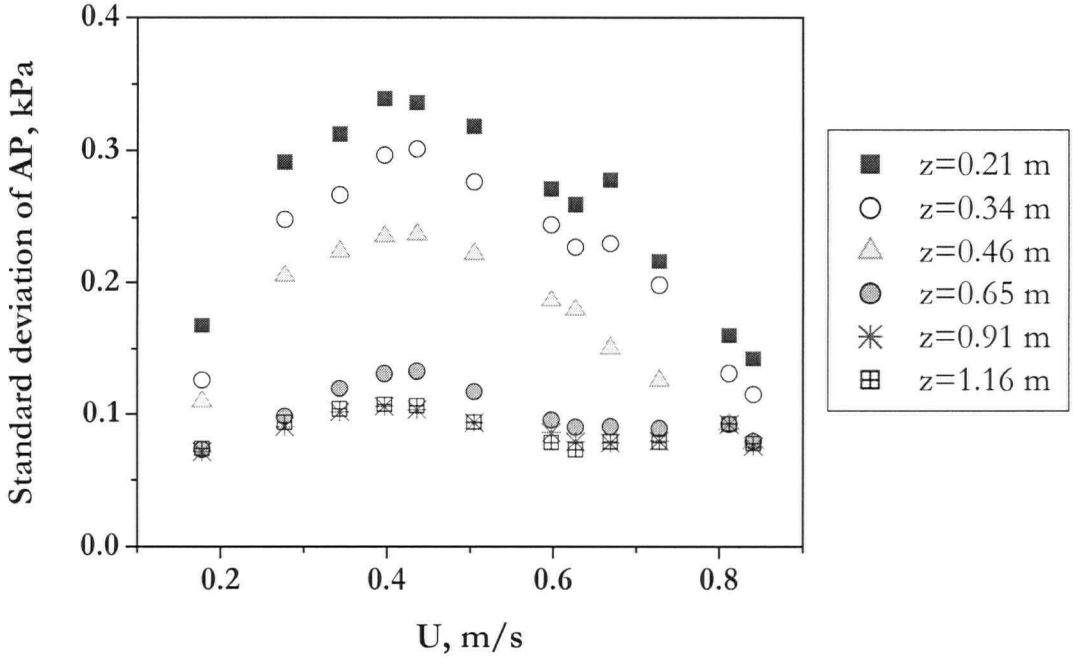

m, H_0=0.51 m, FCC I.

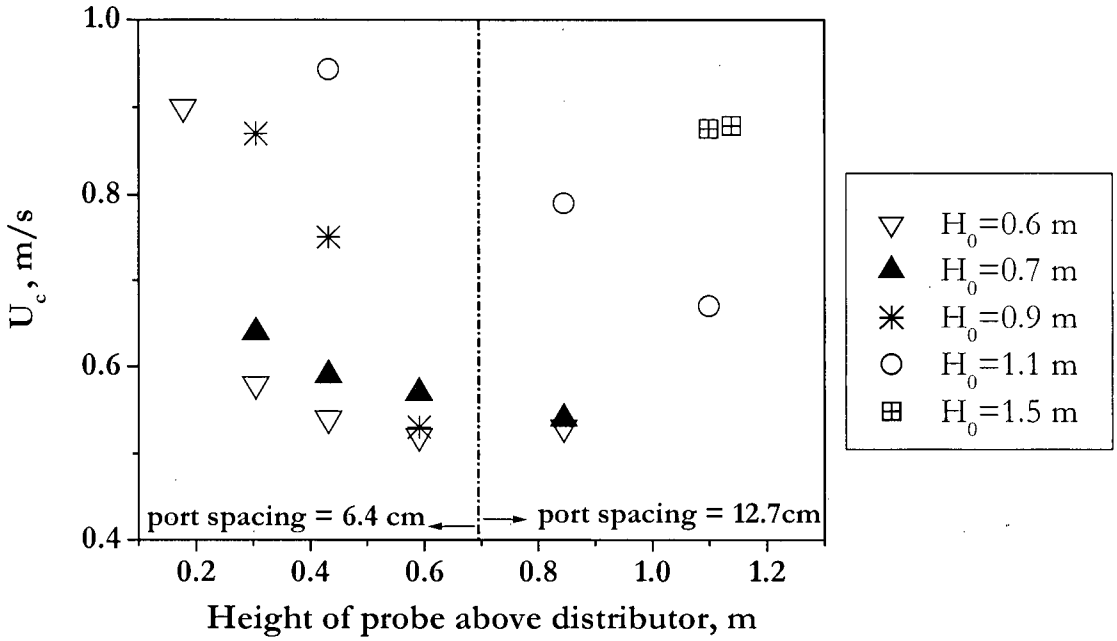

Figure 3.7 Effect of pressure port location on U_c from DP signals. D=0.29 m, FCC I.

It can be seen that U_c values obtained from pressure fluctuation measurements are influenced by local phenomena in the fluidized bed, and that the break-up of voids starts from the top of the expanded bed, as indicated by the decreasing U_c deduced from probes at higher elevations.

From these findings, it is strongly recommended that when reporting U_c, the type of pressure transducer, location of probes and static bed height be specified. Moreover, since U_c deduced from gauge pressure signals seems to reflect the overall change in a fluidized bed, it is simpler to compare U_c from gauge pressure signals for the reason mentioned above. The effect of static bed height on U_c measured by gauge pressure signals is shown in Figure 3.8. It has been reported that U_c measured by gauge pressure signals is unaffected by the H/D ratio providing that it is above 1 (Cai, 1989) or 4 (Grace and Sun, 1991) for FCC particles. The trend is certainly represented in Figure 3.8, where at H/D ~ 3, U_c becomes less sensitive to the aspect ratio, H/D.

3.4.2 Effect of column diameter on U_c

Reliable knowledge about the effect of column diameter on U_c is important to the design and operation of high-velocity fluidized bed reactors. Cai (1989) employed Geldart A and B particles in four columns of diameter 0.05 to 0.48 m, and reported that U_c becomes independent of column diameter beyond a certain diameter. Based on Jin et al. (1986), his data were correlated by

$$\frac{U_c}{\sqrt{gd_p}} = \left(\frac{\mu_{g20}}{\mu_g}\right)^{0.2}\left[\left(\frac{0.211}{D^{0.27}} + \frac{2.42\times10^{-3}}{D^{1.27}}\right)^{\frac{1}{0.27}}\left(\frac{D}{d_p}\right)\left(\frac{\varrho_p - \varrho_g}{\varrho_g}\right)\left(\frac{\varrho_{g20}}{\varrho_g}\right)\right]^{0.27} \quad \text{[D in m]} \quad (3.10)$$

This correlation accounts for the effects of temperature and pressure up to 440°C and 600 kPa, respectively.

Sun and Chen (1989) proposed a correlation for U_c based on the maximum bubble diameter.

$$U_c = 1.74 d_p^2\left(\frac{\varrho_p - \varrho_g}{\varrho_g}\right)^2\left[\frac{\left(\frac{\varrho_p}{\varrho_p - \varrho_g}\right) - \varepsilon_{mf}}{1-\varepsilon_{mf}}\right]^2 \frac{g^{0.5}}{z_c^{1.5}} + U_{mf} \quad (3.11)$$

where

$$z_c = 2.25\sqrt{\frac{0.6D}{d_{b,max} + 0.6D}}\cdot d_{b,max} \quad (3.12)$$

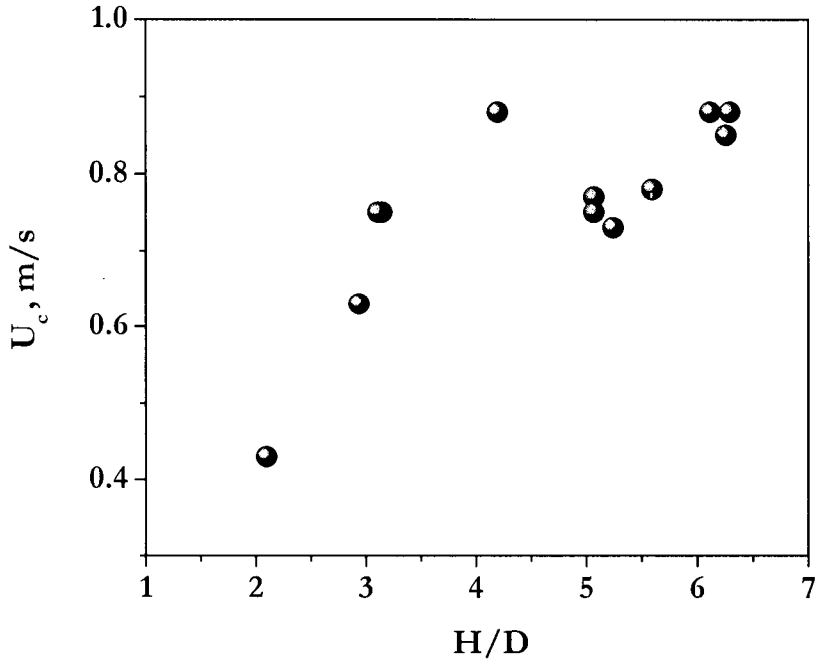

Figure 3.8 Effect of aspect ratio H/D on U_c from gauge pressure signals. D=0.29 m, FCC I.

and
$$\frac{d_{b,max}}{d_p} = 1.32\left(\frac{\varrho_p - \varrho_g}{\varrho_g}\right)\left[\frac{\frac{\varrho_p}{\varrho_p - \varrho_g} - \varepsilon_{mf}}{1-\varepsilon_{mf}}\right] \tag{3.13}$$

The correlation was based on Group A particles fluidized in a column of diameter 0.8 m.

The following correlation suggested by Chehbouni et al. (1995a) is based on experimental data for Group A (FCC) and Group B (sand) particles in 0.082 and 0.20 m diameter columns:

$$Fr_c = \frac{U_c}{\sqrt{gD}} = 0.463\ Ar^{0.145} \tag{3.14}$$

However, none of these correlations has been validated for column diameters exceeding 0.8 m. Existing correlations are overwhelmingly derived from experiments conducted in laboratory-scale fluidized beds operating at atmospheric temperature and pressure, conditions remote from those of most industrial-scale fluidized beds.

Figure 3.9 compares predictions from various correlations with experimental results obtained in columns of diameter 0.29, 0.61 and 1.56 m. Equation 3.14 does not produce a comparable U_c nor does it predict the observed effect of column diameter. U_c appears to be affected by the reactor diameter, at least up to D=1.56 m, in disagreement with previous conjecture (Cai, 1989) that U_c should remain insensitive to D for diameters beyond 0.5 m. The effect of H/D may become increasingly significant in larger columns where greater heights may be needed to reach the maximum stable bubble size.

U_c is plotted against the aspect ratio (H/D) in Figure 3.10. Different trends are observed for shallow ($H/D < 3$) and deep ($H/D \geq 3$) beds. Note that the difference in mean particle diameter (see Table 2.1 in Chapter 2) in the two columns may have contributed to the lower U_c values in the 1.56 m diameter column. However, with the usual exponents on the Archimedes number in equations of the form of Equation 3.2, the effect of the particle diameter variation is not able to fully explain the drop in U_c in passing from the 0.61 m diameter column to the 1.56 m diameter column. Interpretation of U_c as the velocity at which the maximum bubble size is attained may explain U_c being independent of pressure tap location above the level where bubbles/voids have reached their maximum sizes.

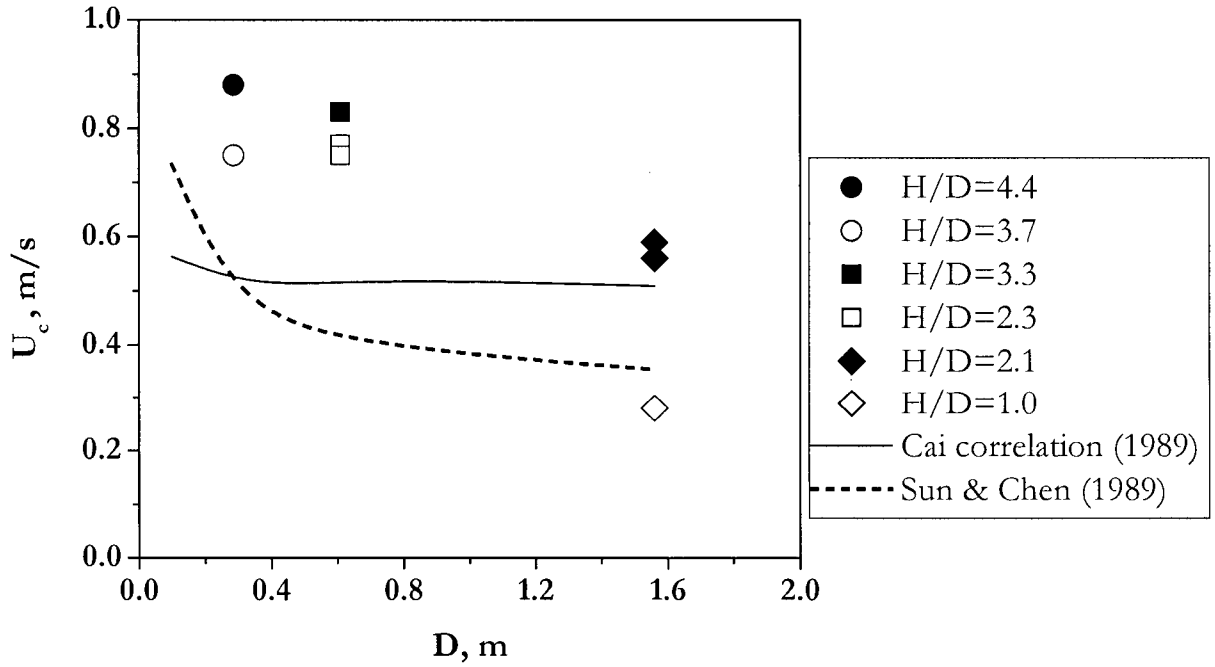

Figure 3.9 U_c obtained in this study from gauge pressure signals as a function of column diameter. FCC.

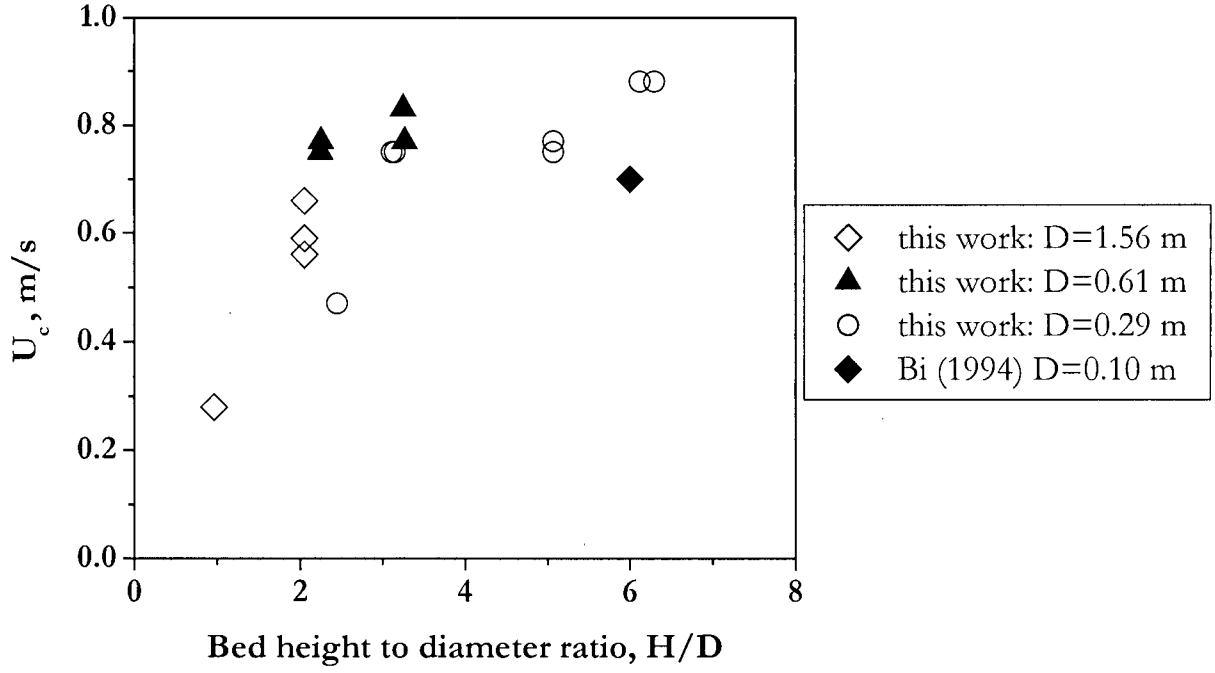

Figure 3.10 U_c based on gauge pressure fluctuations vs. bed aspect ratio for the three columns investigated in this work together with data from Bi (1994). FCC.

U_c data for deep beds ($H/D \geq 3$) are compared with published data (Schnitzlein and Weinstein, 1988; Grace and Sun, 1991; Bi, 1994; Chehbouni et al., 1995a) with FCC particles as the bed material in Figure 3.11. Experiments conducted at different static bed heights in the three columns studied in this work confirm that U_c, based on differential pressure fluctuations increases with decreasing height. This implies that homogeneity of the bed is attained at the top of the bed first; the entire bed is not well into the turbulent flow regime until the gas velocity is well beyond that required for turbulent fluidization at the bed surface. The scatter in the measured U_c for a given column probably originates from different static bed heights, or different particle size distributions in the case of Grace and Sun (1991). Except for the data of Chehbouni et al. (1995a), U_c correlates reasonably well with z/D. Inclusion of the location of the DP cell in the correlation reduces the dependence of U_c on the specific column geometry.

In order to account for the difference in static bed height, the time-mean voidage calculated from DPs from which U_c is obtained is considered in characterizing the bed condition. By plotting voidage and standard deviation from the same DP as in Figure 3.12, ε_c, the voidage at which the maximum standard deviation occurs, is obtained by extrapolation. Assuming that ε_c represents the cross-sectional average voidage at a given D, the effect of column diameter may be removed. Thus, as shown in Figure 3.13, an attempt was made to correlate the voidage with U_c. Due to the scatter and the limited number of data, it is impossible to obtain a clear relationship.

Whilst most studies on U_c are conducted with $D < 0.4$ m (Bi and Grace, 1995), it is of interest to see whether U_c deduced from pressure transducers mounted on the wall is indeed representative of the pressure fluctuation occurring throughout the cross-section of a large-scale reactor. The traversing probe arm constructed at CSIRO for this purpose allowed pressure measurements at the centre of the 1.56 m diameter reactor. Figure 3.14 presents the standard deviation of differential pressure fluctuations. U_c deduced from the standard deviation of pressure fluctuations at $r/R=0.9$ and at the centre appear to be similar, indicating that U_c, though affected by height, is insensitive to radial location. The increased frequency of voids in the centre of the column even at lower gas velocities is indicated by a relatively steep rise in the standard deviation of pressure signals as the gas velocity is increased. Beyond U_c, increased homogeneity of the bed is observed, as indicated by the limited spread in the measured standard deviations.

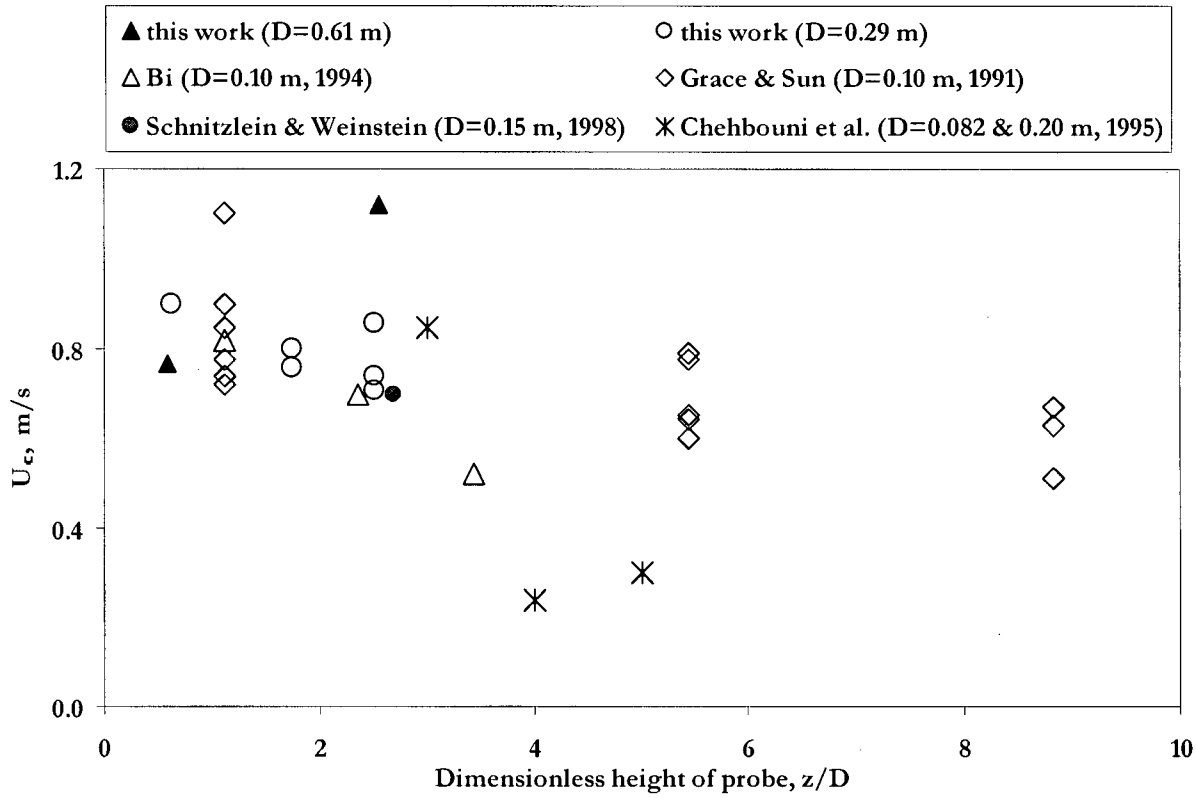

Figure 3.11 Comparison of experimental U_c obtained from DP signals to published data for H/D≥3.

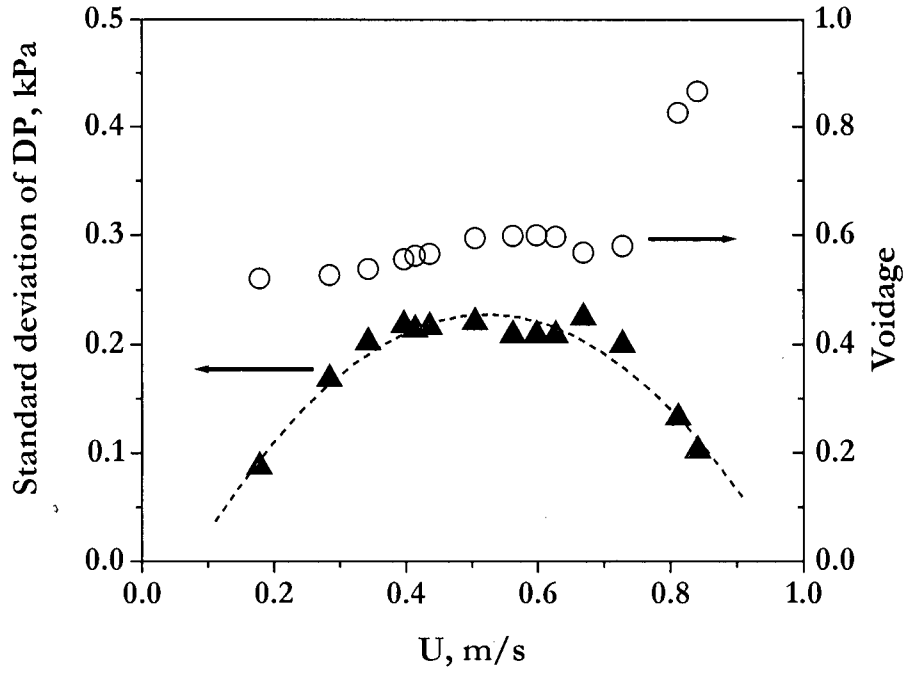

Figure 3.12 Standard deviation of DP signals and voidage plotted against superficial gas velocity. D=0.29 m, FCC I, H_0=0.51 m, z=0.31 m.

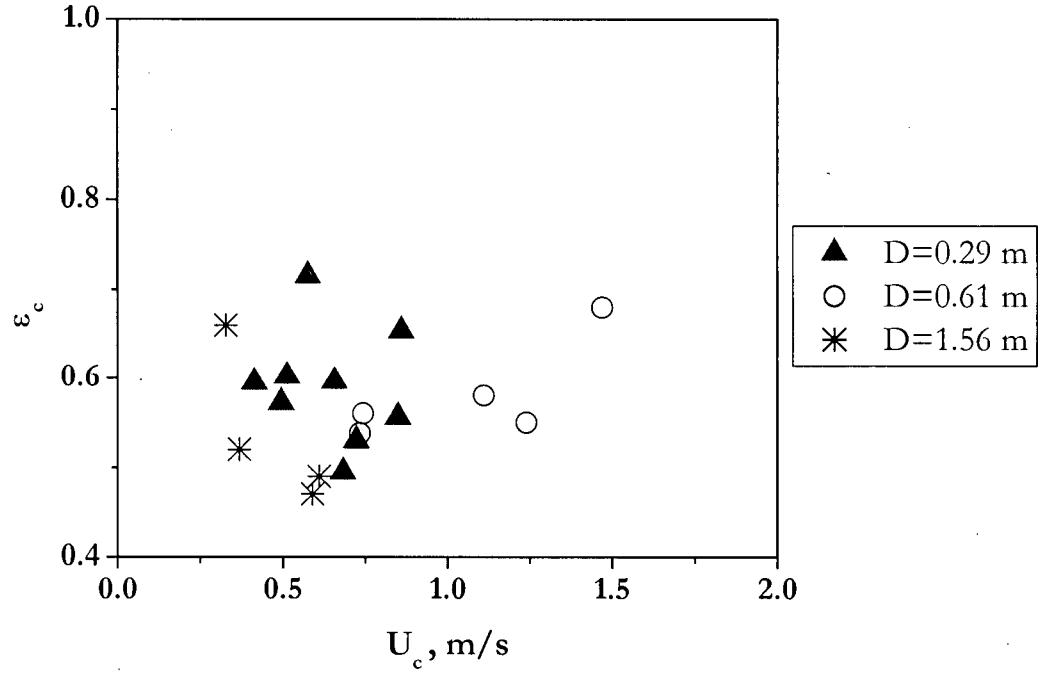

Figure 3.13 Plot of U_c vs. corresponding bed voidage, ε_c. FCC.

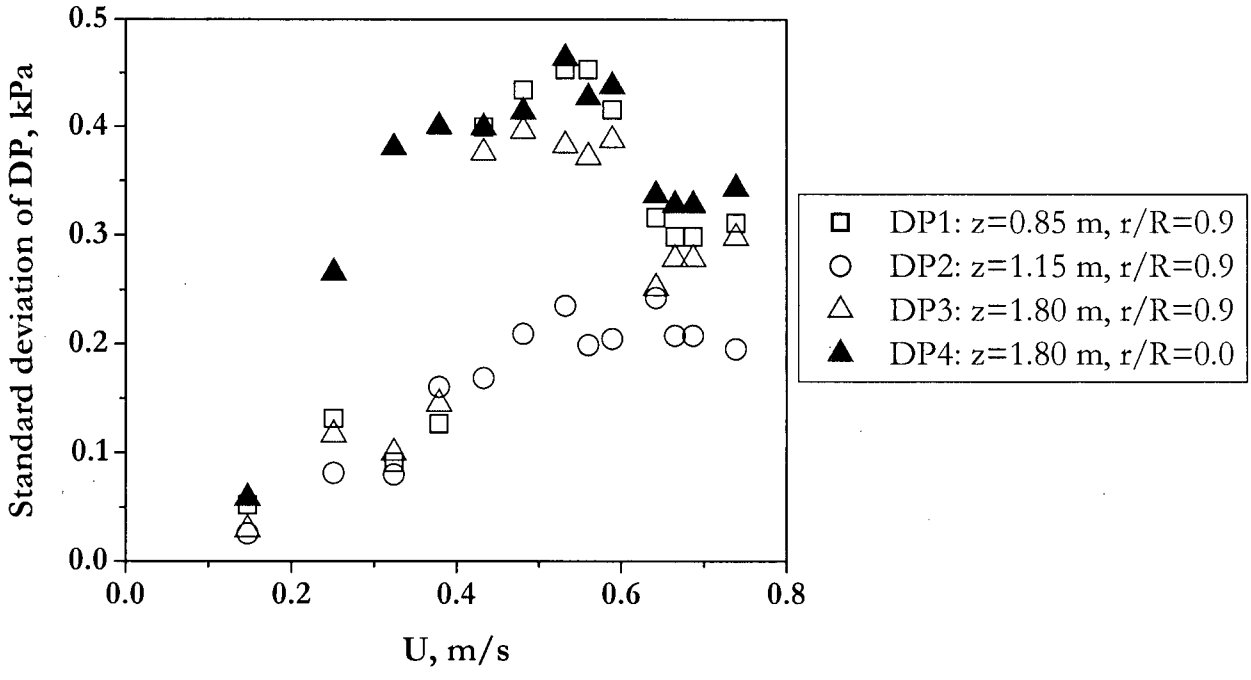

Figure 3.14 Standard deviation of DP signals plotted a s a function of U. D=1.56m, H_0=2 m, FCC II.

3.4.3 Effect of particle properties on U_c

The effect of fines and mean particle size on the 'quality' of fluidization has been the subject of several studies owing to reports suggesting increased chemical conversions with higher proportions of fines (e.g. Yates and Newton, 1986). Bai et al. (1996) have shown the effect of different relative fractions of binary mixtures of FCC particles and silica sand on U_c. Their results correlated well with U_c predicted from Cai (1989) correlation, Equation 3.10, by accounting for the binary distribution in terms of equivalent particle diameter and particle density. The mixture of the narrower and higher mass mean particle diameter sand particles with FCC particles showed a much higher U_c for more than 50% mass fraction of sand to FCC particles. This signified that there was very little effect of the particle size distribution (PSD) of sand on U_c when the mixture consisted of more than 50% FCC particles. Judd and Goosen (1989) indicated a decrease in gauge pressure fluctuations when the reactor diameter increased from 0.05, 0.14 to 0.29 m, with a lower U_c for powders of smaller mean diameter (mass and Sauter means) and larger PSD. In many studies, the change in PSD results in a change in mean particle diameter, and the independent effects of PSD and particle mean diameter cannot therefore be distinguished. Grace and Sun (1991) reported on the enhanced chemical conversion obtained by broadening the PSD yet keeping the mean particle size constant. U_c for FCC particles having a wider PSD indicated an earlier onset of the turbulent fluidization flow regime. This was attributed to the change in the gas flow through the dense phase producing smaller voids for wider-PSD fluidized beds.

In this work, particles displaying a density close to that of FCC particles (1560 kg/m^3) were chosen to obtain experimental values of U_c. The particle size distribution is plotted in Figure 3.15 in comparison to the FCC particles, with properties listed in Table 3.1. Catalyst C had two different size distributions. Both batches of catalysts had the same range of particle size, but Catalyst Cr had a higher content of size cut between 32 and 45 μm, resulting in a smaller mean diameter.

Experiments were conducted in a 0.29 m diameter column with an initial static bed height of 0.60 m for each set of particles. The expanded bed height calculated from the time-average axial pressure measurement, Figure 3.16, indicated much more entrainment for Catalyst Cr than for FCC particles. With Catalysts C and Cr, the return leg often filled up very quickly, indicating that a considerable portion of the bed had been transferred to the return leg.

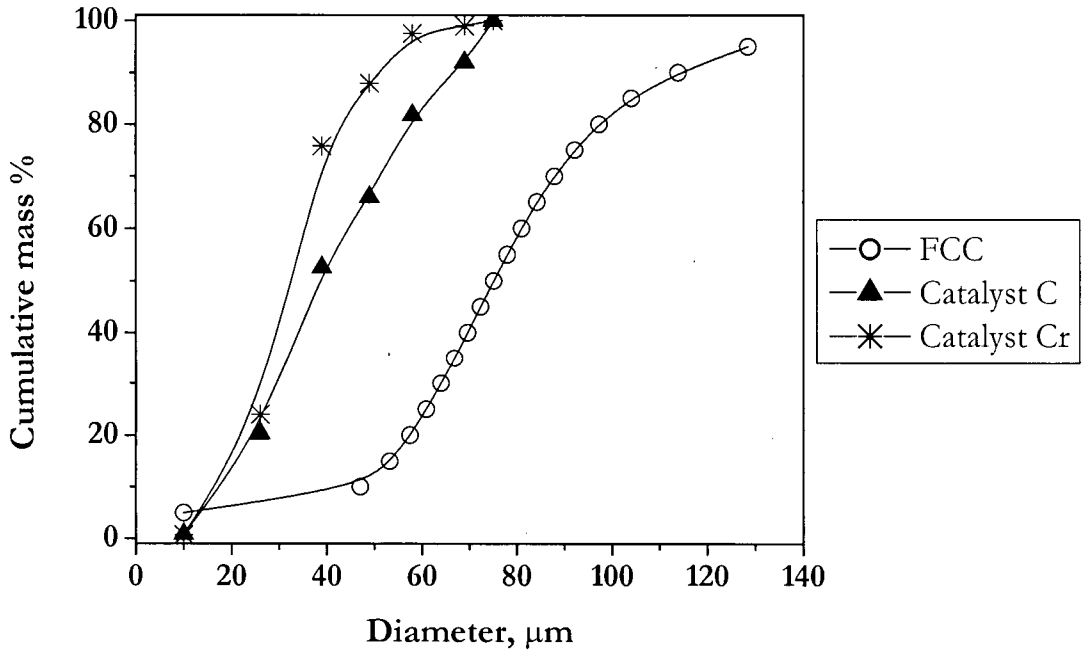

Figure 3.15 Cumulative distribution of particle size based on mass fraction.

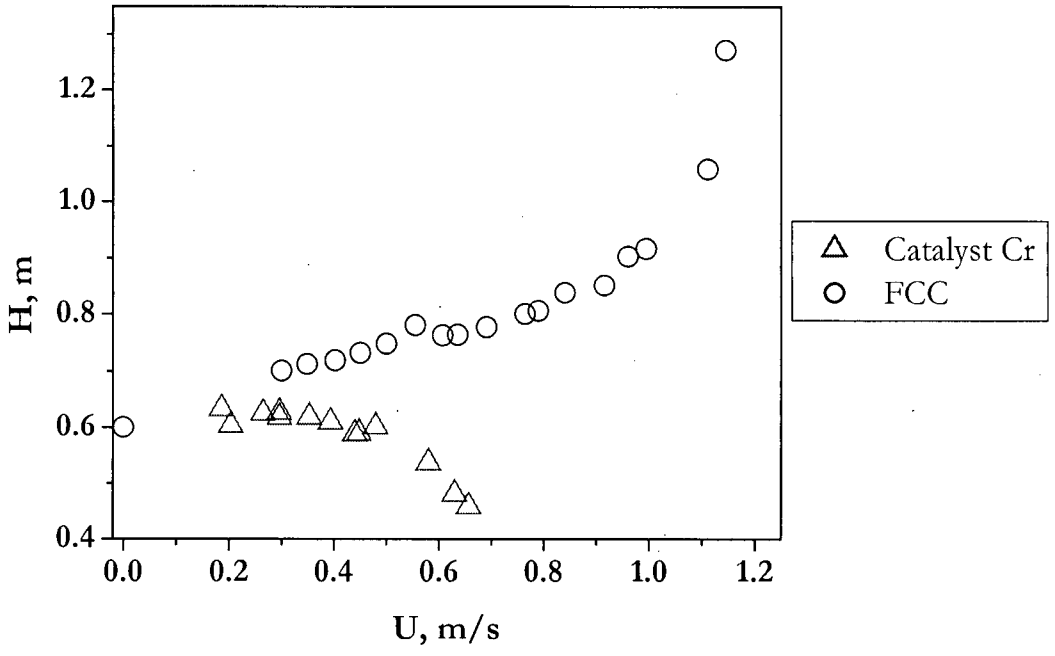

Figure 3.16 Comparison of expanded bed height from axial pressure distribution for FCC and Catalyst Cr. D=0.29 m, H_0=0.6 m.

Therefore, when U_c is plotted against the vertical coordinate as in Figure 3.17, the selected probe heights of 0.18 and 0.43 m ensured that the probe was always located within the fluidized bed. The difference in U_c between Catalysts C and Cr was minimal with the error bars for a 95% confidence interval from curve fitting overlapping. The particle Reynolds number corresponding to U_c from DP signals is plotted against the Archimedes number for mass mean particle diameters in Figure 3.18. Since the effect of height on U_c is not predicted by the correlation in the form of Ar and Re_p, the results are not readily compared with those of previous studies. An attempt was made to correlate U_c deduced from DP fluctuations with height, but this was not successful.

The addition of fines to improve the 'quality' of fluidization is a common practice, and one of the easiest variables to change from the reactor-design point of view. Addition of fines has an effect on the quantity of fines associated with voids (Grace and Sun, 1990), thus affecting pressure fluctuations, and thus the measured value of U_c.

Table 3.1 Particle properties used in 0.29 m diameter column.

Particle	FCC I	Catalyst C	Catalyst Cr
Density, kg/m^3	1560	1580	1580
Ar (mass mean)	23.5	3.94	2.06
$\bar{d}_p$ (mass mean), μm	75.1	41.2	33.3
d_{sm} (Sauter mean), μm	57.4	40.6	36.5

3.4.4 Effect of system pressure on U_c

The effect of system absolute pressure on the bed hydrodynamics including U_c is of vital importance in designing fluid bed reactors, especially with the increasing application of pressurized systems for coal combustion and gasification (Yates, 1996). For Group A powders, an increase in system pressure has been shown to increase the voidage in the dense phase leading to less stable, smaller bubbles. Since the gas density increases with pressure, it is expected, according to correlations of the form of Equation 3.2, that U_c should decrease with increasing pressure. Note that viscosity is virtually unaffected by pressure.

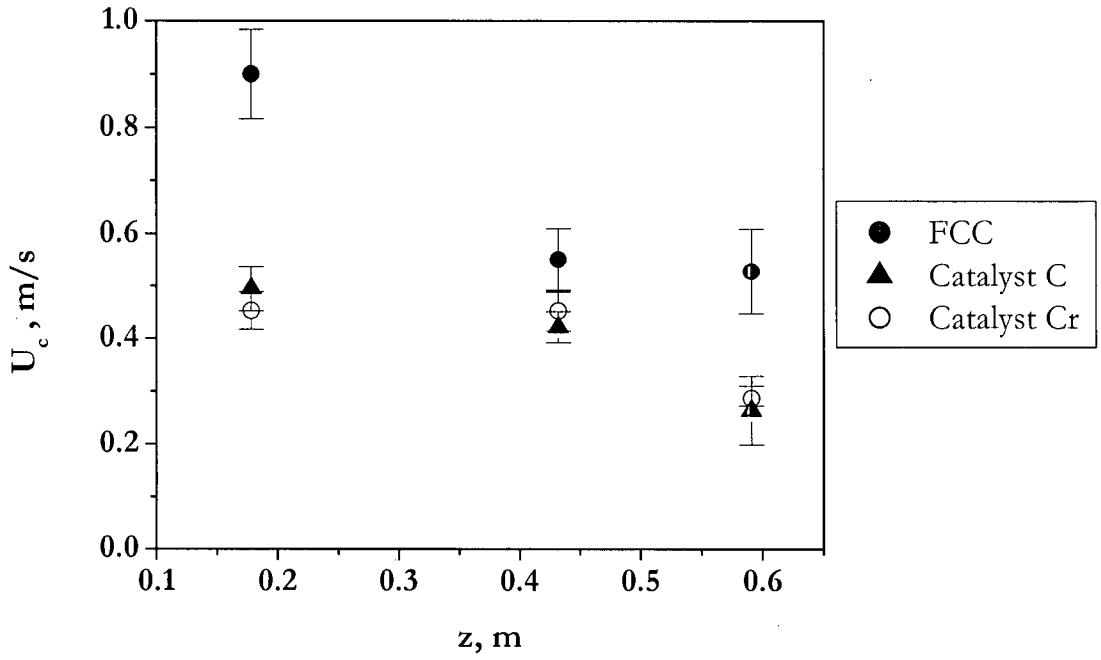

Figure 3.17 Effect of particle properties on axial profiles of U_c from DP signals. H_0=0.60 m, D=0.29 m.

Table 3.2 Published exponents for Equation 3.2.

Source	a	b	Applicable range
Lee and Kim (1988)	0.700	0.485	$0.44 \leq Ar \leq 4.4\times10^7$
Leu et al. (1990)	0.568	0.578	
Horio (1992a)	0.936	0.472	$54 < d_p < 2600$ μm
Nakajima (1991)	0.633	0.467	
Tsukada (1995)	0.791	0.435	
Bi and Grace (1995) DP data	1.243	0.447	$3 \leq Ar \leq 3\times10^7$
Bi and Grace (1995) AP data	0.565	0.461	$3 \leq Ar \leq 2\times10^5$

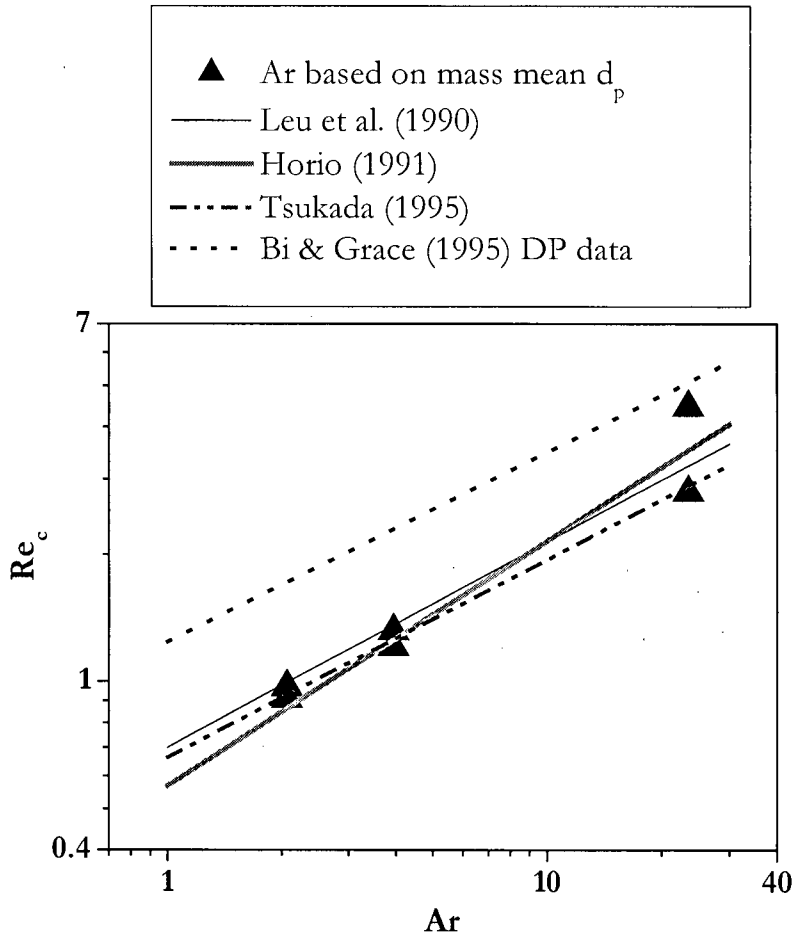

Figure 3.18 Archimedes number vs. particle Reynolds number based on U_c compared to published correlations based on Equation 3.2 and Table 3.2. D=0.29 m.

Cai et al. (1989) examined the effect of pressure up to 0.8 MPa for eight different powders including FCC particles in a 0.28 m diameter column. The resulting correlation for U_c, Equation 3.10, includes the viscosity and density of gas relative to those measured for air at standard conditions, i.e., 20°C and 0.1 MPa. As the pressure increased, the amplitude of pressure fluctuations was found to decrease. The findings are consistent with the findings in the bubbling flow regime showing that bubble size decreases at elevated pressure making the fluidization much smoother (Hoffmann and Yates, 1986). It is expected that the increased bubble break-up will result in a decrease in U_c.

Tsukada et al. (1993) examined the pressure effect on U_c for FCC particles in a 0.05 m diameter CFB. For pressures up to 0.7 MPa, U_c was found to be proportional to $P^{-0.3}$. However, the solids circulation rate was found to be insensitive to the pressure at the regime transition. This implies a structural change within the bed. Simultaneous optical probe measurements indicated a decrease in bubble fraction from 0.4 to 0.3 with increasing pressure.

A study of transition velocity at pressures up to 7.2 MPa was recently reported by Newton et al. (2001) using 13 different powders, including six Geldart Group A powders. U_c was determined through visual inspection of the images taken by X-ray imaging in 0.127, 0.254 and 0.42 m diameter columns. For Group A powders, the correlation of Sun and Chen (1989) showed the best fit. The results for pressures higher than 3 MPa indicated very little effect of pressure on U_c.

As a part of an industrial contract project, the author explored the effects of pressure and temperature on the hydrodynamics in a 0.11 m diameter vessel (Column IV in Chapter 2). Data were sampled at a frequency of 10 Hz with 4000 points (duration ~7 minutes) collected for analysis. Figure 3.19 shows decreasing U_c and decreasing amplitude of pressure fluctuation with increasing system pressure, consistent with the findings of Cai et al. (1989).

The effect of pressure on the minimum fluidization velocity, U_{mf}, has been reported to be more prominent for larger particles (Yates, 1996). This is because the flow around smaller particles is dominated by viscous forces from the gas phase. An increase in pressure has been reported to decrease the apparent kinematic viscosity of the dense phase (King et al., 1981), possibly due to adsorption of gas on particles promoting increased cohesion (Piepers and Rietema, 1989). The resulting increase in interparticle forces in the dense phase may be the cause of dense phase

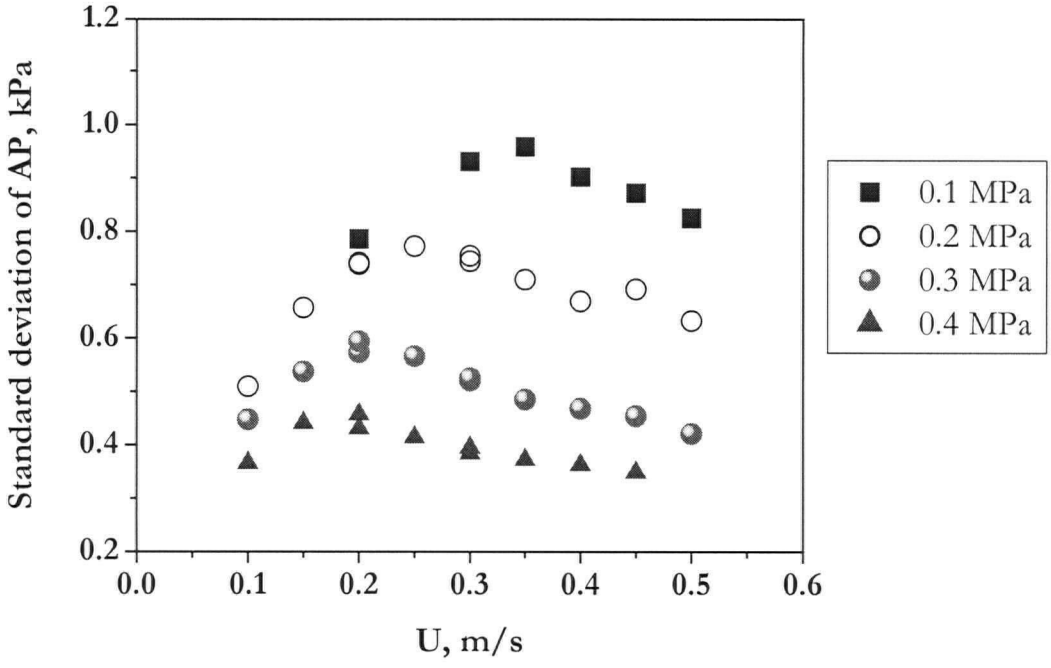

Figure 3.19 Effect of system pressure on U_c. D=0.11 m, z=0.9 m, H_0=0.7 m, Catalyst C fluidized with N_2.

expansion at high pressure causing a lower effective dense phase viscosity. Clift et al. (1974) suggested that a decrease in the apparent kinematic viscosity of the dense phase contributes to the instability of voids. This explanation can be extended to explain the early onset of U_c at higher pressure where voids are smaller and fluidization smoother as pressure is increased.

The effect of system pressure on U_c is summarized in Figure 3.20. For the calculation of U_c using the correlations by Cai et al. (1989), Sun and Chen (1989) and Bi and Grace (1995), gas viscosity, U_{mf} and ε_{mf} are all assumed to be independent of pressure (Kunii and Levenspiel, 1991; Yates, 1996) for Group A powders. Values of 0.565 and 0.461, for a and b, respectively, were taken in applying Equation 3.2 for U_c obtained from gauge pressure fluctuations (Bi and Grace, 1995). The calculations were based on a column diameter of 0.106 m, and therefore do not reflect the range of vessel size represented in the plot. However, the overall trend is well predicted. The effect of column diameter and pressure are not isolated for the Newton et al. (2001) results represented by triangles in Figure 3.20 for D=0.42 m. Since most U_c correlations are deduced from experimental data obtained from relatively small vessels, the effects of vessel size and pressure on U_c should be studied to extend correlations to systems and conditions common in fluidized bed combustors and gasifiers.

3.4.5 Effect of temperature on U_c

Changing temperature affects gas properties, i.e., gas density decreases while gas viscosity increases with increasing system temperature. The viscosity of air at elevated temperature was estimated from:

$$\mu_g = \frac{1.46\times10^{-6}\,(273.15+T)^{1.504}}{(273.15+T)+120} \tag{3.15}$$

(Svoboda and Hartman, 1981).

Chehbouni et al. (1995b) examined the effect of temperatures up to 425°C on U_c and found that U_c decreased with increasing temperature for Geldart A powders, and increased for Geldart B powders in a 0.2 m diameter vessel. Extending the temperature to 960°C, Peeler et al. (1999) reported similar trends for two powders in their 0.08 m riser. On the other hand, an increase in U_c was observed for two types of FCC particles when the temperature was increased from 50 to 250°C in a 0.15 m diameter vessel (Cai et al., 1989). The maximum amplitude of gauge pressure fluctuations decreased with increasing temperature, indicating smaller voids and smoother fluidized bed operation as the system temperature increased.

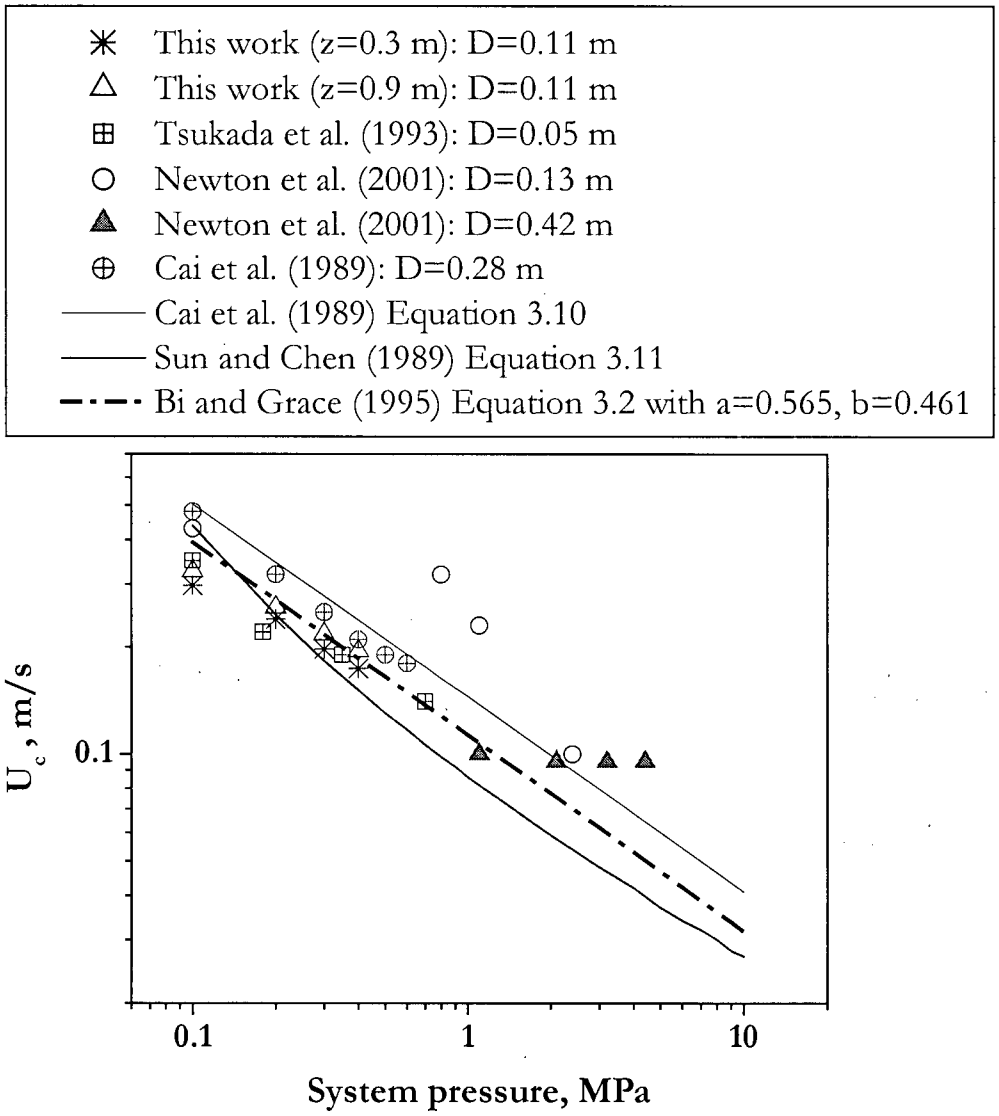

Figure 3.20 Effect of system pressure on U_c. Comparison of this work (D=0.11 m, Catalyst C, fluidizing air: N_2, T=20 °C) to others.

Recent studies on the influence of temperature on the dense phase properties of fluidized beds of FCC particles (Lettieri et al., 2001; Formisani et al., 2002) indicate the contributions from thermal modifications of particle properties, and fluid dynamic effects. Temperature increase was found to influence the interparticle forces which stabilized looser fixed structures. As a result, voidages in the fixed state, at minimum fluidization, and in the dense phase of a bubbling fluidized bed increased linearly with temperature (Yamazaki et al., 1986; Formisani et al., 2002). This suggests that temperature may influence dense phase structure through particle-particle interaction even in high-velocity fluidized beds.

Experimental findings for temperatures of 20, 160 and 240°C at 0.2 and 0.4 MPa are presented in Figure 3.21. From the ideal gas law, gas density is inversely proportional to absolute temperature. However, the change in gas density does not linearly affect the amplitude of the pressure fluctuations, which is a measure of the relative bubble size, indicating that the influence exerted by gas density change does not affect the size of voids. Note that the effect of temperature on U_c is more pronounced at the lower system pressure.

3.4.6 Combined effects of pressure and temperature on U_c

In order to examine the effect of gas viscosity on U_c, the standard deviation of gauge pressure fluctuations is plotted in Figure 3.22 for system temperatures of 20, 160 and 240°C against the volumetric flow rate at standard conditions, i.e., 20°C and 0.1 MPa pressure. By plotting in this manner, the change in gas density with temperature is compensated. If a correlation of the form of Equation 3.2 applies, then

$$Q_c \propto \mu_g^{1-2b} \tag{3.16}$$

The dependence of Q_c on viscosity is therefore given by

$$\frac{Q_{c20}}{Q_{cT}} = \left(\frac{\mu_{g20}}{\mu_{gT}} \right)^{1-2b} \tag{3.17}$$

where the subscript 20 denotes conditions at 20°C. Unfortunately the data do not include an atmospheric pressure system. From Figure 3.23, it is concluded that the effect of temperature represented by the gas viscosity term has less influence on Q_c as pressure is increased. This may suggest less change in the apparent kinematic viscosity of dense phase at higher pressures.

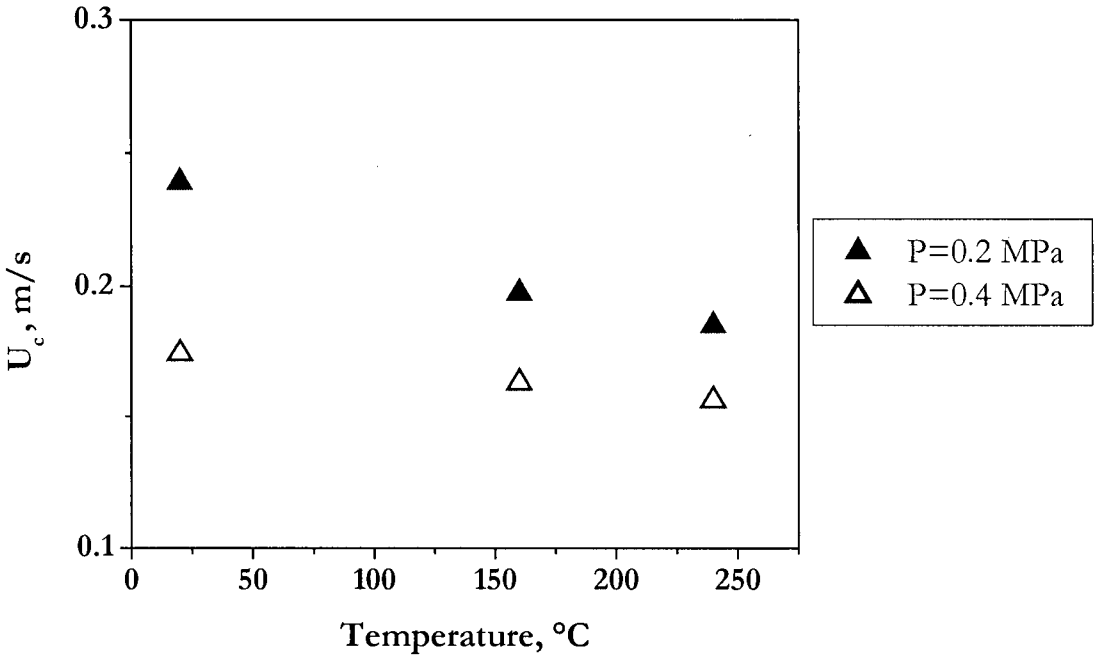

Figure 3.21 Effect of temperature on U_c. D=0.11 m, Catalyst C.

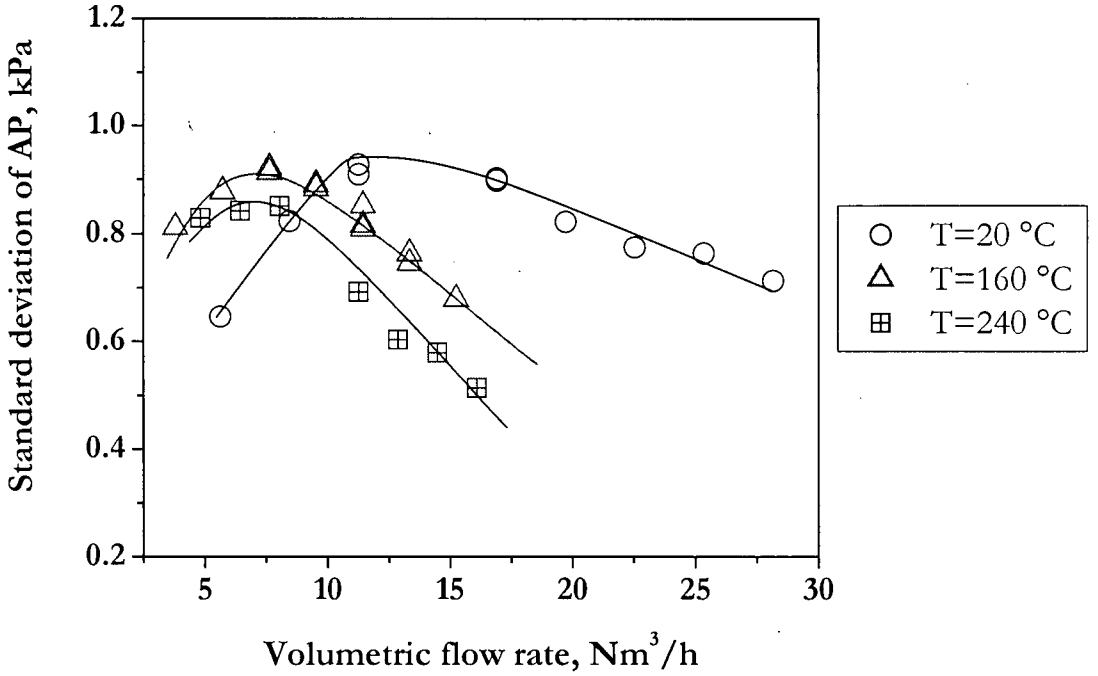

Figure 3.22 Standard deviation of gauge pressure signals against volumetric gas flow rate. D=0.11 m, Catalyst C, P=0.2 MPa.

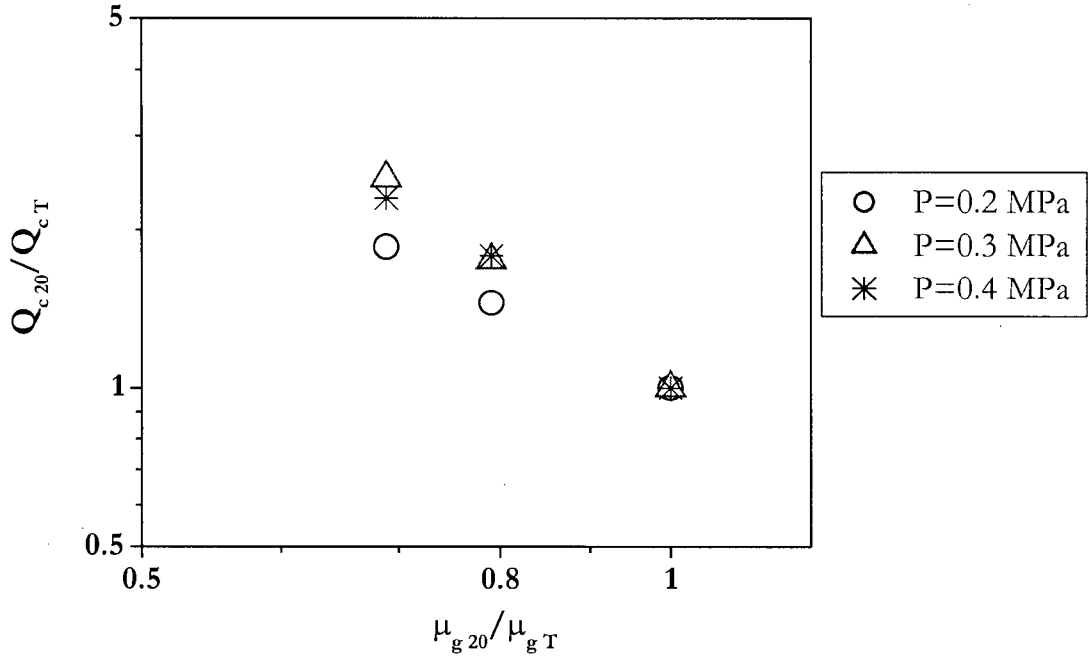

Figure 3.23 Effect of gas viscosity and system pressure on Q_c, transition based on volumetric flow rate. D=0.11 m, Catalyst C. Subscript T denotes system temperature.

Experimental data for U_c from the hot unit for temperatures of 20°C at 0.1, 0.2, 0.3 and 0.4 MPa, and of 160 and 240°C at 0.2, 0.3 and 0.4 MPa are compared to predictions based on the correlations by Cai et al. (1989), Equation 3.10, and Sun and Chen (1989), Equation 3.11, in Figures 3.24 and 3.25, respectively. Figure 3.24 indicates that the correlation by Cai et al. (1989), though based on operating temperatures of 50 to 500°C and pressures of 0.1 to 0.8 MPa, overestimates the transition velocity. Better predictions were obtained from the Sun and Chen correlation (1989) based on Group A particles fluidized in a 0.8 m diameter column.

3.4.7 U_c correlation

Based on the extensive experimental study on U_c from different column sizes, a correlation is proposed taking into account the effect of the aspect ratio, H/D, on U_c deduced from gauge pressure signals. As noted in Section 3.4.1, the effect of H/D on U_c becomes less significant for H/D >~3. In Figure 3.26, U_c for higher aspect ratios is compared to other studies where confirmation of H/D ≥ 3 can be verified. The linear fit on log-log coordinates gives

$$Re_c = 0.371\, Ar^{0.742} \tag{3.18}$$

with R^2=0.989. The exponent b=0.742 is much higher than those previously published, as listed in Table 3.2. This is attributed to this correlation only including Geldart Group A particles, and restricting the data to only include U_c from high H/D and those deduced from gauge pressure fluctuations.

Following the procedure used by Dunham et al. (1993), a correlation is proposed for U_c obtained from gauge (single point) signals measured in the lower H/D fluidized beds as:

$$Re_c = 0.459\, Ar^{0.454} \left(\frac{H}{D}\right)^{0.183 \ln(d_p \varrho_s)+0.83} \tag{3.19}$$

This correlation is compared to the experimental data obtained in columns of three different diameters in Figure 3.27. Combining the two correlations, i.e., Equations 3.18 and 3.19, the overall prediction of U_c is plotted in Figure 3.28 in comparison with the experimental data, resulting in an overall root-mean-square deviation of 0.12. The discontinuity shown between the two correlations is a function of the Ar number, and is a result of limited data available for correlating U_c.

For the purpose of refining the proposed correlations by comparison with other studies, it is recommended that the standard deviation of gauge pressure signals be reported along with the

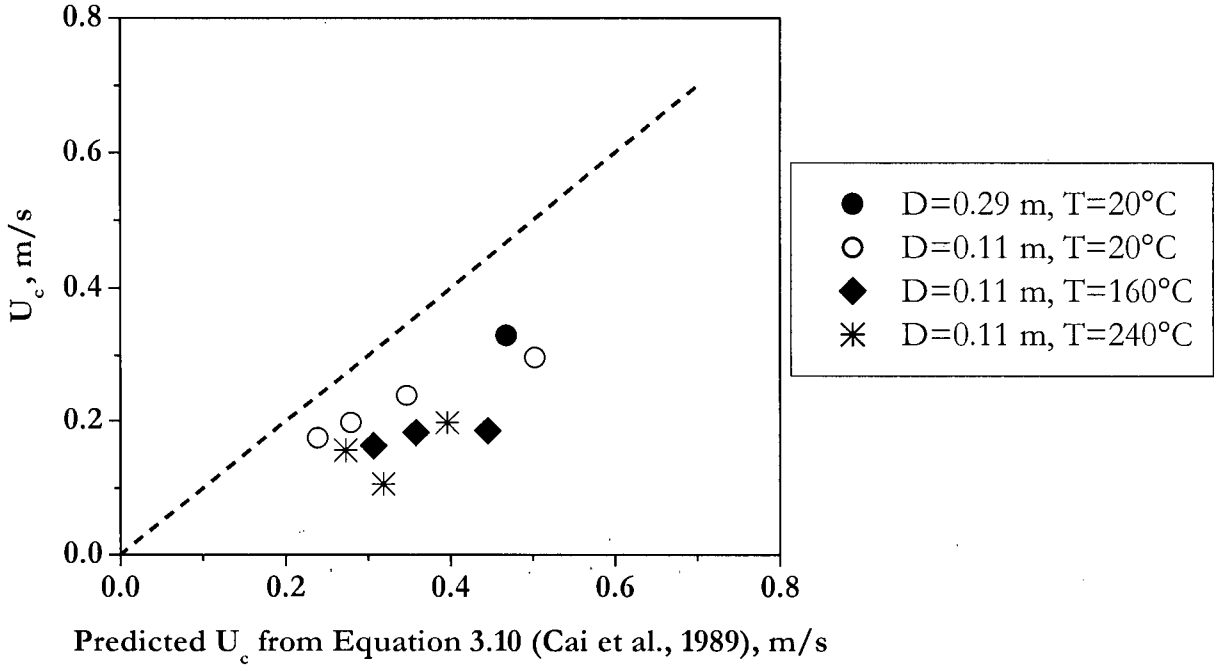

Figure 3.24 Comparison of predictions by Equation 3.10 with experimental U_c. Catalyst C. D=0.11 m diameter column, H_0=0.7 m. D=0.29 m diameter column, H_0=0.6 m.

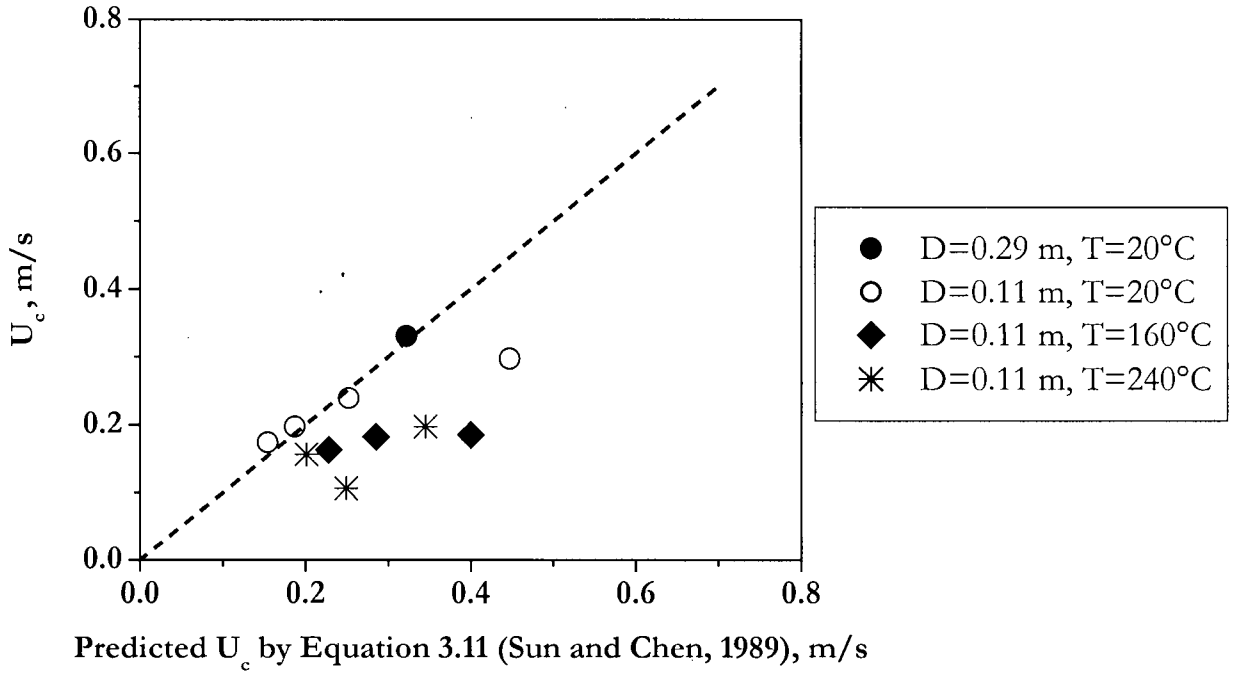

Figure 3.25 Comparison of predictions by Equation 3.11 with experimental U_c. Catalyst C. D=0.11 m diameter column, H_0=0.7 m. D=0.29 m diameter column, H_0=0.6 m.

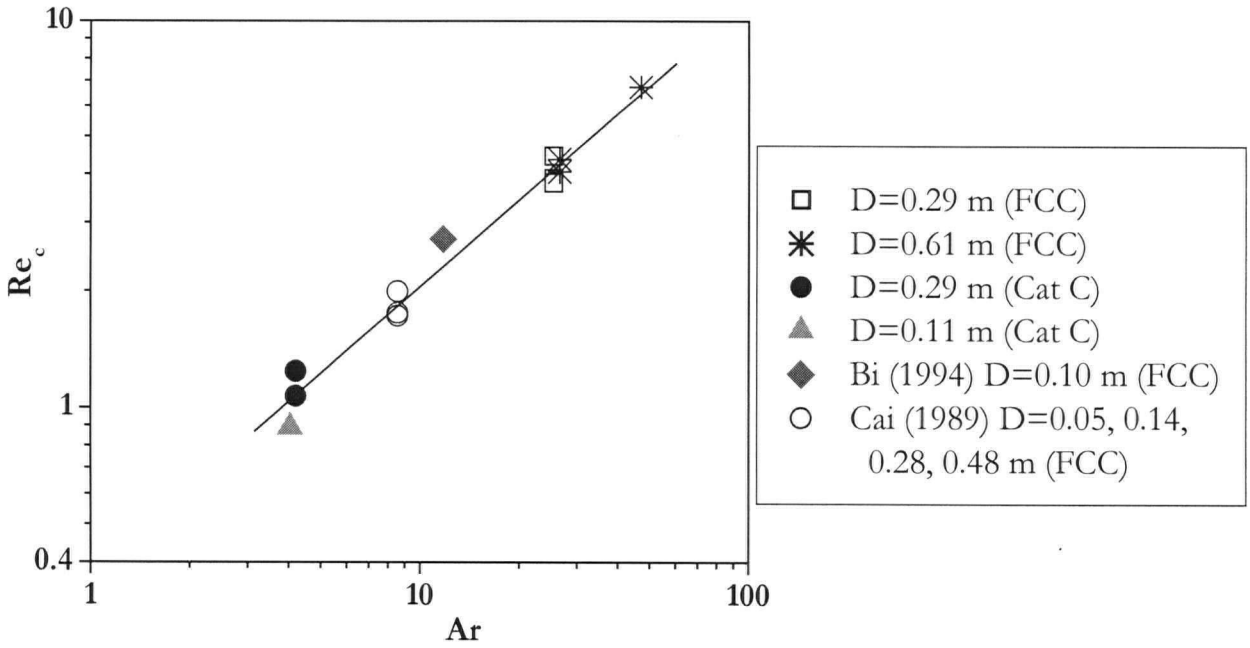

Figure 3.26 Comparison of U_c data from this work to literature data for fluidized bed of Geldart Group A particles from gauge pressure signals.

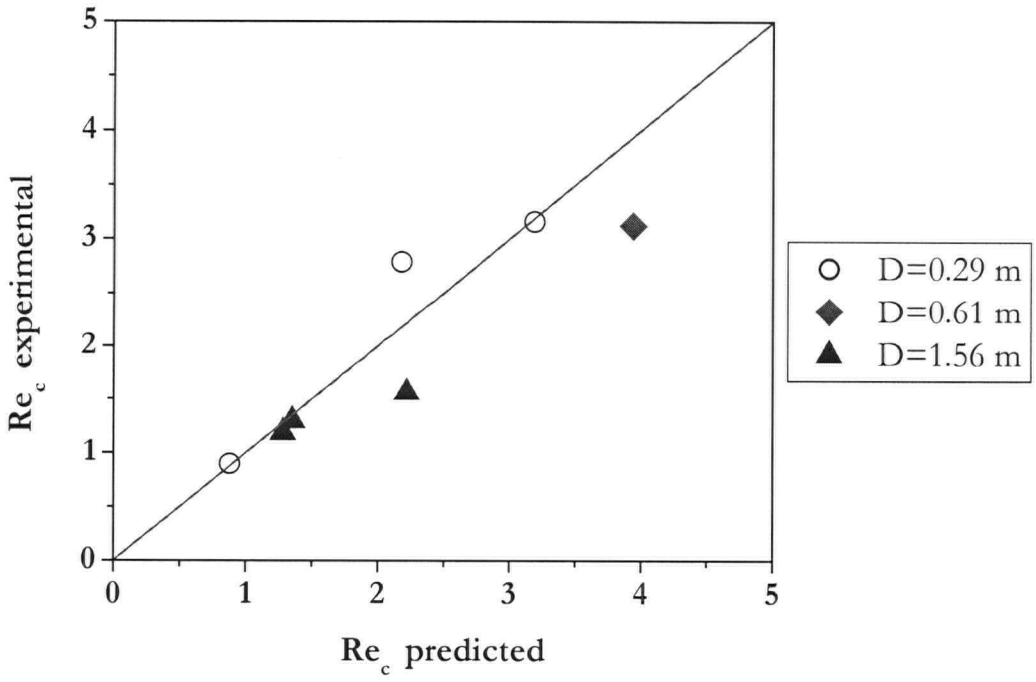

Figure 3.27 Comparison of predictions by Equation 3.19 with experimental U_c. FCC.

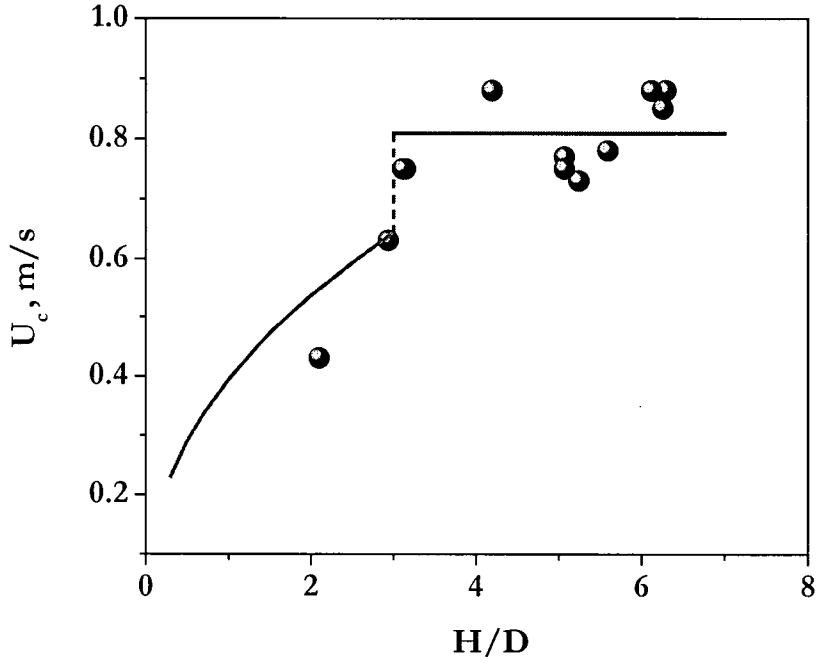

Figure 3.28 Comparison of predictions by Equation 3.18 and 3.19 with experimental U_c from gauge pressure signals. FCC I, D=0.29 m.

information on expanded bed height, particle density and mean diameter, and gas density and viscosity.

3.5 Conclusions and recommendations

Experimental work has been conducted to extend the knowledge of the transition velocity, U_c, using two different powders and four experimental columns. The effect of pressure and temperature was also studied. Transition velocities based on pressure fluctuations were determined in columns much larger than those used in most academic research laboratories. The diameter of the column has been shown to affect the transition to the turbulent flow regime of fluidization.

- The transition velocity, U_c, was found to decrease as the column diameter was increased from 0.29 m through 0.61 m to 1.56 m, and with decreasing static bed height of FCC particles.
- In practice, most pressure measurements are obtained at the column wall for convenience. The validity of the assumption that the wall measurements are representative of the cross-section and give the transition velocity applicable at the centre was confirmed experimentally.
- U_c from DP signals was shown to increase as the location of the sensor descended towards the distributor plate. This implies that, as the superficial gas velocity is increased, homogeneity is attained at the top of the bed first, as indicated by its lower U_c value, before the rest of the bed reaches the turbulent flow regime. The transition velocity decreased with increasing system pressure (to 0.4 MPa) confirming the findings of others. The trend is well predicted on the basis of the change in gas density with increasing pressure.
- The transition velocity was shown to decrease with increasing temperature (to 240°C) for the results obtained in this work. The amplitude of the differential pressure fluctuation indicated very little change in void size with changing temperature.
- Better predictions were obtained by the Sun and Chen correlation for U_c obtained from gauge pressure signals for increased system pressures (to 0.4 MPa) and for elevated temperature (to 240°C).
- Correlations are proposed for predicting U_c in fluidized bed of Geldart Group A particles deduced from gauge pressure signals:

$$Re_c = 0.371\ Ar^{0.742} \tag{3.18}$$

for $H/D \geq 3$, and

$$Re_c = 0.459\ Ar^{0.454} \left(\frac{H}{D}\right)^{0.183 \ln(d_p \rho_s) + 0.83} \tag{3.19}$$

for $H/D < 3$.

Further studies

- Further investigation of U_c is required based on DP signals. The effect of height on U_c should be taken into account when correlating U_c.
- In an attempt to prevent the results from being column specific, ε_c and U_c have been correlated. More data are required before a reliable correlation can be obtained.

CHAPTER 4

VOIDAGE MEASUREMENTS

4.1 Introduction

Voidage is the volumetric fraction of gas in a gas-solid system. Knowledge of the time-mean voidage provides information useful for setting operating conditions and for overall reactor design, while local instantaneous voidage measurements extend understanding of the complex local flow structure in fluidized beds. In a fluidized bed reactor, information on local voidage encompasses determining effects on mass and heat transfer phenomena, and reaction rates (Louge, 1996). Owing to the transient nature of multiphase flow, the instantaneous local voidage measurement method must be able to distinguish the two phases quantitatively and capture signals at relatively high frequencies. Measurement techniques for voidage include non-invasive methods, such as X-rays, computer-assisted tomography (CAT), positron emission tomography (PET), capacitance tomography, gamma ray transmission densitometry, and invasive techniques including capacitance and optical probes. Visualization techniques such as Laser Doppler Anemometry (LDA) are mostly restricted to very dilute systems where the laser can penetrate into the flow of interest, or the wall region, where backscatter can be used.

With the progress of Computational Fluid Dynamics (CFD) in modelling the hydrodynamics of multiphase flows, detailed experimental measurements of the flow structure will play an essential role in validating CFD models. Thus, information on local voidage will help to elucidate the dynamics of multiphase flow and to test the validity of theoretical models.

4.2 Local voidage measurement

Voidage measurements have been executed with various instruments as reviewed by Nieuwland, et al. (1996), Louge (1996) and Werther (1999). Some essential features of the equipment capable of measuring voidage (Werther and Molerus, 1973a) are:

- disturb the bed as little as possible;
- measure local variations;
- respond rapidly to changes in voidage;
- have adequate mechanical strength;
- be movable within the bed;

- be compatible with the bed solids.

For measurements in dense particle phase systems the choice becomes limited.

Since reflective-type optical probes are known to be simpler and less intrusive than most other types of probes (Lischer and Louge, 1992), they have been employed by numerous researchers to determine voidage in fluidized beds (e.g. Reh and Li., 1990; Lischer and Louge; 1992, Cocco et al., 1995; Farag et al., 1997b). Because of their compact size, the measurements are localized with minimum disturbance to the flow dynamics (Zhang et al., 1998). As the light intensity depends on the reflection and penetration of the emitting light, the measuring volume is a function of the solids concentration at the tip of the probe. Thus, careful calibration is critical to obtaining the measurements with high accuracy and precision. Estimation and modelling of the effective measuring volume of a single-fiber reflection probe have been reported by Rensner and Werther (1991, 1993).

A capacitance probe measures voidage through the dielectric constant in the capacitance sensor volume. Thus, signals reflect the change in capacitance due to a change in the local solids concentration if the dielectric constants of the phases differ significantly. Since the probe itself potentially contributes to the capacitance, which varies slightly with temperature, the 'guarded' capacitance probe is capable of suppressing the capacitance from the probe body (Hage and Werther, 1997a,b), especially for applications involving high temperatures. Thus, as summarized by Louge (1997), the 'guarded' capacitance probe is reported to reduce the problem with stray of response, and with increasingly defined measuring volume. However, the sensitivity of the probe to static electricity, and to change in humidity (Herbert et al., 1994) has also been acknowledged.

Very few cases are known in which voidage has been measured successfully under the harsh conditions of industrial high-temperature fluidized bed systems. Recently Johnsson and Johnsson (2001) detected bubbles in a 850°C CFB boiler with a two-fiber reflective type optical probe. Any technological advancements in hydrodynamic measurement methods will certainly be embraced by the fluidization community. In the case of invasive probes in general, the influence of the presence of a probe on the flow structure has generally been neglected, but this assumption needs to be confirmed.

4.3 Voidage in turbulent fluidized beds

The ongoing interest and need to clarify changes in bed structure and flow development through the "gradual" disappearance of discrete bubbles and voids in turbulent fluidization has been addressed in only a few publications pertaining to the hydrodynamics of this flow regime. As listed in Table 4.1, most hydrodynamic studies comprising voidage measurements have been conducted in much smaller columns than industrial scale reactors. The effect of scale on the local flow structure in turbulent fluidized beds must be investigated in order to ensure that excellent contacting between gas and solids can be achieved when the column diameter is increased. Monitoring the local void behaviour while increasing the column diameter should provide valuable insights into how units can be scaled up without loss of conversion or yield.

4.3.1 Radial voidage distribution

The inhomogeneity of the solids holdup in the turbulent fluidized bed was investigated using capacitance probes by Abed (1984). Downward flow along the wall, and accelerated upward flow of higher voidage closer to the centre of the column were reported. From point measurements, the probability density function was computed to obtain hydrodynamic parameters such as void phase fraction and dense phase voidage (emulsion void fraction). A closer look at the radial density profiles reveals that, despite passing into the turbulent flow regime, the gas continued to favour flowing in the core of the fluidized bed, and a different momentum transport mechanism predominated near the walls. Using Geldart group B particles and a capacitance probe, Werther and Wein (1994) showed a shift to higher voidage in the central region as the gas velocity increased from 0.38 to 2.05 m/s.

More recently, Wang and Wei (1997) reported

$$\frac{1-\bar{\varepsilon}}{1-\varepsilon_m} = 0.908 + 0.276\left(\frac{r}{R}\right)^4 \tag{4.1}$$

where ε_m represents the cross-sectional average voidage. The radial voidage distributions in larger columns (D=0.71 m at z=0.23 and 0.36 m by Lu et al., 1996; D=0.47 m at z=0.36 m by Wang and Wei, 1997) show flatter profiles surrounding the centre of the column compared to smaller columns (e.g. D=0.15 m by Abed, 1984; D=0.09 m by Li et al., 1990; D=0.076 m by Issangya, 1998; D=0.09m by Xu et al., 1999) due to less wall effect on the voids in larger columns. Table 4.2

Table 4.1 Summary of reported hydrodynamic parameters in turbulent fluidized beds.

Investigators	Parameters studied	Method	D (m)	d_p (μm)	U (m/s)	H_0 (m)	z (m)
Lanneau (1960)	void size	capacitance probe	0.76	40-80	0.46 0.91	4.6	2.3
Lee and Kim (1989)	void rise velocity	pressure transducer	0.1	362	0.3-1.3	1.0	0.33 0.53
Nakajima et al. (1991)	void phase fraction	optical fiber probe	0.2	64	0.53, 0.66, 0.8, 0.93, 1.06	0.85 1.30	0.1 0.7 0.1 1.3
Yamazaki et al. (1991)	void rise velocity void size	optical fiber probe	0.2	64	0.45-1.1	0.85	0.5
Farag et al. (1997b)	void phase fraction	optical fiber probe	0.3,	65	0.34, 0.40 0.52	0.6, 0.9	0.21, 0.60
	void rise velocity void size		0.5		0.4, 0.55, 0.7	1.6	0.1, 0.4, 0.8, 1.2
Zhang et al. (1997)	void phase fraction void rise velocity void size	optical fiber probe	0.20	77.6	0.39 – 0.98	0.88 1.15	0.15, 0.35, 0.55, 0.75, 0.85
Lu et al. (1997)	void size	optical fiber probe	0.71 0.87	69.2 75	0.41-0.95	0.60	0.23, 0.36, 0.85
Taxil et al. (1998)	void rise velocity, length, and frequency; voidage	optical fiber probe	0.2	95	0.2-1.7	1.3	0.386
Cui et al. (2000)	voidage	optical fiber probe	0.152	70	0.1-0.9	0.3	0.15
Bayle et al. (2001)	void rise velocity, chord length, and frequency; voidage	optical fiber probe	0.19	FCC	0.2-2.0		0.18, 0.8

Table 4.2 Summary of literature data on radial voidage distribution in turbulent fluidized beds.

Investigators	Method	D (m)	d_p (μm)	U (m/s)	H_0 (m)	z (m)
Morooka et al. (1980)	capacitance probe	0.12	65-68	< 0.5	1.0	0.875
Abed (1984)	capacitance probe	0.152	54.8	0.55	-	1.48
Li et al. (1990)	optical fiber probe	0.09	54	-	-	-
Werther and Wein (1994)	capacitance probe	0.6	120	0.38, 2.05	0.65	0.14-2.75 7 levels
Lu et al. (1996)	optical fiber probe	0.71	75	0.41-0.95	0.60	0.6
Wang and Wei (1997)	optical fiber probe	0.47	54	0.38-0.95	0.58	0.36-1.09
Issangya (1998)	optical fiber probe	0.076	70	0.43-0.70	0.46	0.38
Xu et al. (1999)	optical fiber probe	0.09	54	0.11-3.15	-	3.0
Chaouki et al. (1999)	capacitance probe	0.2	120	0.15-0.71	0.5	0.15
Bayle et al. (2001)	optical fiber probe	0.19	FCC	0.2-2.0		0.18, 0.8
Lin et al. (2001)	optical fiber probe	0.186	75	0.025-10.2	-	0.72

summarizes the published work on radial voidage distributions in turbulent fluidized beds. This earlier work is referred to below.

4.3.2 Dense phase voidage

It has been shown (Chaouki et al., 1999) that as the gas velocity is increased in the turbulent regime, the volume fraction of voids increases while the dense phase voidage increases from that of minimum fluidization. The dense phase voidage is often a key parameter in inventory control, process modeling and pressure balance in fluidized bed operations (King, 1989). The measured average void fraction has been used to calculate the dense phase voidage (Yamazaki et al., 1991), suggesting expansion of the dense phase during transition from the bubbling to the turbulent regime. Similarly, Werther and Wein (1994), using Geldart Group B particles, observed a significant increase of dense phase voidage with increasing gas velocity. The dense phase voidage was obtained from the probability density distribution of capacitance probe signals. However, no clear influence of radial position was observed for the particles under investigation. In both of these studies, point density measurements were analyzed to deduce the phase fractions from probability density functions. The threshold value in the probability distribution function strongly influences the resulting phase fraction, especially for high velocity fluidization (Bi, 1994), so that reliance on this method alone is questionable.

Lee and Kim (1989) indirectly measured the dilute phase fraction, and calculated the interstitial gas rise velocity and voidage in the dense phase from measurements of tracer gas concentration in the dense and dilute phases using Geldart group B particles. Cai et al. (1988) and Wang et al. (1997) conducted collapse tests in a column which physically separates the bed and freeboard, making it possible to eliminate accumulation of entrained particles on top of the bed surface as it collapsed. The effect of particle mean size on the performance of the fluidized bed was studied using this configuration. Once entrained and carried over to the freeboard, these particles had no means of returning to the bed, thereby changing the particle mean size in the bed from the initial condition. The dense phase voidage was independent of the gas velocity between 0.1 and 0.5 m/s, in agreement with Yamazaki et al. (1991). No direct measurements of the dense phase voidage have been reported for superficial gas velocities beyond 0.5 m/s, possibly due to the difficulty of conducting experiments such as collapse tests in high velocity fluidized beds.

One method of deducing the local void fraction is by inserting probes which can differentiate local solids concentrations, and thus obtaining the cumulative void contact time which is then divided by the total sampling time. The signals are averaged with respect to time, and the time fraction of the probe in voids is considered to be the local void fraction. Optical fiber probes have revealed an increase in the non-uniformity of local void fractions across the radius in turbulent fluidized beds, with increasing height (Nakajima et al., 1991; Farag et al., 1997a; Zhang et al., 1997), and gas velocity (Nakajima et al., 1991; Zhang et al., 1997). However, once again, difficulty exists in setting a threshold to distinguish the phases, thus resulting in ambiguity and limiting the accuracy of the reported phase fractions.

4.4 Optical probe measuring method principles

Voids in turbulent fluidized beds are known to be intermittent and transient in nature. Because of their simplicity and affordability, fiber optic voidage probes are often chosen to measure voidage fluctuations and distribution. Both emissive and reflective optical measurement systems can be used to deduce the solid volume concentration. However, emission is not suitable for dense suspensions (Louge, 1996; Werther, 1999). Reflective optical fiber probes work on the principle that a small volume of particles is illuminated and the reflected light intensity is correlated to the volumetric concentration within a local measuring volume at the tip of the probe. Voidage fluctuations in a turbulent fluidized bed were investigated in this project to yield instantaneous local solid concentrations. If the instantaneous bed density measurements reflect the characteristics of the passing voids, analysis of the signals should give very localized hydrodynamic information. Voidage measurements using miniature optical fiber probes are slightly invasive, yet they provide insight into the physical phenomena of the fluidized bed.

According to Krohn (1987), different fiber configurations result in different characteristic responses (see Figure 4.1). Thus, the design of optical probes must reflect the size of particles of interest. As depicted in Figure 4.2, the signal from the reflective-type optical probe will capture particle movement when the measuring volume of a probe is comparable in size with the particles. Alternatively, if the measuring volume is large enough to contain a large number of particles, signals transmitted from the probe represent swarms of particles.

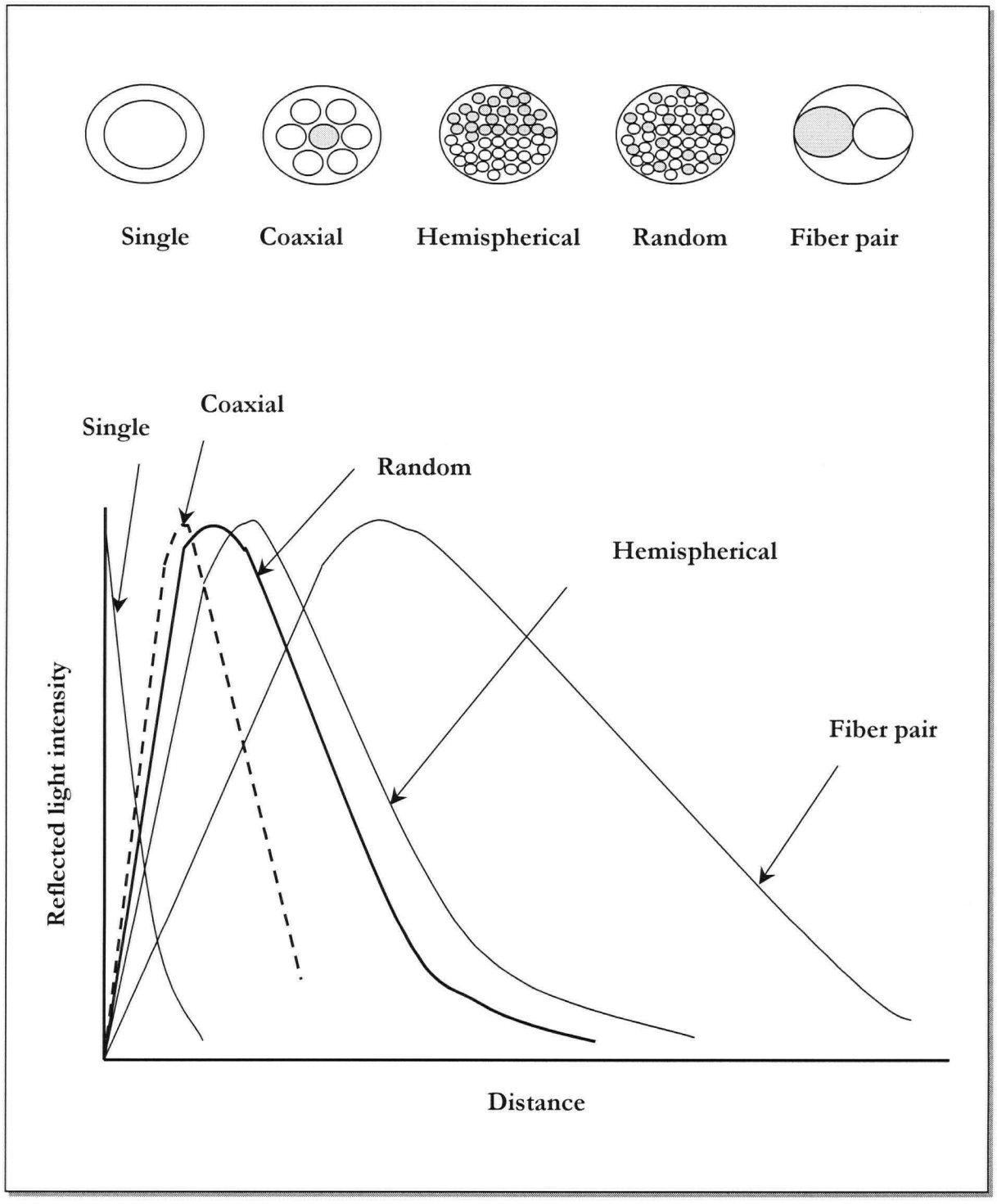

Figure 4.1 Reflective-type optical fiber probe response curves for various fiber configurations (adapted from Krohn, 1987).

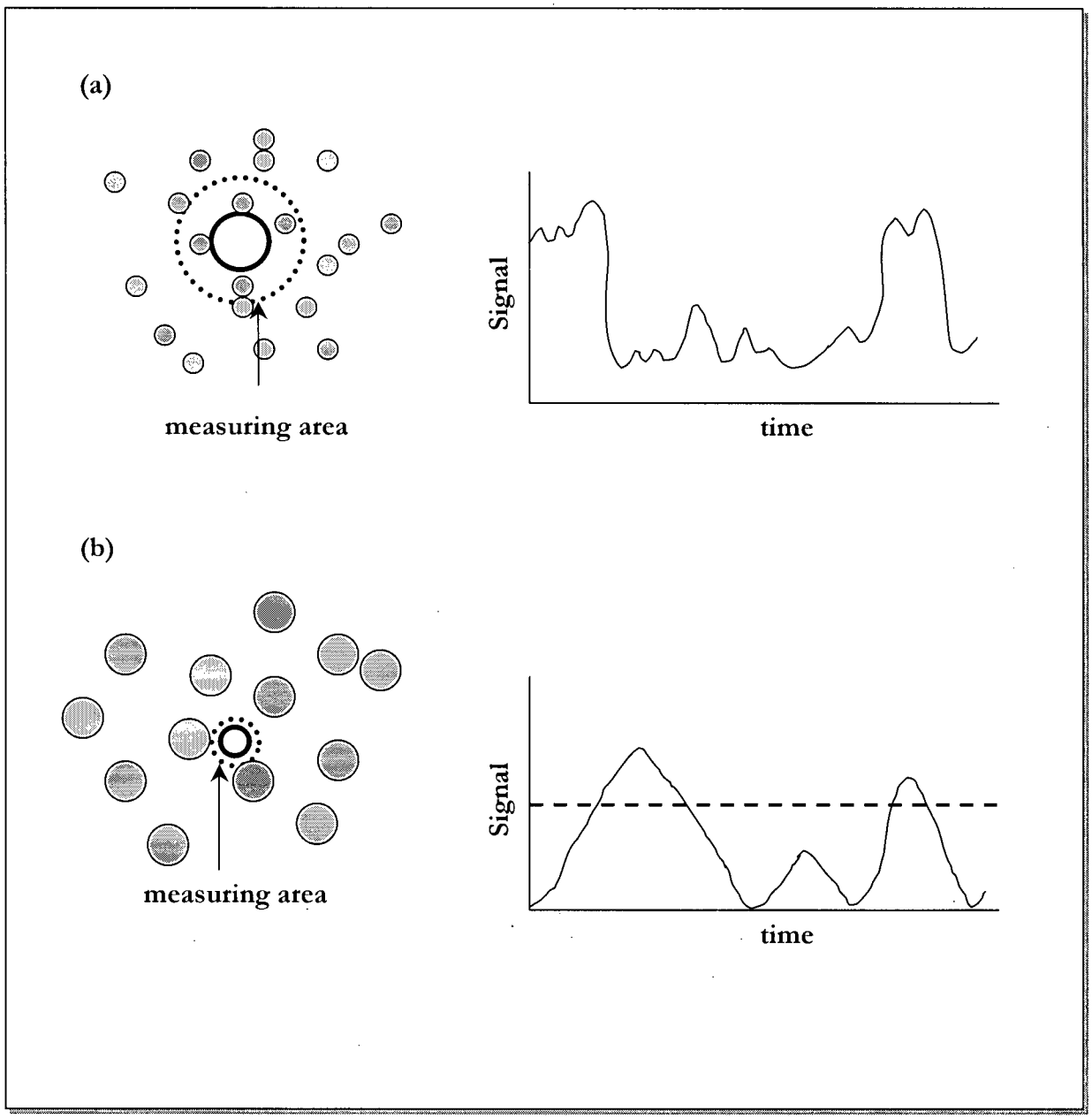

Figure 4.2 Probe tip in relation to particle size. Reflective optical fiber probe detecting (a) swarm of particles; and (b) single particles (adapted from Matsuno et al., 1983).

4.5 Optical voidage probe used in this study

The two identical reflection type optical fiber probes, PC-4 Powder Voidmeter, used for voidage measurements in this work were supplied by the Institute of Chemical Metallurgy of the Chinese Academy of Science in Beijing, China. A schematic diagram of the configuration for the optical fiber probe is shown in Figure 4.3. The probe contains a bundle of fibers projecting light onto a swarm of particles interspersed with light-receiving fibers which measure the intensity of the light reflected from the particles. The bundle diameter is 4 mm, length is 600 mm, and individual fiber diameter is 15 μm. The fibers are arranged in an alternating array of emitting and receiving layers. Because the particle diameter is much smaller than the bundle diameter, light is reflected by many particles in the measurement volume, allowing the probe to detect the instantaneous solids volume concentration from the output voltage, after suitable calibration. The measuring volume of the reflective-type optical probe is dependent on the solids concentration at the tip. Thus, careful calibration of the response signal to the solids concentration is required for accurate measurement of voidage. This is discussed in the next section.

The local voidage measurement system includes a reflective optical fiber probe, light source, photo-multiplier, A/D converter and data acquisition system (Figure 4.4). The PC-4 Powder Voidmeter allows auto-adjustment of the photomultiplier in order to compensate for variation of the light source through re-adjustment using the reference light. The emitting and receiving diode circuits can be adjusted separately allowing the control of the sensitivity, maximum signal output and offset value. Before and after each set of runs, the voidmeter was calibrated against a dense bed (to give ~5 V) and the 'black box', a tube painted black to prevent reflection of light, representing the no solid condition (set at ~0 V). Any shifts of the upper and lower settings were corrected through the calibration equation, having the form of Equation 4.5, when converting the voltage signals to local voidages.

Measurements of instantaneous voidage fluctuations were captured through voltage output logging using LABTECH® Notebook 10.1 sampling at 100 Hz for periods of 100 s.

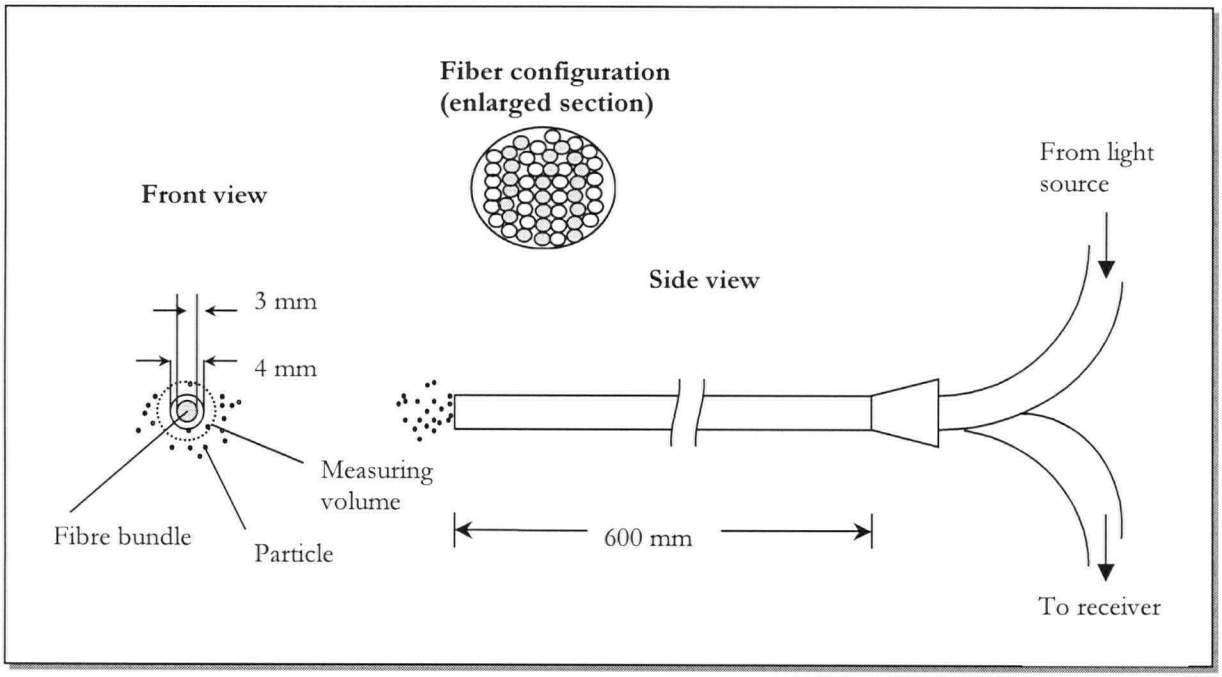

Figure 4.3 Optical fiber probe for measuring local particle concentrations: the probe is shown detecting a swarm of particles.

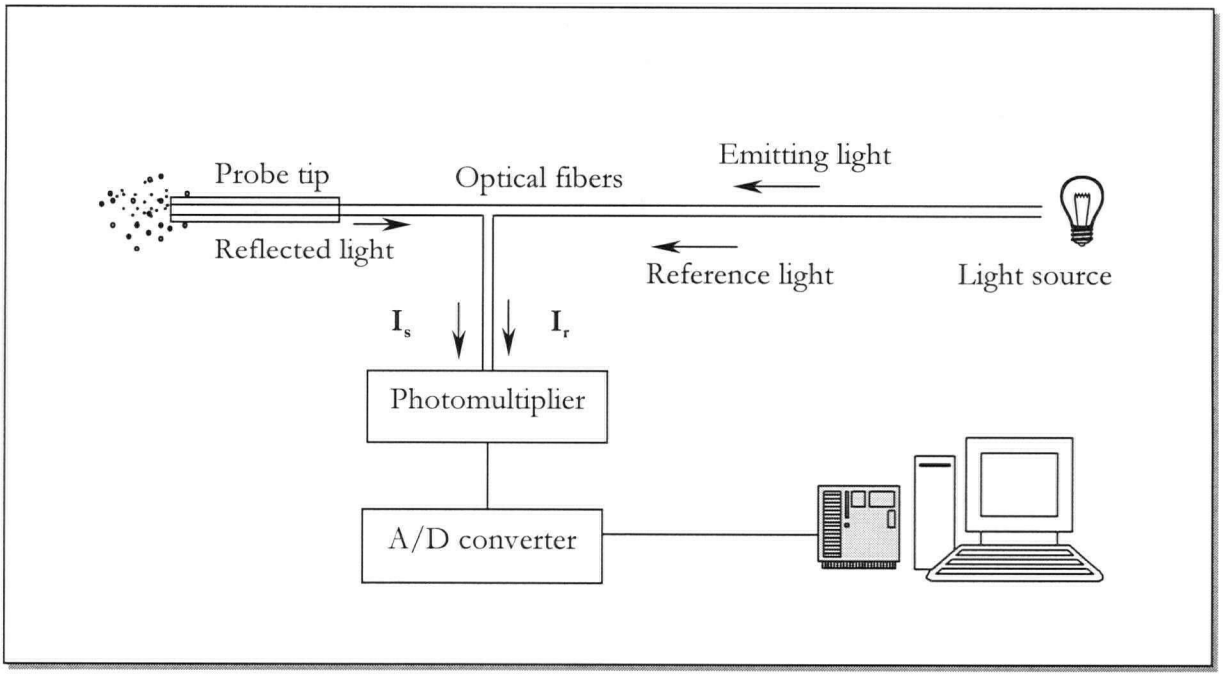

Figure 4.4 Schematic of local voidage measurement apparatus and configuration.

4.5.1 Optical probe calibration

As emphasized by numerous researchers (e.g. Amos et al., 1996; Zhang et al., 1998), one of the disadvantages of otherwise simple and relatively inexpensive reflective-type optical fiber probe is the difficulty in obtaining an accurate calibration of voidage as a function of reflected light intensity, especially in gaseous suspensions. Due to the nature of heterogeneous suspensions in gaseous media, an accurate and reproducible calibration procedure has been elusive (Herbert et al., 1994). Zhang et al. (1998) reviewed the calibration methods employed by earlier researchers. More recent researchers prefer that the calibration be done in the medium of interest. Thus, extrapolating calibration results from a liquid fluidized bed to a gas-solid riser (Hartge et al., 1986) has been criticized for not considering the difference in refractive index between water and gas. Furthermore, the method of calibration must reflect the required scale and flow dynamics. For instance, the average cross-sectional voidage measured by pressure transducers was used to calibrate the optical probe response by Tung et al. (1989). Calibration against time-mean values may introduce uncertainties (Lischer and Louge, 1992) when measuring instantaneous values. Calibration against a capacitance probe (Lischer and Louge, 1992; Herbert et al., 1994) introduces a difference in measuring volume and shape, no doubt altering the calibration. Furthermore, use of linear relationships for comparison between different measuring volumes is questionable (Zhang et al., 1998).

Mathematical simulation using a Monte Carlo method was carried out by Lischer and Louge (1992). The influences of particle size, numerical aperture of the optical fibers, and the ratio of the refractive indices of the particles and the suspending medium were tested. Amos et al. (1996) investigated the probe reflection curve and response function for a fiber diameter of 1 mm, and concluded that the relation of the fiber diameter to the effective penetration of light in to the suspension was the controlling variable. Thus, the inclusion of particle diameter was necessary. Bergougnoux et al. (1999) and Bellino et al. (2001) improved on the Monte Carlo simulation by incorporating such factors as: the volume fraction of suspension; scattering properties of particles (i.e., refractive index, size and shape); geometric properties of the sensor (i.e., fiber diameter and distances between emitting and receiving fibers), for a bundle of fibers with a central emitting fiber surrounded by two bundles of receiving fibers.

Calibration of local particle concentration has been examined theoretically by Liu (2001).

Eliminating the 'blind zone' (e.g. Figure 5.2), and obtaining a monotonic reflective function by placing a protective quartz window in front of the probe tip, suggested by Cocco et al. (1995), were confirmed by the simulation results (Liu, 2001). For a typical fiber diameter of 40 μm for a multi-fiber optical probe, a window thickness of 80 μm resulted in a nearly linear calibration curve.

4.5.2 Experimental calibration of optical voidage probe

Measurement of voidage in turbulent fluidized beds requires that the voidage probe capture the full spectrum of voidages, i.e., from dense bed to 100% void. The calibration was accomplished with the same particles and the same suspending medium, i.e., air as were used in the fluidization experiments. The optical probe system had to be turned on for half an hour or so before calibration for the system to stabilize. Failure to do so resulted in shifting signals. The FCC particles were put in a container designated for dense bed calibration to set the upper voltage, while a 'black box' supplied by the Institute of Chemical Metallurgy was used to set the lower voltage. The black box was a tube with an inner coating of black paint to absorb all visible light emitted from an optical fiber probe, thus providing conditions equivalent to no solid suspension. An iterative procedure was adopted to adjust the upper and lower voltages to enhance the probe sensitivity by setting the full-scale limits of the probe.

Calibration was conducted in the same unit as was used by Liu (2001) based on the dropping/trapping techniques described by Issangya (1998) and Issangya et al. (2000). The calibration set-up, shown in Figure 4.5, is comprised of an incipiently fluidized hopper section at the top where solids are introduced, a 12.7 mm ID tube to develop the solids flow, a pair of externally connected slide valves to trap the solids, and a collection vessel at the bottom. Once a steady fall of solids is attained, the optical probe signals are recorded at 100 Hz for 10 s before trapping the solids between the slide valves by simultaneously shutting the two valves. The collected solids are weighed to calculate the volumetric solids concentration, which is correlated to the recorded signal. By changing the feeding tube in the hopper and the flow of aeration air, a wide range of solids concentrations could be attained. The optical probe was calibrated using the FCC I particles with and without the glass window (see Figure 4.6). However, this method produced considerable scatter of the equivalent voidage calculated from the captured solids between the slide valve. This was considered to be mainly due to the imperfect closing of the slide valve, and fluctuation of the downflow of solids. Another difficulty encountered was the presence of electrostatic charges, which caused solids to adhere to the tip of the probe.

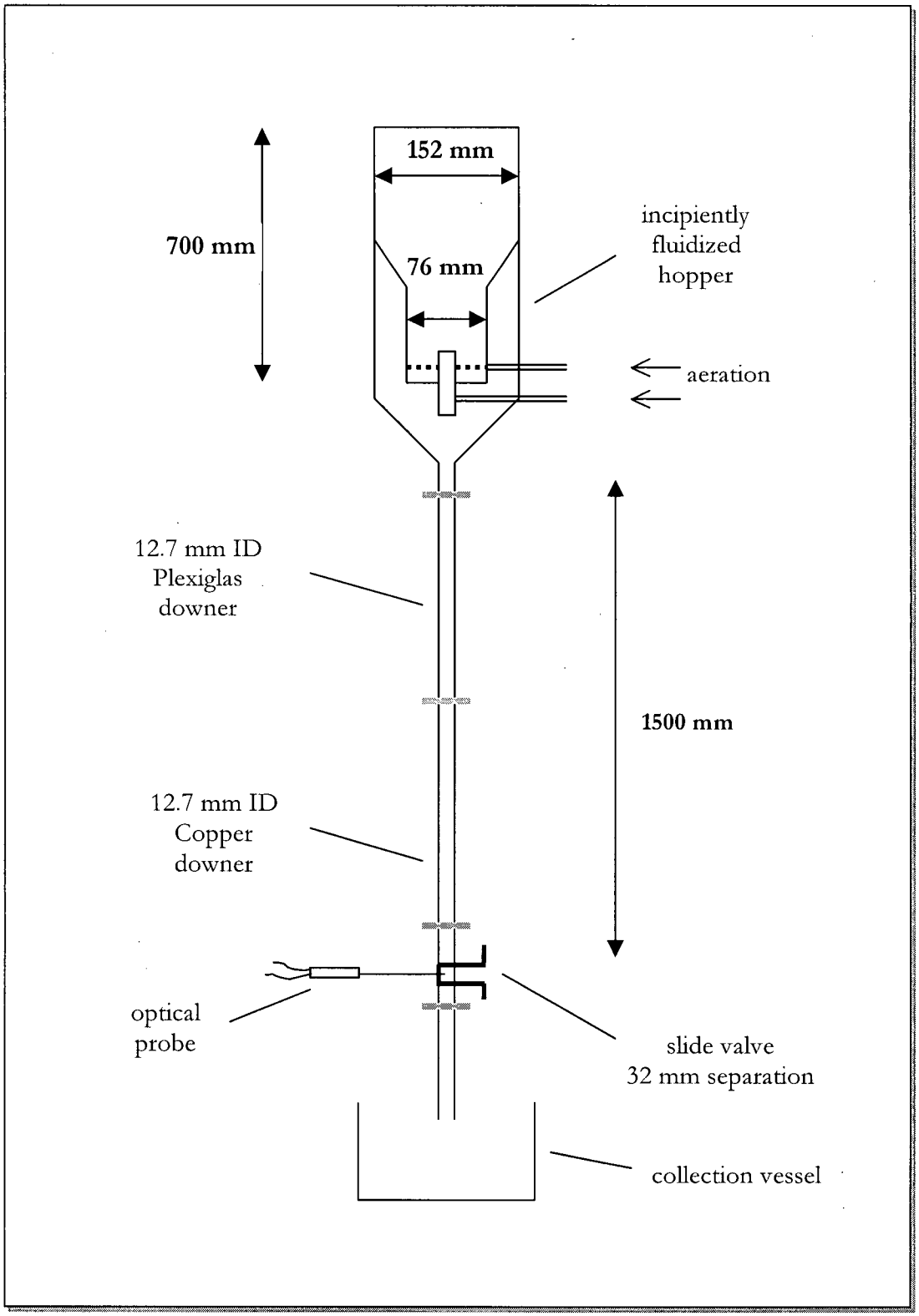

Figure 4.5 Schematic of optical probe calibration equipment applying "drop-trap" technique.

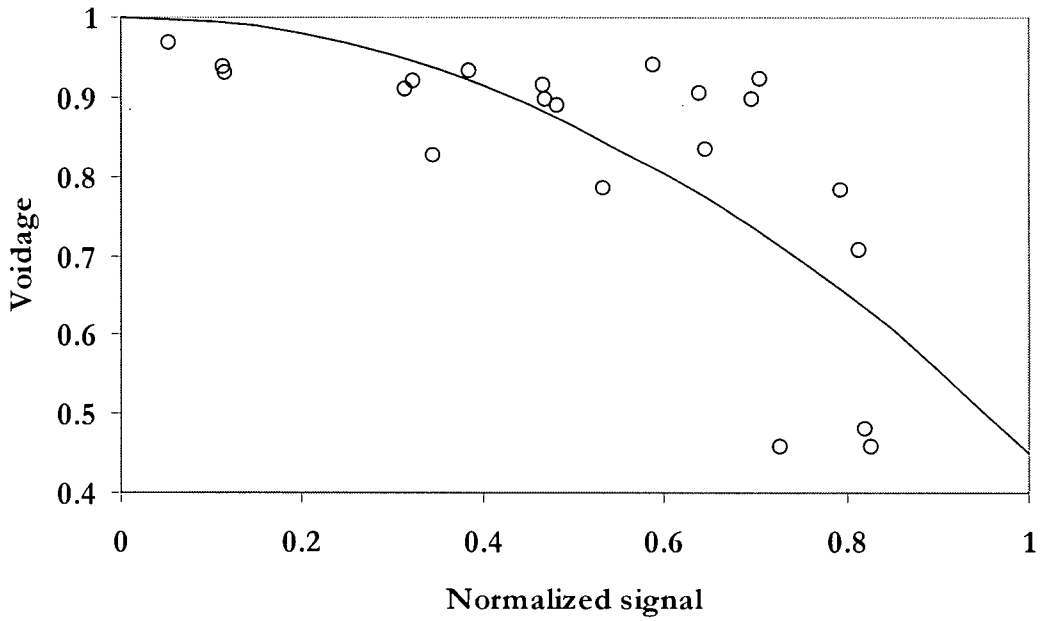

Figure 4.6 Response curve for calibration of optical probe using FCC I without glass window. The line represents the calibration curve of Issangya (1998).

Another method was devised to measure the signal response to reflect the solid concentration using FCC and coke particle mixtures. Both FCC and coke particles were sieved using screen sizes of 90 and 150 μm with a mean particle size of 120 μm. Different concentration mixtures were obtained by combining a known ratio of the two types of solids, FCC reflecting light and coke particles absorbing light, and detected by the optical voidage probe. Compared to the response from the bare probe, the results with the glass window at the tip of the probe show a near-linear response to the equivalent voidage calculated from the concentration of FCC in mixture, as shown in Figure 4.7. The near-linearity is further supported by examining the effect of the glass window in the following section.

In addition, the optical probe with the glass window (see below) was placed in a beaker where FCC II particles were suspended in water through stirring. As the refractive index of water differs from that of air, i.e., 1.33 and 1 in vacuum, respectively, quantitative calibration cannot be obtained through suspension in liquid media. However, the trend shown in Figure 4.8 suggests an improved linearity of response, comparable to that reported by Liu (2001).

4.5.3 Glass window

One of the difficulties encountered with voidage measurements using the optical fiber probe was accumulation of static charges, not completely eliminated by the addition of Larostat 519, an anti-static agent. The presence of static electricity was evident from touching the exterior surface of the Plexiglas column and having solids congregate around this point, hearing sparks at the top of the column, and observing flashes of light at the tip of the optical probe. The well-reported problem of electrostatic charges (e.g. Zhang et al., 1998; Geldart, 1986) could affect the optical measurement in turbulent fluidized beds as the operating gas velocities are not high enough to sustain the solids in dilute suspension, or to sweep the particles away from the probe tip.

Another phenomenon that was noticed was the probe response signal exceeding the pre-set maximum value. As shown in Figure 4.9, despite setting the upper and lower voltages to dense bed and black box values, once the probe was placed in the bubbling fluidized bed, the signals frequently reached values beyond the maximum. At a superficial velocity of 0.15 m/s with the probe in the centre, it is expected that the optical probe will pick up the movements of voids passing the tip. However, the signal obtained is difficult to comprehend in terms of void dynamics.

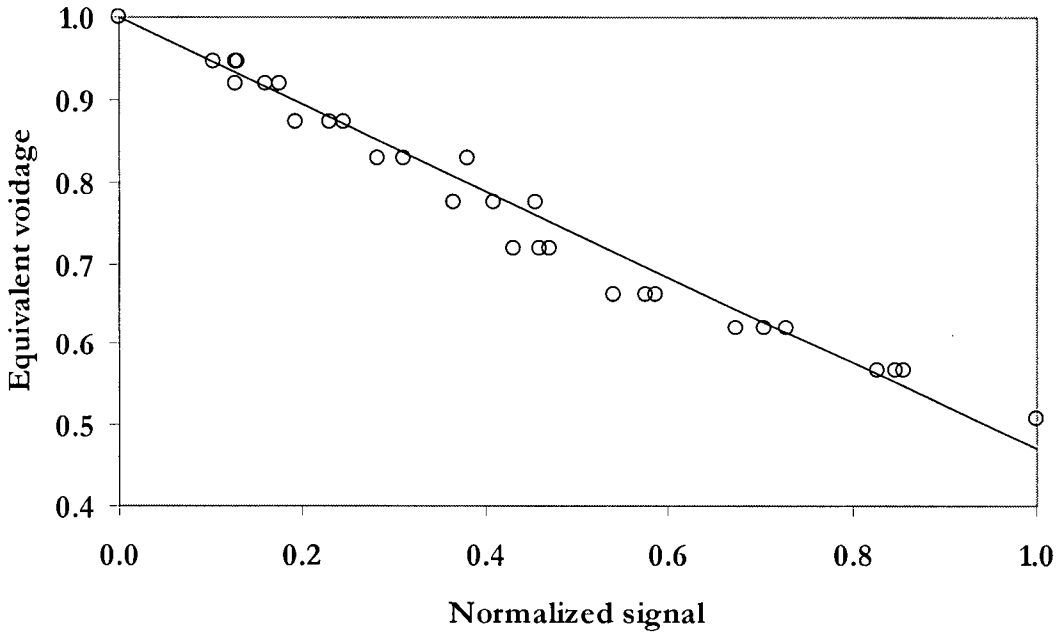

Figure 4.7 Response curve for calibration of optical probe using FCC I and coke particles with glass window.

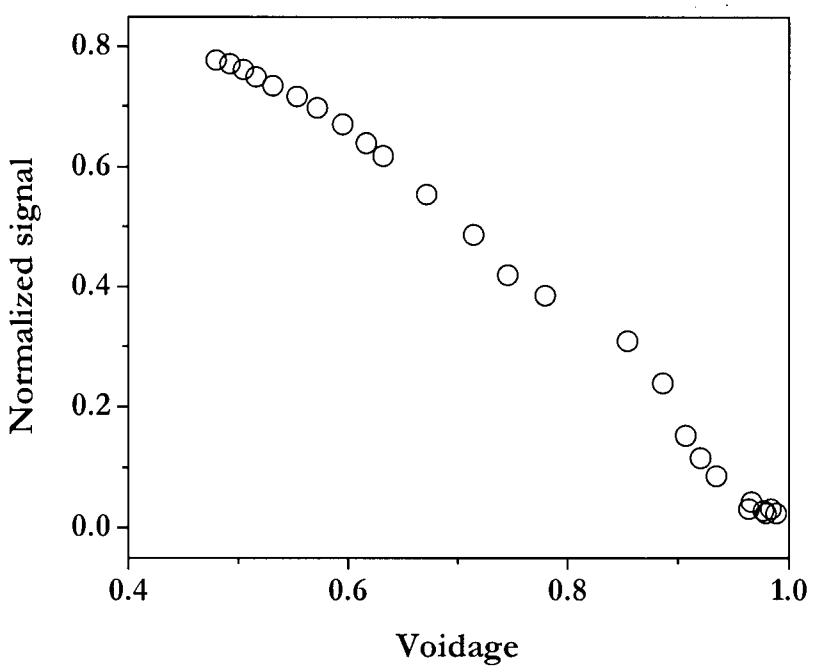

Figure 4.8 Response signal of experimental calibration curves for FCC II with glass window in water-solids system.

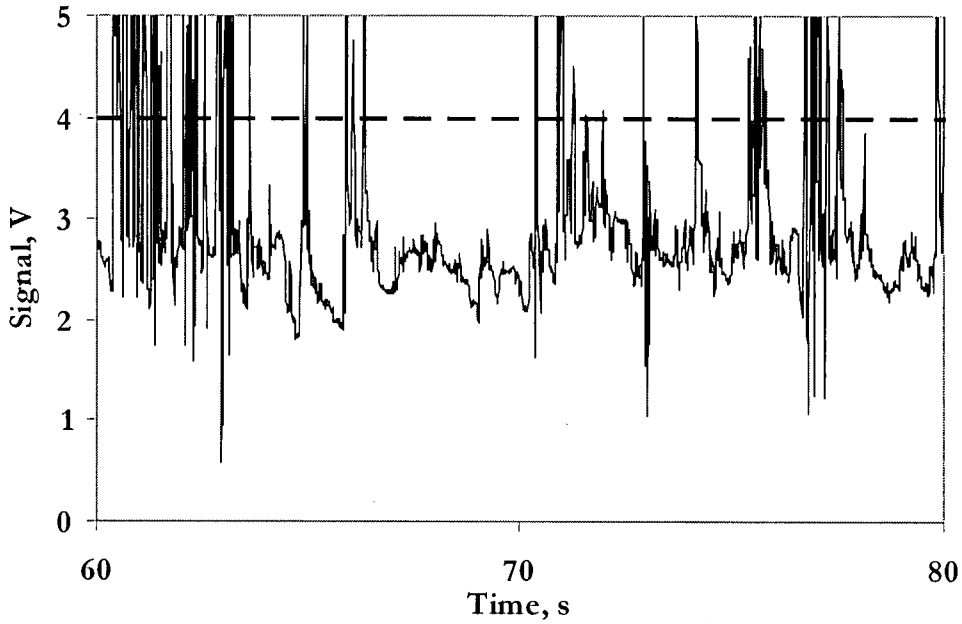

Figure 4.9 Signal obtained from optical probe without glass window. (Dotted line represents the maximum calibrated value.) D=0.29 m, U=0.15 m/s, z=0.15 m, r/R=0.0, FCC I.

As shown in Figure 4.4, the signal obtained through the photomultiplier is the relative intensity between the reflected light and the reference light, i.e.,

$$I = \frac{I_{signal}}{I_{reference}} \tag{4.2}$$

Since the intensity is converted to voltage, when the signal intensity is higher than $I_{reference}$, as shown in Figure 4.10 (a), the relative intensity becomes larger than 1, translating to a voltage beyond 5 V. However, when a quartz glass window of 0.5 mm thickness, custom made by Canadian Scientific Glass Blowing, covered the probe tip, as depicted in Figure 4.10 (b), the signal intensity was always less than the maximum reference intensity. Figure 4.11 shows the difference in the measured voltage for the same operating condition as in Figure 4.9, but with the glass window covering the tip. Evidently, the 'blind zone' was eliminated and the probe response was altered. The basis for the linear response of the probe with the 'blind zone' being eliminated is reported by Liu (2001).

The routine measurement of local voidage using the optical voidage probe involved obtaining the upper and lower voidage limits, with the black box and dense phase, respectively. Linearity was then assumed to be valid for voidages between these two limits.

The 0.29 m Plexiglas column was covered with black curtains to ensure there was no external light permeating through the column to give erroneous results.

4.6 Capacitance probe

As noted before, capacitance probes measure the dielectric constant between two poles, with the signal being a function of the solids concentration between the poles. By maintaining the voltages of the guard and sensor at the ground voltage, the probes and guard circuit reported by Acree and Louge (1989) did not induce electrostatics, nor did they attract charged particles. As highlighted by Wiesendorf and Werther (2000), the linear relationship between voidage and capacitance signal generally applies well for gas-solid suspensions, although linearity may not hold for systems at high temperature due to the relative dielectric constant of solids being affected by increasing temperature. Disadvantages of capacitance probes include the measuring volume being not well defined, and the sensitivity of the capacitance probe to humidity (Zhang et al., 1998). The output signal of the capacitance probe in voltage, is given by

$$V = \frac{Q_s}{[gain] \times C} \tag{4.3}$$

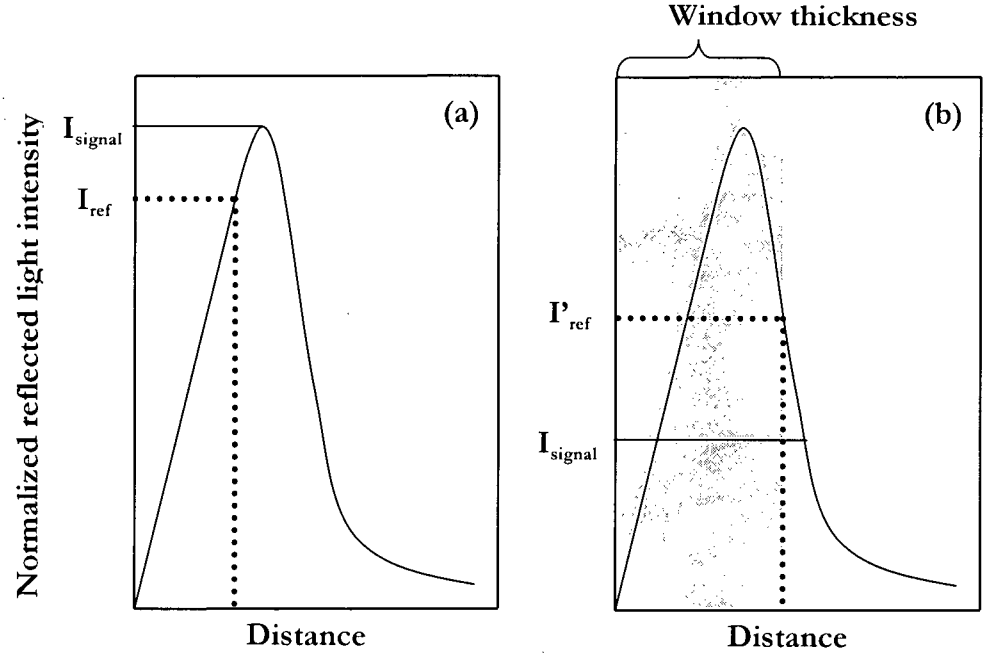

Figure 4.10 Setting the upper intensity in dense bed: (a) without window; (b) with window.

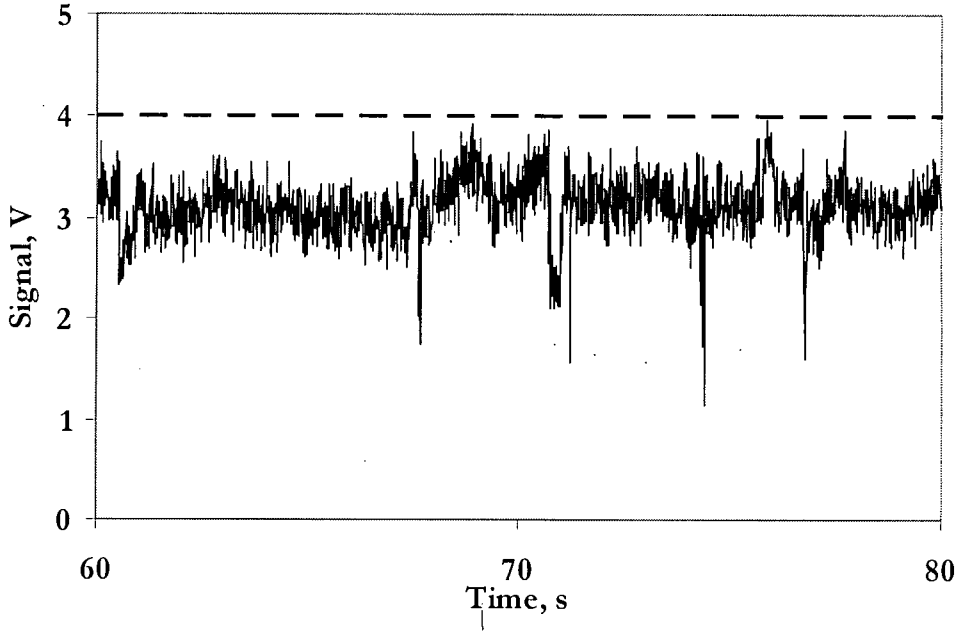

Figure 4.11 Signal obtained from optical probe with glass window. (Dotted line represents the maximum calibrated value.) D=0.29 m, U=0.15 m/s, z=0.15 m, r/R=0.0, FCC I.

where Q_s is the constant charge amplitude supplied by the amplifier. The effective relative dielectric permittivity, K_{eff}, is a function of local voidage, particle size, sphericity, and particle size distribution for particles of negligible conductivity (Louge and Opie, 1990). If the gain and charge are constant, then K_{eff} can be expressed as:

$$K_{eff} \propto \frac{C}{C_0} \propto \frac{V_0}{V} \tag{4.4}$$

where C is the capacitance between the probe surface and ground.

The capacitance probe used in this study was developed in-house at CSIRO and used exclusively in the 1.56 and 0.61 m diameter columns. The probe schematic presented in Figure 4.12 has a very similar design and construction to the one used also at CSIRO and reported by White and Zakhari (1999). The probe is connected to a capacitance meter with a driven-shield to minimize electrical noise such as stray and cable capacitances. Initially, the upper and lower capacitance response limits were set by placing the probe into the column prior to injecting solids, i.e., in air for the upper voidage limit, and into the static bed in the column after solids injection.

Calibration of the capacitance probe with FCC particles suspended in water was conducted to obtain the response and to extrapolate the results to the gas-solid system. The capacitance probe was placed in a beaker where FCC particles were suspended in water by means of stirring. Figure 4.13 depicts the normalized response vs. volumetric solids concentration in water. The effect of solid concentration on the effective relative dielectric permittivity of a suspension, K_{eff}, is presented in Figure 4.14 and compared to calibration models applied to the water-solids system. The relative dielectric permittivity of FCC material, K_p, is estimated to be 14 for all models, based on the findings of Louge and Opie (1990). At very dilute conditions, the effective relative dielectric permittivity, K_{eff}, of a FCC-water suspension is seen to be well represented by the linear model. However, the capacitance response becomes fairly insensitive to the volumetric solid fraction beyond 0.03, as depicted in Figure 4.14. The discrepancies between measured response and the models are attributed to the difficulty in assessing the wetting behaviour of porous FCC with an unknown amount of water penetration into the pores.

Therefore, as suggested by Wiesendorf and Werther (2000), the linear signal response was taken to be adequate for measurements in gas-solids suspensions, and thus applied in this case.

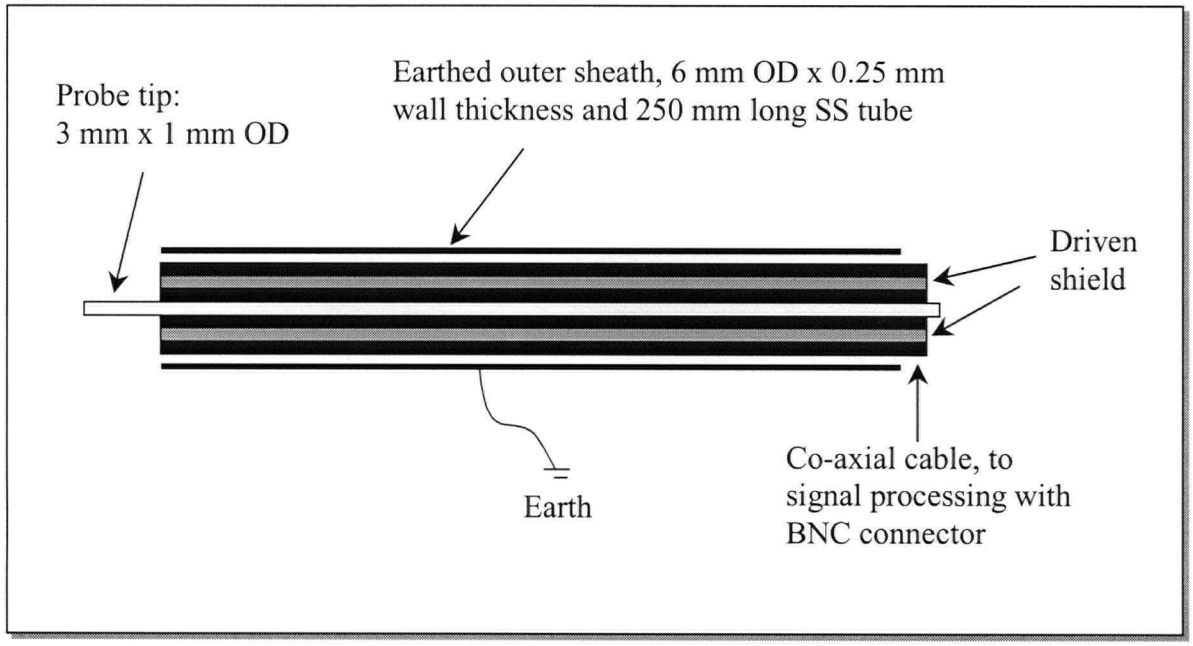

Figure 4.12 Schematic of needle-type capacitance probe.

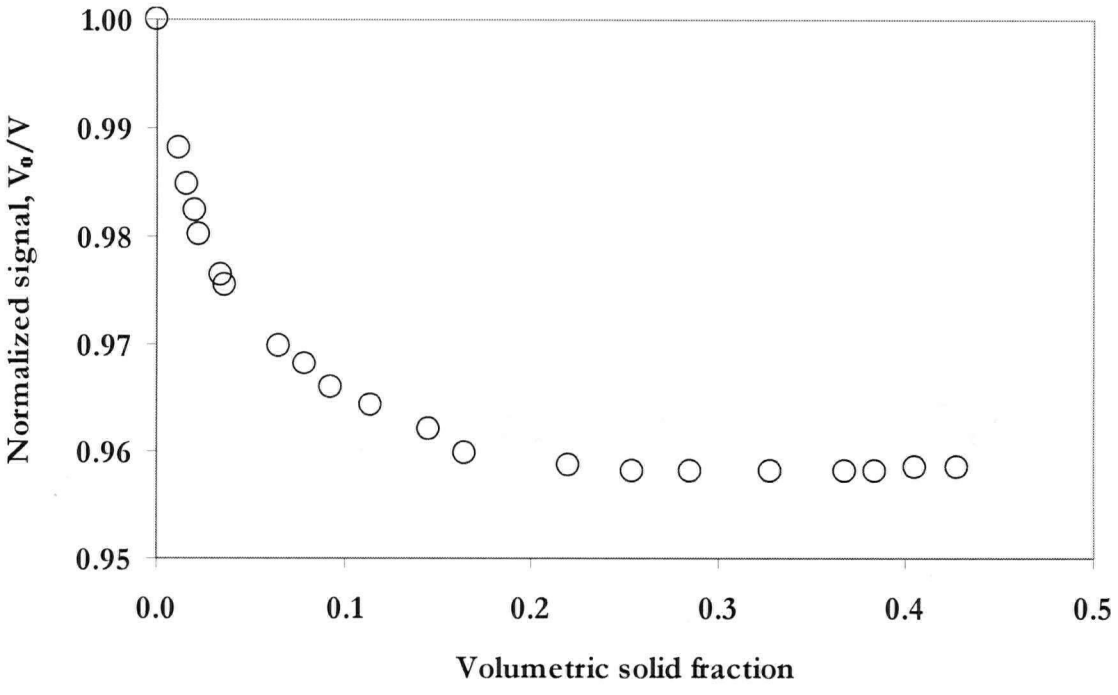

Figure 4.13 Signal response of capacitance probe with FCC II in water-solids suspensions.

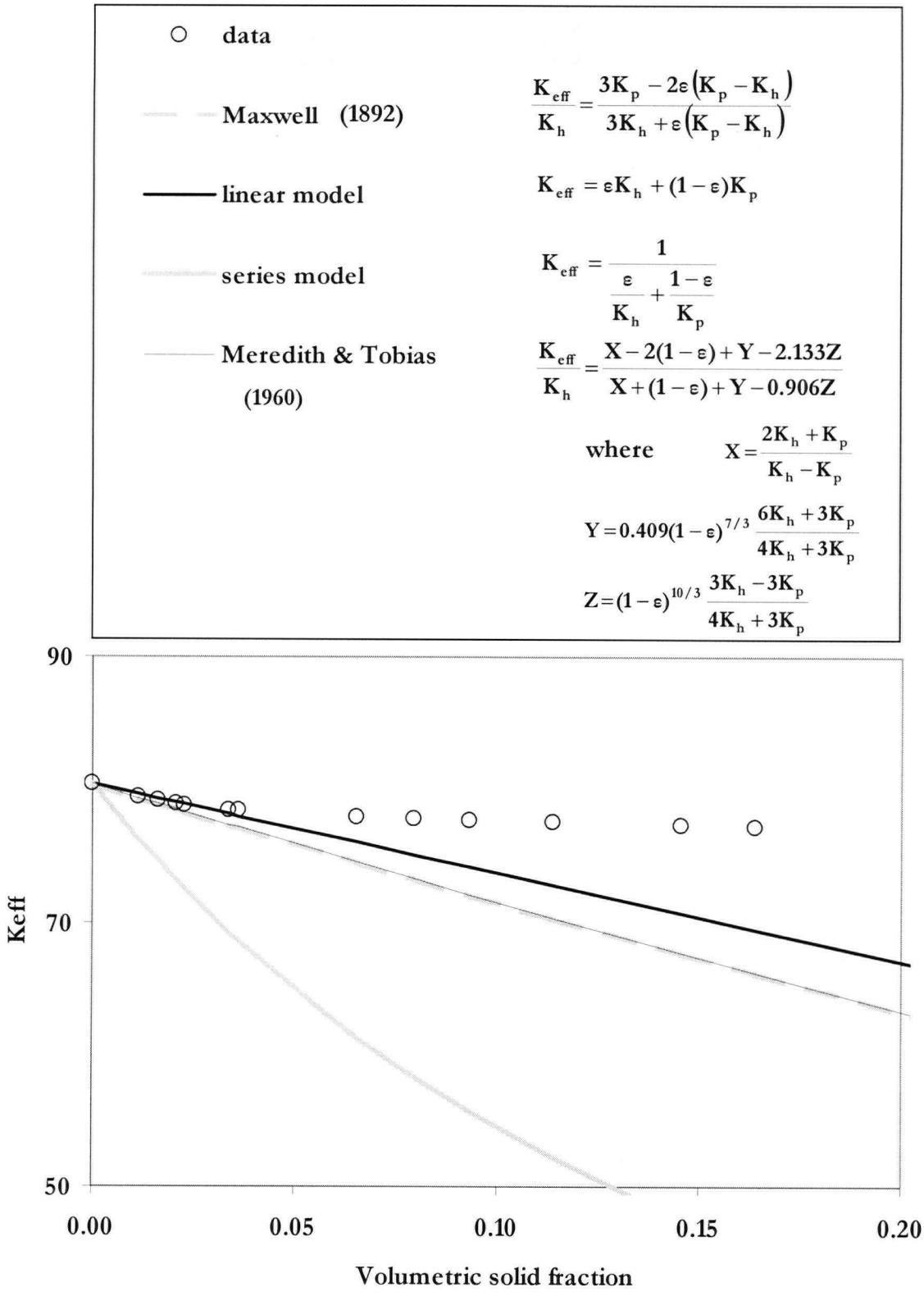

Figure 4.14 Effect of volumetric solids fraction on the effective relative dielectric permittivity of a water-FCC system. All models assume K_p = 14 and K_h = 80 for FCC and water, respectively, based on Louge and Opie (1990).

The temperature of the fluidizing air ranged from 18 to 66°C, a range which was considered to be small enough that there was negligible change in the relative dielectric constant of FCC (Wiesendorf and Werther, 2000).

4.7 Results

4.7.1 Optical fiber probe

Local voidages were captured by the optical fiber voidage probes by sampling at 100 Hz for durations of 100 s. Voltage signals were converted to voidages by

$$\frac{1-\varepsilon}{1-\varepsilon_{mf}} = \left(\frac{V - V_0}{V_{mf} - V_0} \right)^n \tag{4.5}$$

where V_0 is the voltage signal obtained from the black box where negligible light is reflected, representing a voidage of 1, and V_{mf} is the signal when the probe is immersed in a container of static solids representing closely the voidage at minimum fluidization. The power n was taken as 1 for a linear response of voltage against voidage. The two end points, V_0 and V_{mf}, were calibrated several times during experimental runs to detect any shift in signal output. In general, allowing sufficient time to warm up the equipment resulted in stable V_0 and V_{mf} readings.

Occasionally when converting voltage measurements to voidage signals, signals were recorded outside the range set by the two end points, i.e., the black box and dense phase limits. Distinction criteria were set between noisy signals, i.e., electrical spikes, and the shifts in the range of signals were observed to be mostly linear. For a given set of data, V_{max} and V_{min} were plotted chronologically for each set to assess against the V_{mf} and V_0 values. Any gradual shifts or isolated shifts were further investigated by plotting the probability distribution curve for each set. Data points of probability <0.5 % for the lower limit (if $V_{min} < V_0$), or > 99.5 % for the upper limit (if $V_{max} > V_{mf}$) were considered to be outliers. Otherwise, probability distribution curves for data sets before and after the one under investigation were assessed to examine if any shift in output could be observed. On average, a 3% difference in voidage was observed by re-adjusting the signal limits, with as high as 7.6% within the data set studied.

4.7.2 Radial voidage profile

The time-mean local voidage was calculated from

$$\bar{\varepsilon} = \frac{1}{T}\int_0^T \varepsilon_t \, dt = \frac{1}{N}\sum_{i=1}^{N} \varepsilon_{t_i} \tag{4.6}$$

Figure 4.15 represents a typical radial voidage profile at three axial levels in a 0.29 m diameter column containing FCC I particles with a static bed height of 0.51 m. At the level closest to the distributor plate, the flow was not fully developed, as signified by the asymmetric distribution. The return leg re-introducing entrained solids into the column was positioned at 90° to the plane of the plot in Figure 4.15 at z between 0.051 and 0.18 m which may affect the local voidage at z=0.15 m.

At the next level of z=0.27 m, better symmetry is observed. An increase in gas velocity clearly increases the local voidage at most radial locations. The difference in voidage measurement near the wall represented by r/R=-0.98 and 0.98 are likely due to the probe insertion from one side. The optical voidage probe was inserted into the column at r/R=1 and extended to measure voidage at r/R=-0.98. The short distance between the tip of the probe and the wall may have disturbed the local flow. Asymmetry of the radial voidage profile is observed at the level of z=0.40 m. This may be due to the effect of solids movement near the fluctuating expanded bed surface.

The cross-sectional average voidage, ε_m, was obtained by integration of the polynomial curve fit of local time-mean voidage over the column cross-section.

$$\varepsilon_m = \frac{1}{R^2}\int_0^R 2\bar{\varepsilon} r dr = \int_0^1 2\bar{\varepsilon}\varphi d\varphi \tag{4.7}$$

where φ=r/R. Figure 4.16 depicts the cross-sectional average calculated from the data shown in Figure 4.15. The trend is as expected, with the overall cross-sectional voidage remaining relatively constant within the bed, and starting to increase close to the top of the expanded bed, i.e., at z=0.40 m. U_c measured from the standard deviation of DP reading located between z=0.40 and 0.463 m is 0.495 ±0.015 m/s, beyond which point a sudden increase in cross-sectional average voidage is observed at z=0.40 m in Figure 4.15.

Cross-sectional average voidages from the optical probe are compared with those from DP measurements at z=0.27 m in Figure 4.17. Cross-sectional average voidages from the optical probe tend to be somewhat higher than from DP signals. This may be due to the DP measurements being

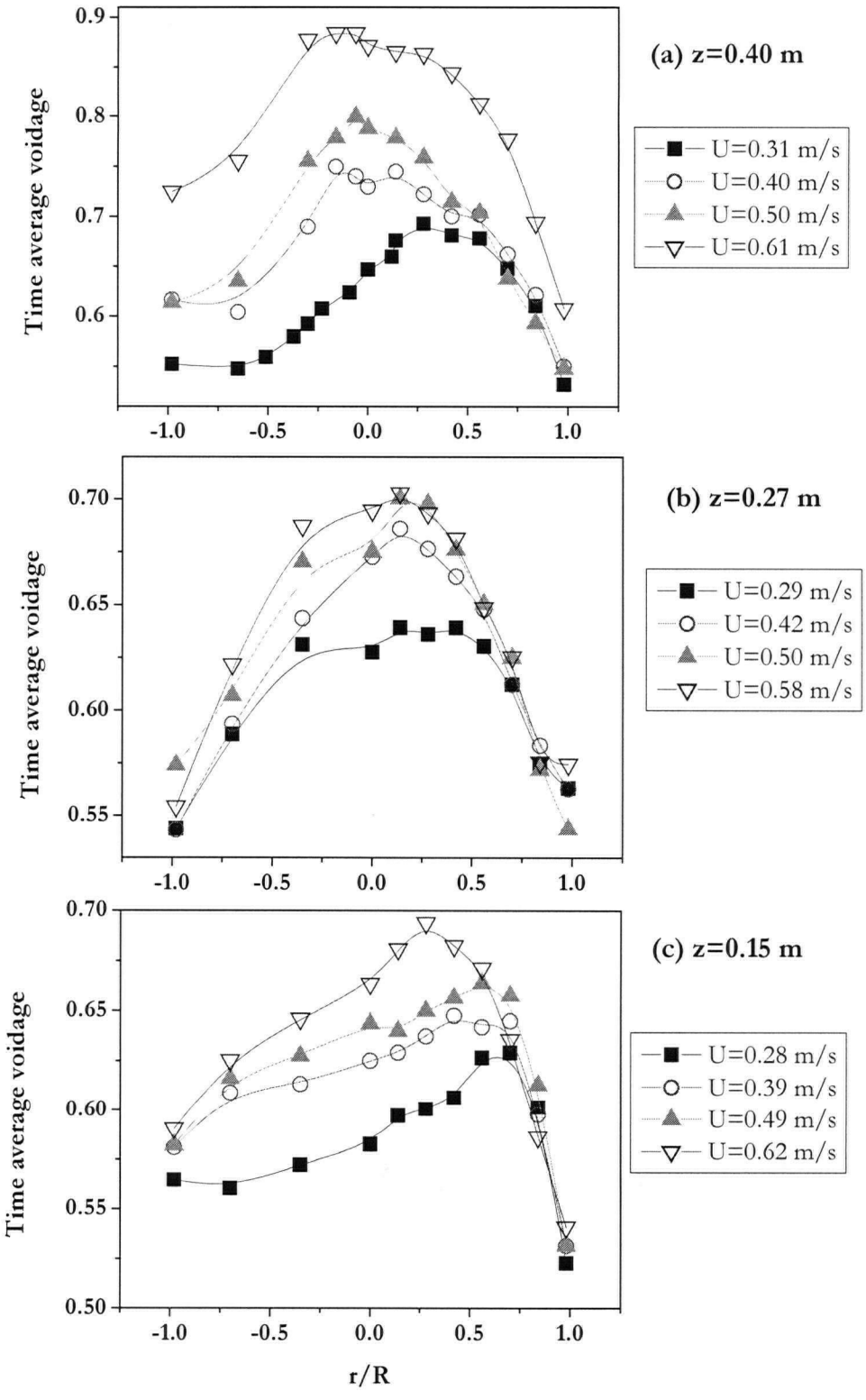

Figure 4.15 Radial voidage distributions. H_0=0.51 m, D=0.29 m, FCC I. U_c ($\bar{z}$ =0.43 m, DP) = 0.49 ± 0.015 m/s.

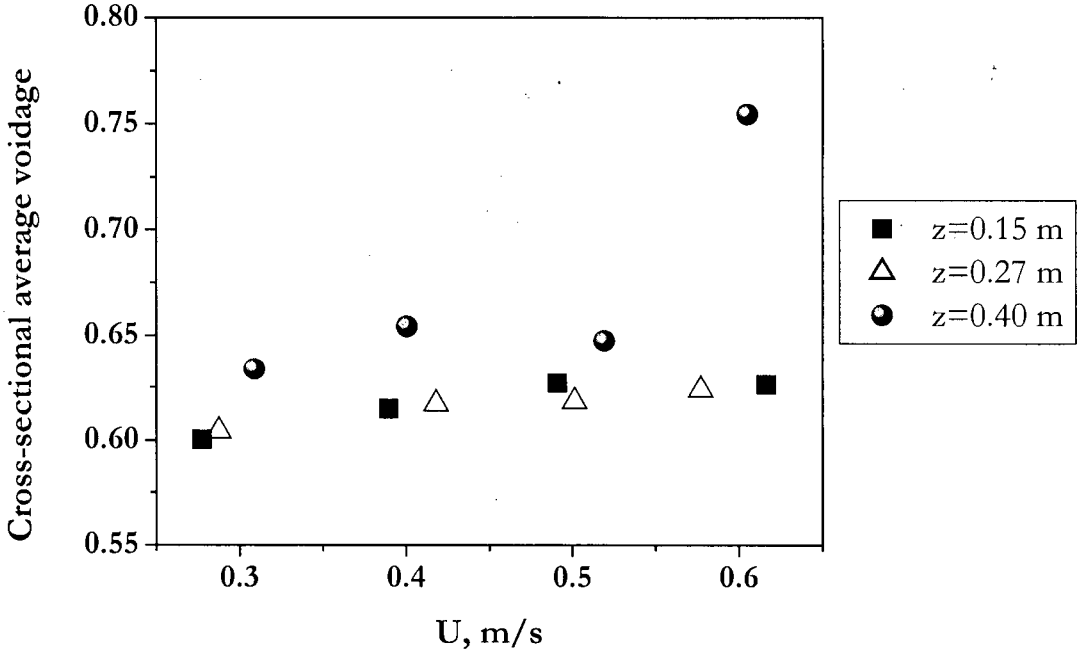

Figure 4.16 Cross-sectional average voidage from local radial voidage measurements from optical probe. H_0=0.51m, D=0.29 m, FCC I.

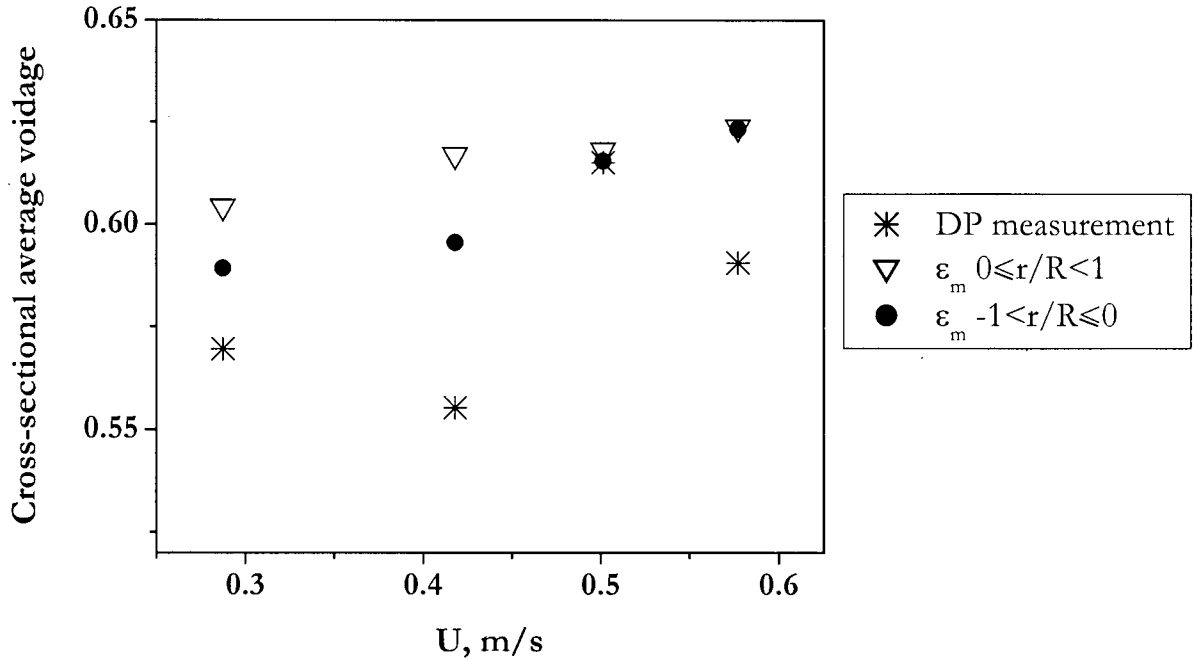

Figure 4.17 Comparison of cross-sectional average voidage from optical signal to that from DP. H_0=0.51 m, D=0.29 m, z=0.27 m FCC I.

more influenced by void dynamics near the wall where the DP ports are positioned compared to the void dynamics closer to the axis of the column.

Figure 4.18 and 4.19 portray normalized time-mean voidage profiles, $\bar{\varepsilon}/\varepsilon_m$. For an initial static bed height of 1.1 m, U_c measured through DP fluctuations between axial heights of 0.53 and 0.65 m was 0.657 ± 0.040 m/s. Thus, the normalized voidage profiles for gas flow rates of 0.40 and 0.80 m/s represent below- and beyond-U_c values.

In the bubbling flow regime, the highest voidage does not necessarily occur at the column axis. In fact, Werther and Molerus (1973b) reported coalescence and evolution of bubbles in bubbling fluidized beds depicting the highest frequency of bubbles at $r/R \approx 0.6$ to 0.7. Beyond U_c, the maximum voidage shifts closer to the axis. The profile between r/R=0.7 to near the wall seems insensitive to height and gas velocity, while that towards the column axis varies with axial position and gas velocity when H_0=1.1 m. Similar profiles obtained by Abed (1984) have been employed (Geldart and Rhodes, 1985; Wang and Wei, 1997) to support the idea of the existence of flow heterogeneity in turbulent fluidized beds. The macroscopic non-uniformity observed in radial distribution of time-mean voidage is interpreted as not having unique enough features to call the turbulent fluidization flow regime an independent regime by some researchers (e.g. Xu et al., 1999). However, the notion of a turbulent fluidized bed becoming increasingly homogeneous beyond a certain transition originated qualitatively through photographs such as those of Zenz and Othmer (1960) and Kehoe and Davidson (1970). In order to quantitatively analyze the breakdown of larger voids into smaller transient voids, the scales of time and space must reflect the hydrodynamics of interest.

Figure 4.20 indicates a decrease in voidage fluctuations with increasing gas flow rate. Given that the average voidage increases with increasing gas flow rate, this denotes an increase in the lower limit of the voidage. Furthermore, the voidage fluctuations gradually decrease from the wall inwards, signifying the influence of the denser structure.

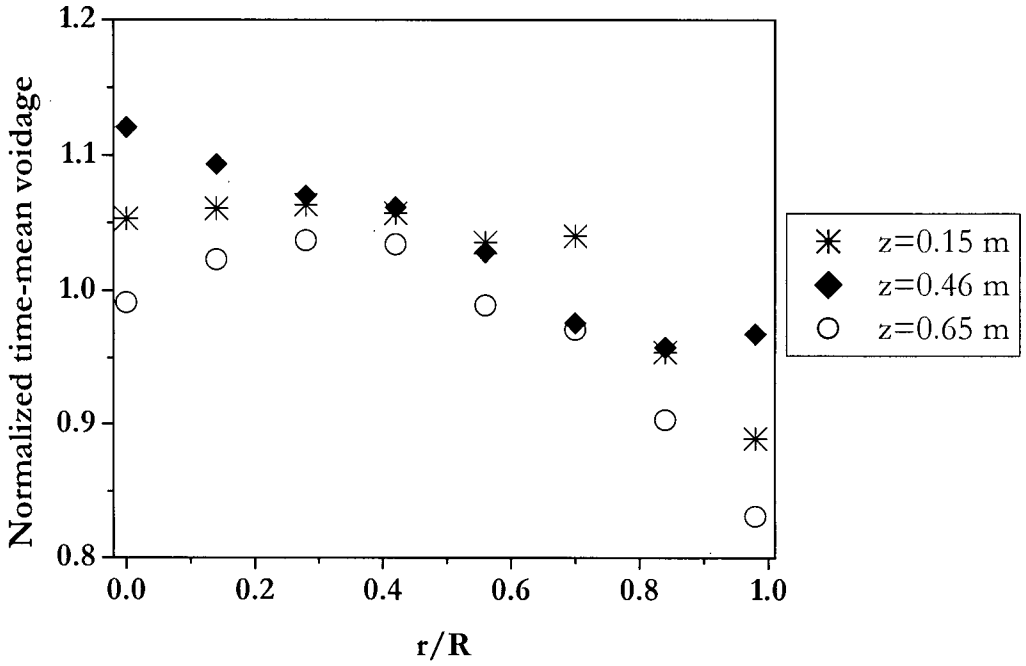

Figure 4.18 Radial profile of normalized time-mean average voidage. H_0=1.1 m, D=0.29 m, FCC I, U=0.40 m/s.

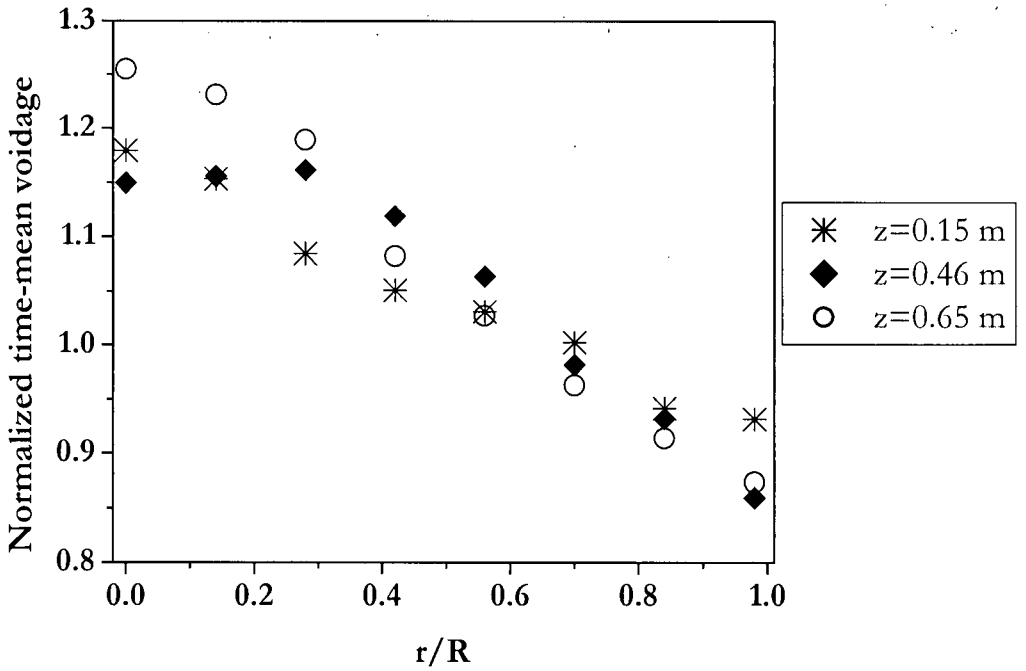

Figure 4.19 Radial profile of normalized time-mean average voidage. H_0=1.1 m, D=0.29 m, FCC I, U=0.80 m/s, U_c ($\bar{z}$ =0.85 m, DP)=0.73 m/s .

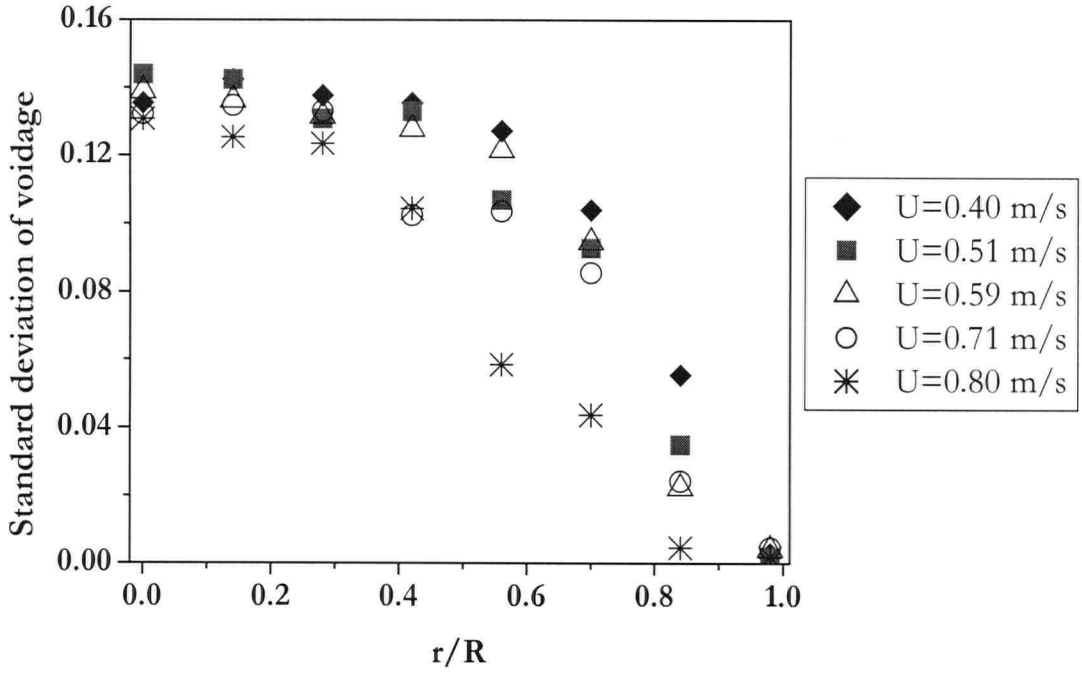

Figure 4.20 Radial profile of voidage fluctuation represented by standard deviation of local voidage measured by optical probe. D=0.29 m, H_0=0.8 m, z=0.40 m, U_c=0.75 m, FCC I.

Figure 4.21 presents the evolution of the probability density function at z=0.40 m and at the column axis with the superficial gas velocity. The function is a non-linear gas-solid distribution as reported by Cui et al. (2000). The shift in voidage distributions from $U < U_c$ to those beyond U_c is clearly shown at this level. From U=0.60 to 0.79 m/s, the cumulative probability distribution of local voidage remains nearly unchanged. This is also indicated by the relatively unchanged average bed voidage around U_c, as shown in Figure 2.9 (H_0=0.8 m), also reported by Lancia et al. (1988) and Tannous et al. (1996). The plateau of average voidage with increasing U may indicate competing mechanisms of void splitting, coalescence and acceleration.

At z=0.78 m in Figure 4.22, the voidage probability distributions exhibit wider spread with increasing U than in Figure 4.21, where the data were measured simultaneously. These results indicate a monotonically increasing gas flow at r/R=0 with increasing height at all gas velocities between 0.4 and 0.9 m/s. This supports the trend displayed in Figure 4.15 for a lower static bed height of 0.51 m.

The contour plots shown in Figure 4.23 through Figure 4.26 are based on 64 and 80 cells of time-mean voidage for static bed heights of 1.1 and 1.5 m, respectively. The qualitative observations suggest higher time-mean voidage around r/R=0.5 for below-U_c, than for beyond-U_c. The effect of static bed height on the voidage mapping for U=0.9 m/s indicates an increased dispersion of voidage for deeper beds. In other words, for H_0=1.1 m, there seems to be a definite pattern of higher voidage toward the axis, while for H_0=1.5 m, the higher voidage areas are more dispersed, suggesting possible local circulating flows. This, however, cannot be confirmed without making velocity measurements.

4.7.3 Scale effect on radial voidage profile

The published work summarized in Table 4.2 does not elucidate the effect of scale on the radial voidage profile, as very limited data are available in this respect from reactor sizes comparable to industrial scale units. To a certain point, the increase in reactor size increases the maximum bubble diameter attainable from coalescence, $d_{b,max}$, as expressed by Mori and Wen (1975),

$$d_{b,max} = 0.652\left[A\left(U - U_{mf}\right)\right]^{0.4} \tag{4.8}$$

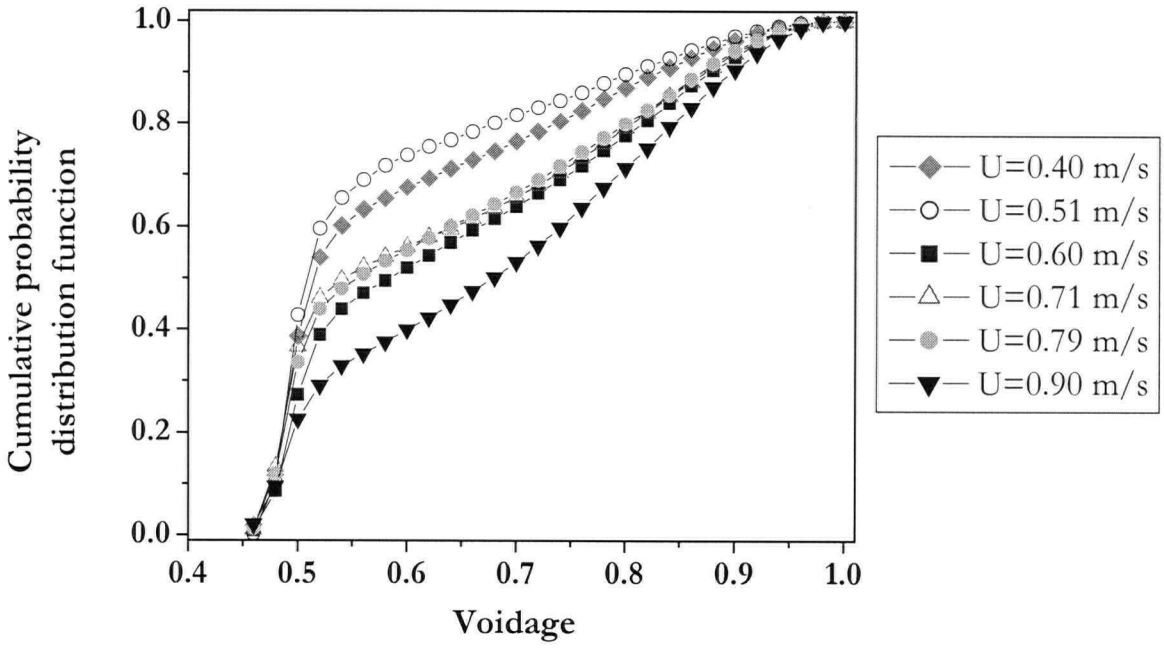

Figure 4.21 Probability distribution function of local voidage measured by optical probe. U_c DP ($\bar{z}$ =0.85 m)= 0.727 ± 0.039 m/s, H_0=1.1m, D=0.29 m, r/R=0.0, z=0.40 m, FCC I.

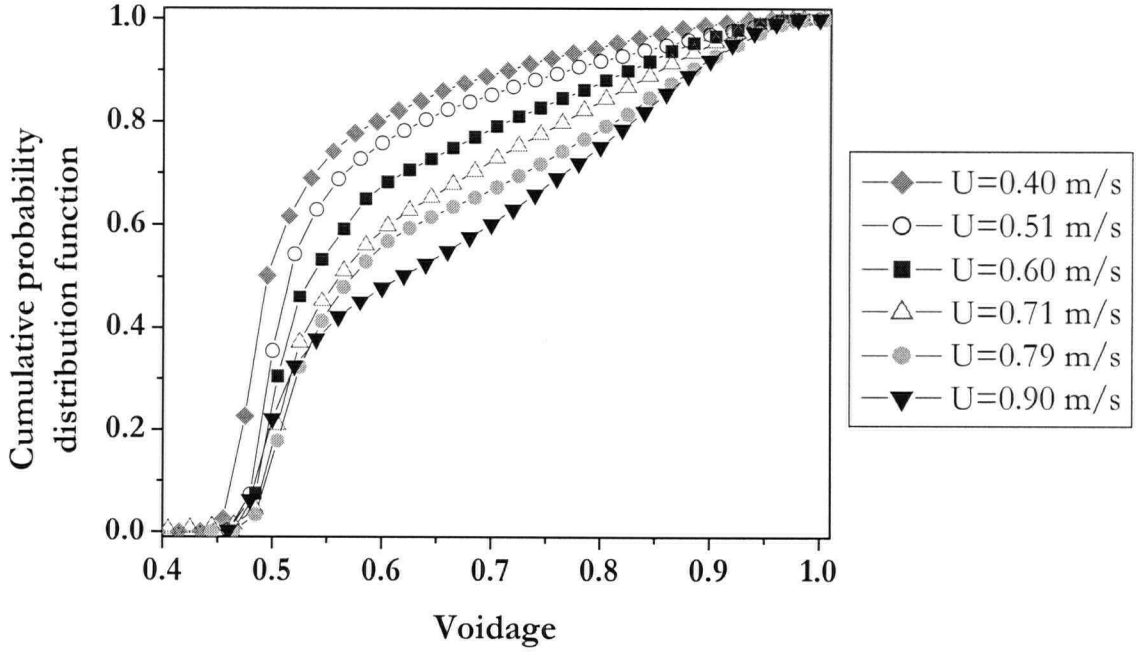

Figure 4.22 Probability distribution function of local voidage measured by optical probe. U_c DP ($\bar{z}$ =0.85 m)= 0.727 ± 0.039 m/s, H_0=1.1m, D=0.29 m, r/R=0.0, z=0.78 m, FCC I.

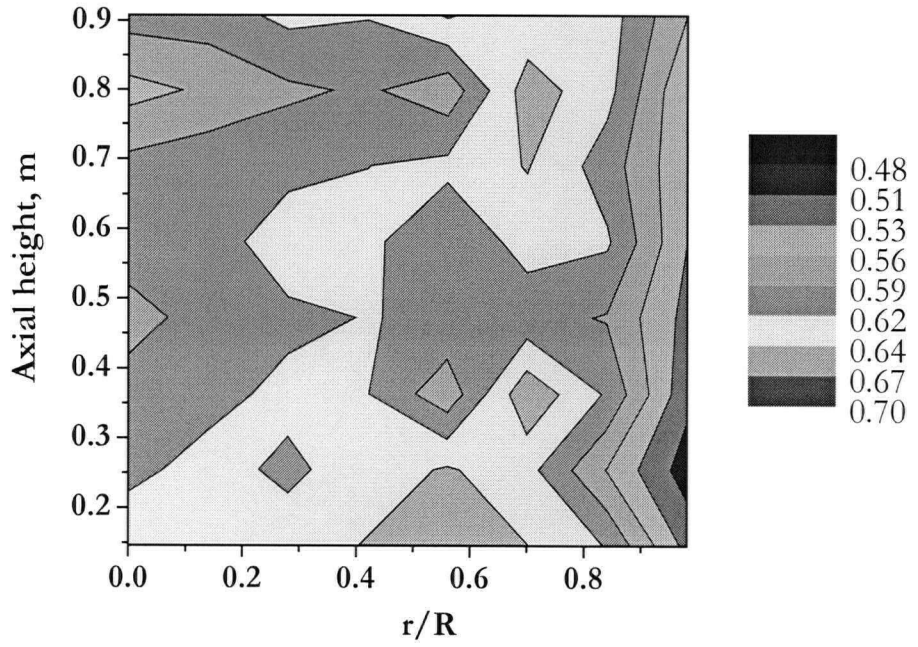

Figure 4.23 Contour plot of time-mean local voidage measured by optical probe. D=0.29 m, FCC I, H_0= 1.1 m, U=0.4 m/s.

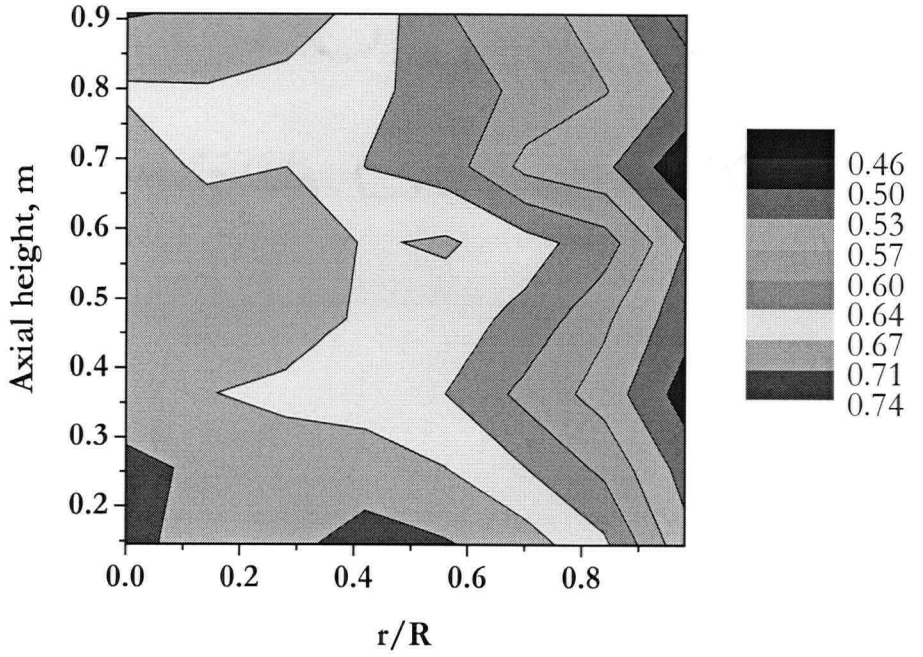

Figure 4.24 Contour plot of time-mean local voidage measured by optical probe. D=0.29 m, FCC I, H_0= 1.1 m, U=0.9 m/s

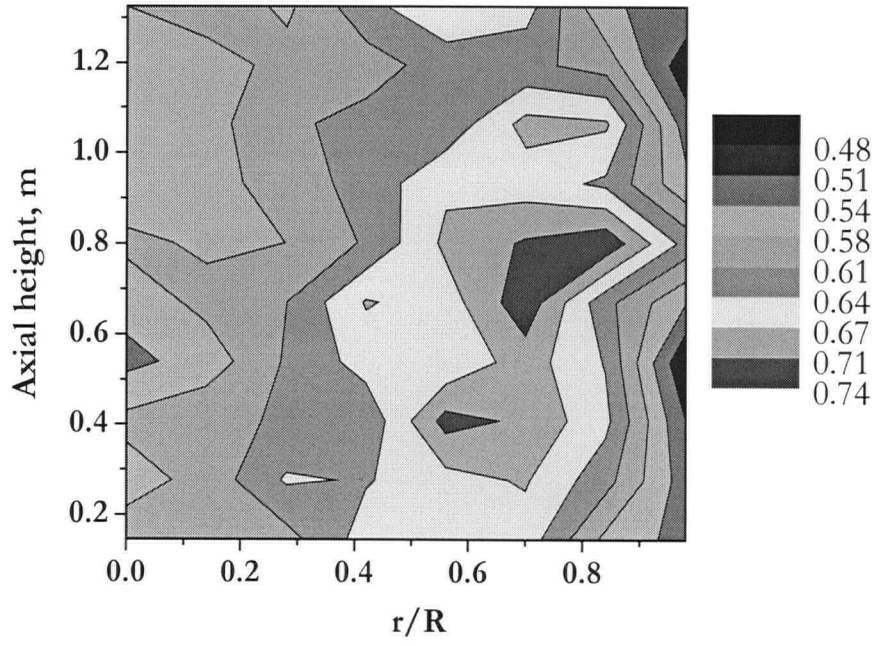

Figure 4.25 Contour plot of time-mean local voidage measured by optical probe. D=0.29 m, FCC I, H_0=1.5 m, U=0.4 m/s

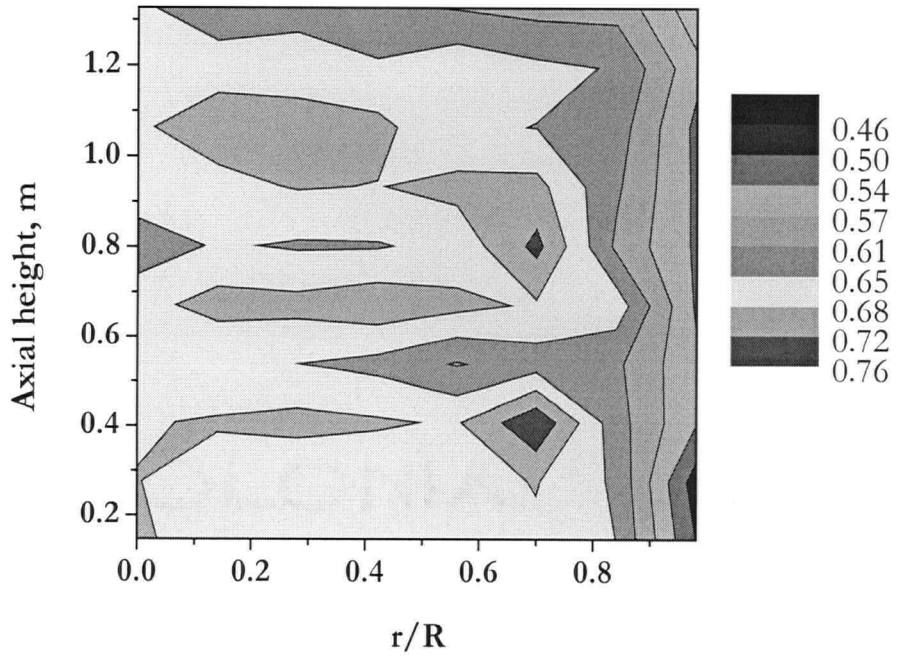

Figure 4.26 Contour plot of time-mean local voidage measured by optical probe. D=0.29 m, FCC I, H_0=1.5 m, U=0.9 m/s

where A is the reactor cross-sectional area. U_c is considered to be the superficial gas velocity at which the maximum bubble size is attained by coalescence. Increasing U beyond U_c results in bubble break-up being more dominant than coalescence (Sun and Chen, 1989; Cai et al., 1990). Equation 4.8 then no longer applies. As conversion in a fluidized bed catalytic or gas-solid reactor is affected immensely by gas-solid contacting, monitoring the local void behaviour with increasing column diameter should provide valuable knowledge into scale-up effects. The same optical voidage system used at UBC was used to acquire voidage data from reactor diameters of 0.61 and 1.56 m at CSIRO.

4.7.3.1 Results from 0.61 m diameter fluidization column

Similar radial voidage profiles were observed for the 0.61 m and 0.29 m diameter columns. As depicted in Figures 4.27 and 4.28, the maximum time-mean voidage occurred near r/R=0.5 for $U < U_c$, while it was closer to the column axis for $U > U_c$. This trend is consistent with other runs, as well as that reported by Nakajima et al. (1991) in a 0.20 m diameter column. Moreover, the profile was similar for a given gas flow rate at two levels, z=0.8 and 1.55 m. This provides a strong indication that in the turbulent fluidized bed flow regime, the radial voidage profile examined through time-mean local voidage measurements becomes fully developed at $z/D \approx 1.3$.

As shown in Figure 4.29, the cross-sectional voidage calculated from local voidages based on optical probe signals was in good agreement with that from DP measurements.

4.7.3.2 Results from 1.56 m diameter fluidization column

In order to obtain simultaneous measurements of DP, AP, and voidages from optical and capacitance probes in the column of diameter 1.56 m, traversing swivel arms were designed and constructed as described in Chapter 2. The effect of the swivel arms on the flow was not investigated; however, due to the relative size, i.e., 1.56 m diameter vs. a 0.064 m diameter head attached to a 0.038 m diameter tube, with the optical voidage probe at the tip of the arm measuring local light reflection, the blockage effect was likely minimal. The radial positions were determined from the penetration length and the swivel angle, which covered the desired radial positions on a fan-shaped plane rather than a line connecting the wall and the column centreline.

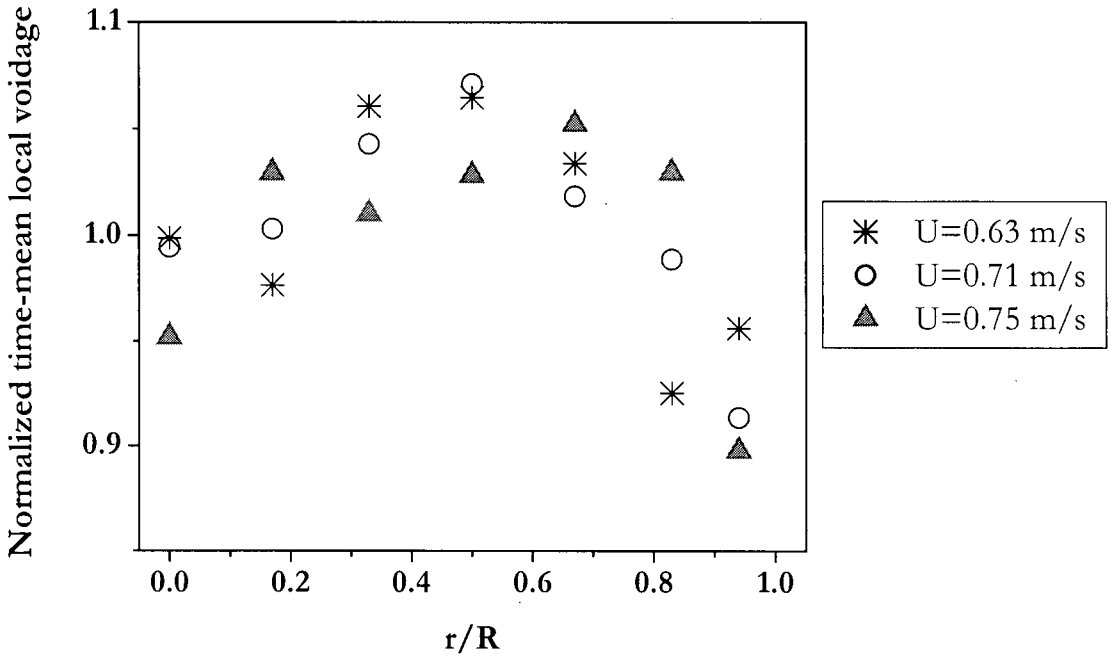

Figure 4.27 Radial profile of time-mean voidage from optical probe signals. H_0=1.1-1.3m, D=0.61 m, z=0.8 m, FCC III, U_c=0.83 m/s (z=0.8m, DP).

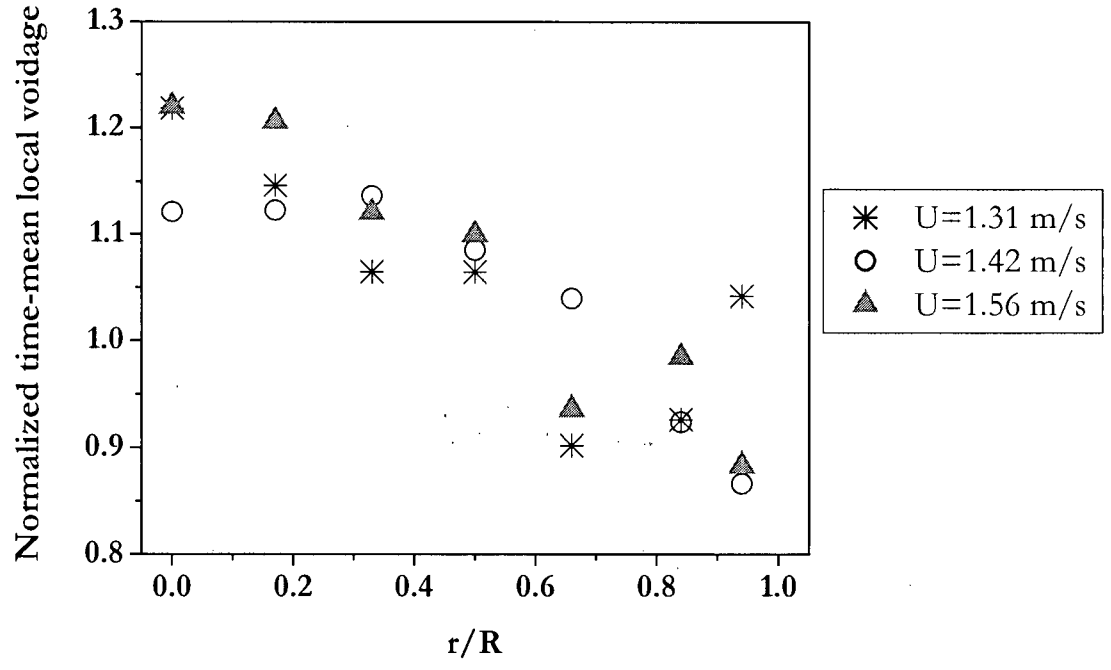

Figure 4.28 Radial profile of time-mean voidage from optical probe signals. H_0=2 m, D=0.61 m, z=1.55 m, FCC IV, U_c=1.12 m/s (z=1.5 m, DP).

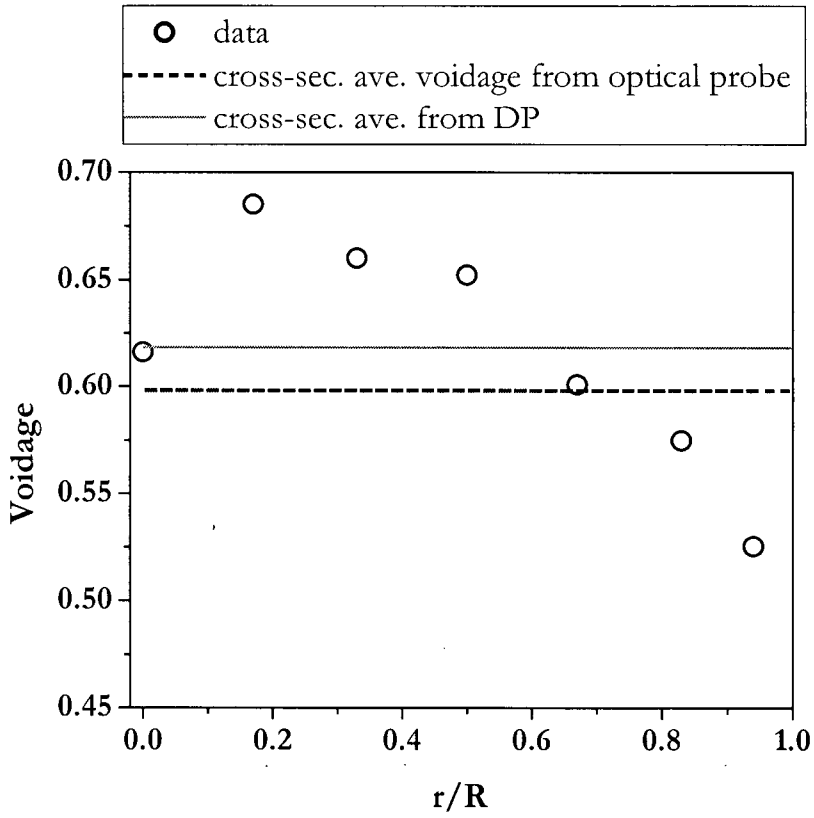

Figure 4.29 Radial profile of time-mean voidage from optical probe signals. H_0=1.7 m, D=0.61 m, U=0.85 m/s, z=0.8 m, FCC III, U_c=0.77m/s (z=0.36 m, DP).

The radial profile for H_0=1.2m at z=0.84 m is shown in Figure 4.30. For both superficial gas velocities, the trend shows increased voidage near the wall. This was attributed to the centre of the column being non-uniformly aerated. The increase in U naturally increased the voidages. Two points from these data are chosen to examine the probability density of voidages portrayed in Figure 4.31. The time-mean voidages are 0.69 and 0.72 for r/R=0.9 and 0.0, respectively. However, the profiles of the probability density distribution indicate a slight difference between the two radial positions, with less high-density phase and an increased presence of voids near the wall. Although these two measurements were obtained from different runs, the trend was confirmed to be reproducible.

For a deeper bed, i.e., H_0=2.2 m, the general trend of radial profile is represented by that for U=0.62 m/s in Figure 4.32. For r/R=0.0 the time-mean voidage peaked at around U_c as demonstrated in Figure 4.33. This trend was also indicated for r/R=0.23 and 0.50. After examining the probability density distribution of voidages for $U > U_c$ at r/R=0.8, 0.6 and 0.0, it was concluded that fewer voids and a denser dense phase were detected at gas velocities beyond U_c.

Curiously, the trend did not reflect the increase in gas flow rate. From the cross-sectional averaged voidage based on DP measurements against gas velocity, e.g. Figure 2.27, albeit at a different H_0, an overall increase in voidage is evident. For the 1.56 m diameter column, the axial position of the return leg was between 0.2 and 0.8 m. At higher gas velocities resulting in increased entrainment, more solids were re-injected into the column. With the traversing probe arm position at 0.84 m the results may have reflected the influence of the returning solids resulting in lower local voidages. In fact, when time-mean voidages were compared for the probe swinging from the left to the right, it was observed that for $U > U_c$ the probe positioned closer to the return leg indicated a lower voidage.

4.7.3.3 Scale effect

The normalized radial profiles of time-mean voidage are compared to several of the works listed in Table 4.2 in Figure 4.34. It shows that the profiles are quite similar for column diameters ranging from 0.076 to 0.71 m. Due to the non-uniform aeration in the 1.56 m diameter column, data from the largest column are not included. Therefore, there is not enough evidence to say whether the radial profile in Figure 4.34 is valid when column diameter is scaled-up beyond 0.71 m. Nevertheless, the results provide an indication of the radial variation of the flow structure.

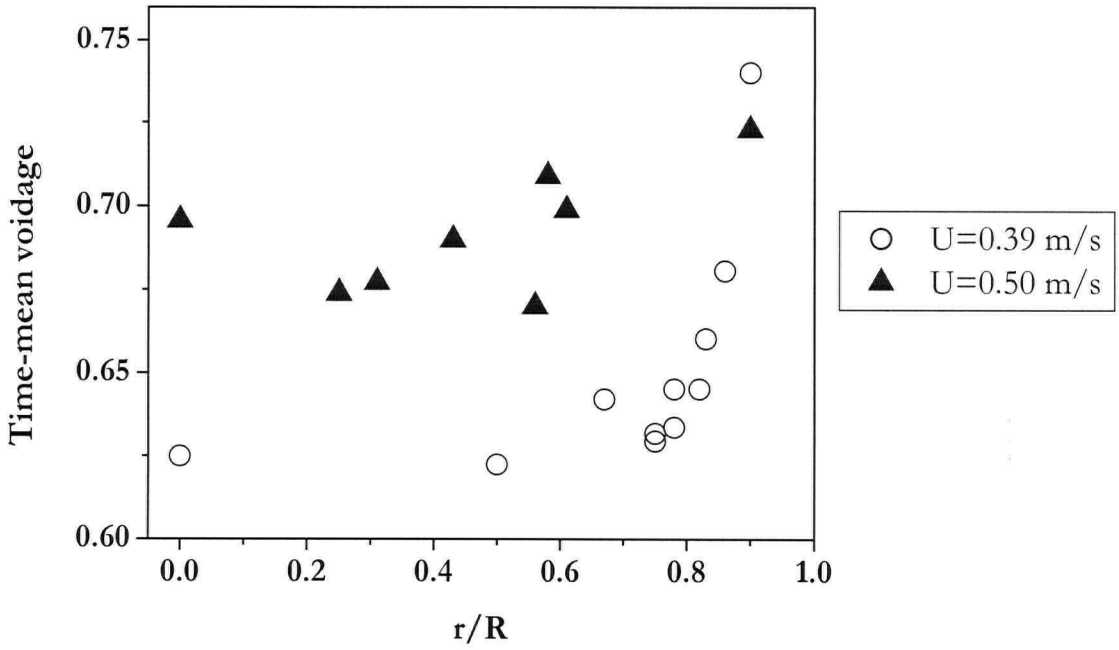

Figure 4.30 Radial profile of time-mean voidage from optical probe signals. z=0.84 m, D=1.56 m, H_0=1.2 m, FCC II, U_c (z=0.84 m, DP)=0.39 m/s.

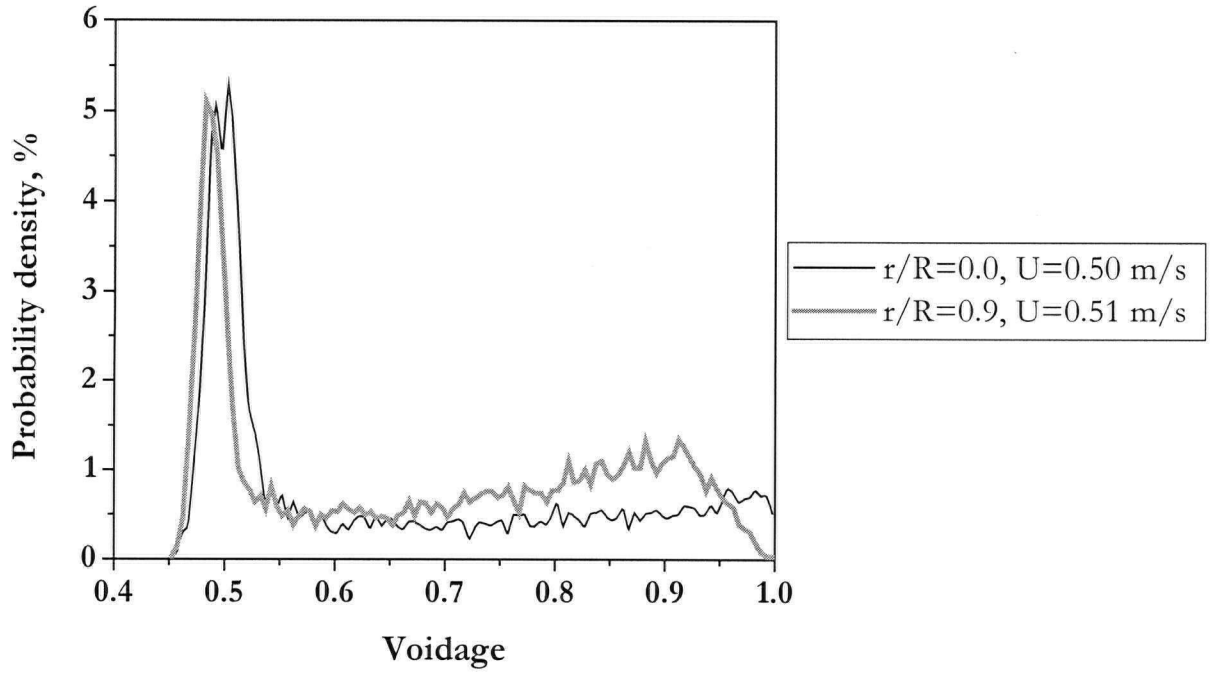

Figure 4.31 Probability density of voidage obtained from optical probe signals measured at r/R=0.90 and 0.0. D=1.56 m, H_0=1.2 m, FCC II, z=0.84 m.

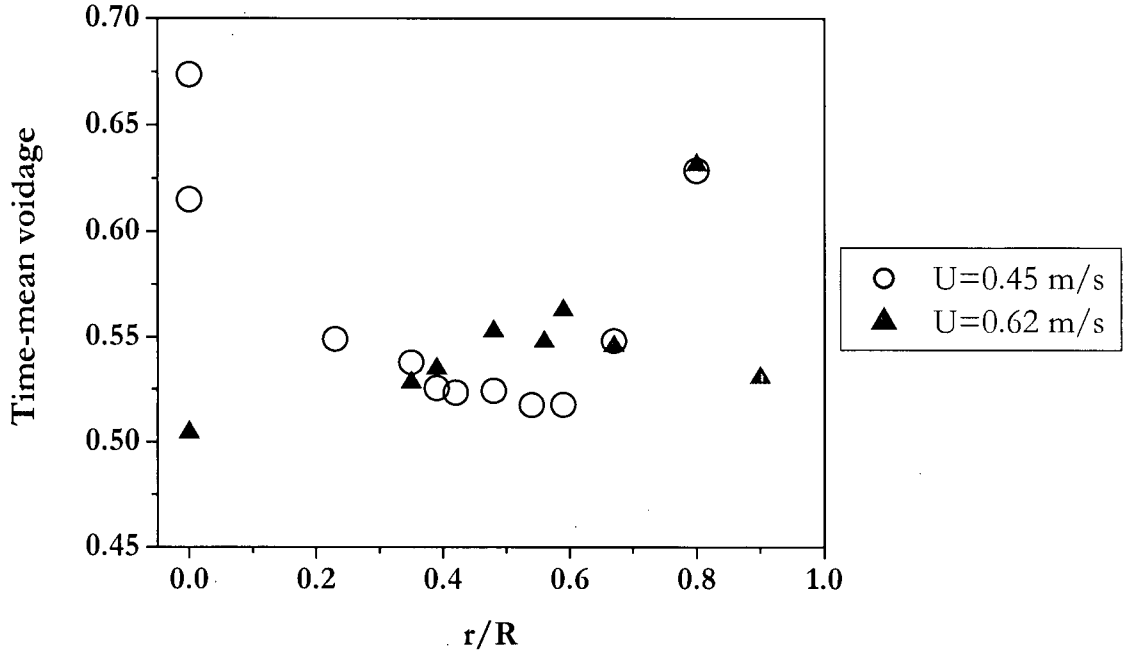

Figure 4.32 Radial profile of time-mean voidage from optical probe signals. D=1.56 m, z=0.84 m, H_0=2.2 m, U_c (z=0.85 m, DP)=0.53 m/s, FCC II.

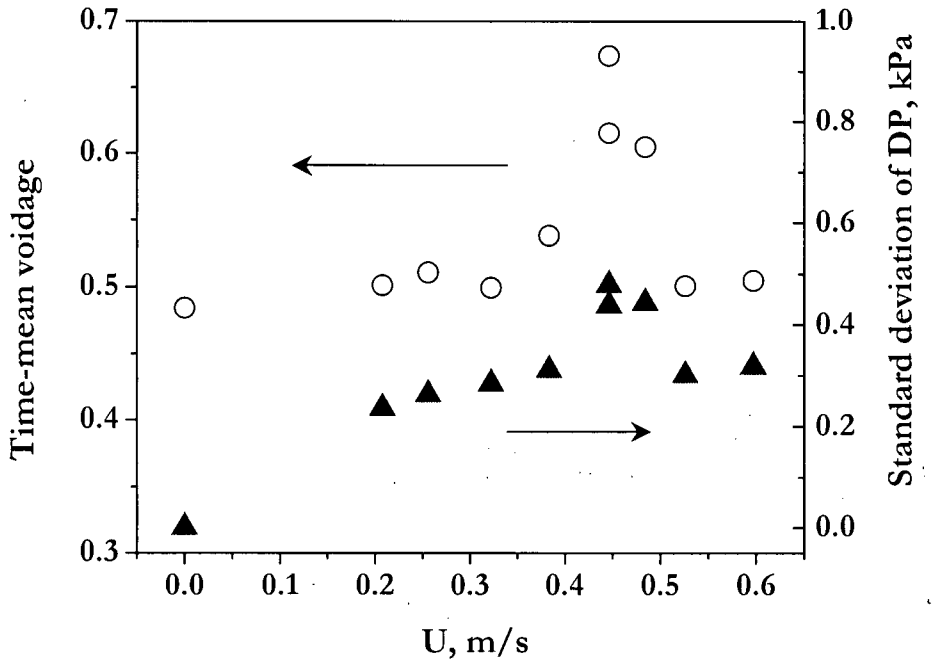

Figure 4.33 Effect of U on time-mean voidage and DP fluctuation at r/R=0.0. D=1.56 m, z=0.84 m, H_0=2.2 m, U_c (z=0.85 m, DP)=0.53 m/s, FCC II.

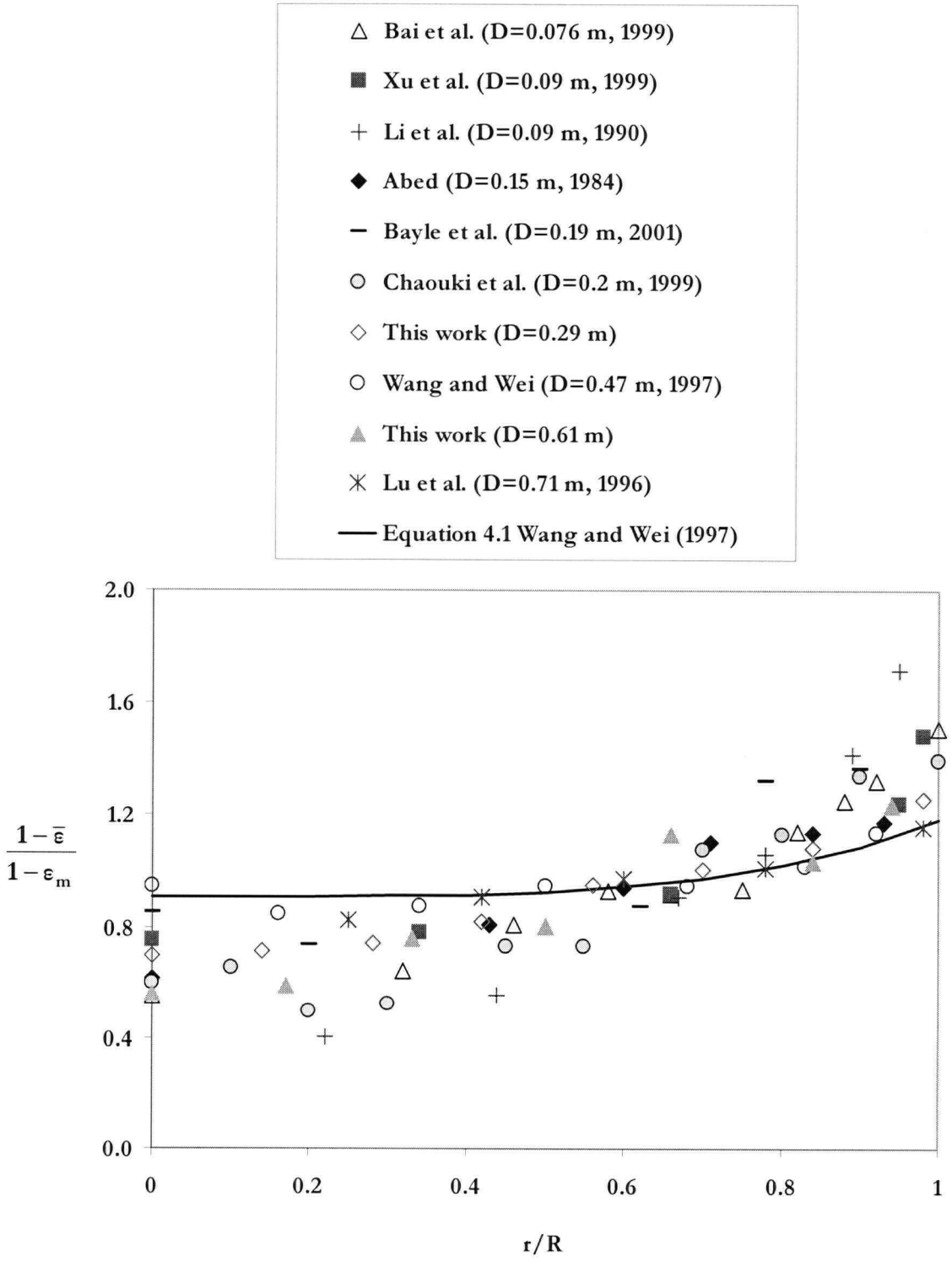

Figure 4.34 Radial profile of normalized time-mean voidage. Comparison of experimental data to other publications. Particle properties and operating conditions listed in Table 4.2.

Figure 4.35 presents the effect of normalized superficial gas velocity on the normalized radial profile of time-mean voidage. The voidage near the axis increases with increasing normalized superficial gas velocity. For the range of column diameters under investigation, the effect of column diameter on the radial voidage profile is shown to be less significant compared to the effect of U, as the profile for U/U_c=1.39 and D=0.61 m is similar to that for U/U_c=1.38 and D=0.15 m in Figure 4.35.

4.7.4 Dense phase voidage

The strong interaction between the dense and dilute phases is one of the characteristics of turbulent fluidized beds. Deviation from the two-phase theory prediction has been reported by Nakajima et al. (1990) through local bubble fraction measurements using an optical probe. Chaouki et al. (1999) estimated the dense phase voidage to be the lower limit of the probability distribution function of local voidage measured with a capacitance probe. Their findings suggest that the dense phase voidage increases with increasing gas velocity while the dilute phase voidage remains constant beyond U_c for FCC particles.

Figure 4.36 depicts the probability density of voidage at three radial locations. The voidage distributions indicate heterogeneity across the radius. The voidage value at zero probability, ε_c, shifts with radial position with the value corresponding to r/R=0.0. Accordingly, the peaks of the voidage probability, representing the maximum crossing voidage, shift with radial position. The broad probability distribution function for r/R=0.0 supports the notion of breakdown of a two-phase structure.

The breakdown of the two-phase structure is further illustrated in Figure 4.37, where the voidage distribution is compared for columns of diameter 0.29 and 1.56 m. At similar normalized superficial gas velocities, the voidage distribution in the larger column exhibits a broad bimodal distribution, while that in the smaller column appears to be unimodal. The wall effects may be the cause of this difference in voidage distributions.

4.7.5 Capacitance probe measurements

The local voidage was also measured using the capacitance probe, which recorded the local dielectric constant in the 0.61 and 1.56 m diameter fluidized beds. A linear relationship between the capacity response and the solids concentration was assumed as explained in Section 4.6.

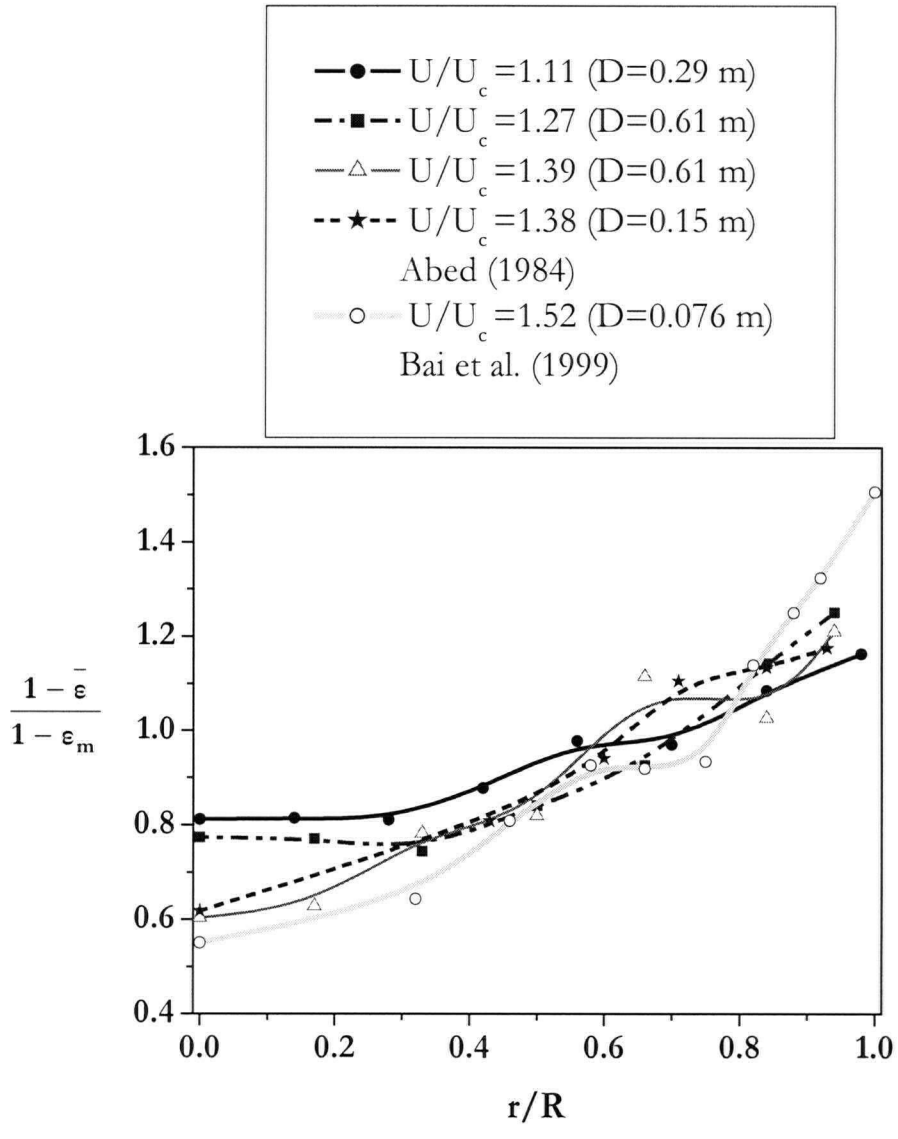

Figure 4.35 Effect of U/U_c on radial profile of normalized time-mean voidage. FCC.

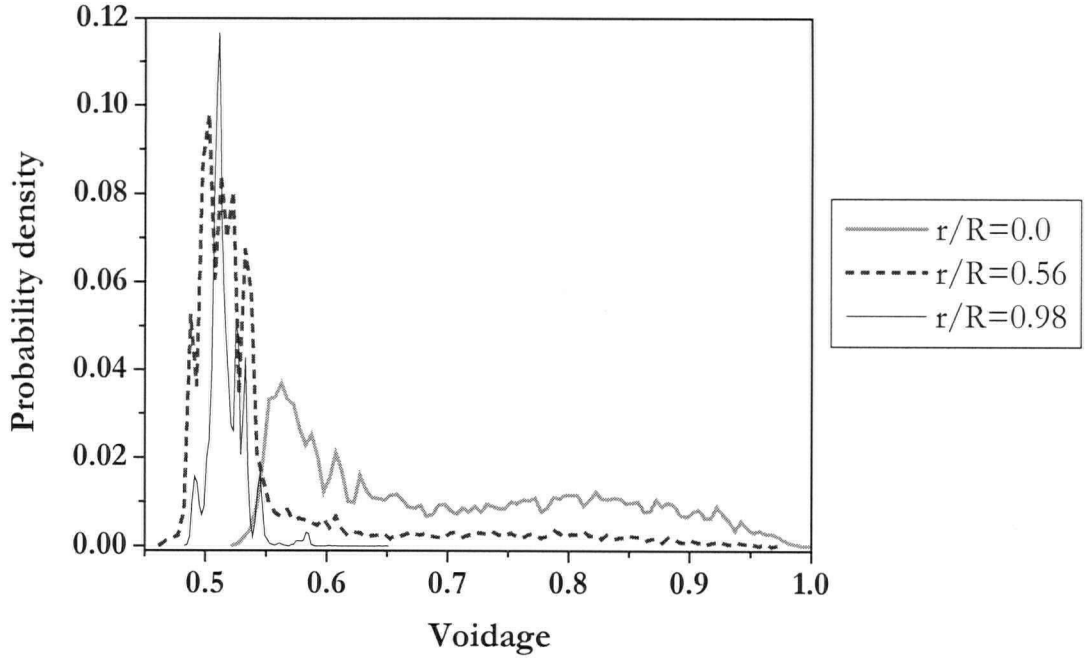

Figure 4.36 Probability density of voidage from optical probe signals. D=0.29 m, z=0.527 m, U=0.78 m/s, FCC I, H_0=0.8m.

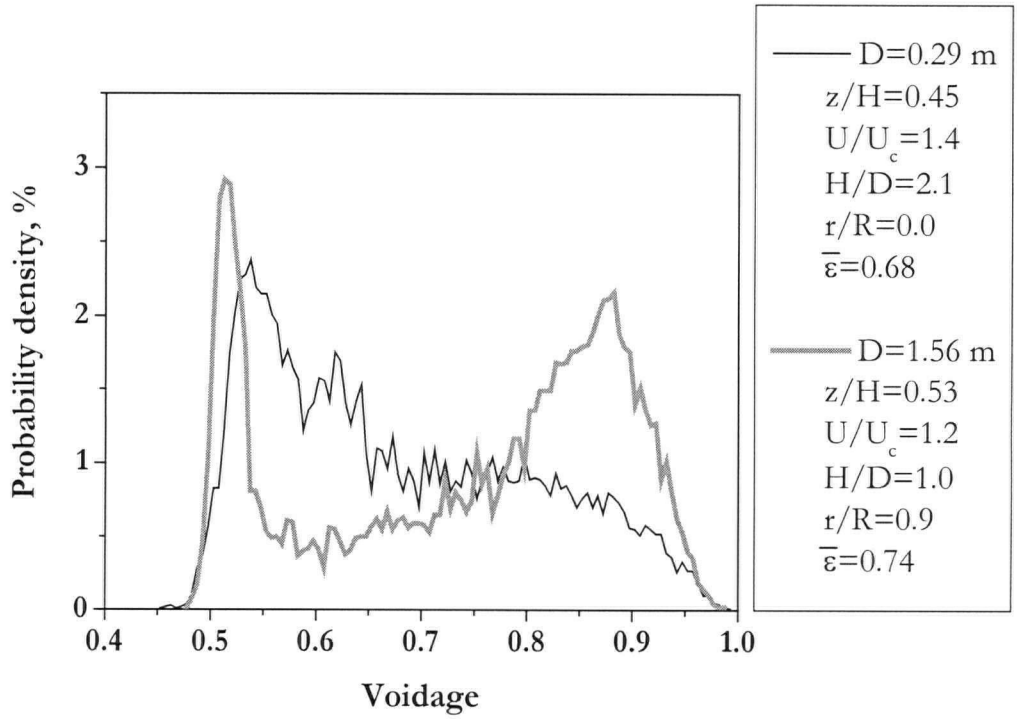

Figure 4.37 Probability distribution of voidage measured by optical probes. D=0.29 m (FCC I). D=1.56 m (FCC II).

The probability density distributions of the voidage measured by the capacitance and optical probes, compared in Figure 4.38, exhibit significantly different profiles. Time-mean voidage was calculated to be 0.58 and 0.57 from capacitance and optical probe signals, respectively. The broader peaks imply that the measured capacitance of the gas-solid mixture covers a larger measuring volume than the optical measurement.

4.8 Conclusions

Local voidage measurements were obtained experimentally through the use of optical fiber and capacitance probes in 0.29, 0.61 and 1.56 m diameter columns for fluidized beds of FCC particles, operated in the bubbling and turbulent fluidized bed flow regimes. The signals showed continuous distributions of probability distribution and rapid fluctuations, indicating a breakdown in the two distinct phases (discrete dense and dilute phases) usually assumed in the bubbling bed flow regime.

- Symmetry of the radial voidage profile was confirmed for z/H=0.5 in the D=0.29 m column.
- Cross-sectional average voidages obtained from optical probe measurements compared well with those derived from differential pressure measurements for D=0.61 and 1.56 m.
- Time-mean radial voidage profiles tended to be different for the bubbling and turbulent fluidization flow regimes: for $U < U_c$ there was a maximum voidage at a non-axis position; on the other hand, for $U > U_c$, the maximum voidage was at the column centre.
- The standard deviation of voidage decreased with increasing superficial gas velocity.
- Contour plots of time-mean voidage from optical probe signals for the D=0.29 m column showed that static bed height and superficial gas velocity affect the overall flow structure.
- A comparison of voidage distributions for D=0.29 m and 1.56 m revealed a bimodal distribution for the larger column and a unimodal one for the smaller column. The breakdown of the two-phase structure for the smaller column is presumably due to a greater wall effect.
- Results from the optical probe and capacitance probe differed substantially. This is attributed to the fact that the measuring volume of the capacitance probe is much larger than that of the optical probe.

Further analyses on the local voidage measurements are pursued in Chapter 6.

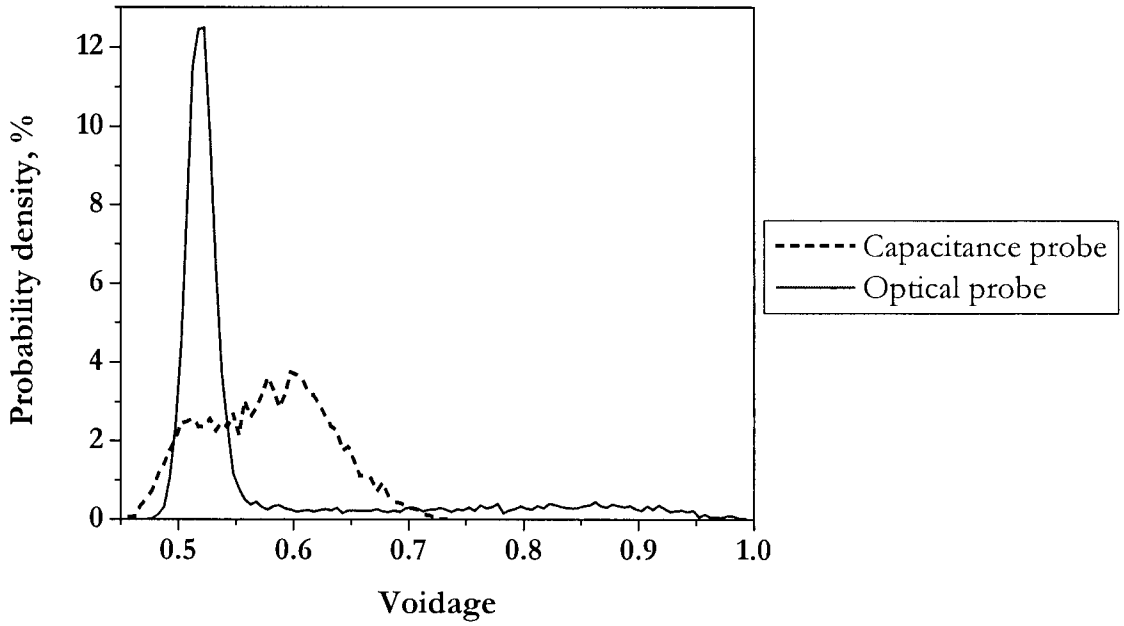

Figure 4.38 Probability density of voidage from capacitance and optical probe signals. D=0.61 m, U=0.86 m/s (capacitance); U=0.85 m/s (optical), H_0=2 m, z=1.55 m, FCC III, r/R=0.83.

CHAPTER 5

VELOCITY MEASUREMENTS

5.1 Introduction

One of the more fundamental measurement quantities related directly to the physics of two-phase flows is the velocity of each phase. Numerous studies have been reported on direct measurements of particle and/or bubble/void velocities in fluidized beds, often in attempts to verify hydrodynamic theories and models that can depict the complex flow dynamics (e.g. Horio et al., 1992b; Seville et al., 1995; Zhu et al., 2001). This chapter deals with the experimental void and particle velocity measurements for obtaining reliable data to contribute to the understanding of the local heterogeneity of the two-phase flow structure.

5.1.1 Void velocity

Many hydrodynamic studies of the turbulent fluidization flow regime have adopted the terminology applied in the bubbling flow regime where the dense phase forms a continuous phase and the gas phase remains discontinuous. One of the first reports published on the void velocity in or close to the turbulent fluidization flow regime was by Lanneau (1960) using dual capacitance probes positioned 0.076 m apart in a 0.076 m diameter column. Beyond a superficial gas velocity of 0.6 m, the voids were reported to be small, rapid, and losing their identity, making the measurement unattainable. The trend is such that the bubble phase velocity approaches the superficial gas velocity as U is increased. Lee and Kim (1989) analyzed the cross-correlation of two pressure fluctuation signals to deduce the void rise velocities in a turbulent fluidized bed. Their fluidized bed of glass beads in a 0.1 m diameter column encountered the slugging regime prior to the turbulent flow regime. The reported average void rise velocity remained around 1.6 m/s once in the turbulent fluidization flow regime. In measuring the slug rise velocity, the correlation of pressure fluctuations at the wall, approximately equal to cross-sectional average pressures, seems to be a viable choice. However, once in the turbulent fluidized flow regime, due to the transient nature of voids, the average void velocity may not be obtainable from a cross-correlation of the gauge pressure signals. Similarly, Yamazaki et al. (1991) found a maximum void rise velocity at U_c=0.55 m/s, followed by a plateau at a superficial gas velocity of around 0.8 m/s for a bed of FCC catalyst particles (D=0.2 m). Ege (1995) reported on the bubble rise velocity in 0.3 and 0.5 m diameter columns with FCC particles using two optical fiber probes. Considerable scatter in the radial profile of void rise velocity

was observed for both columns at a superficial gas velocity of 0.55 m/s. In general, the void rise velocity decreased with increasing distance from the grid. This was shown to coincide with decreasing void length, and decreasing void frequency.

Local measurements have been reported in investigating bubble characteristics such as rise velocity and chord length (e.g. Zhang et al., 1997; Lu et al., 1997). Lu et al. (1997) found an increase in the average void chord length with increasing height from z=0.15 to 0.85 m, while there was no significant difference in the void rise velocity for the three superficial gas velocities under investigation (0.59, 0.78, 0.98 m/s). The results of Taxil et al. (1998) indicate significant scattering of lengths and velocities, with 15% of the voids having chord lengths greater than the column diameter of 0.2 m. Comparison of the void lengths reported by Lu et al. (1997, D=0.71 m) with those of Taxil et al. (1998) reveals a 3-fold difference, highlighting the challenge in identifying void structure and dynamics due to the distorted and transient nature of the voids in turbulent fluidized beds.

5.1.2 Particle velocity

Local particle velocity measurements coupled with the volumetric solid concentration can provide vital information on the heterogeneity of the flow. However, very few reports pertain to the turbulent fluidization flow regime, especially for Group A particles, due to the experimental difficulty in obtaining reliable results from experiments conducted in dense phase beds. Van den Moortel et al. (1998) reported on the velocities of particles in a circulating fluidized bed. Their superficial gas velocity of 1 m/s for Group A glass beads (ρ_p = 2400 kg/m^3, d_p = 120 μm) almost certainly corresponds to the turbulent fluidization flow regime, and this is consistent with the reported solid circulation flux of 0.22 kg/m^{2}s. However, in order to capture the particle movement with a phase Doppler particle analyzer, the volume fraction was restricted to 1.5%, resulting in a very dilute suspension, implying a situation where no distinct voids are present and particles are carried upwards by the gas as a dilute suspension. Reported lateral instantaneous particle velocities ranged from –0.9 to 2.5 m/s. Dencs (1995) used a reflective fiber optical probe, consisting of fibers of diameter 50 μm, in a bubbling fluidized bed of particles of size range 600 to 2500 μm with superficial gas velocities up to 1.3 m/s. The average particle velocity increased with both height and superficial gas velocity. However, possibly due to the blockage of a 0.02 m diameter area in the centre of the distributor plate in a 0.1 m diameter column, the radial profile of the average local particle velocity exhibited higher values (0.46 m/s) at the wall than in the centre (0.33 m/s) for U = 1.0 m/s and z/D = 1. No details on the optical probe used to determine the velocities were

provided. A reflective fiber optical probe with seven receiving fibers was applied to a bubbling bed of FCC particles with fluorescent-coated FCC as tracer particles by Tayebi et al. (1999). By detecting tracer particles that give uniquely intense signals, two-dimensional local particle and void velocities were measured. The results showed tracer particle velocities in all directions up to 0.92 m/s for U = 0.065 m/s. The fiber orientation provides the advantage of allowing the motion of particles in different directions to be determined.

In this study, a novel velocity probe developed at UBC is used to report on the local velocities of voids and particles in turbulent fluidized beds.

5.2 Optical fiber probe

Two types of probes were employed in this study. The first is the multi-functional optical fiber probe designed at UBC by Liu (2001) and manufactured by the Institute of Chemical Metallurgy in Beijing, China, for simultaneous measurement of local instantaneous voidage, particle velocity and solids flux. This probe was originally used in a high density circulating fluidized bed, but is intended for a wide range of two-phase systems. As shown in Figure 5.1, the probe contains three 0.26 mm diameter fibers; one light emitting, and two light receiving, with a physical centre-to-centre separation distance of 0.53 mm, and an effective separation distance of 0.18 mm between adjacent fibers. Since the diameter of the fibers is similar to the mean size of the FCC particle used in this work (75 μm), single particle movements can be detected. Mathematically, by acquiring data at a frequency higher than 27.8 kHz, this method can capture one-dimensional axial particle velocities up to 5 m/s travelling over the effective separation distance of 0.18 mm. In order to prevent particles from occupying the blind zone (see Liu, 2001; Cui et al., 2001), a glass cover was placed over the probe tip, as depicted in Figure 5.2. This helps to ensure a linear relationship between the signal and voidage measurements. Details of the optical velocity probe and the verification of velocity measurements can be found in Liu (2001), Liu et al. (2003a), and Liu et al. (2003b).

The second type of sensor utilizes two identical optical fiber voidage probes separated by a known distance to obtain voidage fluctuations, thus capturing the lag time between the signals from the two probes. The detailed concept of the optical voidage probe is covered in Chapter 4. As shown in Figure 4.2, the size of the fibers relative to that of the particles affects the measurements. In this case, the diameter of the fiber bundle is much larger than that of the particles.

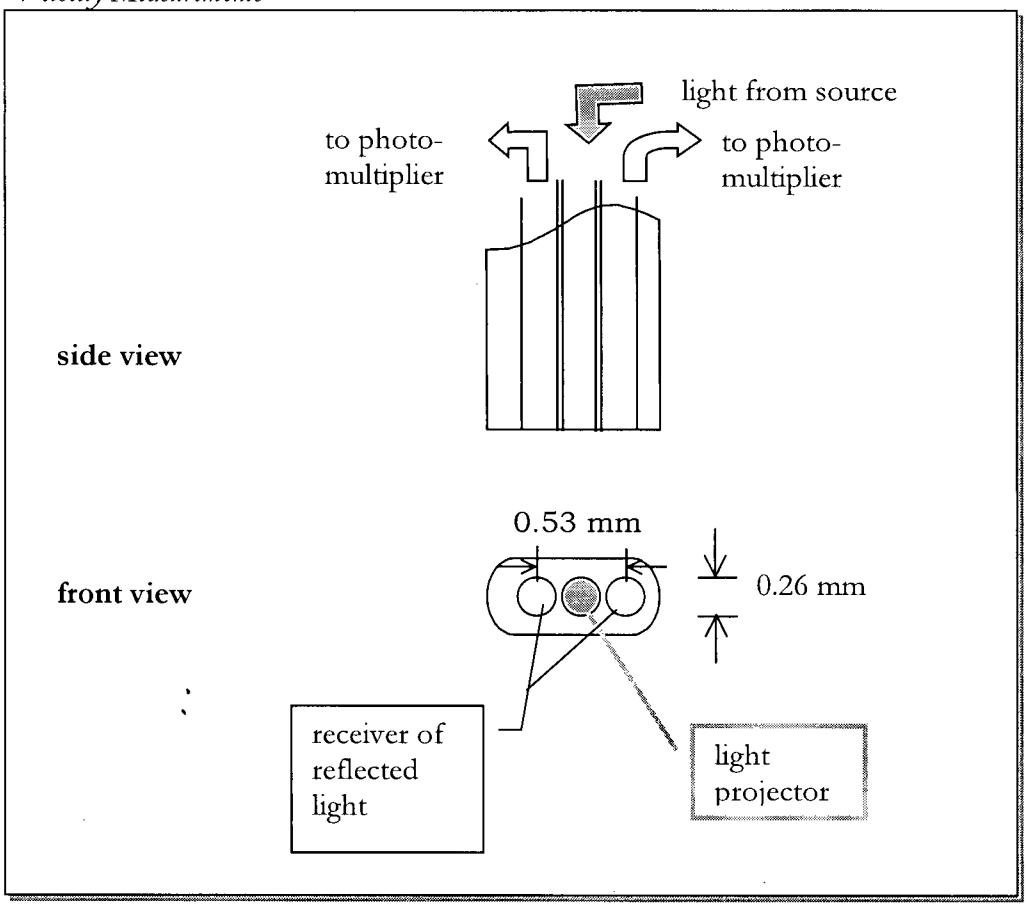

Figure 5.1 Details of optical fiber velocity probe.

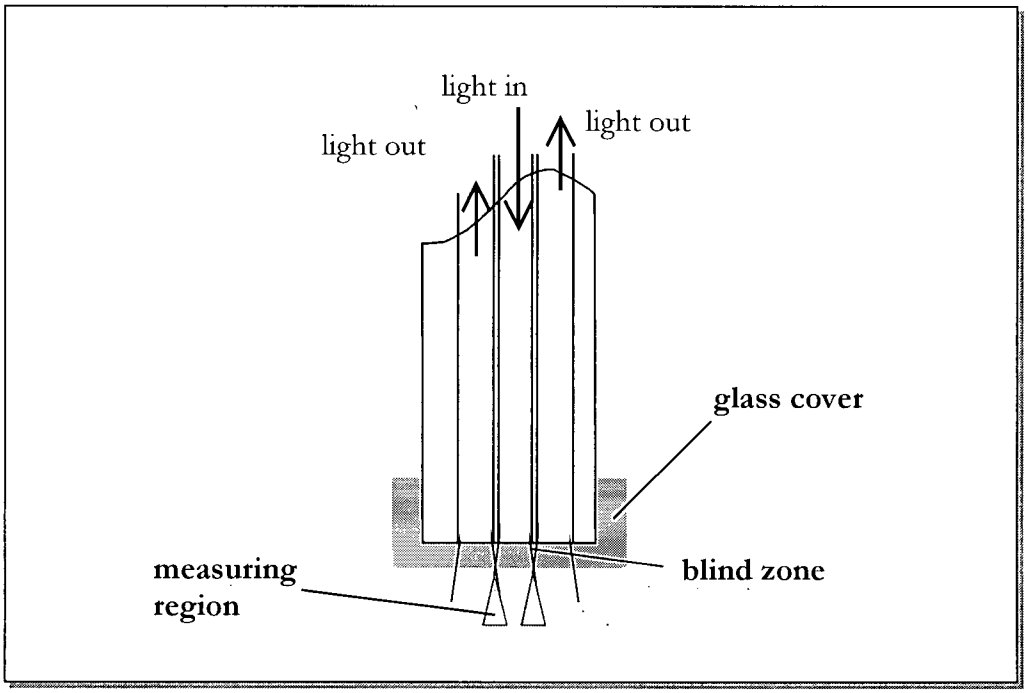

Figure 5.2 Schematic of optical velocity probe tip showing measurement volume and elimination of 'blind zone' by addition of glass cover.

As a result, this type of optical probe receives light reflected from a swarm of particles, as typified in Figure 5.3, and cannot distinguish signals from individual particles. Due to the sufficient separation of the two probes, the effective distance between the probes is considered to be identical to the physical separation distance as there is no overlapping measuring volume in this case. However, correlation of the signals from the probes becomes poor as the distance between the two probes is increased. This method is advantageous for capturing void movements from acquisition of data at much lower frequencies than those required by the particle velocity probe described in the previous paragraph. The drawback is the relatively poor correlation of signals, especially in turbulent fluidized beds due to considerable distortion and deviation in the shapes, sizes and directions of motion of voids and particles travelling between the two probes. As indicated by the traces in Figure 5.3, the irregularity of the voidage fluctuation signals makes the analysis difficult, inevitably leading to some uncertainty and error.

5.3 Data acquisition and analysis

The optical fiber velocity probe and the high-speed data acquisition card were supplied by the Institute of Chemical Metallurgy in Beijing, China. The high-speed data acquisition software for the optical velocity probe is written in Turbo C based on a program written by Liu (2001) without the user interface. The typical sampling rate was between 13 and 30 kHz with durations of 60 to 140 s. As shown in Figure 5.4, two signals from fibers A and B are acquired at high speed, followed by off-line analysis of the cross-correlation between the signals and conversion to voidage. In order to pursue the analysis in an unbiased manner, pre- and post- processing of data was carried out according to the algorithms, written in MATLAB®, listed in Table 5.1. Cross-correlation was performed on the raw data as well as on data that had been pre-processed with binary coding and cut-off methods. Further details on the pre-conditioning of data and analysis methods are described in Appendix B.

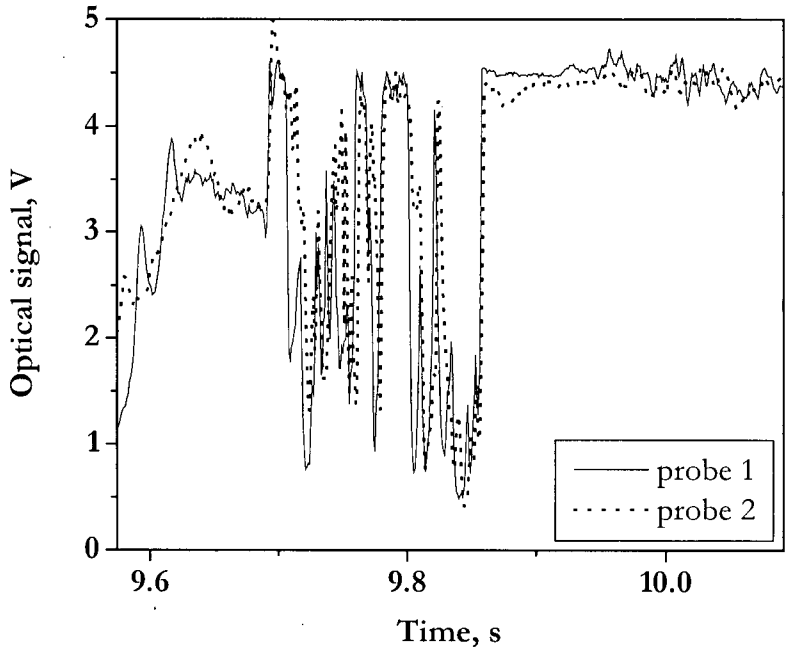

Figure 5.3 Typical optical signal obtained by two identical voidage probes separated by 0.01 m. D=0.29 m, z=0.78 m, U=0.90 m/s, r/R=0.70, H_0=1.5 m, FCC I.

Table 5.1 MATLAB® functions written for data analysis.

File name	Function
corr_fun.m	performs cross-correlation on group number
eliminate.m	imposes elimination criteria on correlated data
dense.m	extracts data points related to dense-phase
binary.m	converts raw data into binary code based on assigned threshold value

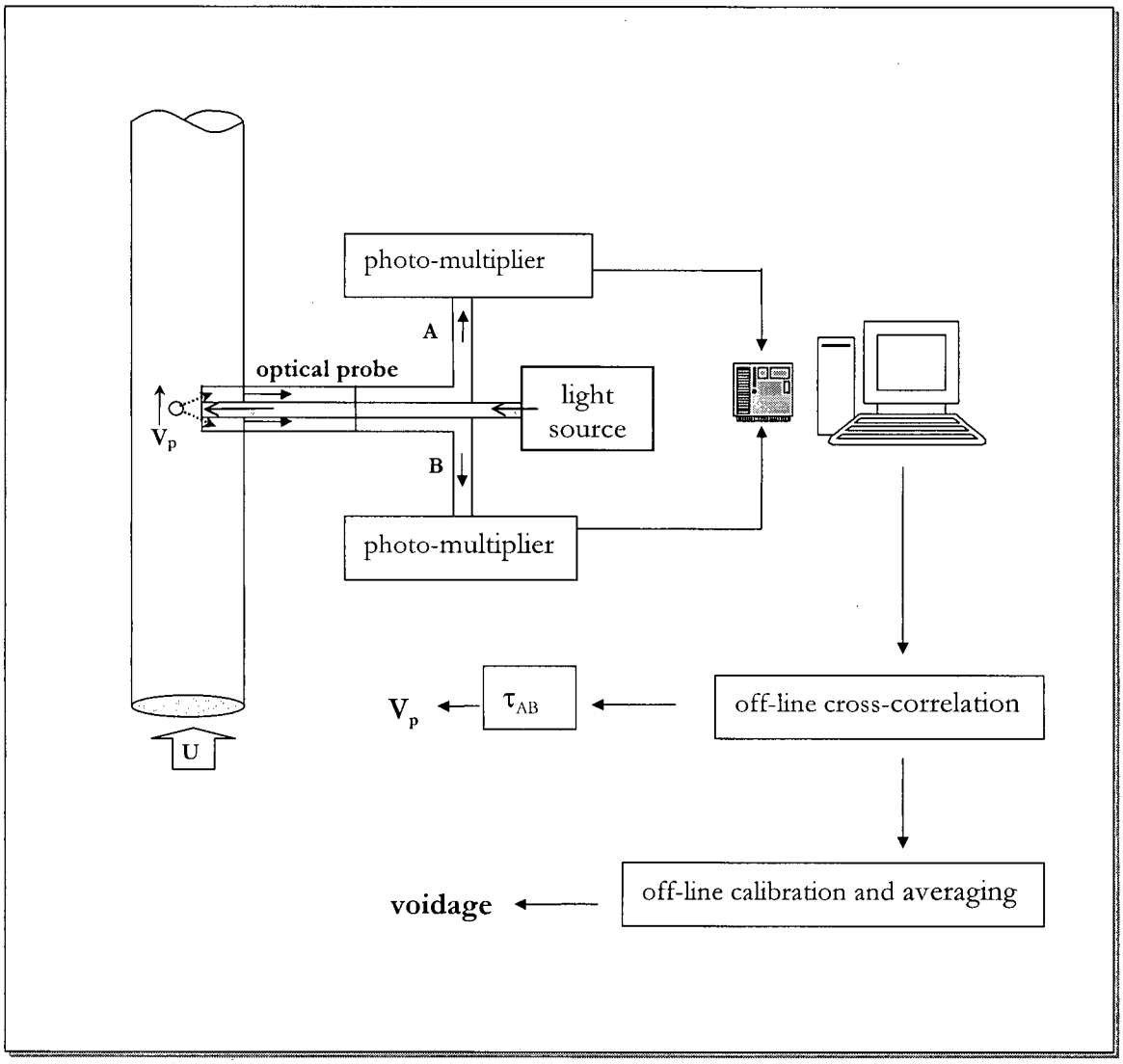

Figure 5.4 Schematic of the optical fiber velocity probe system for simultaneous measurement of local solids concentration and particle velocity.

5.4 Results

5.4.1 Particle velocities in 0.61 m diameter column

The time-average overall axial voidage profile from the wall mounted differential pressure (DP) transducer for the velocity measurement runs performed in the 0.61 m diameter column is shown in Figure 5.5. The results indicate an increased difference in time-mean voidage at z=1.55 m compared to z=0.80 m with increasing superficial gas velocity.

Figure 5.6 depicts the cumulative void-associated particle velocity profile for U=1.56 m/s, z=1.55 m. As the optical fiber velocity probe is moved towards the centre, the profile shifts to higher velocity, coinciding with an increase in time-average voidage. Figure 5.7 exhibits a typical probability distribution of voidage at four different radial positions. As the optical probe is traversed towards the axis of the column, the voidage distribution changes from dominantly representing the dense phase to a bimodal distribution of dense and dilute phases. A further increase in superficial gas velocity results in a radial profile resembling a core/annulus structure in a circulating fluidized bed. For all of the superficial gas velocities examined, a bimodal distribution, suggesting dense and dilute phases, is present near the centre.

Radial profiles of average void-associated particle velocity and voidage for superficial gas velocities of 1.56 and 0.82 m/s are shown in Figure 5.8. The method of distinction between the void- and dense-phase-associated particle velocities is discussed in Appendix B. At the measurement height of 1.55 m, the cross-sectional time-average voidages for the two velocities are similar, i.e., 0.88 and 0.87, respectively. The particle velocity profile is rather scattered for U=0.82 m/s, which is very close to U_c, as determined according to the pressure fluctuations. It is concluded that the average velocity may not necessarily be representative of the flow conditions given the considerable fluctuations in both pressure and solids velocities.

The curves in Figure 5.9 display a shift in void-associated particle velocity distribution with superficial gas velocity as well as with position. For both r/R=0.09 and 0.5, particle velocity is higher for z=0.80 m (at U=0.81 m/s) than for z=1.55 m (at U=0.82 m/s). The operating conditions expressed in terms of average pressure drop measurements along the axial height, and the average

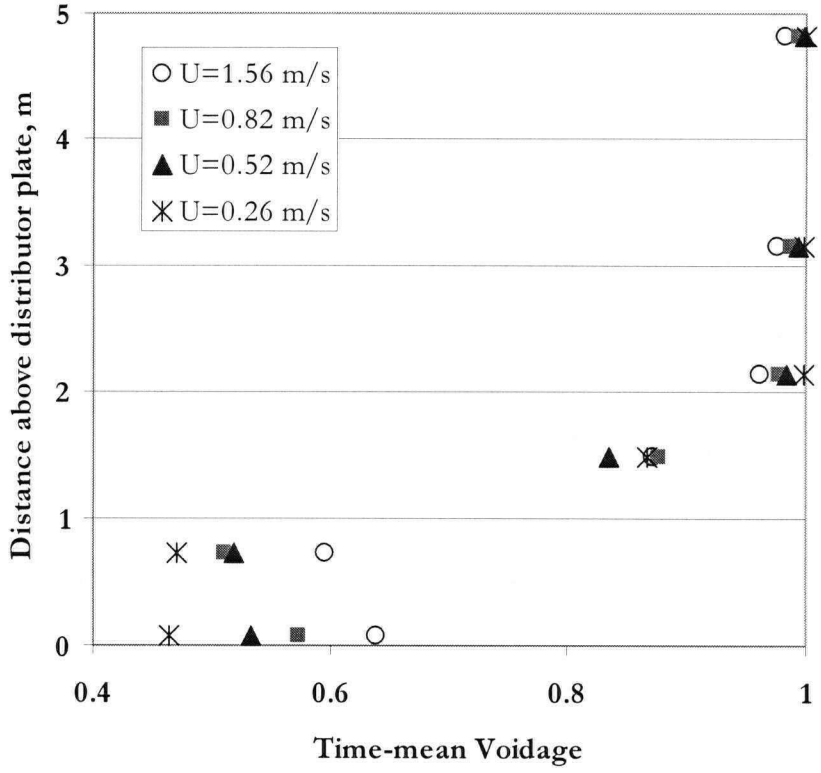

Figure 5.5 Axial profile of time-mean voidage determined from differential pressure signals. D=0.61 m, H_0=2 m, FCC IV, U_c (DP at $\bar{z}$ =1.55 m)=1.12 m/s.

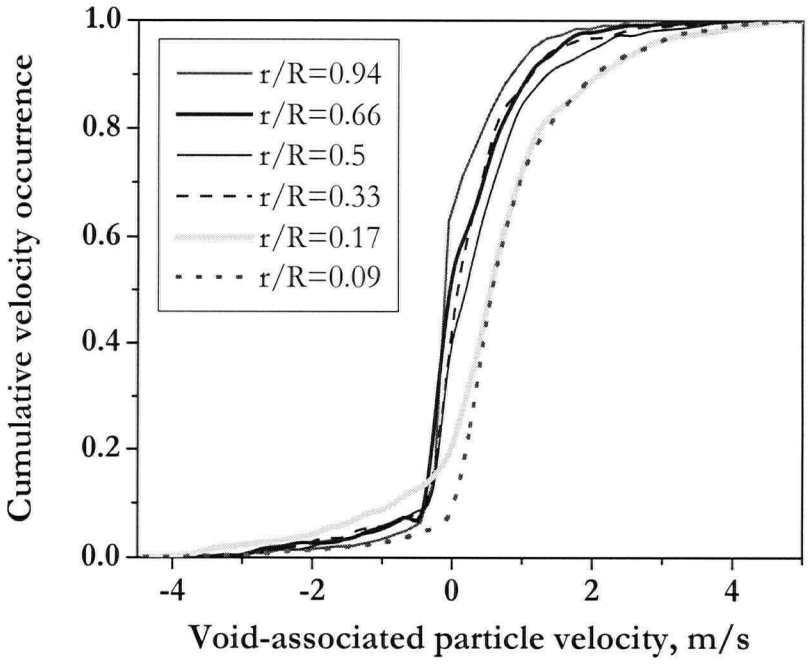

Figure 5.6 Cumulative void-associated particle velocity profile. D=0.61 m, U=1.56 m/s, z=1.55 m, H_0=2 m, FCC IV.

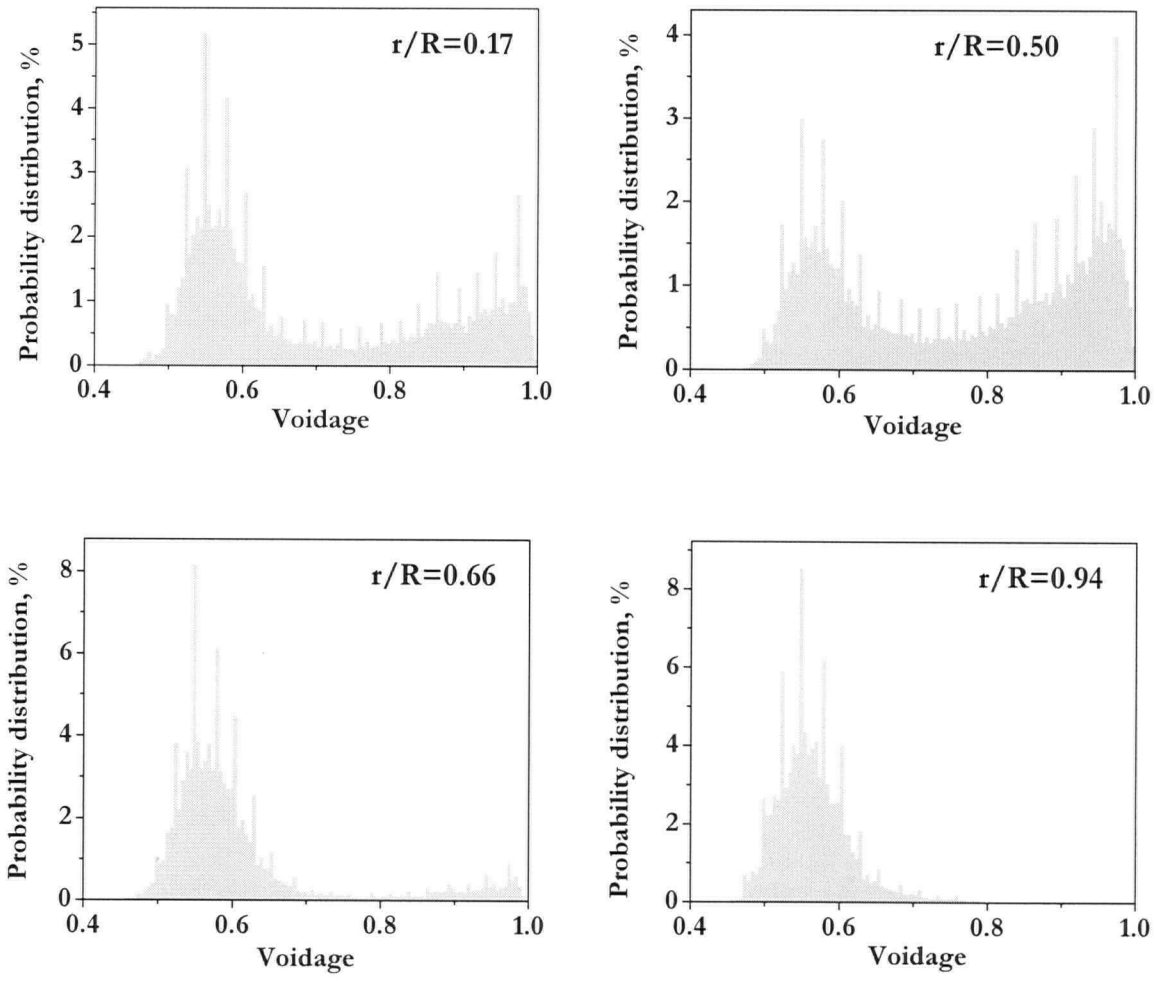

Figure 5.7 Probability distribution of voidage. D=0.61 m, U=0.82 m/s, z=1.55 m, H_0=2 m, FCC IV.

Table 5.2 Average voidage. D=0.61 m, H_0=2 m, FCC IV.

Voidage comparison	r/R = 0.5	r/R=0.09
z=0.80 m (U=0.81 m/s)	0.76	0.66
z=1.55 m (U=0.82 m/s)	0.77	0.71

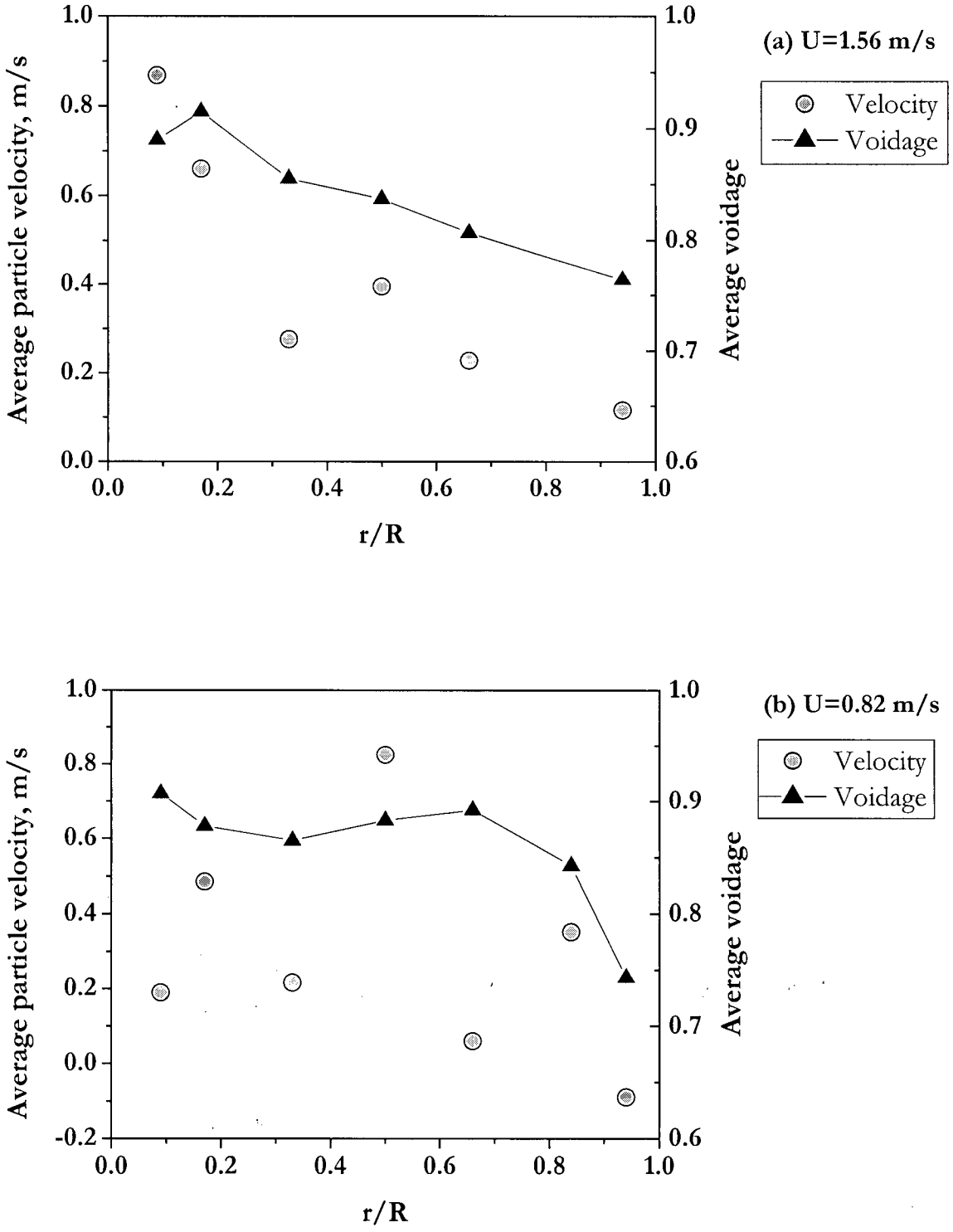

Figure 5.8 Radial profile of time-mean void-associated particle velocity (●)and voidage (▲)distributions: (a) U=1.56 m/s; (b) U=0.82 m/s. D=0.61 m, z=1.55 m, H_0=2 m, FCC IV.

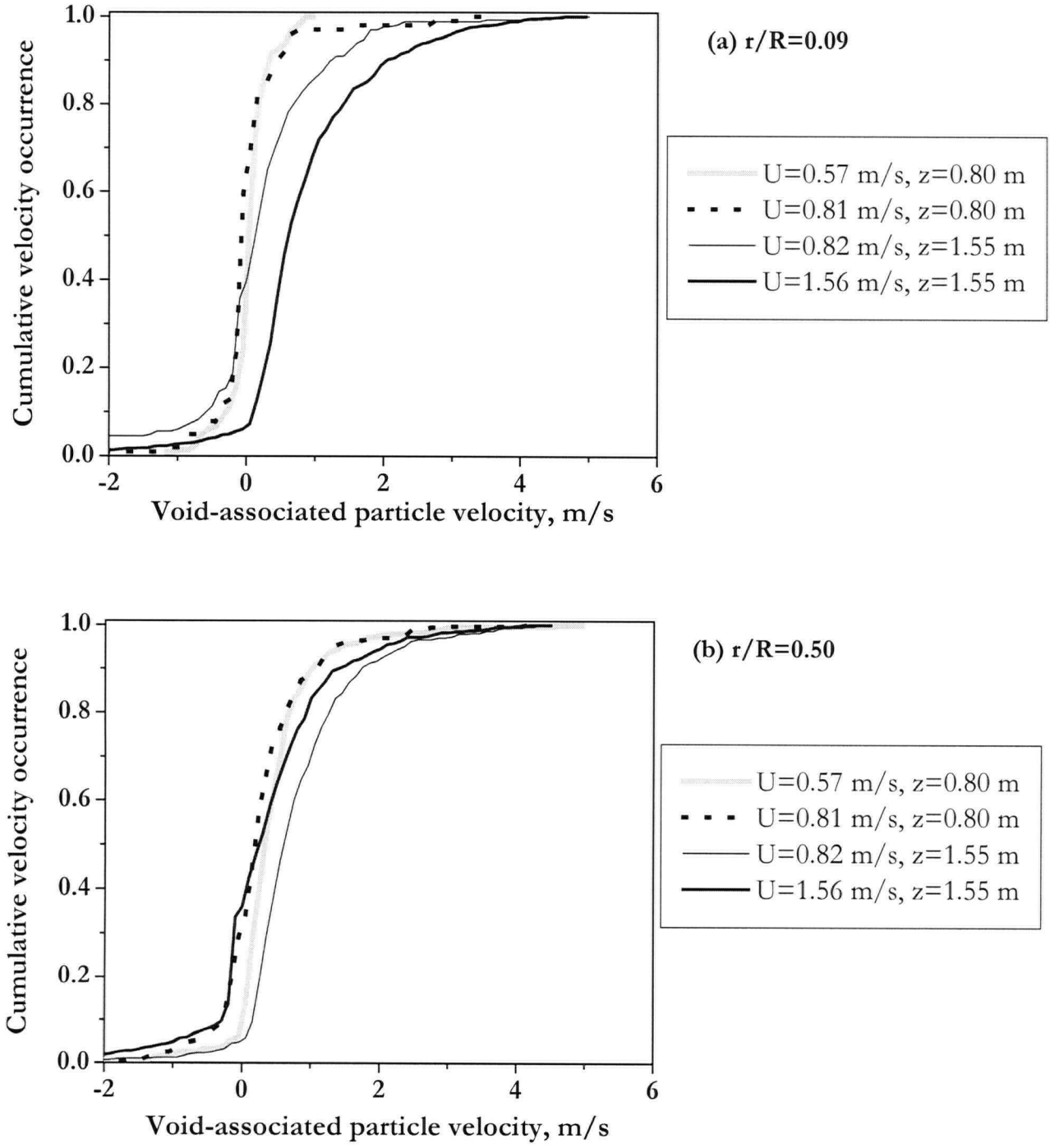

Figure 5.9 Cumulative void-associated particle velocity occurrence at (a) r/R=0.09 and (b) r/R=0.50. D=0.61 m, H_0=2 m, FCC IV.

local voidage measurements at four spatial locations (i.e., combination of z=0.80 and 1.55 m, and r/R=0.09 and 0.5) are examined in Table 5.2. The results from Figure 5.9 compared to the values in Table 5.2 confirm that fewer particles are moving much faster as they travel mostly upward with the voids near the column axis

The cumulative velocity distribution, Figure 5.9, also indicates numerous occurrences of particle velocity close to 0 for z=0.80 m, particularly for r/R=0.09. This is attributed to being close to the solids return position, as illustrated in Figure 2.14, and is supported by the decrease in time-average voidage at these locations. The particles re-entering the fluidized bed have little axial momentum, and they frequently change directions. The effect of the solids return on the hydrodynamics in the turbulent fluidized bed intensifies with increasing solids circulation rate.

5.4.2 Effect of superficial gas velocity on particle velocity

In order to examine the effect of superficial gas velocity on particle velocity, data have been analyzed for eight superficial gas velocities between 0.82 and 1.56 m/s, as shown in Figure 5.10. By choosing these particular runs, the change in hydrodynamics is investigated as U varies from below U_c to beyond U_c.

Figure 5.11 indicates that the void-associated particle velocity exhibits a steady increase with increasing U, despite the maximum standard deviation from the gauge pressure being attained at around 1 m/s. The dense-phase-associated particle velocities do not rise until U is beyond U_c. As reported in Chapter 4, one of the characteristic changes in the local structure, once within the turbulent fluidization flow regime, occurs in the dense phase. A further analysis of the data yields the standard deviation of the particle velocity fluctuation reported in Figure 5.12. This may indicate, though quite scattered, that the fluctuation of the dense-phase-associated particles generally increases with U. Note that at U=1.56 m/s, the signals from the dense to the dilute phases are still distinguishable, i.e., there are two major peaks in the pdf of voidage, with the standard deviation of the pressure fluctuation decreasing, and the particle movement becoming less dominated by void dynamics. The particle velocity fluctuations originate from collisions between particles and interactions with the gas phase in the form of shear stress, and are characteristics of the particle phase turbulence. In essence, the trend beyond U_c can be interpreted as particles in the dense phase becoming increasingly spaced apart, gaining turbulent energy by having less energy loss as a consequence of inelastic particle-particle collisions. Once local pressure gradients and fluctuations

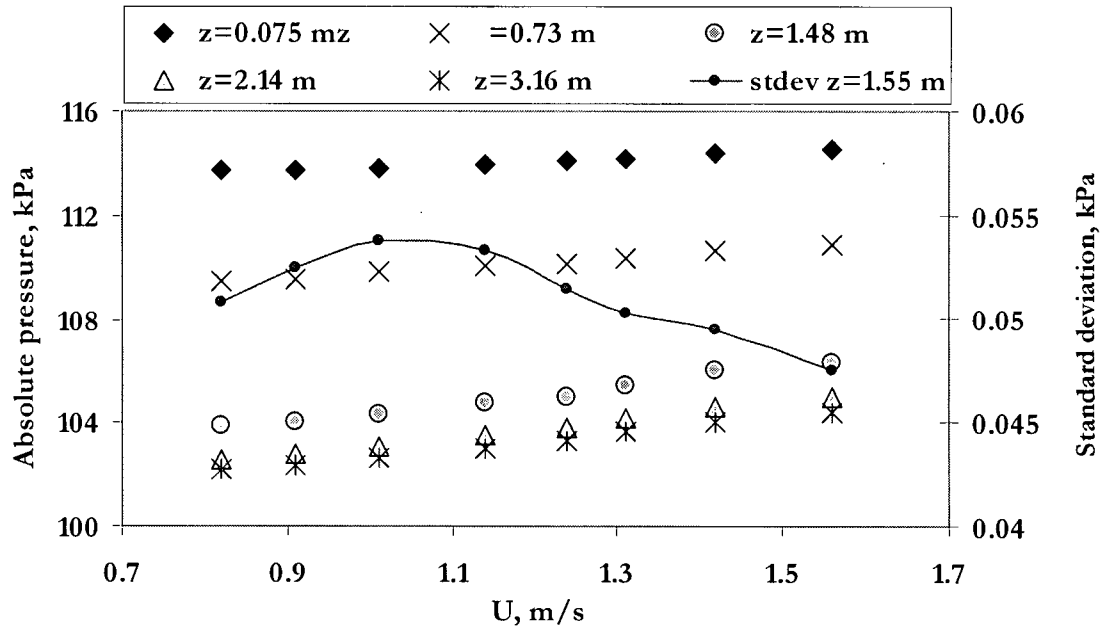

Figure 5.10 Wall measurements of gauge pressure and standard deviation of pressure fluctuation. D=0.61 m, H_0=2 m, FCC IV.

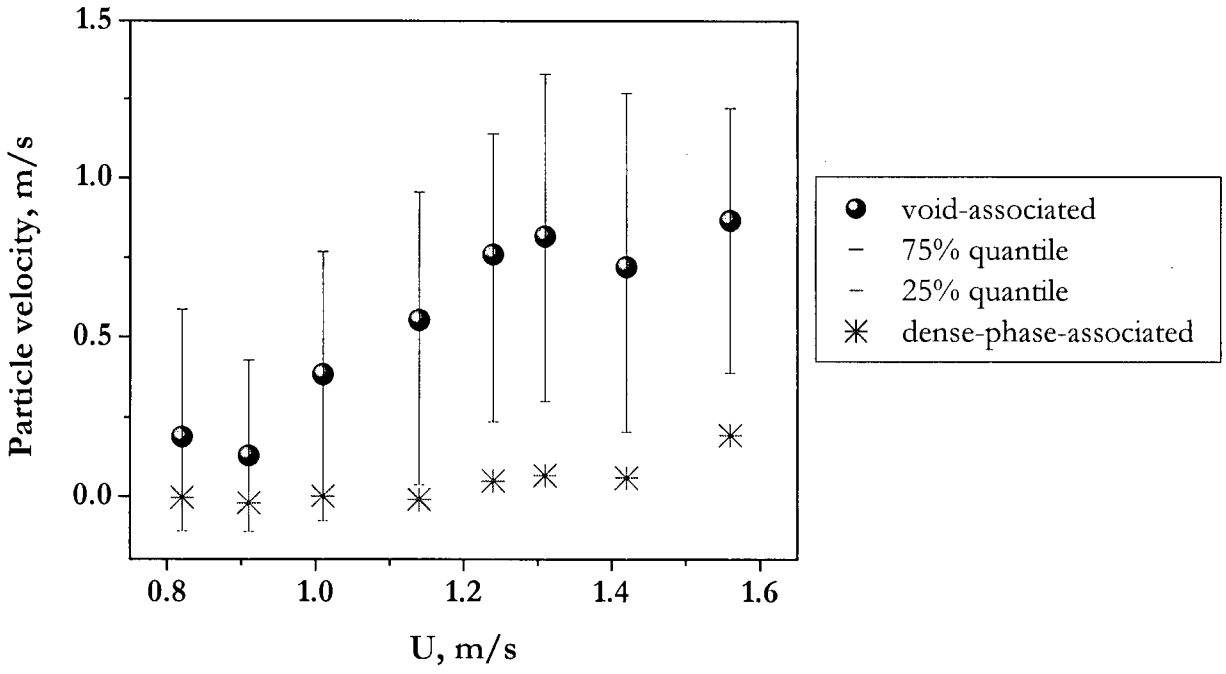

Figure 5.11 Effect of U on average particle velocities. r/R=0.09, D=0.61 m, H_0=2 m, FCC IV, U_c =1.12 m/s (DP at $\bar{z}$ =1.55 m).

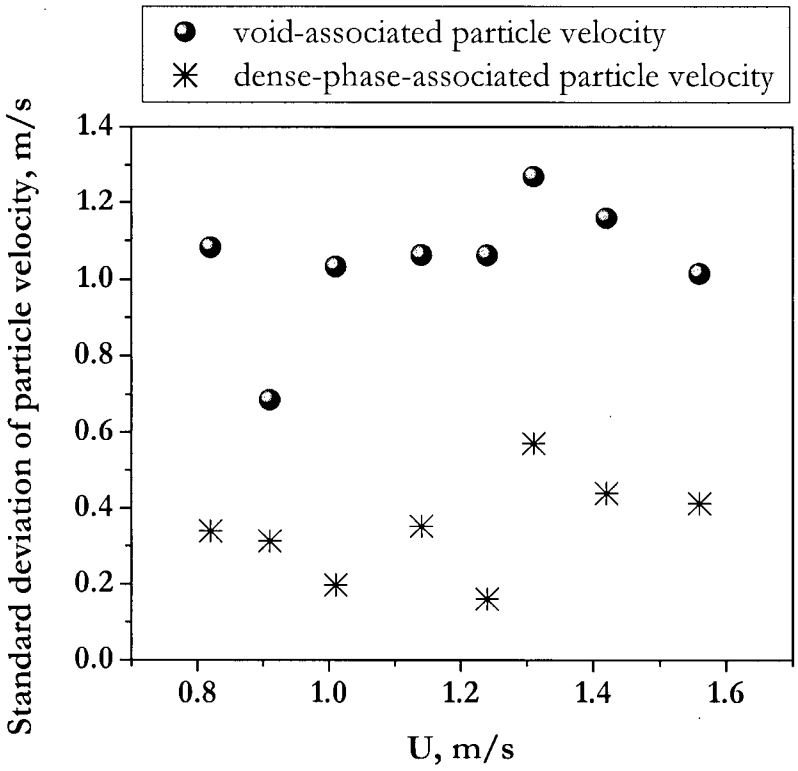

Figure 5.12 Standard deviation of particle velocities. D=0.61 m, z=1.55 m, r/R=0.09, U_c=1.12 m/s (DP at z=1.55 m), FCC IV.

due to voids become reduced, the extra lift exerted on particles from the Saffman force should decrease. Assuming that the majority of voids are travelling vertically, the reduction in the lift force may further promote radial movement of particles.

5.4.3 Particle velocity and voidage

Another set of data is examined next to interpret the results based on a continuous distribution of voidage rather than separated into binary phases. For consistency, a group number of 200 was chosen for this analysis of the data, with the probability distribution of particle velocities measured at superficial gas velocities of 0.42 and 1.00 m/s in the 0.61 m diameter column. Figure 5.13 (a) depicts a close-to-symmetrical probability distribution of particle velocities for U=0.42 m/s. At U=1.00 m/s, Figure 5.13 (b), the distribution becomes increasingly skewed and asymmetric, especially for the central location. More negative particle velocities were recorded near the wall than in the core for U=1.00 m/s.

By plotting the particle velocity against voidage, the change in two-phase flow dynamics becomes obvious. Figure 5.14 shows that most particle movement is associated with denser voidage for the radial positions r/R=0.94 and 0.50, while the particle dynamics exhibit a near binary voidage region near the centre-most radial position. The lack of particle movement for $\varepsilon \approx 0.7$ indicates that the distinction between being in a void and in the dense phase is clear, similar to typical void characteristics in bubbling fluidized beds. With U increased to 1.00 m/s, Figure 5.15 shows more intermediate voidage data, while particle velocities shift toward more to the positive domain for r/R=0.09. This confirms that as the superficial gas velocity is increased to the turbulent fluidized bed flow regime, particles are found over a wide spectrum of concentrations, i.e., the distinction between the dense and dilute phases becomes increasingly diffuse.

Voidage and particle velocity data were also obtained at the higher superficial gas velocity of 1.56 m/s, though at a different level, z=1.55 m, and the results are shown in Figure 5.16. There is very little distinction between the structures detected at r/R=0.50 and 0.09 both for the voidage and particle velocity distributions. Even near the wall, the voidage is widely distributed. It is quite noticeable that a significant number of particle velocities are positive. A further increase in the superficial gas velocity should reveal the local structural change as the transition to the fast fluidization flow regime is approached.

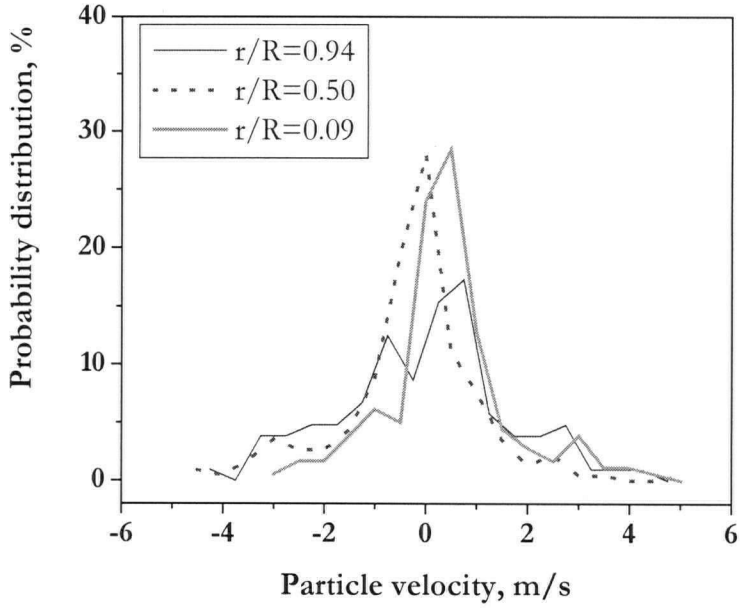

(a) U=0.42 m/s

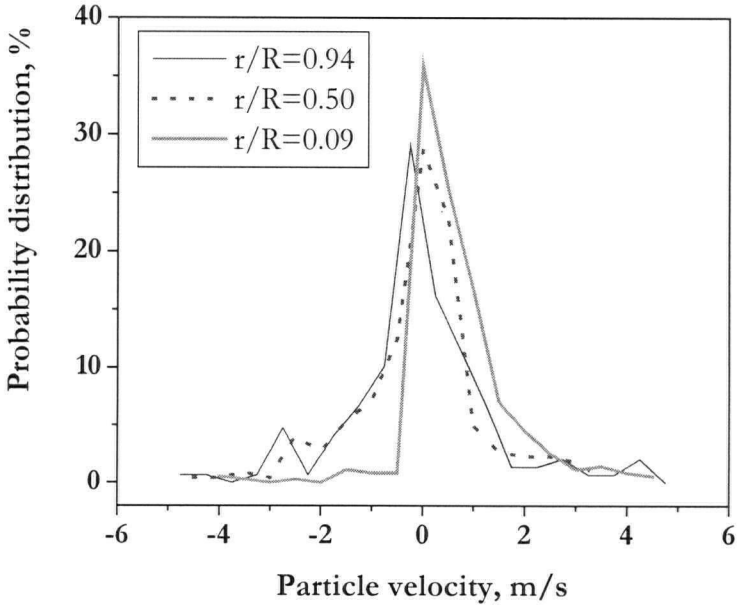

(b) U=1.00 m/s

Figure 5.13 Probability distribution of particle velocities for (a) U=0.42 m/s, and (b) U=1.00 m/s at radial positions of 0.94, 0.50, and 0.09. D=0.61 m, z=0.80 m, FCC IV.

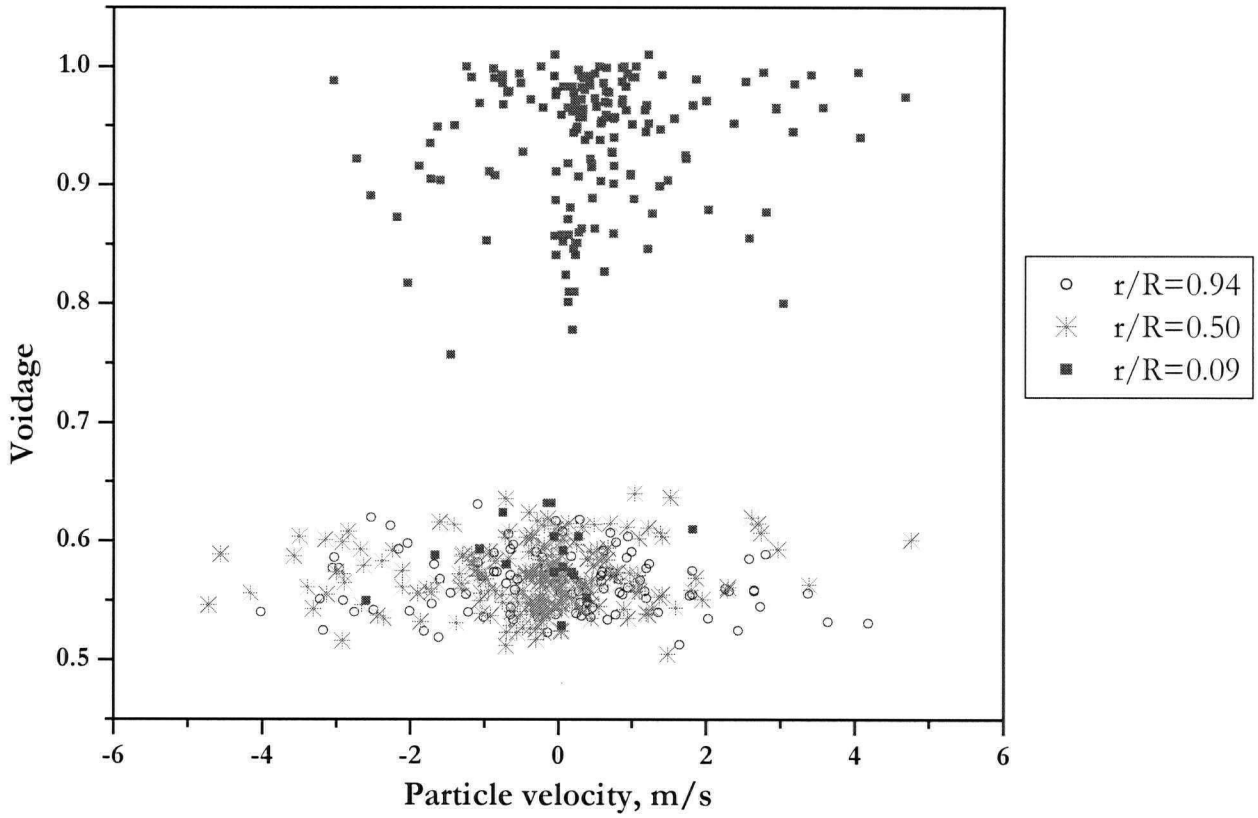

Figure 5.14 Particle velocity and voidage distribution for U=0.42 m/s at radial positions of 0.94, 0.50, and 0.09. D=0.61 m, z=0.80 m, FCC IV.

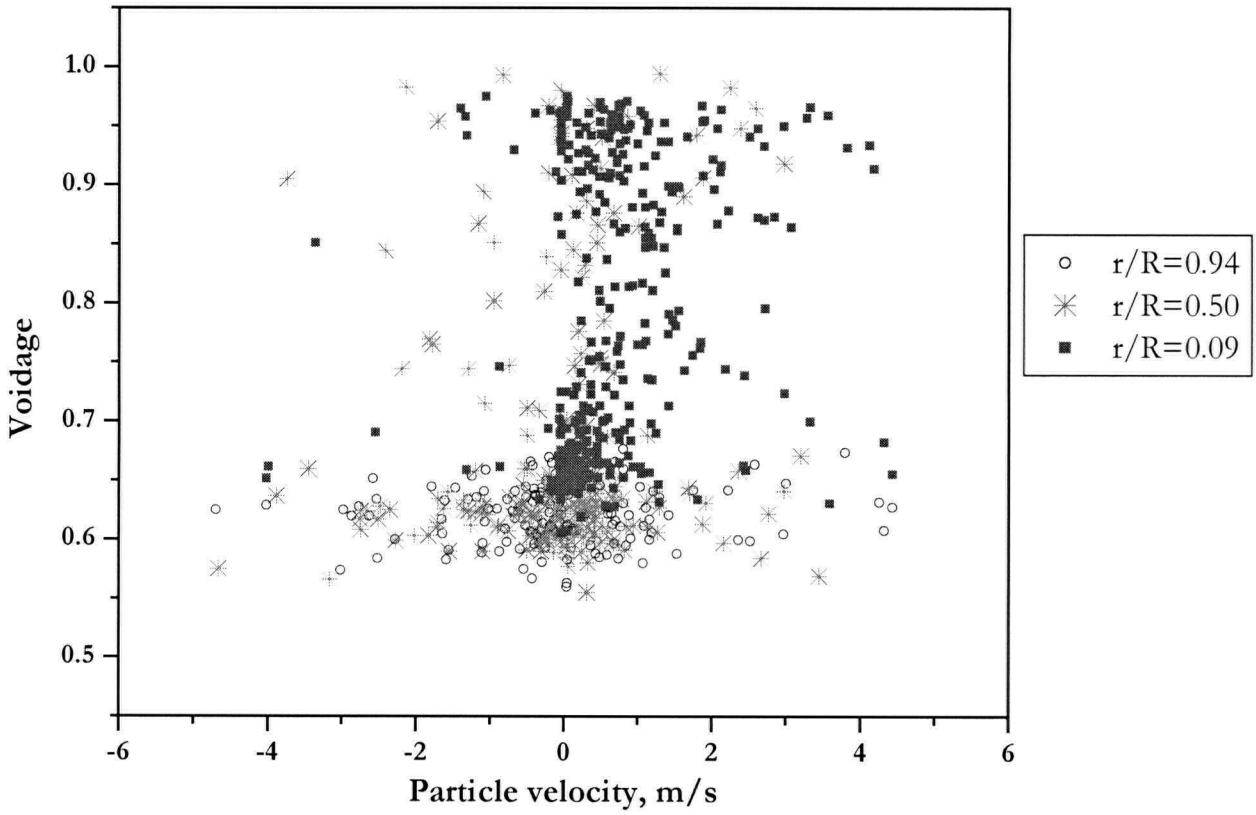

Figure 5.15 Particle velocity and voidage distribution for U=1.00 m/s at radial positions of 0.94, 0.50, and 0.09. D=0.61 m, z=0.80 m, FCC IV.

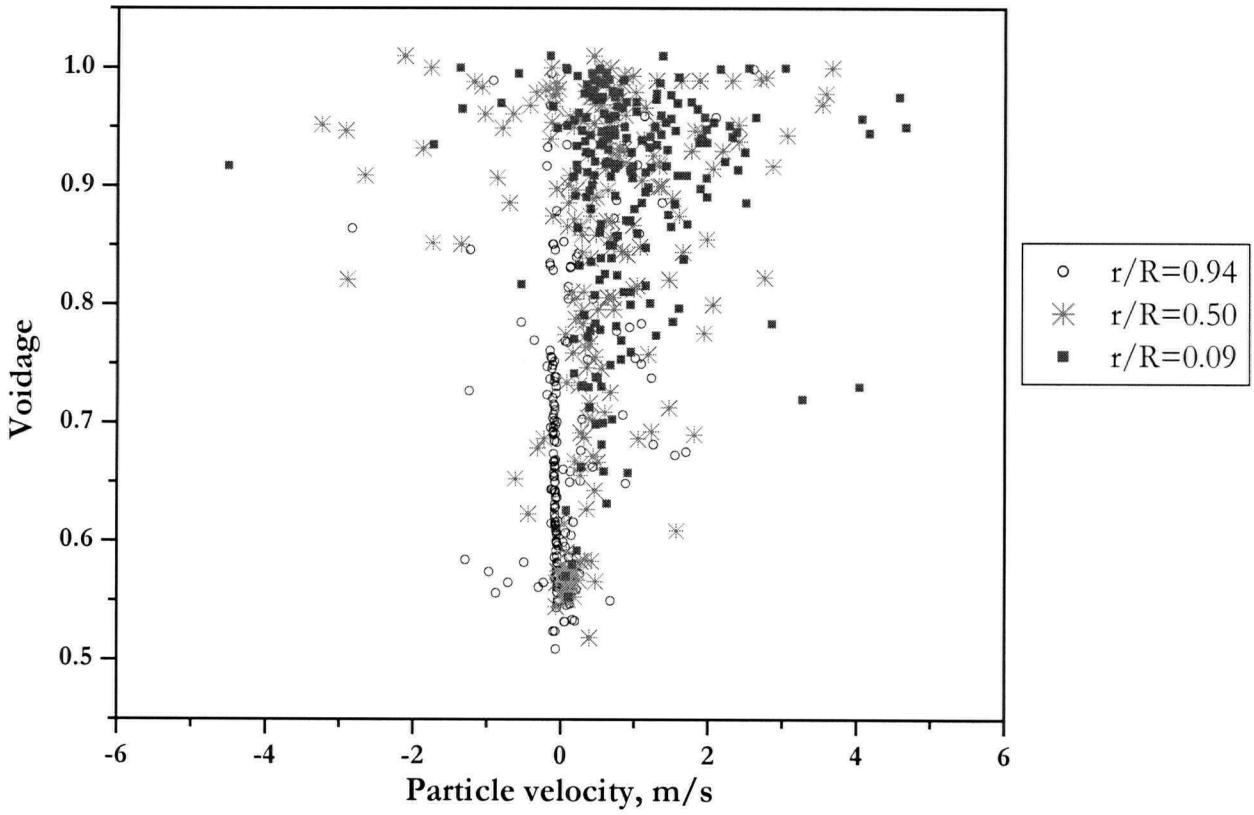

Figure 5.16 Particle velocity and voidage distribution for U=1.56 m/s at radial positions of 0.94, 0.50, and 0.09. D=0.61 m, z=1.55 m, FCC IV.

5.4.4 Particle velocities in the 0.29 m diameter column

Velocity measurements using the optical fiber velocity probe with high-speed data acquisition have been analyzed to obtain the effect of superficial gas velocity on the one-dimensional particle velocities associated with voids and dense phase in a 0.29 m diameter column. The procedures are described in Appendix B.

For the data set from the optical velocity probe used for the 0.29 m diameter column, sampling frequencies of up to 13,357 Hz were acquired for the fiber separation of 0.18 mm. This means that particle velocities beyond 2.4 m/s could not be captured. As this may not be sufficient for the conditions under study, only particle velocities primarily associated with the dense phase are analyzed in this section.

The dense-phase-associated particle velocity distribution is shown in Figure 5.17 with statistical moments calculated in Table 5.3. The mean particle velocity distribution approaches zero with increasing U, while the skewness of particle velocity distribution decreases, indicating increasing symmetrical distribution of the probability distribution function. High kurtosis numbers (=3 for Gaussian distribution) may suggest intermittency in the dense-phase-associated particle velocities. Changes in the dense-phase-associated particle velocity distribution may indicate a different solids circulation pattern in the fluidized bed. Unfortunately, the data at hand for the 0.29 m diameter column did not allow verification of the trend beyond U_c, around 0.7 m/s.

5.4.5 Void velocities in the 0.29 m diameter column

The method described in Section B.7 in Appendix B using optical voidage probes was adopted to capture the void velocities in the 0.29 m diameter column. The cut-off method using the threshold value set by Method (a) in Section B.6 was used to eliminate fluctuations corresponding to the dense-phase prior to performing the cross-correlation. The group number was set at 300, which for a sampling frequency of 1,000 Hz, represented 0.3 s correlating segments. The distance between the two probes was varied from 0.01 to 0.04 m.

Figures 5.18 (a) and (b) portray the void velocity distribution for r/R=0.0 and 0.7. These indicate increasing skewness at the centre position compared to r/R=0.70. The transition velocity, U_c, was determined to be 0.82 m/s from gauge pressure measurements at z=0.65 m. Thus, at a superficial

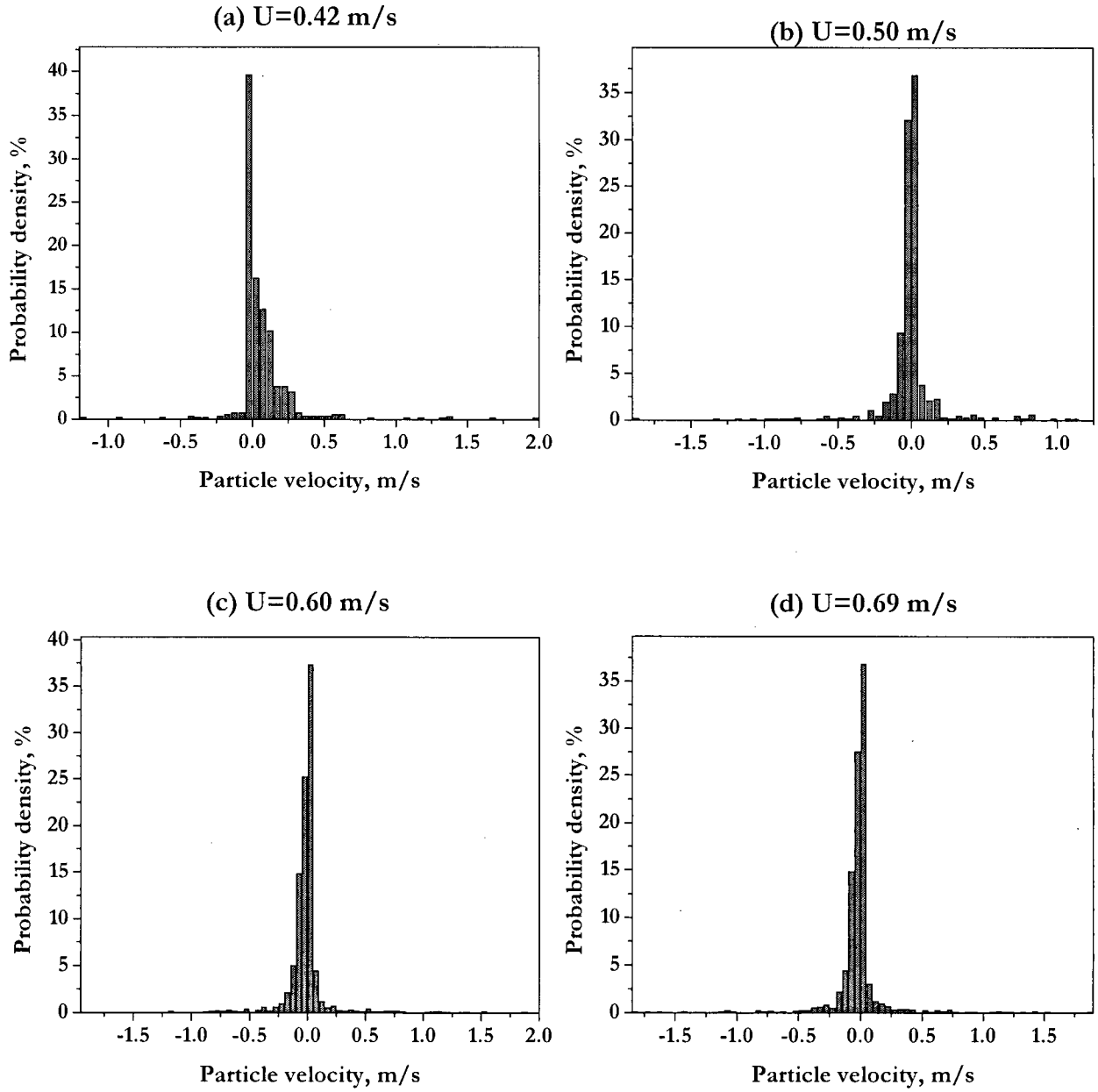

Figure 5.17 Distribution of particle velocities associated with dense-phase. D=0.29 m, r/R=0.70, z=0.78 m, H_0=1.0 m, FCC I.

Table 5.3 Moments of particle velocity distributions. D=0.29 m, z=0.78 m, r/R=0.55, FCC I.

Moments	U=0.42 m/s	U=0.50 m/s	U=0.60 m/s	U=0.69 m/s
Mean	0.06717	-0.009676	-0.01798	-0.02198
Std Dev	0.218	0.207	0.236	0.218
Std Err Mean	0.00954	0.00804	0.00538	0.00553
upper 95% Mean	0.0859	0.00610	-0.00742	-0.0111
lower 95% Mean	0.0484	-0.0255	-0.0285	-0.0328
Sample Number	520	663	1917	1557
Sum Weights	520	663	1917	1557
Sum	34.9	-6.41	-34.5	-34.2
Variance	0.0474	0.0428	0.0556	0.0476
Skewness	3.24	-1.40	0.554	-0.494
Kurtosis	26.9	22.5	26.1	25.8
Coef. variance	323	-2138	-1311	-993

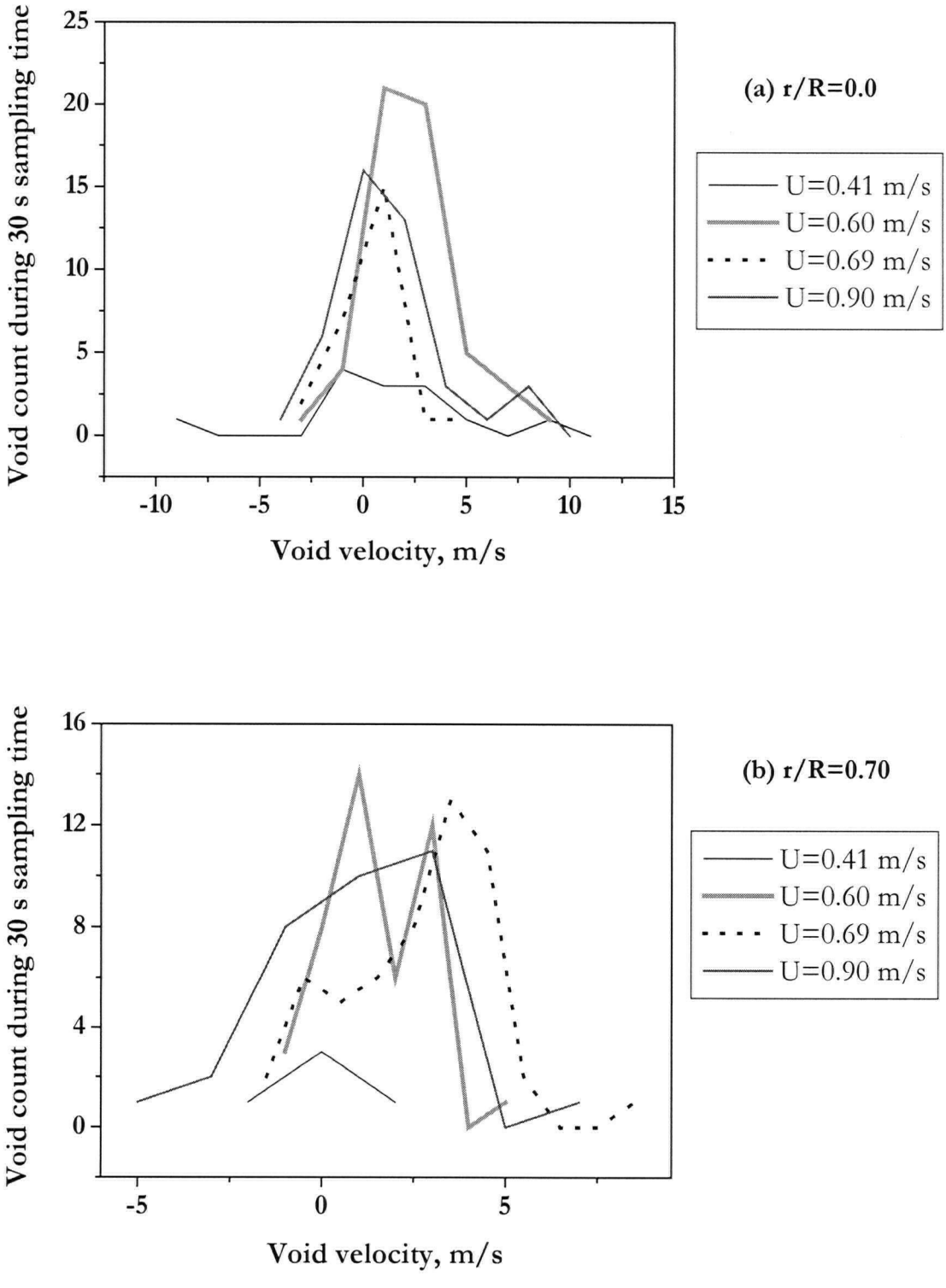

Figure 5.18 Void velocity distribution for (a) r/R=0.0, and (b) r/R=0.70. D=0.29 m, z=0.78 m, Δz=0.02 m, H_0=1.5 m, FCC I.

gas velocity of 0.90 m/s, the standard deviation of pressure fluctuations is on the decrease. The increased number of occurrences of negative void velocities, particularly at U=0.90 m/s and r/R=0.70, was verified by examining the original data and with the peak picking method. This, coupled with the dense-phase-associated particle velocity distribution in the previous section, may suggest void-induced downward flow of solids at r/R=0.7. Further analysis can be conducted to study the gas mixing behaviour, which is not only associated with void movement, but is also related to a back-mixing phenomenon.

In Figure 5.19, the average void velocity is plotted against the superficial gas velocity for three radial positions. Very crudely, the results can be interpreted as showing the average void velocity increasing at r/R=0.70, and decreasing near the wall with increasing superficial gas velocity. The void velocities are within the same range as the findings of Taxil et al. (1998) in a 0.2 m diameter column with FCC particles of 95 μm mean diameter. However their study merely mentions downflowing voids "from time to time", without indicating any negative velocities in the reported data.

The average void frequency is plotted in Figure 5.20 against radial position for four superficial gas velocities. Though very much threshold-value dependent, the frequencies are similar to those reported by Bayle et al. (2001), Taxil et al. (1998) and Ege (1995). Ege (1995) indicated void frequencies as high as 20 Hz for a 0.3 m diameter column with FCC particles of 65 μm mean diameter fluidized at U=0.55 m/s. Bayle et al. (2001) presented void frequencies up to 6 Hz at U=0.80 m/s in a 0.2 m diameter column with FCC particles of 95 μm mean diameter. This underlines the strong dependency of the void frequency on the analysis method. The frequency range indicated in Figure 5.20 is comparable to the major frequency from the differential pressure fluctuation signals reported in Chapter 6 (Figure 6.3), which provides evidence that the DP signals can capture the void dynamics.

5.5 Conclusions and recommendations

Experimental work has been conducted to capture simultaneous measurements of local voidage, particle velocity and void velocity in 0.29 and 0.61 m diameter columns for FCC particles, operated in the bubbling and turbulent fluidized bed flow regimes. The results confirm previous reports that void movement is erratic and transient in the turbulent fluidized bed.

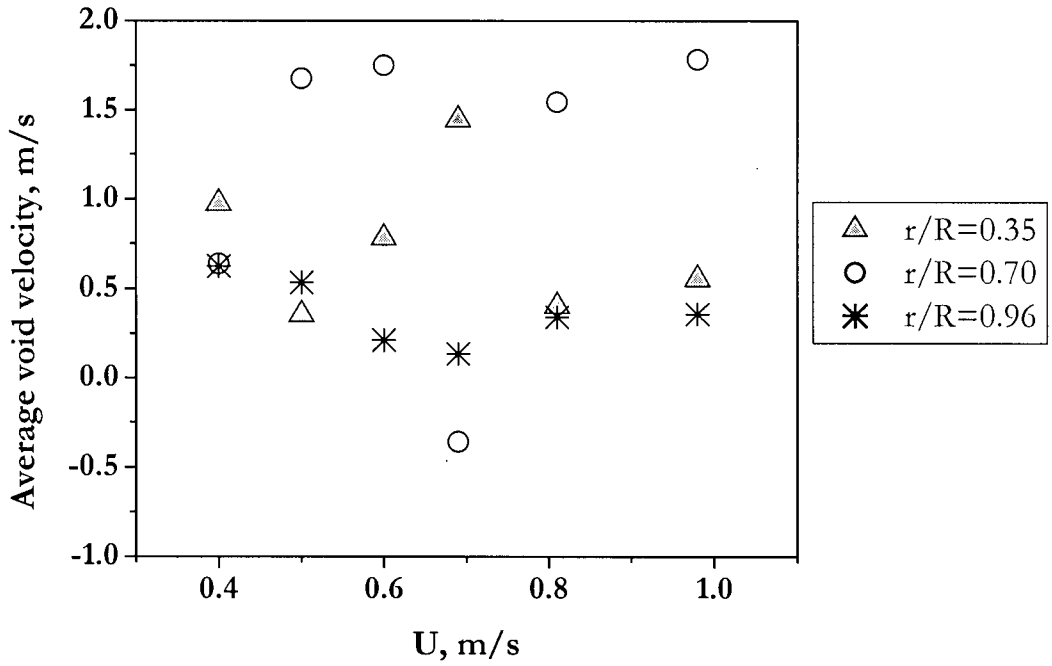

Figure 5.19 Average void velocity. D=0.29m, z=0.78 m, Δz=0.02 m, H_0=1.5 m, FCC I.

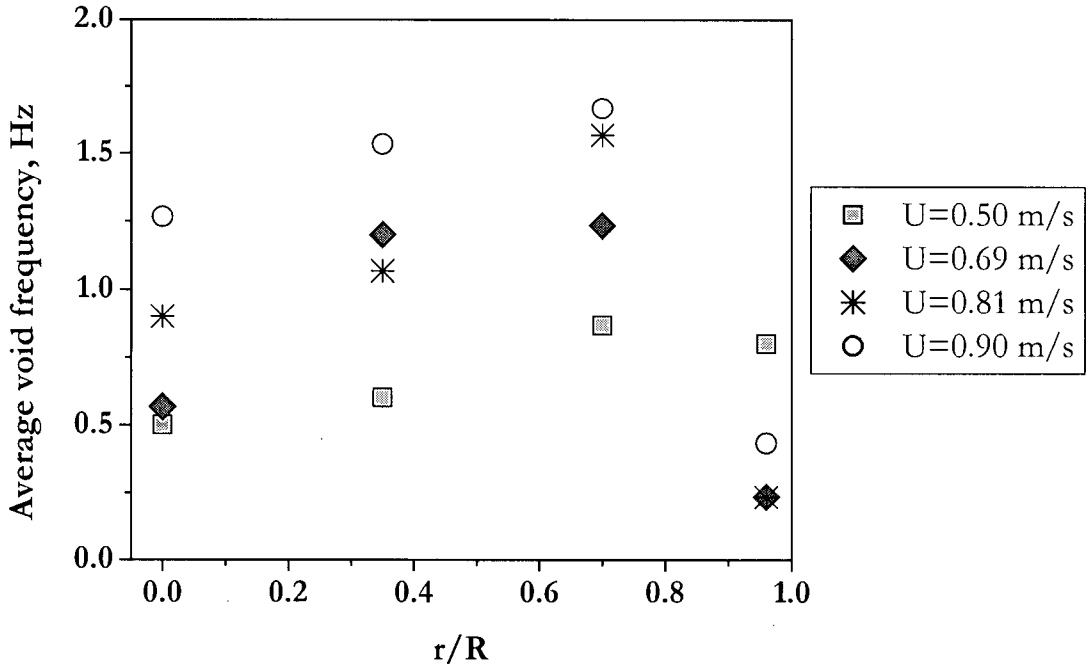

Figure 5.20 Radial distribution of average void frequency. D=0.29m, z=0.78 m, Δz=0.02 m, H_0=1.5 m, U_c (z=1.16 m, AP)=0.85 m/s, FCC I.

Particle velocity

- The void-associated particle velocity distribution shifted to higher velocities with increasing height, as well as with increasing superficial gas velocity.
- The average particle velocity associated with voids increased monotonically with increasing superficial gas velocity, while that associated with the dense-phase only started to increase beyond U_c.
- The standard deviation of particle velocity fluctuations for dense-phase associated particle velocities increased slightly beyond U_c.
- The relationship between simultaneously measured particle velocities and voidages indicated a change in the local two-phase flow structure when the superficial gas velocity exceeded U_c.
- Radial variations of voidage and void-associated particle velocity indicate a core/annulus structure at the highest superficial gas velocity examined (i.e., 1.56 m/s).

Void velocity

- Considerable scatter in the void velocity was detected for both the bubbling and turbulent fluidization flow regimes.
- The void frequency range corresponded closely with the major frequencies from a frequency analysis of DP signals (in Chapter 6).
- The void velocity distribution became wider as the superficial gas velocity increased.

The effect of solids flux from the return leg was found to be significant with respect to the hydrodynamics of the bed, especially for a larger column at higher solids net mass fluxes.

The major drawback to the current velocity measurement system is the limitation of obtaining only a one-dimensional velocity due to having two receiving fibers. The assumption of measuring a known flow direction in a turbulent fluidized bed may not be justified in certain positions in the dense bed, such as those close to the solids return leg. By applying an optical probe like the one reported by Tayebi et al. (1999) (seven-fiber probe), it would be possible to deduce the maximum cross-correlation for the two-dimensional flow. However, such a probe would inevitably be more intrusive and therefore perturb the flow more than a two-fiber probe. The present work is significant as it provides important experimental evidence regarding the dynamic nature of the flow structure.

Further studies

- Acquisition of additional data on particle and void velocities from different column diameters would enhance the knowledge of the effect of column size on the velocity distribution. In particular, the effect of scale on the chord length of voids would provide insight into the size of voids in the turbulent fluidization flow regime where bubble diameter correlations are no longer valid.
- Simultaneous measurement of void velocities at two axial locations can reveal void growth and coalescence with varying superficial gas velocity.
- The design and fabrication of an optical probe capable of simultaneously measuring particle and void velocities, and voidage, would lead to experimental data that could advance understanding of how particle velocities are affected by void dynamics.
- Comparison of results obtained from void velocity measurements and a simultaneous gas mixing study would be helpful in interpreting data.
- A computer program should be written to detect the passing of voids and to cross-correlate the signals according to the group number reflective of each void.
- Addition of fluorescent FCC particles to the bed of regular FCC particles will 'tag' some particles within the system. The unique reflective properties will help validate the particle velocity measurements.
- Tracking the particle velocity at the top of the expanded bed should enable the change in particle momentum and flow structure to be studied, especially near the transition from the turbulent to the fast fluidization flow regimes.
- Radial particle transport mostly depends on particle-particle collisions and particle acceleration due to eddy and particle interactions. If the configuration of the optical velocity probe could be such that the radial particle velocity can be measured without disturbing the particle flow, vital information could be obtained on the radial solids flux. This may be accomplished by simultaneously measuring the voidage to discriminate single particles hitting the probe and changing directions from particles in the dense phase moving radially as a result of momentum exchange.

CHAPTER 6

SIGNAL ANALYSES AND INTERPRETATION

6.1 Introduction

The complex hydrodynamics of multiphase flows cannot be represented by time- or volume-averaged parameters alone for the design and scale-up of such systems (Mudde et al., 1997). Various statistical analysis methods have been employed, as demonstrated in Chapters 2 through 5. In this chapter, the linear analysis techniques such as frequency (FFT), cross-correlation, and autocorrelation analyses, as well as nonlinear analysis techniques including chaos analysis, are applied to gain further insight into the nature of the flow structure, and to extract dynamically meaningful information.

6.2 Frequency analysis of pressure fluctuations in fluidized beds

Pressure fluctuations in gas-solid fluidized beds have often been investigated owing to their relative ease of measurement, even under challenging industrial conditions. Pressure measurements can be used to infer stability, quality of fluidization, flow structure and regime transitions (e.g. Trnka et al., 2000). Pressure signals reflect complex phenomena, including effects of absolute pressure, temperature, gas turbulence, and the formation, coalescence and eruption of voids. Time, frequency, and state-space analyses of such measurements have been interpreted in terms of both macro-flow and detailed structures of gas and solids flow (Johnsson et al., 2000).

It is commonly held that a fundamental frequency exists for a fluidized bed of given geometry, particle and fluid properties, and flow conditions. However, the origin of the pressure fluctuations requires further inquiry. One of the strong associations between pressure fluctuations and the behaviour inside a fluidized bed at low gas velocities is the movement of bubbles. Their eruptions at the surface of the bed instigate pressure waves which propagate throughout the bed. Fan et al. (1984) suggested that the frequency of pressure fluctuations is affected by the mean bubble residence time, average windbox pressure, plenum volume, column cross-sectional area, and bed mass, indicating that the bed surface is not the only source of fluctuations. As reviewed by M'chirgui et al. (1997), studies show that the fundamental frequency in a fluidized bed is strongly affected by the static bed height (e.g. Verloop and Heertijes, 1974; Baskakov et al., 1986). Analysis of pressure

signals from a fluidized bed at minimum fluidization has shown distinct pressure waves, propagating upwards and downwards, originating from bubble formation and from bubble eruptions at the bed surface (van der Schaaf et al., 1998). Kage et al. (2000) identified three principal frequencies from the power spectra of pressure signals in a plenum chamber corresponding to the natural frequency of the fluidized bed, the bubble eruption frequency and the bubble generation frequency. The latter two were confirmed from local voidages, determined by an optical probe, and visualization of bubble eruption by a video camera. However, their study was restricted to the bubbling fluidization regime.

The macroscopic behaviour of a fluidized bed inferred from pressure measurements has been elucidated by local measurements. Simultaneous measurements of gauge pressure and voidage using an optical probe (Xu et al., 1998) indicated that the pressure waves did not correspond to the heterogeneous flow structure. Bi et al. (1995) reported that gauge pressure measurements tend to reflect more macroscopic behaviour of fluidized beds, whereas differential pressure measurements, with the separation distance between the two ports of the order of a few centimetres, are able to differentiate between the dense and dilute phase behaviour. Even with closely spaced differential pressure probes, the information from pressure probes differed from that corresponding to local optical fibre probes measurements.

In the turbulent fluidization regime, pressure fluctuations are commonly employed to delineate a transition velocity, U_c, at which the standard deviation attains a maximum. This is commonly taken to indicate the onset of the turbulent fluidization flow regime. U_c has been reported to be influenced not only by the fluid and particle properties, but also by column geometry, static bed height and the location of the measurements (Cai, 1989; Dunham et al., 1993; Bi and Grace, 1995). Reported values of U_c tend to be empirical and geometry-specific.

Industrial fluidized beds often operate at gas velocities corresponding to the turbulent fluidization flow regime. Monitoring fluidization quality in commercial scale units using pressure measurements can be a convenient method of ensuring excellent contacting between the gas and solids. It is crucial to ensure that the natural frequency of the structure differs appreciably from the major frequency range of the bed, for vibrations tend to be increasingly significant as units are scaled-up (Pell, 1990). Thus, understanding the source and propagation of pressure waves and the fundamental frequency of a given unit is crucial, especially for scale-up.

In order to further investigate the origin of these fluctuations and their effect on scale-up, turbulent fluidization experiments were conducted in this work in four different columns. The macroscopic behaviour of the fluidized beds inferred from the pressure waves is compared below to local measurements obtained using optical fibre probes.

6.2.1 Fourier transform

The Fast Fourier Transform, FFT, transforms time domain functions into frequency domain representations. Although this is a well-established method of analysis in engineering (Chatfield, 1996), the transform is briefly reviewed in Appendix C in order to highlight the difference between the Fourier transform and the wavelet transform discussed in the next chapter.

6.2.2 Experimental data analysis

In order to examine the pressure waves in a turbulent fluidized bed, simultaneous pressure signals were recorded at 8 different vertically aligned locations, the windbox and across the distributor plate of the 0.29 m diameter column. Amplitude spectra of gauge and differential pressure signals obtained by FFT analysis from vertically aligned pressure probes are shown in Figure 6.1 for a superficial gas velocity of 0.65 m/s. The following criteria were used:

- Frequencies less than 0.5 Hz are taken as the leakage of the Fast Fourier transformation depending on the window function; therefore, peaks below 0.5 Hz are ignored.
- Since the typical frequency range of interest in fluidized beds is 0-10 Hz, frequencies above 10 Hz are not considered.
- The combined results of differential pressure, DP, and gauge pressure, AP, signals enable peaks related to predominantly global phenomena to be differentiated from those reflecting local voids.

The amplitude of the strong peak present throughout the bed (and even in the windbox) in the spectra of gauge pressure signal remains relatively constant suggesting global pulsations resulting from particle oscillations. The recurrent peaks of gauge pressure signals in Figure 6.1 indicated by "n" provide the experimentally determined f_n. This "natural frequency," characteristic of global dense phase movement, has been predicted by Verloop and Heertjes (1974) based on a balance of frictional and gravitational forces in gas-solid fluidized beds as:

$$f_n = \frac{1}{2\pi}\sqrt{\frac{(1-\varepsilon)(\varrho_p-\varrho_f)g(2-\varepsilon)}{\left[(1-\varepsilon)\varrho_p+\varepsilon\varrho_f\right]H\varepsilon}} \tag{6.1}$$

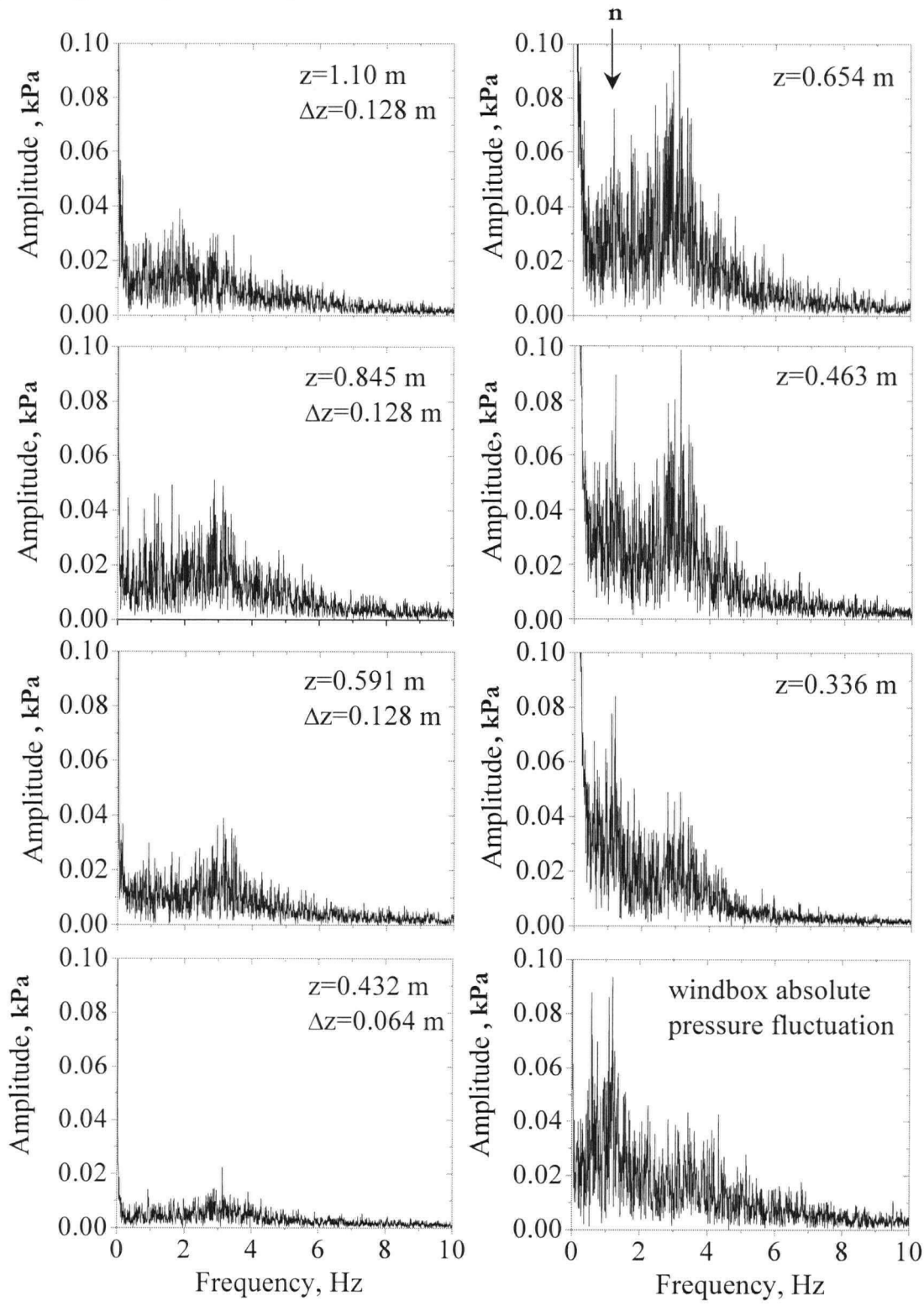

Figure 6.1 Power spectral density functions of pressure fluctuations. U=0.65 m/s, H=1.1 m, r/R=1, FCC I. (n identifies recurrent "natural frequency")

which can be simplified for $\varrho_p \gg \varrho_f$ to $f_n = \sqrt{g(2-\varepsilon)/H\varepsilon} \; / \; 2\pi$. Figure 6.2 summarizes the effect of expanded bed height on the observed natural frequency from gauge pressure signals. The predicted f_n from Equation 6.1 gives better predictions with increasing bed height.

The amplitude of the power spectral density function from differential pressure fluctuations confirms that vigorous fluctuations in the windbox are largely filtered out, with DP signals then reflecting local phenomena between the two ports. The broadband peak at around 3.2 Hz increases in intensity and shifts towards 2.8 Hz before diminishing beyond 1.10 m above the distributor plate. The frequency of the major peak from the DP signals, f_{DP}, can be attributed mainly to voids which coalesce moving upward, thus exhibiting decreased f_{DP} and increasing intensity. Gauge pressure signals support this trend, with the intensity of peaks increasing with height. The eruption of voids at the top of the bed is difficult to identify owing to the diffuse bed surface in a turbulent fluidized bed. Further frequency analysis of DP signals using an FFT smoothing function was pursued to study the effect of U on f_{DP} in Figure 6.3. This confirms the void growth with increasing height for $U < U_c$. Beyond U_c, the fluidized bed becomes increasingly homogeneous, while f_{DP} continues to decrease. A similar trend was observed by Taxil et al. (2000) where the dominant frequency from DP signals continued to decrease far beyond U_c. The f_{DP} peaks for the 0.61 and 1.56 m diameter columns were increasingly clear, especially for deeper beds, probably due to larger voids under these conditions. As portrayed in Figure 6.4, the same trend of decreasing f_{DP} as U approaches U_c is present; however, f_{DP} reaches a plateau around U_c, possibly because of the competing phenomena of void growth and splitting.

The major frequencies from DP signals in columns of different diameter are compared in Figure 6.5 in terms of the Strouhal number, Sr, based on expanded bed height and U_c, versus the Froude number, based on superficial gas velocity and column diameter. Plotting in this manner yields a good correlation with other data reported in the turbulent flow regime. The data indicate that f_{DP} increases with decreasing gas velocity and with increasing column diameter for $U > U_c$.

6.2.3 Crossing frequency

In order to confirm the source of the fluctuations observed in the FFT spectra, the dynamic behaviour of local voids was also captured using optical fibre probes. Probability distribution curves

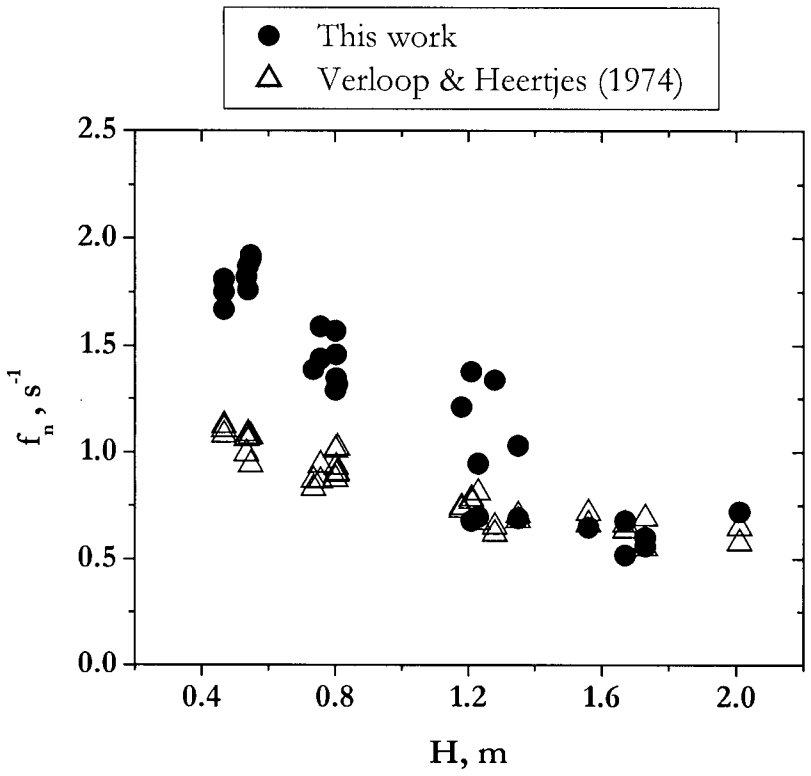

Figure 6.2 Effect of expanded bed height on natural frequency from AP signals with comparison to calculated values based on Equation 6.1. D=0.29m, FCC I.

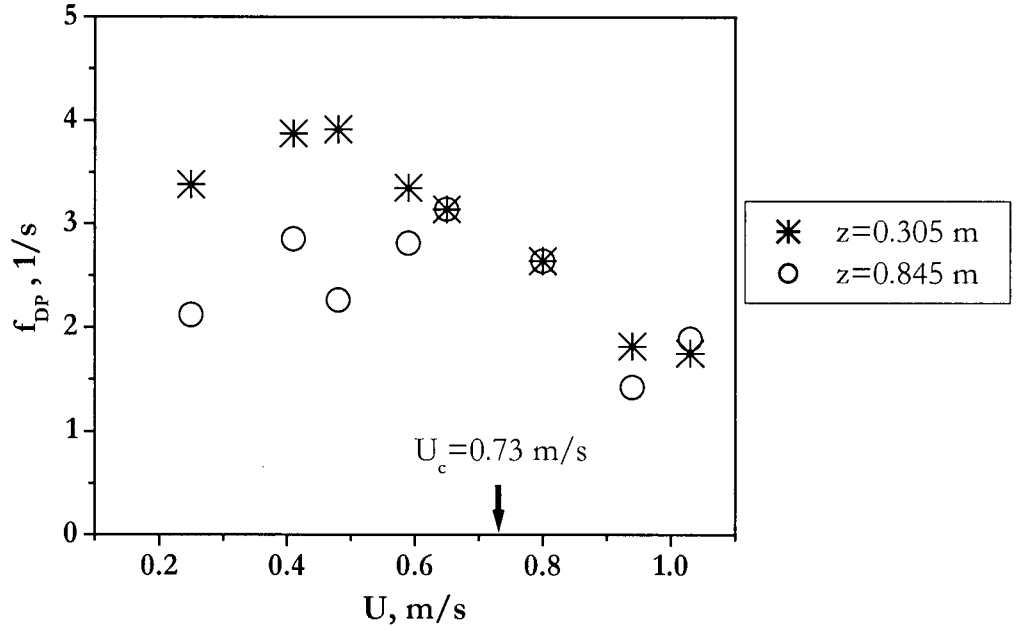

Figure 6.3 Effect of superficial gas velocity on major frequency from DP signals. D=0.29 m, H_0=1.1 m, FCC I.

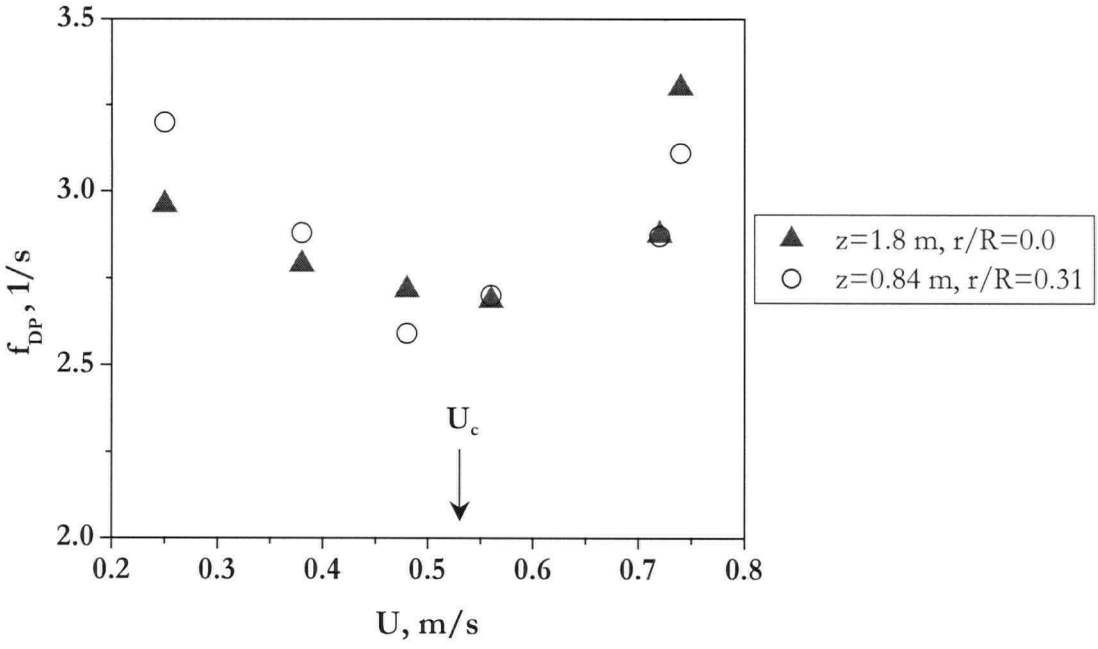

Figure 6.4 Variation of dominant frequency, f_{DP}, with superficial gas velocity. D=1.56 m, H_0=2.2 m.

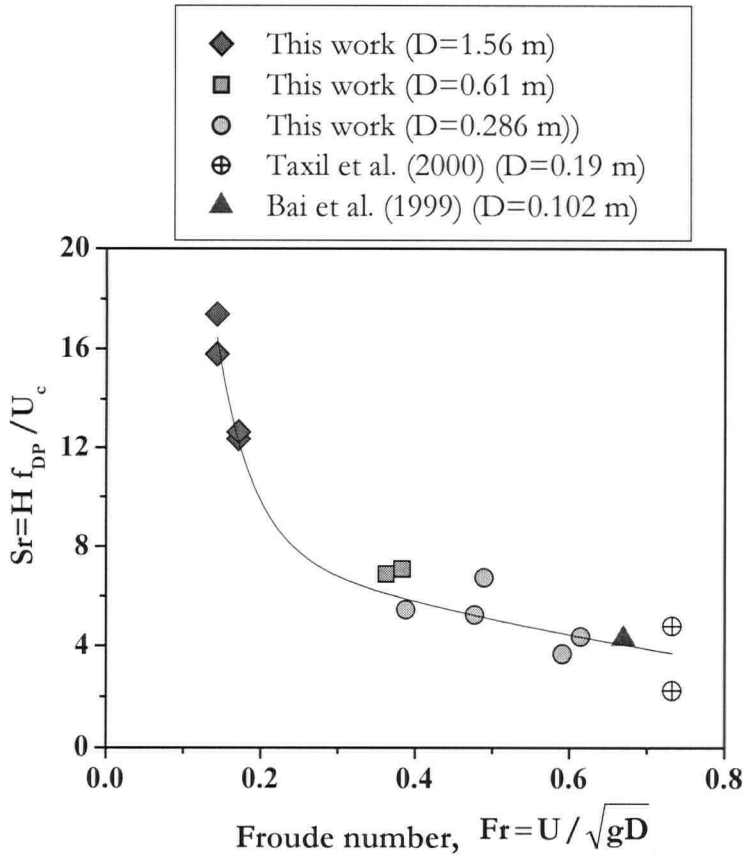

Figure 6.5 Strouhal number vs. Froude number correlation for $U > U_c$, FCC.

of the voidage at given conditions reveal bimodal distributions, even for gas velocities well beyond U_c. It is difficult, however, to distinguish between small frequent voids and large sparse voids from a cumulative function. Therefore, the data were analyzed in terms of a crossing frequency, i.e., the number of times the signal passes through a threshold value over a given time, expressed as:

$$f_c = \frac{(\text{number of crossings})/2}{\text{duration of time series}} \tag{6.2}$$

The threshold value for counting was set to give the maximum number of crossings, which corresponds to the threshold value setting of method (d) in Figure B.9 in Appendix B. Figure 6.6 plots radial profiles of both the average local voidage and the average crossing frequency from Equation 6.2 at two levels. The average crossing frequency remains similar when void activity is dominant, i.e., for $0 \leq r/R \leq 0.6$, z=0.40 and 0.78 m, implying that flow is fully developed and that any excess gas is carried by the dense phase, as indicated by the increase in average voidage. Higher f_c towards the wall indicates frequent signal fluctuations in the dense phase. The effect of U on the crossing frequency in comparison with f_{DP} in Figure 6.3 is shown for the 0.29 m column in Figure 6.7. The overall trend of f_c resembles that of the f_{DP} with respect to U. Moreover, f_c is of the same order of magnitude as f_{DP} for measurement intervals of 0.1 m or less. The discrepancy between f_c and f_{DP} is due to f_c being a localized measurement, and cannot be fully integrated to be compared to f_{DP} at the wall. The latter is considered to reflect the cross-sectional void activities. Use of two traversing probe arms in the 1.56 m diameter column (see Chapter 2) allowed pressures and voidages to be measured simultaneously at various radial positions. The crossing frequency from optical probe measurements showed a decrease in f_c with increasing U, implying larger voids as U approached U_c. Further investigation is required to determine void dimensions directly in confirming the breakdown of voids while maintaining high gas throughput for $U > U_c$.

6.2.4 Sensitivity of threshold value to crossing frequency

Further investigation into the crossing frequency revealed the sensitivity of the resulting crossing frequency to the threshold value. Taking the threshold value as the time-mean voidage, the crossing frequency was calculated as shown in Figure 6.8, where the radial variations of crossing frequency indicate a more profound influence of U, compared to Figure 6.6. Furthermore, the trend of crossing frequency with increasing U at the column centre shown in Figure 6.9, indicates a reversal of the trend compared to the dominant frequency deduced from DP, shown in Figure 6.3. The sensitivity to the threshold value is caused mainly by the signal repeatedly crossing the threshold value. Thus, it may not necessarily pick up the dominant frequency present in the signal.

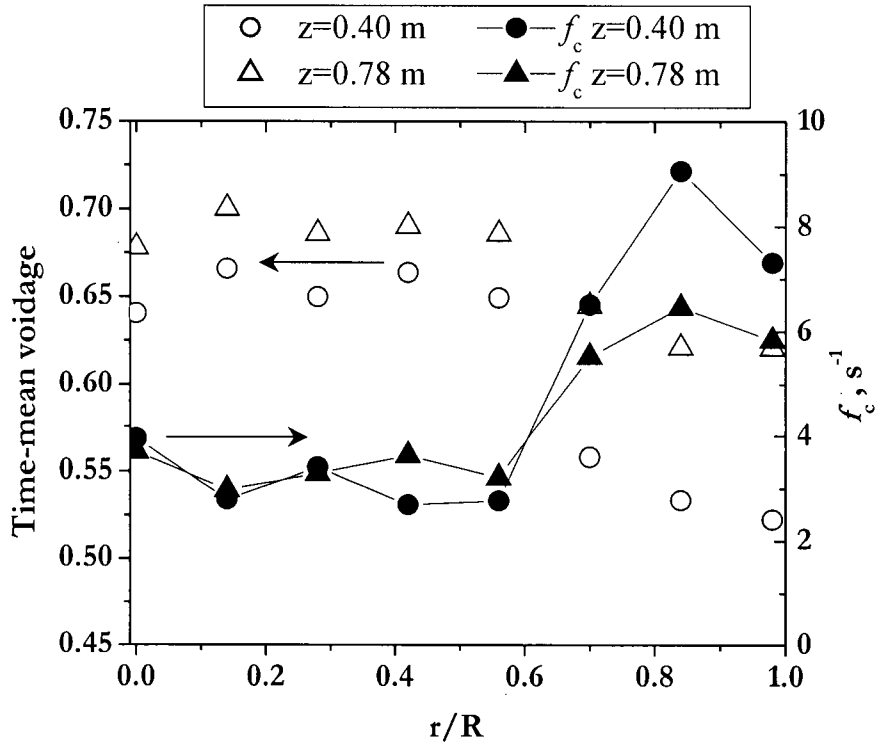

Figure 6.6 Radial profiles of voidage and crossing frequency. D=0.29 m, H_0=1.1 m, U=0.70 m/s, FCC I.

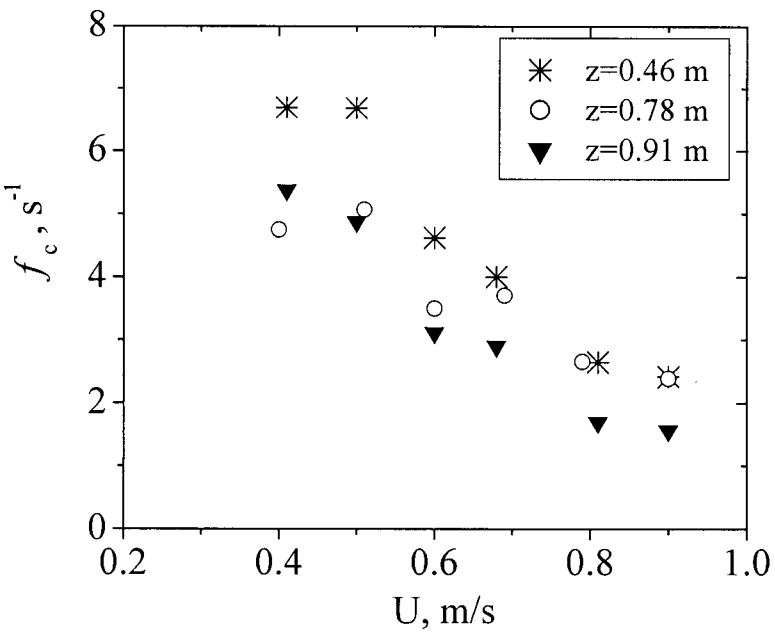

Figure 6.7 Effect of superficial gas velocity and height on crossing frequency. D=0.29 m, H_0=1.1 m, U_c=0.68-0.73 m/s, r/R=0.0, FCC I.

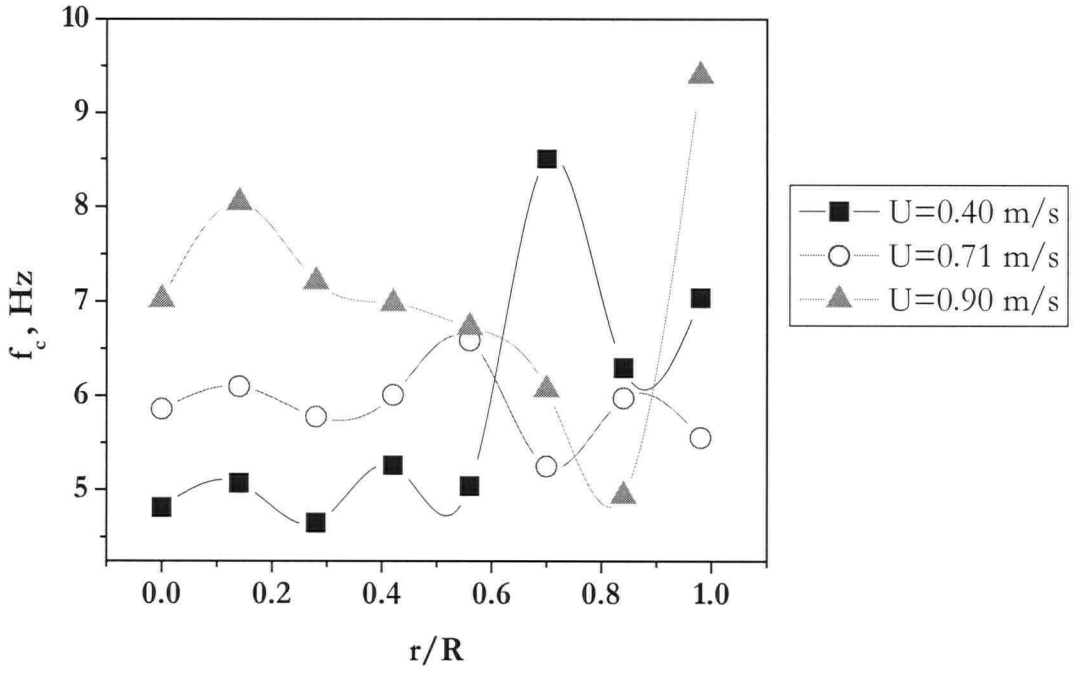

Figure 6.8 Radial profiles at different superficial gas velocities of crossing frequency calculated from threshold value of time-mean voidage. D=0.29 m, H_0=1.1 m, z=0.78 m, FCC I.

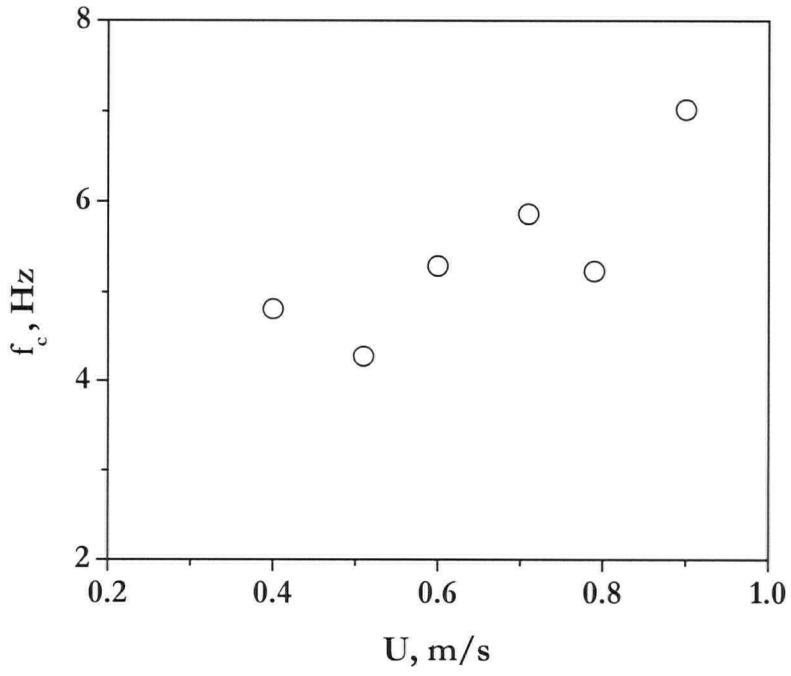

Figure 6.9 Effect of superficial gas velocity on crossing frequency calculated from threshold value of time-mean voidage. D=0.29 m, H_0=1.1 m, z=0.78 m, r/R=0.0, FCC I.

Crossing frequencies with two different threshold values have been sought and compared with the dominant frequencies deduced from DP. The sensitivity of the threshold value to the crossing frequency causes ambiguity in the analysis. Thus, evidence of the origin of f_{DP} from FFT is further pursued through analysis of voidage signals with respect to the cycle time in Section 6.6.

6.2.5 Effect of air-feed system

One of the main concerns raised in assigning peaks from the frequency analysis of pressure fluctuations is the origin of the fluctuations. As in previous sections, pressure measurements in fluidized beds reflect natural oscillation of the bed as well as bubble/void dynamics. The air-feed system may also be important, affecting the boundary conditions for numerical modelling (Johnsson et al., 2002). Roots blowers, in particular, have been reported to be a source of pressure fluctuations (Dhodapkar and Klinzing, 1993). For example, Chyang and Lin (2002) found that the characteristic frequency resulting from a Roots blower was comparable to the simultaneous pressure measurements in 0.29 and 0.10 m diameter fluidization columns. The existence of this characteristic frequency was confirmed to be independent of the static bed height and windbox volume, and to be a function of the blower impeller speed. The influence of the pressure pulsations became less significant with increasing superficial gas velocity, possibly due to an increased pressure drop across the distributor plate. In most reported cases of laboratory-scale fluidized beds attached to in-house pressurized air systems, the effect of air-feed system may not be significant (Johnsson et al., 2002). However, in industrial-scale fluidized beds, the entire air-feed system may contribute to the transient effects of pressure and flow fluctuations.

6.2.5.1 Experimental investigation of dominant frequency from air-feed system

Simultaneous pressure fluctuations in the windbox, across the distributor plate, and at the bottom of the bed were measured for FFT analysis in a 0.29 m diameter column with a static bed height of 1.5 m. The peaks in Figure 6.10 (b) and (c) at around 13.5 Hz are for data obtained in the windbox and at the distributor plate. The signal at the frequency of 13.5 Hz was only present in the windbox. As the blower impeller speed is fixed and the gas flow rate is controlled by the by-pass line, the peak corresponding to the blower should remain constant. Moreover, by using the fluidizing gas from the compressed building air supply, the peak at 13.5 Hz was not observed from fluidizing at U=0.19 m/s. It was concluded that the peak at 13.5 Hz was due to the air-feed system. More importantly, the frequency of the air-feed system did not interfere with the frequency range of interest for bed dynamics.

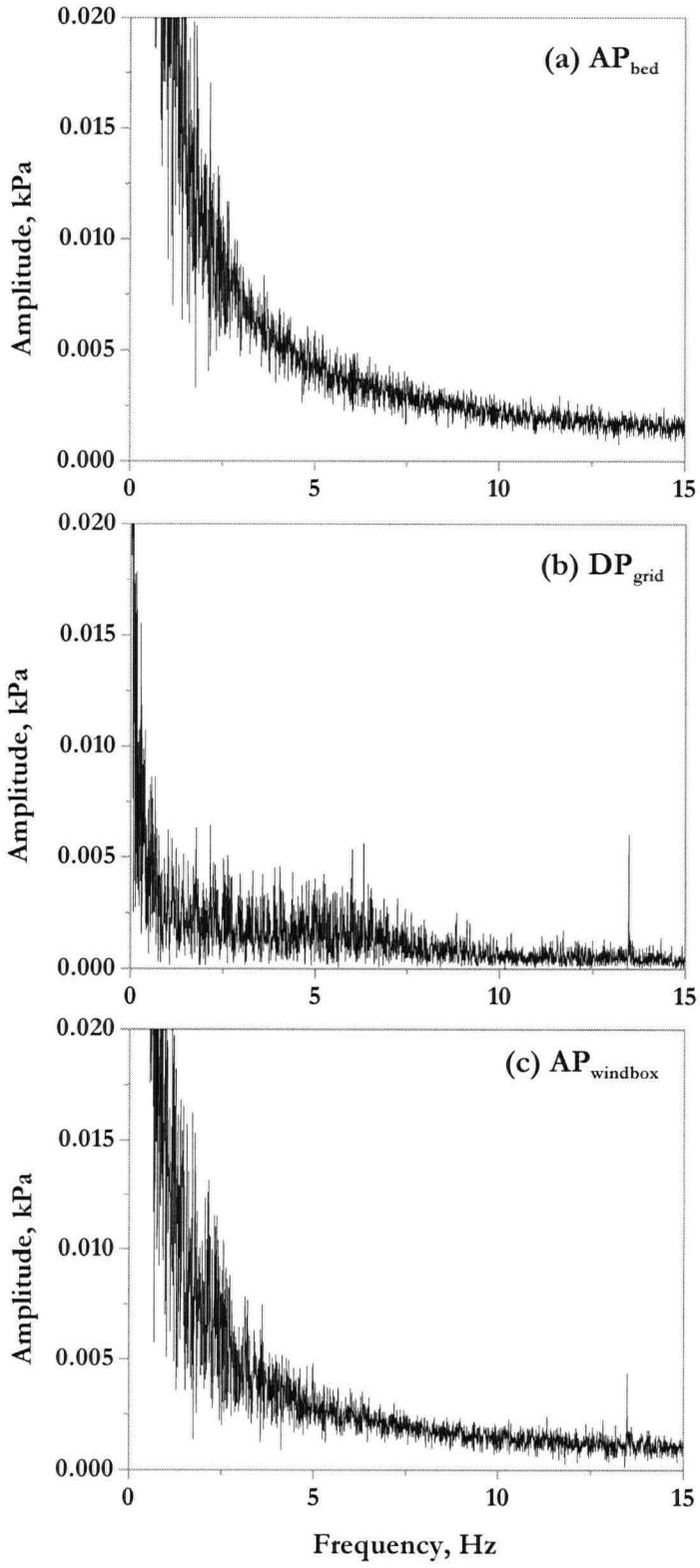

Figure 6.10 Fast Fourier Transform of pressure fluctuations: (a) AP at z=0.15 m; (b) DP across grid; (c) AP in windbox. D=0.29 m, H_0=1.5 m, U=0.19 m/s.

6.3 Cross-correlation function

From bivariate time series, cross-correlation coefficients can provide empirical indications of possible relationships between the variables. The cross-correlation coefficient function is defined as:

$$\varrho_{I_1 I_2} = \frac{C_{I_1 I_2}(\tau)}{\sqrt{C_{I_1}(0) C_{I_2}(0)}} \tag{6.3}$$

which satisfies, for all τ,

$$-1 \leq \varrho_{I_1 I_2} \leq 1 \tag{6.4}$$

$C_{I_1 I_2}$ is the covariance functions at arbitrary fixed values of $t_1 = t$ and $t_2 = t+\tau$, defined by:

$$C_{I_1 I_2} = E\left[\left(x(t) - \overline{x(t)}\right)\left(y(t+\tau) - \overline{y(t+\tau)}\right)\right] \tag{6.5}$$

E[ ] represents the expected value over the index t and $t+\tau$. A typical cross-correlation function is shown in Figure 6.11. The value of τ at which $\varrho_{I_A I_B}$ is a maximum represents the lag between the two signals. In Chapter 5, the same analysis method was applied to obtain the time shift to calculate the velocity at which particles or voids passed the tip of two optical fibers. The value of ρ_{xy} measures the linear dependence between two signals for a displacement of τ in signal 2 relative to signal 1. At $\tau=0$, ρ_{xy} represents the correlation coefficient. The correlation function coefficient is calculated for local voidage signals obtained from optical voidage probes. However, it must be noted that the cross-correlation function fails when the linearity assumption is not valid (Bendat and Piersol, 1971).

6.3.1 Correlation function coefficient of voidage signal

A Plexiglas plate with 10 equally spaced 4 mm holes was mounted on the exterior of the column 0.77 m above the distributor plate. This allowed two identical optical voidage probes to be inserted into the column a known distance apart. The multi-fiber probes are capable of capturing the reflected light intensity from swarms of particles. The correlation will be stronger if the scale length of the measurements matches the size of voids. Thus, the cross-correlation function is a function of the probe distance, void velocity, sampling frequency, and size of voids. The distance between the two probes was varied from 10 to 50 mm in 10 mm increments. Intuitively, voids of chord length close to or larger than the separation distance of the probes should give higher cross-correlations. As shown in Figure 6.12, most maxima of cross-correlation function indicate higher values for smaller probe separation distance. For a separation distance of 0.01 m, the highest correlation occurs near U=0.7 m/s, which is close to U_c obtained though gauge pressure signals. As the separation distance

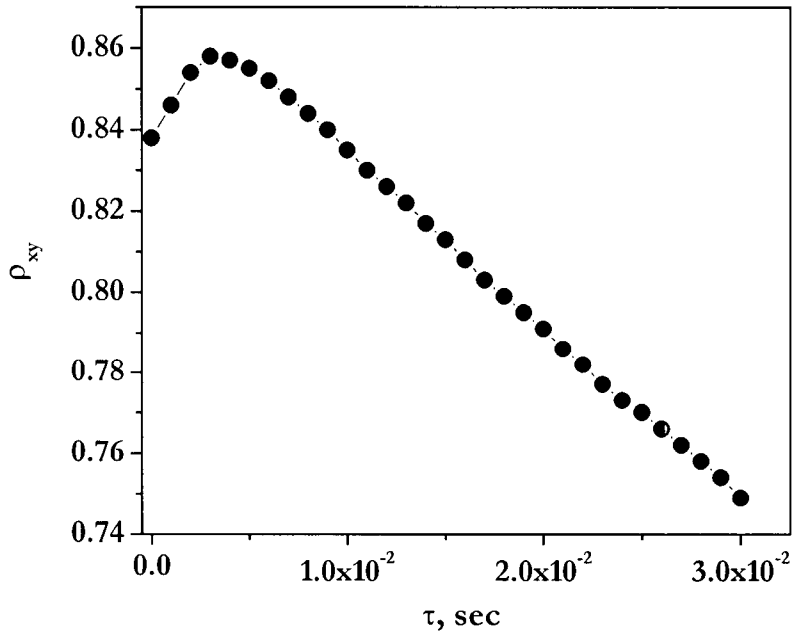

Figure 6.11 Cross-correlation function of optical voidage probe signals. D=0.29 m, H_0=1.5 m, distance between probes=0.01 m, r/R=0.70, U=0.90 m/s, FCC I.

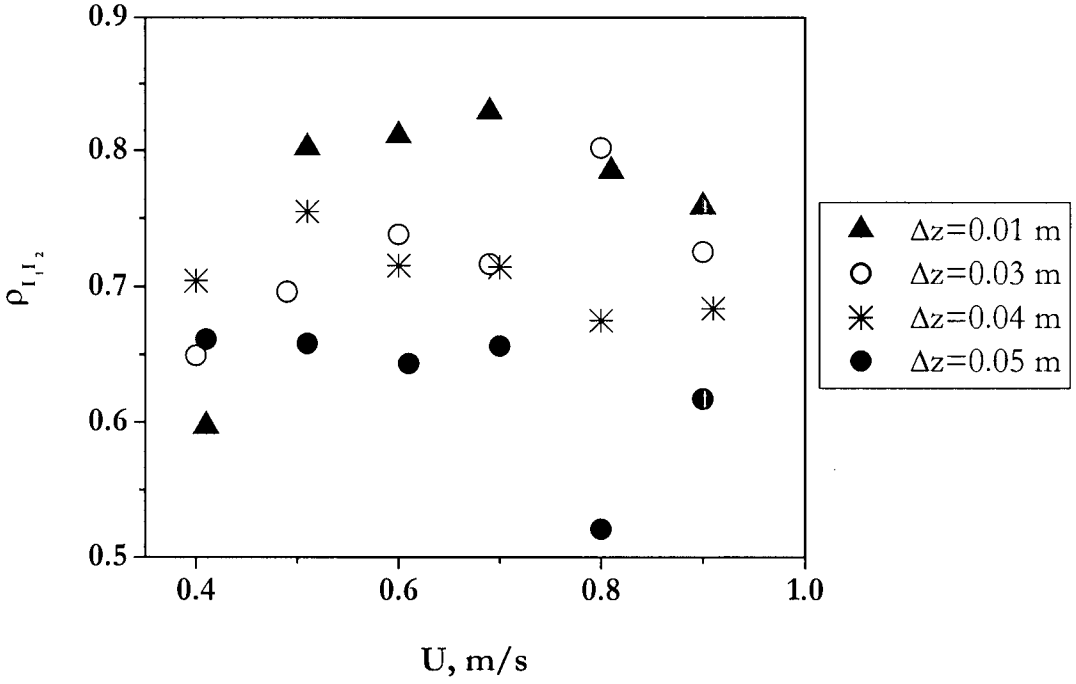

Figure 6.12 Variation of correlation function coefficients with superficial gas velocity. D=0.29 m, H_0=1.5 m, r/R=0.35, U_c=0.75 m/s , H_0=1.5 m, $z_{\text{lower probe}}$ =0.77 m, FCC I.

increased, the maximum occurred at different gas velocities. However, owing to the scatter, definite trends are difficult to identify.

Figure 6.13 (a) and (b) represent cross-correlation function coefficients for U=0.40 and 0.90 m/s, respectively. The high correlation coefficients indicate the coherence between the probe distance and the size of voids. However, owing to the limited and fixed distances between the probes, this method is considered to be disadvantageous in deducing the length scale of voids. The increased scatter of the cross-correlation function coefficient for the shortest distance in the bubbling regime (Figure 6.13 (a)) may suggest that the probe interferes with the flow.

6.4. Autocorrelation

The autocorrelation function of random data relates the influence of values at any time to values at a future time (Bendat and Piersol, 1971). It is useful in detecting non-randomness in data, and to identify an appropriate time series model for periodic signals (Box and Jenkins, 1976). Any deterministic data will have an auto-correlation function that persists over all time displacements, as opposed to random data, whose auto-correlation function approaches zero over large time displacements. The function is defined as:

$$\gamma(\tau)=\frac{\frac{1}{N-\tau}\sum_{i=1}^{N-\tau} x_i\, x_{i+\tau}}{\frac{1}{N}\sum_{i=1}^{N} x_i\, x_i} \tag{6.6}$$

if it is calculated directly, or it may be calculated by the inverse transform following FF transformation of signal. This function has been applied to various fluidized bed systems to assess the quality or to detect the deterministic nature of the data, which might be masked in a random background (Saxena and Waghmare, 2000; Johnsson et al., 2000).

The characteristic shape of the autocorrelation function for a purely random process fluctuates randomly about zero indicating that the process at any instant has no 'memory' of the past (Tsonis, 1992). A chaotic system can be characterized by a characteristic time, τ_c, which signifies the time over which the system retains previous information.

This particular statistical method was applied to voidage measurements from optical probes. As shown in Figure 6.14, the autocorrelation function rapidly decays with lag time, τ, and oscillates

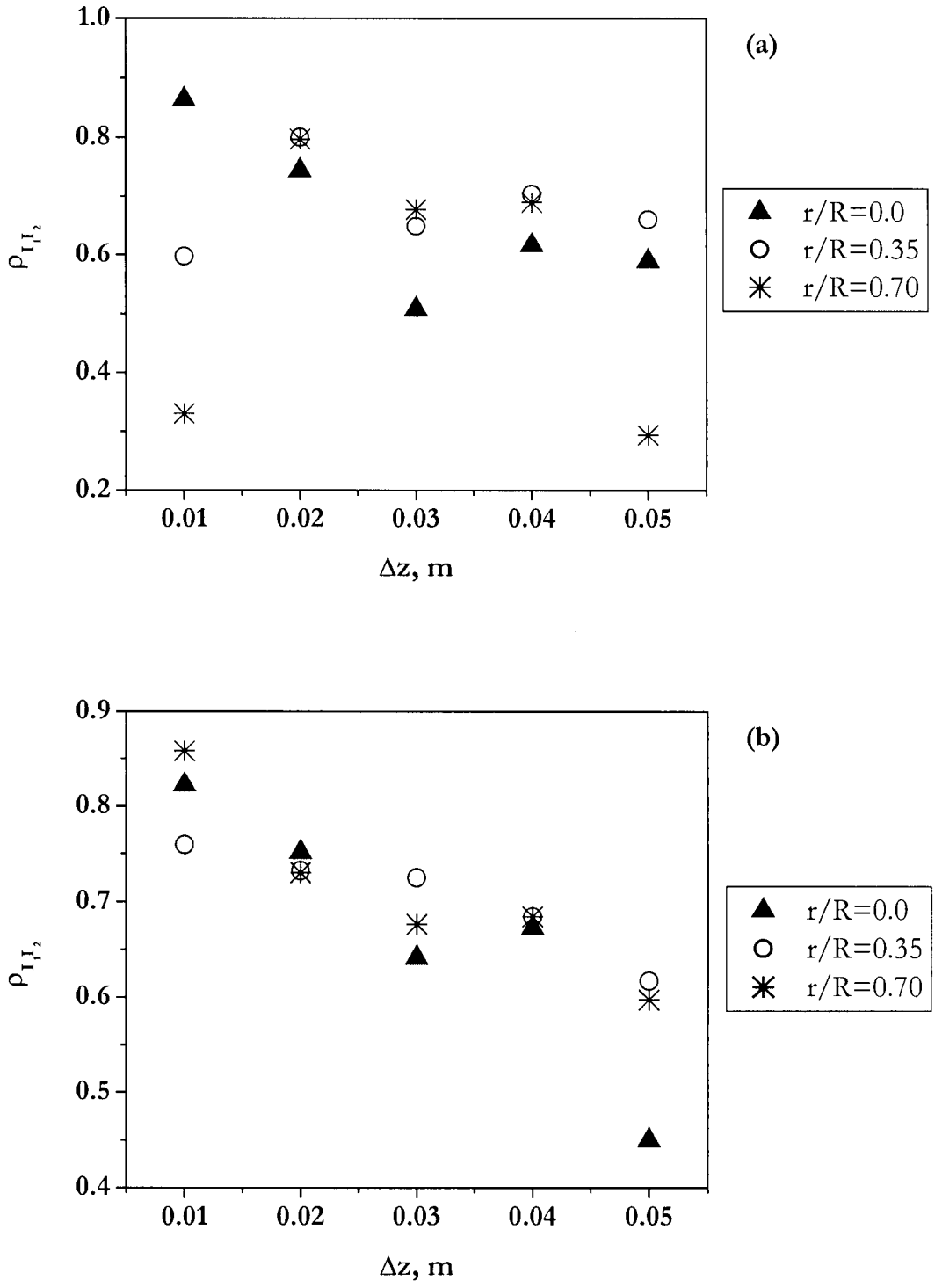

Figure 6.13 Effect of optical probe separation distance on cross-correlation function coefficient. (a) U=0.40 m/s; (b) U=0.90 m/s. D=0.29 m, H_0=1.5 m, $z_{lower\ probe}$ =0.77 m, FCC I.

about zero implying a random signal. The radial profile of the characteristic time of autocorrelation function, τ_c, is illustrated in Figure 6.15 for U=0.9 m/s at axial heights of 0.40 and 0.78 m above the distributor. Since the signal strongly reflects the void dynamics, the lower the value of τ_c, i.e., the faster the autocorrelation function decays, implies higher intensity of void motion. The simultaneous measurement of the two signals allows the change in void motion intensity with height to be determined. The similarity in τ_c for the outer region of $0.5 \leq r/R < 1.0$ suggests less change in void dynamics compared to the core region. Furthermore, the radial profile of the time-mean voidage shown in Figure 6.16 indicates very little change in voidage between z=0.40 m and z=0.78 m. This suggests coalescence of voids between the two axial positions in the core region. In fact, the standard deviation of DP at these two levels indicates an increasing trend, suggesting $U < U_c$.; U_c is measured at 0.73 m/s at z=0.85 m from gauge pressure fluctuations. The effect of U on τ_c, shown in Figure 6.17, indicates considerable scatter for measurements at the higher level. This may reflect the complex dynamics of void coalescence and splitting at higher position. The decrease in τ_c at the lower position implies increased intensity of the void motion with increasing superficial gas velocity. The underlying assumption of the autocorrelation function is that there is a linear functional relationship between the data points. The autocorrelation function may not be appropriate for signals produced by nonlinear systems (Karamavruç and Clark, 1997). Thus, the purpose of applying the autocorrelation function will be to assess the deterministic nature of voidage fluctuations.

6.5 Coherence structure and characterization

Turbulence leads to the presence of localized coherent structures, i.e., organized patterns containing most of the energy. The coherence according to Robinson (1991), is in general terms defined as: "a three-dimensional region of the flow over which at least one fundamental flow variable (velocity component, density, temperature, etc.) exhibits significant correlation with itself or with another variable over a range of space and/or time that is significantly larger than the smallest local scales of the flow". Turbulent signals in the context of component analysis and pattern recognition for the study of turbulent coherent motions have been characterized through a variety of statistical analysis tools, such as auto- and cross-correlation coefficients, and spectra and coherence functions.

However, the capability of the statistical approaches to deduce dynamic and quantitative information about the turbulent flow structure is questionable (Ferré and Giralt, 1993; Kevlahan et al., 1993), due to the necessity to distinguish between global and local self-similarities in characterizing coherent

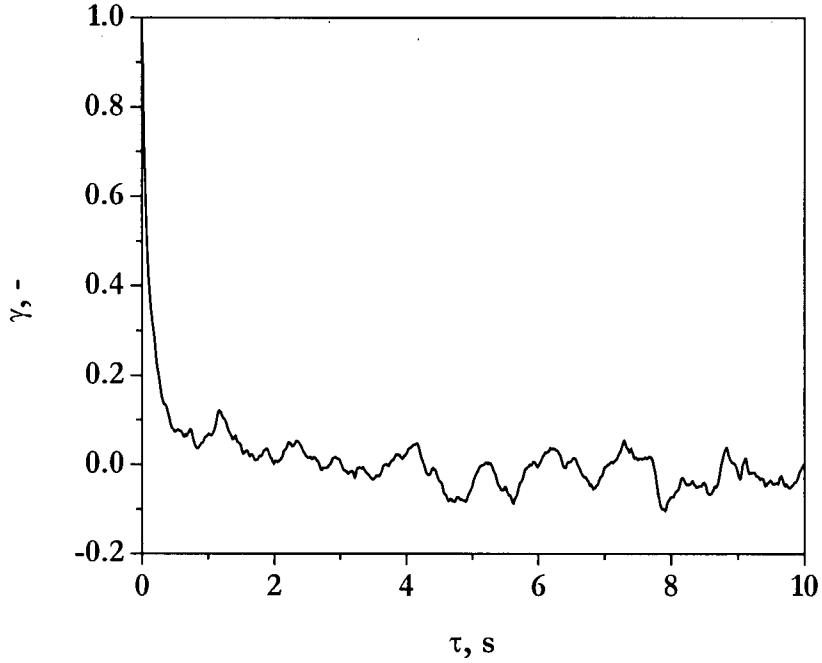

Figure 6.14 Autocorrelation function of voidage signal. D=0.29 m, U=0.90 m/s, z=0.78 m, r/R=0.0, H_0=1.1 m, FCC I.

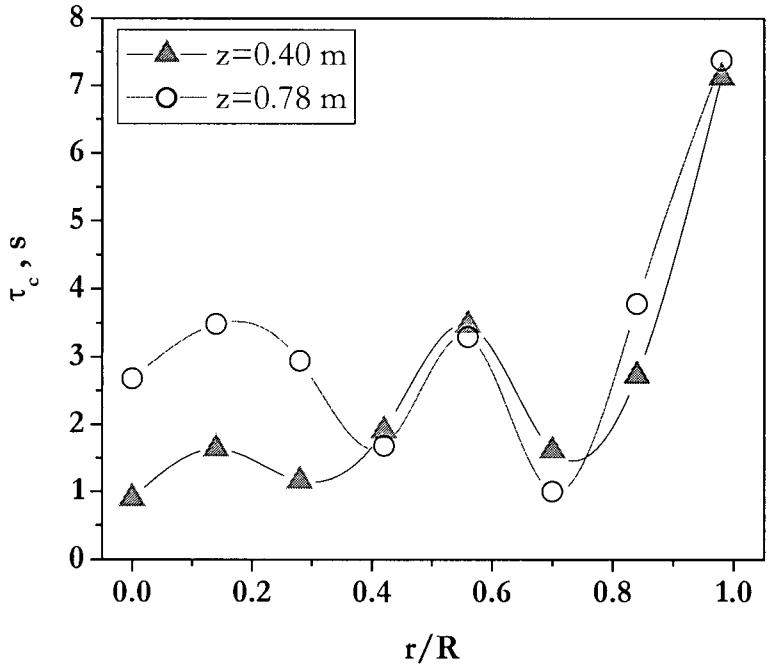

Figure 6.15 Radial profile of characteristic time of autocorrelation function from voidage measurements. D=0.29 m, U=0.90 m/s, H_0=1.1 m, FCC I.

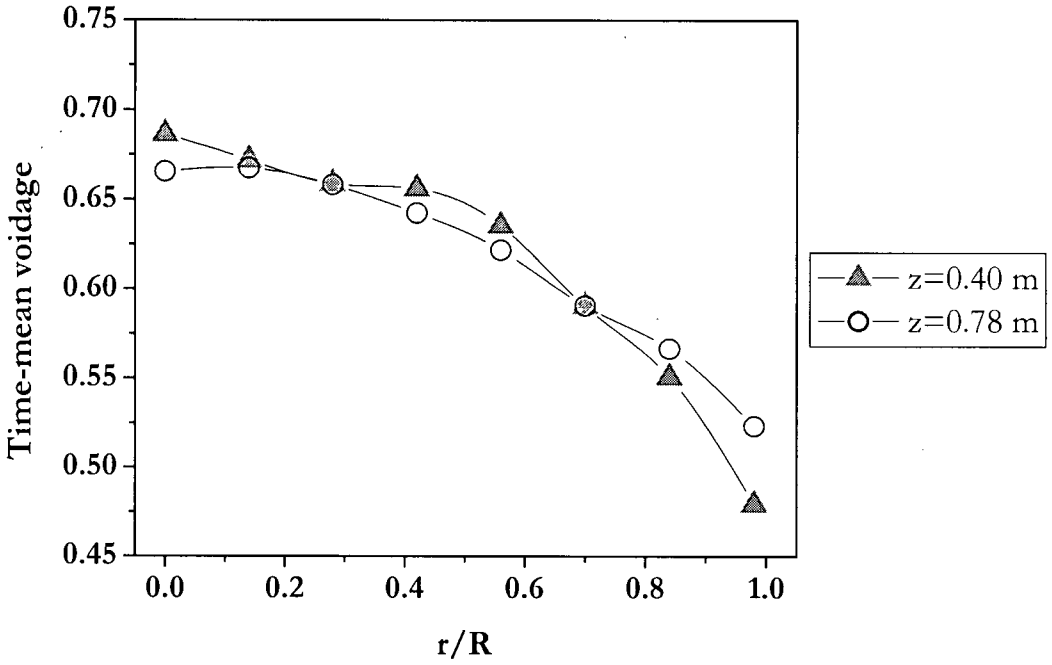

Figure 6.16 Radial profile of time-mean voidage for data presented in Figure 6.15. D=0.29 m, U=0.90 m/s, H_0=1.1 m, FCC I.

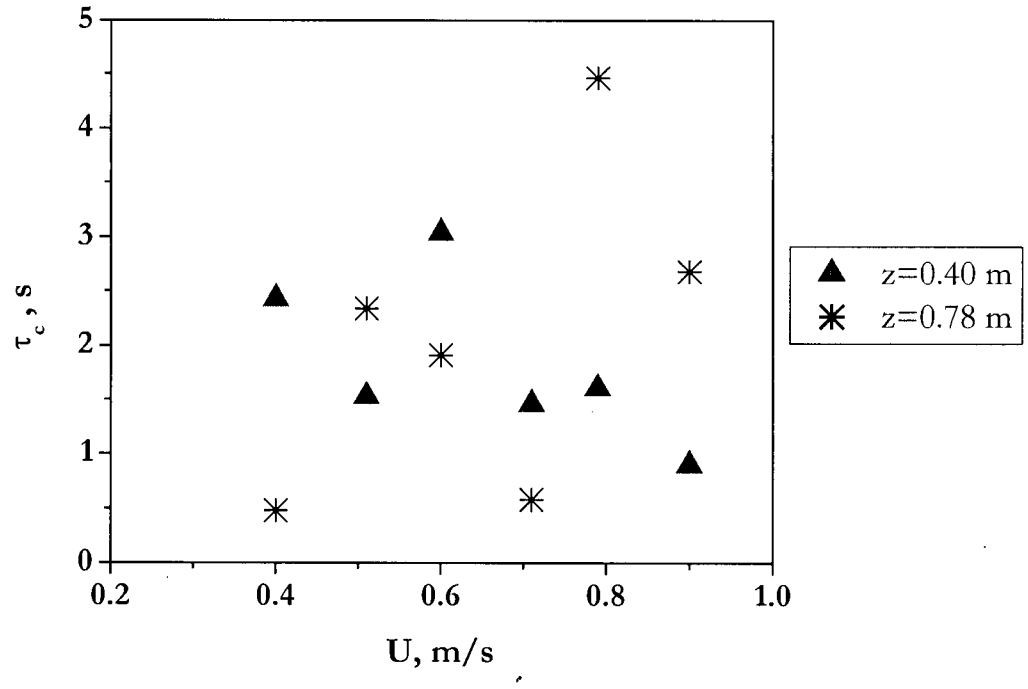

Figure 6.17 Effect of U on τ_c. r/R=0.0, D=0.29 m, H_0=1.1 m, FCC I.

structures. Furthermore, the analysis tool must be able to characterize quasi-periodic repeating patterns of the coherent motion in the flow (Robinson, 1991). For single-phase flow, coherent motion has been described as a burst-sweep process where the violent outward ejections of low-speed fluid are followed by the rapid inrushing sweeps of high-speed fluid (McComb, 1990). Multiple bursts occurs per sweep of fluid velocity of 30-60 times that of mean flow velocity. As a result, the coherence motion is reported to be responsible for most turbulence production in the near-wall region and for increased drag and mixing. Recent experimental and numerical investigations show that this bursting process is more intermittent in space than in time (Robinson, 1991).

A recent summary by Van Den Akkar (1998) portrays coherent structures in multiphase systems. These may originate from the slip velocity created from the density difference between the two phases, or the shear over no-slip walls. Regardless of the origin, the local turbulence and vorticity levels may intensify as a result of local differences in mixture density. The resulting flow regimes with typical phase re-distributions are a consequence of energetically favourable structures in multiphase flows. The interactions of particles and coherent structures in a turbulent boundary layer were summarized by Hetsroni (1989), albeit only for very dilute cases. Coherent structures in bubble columns have been investigated through particle image velocity measurements (e.g. Tzeng et al., 1993, Chen et al., 1994) and through Laser-Doppler Velocimetry (Groen et al., 1996; Mudde, et al., 1997). In a recent review, Joshi et al. (2002) attributed the increased number of publications dealing with the dynamics of bubble columns using CFD to progress in computational power fuelling further understanding of circulation cells and coherent structures.

Perhaps due to the difficulty in making velocity measurements in dense-phase gas-solid fluidized beds, the analysis from the viewpoint of turbulent fluctuations or vortical structures has not been as common as for gas-liquid bubble columns. Transient wave-like flow patterns were reported through image analysis of a two-dimensional circulating fluidized bed by Kono et al. (1999), without any quantitative analysis. The coherence function defined as:

$$\gamma_{xy}^2(f) = \frac{\left|G_{xy}(f)\right|^2}{G_{xx}(f)G_{yy}(f)} \leq 1 \tag{6.7}$$

(Bendat and Piersol, 1971) was applied for regime identification by Vial et al. (2001) and Letzel et al. (1997) in bubble columns and airlift reactors, and by Cai et al. (1990) in a gas-solid turbulent

fluidized bed. The ratio of the auto power spectral density and cross power spectral density in the frequency domain characterizes the coherence between two signals reflecting the instantaneous flow structure: the ratio is then 1 for totally analogous signals at a given frequency; and 0 for signals being completely different. Moreover, the ratio is a measure of linearity between two related signals (Bendat and Piersol, 1971). In order to characterize the flow structure at a given gas flow rate, Cai et al. (1990) arbitrarily proposed the average coherence function as:

$$\overline{\gamma_{xy}^2} = \frac{1}{f_2 - f_1} \int_{f_1}^{f_2} \gamma_{xy}^2(f)\,df \tag{6.8}$$

with f_1 and f_2 as 0 and 10 Hz, respectively. As shown in Figure 6.18, the average coherence function exhibited a peak close to U_c, determined by the maximum standard deviation from gauge pressure fluctuations, when plotted against the superficial gas velocity. The trend in the average coherence function between A and B is attributed to enhanced bubble variations with increasing gas velocity. With the increase in standard deviation for this sub-region, the dominant bubble mechanism is coalescence. Once into the sub-region between B and C, it was explained that the bubble size was of the same order of magnitude as the probe separation distance, in this case 0.1 m. This is called the transition region where signal similarity improves without much variation in pressure fluctuations. Point C was found to be insensitive to port separation distances up to 0.3 m. Further increasing the superficial gas velocity decreases the average coherence function represented in the C-D sub-region. The variation of bubbles is enhanced, represented by the decrease in coherence function. As well, bubble break-up becomes predominant as indicated by the decrease in standard deviation of pressure fluctuations.

As examined in Section 6.2, major frequencies from gauge pressure signals are always below 10 Hz for gas-solid fluidized beds. Thus, the average coherence function calculated between 0 and 10 Hz covers almost all of the phenomena reflected by pressure fluctuation. However, by using gauge pressure to calculate the coherence function, one picks up not only frequencies reflecting void movements, but also global pulsations of the bed and other local and non-local phenomena within the bed (see, for example, Figure 6.1 (b)). Another aspect for consideration is the probe separation distance. Cai et al. (1990) claimed to have observed the same trend as in Figure 6.18 for separation distances up to 0.3 m. The length scale of coherent structure may change considerably and rapidly once in the turbulent flow regime. The initial decrease in average coherence function may represent this change in length scale; however, it becomes difficult to assess if the decreasing trend is due to a change in void characteristics, or to a change in global circulation frequency. Despite these

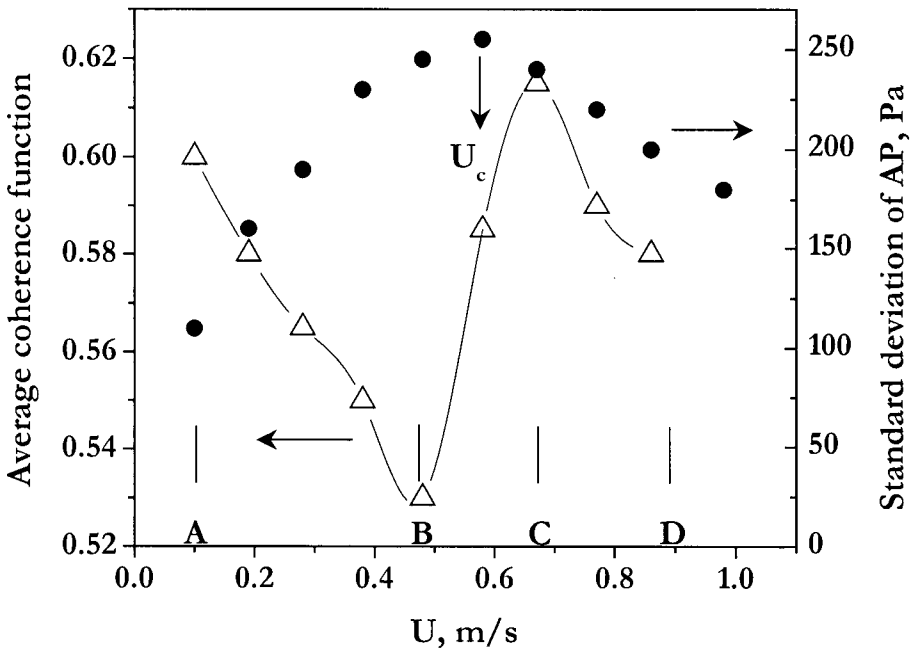

Figure 6.18 Coherence function and standard deviation vs. superficial gas velocity. (Adapted from Cai et al., 1990; D=0.139 m, d_p=280 μm, probe separation distance=0.1 m)

comments, the coherence function appears to be promising in identifying and characterizing the coherence structure in turbulent fluidized beds. Moreover, the three main types of statistical functions in expressing the joint properties of two signals are: joint probability density function; cross-correlation functions; and cross-spectral density functions, providing information regarding the joint properties in the amplitude, time and frequency domains, respectively. As indicated in Section 6.3, dynamic phenomena in fluidized beds exhibit frequency dependency through pressure signals, making cross-correlation unsuitable (Bendat and Piersol, 1971). Thus, the coherence function based on power spectral and cross-spectral density functions seems to be a viable choice, and is pursued further.

Another approach has been taken to express the coherence related to the power spectral density function from bivariate pressure fluctuation measurements. The coherent-output power spectral density (COP) and incoherent-output power spectral density (IOP) are defined (van der Schaaf et al., 1998; van der Schaaf, 2002) as:

$$\mathrm{COP}(f)=\gamma_{xy}^2\,\Phi_{yy} \tag{6.9}$$

$$\mathrm{IOP}(f)=\left(1-\gamma_{xy}^2\right)\Phi_{yy} \tag{6.10}$$

where Φ_{yy} represents the power spectral density of time series measured at position y. The above definitions distinguish the power spectral density from fast pressure fluctuations, COP, from that due to gas bubbles or turbulence, IOP. From the standard deviation of IOP, the characteristic bubble scale was calculated in a bubbling fluidized bed, while that for voidage in the dense bed region of the circulating fluidized bed rise was estimated from the pressure signal. The power-law fall-off in the IOP characterizes the gas bubble dynamics.

The IOP was applied to gauge pressure measurements from the turbulent fluidized bed of diameter 0.29 m in Figure 6.19 for U=0.33 and 0.87 m/s. Based on van der Schaaf (2002), the standard deviation of IOP is correlated to the average bubble diameter:

$$D_b \sim \frac{\sigma_{IOP}}{\varrho_s g(1-\varepsilon_{mf})} \tag{6.11}$$

For the case shown in Figure 6.19, increasing U led to a decrease in characteristic length scale from 1.36×10^{-5} to 1.24×10^{-5} m. Although the physical meaning of this characteristic length is unclear, especially in the context of turbulent fluidized beds where voids are transient, the standard deviation of IOP suggests a decreasing value with increasing U. Further study on the effect of probe

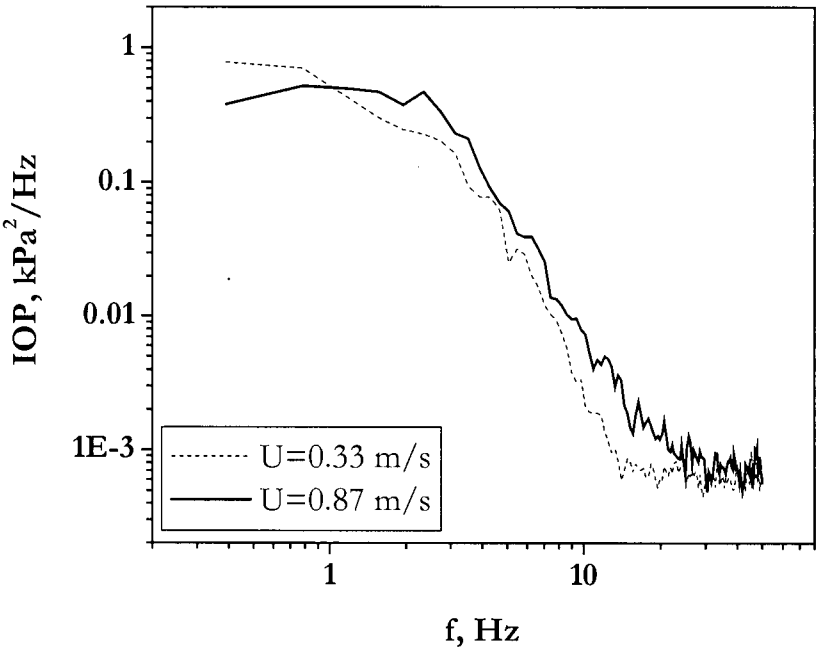

Figure 6.19 Incoherent-output power spectral density (defined in Equation 6.10) from gauge pressure fluctuations for two superficial gas velocities. D=0.29 m, z_1=0.21 m, z_2=0.34 m, H_0=1.5 m.

Table 6.1 Transducer positions for Figure 6.22.

Channel identification	$\bar{z}$, m	Δz, m
ch1	0.305	0.064
ch2	0.432	0.064
ch3	0.591	0.128
ch6	0.845	0.128

separation distance on this characteristic length scale may reveal the physical significance of this parameter. For the purpose of this study, the average coherence function is applied to characterize the change in bed dynamics with U.

6.5.1 Coherence function from pressure measurements

As shown in Figure 6.20, the coherence function of two pressure measurements exhibits a fall-off at $f \approx 3$ Hz. Assuming that most bed dynamic coherence can be captured between 0 and 10 Hz, and following the method described by Cai et al. (1990), the average coherence function is calculated by integrating the function between 0 and 10 Hz. Figure 6.21 portrays the effect of superficial gas velocity on the average coherence function at various heights from simultaneous measurements of five gauge pressure transducers. As separation distance increases, the coherence functions suggest decreased similarity between signals in the 0 to 10 Hz frequency range. The trend from this work is similar to that shown in Figure 6.18 from Cai et al. (1990), although with much smaller dips. Dips are, however, indicated for three cases, namely separation distances of 0.13, 0.25, and 0.45 m, for U close to U_c. At a separation distance of 0.70 m, the average coherence function remains below 0.2, with a slight increase for $U > 1.0$ m/s, attributed to the decrease in power spectra at high U. At such a low coherence function, conclusions other than that the signals are incoherent are difficult. Figure 6.22 reveals that the average coherence function based on DP signals is lower than from gauge pressure signals. This may be because the DP signals reflect more local phenomena. The detailed locations of the transducers are listed in Table 6.1. The higher value of the average coherence function for the lower DP pair of pressure taps, i.e., between channels 1 and 2 for U beyond 0.7 m/s in Figure 6.22, may reflect the void break-up mechanism becoming predominant at higher axial positions. The overall trend of decreasing average coherence function with increasing superficial gas velocity indicates decreasing coherence of the two signals captured by DP measurements.

6.5.2 Coherence function from optical probe voidage measurements

In this section, coherence function analysis is extended to optical probe voidage measurements, reflecting local behaviour of voids, to provide further insight into bed dynamics. Figure 6.23 plots the average coherence function and correlation function coefficient defined by Equation 6.3. The absolute value of the coherence function is a function of the probe separation distance. According to Cai et al. (1990) if the void size matches the probe separation distance, the two signals will exhibit a high correlation.

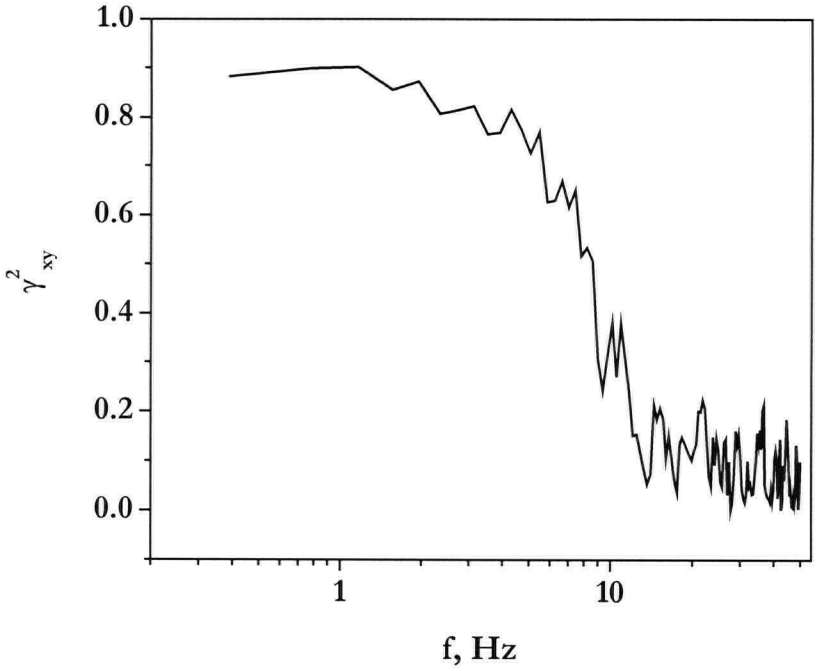

Figure 6.20 Typical coherence function. D=0.29 m, U=0.87 m/s, r/R=0.0, z=0.40 and 0.46 m, H_0=1.5 m, FCC I.

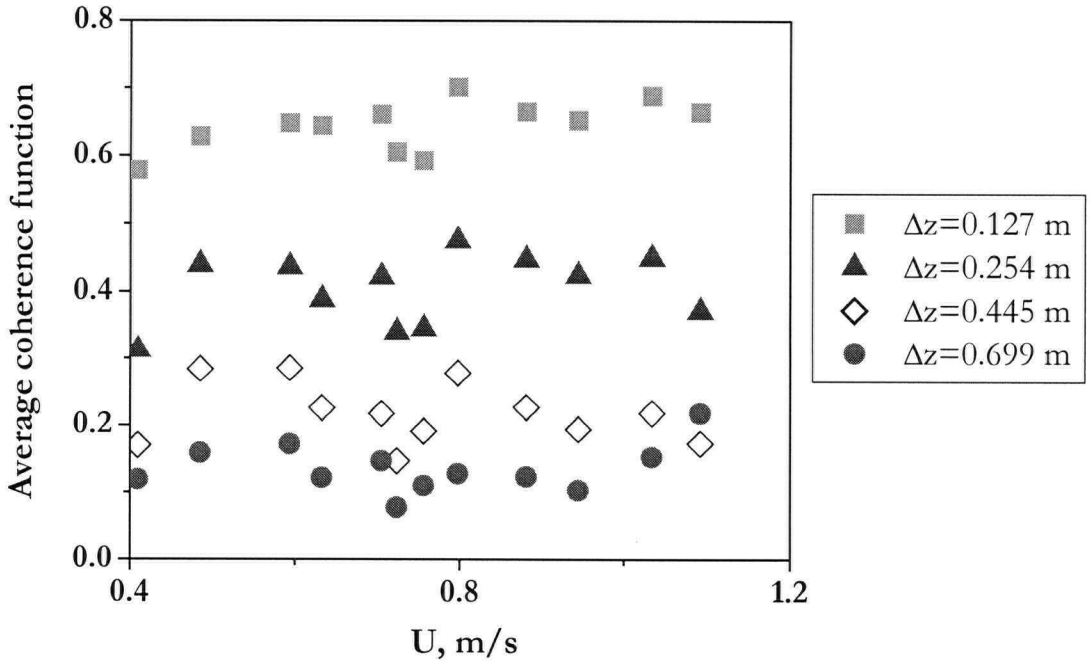

Figure 6.21 Average coherence function from gauge pressure signals. D=0.29 m, H_0=1.1 m, U_c=0.73 m/s, FCC I.

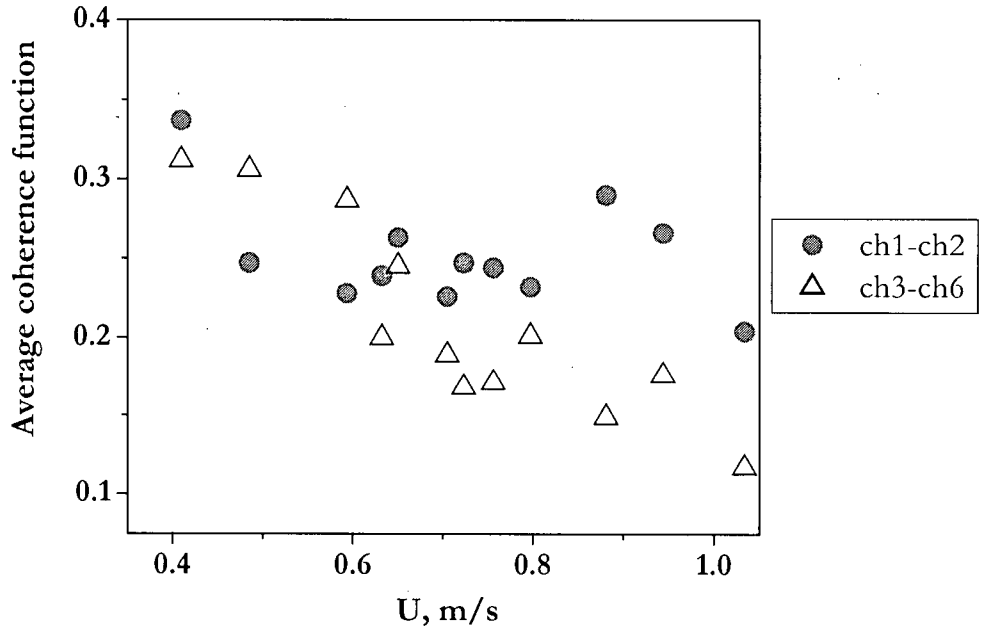

Figure 6.22 Average coherence function from DP signals. D=0.29 m, H_0=1.1 m, ch1 locations, U_c ($\overline{\Delta z}$ =0.845 m) = 0.727±0.039 m/s, FCC I.

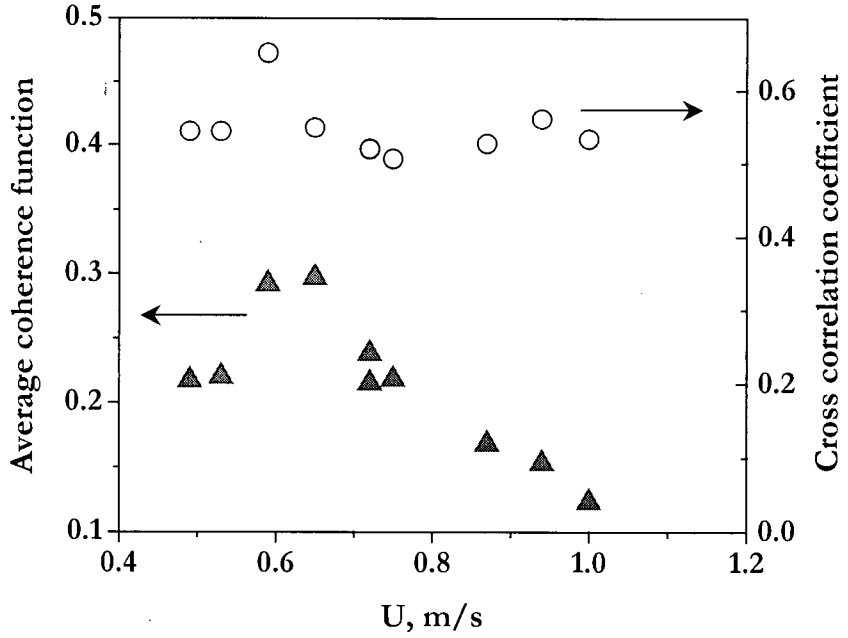

Figure 6.23 Average coherence function and correlation function coefficient. D=0.29 m, r/R=0.0, U_c=0.75 m/s, probe separation distance=0.063 m, z=0.40 m and 0.463 m, H_0=1.5 m, FCC I.

When the average coherence function in Figure 6.23 reaches a peak, the dominating void dynamics in the bed are coherent with a length scale of 0.063 m, the distance between the two probes. From the cross-correlation of the signals, the void rise velocity was calculated to be approximately 0.63 m/s. The power spectral density of the voidage measurement corresponding to the peak in Figure 6.23, i.e., at U=0.65 m/s, is shown in Figure 6.24. No obvious dominant frequency can be distinguished. However, as depicted in Figure 6.25, the coherence function of the same data including the second probe signal at U=0.65 m/s, indicated a strong peak at 3.2 Hz, very close to the dominant frequency obtained from DP signals as indicated in Figure 6.3, albeit for a different static bed height. This indicates a useful method from which to deduce the coherent cycle from bivariate time series measured at the appropriate length scale. A further increase in U resulted in a decrease in coherence between two measurements. At this point, it is not clear whether the decrease in coherence is related to an unsuitable length scale set by the distance between the measuring probes alone, or due to increased turbulence intensifying the void dynamics. As the measurements were from optical voidage probes, bed dynamics at the particle level could not be picked up. Further investigation is pursued with the same optical voidage probes 0.01 m apart. As shown in Figure 6.26, much higher average coherence function values result as the probe separation distance is decreased from 0.063 m to 0.01 m. In all cases, the average coherence function was smallest near the wall of the column. The coherence function at U=0.9 m/s for r/R=0.70 did not indicate any dominant frequency between 0 and 10 Hz. Rather, the distribution was very broad reflecting the broad range of frequencies of voidage fluctuation for this operating condition. The effect of U on the average coherence function, shown in Figure 6.27, indicates scattering of points at r/R=0. As the average over the frequency range of 0 to 10 Hz is arbitrary, the averages for 0 to 30 Hz and 0 to 100 Hz were calculated for comparison, with hardly any change.

In this section, the applicability of the coherence function to pressure and voidage signals has been investigated. Stronger coherence was indicated mainly in the bubbling fluidization regime when the void length scale was similar to the probe separation distance. In the turbulent fluidized bed exhibiting erratic void movements, the coherence function alone may not be sufficient to capture trends at different frequencies. In order to detect the 'footprints' of the coherence structure (Toyoda et al., 1993) from experimental measurements, the length scale(s) of the phenomena of interest need to be considered carefully.

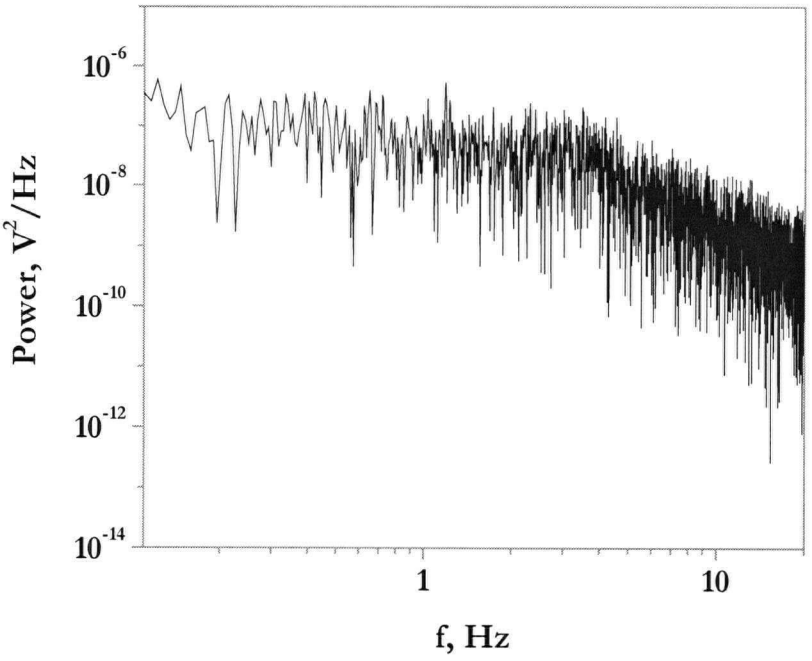

Figure 6.24 Power spectra density of voidage data at U=0.65 m/s. D=0.29 m, r/R=0.0, z=0.46 m, H_0=1.5 m, FCC I.

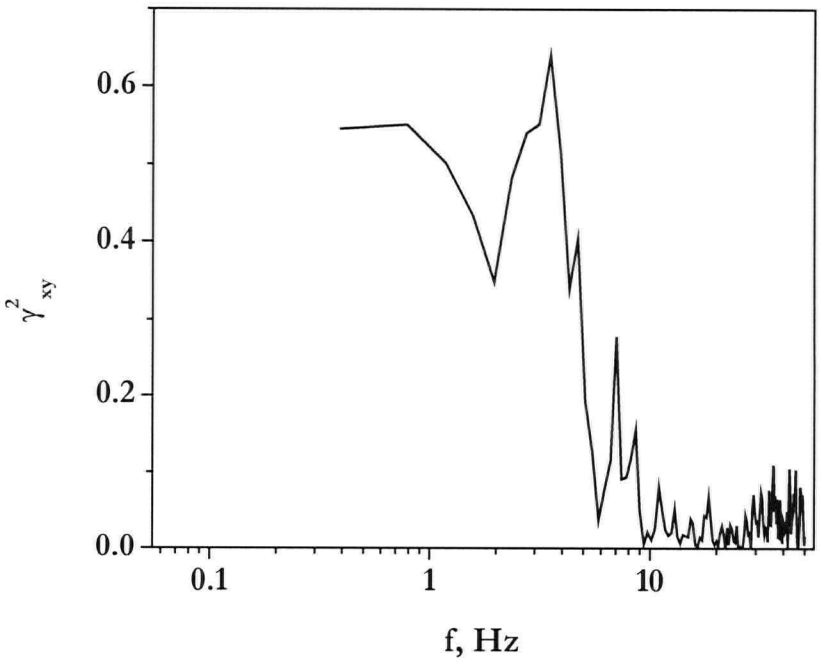

Figure 6.25 Coherence function of voidage data at U=0.65 m/s. D=0.29 m, r/R=0.0, probe separation distance=0.063 m, z=0.40 m and 0.463 m, H_0=1.5 m, FCC I.

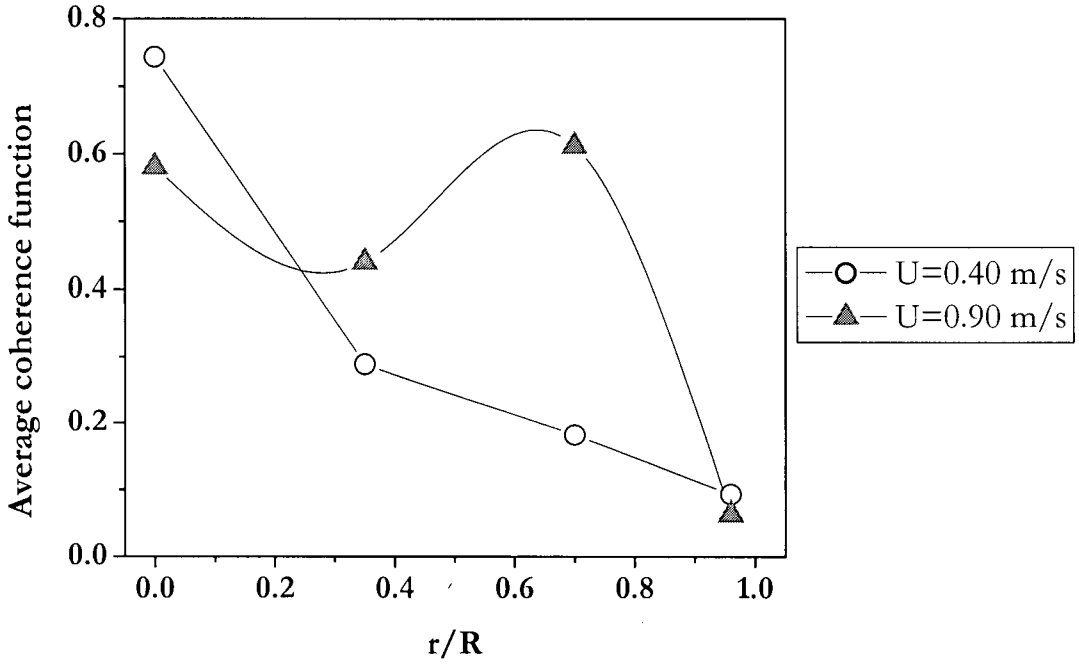

Figure 6.26 Radial profile of average coherence function. D=0.29 m, Δz=0.01 m, H_0=1.5 m, FCC I.

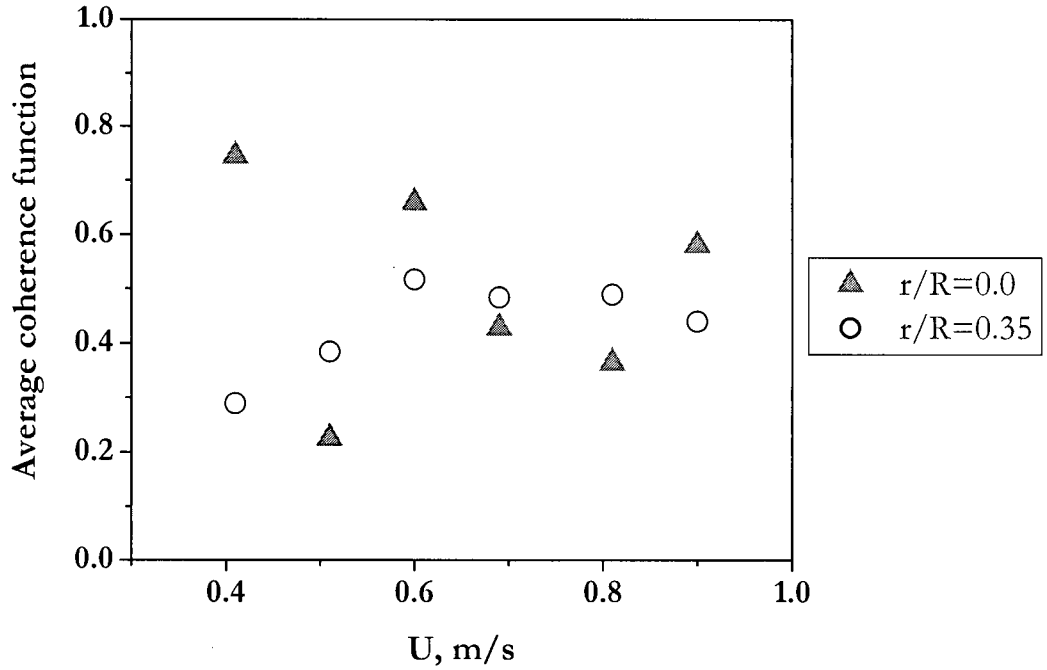

Figure 6.27 Effect of U on average coherence function form voidage measurements. D=0.29 m, z=0.77 m and 0.78 m, distance between probes=0.01 m, H_0=1.5 m, FCC I.

6.6. Chaotic analysis

In the study of non-linear dynamics, irregular but deterministic systems have been investigated in recent decades through chaotic analysis. Although the conventional method of characterizing fluidized bed hydrodynamics has been to use time-averaged properties, such as average void diameter, void rise velocity, average solids holdup and bed voidage, time-dependent components have gained more attention in recent years. Schouten et al. (1996) argue that all of the analytical methods considered above neglect the time-dependent dynamic behaviour of the fluidized bed, and that the analysis must take account aperiodicity and nonlinearity of the dynamics, leading to chaos analysis. Following the hypothesis of Stringer (1989) that a fluidized bed is a chaotic dynamic system, several researchers (Daw and Halow, 1991; Schouten et al., 1992; Skrzycke et al., 1993) have experimentally confirmed this. Chaos analysis has been applied to scale-up, transition detection and regime identification.

The dynamics of a chaotic system are fully represented by the "attractor" in phase space (Hilborn, 1994). An attractor can be estimated from the time series of only one of the system's characteristic variables, with pressure fluctuations most commonly used in fluidized bed studies. Spectral analysis has also been used to obtain the dominant frequency of the fluctuations (Jin et al., 1986; Lee and Kim, 1988; Chehbouni et al., 1994). Cai et al. (1990) used the coherence function on signals from two pressure transducers. The signal variations were related to the movement of bubbles, and the coherence function plotted against a gas velocity showed higher values at which two signals were similar at frequency f. The Kolmogorov entropy, one of the chaotic invariants, seems to be sensitive to changes in operating conditions, resulting in its use in examining the change in dynamics in fluidization regimes and transition from fixed bed to dilute transport flow (Zijerveld et al., 1998; Bai et al., 1999). Increasing the solid loading of FCC in a CFB, Huilin et al. (1997) observed less 'chaos' in the system through the correlation dimension, suggesting that solids dampen the turbulence and reduce the complexity of the flow.

Although pressure measurements have been the most common parameter in characterizing the flow in a fluidized bed, due to the propagation of pressure waves affecting the local pressure measurements (Bi et al., 1995), pressure fluctuations measured in the bed do not truly represent localized phenomena. In order to reveal the local behaviour, voidage measurements should be better for chaotic analysis than pressure measurements. In this section, deterministic chaos theory is

applied to time-dependent data on pressure and voidage fluctuations as a quantitative tool to characterize the behaviour of a turbulent fluidized bed.

6.6.1 Hurst exponents

Hurst (1951) introduced the rescaled range (R/σ) analysis for the time series of natural phenomena. The Hurst exponent describes the self-similarity of a signal and reveals the detail differences in different scales (Tsonis, 1992). The 'fractality' in a time series can be expressed by

$$\tau_H \propto \frac{R(t,\tau)}{\sigma(t,\tau)} \tag{6.12}$$

and

$$R(t,\tau) = \max_{0<i\leq\tau} c(t,i) - \min_{0<i\leq\tau} c(t,i) \tag{6.13}$$

where c(t, i) is the cumulative departure of $x(t+\tau_H)$ from the mean; max(c) and min (c) are the maximum and minimum value of c over the subperiods, τ_H; and σ is the standard deviation. A detailed procedure for obtaining the Hurst exponent is reported by Briens et al. (1997). The rescaled range analysis has been found to be useful in characterizing fluidized bed systems (Hey et al., 1995; Karamavruç and Clark, 1997; Briens et al., 1997; Bai et al., 1997; Taxil et al., 2000).

A Hurst exponent of 0.5 indicates a pure Brownian motion, or random walk; for H=0, the position becomes independent of time (Tsonis, 1992). For H > 0.5, the position follows a biased random walk where the next position is more likely to repeat the present event, and the system is considered to be nonlinear or chaotic. A typical plot of the rescaled range analysis is shown in Figure 6.28. Two distinct Hurst exponents can be deduced from a signal for the bubbling regime, suggesting bifractal flow behaviour (Bai et al., 1999). The minimum Hurst exponent, the slope at higher τ (or lower frequency), is found to be less than 0.5 for measurements in the bubbling flow regime, indicating the pressure fluctuations are less likely to repeat the present pattern, i.e., it is an antipersistent system. This may be attributed to void coalescence and splitting. On the other hand, the maximum Hurst exponent, the slope at smaller τ (or higher frequency), is observed to be higher than 0.5, representing a divergent system.

6.6.2 Cycle time and V statistic

The cycle time of a system can be obtained through Hurst analysis from a break in the plot of $\log(R/\sigma)$ vs. $\log(\tau)$ (Peters, 1994). The method has been applied to obtain the average cycle time

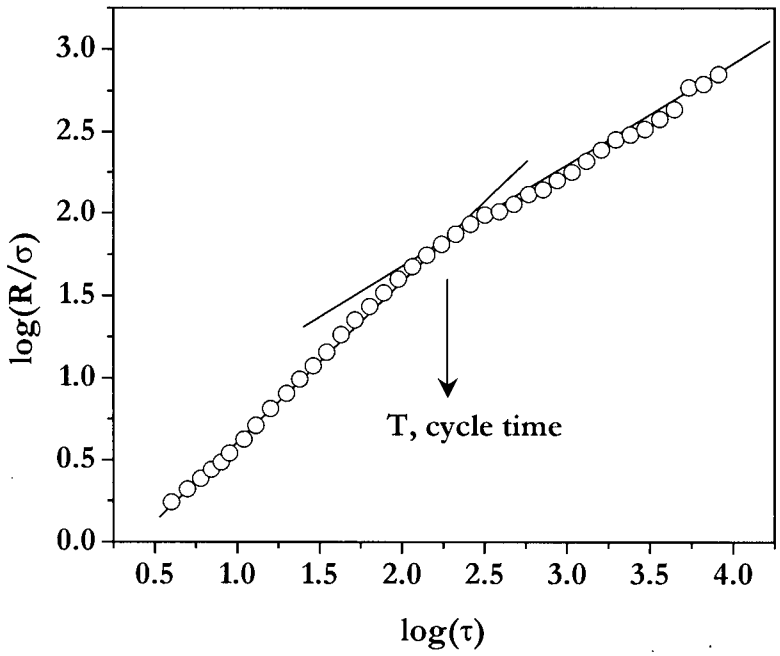

Figure 6.28 Variation of the rescaled range with sub-period length for gauge pressure fluctuation. Sampling frequency=500 Hz, sampling duration=200 s, U=0.39 m/s, D=0.29 m, z=0.65 m, H_0=0.97 m, FCC I.

used to calculate the delay time to reconstruct the phase space of further chaotic analysis (Hay et al., 1995). More recently, Briens and Briens (2002) have compared this method to the V statistic (Peters, 1994) to detect cycle times in various multiphase systems. As a part of the on-going collaboration between Lauren Briens and the author, some analysis is pursued here based on methods described by Briens (2000).

Detection of the break in the $\log(R/\sigma)$ vs. $\log(\tau)$ curve is enhanced by using the V statistic suggested by Peters (1994).

$$V_\tau = \frac{(R/\sigma)_\tau}{\sqrt{\tau}} \tag{6.14}$$

The V statistic, derived from the rescaled range analysis, was applied to the local heat transfer in a circulating fluidized bed (Kikuchi and Tsutsumi, 2001) reporting increasingly uniform and deterministic gas-solid flow structure with increasing circulating solid mass flux. The underlying assumption in the V statistic is that the intersection of the slope is between Hurst exponents higher and lower than 0.5. Both exponents indicate values lower than 0.5 when there is no cycle in the signal, or a cyclic signal without slope switching from smaller to larger than 0.5 (Briens and Briens, 2002). For such cases, the P statistic is used to determine the cycle time (Briens, 2000), where

$$P_\tau = \frac{(R/\sigma)_\tau}{\tau^\gamma} \tag{6.15}$$

Here γ is an exponent between 0 and 1. One advantage of the cycle time analysis through rescaled range analysis is that as long as it is a linear operation, the Hurst exponent is tolerant to the minor shifts in the calibration constants of the measuring probes (Briens and Briens, 2002).

The detailed procedure for calculating the regularities is given in Briens and Briens (2002). The regularity of a cycle time is defined as:

$$R_T = \frac{V_T \Delta t}{\sqrt{T}} = \frac{P_T \Delta t}{T^{1-\gamma}} \tag{6.16}$$

where T is the cycle time, and Δt is the sampling time interval.

6.6.3 Results from pressure signals

The Hurst exponent from DP signals is presented in Figure 6.29. Bimodal plots as in Figure 6.28 lead to two Hurst exponents. A peak in the minimum Hurst exponent is indicated, consistent with the findings of Bai et al. (1999). In the bubbling fluidization flow regime, the minimum Hurst

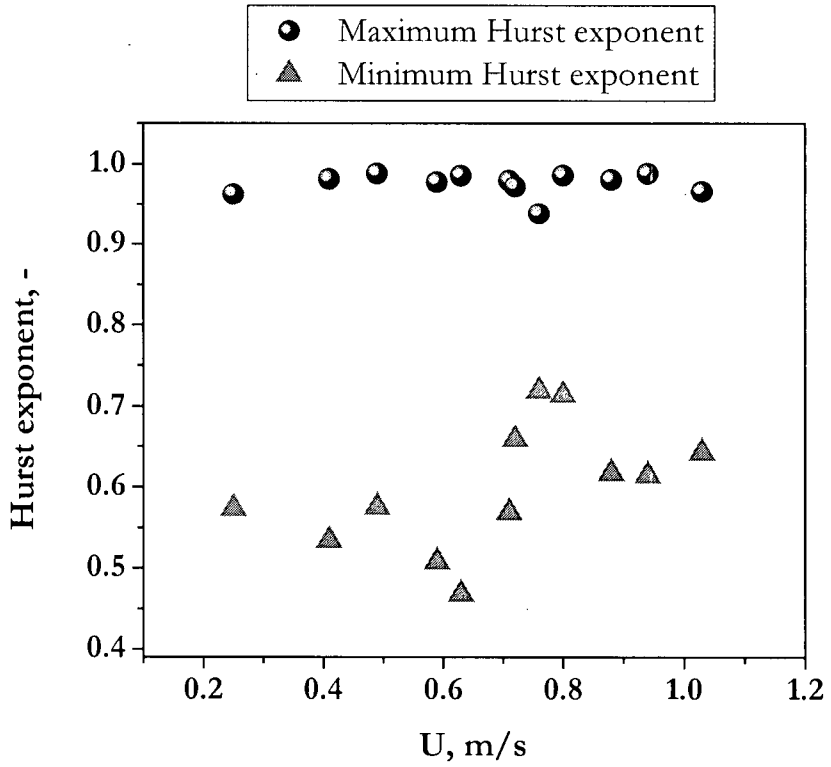

Figure 6.29 Variation of the Hurst exponents from DP signals with superficial gas velocity. D=0.29 m, H_0=1.1 m, $\bar{z}$=0.59 m, Δz =0.12 m, sampling frequency=100 Hz, sampling duration=100 s.

exponent decreases to below 0.5, implying a convergent system. This can be attributed to the splitting and coalescence of bubbles reflecting reversing phenomena. Though not showing as clear a trend as in Figure 6.29, Taxil et al. (2000) reported a similar trend for Hurst exponents in their 0.19 m diameter column with FCC particles. The maximum Hurst exponent, reflecting higher frequency phenomena, is shown to be consistently above 0.5 for DP signals measured at the wall, suggesting a divergent system. At around U=0.76 m/s, the difference between the two Hurst exponents becomes smaller, suggesting less phase segregation near U_c.

The cycle time calculated from the intercept of the two slopes of Hurst exponents represents a lag time caused by a dominant periodic component of a signal (Fan et al., 1993). This is also indicated in Figure 6.28. The variation of the cycle time with the axial position of the pressure taps for DP and gauge pressure signals appear in Figures 6.30 (a) and (b), respectively. Three superficial gas velocities are chosen as representative U values, corresponding to $U < U_c$, $U \approx U_c$, and $U > U_c$. Increasing U increases the cycle time for all superficial gas velocities at DP locations close to the distributor, indicating gradual growth in voids due to coalescence with height. The range of cycle time of 0.3-0.55 s corresponds well to the dominant frequency detected from FFT of DP signals of 1.5-3 Hz, e.g. see Figure 6.3. At z=1.1 m for U=1.0 m/s, the trend in cycle time reverses, suggesting dominance of void splitting over coalescence. The bed above this point becomes dominated by smaller voids, contributing to the increased homogeneity of the turbulent fluidized bed.

The trend shown from gauge pressure signals, Figure 6.30 (b), indicates two distinct regions: one nearer the distributor corresponding closely to the natural frequency of the bed, and the other indicating much lower cycle times. As signals from gauge pressure reflect global phenomena in a fluidized bed, the origin, propagation, and attenuation of pressure waves may be picked up. Following the analysis of Bi et al. (1995), the higher cycle time near the bottom of the fluidized bed may indicate pressure waves much lower in frequency than the natural frequency of the bed, implying that the bed is acting "as a wave propagation medium". On the other hand, at z=0.46 m and beyond, the imposed pressure waves have frequencies higher than the natural frequency of the bed resulting in oscillatory motion. Oscillations are dampened by energy loss from interparticle collisions, and friction between particle-gas or the wall, but sustained by the continuous supply of pressure waves. In a turbulent fluidized bed, it is extremely difficult, if not impossible, to pin-point

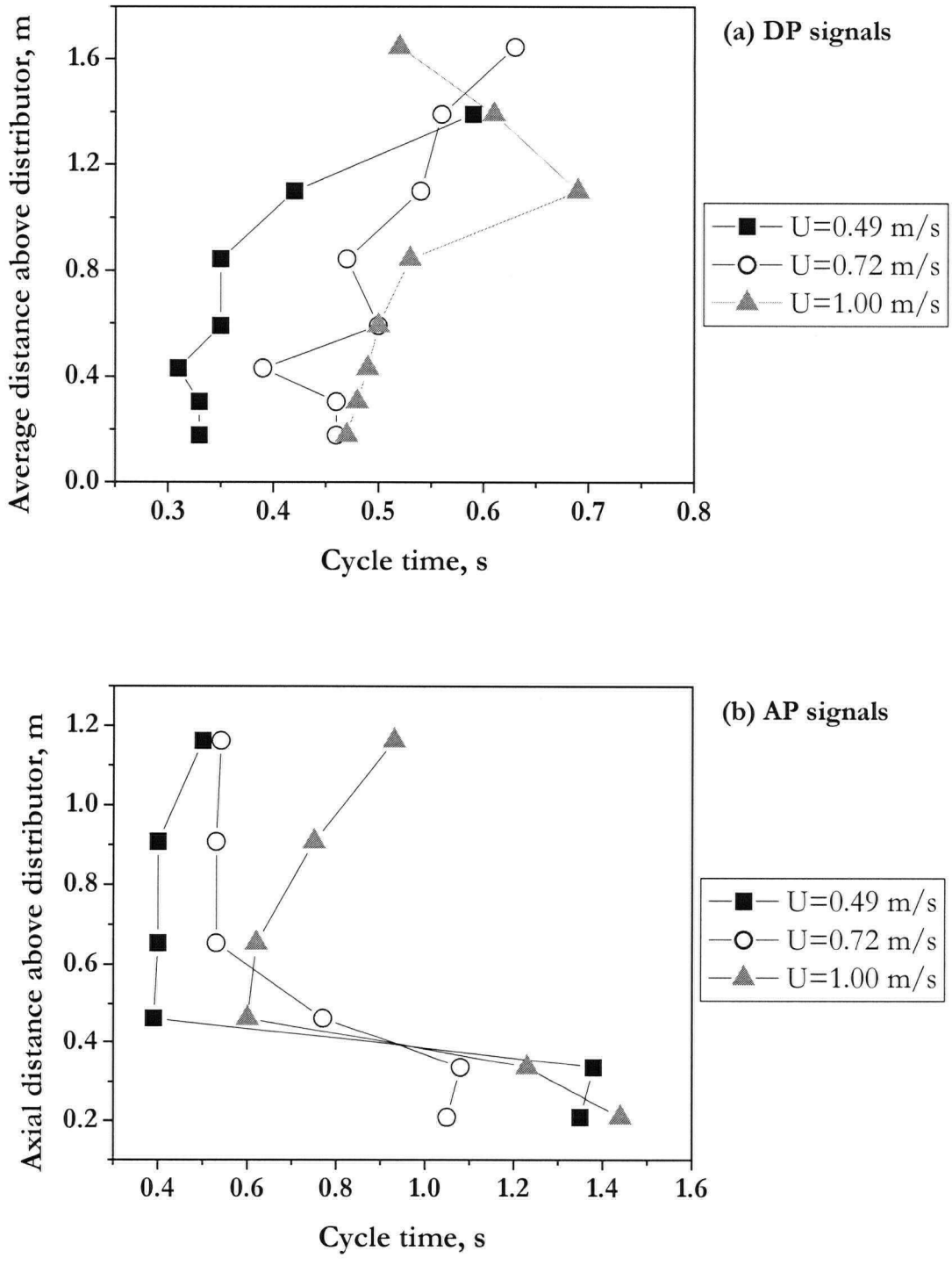

Figure 6.30 Axial profiles of cycle time from (a) DP, and (b) AP signals. D=0.29 m, H_0=1.5 m, r/R=1, FCC I.

the factors contributing to the pressure fluctuation owing to the complex dynamics. However, extending the analysis of such pressure waves from fluidized beds at minimum fluidization or minimum bubbling velocities (Musmarra et al., 1995; Bi et al., 1995; van der Schaaf, 2002) may provide insight into the understanding of energy supply and dissipation.

The effect of column diameter on the cycle times calculated from the rescaled range analysis of DP signals is illustrated in Figure 6.31. By comparing the cycle time variation with normalized axial probe height with expanded bed height, i.e., z/H, it is seen that there is a shift in trend in cycle time at certain axial heights for $U > U_c$. This implies that once in the turbulent fluidization flows regime, cycle time shifts to smaller values with height reflective of void splitting for the three columns in this study. The cycle time for the 0.61 m diameter column is indicated to be much larger than for the two other columns. This can be attributed to the distributor plate design, as well as the particle size distribution, which was widest for the 0.61 m diameter column. The cycle time regularity, defined in Equation 6.16, for DP signals obtained from the three columns are represented by Figure 6.32. The regularity from the rescaled range analysis indicates a decline with increasing U, except for the one point for the 1.56 m diameter column at $U/U_c=1.24$, which is considered to be inconclusive for the amount of information at hand.

6.6.4 Results from voidage signals

The rescaled range analysis is extended to voidage signals in this section. As noted by Briens et al. (1997), increasing the measurement volume with different measuring probes increases the Hurst exponent, implying increasingly persistent behaviour of phenomena occurring globally. The voidage signals obtained from optical voidage probes reflect much smaller measuring volumes than AP or DP signals, as discussed in Chapter 4. Thus, more localized behaviour should be revealed. Figure 6.33 illustrates radial profiles of the Hurst exponents for U=0.40 and 1.0 m/s. The maximum Hurst exponent remains close to 0.5 for U=0.40 m/s near the column axis indicating random motion. Though their Hurst exponents were much higher, Bai et al. (1999) reported a similar radial profile for the bubbling flow regime. However, in the turbulent fluidization flow regime, both maximum and minimum Hurst exponents indicated values above 0.5, increasing towards the wall. Figure 6.33 indicates smaller differences between maximum and minimum Hurst exponents near the wall implying less phase separation than in the core of the column.

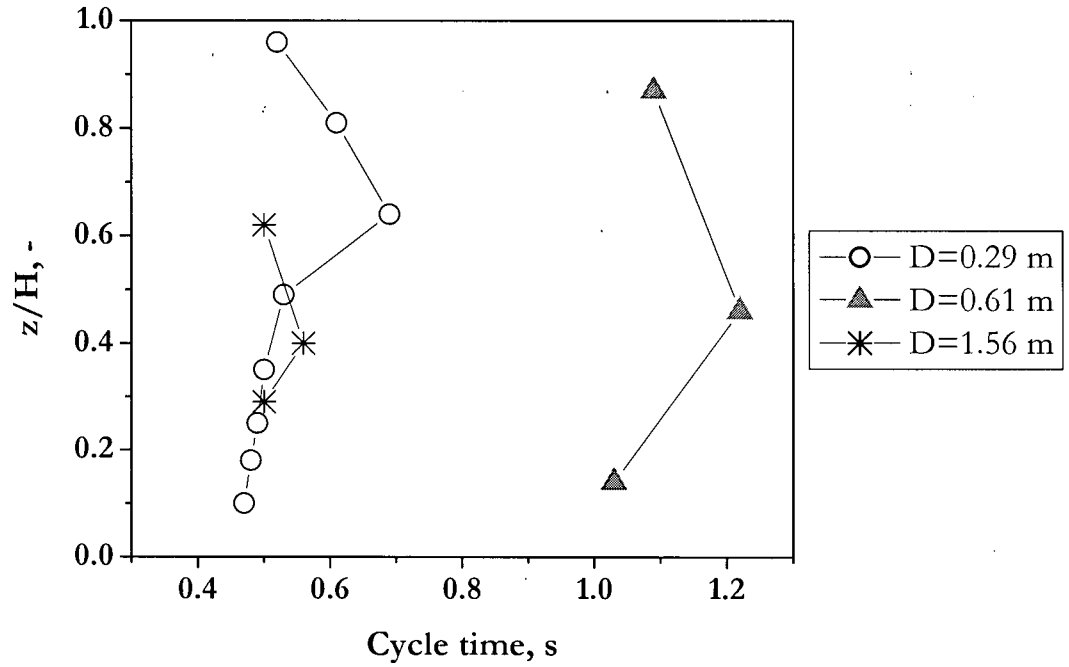

Figure 6.31 Variation of cycle time with dimensionless height for $U > U_c$ from DP signals.

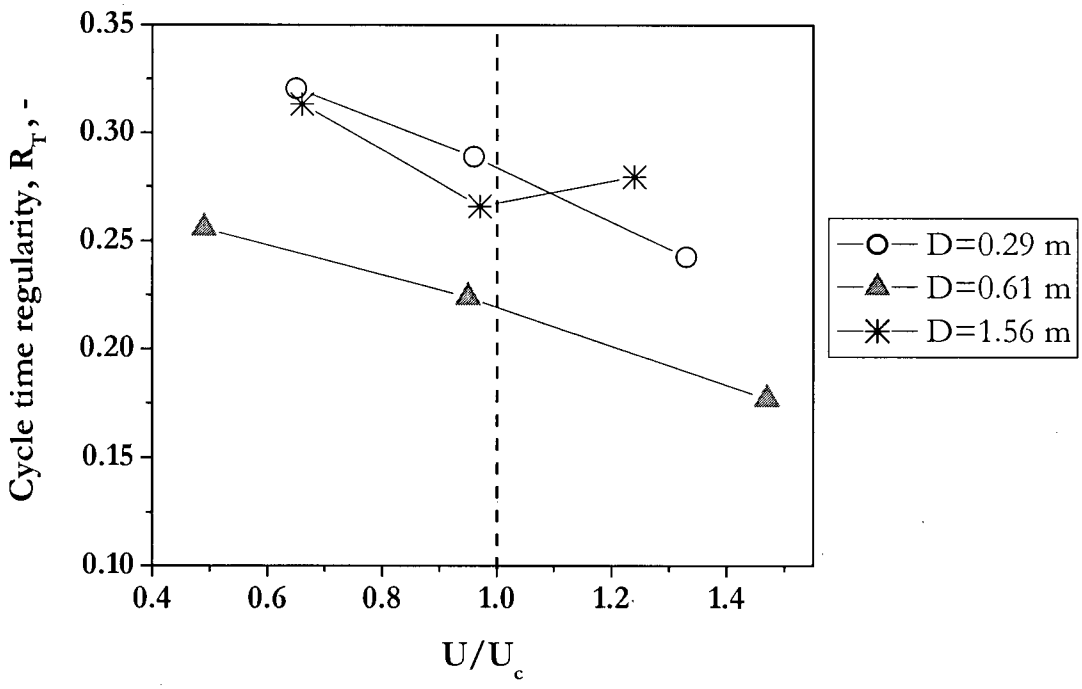

Figure 6.32 Variation of cycle time regularity with dimensionless superficial gas velocity. Axial positions: D=0.29 m (z/H=0.64); D=0.61 m (z/H=0.87); D=1.56 m (z/H=0.62).

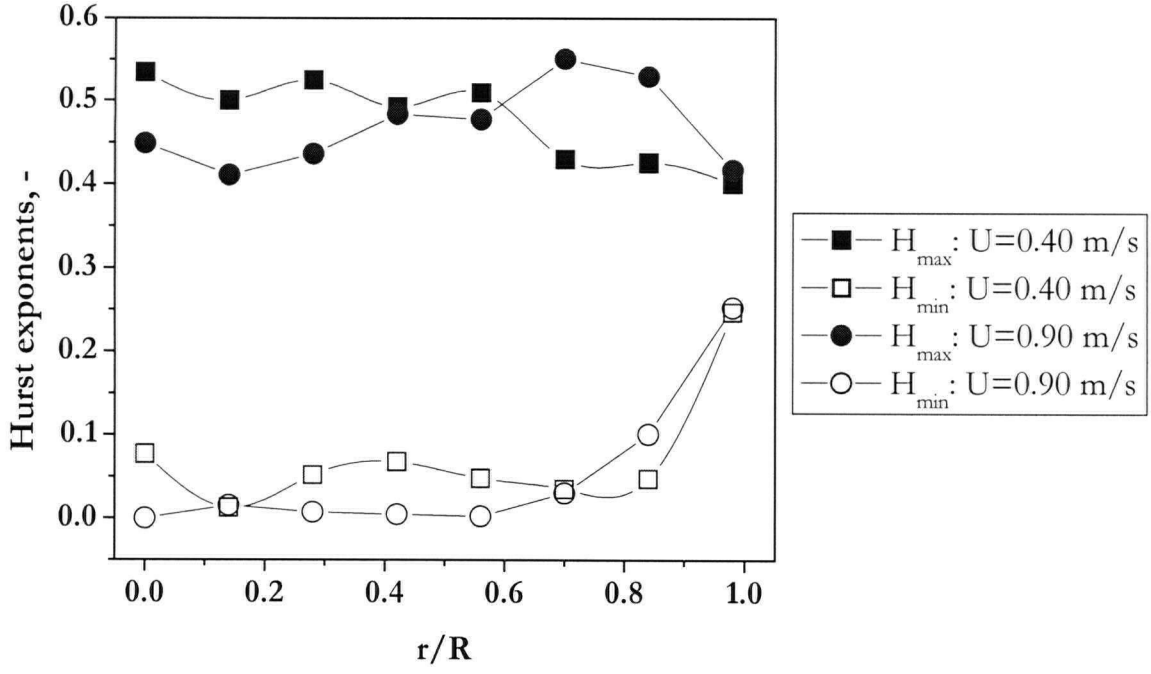

Figure 6.33 Radial profile of Hurst exponents for U=0.40 and 0.90 m/s. D=0.29 m, z=0.78 m, H_0=1.1 m, FCC I.

The maximum Hurst exponent, H_{max}, from the local voidage measurements shows a sudden drop with increasing superficial gas velocity, see Figure 6.34, indicating a change in the high frequency fluctuations. The velocity at which this abrupt drop occurs may correspond to the transition into the turbulent fluidization flow regime. The drop in H_{max} also corresponds to a slight decrease in Figure 6.29 from DP measurements. The sensitivity of the H_{max} from voidage signals to the change in local fluctuation may suggest a viable means of deducing the transition velocity, U_c.

The cycle time deduced from rescaled range analysis for voidage signals is shown in Figure 6.35. Considerable scatter of cycle time is observed with no definite trend indicated by the transition, as shown in Figure 6.34. The general trend of decreasing cycle time with increasing U indicates increasing cycle frequency of voidage fluctuations. The range of cycle frequency, i.e., reciprocal of cycle time, indicates close correspondence with the range of frequencies observed from FFT of DP signals, as shown in Figure 6.4. Thus with the optical signal capturing the local void movements, f_{DP} reflects void dynamics. Moreover, the superiority of the rescaled range analysis in deducing cycle time over the crossing frequency is highlighted.

6.7 Conclusions

Various statistical, spectral and chaotic analysis methods were employed to interpret pressure and voidage data in fluidization columns of diameter 0.29, 0.61 and 1.56 m. The results may be summarized as follows:

- Pressure signals were examined to study the hydrodynamic behaviour of turbulent fluidized beds in columns of different diameter. The natural frequency of the bed based on gauge pressure signals decreased with increasing bed height. FFT analysis of DP signals at different axial positions revealed a shift towards lower frequency distributions with increasing height, due to an increase in void sizes for $U < U_c$. Once in the turbulent fluidization flow regime, f_{DP} became less sensitive to height. This trend was supported by the crossing frequency, defined in Equation 6.2, deduced from local voidage measurements via an optical fibre probe within the bed. Figure 6.5 gives a graphical correlation for the pressure fluctuation frequency which includes the influence of column diameter and gas velocity in the turbulent fluidization flow regime.
- The correlation function coefficient was applied to characterize simultaneous voidage signals from two identical optical voidage probes. Higher correlation function coefficients were obtained for a probe distance similar to the length scale of the voids. Once in the turbulent

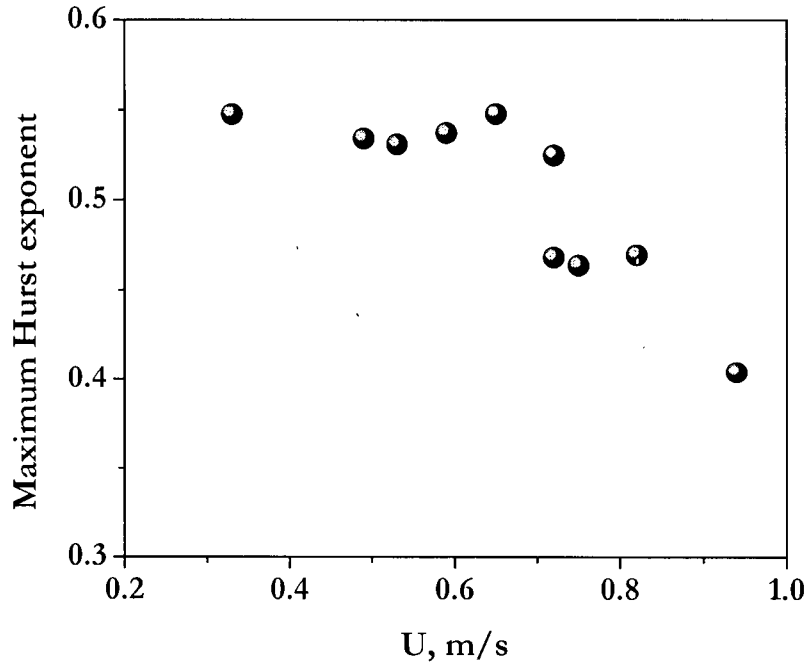

Figure 6.34 Variation of maximum Hurst exponent from optical voidage probe signals with superficial gas velocity. D=0.29 m, z=0.40 m, U_c=0.75 m/s, r/R=0.0, H_0=1.5 m, FCC I.

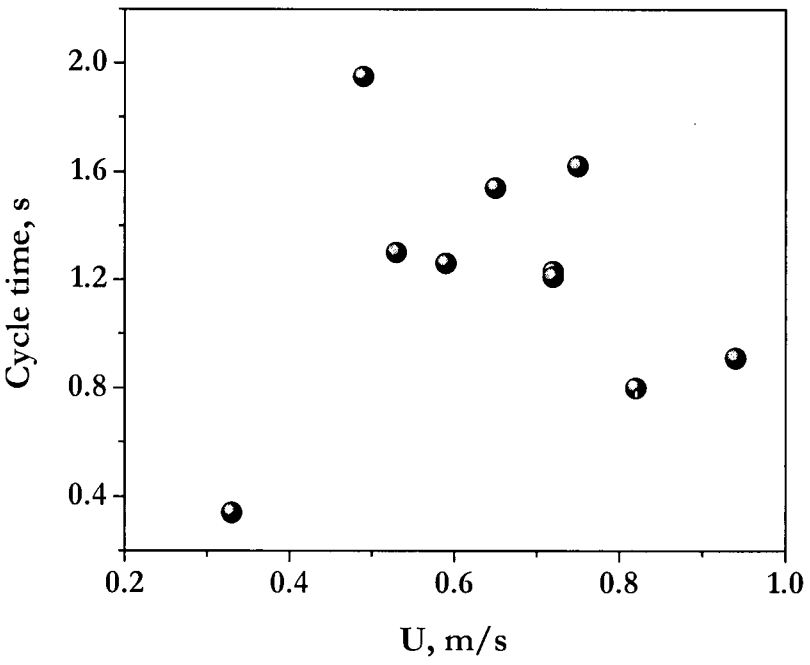

Figure 6.35 Variation of cycle time with superficial gas velocity for optical voidage probes signals. D=0.29 m, z=0.40 m, r/R=0.0, H_0=1.5 m, U_c=0.75 m/s, FCC I.

fluidization flow regime, less radial variation of the correlation function coefficient was observed, possibly indicating a narrow range of physical length scale of voids in the turbulent bed. This method of deducing the length scale is not considered to be practical, without *a priori* knowledge of the length scale to be detected, as the physical separation distance of probes dictates what scales can be detected.

- The autocorrelation function was applied to assess the non-randomness of voidage measurements from optical probes. The autocorrelogram in Figure 6.14 suggests a chaotic signal from a system which 'forgets' previous information. Simultaneous voidage measurements at two axial locations indicate longer lag times for the higher probe position indicating void coalescence being dominant as voids rise at U=0.9 m/s. Further analysis using autocorrelation function was not pursued as it is based on the underlying assumption of a linear relationship between data points, which is unlikely for void dynamics in turbulent fluidized beds.
- The coherence function measures the coherence of a set of signals at a given frequency. Strong coherence was indicated between the two probes when their separation distances corresponded to the length scale of the voids, which occurred in the bubbling flow regime. Once in the turbulent fluidization flow regime, the coherence function declined with increasing U. As for the autocorrelation function, the probe separation dictates the length scale to be detected.
- Rescaled range analysis was applied to pressure and voidage signals. The minimum Hurst exponent indicated a maximum at $U \approx U_c$. Cycle times calculated from the V and P statistics indicated a shift in cycle time at $U > U_c$. This may suggest that at a certain height above the distributor plate, void splitting may become more dominant than coalescence. Cycle time obtained from voidage signals indicated a range of cycle frequencies similar to those detected by the dominant peak from Fast Fourier Transformation of pressure signals. It strongly suggests that FFT peaks from DP signals reflect void dynamics, as supported by cycle times obtained from voidage signals.

CHAPTER 7

MULTISCALE RESOLUTION

7.1 Introduction

This chapter continues the exploration of the hydrodynamic complexity of the turbulent fluidized flow regime from a multiscale resolution viewpoint. Nonlinear dynamics and their implications with respect to the flow were discussed through chaotic analysis in the previous chapter, shedding light on the challenges of understanding dynamics from observations of systems where non-linearities are important. It is important to determine whether or not the rapid inversion of continuous and discontinuous phases between low- and high-density phases in turbulent fluidized bed can be explained or modeled through energy-based hypotheses and the dominance of one phase over the other between two phases (Li et al., 1998). Here, both velocity and voidage fluctuations are analyzed and interpreted as footprints for the flow structure in an attempt to understand the system from an energy dissipation point of view. The analysis tool used for this task is wavelet analysis, a technique which is being widely recognized as a powerful tool to interpret the physics of non-linear data (Ross and Pence, 1997). Noting that the quantification of dynamics drawn from experimental data is basically bounded by the underlying theory, the fundamental equations governing the two-phase flow based on fluid dynamics are discussed in Appendix D.

7.2 Turbulence – two phase flow

Single-phase turbulence from a statistical fluid mechanic viewpoint is characterized as highly non-linear (inherent in the Navier-Stokes equations), subject to irregular fluctuations of velocity, cascading energy, and intermittency of the dynamically active regions (e.g. Argoul et al., 1989; McComb, 1990). Turbulent events include acceleration, deceleration, rotation or vortex, or a constant velocity experienced by eddies. The Reynolds number dictates the ratio of the nonlinear convective motions, inducing flow instability, to the linear dissipative damping, which converts kinetic energy into thermal energy (Farge et al., 1996).

Gas-particle interaction is an important research topic steadily gaining in attention owing to its dominant influence on heat and mass transfer in gas-solid flows, as encountered in many industrial processes. The structure and motion of turbulence are greatly influenced by the presence of turbulent eddies of different sizes and orientations. Eddies affect the transfer of momentum found

in turbulent flow. Instantaneous shear stresses near the wall are key factors in the production of turbulent eddies in concurrent-upward gas-solid flows.

As Townsend (1976) stated: the necessary connection between diffusion and the supply of energy to the turbulent motion is a fundamental characteristic of turbulent flow. The primary eddies are produced by an energy source and are dissipated into smaller eddies. The eddies responsible for macroscopic transport are mainly the large-scale ones which contain the major portion of the turbulent energy (Zethræus et al., 1992). Baird and Rice (1975) attempted to connect the energy dissipation rate per unit mass of fluid by applying the Kolmogorov's theory of isotropic turbulence.

The behaviour of the suspended solids in a turbulent two-phase fluid depends largely on the concentration of the particles, and on the size of the particles relative to the scale of turbulence of the fluid (Hinze, 1959). The particles can dampen or enhance the gas turbulence. According to Sinclair and Jackson (1989), the interactions can be categorized as:

- Interaction between particles and gas resulting from the difference between their mean velocity fields, leading to drag forces that propel the non-random part of the particle motion.
- Interaction of the particles with the fluctuating component of the gas velocity. This may cause a flux of kinetic energy in either direction between the fluctuating components of velocity of the two phases, either damping the fluctuations of gas velocity and stimulating fluctuations in particle velocity, or vice versa.
- Interactions of the fluctuating part of the particle motion with the mean particle motion through interaction between the particles. These generate stresses in the particle assembly and give rise to its apparent viscosity.
- Interactions between the turbulent fluctuations of gas velocity and the mean motion of the gas, generating the well-known Reynolds stresses.

Key features of fluidized beds such as bubbles and slugs can be traced to inertial instability in the gas phase, as well as the solid phase (Dasgupta et al., 1994). Motion of the particles can be partitioned into three components: the mean and the fluctuating velocities associated with the organized motion of collections of particles; and fluctuations at the level of individual particles. From the previous investigation of particle-turbulence interaction by Hetsroni (1989) and given the operating conditions of turbulent fluidized bed systems, turbulence due to the influence of particles should be suppressed.

7.3 Multiple scales in fluidized beds

In systems such as a fluidized bed where multiple scales of dynamics are omnipresent, it is surprising to see how few studies have adopted a multiscale point of view. In Li (2000), extending a paper of Li et al. (1998), eight parameters emerge, namely ε_f, ε_c, f_d, U_{gf}, U_{gc}, U_{df}, U_{dc}, d_{cl}, together with three scales of interaction associated with the heterogeneous gas-solid flow. The three scales are a macro-scale of the overall processing unit; a meso-scale of clusters or bubbles; and a micro-scale of individual particles.

The macroscale in a fluidized column is the column geometry represented by the macroscopic variables such as pressure, temperature and volume. It is characterized by radial and axial heterogeneity. Fluctuations in the motion of the two phases and the interactions between the dense and dilute phases are observed. Key phenomena originate from instabilities of shear flow associated with the presence of the column walls, with the largest eddy size being the column diameter. The macroscopic length scale of the flow is much larger than the particle diameter, so that a continuum description of the suspension can be assumed.

In the intermediate (meso) length scale, lengths of interest (e.g. bubble diameter, cluster size) that are larger than the diameter of the particles but limited by the averaging volume are considered. This mesoscale range deals with what is usually called a "local" measurement with respect to the solids such as from optical fiber probes. Li (2000) proposes a particle-fluid compromising interaction scheme where both 'ordered' and 'irregular' behavioural changes occur.

The smallest (micro) scale is characterized by the particle diameter and the separation between neighbouring particles, but is still much larger than the gas molecular mean free path. For Group A and B solids, the flow at the microscale level is no longer turbulent but viscous and dominated by molecular effects. Variations in gas velocity result from streamline deformation around a particle. Individual particle velocities differ as a result of interactions such as collisions or due to fluctuations in the interstitial gas velocity. At the smallest scale, viscous dissipation forces become important and tend to damp the eddy motion. Interactions at the micro-scale can be particle-dominated in a dense-phase cluster, or fluid-dominated within a dilute phase.

7.3.1 Kolmogorov scale of turbulence

The hypothesis of Kolmogorov depicts the cascading of energy from the largest scales to the smallest through the non-linear terms of the Navier-Stokes equations (McComb, 1990). At the smallest scale of turbulence, viscous forces dominate over inertial forces resulting in dissipation of turbulent kinetic energy where the velocity gradients are large. In an open system, the external forces act only on the largest scales. For an intermediate range of scales, Kolmogorov states that the energy cascaded from the larger scales is transferred to the small scale at a constant rate (Farge et al., 1996). In dilute suspensions, discrete particles only respond to turbulent eddies larger than the particle diameter. For eddies of size

$$\eta=\left(\frac{\mu^3}{\varrho^3\sigma}\right)^{1/4} \tag{7.1}$$

and smaller, where σ is the rate of energy dissipation per unit mass, the kinetic energy of turbulent motion is dissipated as heat. Reade and Collins (2000) suggest that the Komogorov scale dominates the particle clustering process since motions of this scale contain most of the fluid vorticity responsible for centrifuging the particles. On the other hand, Crowe (2000) suggests that the Komogroff scale is no longer appropriate for a fluid-particle flow since the presence of the particles provides surfaces that can support stresses.

7.3.2 Time scale

The parametric dependence on the small-scale particles can be characterized by the Stokes number,

$$St=\frac{\tau_p}{\tau_\eta}=\frac{1}{18}\left(\frac{\varrho_p}{\varrho_g}\right)\left(\frac{d_p}{\eta}\right)^2 \tag{7.2}$$

Small scale dissipative eddies contribute to the local non-uniform particle distribution which is most pronounced when the ratio of the particle response time, τ_p, to the Kolmogorov time scale, τ_η, is close to unity. This phenomenon of local vorticity centrifuging particles out of regions of high vorticity into regions of high strain is called "preferential particle concentration." However, for large values of the particle Stokes number, e.g. $St\approx\sqrt{Re_\lambda}$, particles become less correlated, thus increasing the collision frequency (Reade and Collins, 2000).

The particle relaxation time is defined as the time taken for a particle at rest to be accelerated to within ~63% of the fluid velocity. In a dilute two-phase suspension, particle velocities follow the

fluid eddy velocities when the oscillation period or eddy time scale is much larger than the particle relaxation time,

$$\tau_c >> \frac{d_p^2\left(2\varrho_p/\varrho_g+1\right)}{36\upsilon} \tag{7.3}$$

When the two times scales are of the same order of magnitude, particles fluctuate less as a result of interactions with eddies. However, the presence of many discrete particles in a turbulent flow indirectly influences the fluid-velocity field in the interspace between particles, consequently changing the length and time scales, and hence the energy spectrum of the fluid.

7.4 Turbulence energy decomposition - phase space

In employing functions to characterize the flow phenomena, one must understand the intrinsic structure of the field to be analyzed. Farge (1992) points this out in modeling turbulent flows where an appropriate segmentation of the energy density in phase space must be identified to understand the interactions of the dynamically relevant quantities. For example, if a signal is composed of superimposed waves, the wave number through the Fourier spectrum is the appropriate analyzing function for characterizing the phenomena. On the other hand, a different analyzing function must be employed for a flow field composed of superposed point vortices. Only when an appropriate decomposition of the flow field is obtained, can the flow dynamics be meaningfully interpreted.

7.5 Wavelet analysis

The wavelet transform, WT, is an analysis tool for decomposing data into different frequency components, and then for resolving the positions and scales as independent variables. It is capable of isolating singular sequences of events related to particular scales (Daubechies, 1992; Hlawatsh and Boudreaux-Bartels, 1992; Weng and Lau, 1994). Through wavelet analysis, a one-dimensional time series is transformed into a two-dimensional region displaying wavelet coefficient amplitudes as a function of both time and frequency. This enables time localization of spectral components to be interpreted (Hlawatsch and Boudreaux-Bartels, 1992). A wide range of applications of wavelet transforms is found in geophysics, image analysis, seismology and fluid dynamics. Recently, wavelet transformations have been gaining attention in studies of single-phase turbulence. In single phase turbulent flow, the WT has been applied to analyze the intermittent nature and multiscale aspects of the turbulent flow (Farge et al., 1996); in investigations of intermittency and the passage of turbulent coherent structures (Camussi and Guj, 1997); and in characterizing local turbulent or eddy structures (Katul et al., 2001). The potential efficacy of wavelet transformation in understanding the local

structure of turbulence has been highlighted, e.g. by Farge et al. (1996), Camussi and Guj (1997), Chainais et al. (1999), Katul et al. (2001), in identifying the points of intermittency in large and small-scale turbulence; in displaying fractal characteristics of cascading phenomenon; and in analyzing the physics of nonlinear data (Ross and Pence, 1997). Dynamic behaviour has also been analyzed through wavelet transformation elucidating intermittency, structural resolution, phase separation, turbulent density and energy, and principal time scales in bubble columns and in circulating fluidized beds (Bakshi et al., 1995; Ross and Pence, 1997; Lu and Li, 1999; Zhou et al., 2000; Ren et al., 2001; Kulkarni et al., 2001). According to Ren et al. (2001), local voidage measurements from a fluidized bed can be decomposed into three scales: micro-scale (particle and fluid), meso-scale (voids, two phase structure), and macro-scale (equipment, global). The wavelet filtering method has been applied to phase decomposition of voidage measurements in identifying the transition points between dilute and dense phases, enabling the determination of the volume fraction of each phase and cluster duration time, without resorting to pre-set threshold values.

Prior to applying this recent mathematical tool to data form turbulent fluidized bed systems, a brief overview is presented and its applicability to this project is discussed in Appendix C, as the method is not yet well established compared to Fourier analysis.

7.5.1 Wavelets and turbulence

Wavelet analysis has been shown to be an effective tool in studying fully developed turbulence (Meyer, 1993). Modern understanding and characterization of turbulence are built upon considerable research conducted by early researchers in the field such as Kolmogorov, Karman, Prandtl, and Taylor as described by Hinze (1959), Batcheleor (1967), and Townsend (1976). Turbulent flow is depicted as unsteady, three-dimensional vortical flow, leading to high dissipation of energy into heat and rapid dispersion over wide ranges of frequencies and scales. The statistical approaches to turbulence investigate the partition of energy, at different scales, in solving the Navier-Stokes equations (Meyer, 1993). Some of the statistical tools applied are averaging, characterization of fluctuations, probability density functions, space and time correlations, spectra, conditional averaging, Lagrangian statistics, and volume averaging (Libby, 1996). The Fourier transform provides a good representation to solve the linear dissipation term, but is not able to represent the nonlinear convection term, which becomes dominant in high Reynolds numbers (Farge et al., 1996). When there is spatial intermittency in the flow, the Fourier transform is capable of representing the velocity field in a combination of plane waves; however, the position in physical space is not

revealed (Meneveau, 1991). Wavelet analysis, on the other hand, provides the means for "conditional averaging and seeking atomic decomposition of phase space, defined in both space and scale" (Farge et al., 1996), enabling flow intermittency to be treated as localized pulses, rather than as extended waves. Numerous publications on various aspects of turbulent flow based on wavelet analysis have been published. For example, see Lewalle et al. (2000) for clarification of coherent structures and Camussi and Guj (1997) for a study of intermittency and coherence structures.

7.6 Analysis method

7.6.1 Application of wavelet transform to de-noising signals

In de-noising signals, the linear band-pass filters based on the frequency domain allow some frequency signals to pass unaltered, while other frequencies are blocked. This method is useful in removing frequencies that are present throughout the signal, but does not allow time localization. De-noising signals using wavelets takes advantage of the their excellent time-frequency localization and multi-resolution analysis.

Recognizing these features, the method is applied here to transpose voidage signals to different physical scales by means of frequency decomposition. Ren et al. (2001) reported on the application of wavelet analysis to decompose voidage signals into three scales of components: micro-scale (particle size); meso-scale (cluster size); and macro-scale (unit size), thus avoiding the effect of the pre-set threshold on the resulting cluster-size distribution.

The effect of threshold value in determining void velocities was raised in Chapter 5 and reported in Appendix B. As investigated in Section 5.4.5, the cut-off method was applied in order to remove the interference of dense phase fluctuations prior to cross-correlating void velocity signals. The resulting velocity was shown to be affected by the threshold value for the cut-off voidage and the number of data points used for the sectional cross-correlation. The new approach proposed here applies wavelet decomposition to eliminate dense phase fluctuations of the voidage signals.

7.6.1.1 Crude method

One way to eliminate signals of certain frequencies using wavelets is to decompose the signals and reconstruct the signal without certain components known to contain noise. The one-dimensional Daubechies wavelet, db, is chosen here to demonstrate the reconstruction of approximation coefficients to show the signals without certain scales. Figure 7.1 compares the original voidage

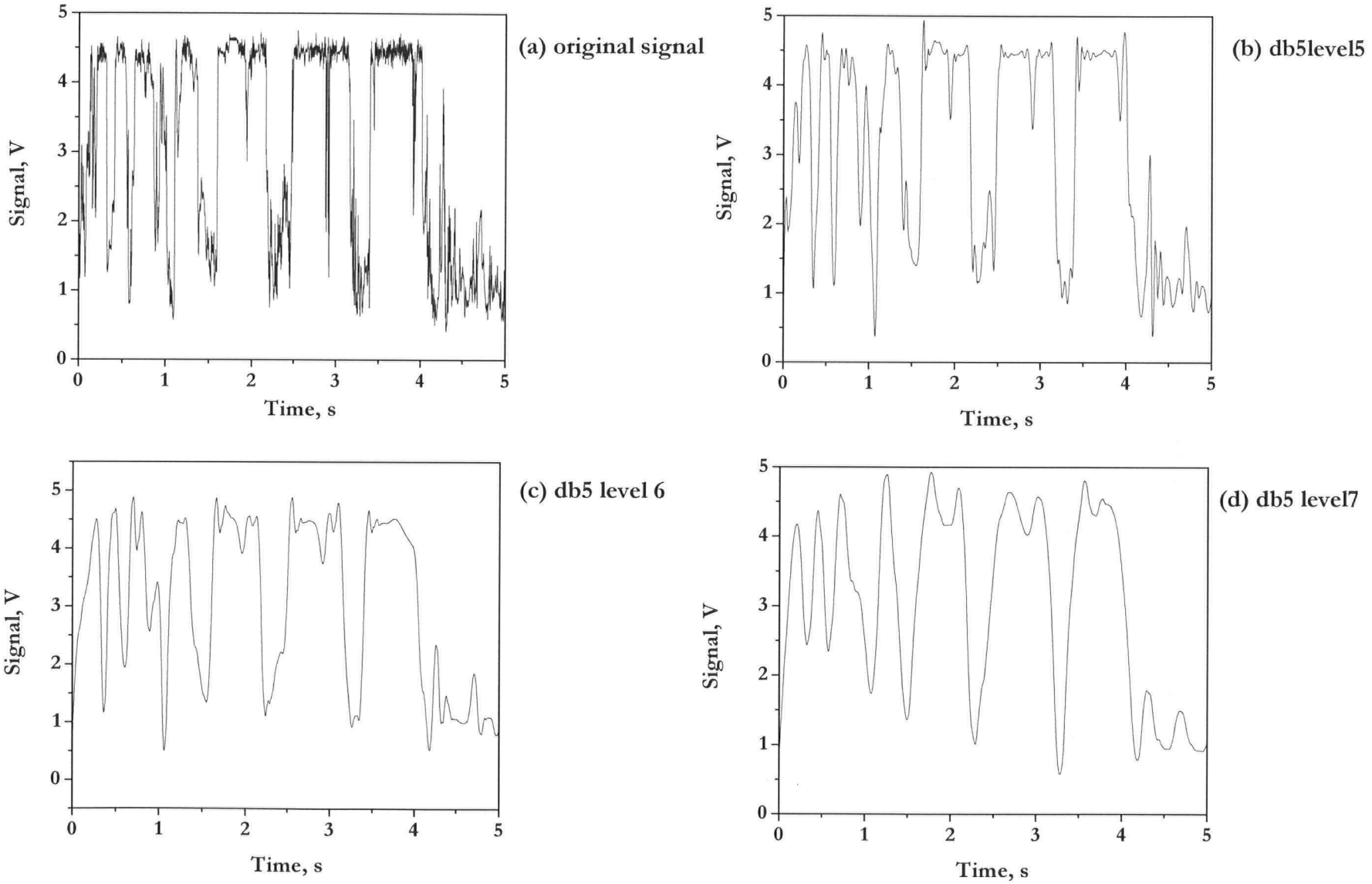

Figure 7.1 Original and de-noised signals.

signal and the reconstruction of the approximation confidences at specific levels. Since the purpose of the decomposition is to retain the void fluctuation, yet to eliminate the small-scale fluctuations associated with particle dynamics, the appropriate wavelet must be chosen. Increasing levels of decomposition results in eliminating the sharpness of the edges. Moreover, the signal reconstruction from approximation coefficients loses the sharpest features of the original data, which may well be undesirable.

7.6.1.2 Thresholding

In recovering signals from noisy and incomplete data, both parametric and nonparametric regression models are applied. The former includes linear or polynomial regression, and produces estimators influenced by *a priori* knowledge of the functional form of data. Nonparametric regression, on the other hand, seeks to track the average values of the dependent variables as a function of the independent variables with minimal assumptions about the form of the relationship. Nonlinear wavelet estimators have gained considerable attention in recent years as an approach to nonparametric regression (Ogden, 1997). Further discussion is reported in Section C.2.5 in Appendix C.

The methodology of nonparametric regression was applied to de-noise the same signal prior to cross-correlation. Daubechies wavelet N=3 at level 5, equivalent to the condition on Figure 7.2, was used to decompose the signal. The soft thresholding method was applied with threshold equal to $\sqrt{2\log(n)}$ and rescaling of the threshold using level-dependent estimation of the level noise. The resulting reconstructed signal is shown in Figure 7.3. Comparing visually with the approximation reconstruction in Figure 7.2, sharper edge jumps are observed. Furthermore, the cross-correlation of the de-noised signals results in void velocity distribution much closer to the cut-off method as shown in Figure 7.4. The non-linear wavelet method eliminates the dependency on the threshold value in determining the void edge. Treating high-frequency, small-scale voidage fluctuations from the particle dynamics as noise, and effectively de-noising the signal, wavelet analysis is seen to be successful in pre-conditioning the voidage signals for cross-correlation.

7.6.2 Local intermittency measure

The notion of intermittency originated from the transition from laminar to turbulent flows where periods of laminar motion and turbulent bursts succeed each other in a random sequence

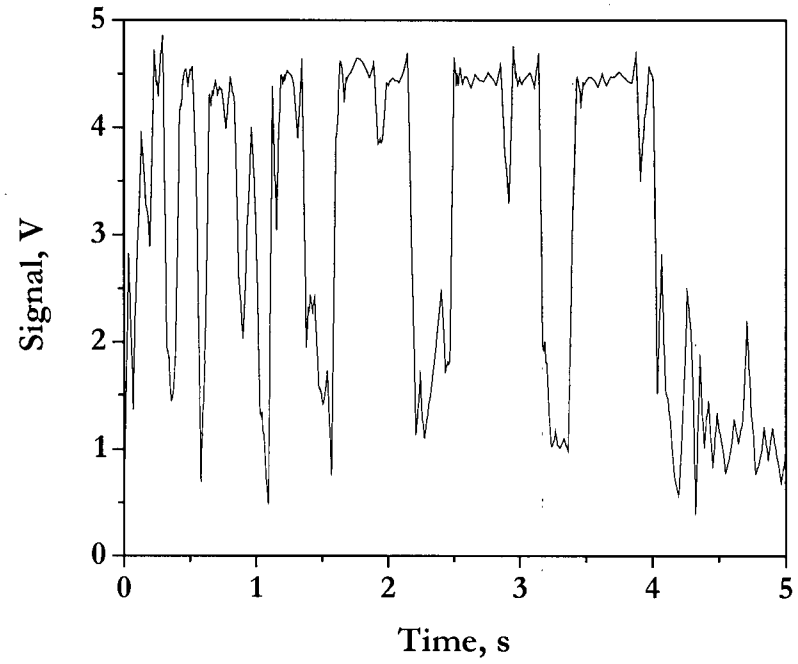

Figure 7.2 De-noising signal using Daubechies 3 wavelet level 5.

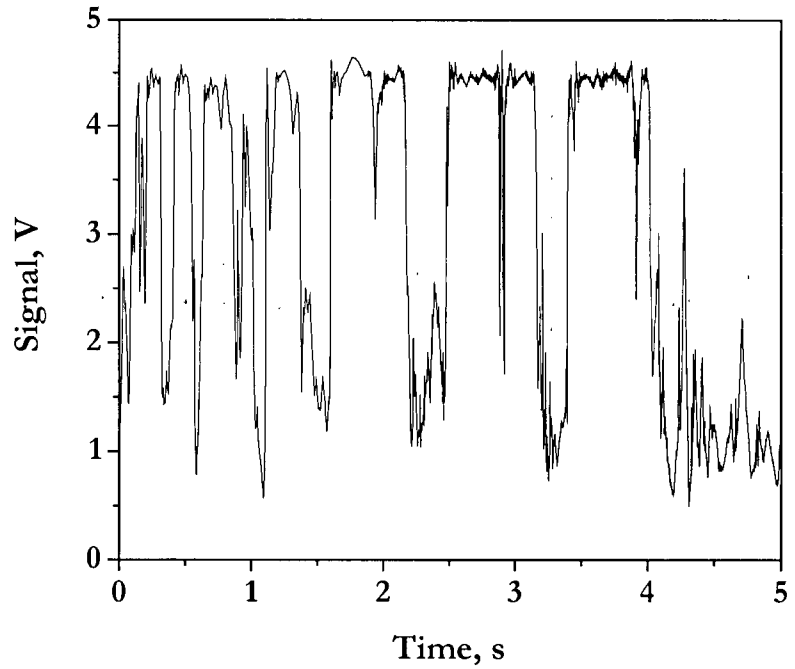

Figure 7.3 De-noising signal using Daubechies 3 wavelet level 5 with soft thresholding method.

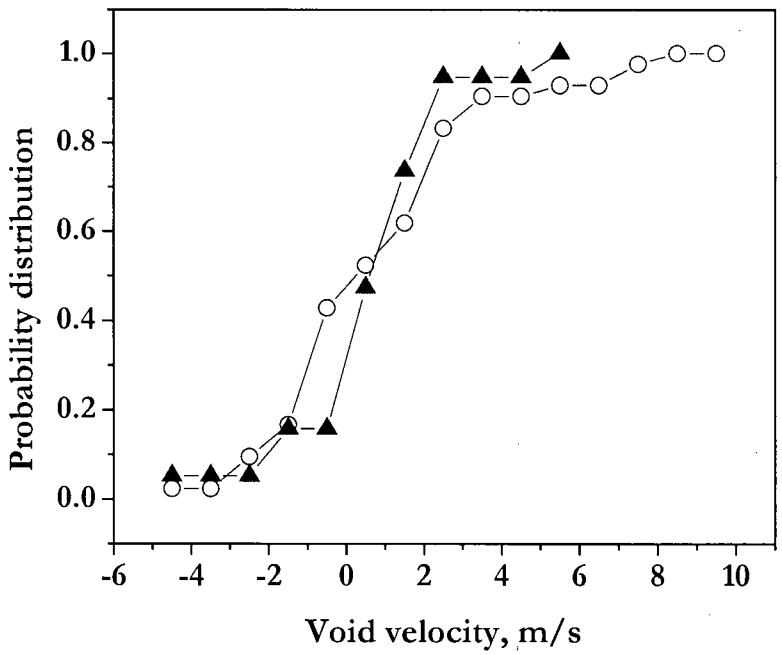

Figure 7.4 Comparison of void velocity distribution between cut-off method (○); and db3 level 5 wavelet transform with soft thresholding (▲) (data of Figure 7.6a).

(Schlichting, 1979). In recent years, intermittency has been associated with various types of regular or quasi-deterministic behaviour, termed coherent structures. Coherent structures affect the energy cascade and other aspects of turbulent flow. They constitute a relatively new area of study, as summarized by McComb (1990). Various authors have investigated the relationship between temporal and spatial intermittency of turbulent flows to the presence of coherent structures through wavelet analysis (Farge et al., 1996; Camussi and Guj, 1997; Chainais et al., 1999). Coherent structures are characterized in Chapter 6. Here, some of the quantitative methods in characterizing the intermittency through coherent structures are applied.

The passage of highly coherent vortical structures can be characterized by strong velocity gradients considered to be responsible for momentum transfer (Li, 1998) through viscous dissipation of turbulent kinetic energy. Application of wavelet analysis in distinguishing the coherent and non-coherent components of turbulent flows and characterizing the intermittency related to coherent structures of energy bursts should provide insight into the flow structures.

The local intermittency index based on the non-uniform distribution of energy in space represented by scalar x has been defined as:

$$LIM_j(i) = \frac{\left|x_j(i)\right|^2}{\left\langle \left|x_j(i)\right|^2 \right\rangle_N} \tag{7.4}$$

where < > denotes the arithmetic average over N data points. This index has been applied to measure intermittency in turbulent flows (Farge, 1992; Camussi and Guj, 1997) and to velocity measurements in a bubble column (Kulkarni et al., 2001).

7.6.2.1 Wavelet analysis applied to particle velocity

The experimental data obtained in this project using the optical velocity probe capable of capturing fluctuations at a particle scale have been analyzed to quantify the presence of energetic microstructures through the local intermittency index. The bivariate time series of voidage fluctuation, shown in Figure 7.5 is converted to "instantaneous" particle velocity fluctuation based on the methodology described in Appendix B. Particle velocities corresponding to 142.5 ms bursts have been calculated via cross-correlation and are shown in Figure 7.6. The resulting velocity fluctuation is decomposed through Deubechies 5 wavelets (db5) for 6 levels.

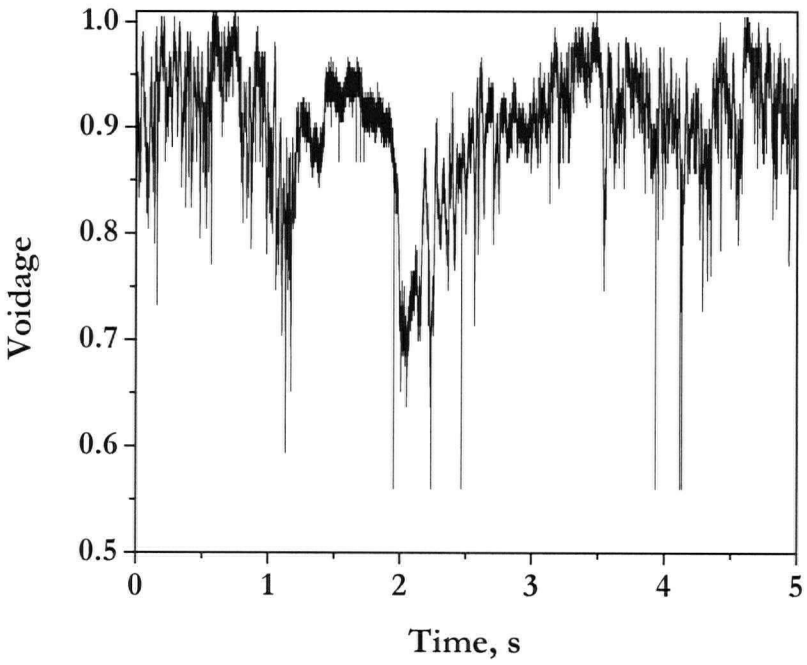

Figure 7.5 Voidage fluctuation captured by optical velocity probe. Sampling frequency, 28,741 Hz, D=0.61 m, U=1.56 m/s, r/R=0.09, z=1.55 m, z=1.55 m, H_0=2 m, FCC IV.

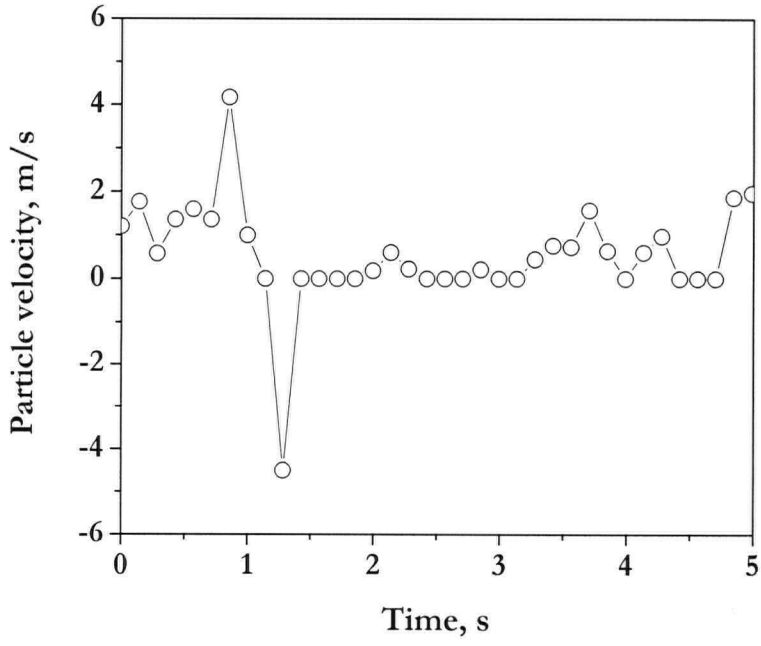

Figure 7.6 Particle velocity fluctuation of data from Figure 7.10 based on cross-correlation of 4096 data points, representing 142.5 ms. D=0.61 m, U=1.56 m/s, r/R=0.09, z=1.55 m, H_0=2 m, FCC IV.

The maximum number of levels of decomposition depends on the sample size, N, as:

$$\max(j)=\log_2 N \tag{7.5}$$

The detailed coefficient at levels 1 through 6 are reconstructed to calculate LIM according to Equation 7.4. The local intermittency index represents the normalized energy distribution at various scales j. A large magnitude of LIM signifies high energy variation and content. Thus, the graphical representation of LIM has been used to identify the passage of high-energy coherent structures (Kulkarni et al., 2001).

Typical contour plots for U less than, close to, and larger than, U_c are shown in Figures 7.7, 7.8, and 7.9, respectively. Comparison of the three plots suggests a general shift in distribution of the energetic microstructures at a given measurement location in time. For $U < U_c$, the local intermittency index indicates energy variations across the scale; on the other hand, at U=1.56 m/s, Figure 7.9 indicates that most of the energy variations occur at a smaller scale representing higher frequency. Moreover, these structures are much shorter lived in Figure 7.9 than in Figure 7.7 or Figure 7.8. This highlights the change in flow structure in passing from bubbling to the turbulent fluidization flow regime.

Probability distributions of LIM at three superficial gas velocities, U=0.42, 0.82, and 1.56 m/s, are shown in Figures 7.10 (a) and (b) for the smallest and largest scales, i.e., j=1 and 6, respectively, for r/R=0.09. By conducting analysis at different scales, certain trends become apparent. As shown in Figure 7.10 (a) at the smallest scale of analysis for r/R=0.09, the local intermittency indicates similar distribution among the three superficial velocities. As the optical velocity probe reflects voidage variations at the particle level, it is plausible that the burst of energy reflects particle velocity fluctuation. However, it is difficult to pinpoint the relevant frequency. As shown in Figure C.2, as the scale, a, is reduced, the frequency band increases with superior time localization.

Though this method of decomposing the signal and quantifying the energy distribution is shown to be effective, it must be noted that the particle velocity data are unsuitable owing to discontinuities due to cross-correlation and elimination criteria. As reported in Appendix B, 20 to 40% of data are rejected owing to poor correlation of the two-voidage signals. For the above velocity data, zero velocity is assumed when there is poor correlation.

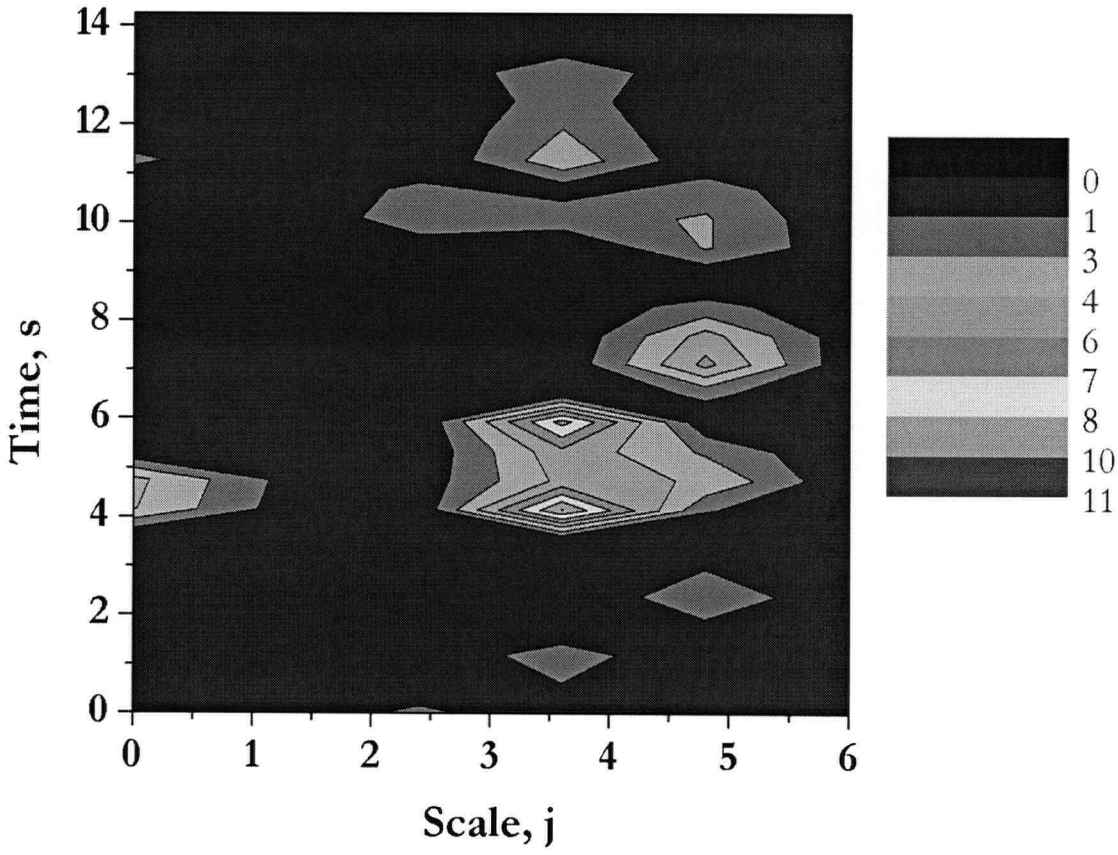

Figure 7.7 Contour plot of LIM for 6 levels depicting passage of energetic microstructure centred around scale 3. U=0.42 m/s, r/R=0.09, D=0.61 m, z=1.55 m, H_0=2 m, FCC IV.

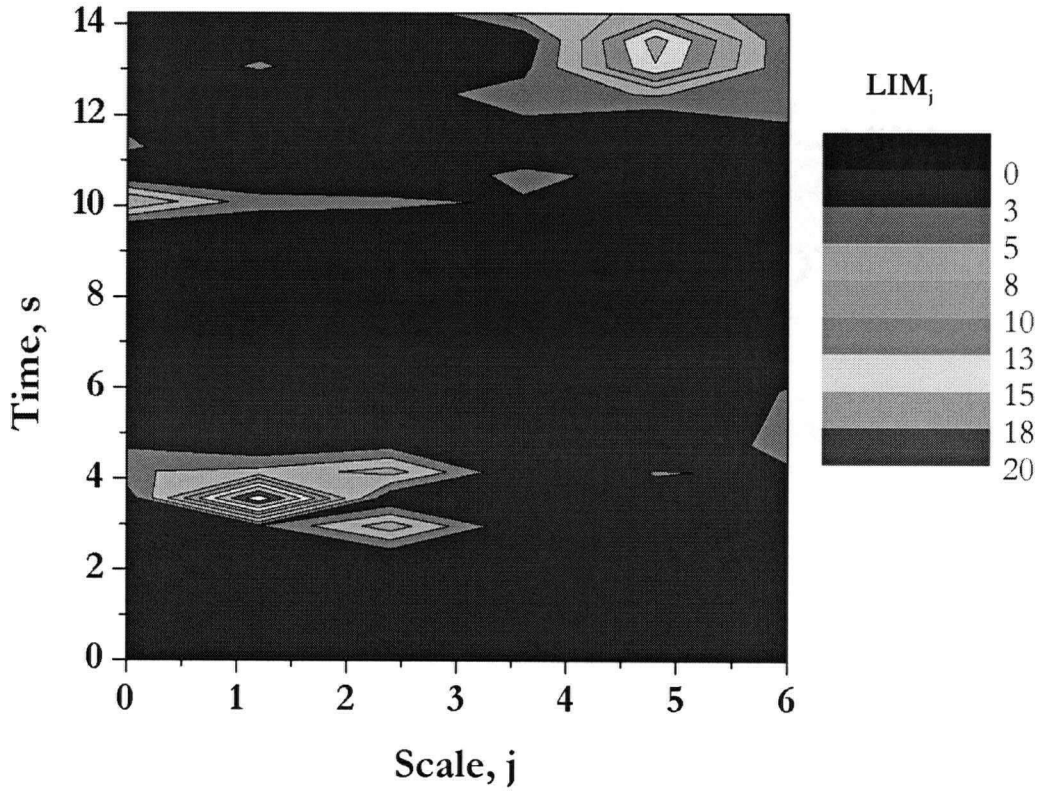

Figure 7.8 Contour plot of LIM for 6 levels depicting passage of energetic microstructure centred at all scales of analysis. U=0.82 m/s, r/R=0.09, D=0.61 m, z=1.55 m, H_0=2 m, FCC IV.

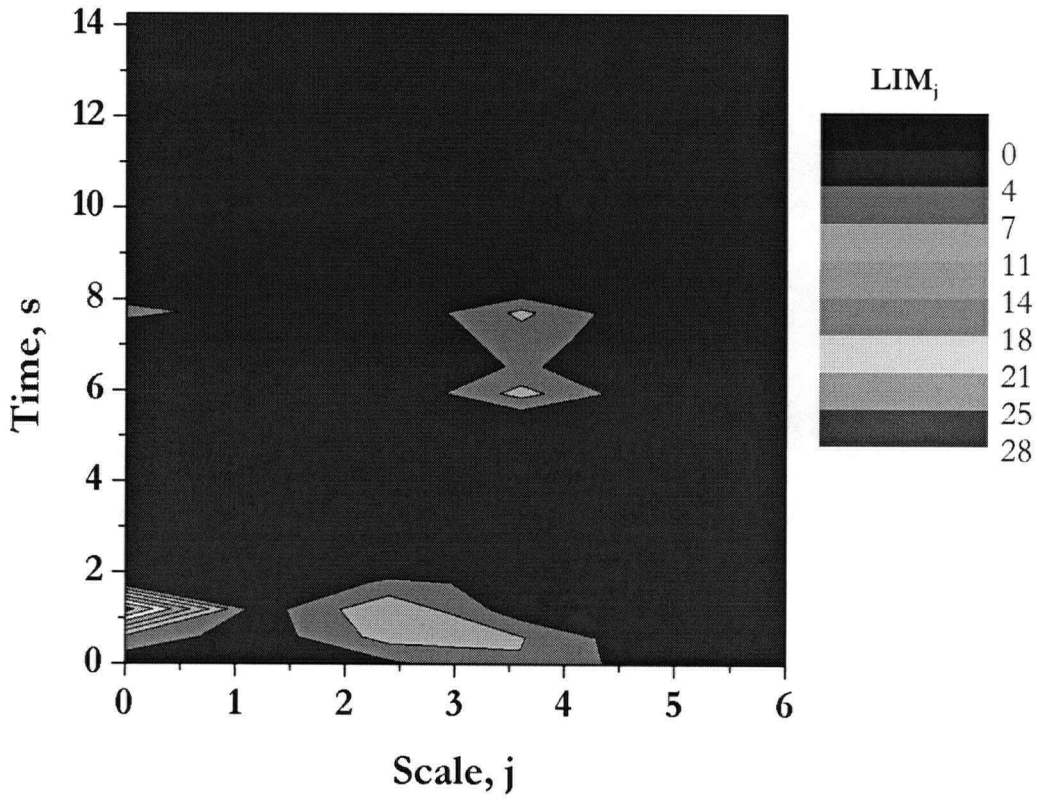

Figure 7.9 Contour plot of LIM for 6 levels depicting passage of energetic microstructure mostly at small scales of analysis. U=1.56 m/s, r/R=0.09, D=0.61 m, z=1.55 m, H_0=2 m, FCC IV.

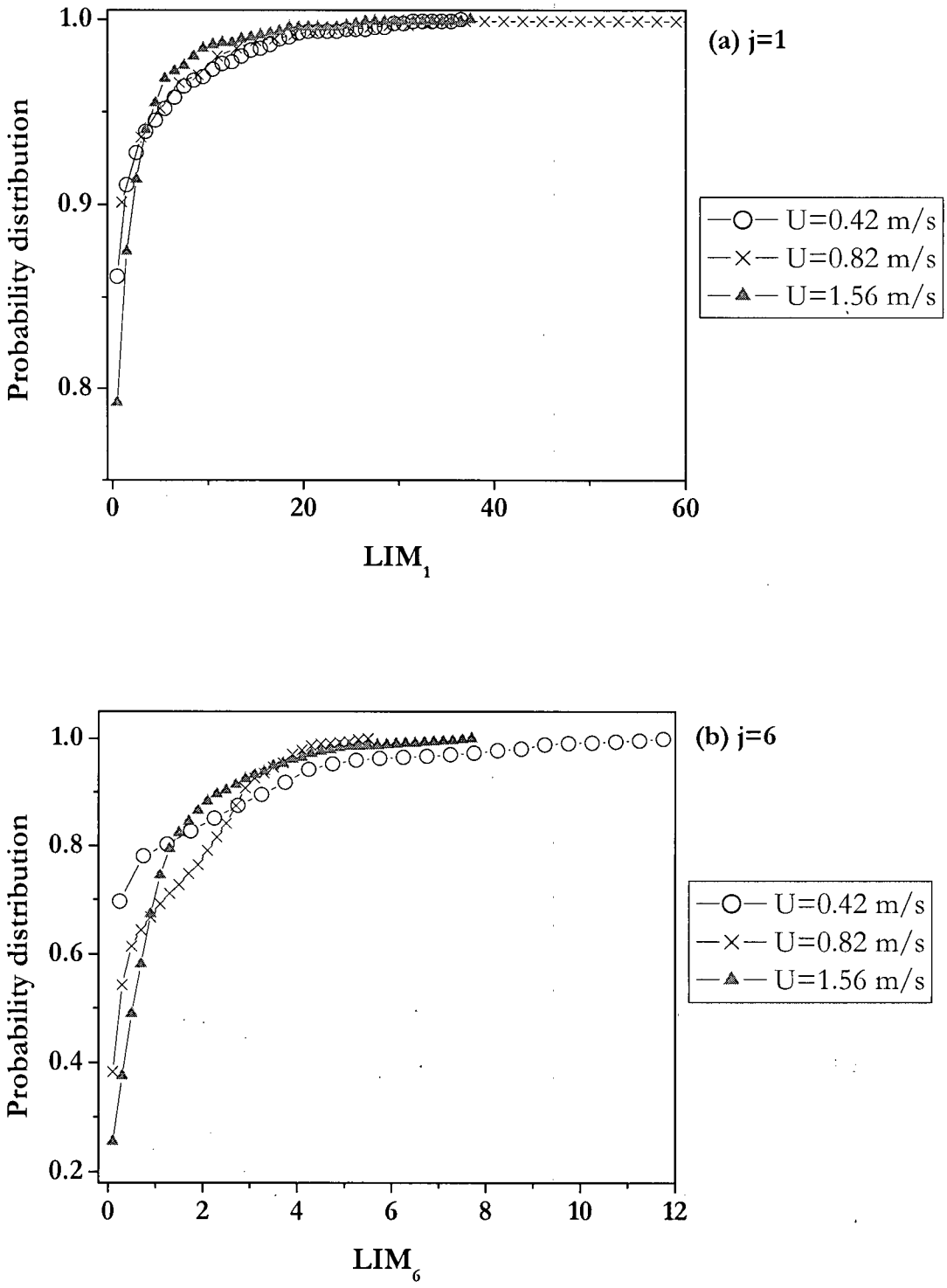

Figure 7.10 Effect of superficial gas velocity on probability distribution of LIM at: (a) level 1; and (b) level 6. D=0.61 m, r/R=0.09. z=0.80 m for U=0.42 m/s; z=1.55 m for U=0.82 and 1.56 m/s, H_0=2 m, FCC IV.

7.6.2.2 Wavelet analysis applied to voidage fluctuation

To gain better understanding of the signal fluctuations at the particle level, data from the optical velocity probe sampled at 7333 Hz are analyzed using the Daubechies wavelet 5. The local intermittency measure, LIM_j, at scale j=1 and 6 is compared for three superficial gas velocities, 0.57, 0.82 and 1.56 m/s, for r/R=0.09 in Figure 7.11 (a) and (b). At the larger scale, the three distributions are very similar. However at the small scale, the energy variation due to particle voidage fluctuation increases with U as indicated by the shift in the probability distribution of LIM_1 in Figure 7.11 (a).

As depicted by the voidage signals for three superficial gas velocities of 0.57, 0.82 and 1.56 m/s in Figures 7.12 (a), 7.13 (a) and 7.14 (a), respectively, the erratic voidage fluctuations at the measurement scale and frequency captured by the 0.26 mm diameter fiber increases with gas velocity. By employing the time localization capabilities of the wavelet analysis, a section from each gas velocity trace representing the dense phase is extracted from the LIM values. LIM values from 9.96 to 10.06 seconds in the time series are plotted in Figures 7.12 (b), 7.13 (b) and 7.14 (b). Increasing U towards U_c increases the LIM, particularly at the smallest scale, i.e., j=1, and the larger scales of j=5 and 6. Increasing U beyond U_c results in the LIM distribution becoming increasingly uniform in the high-density phase near the column axis. Extending U to examine the distribution of LIM in clusters would be of great interest in bridging the transition between turbulent and fast fluidization flow regimes. Nevertheless, the energy variations in the high-density phase near the axis become increasingly homogeneous with increasing scale.

On the other hand, measurements near the wall reveal an increase in larger scale energy variations with increasing U as shown in Figures 7.15 (a) and (b). The significance of these findings can be associated with the increasing size of eddies near the wall, leading to higher energy dissipation affecting the larger scale of turbulence reflected by the higher energy variation at larger scale.

The time series of LIM_j for four different situations in a fluidized bed are shown in Figures 7.16 (a) through (d). The high LIM peaks are linked to indicate the presence of coherent structure corresponding to high energy level (Camussi and Guj, 1997). High-energy fluctuations are indicated at r/R=0.09, with the probe reflecting very fast movement of regions of different voidage, e.g. passing of fast voids. The energetic microstructure is shown at a small scale to pass near the axis while the larger scale is near the wall.

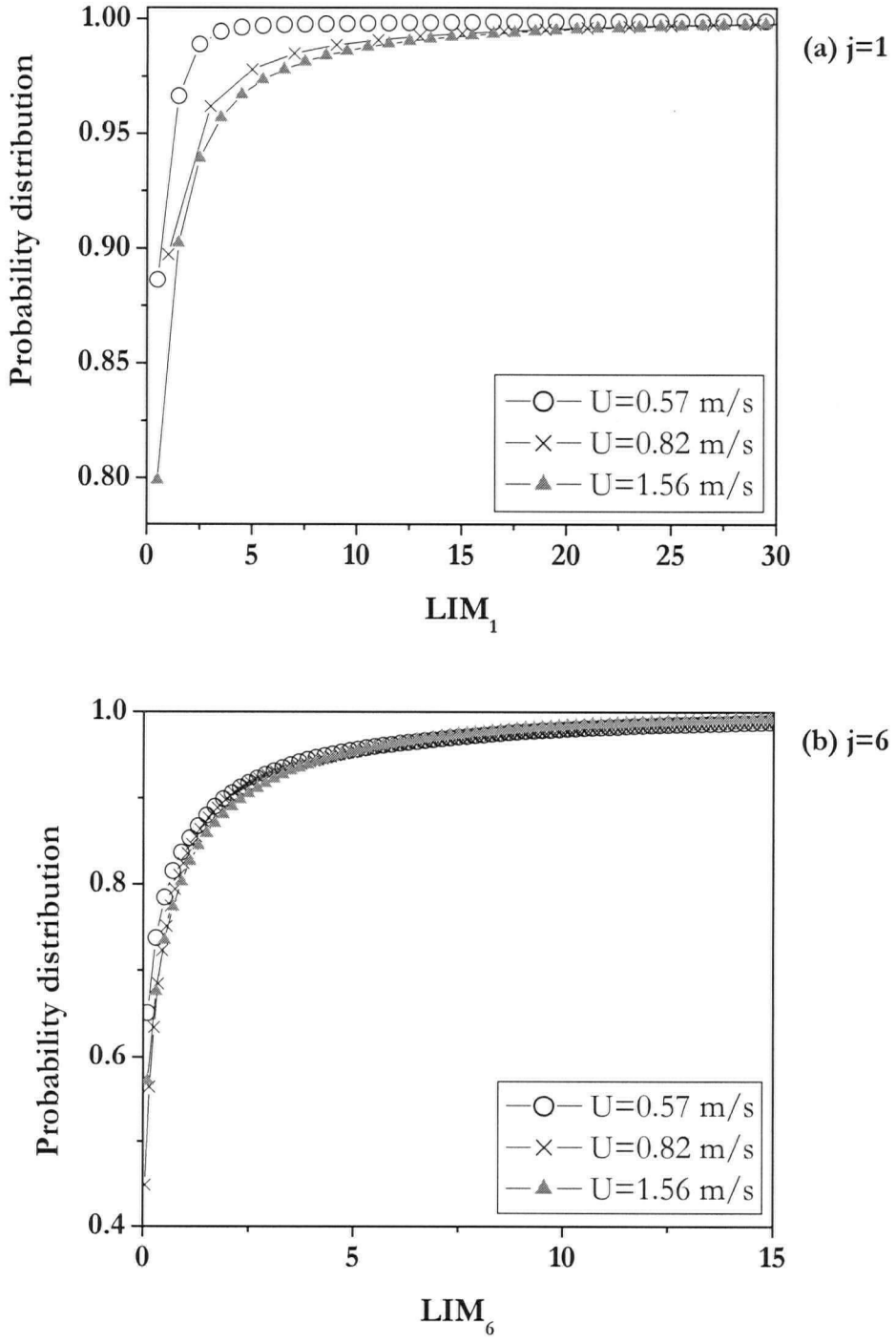

Figure 7.11 Effect of scale on probability distribution of LIM_j. D=0.61 m, r/R=0.09. z=0.80 m for U=0.42 m/s; z=1.55 m for U=0.82 and 1.56 m/s, H_0=2 m, FCC IV.

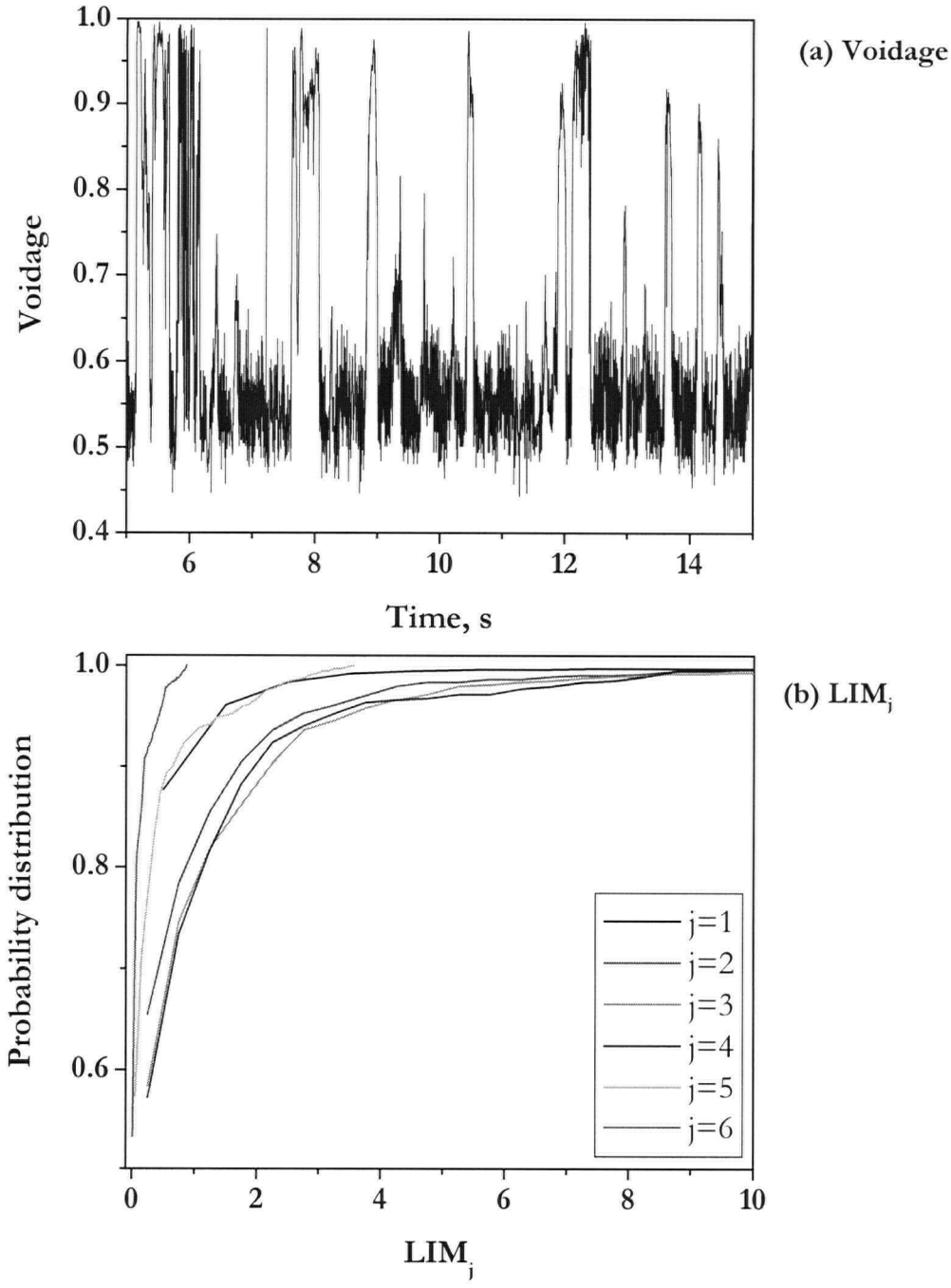

Figure 7.12 Voidage fluctuation signal from optical velocity probe and probability distribution of LIM at 6 scales. U=0.57 m/s, r/R=0.09, D=0.61 m, z=0.80 m, H_0=2 m, FCC IV.

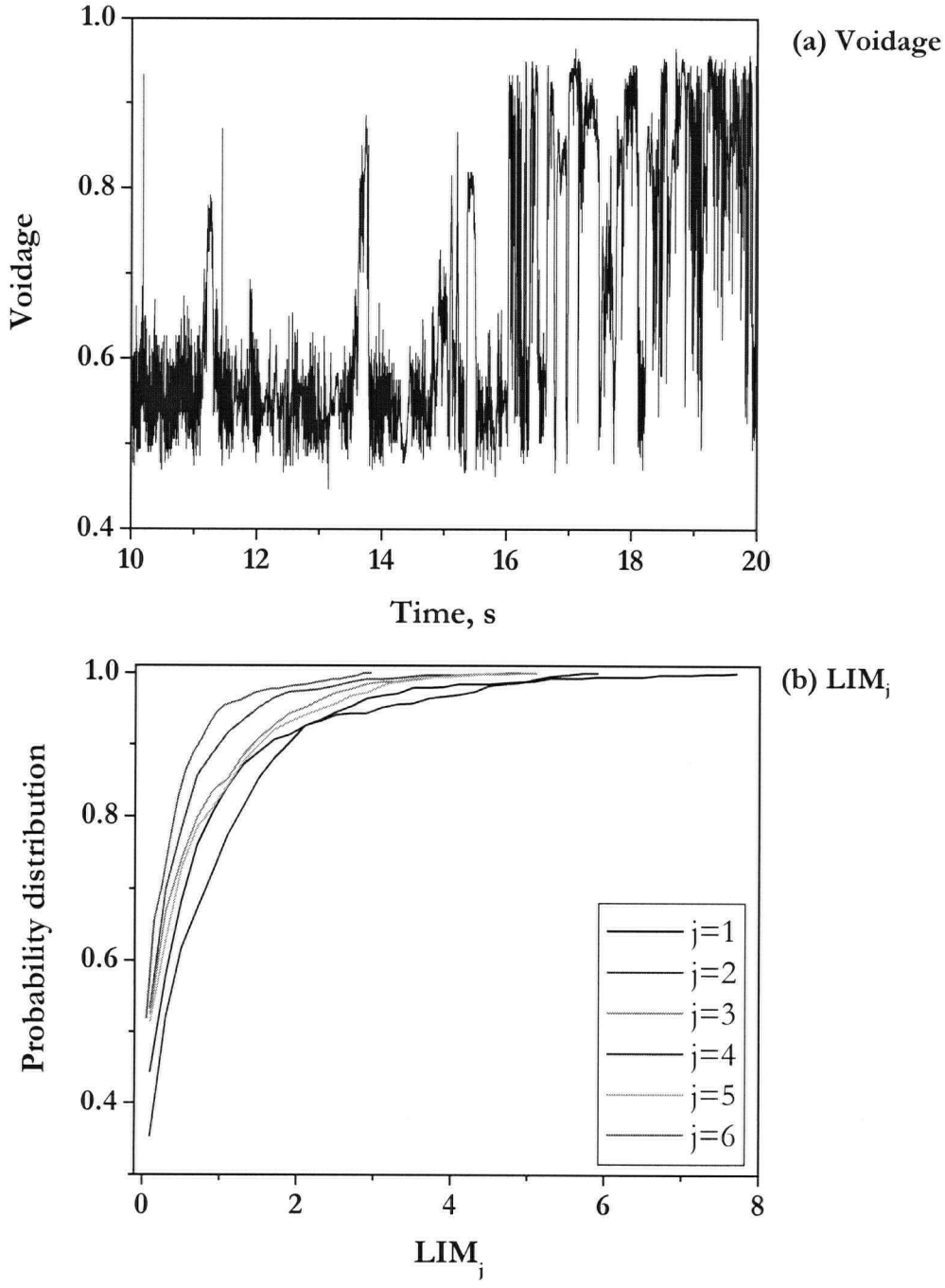

Figure 7.13 Voidage fluctuation signal from optical velocity probe and probability distribution of LIM at 6 scales. U=0.82 m/s, r/R=0.09, D=0.61 m, z=1.55 m, H_0=2 m, FCC IV.

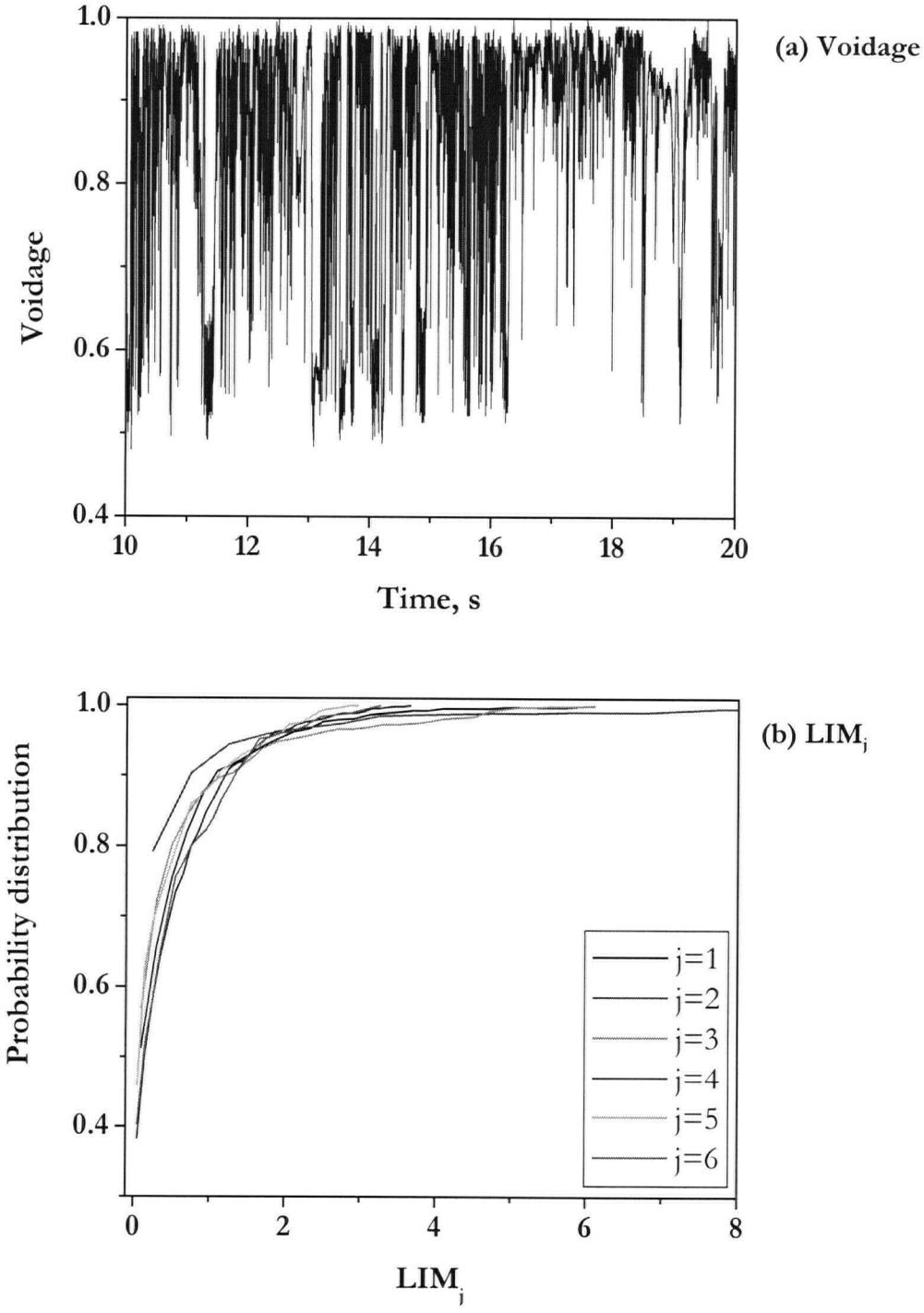

Figure 7.14 Voidage fluctuation signal from optical velocity probe and probability distribution of LIM at 6 scales. U=1.56 m/s, r/R=0.09, D=0.61 m, z=1.55 m, H_0=2 m, FCC IV.

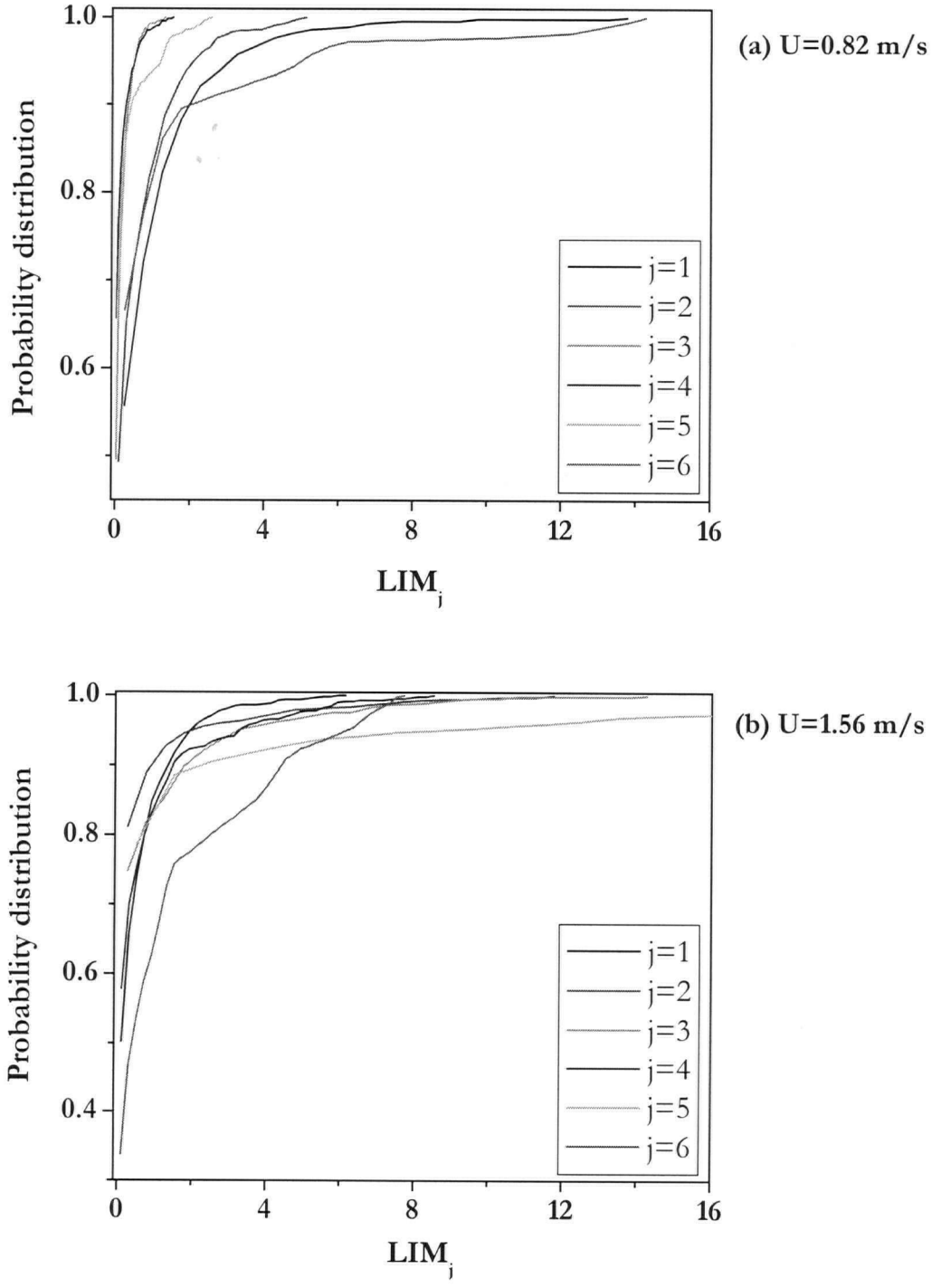

Figure 7.15 Effect of U on probability distribution of LIM at 6 scales for r/R=0.94. D=0.61 m, z=1.55m, H_0=2 m, FCC IV.

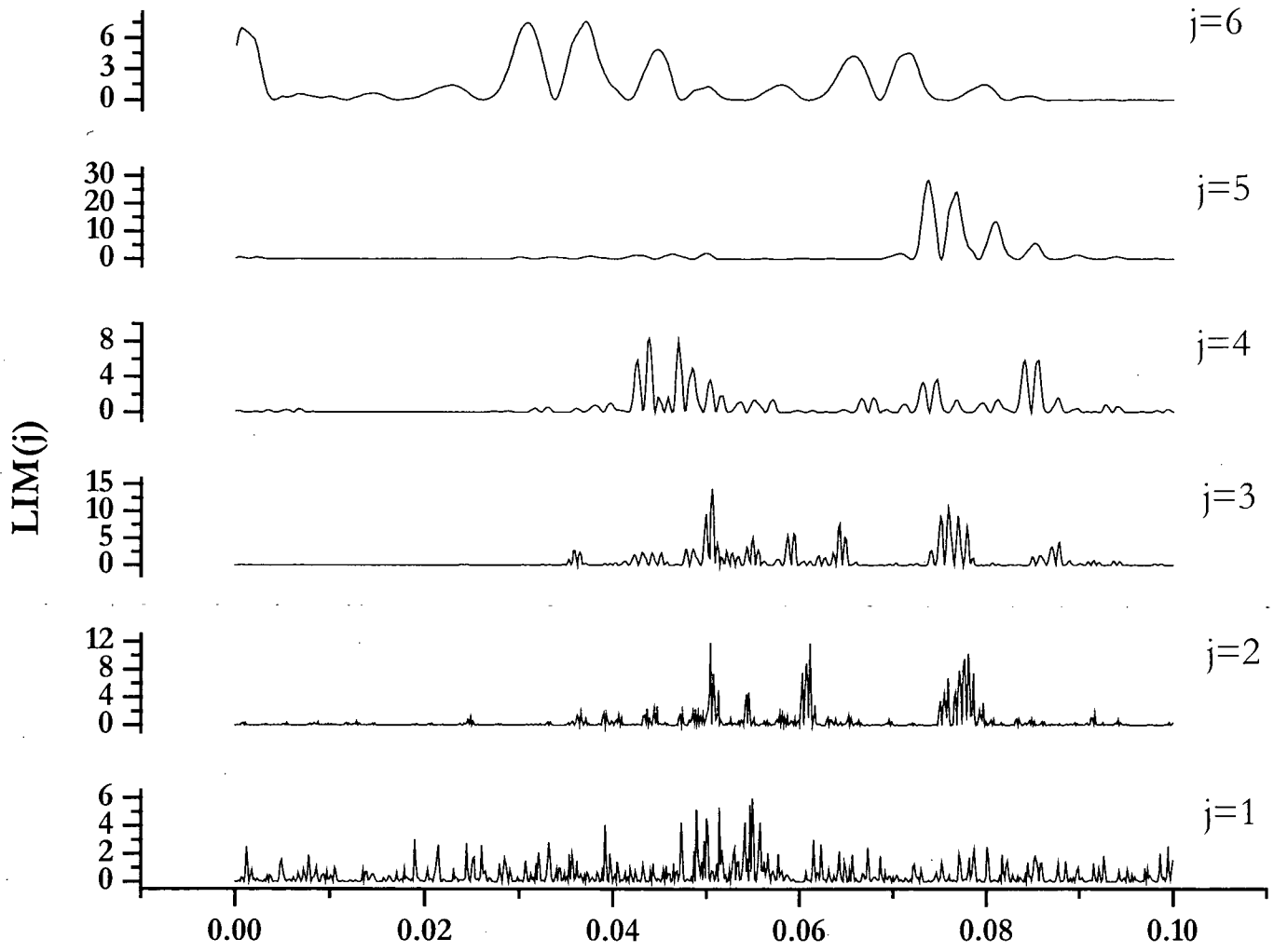
LIM(j)
6
3
0
j=6
30
20
10
0
j=5
8
4
0
j=4
15
10
5
0
j=3
12
8
4
0
j=2
6
4
2
0
j=1
0.00
0.02
0.04
0.06
0.08
0.10
Time, s

Figure 7.16 (a)

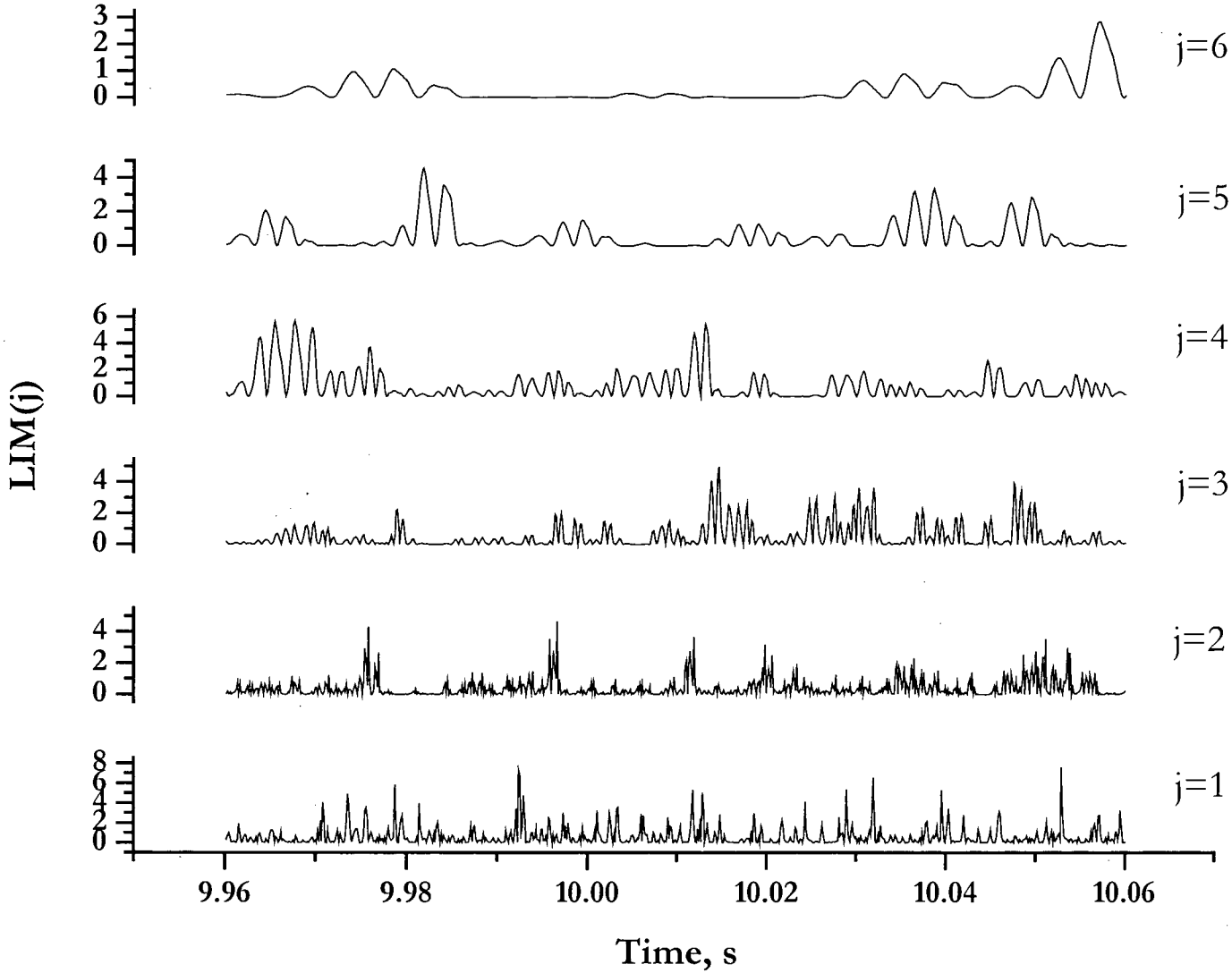

Figure 7.16 (b)

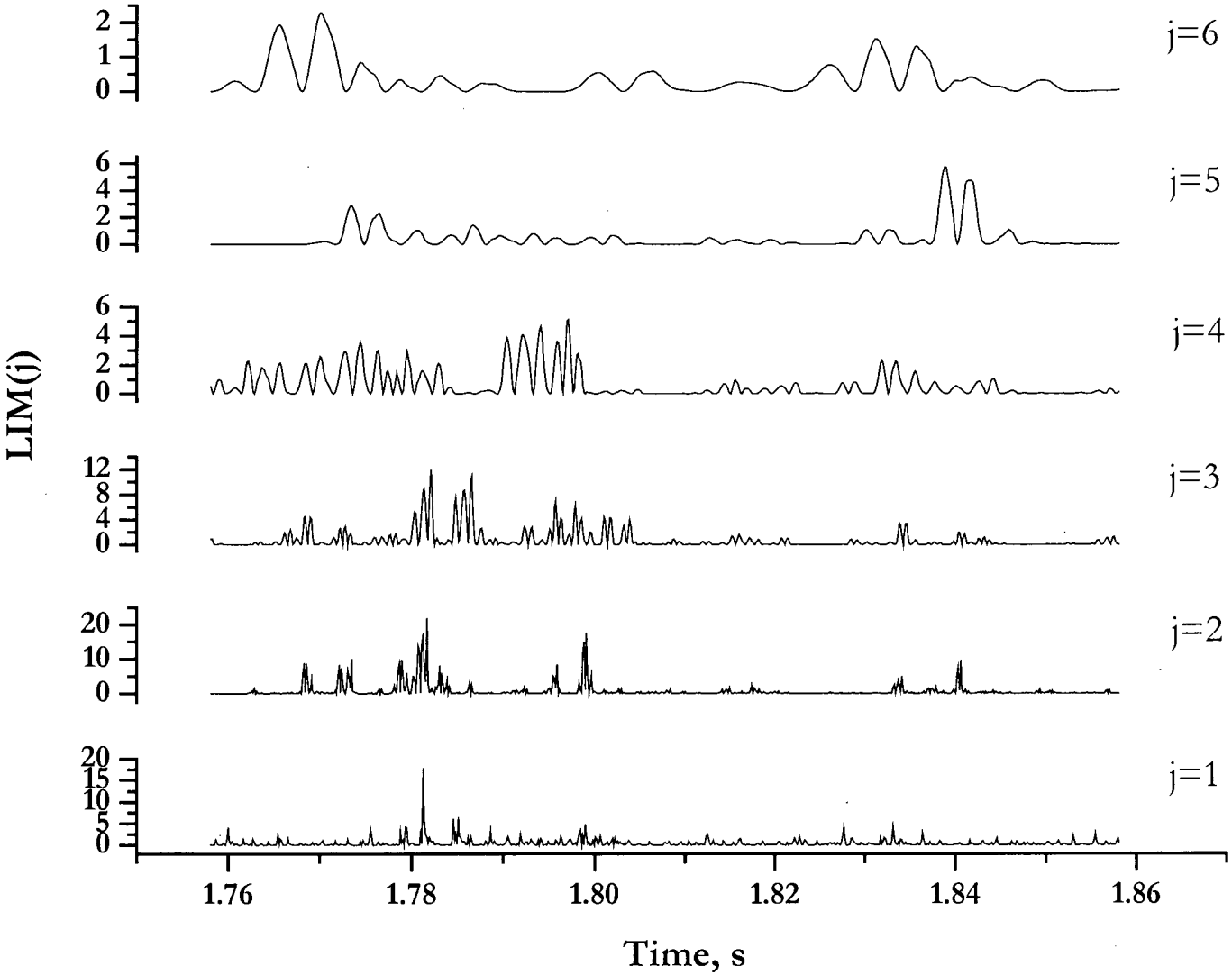
LIM(j)
2
1
0
j=6
6
4
2
0
j=5
6
4
2
0
j=4
12
8
4
0
j=3
20
10
0
j=2
20
15
10
5
0
j=1
1.76
1.78
1.80
1.82
1.84
1.86
Time, s

Figure 7.16 (c)

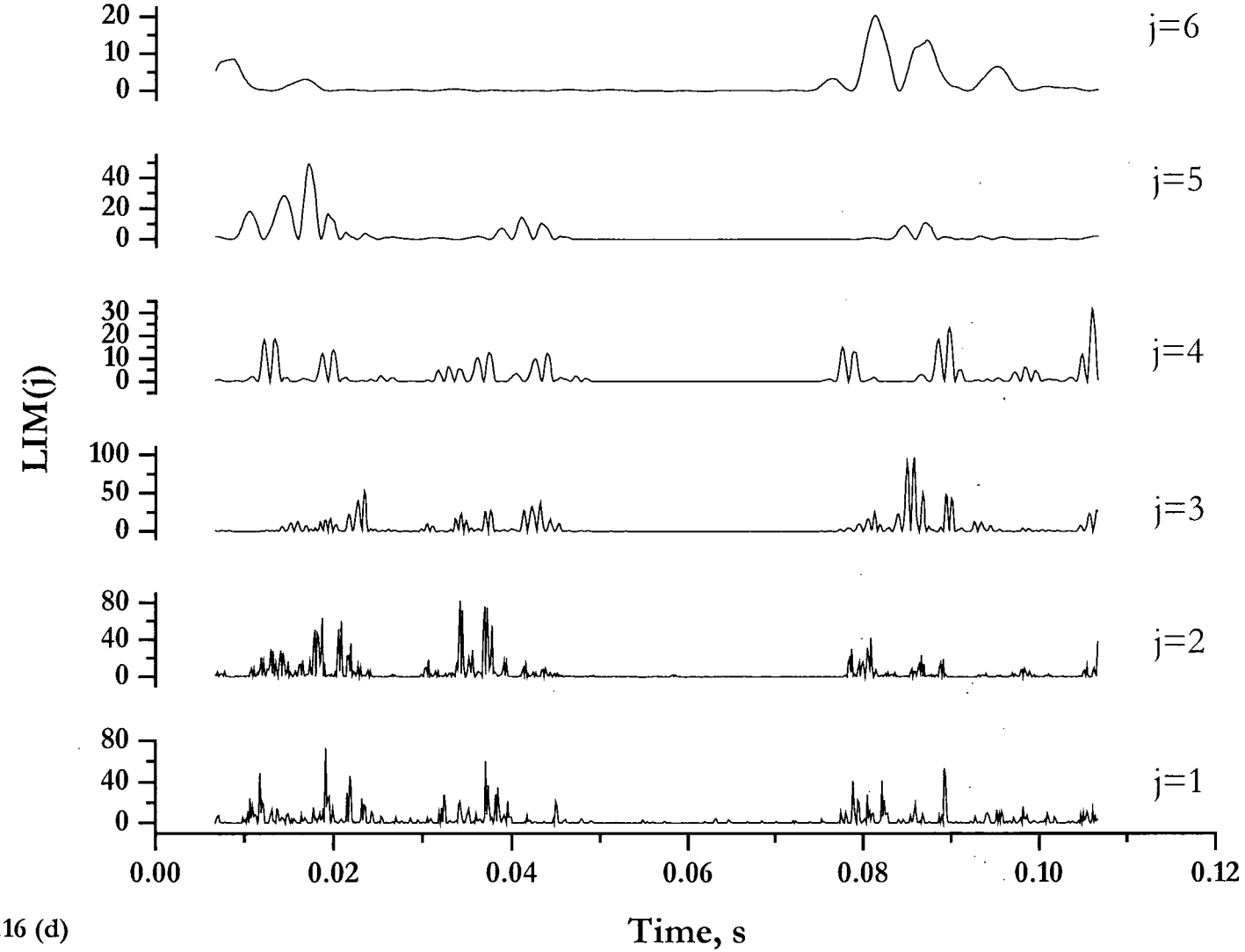

Figure 7.16 (d)

Figure 7.16 Comparison of LIM_j of 6 scales for probe in various radial position and phases: (a) r/R=0.94; (b) r/R=0.09, high-density phase; (c) r/R=0.09, low-density phase; (d) r/R=0.09, fluctuating phase. D=0.61 m, U= 1.56 m/s, z=1.55 m, H_0=2 m, FCC IV.

7.6.3 Qualitative analysis using wavelet

A more qualitative analysis is presented here based on wavelet transform. The scalogram of a decomposed signal on a wavelet provides information regarding the time and frequency variation of signals. Ross and Pence (1997) reported on the continuous wavelet transform using the Morlet wavelet of the heat transfer coefficients obtained in a bubbling bed of 345 μm particles. Bifurcating and trifurcating structures were revealed in the scalogram. Bakshi et al. (1995) used the wavelet packets basis in visualizing the contributing physical phenomena of local gas holdup signals in gas-liquid bubble columns. Time- and scale-localized energy distributions were shown to provide a rigorous tool in extracting phenomenological features of the flow. Moreover, wavelet analysis was shown to unify the interpretive results obtained through statistical, spectral and fractal analysis methods.

Continuous wavelet transform and the Morlet wavelet were applied to the voidage data to obtain wavelet coefficients. Figures 3.17 (a) and (b) display the scalogram based on a sampling frequency of 100 Hz for 100 s data, with U=0.32 and 1.0 m/s. The bright red colour indicates strong variations of signal fluctuation related to energy distribution. In the bubbling fluidized flow regime, e.g. Figure 7.17 (a), the voidage fluctuation dominates the energy distribution with minor amounts of energy distribution in the higher frequency range. Comparison of the two figures shows increased energy at the higher frequency and more energy dissipation at lower frequency, while the extent of variations decreases with increasing frequency at U=1.0 m/s. In the flow regime of turbulent fluidization, the voids transfer energy erratically in various frequency ranges.

Figure 7.18 shows the energy dissipation during defluidization of the bed after the air supply has been cut off from the 1.56 m diameter column. Bursts of energy at lower frequency from the void dynamics are no longer present, and the energy is mostly dissipated at high frequency from particle fluctuation. The above analyses reveals the effectiveness of the continuous wavelet transform in displaying the properties of signals in a time-frequency domain and providing insights which aid physical interpretation.

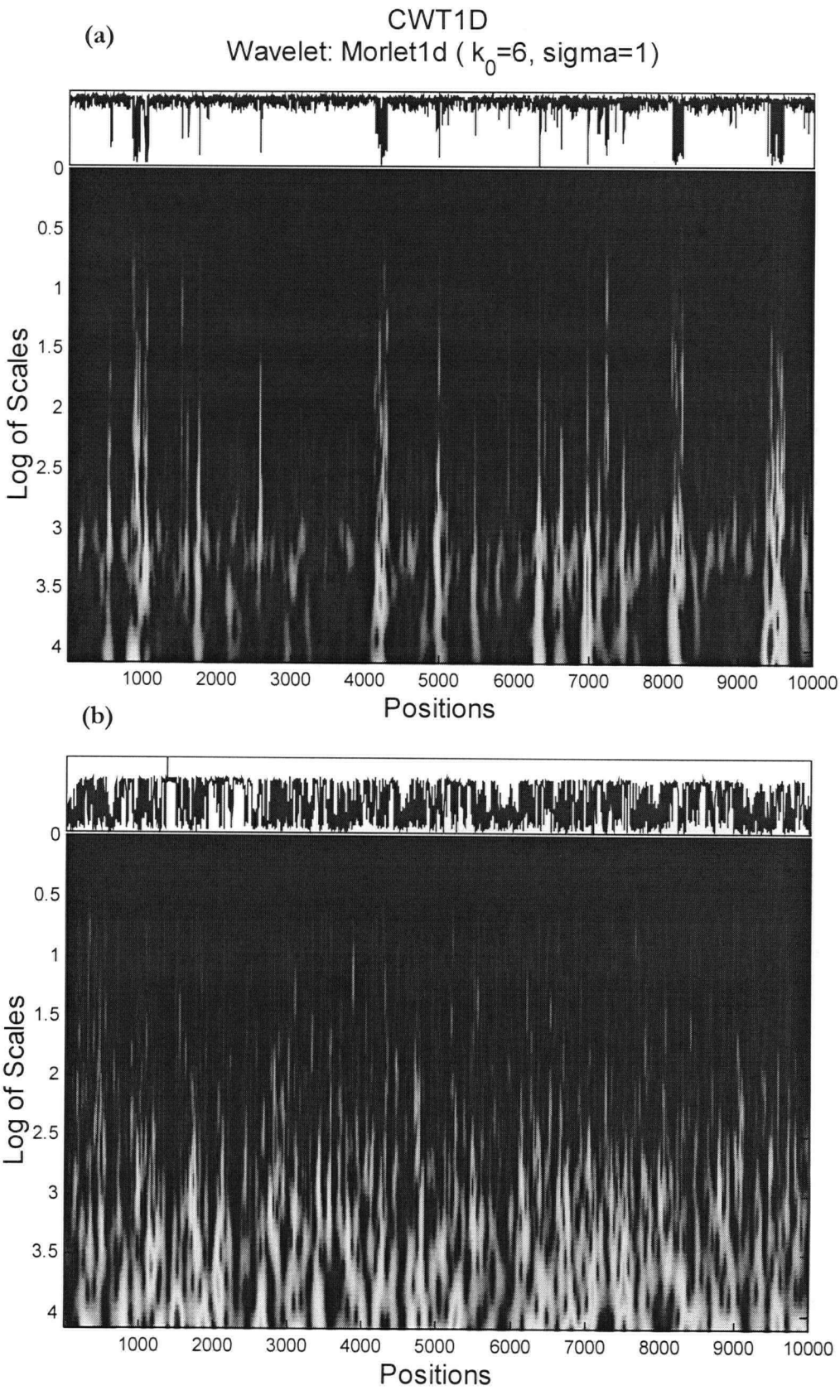

Figure 7.17 Continuous wavelet transform using Morlet wavelet. (a) U=0.32 m/s; and (b) 1.0 m/s. D=0.29 m, z=0.77 m, r/R=0.0. (lowest scale corresponding to 50 Hz)

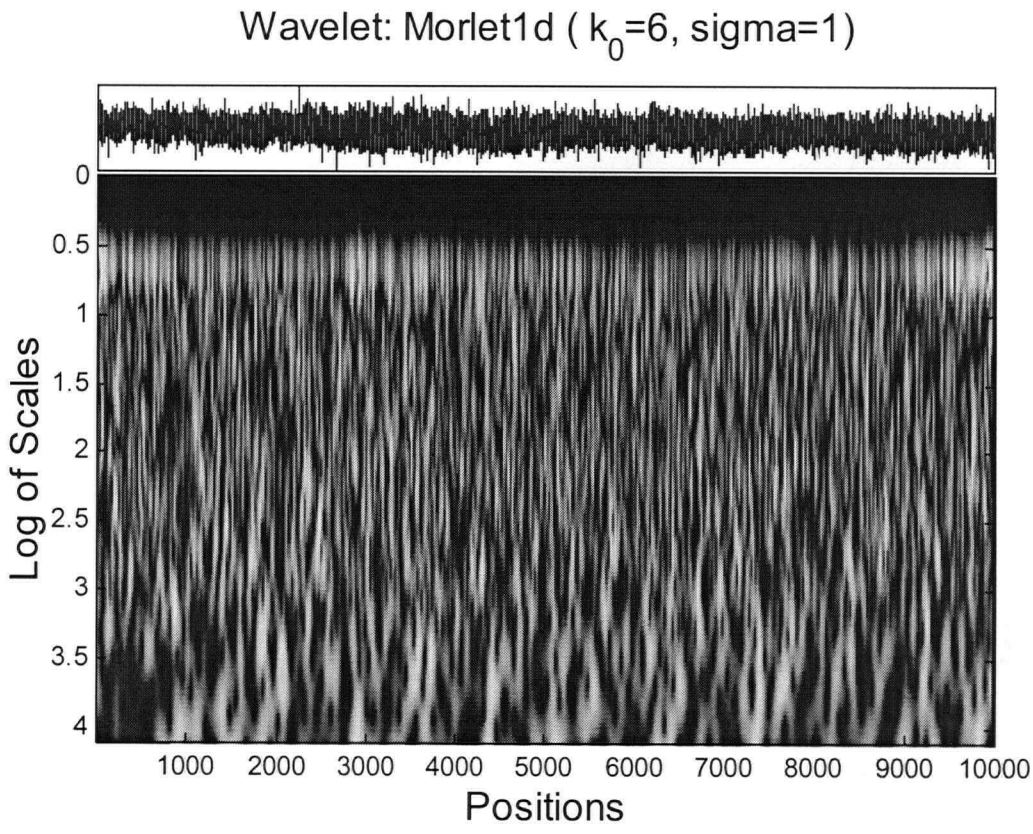

Figure 7.18 Distribution of energy in the time-frequency plane of voidage signal using continuous wavelet transform with Morlet wavelet during defluidization. D=1.56 m, r/R=0.5, z=0.84 m, H_0=2.0 m, FCC II.

7.7 Multiple scales in turbulent fluidized beds

As explained in Section 7.3, flow structures in fluidized beds can be divided into three different scales. The dynamic behaviour of solids and gas influences the interactions at different scales and under different operating conditions.

At the macroscale, the axial voidage distribution indicated a smooth transition from the bed to the freeboard, as shown in Figure 2.17. The expanded bed height was greatly influenced by the configuration of the solids collection and return system. At the macroscopic level, the radial voidage distribution, as depicted in Figure 4.34, exhibited heterogeneity. The turbulent fluidization flow regime at this scale clearly indicated a smooth transition between a bubbling regime and fast fluidization with the dense bed expanded by the increasing superficial gas velocity, while an increasing fraction of the solids inventory was transferred to the freeboard.

On the meso-scale, void dynamics prevail in the turbulent fluidization flow regime. The rise and fall of pressure fluctuations correspond to occurrences of void coalescence and splitting. As depicted in Figure 6.30 (a), the cycle time obtained from DP signals through rescaled range analysis indicated a shift at $U > U_c$. This may suggest that at a certain height above the distributor plate, void splitting becomes increasingly dominant over coalescence. Furthermore, the increased overall voidage at $z/H > 0.5$ from pressure drop measurements, plotted in Figure 2.13, and the decrease in standard deviation of voidage fluctuations from optical probe measurements, shown in Figure 4.20, suggest an increasingly diffuse bed subject to high frequency voidage fluctuations. This is also consistent with the average void frequency, shown in Figure 5.20. Note that the amplitude of such fluctuations decreased with increasing voidage as U was increased, resulting in a decrease in pressure fluctuations for $U > U_c$. The homogeneity of the bed, an often-cited characteristic of the turbulent fluidization flow regime, originates from the breakdown of the two-phase structure, i.e., dense and dilute phases at the meso-scale, as shown in Figure 4.37. This breakdown occurred gradually with increasing U.

At the microscale, i.e., particle level, a significant number of upward particle velocities are indicated for $r/R=0.09$ and 0.50 with increasing U, as depicted in Figures 5.14 through 5.16. These particle velocities were associated with higher voidages, especially at $r/R=0.09$. The increase in voidage, i.e., interstitial gas between particles, may suggest less energy loss as a consequence of inelastic particle-particle collisions, and an increase in the turbulent energy of particles.

High frequency voidage fluctuations, as shown in Figure 7.14 (a) may be linked to the passage of high-energy structures according to Figure 7.16 (d) at the smaller scales, i.e., reflecting fluctuations at the particle level.

7.8 Conclusions

Numerous methods have been introduced (Motard and Joseph, 1994) to provide improved signal processing in contemporary science and engineering. All are aimed at analyzing and interpreting complex time series. Though it has not been possible to cover them all, some promising methods have been considered in this and the preceding chapters. In particular, multiresolution analysis has been introduced in this chapter and applied to local data from turbulent fluidized beds. The following observations are made:

- De-noising voidage fluctuation signals using a nonlinear wavelet transform through soft thresholding was successful in pre-conditioning the signal for cross-correlation of bivariate time series. *A priori* knowledge of the signal must be applied to set the appropriate criteria to eliminate certain frequencies and time domains of the signal. The successful application of this technique eliminates the necessity to set threshold values in distinguishing voidage signals from dense to dilute phases, as described in Chapter 5.
- The time- and frequency-localization capabilities of the wavelet transform enable further analysis of signal characteristics. Local intermittency measures defined to characterize energy distribution in space were applied to velocity and voidage fluctuations in turbulent fluidized beds, revealing the presence and passage of energetic microstructures with different scales. Multiresolution analysis must consider the physical scale for which the signal was obtained, as well as the frequency scale.
- Continuous wavelet transformation was applied to visualize the contributing physical phenomena, which can be extracted for further analysis.
- Multiresolution analysis can help in understanding the complex flow dynamics of fluidized beds. Preliminary indications of the applicability of wavelet transform for scalewise decomposition of signals from fluidized beds are promising. As stated by many wavelet researchers, e.g. Farge, 1992, wavelet transform can be regarded as a tool to better 'see' the phenomena, and from which to conduct further analysis leading to conclusions, rather than a method to present solutions to underlying phenomena.
- The presence of intermittency from velocity and voidage measurements can be qualitatively shown; however, there is no analogy to connect the observations to the flow structure.

Further studies

- Further investigations in applying wavelet transform to reveal complex dynamics in fluidized beds from specific scale related measurements and decomposition are required to contribute to the maturity of analysis methods in fluidization research.
- Multiscale analysis has recently been applied to the bivariate relationship between two time series (Arneodo et al, 1998; Whitcher, et al., 2000). This indicates progress in wavelet analysis, and the potential for further advanced analysis methods.

CHAPTER 8

CONCLUSIONS

From the extensive experimentation presented in this work involving measurements of gauge and differential pressure, voidage and particle velocity fluctuations as functions of gas velocity at ambient temperature, at elevated pressure and temperature, and in four columns of different diameters, a number of conclusions have been drawn. The underlying idea of understanding the complex flow in the turbulent fluidized bed from the perspective of gas-solids transient flow has been explored. As a way of tackling this complexity and gaining insight into the mechanisms involved, various analysis methods have been employed. The findings are collectively summarized in this chapter.

Differences of opinion persist with respect to what constitutes the turbulent fluidized bed flow regime, even after 20 years of work by industrial and academic researchers. Furthermore, and perhaps because of that, definitions of transition on both ends of the turbulent fluidized bed flow regime still fuel heated discussions at fluidization conferences. Once, at an international chemical engineering congress, I was asked about my philosophical view of these transitions as a young researcher getting into this field. Displaying common objective propositions happens far too infrequently. As a result, reports characterizing turbulent fluidization lack standardization on reporting methods and do not display acceptance of some common perspectives. For example, hydrodynamic characteristics are still reported by some for units considered to be operated as turbulent fluidized beds from observing breakdown of voids solely by visual observations or through X-rays. Common understanding of key operating parameters affecting hydrodynamics and operations should be sought in the quest for substantiating past findings and advancing knowledge in this field. The realization of the lack in standardized terminology, on system characterization and experimental methodology was apparent through surveying the literature, and thus served as a starting point for this research project.

Key conclusions are summarized as follows.

- The transition velocity, U_c, was defined as the superficial gas velocity at which the standard deviation of pressure fluctuations attains a maximum, and was found to decrease as the column diameter increased from 0.29 m through 0.61 m to 1.56 m, and with decreasing initial

static bed height. Results indicated a different trend in U_c between shallow ($H/D < 3$) and deep beds ($H/D \geq 3$). Correlations are proposed for high H/D as:

$$Re_c = 0.371\ Ar^{0.742}$$

and for low H/D as:

$$Re_c = 0.459\,Ar^{0.454}\left(\frac{H}{D}\right)^{0.183\ln(d_p \rho_s)+0.83}$$

These equations are for Geldart Group A particles with U_c deduced from gauge pressure fluctuations.

- U_c from differential pressure signals was found to increase as the location of the sensor descended towards the distributor plate. This implies that homogeneity of the fluidized bed was attained at the top of the bed first, before the rest of the bed reached the turbulent fluidization flow regime as the superficial gas velocity increased. No conclusive correlation was obtained for predicting U_c from DP signals due to this height effect.

- The transition velocity decreased with increasing system pressure (up to 0.4 MPa), and with increasing temperature (up to 240°C), for a commercial catalyst. The correlation by Sun and Chen (1989) displayed better predictions of U_c for the conditions under investigation than the correlation of Cai et al. (1989). The effect of particle size distribution on U_c was well predicted by existing correlations based on Ar and Re_c numbers reflecting the change in mean particle size. However, discrepancy was observed when existing correlations were used to predict the effect of column diameter on U_c. The validity of the assumption that the wall measurements are representative of the cross-section and give the transition velocity applicable at the centre was confirmed experimentally.

- Axial pressure profiles indicated diffuse bed surfaces, with increasing gauge pressure in the freeboard with increasing superficial gas velocity due to solids entrainment. With an efficient solids return system, bed voidage in the 0.61 m diameter column remained at ~0.6, for operation in the turbulent fluidized flow regime. Increases in both the absolute pressure and bed temperature, investigated in the 0.11 m diameter column, caused increases in bed voidage, with pressure having a greater influence than temperature.

- Spectral analysis of pressure fluctuations revealed dominant peaks amongst a broad range of frequencies. The natural frequency of the bed based on gauge pressure signals decreased with increased bed height. FFT analysis of DP signals at different axial positions indicated a shift towards a lower frequency distribution with height, due to an increase in void size for $U < U_c$. This trend was confirmed by local measurements obtained by optical probes, based on the crossing frequency.

- A novel probe was employed to capture simultaneous measurements of local voidage and particle velocity in a turbulent fluidized bed of FCC particles. The results confirm previous reports that void movement is erratic and transient. Particle velocity fluctuations increased at $U > U_c$, indicating an increase in particle turbulence. Increasing U led to increasing migration of solids to wider range of voidages, and to increasing occurrence of upward particle velocities at the wall. Particle velocity fluctuations originate from collisions and other interactions between particles and from interactions with the gas phase. In a dense suspension, interparticle frictional forces dominate over kinetic and collisions forces. It is shown that particle velocity fluctuations increase for $U > U_c$. The trend can be explained as particles in the dense phase becoming increasingly spaced apart, gaining turbulence energy by higher fluctuations and having less energy loss as a consequence of inelastic particle-particle collisions. At U=1.56 m/s, there were more close-to-zero particle velocities and a shift to a higher voidage distribution. Since the optical velocity probe is only capable of capturing vertical velocities, an increased occurrence of near zero velocities may indicate increased radial movement of particles.

- The effect of solids flux from the return leg was found to be significant with respect to the hydrodynamics of the bed, especially for a larger column with a highest mass flux. In systems where the solids circulation rate is not controlled, it is difficult to characterize of the overall operating conditions in terms of bed expansion alone.

- Using identical optical probes, void velocity was calculated from the cross-correlation of signals. At $U > U_c$ determination of the threshold for removing dense-phase voidage fluctuation prior to cross-correlation became extremely sensitive to the resulting velocity distribution. This suggests that treating turbulent fluidized beds as two discrete phases, i.e., voids and dense phases, may not be applicable. A new method is proposed to remove high-

frequency voidage fluctuations from the signal based on a non-linear thresholding method involving wavelet transformation. This method eliminates the dependency on the threshold value in determining the void edge, and is seen to be successful in pre-conditioning the voidage signals for cross-correlation.

- In order to determine the cycle of void renewal in characterizing the change occurring at $U \approx U_c$ without differentiating between void and dense phases, rescaled range analysis was employed. The cycle frequency detected in voidage fluctuations exhibited a change in trend at $U \approx U_c$ with cycle frequencies comparable to those represented by the dominant frequency in the DP fluctuations. In addition, rescaled range analysis used to detect cycle times in pressure fluctuations provided a means of confirming the change in void dynamics with height. Cycle time from DP fluctuations for $U < U_c$ increased monotonically with increasing height, indicating general dominance in void growth. At $U > U_c$, an increase in cycle time occurred suggesting larger voids closer to the distributor plate until a decreasing trend emerges higher in the bed. This may suggest relative dominance of void splitting at the higher levels.

- Wavelet analysis provided an excellent means of time-frequency localization of signals. The local intermittency measure (LIM) calculated based on wavelet coefficients was shown to describe the non-uniform distribution of energy resolved in time and frequency. The strong velocity gradient considered can be characterized by coherent vortical structures. Thus, LIM can identify the passing of energetic structures. At $U > U_c$, the LIM near the column wall indicates more frequent passage of large-scale energetic structures. This may be due to increasing particle velocity fluctuations as particles respond to the movement of eddies generated near the wall. Wavelet transforms appear to be promising for scalewise decomposition of signals from fluidized beds.

- The coherence function characterizing the coherence between a set of signals at a given frequency was shown to decrease with increasing superficial gas velocity. In the turbulent fluidized bed exhibiting erratic void movements, the coherence function alone may not be sufficient to capture trends at different frequencies. The length scales of the phenomena of interest must be considered before making experimental measurements.

- A preliminary investigation was carried out to simulate a turbulent fluidized bed of FCC particles using a commercial CFD software package CFX, based on the two-fluid model. Due to time constraints, a successful simulation was not attained. Owing to the difficulty of conducting precise experimental measurements to obtain such coupling terms as solid stress, drag force, and energy dissipation as a result of particle collisions, it is very difficult to validate the parameters incorporated in the two-fluid model. Much work is needed to make CFD a viable tool for the simulation of hydrodynamics of turbulent fluidized beds.

NOMENCLATURE

A	cross-sectional area	m^2
AP	single-point pressure (referred to as gauge pressure)	kPa
Ar	Archimedes number, $= \frac{\varrho(\varrho_p - \varrho) g d_p^3}{\mu^2}$	-
a	wavelet scale in Equation C.14	-
a	approximate wavelet coefficient	-
a, b	coefficients in Equation 3.2	-
b	translation parameter in Equation C.14	-
C	signal capacitance	pF
C_0	capacitance without solids present	pF
C_D	drag coefficient	-
C_{Ds}	drag coefficient of a single sphere in an infinite expanse of fluid	-
$C_{I_1 I_2}$	covariance function	-
c	instantaneous particle velocity	m/s
D	column diameter	m
D_b	bubble diameter	m
DP	differential pressure	kPa
d	detailed wavelet coefficients	-
d_{cl}	cluster diameter in Table D.2	m
$d_{b,\,max}$	maximum bubble diameter	m
$d_{j,\,k}$	wavelet coefficient	-
d_p	mean particle diameter	m
d_{sm}	Sauter mean particle diameter	m
E	expected value	-
e	restitution coefficient	-
e_{eff}	effective coefficient of restitution	-
e_w	particle-wall restitution coefficient	-
Fr	Froude number based on U, $= U\sqrt{gD}$	-
Fr_c	Froude number based on U_c in Equation 3.14, $= U_c\sqrt{gD}$	-

f	sampling frequency	1/s
f_c	crossing frequency from Equation 6.10	1/s
f_c	crossing frequency in Table B.2 (with defined threshold value)	1/s
f_{DP}	major frequency from DP signals	1/s
f_d	volume fraction of dense phase in Table D.2	-
f_n	natural frequency from AP signals	1/s
G(f)	cross-spectral density function	
G(ε)	solid pressure function	
g	gravitational acceleration	m/s^2
g_0	radial distribution function for a uniform distribution of given mean porosity	
g^{J0-1}	detailed wavelet function	
g(r)	radial distribution function	
H	expanded bed height	m
H	Hurst exponent	-
H′	dense bed height corresponding to voidage at minimum fluidization	m
H_{max}	maximum bed expansion	m
H_{max}	maximum Hurst exponent	-
H_{min}	minimum Hurst exponent	-
H_0	initial static bed height	m
I	relative intensity of reflected light to reference light	-
I	identity tensor in Equation D.12	
$I_{A, B}(t)$	time series of relative light intensities from fibers A and B, respectively	-
i	time index	-
j	wavelet scale	-
K_{eff}	effective relative dielectric permittivity of a suspension in Equation 4.4	-
K_h	relative dielectric permittivity of host fluid	-
K_p	relative dielectric permittivity of particles	-
k	wavevector/translation parameter	
k	thermal conductivity	$W \cdot m^2 \cdot K$
k	unit vector along line from centre of particle 1 to 2 in Equation D.20 and D.21	

k_0	number of levels corresponding to scale	-
$L^2(I)$	set of square-integrable functions on the interval, I, defined in Equation 6.1	
LIM	local intermittency measure defined in Equation 7.4	
M	largest resolvable wavelet scale	
M_b	mass of solids in the dense bed	kg
M_s	mass of solids	kg
m	mass of particles in Equation D.14	kg
max(j)	maximum number of levels of wavelet decompositions in Equation 7.5	-
m_i	thermodynamic mass transfer term in Equation D.7	$kg/m^3 \cdot s$
m_s	particle mass loading: mass of particles/mass of gas in computational domain	-
N	number of data points analyzed in time series/group number	-
N	number of vanishing moments in wavelet	-
n	number of determinants	
n	coefficient used in Equation 2.1	-
P	pressure	kPa
Pg	gauge (single point) pressure	kPa
P_τ	P statistic defined in Equation 6.15	$s^{-\gamma}$
Q_c	volumetric flow rate at which standard deviation of pressure fluctuation reaches a maximum	kg/m^3
Q_s	constant charge amplitude	Coulombs
r	radial coordinate	m
R	column radius	m
Re_c	Reynolds number based on U_c, $= \frac{d_p \varrho_g U_c}{\mu_g}$	-
Re_c	Reynolds number in dense phase in Table D.2	-
Re_D	Reynolds number based on column diameter, $= \frac{D \varrho_g U}{\mu_g}$	-
Re_f	Reynolds number in dilute phase in Table D.2	-
Re_p	particle Reynolds number, $= \frac{d_p \varrho_g U}{\mu_g}$	-

Re_p'	particle Reynolds number based on relative velocity, $= \frac{d_p \varrho_g \lvert \upsilon_g - \upsilon_s \rvert}{\mu_g}$	-
Re_λ	Taylor microscale turbulent Reynolds number	-
$R(t, \tau)$	range over the subperiod, τ, defined in Equation 6.13	
R_T	regularity of cycle time defined in Equation 6.16	
$(R/\sigma)_\tau$	rescaled range for the subperiod of length τ	
Sr	Strouhal number based on dominant frequency, $=f_{DP}H/U_c$	
St	Stokes number, τ_p / τ_η	-
sigma	moment of wavelet function	-
T	temperature	°C
T_c	time required for distance between particles to return to original value	s
T_n	time scale in Equation D.23	s
T_r	relaxation time in Equation D.23	s
U	superficial gas velocity	m/s
U_c	transition velocity at which standard deviation of pressure fluctuations attains a maximum	m/s
U_c	superficial gas velocity in dense phase in Table D.2	m/s
U_f	superficial gas velocity in dilute phase in Table D.2	m/s
U_{dc}	superficial particle velocity in dense phase	m/s
U_{df}	superficial particle velocity in dilute phase	m/s
U_{gc}	superficial gas velocity in dense phase	m/s
U_{gf}	superficial gas velocity in dilute phase	m/s
U_k	superficial gas velocity corresponding to levelling out of pressure fluctuation amplitude with increasing U	m/s
U_{mb}	minimum bubbling velocity	m/s
U_{mf}	minimum fluidization velocity	m/s
U_p	velocity vector of particles	m/s
U_t	particle terminal settling velocity	m/s
U_t^*	effective cluster terminal velocity	m/s
U_{tr}	transport velocity	m/s
V	voltage signal	V
V_0	optical fiber signal in black box	V

V[k]	Fourier transformation of x[n]	
V_{mf}	optical fiber signal of dense bed/packed state	V
V_r	ratio of terminal velocity of a group of particles to that of an isolated particle	-
V_τ	V statistic defined in Equation 6.14	$s^{-0.5}$
v_g	gas velocity	m/s
v_s	particle velocity	m/s
$w_j(k)$	wavelet coefficient	
w[n]	window function in Equation C.6	
x	time series data value	
x(i)	signal	
$x_j(i)$	wavelet transform of x(i)	
Z	set of integers	-
z	axial distance above distributor	m
z	coordinate in direction of flow	m
z	statistic defined in Equation 3.8	
z_c	coefficient defined in Equation 3.12	
$\bar{z}$	average height between two ports from distributor plate	m

Symbols

β	fluid-particle friction coefficient	$kg/m^3 \cdot s$
β_i	regression parameters in Equation 3.4 (i=0, 1, 2)	-
γ	exponent for P statistic in Equation 6.15	-
γ_s	collision rate of dissipation per unit volume	-
$\gamma(\tau)$	autocorrelation function defined in Equation 6.6	-
γ^2_{xy}	coherence function defined in Equation 6.7	
ΔP	pressure drop	Pa
ΔP_{bed}	bed pressure drop extrapolated from gauge pressure profile	Pa
ΔP_{total}	total pressure drop	Pa
Δt	time interval	s
Δz	vertical separation between two ports/probes	m
$\Delta\omega$	frequency band	Hz
ε	voidage	-

ε_0	compaction gas phase volume fraction	-
$\overline{\varepsilon}$	time-mean voidage	-
ε_c	voidage corresponding to maximum standard deviation of pressure fluctuations	-
ε_c	voidage in dilute phase	-
ε_e	voidage at zero probability (lower limit of voidage)	-
ε_f	voidage in dense phase	-
ε_m	cross-sectional average voidage	-
ε_{mf}	voidage at minimum fluidization	-
ε_s	solids volume fraction	-
$\varepsilon_{s,\,max}$	maximum solids compaction fraction	-
ε_t	voidage signal as a function of time (Equation 4.6)	-
η	eddy size defined in Equation 7.1	m
Θ	granular temperature	m^2/s^2
φ	normalized radial coordinate in Equation 4.8, r/R	-
λ	threshold value used in Equation C.29	
λ_{mfp}	mean free path of particles	m
λ_s	solids bulk viscosity	Pa·s
μ_{cf}	coefficient of friction in Equation D.22	
μ_g	gas viscosity	Pa·s
μ_{g20}	gas viscosity at 20°C	Pa·s
μ_s	solids shear viscosity	Pa·s
ρ_g/ρ_f	gas density	kg/m^3
ρ_{g20}	gas density at 20°C and 0.1 MPa	kg/m^3
ρ_p/ρ_s	particle density	kg/m^3
ρ_{xy}	cross-correlation coefficient function	
σ	standard deviation defined in Equation 3.1	
σ	solids normal stress in Equation 2.2	Pa
τ	time lag	s
$\overline{\overline{\tau}}$	shear stress tensor	Pa
τ_c	characteristic time of autocorrelation function	s
τ_e	eddy time scale	s
τ_{Hi}	subperiods in Equation 6.12	

τ_p	particle response time	s
τ_{wg}	wall shear due to gas	Pa
τ_{ws}	wall shear due to solids	Pa
τ_η	Kolmogorov time scale	s
$\Phi_{I_A I_B}$	cross-correlation function	
$\Psi_j(k)$	Mother wavelet	
$\hat{\Psi}_j(k)$	wavelet function in frequency space	
ψ_0	wavelet basis function	
$\psi_j(k)$	wavelet function in time space	
$\Re$	set of real numbers $(-\infty,\infty)$	

Operations

[a,b)	half-open interval $\{x: a \leq x < b\}$
$\langle f, g \rangle$	L^2 inner product
$f \perp g$	functions f and g are orthogonal, i.e., $\langle f, g \rangle = 0$
∇	gradient
∇^T	transpose of gradient

Abbreviations

AP	single-point (gauge) pressure	kPa
CFB	circulating fluidized bed	
CFD	computational fluid dynamics	
COP	coherent-output power spectral density defined in Equation 6.9	
CSIRO	Commonwealth Scientific and Industrial Research Organisation	
CWT	continuous wavelet transformation	
db	Deubechies wavelet	
DEM	discrete element method	
DP	differential pressure	kPa
FCC	fluid cracking catalyst	
FFT	fast Fourier transformation	
ID	internal diameter	m
IOP	incoherent-output power spectral density defined in Equation 6.10	

LIM	local intermittency measure defined in Equation 7.4	
OD	outside diameter	m
PSD	particle size distribution	
UBC	University of British Columbia	

Subscripts

b	bubble
g	gas
p	particle
R	range
s	solids
x	time-series data
y	time-series data
τ	subperiod

REFERENCES

Abba, I.A., *A Generalized Fluidized Bed Reactor Model Across the Flow Regimes*, Ph.D. Dissertation, UBC, Vancouver, Canada (2001).

Abed, R., "The Characterization of Turbulent Fluid-Bed Hydrodynamics", in *Fluidization IV*, Ed. Kunii, D. and Toei, R., Engineering Foundation, pp.137-144 (1984).

Acree, R.C. and Louge, M., "Quantitative Capacitive Measurements of Voidage in Gas-Solid Flows", Particulate Sci. Tech., 7(1-2), 51-59 (1989).

Amos, G., Rhodes, M.J. and Benkreira, H., "Calculation of Optic Fibres Calibration Curves for the Measurement of Solids Volume Fractions in Multiphase Flows", Powder Tech., 88, 107-121 (1996).

Anderson, T.B. and Jackson, R., "A Fluid Mechanical Description of Fluidized Beds", Ind. Eng. Chem. Fundam., 8(1), 137-144 (1969).

Antoniadis, A. and Gijbels, I, "Detecting Abrupt Changes in Wavelet Methods", J. Nonparametric Stat., 14 (1-2), 7-29 (2002).

Arastoopour, H., "Numerical Simulation and Experimental Analysis of Gas/Solid Flow Systems: 1999 Fluor-Daniel Plenary Lecture", Powder Tech., 119, 59-67 (2001).

Argoul, F., Arneodo, A., Grasseau, G., Gagne, Y., Hopfinger, E.J. and Frisch, U., "Wavelet Analysis of Turbulence Reveals the Multifractal Nature of the Richardson Cascade", Nature, 338, 51-53 (1989).

Arneodo, A., Bacry, E., Manneville, S. and Muzy, J.F., "Analysis of Random Cascades Using Space-Scale Correlation Functions", Physical Review Letters, 80(4), 708-711 (1998).

Avidan, A.A., *Bed Expansion and Solid Mixing in High Velocity Fluidized Beds*, Ph.D. Dissertation, The City University of New York, New York (1980).

Avidan, A.A. and Yerushalmi, J., "Bed Expansion in High Velocity Fluidization", Powder Tech., 32, 223-232 (1982).

Bai, D., Bi, H.T. and Grace, J.R., "Chaotic Behavior of Fluidized Beds Based on Pressure and Voidage Fluctuation", AIChE J., 43, 1357-1361 (1997).

Bai, D., Issangya, A.S. and Grace, J.R., "Characteristics of Gas-Fluidized Beds in Different Flow Regimes", Ind. Eng. Chem. Res., 38, 803-811 (1999).

Bai, D., Masuda, Y., Nakagawa, N. and Kato, K., "Transition to Turbulent Fluidization in a Binary Solids Fluidized Bed", Can. J. Chem. Eng., 74, 58-62 (1996).

Baird, M.H.I. and Rice, R.G., "Axial Dispersion in Large Unbaffled Columns", Chem. Eng., J. 9, 171-174 (1975).

Bakshi, B.R., Zhong, H., Jiang, P. and Fan, L.-S., "Analysis of Flow in Gas-Liquid Bubble Columns Using Multi-Resolution Methods", Trans., I. Chem. E., 73, part A, 608-614 (1995).

Balzer, G. and Simonin, O., "Extension of Eulerian Gas-Solid Flow Modelling to Dense Fluidized Bed", in *Proc. 5th Int. Symp. on Refined Flow Modelling and Turbulence Measurements*, Ed. Viollet, P.L., Paris, pp. 417-424 (1993).

Baskakov, A.P., Tuponogov, V.G. and Filippovsky, N.F., "A Study of Pressure Fluctuations in a Bubbling Fluidized Bed", Powder Tech., 45, 113-117 (1986).

Batchelor, G.K., *The Theory of Homogeneous Turbulence*, Cambridge University Press, London (1967).

Bayle, J., Mege, P. and Gauthier, T., "Dispersion of Bubble Flow Properties in a Turbulent FCC Fluidized Bed", in *Fluidization X*, Ed., M. Kwauk, J. Li and W.-C. Yang, United Engineering Foundation, N.Y., pp. 125-132 (2001).

Bellino, I., Bergougnoux, L., Misguich-Ripault, J. and Firpo, J.-L., "Particle Size Effects on an Optical Fiber Sensor Response", Powder Tech., 115, 68-74 (2001).

Bendat, J.S. and Piersol, A.G., *Random Data: Analysis and Measurement Procedures*, Wiley-Interscience, New York (1971).

Benyahia, S., Arastoopour, H. and Knowlton, T., "Numerical Analysis of Two-Dimensional Transient Gas-Solid Flow in a Pneumatic Conveying Line and in a Fluidized Bed with a Central Jet", ASME Fluids Eng. Div. Summer Meeting FEDSM '97 (1997).

Bergougnoux, L., Firpo, J.-L. and Misguich-Ripault, J., "Optical Fiber Sensor for Measuring High Particle Concentrations", Powder Tech., 105, 413-417 (1999).

Bi, H. and Fan, L.-S., "Existence of Turbulent Regime in Gas-Solid Fluidization", AIChE J., 38(2), 297-301 (1992).

Bi, H.T. and Grace, J.R., "Effect of Measurement Method on the Velocities Used to Demarcate the Onset of Turbulent Fluidization", Chem. Eng. J., 57, 251-271 (1995).

Bi, H.T. and Su, P.-C., "Local Phase Holdups in Gas-Solids Fluidization and Transport", AIChE J., 47(9), 2025-2031 (2001).

Bi, H.T., Ellis, N., Abba, I.A. and Grace, J.R., "A State-of-the-Art Review of Gas-Solid Turbulent Fluidization", Chem. Eng. Sci., 55, 4789-4825 (2000).

Bi, H.T., Grace, J.R. and Zhu, J., "Propagation of Pressure Waves and Forced Oscillations in Gas-Solid Fluidized Beds and Their Influence on Diagnostics of Local Hydrodynamics", Powder Tech., 82, 239-253 (1995).

Bi, X., *Flow Regime Transitions in Gas-Solid Fluidization and Transport*, Ph.D. Dissertation, UBC, Vancouver, Canada (1994).

Bird, R.B., Stewart, W.E. and Lightfoot, E.N., *Transport Phenomena*, John Wiley and Sons, 2nd Ed. (2002).

Boemer, A., Qi, H., Renz, U., Vasquez, S. and Boysan, F., "Eulerian Computation of Fluidized Bed Hydrodynamics – A Comparison of Physical Models", in *Proceedings of the 13th International Conference on Fluidized Bed Combustion*, Orlando, vol. 2, pp. 775-787 (1995).

Bolio, E.J., Yasuna, J.A. and Sinclair, J.L., "Dilute Turbulent Gas-Solid Flow in Risers with Particle-Particle Interactions", AIChE J., 41(6), 1375-1388 (1995).

Bouillard, J.X., Lyczkowski, R.W. and Gidaspow, D., "Porosity Distributions in a Fluidized Bed with an Obstacle", AIChE J., 35, 908-922 (1989).

Box, G.E.P. and Jenkins, G.M., *Time Series Analysis: Forecasting and Control*, Holden-Day, San Francisco, Revised Ed. (1976).

Brereton, C.M.H. and Grace, J.R., "The Transition to Turbulent Fluidization", Trans IChemE, 70, part A, 246-251 (1992).

Briens, C.L., Bergougnou, M.A., Inculet, I.I., Baron, T. and Hazlett, J.D., "Size Distribution of Particles Entrained from Fluidized Beds: Electrostatic Effects", Powder Tech., 70, 57-62 (1992).

Briens, C.L., Mirgain, C., Bergougnou, M.A., Del Pozo, M. and Loutaty, R., "Evaluation of Gas-Solids Mixing Chamber Through Cross Correlation and Hurst's Analysis", AIChE J., 43(6), 1469-1479 (1997).

Briens, L.A. and Briens, C.L., "Cycle Detection and Characterization in Chemical Engineering", AIChE J., 48(5), 970-980 (2002).

Briens, L.A., Briens, C.L., Margaritis, A. and Hay, J., "Minimum Liquid Fluidization Velocity in Gas-Liquid-Solid Fluidized Beds", AIChE J., 43(5), 1180-1189 (1997).

Briens, L.A., *Identification of Flow Regimes in Multiphase Reactors by Time Series Analysis*, Ph.D. Thesis, Univ. of Western Ontario, London, Canada (2000).

Cai, P., Jin, Y., Yu, Z.-Q. and Wang, Z.-W., "Mechanism of Flow Regime Transition from Bubbling to Turbulent Fluidization", AIChE J., 36(6), 955-956 (1990).

Cai, P., Chen, Z.Q. and Wang, Z.W., "Effect of Operating Temperature and Pressure on the Transition from Bubbling and Turbulent Fluidization", AIChE Symp. Ser., 85(270), 37-43 (1989).

Cai, P., Jin, Y., Wang, Z. and Yu, Z., "Dynamic Pressure Tracking Technique for Collapsing Fluidized Bed Analysis", in *Fluidization '88 Science and Technology*, Third China-Japan Symposium, Ed. Kwauk, M. and Kunii, D., Beijing, pp. 82-87 (1988).

Cai, P., *The Transition of Flow Regime in Dense Phase Gas-Solid Fluidized Bed*, Ph.D. Dissertation, Tsinghua Univ., Beijing, and Ohio State University (1989).

Calis, H.P.A., Nijenhuis, J., Paikert, B.C., Dautzenberg, F.M. and van den Bleek, C.M., "CFD Modelling and Experimental Validation of Pressure Drop and Flow Profile in a Novel Structured Catalytic Reactor Packing", Chem. Eng. Sci., 56, 1713-1720 (2001).

Campbell, C.S. and Wang, D.G., "A Particle Pressure Transducer Suitable for Use in Gas-Fluidized Beds", Meas. Sci. Tech., 1, 1275-1279 (1990).

Campbell, C.S. and Wang, D.G., "Particle Pressures in Gas-Fluidized Beds", J. Fluid Mech., 227, 495-508 (1991).

Camussi, R. and Guj, G., "Orthonormal Wavelet Decomposition of Turbulent Flows: Intermittency and Coherent Structures", J. Fluid. Mech., 348, 177-199 (1997).

Carnahan, N.F. and Starling, K.E., "Equation of State for Nonattracting Rigid Spheres", J. Chem. Phys., 51, 635-636 (1969).

CFX 4.4 Solver, User Manual, CFX, AEA Technology, Harwell Laboratory, UK (2001).

Chainais, P., Abry, P. and Pinton, J.F., "Intermittency and Coherent Structures in a Swirling Flow: A Wavelet Analysis of Joint Pressure and Velocity Measurements", Phys. of Fluids, 11(11), 3524-3539 (1999).

Chaouki, J., Gonzalez, A., Guy, C. and Klvana, D., "Two-Phase Model for a Catalytic Turbulent Fluidized-Bed Reactor: Application to Ethylene Synthesis", Chem. Eng. Sci., 54, 2039-2045 (1999).

Chapman, S.C. and Cowling, T.G., *The Mathematical Theory of Non-Uniform Gases*, Cambridge Univ. Press, 3rd Ed. (1970).

Chatfield, C., *The Analysis of Time Series*, Chapman and Hall, London, 5th Ed. (1996).

Chehbouni, A., Chaouki, J., Guy, C. and Klvana, D., "Characterization of the Flow Transition between Bubbling and Turbulent Fluidization", Ind. Eng. Chem. Res., 33 1889-1896 (1994).

Chehbouni, A., Chaouki, J., Guy, C. and Klvana, D., "Effets de Differents Paramètres sur les Vitesses de Transition de la Fluidisation en Rēgime Turbulent", Can. J. Chem. Eng., 73, 41-50 (1995a).

Chehbouni, A., Chaouki, J., Guy, C. and Klvana, D., "Effect of Temperature on the Hydrodynamics of Turbulent Fluidized Beds" in *Fluidization VIII*, Ed. Large, J.-F. and Laguérie, C., Engineering Foundation, N.Y., pp. 149-156 (1995b).

Chen, R.C., Reese, J. and Fan, L.-S., "Flow Structure in a Three-Dimensional Bubble Column and Three-Phase Fluidized Bed", AIChE J., 40(7), 1093-1104 (1994).

Cheng, Y., Wei, F., Guo, Y.-C., Jin, Y. and Lin, W.-Y., "Modeling the Hydrodynamics of Downer Reactors Based on Kinetic Theory", Chem. Eng. Sci., 54(13-14), 2019-2027 (1999).

Chyang, C.-S. and Lin, Y.-C., "Influence of the Nature of the Roots Blower on Pressure Fluctuations in a Fluidized Bed", Powder Tech., 127, 19-31 (2002).

Clift, R., Grace, J.R. and Weber, M.E., "Stability of Bubbles in Fluidized Beds", IEC Funds., 13, 45-51 (1974).

Clift, R., Weber, M.E. and Grace, J.R., *Bubbles, Drops, and Particles*, Academic Press, New York (1978).

Cocco, R., Cleveland, J., Harner, R. and Chrisman, R., "Simultaneous In-Situ Determination of Particle Loading and Velocities in a Gaseous Medium", AIChE Symp. Ser., 91, no. 308, 147-153 (1995).

Cohen, A., Daubechies, I., Jawerth, B. and Vial, P., "Multiresolution Analysis, Wavelets, and Fast Algorithms on an Interval", Comptes Rendus Acd. Sci. Paris (A) 316, 417-421 (1993).

Crowe, C.T., "On Models for Turbulence Modulation in Fluid-Particle Flows", Int. J. Multiphase-Flow, 26, 719-727 (2000).

Cui, H., Li, J., Kwauk, M., An, H., Chen, M., Ma, Z. and Wu, G., "Dynamic Behaviours of Heterogeneous Flow Structure in Gas-Solid Fluidization", Powder Tech., 112, 7-31 (2000).

Cui, H., Mostoufi, N. and Chaouki, J., "Comparison of Measurement Techniques of Local Particle Concentration for Gas-Solid Fluidization", in *Fluidization X*, Ed. Kwauk, M., Li, J. and Yang, W.-C., United Engineering Foundation, Beijing, pp. 779-786 (2001).

Dasgupta, S., Jackson, R. and Sundaresan, S., "Turbulent Gas-Particle Flow in Vertical Risers", AIChE J., 40, 215-228 (1994).

Daubechies, I., *Ten Lectures on Wavelets*, Soc. for Industrial and Applied Mathematics, Philadelphia, PA (1992).

Daw, C.S. and Halow, J.S., "Characterization of Voidage and Pressure signals from Fluidized Beds Using Deterministic Chaos Theory", in *11th Int. FBC Conference: Clean Energy for the World*, Ed. Anthony, E.J., ASME, pp. 777-786 (1991).

Dencs, B., "Particle Velocity Measurements in Dense Fluidized Beds", Part. Part. Syst. Charct., 12, 314-317 (1995).

Dhodapkar, S.V. and Klinzing, G.E., "Pressure Fluctuations in Pneumatic Conveying Systems", Powder Tech., 74, 179-195 (1993).

Donoho, D.L., "Nonlinear Wavelet Methods for Recovery of Signals, Densities, and Spectra from Indirect and Noisy Data", in *Proc. of Symp. Appl. Math.*, Ed. Daubechies, I., American Math Soc., vol. 47, pp. 173-205 (1993).

Donoho, D.L., Johnstone, I.M., Kerkyacharian, G. and Picard, D., "Wavelet Shrinkage – Asymptopia", J. Royal Stat.Soc. Ser. B, 57(2), 301-337 (1995).

Drew, D.A. and Passman, S.L., *Theory of Multicomponent Fluids*, Springer, New York (1999).

Dunham, G.E., Mann, M.D. and Grewal, N.S., "Dependence of Transition to Turbulent Fluidization on Static Bed Depth in a Fluidized Bed", in *Preprints for the 4th International Conf. on CFB* (1993).

Edwards, M. and Avidan, A., "Conversion Model Aids Scale-up of Mobil's Fluid-Bed Process", Chem. Eng. Sci., 41(4), 829-835 (1986).

Ege, P.E., *Investigation of the Flow Structure in Turbulent Fluidized Beds*, Ph.D. Dissertation, University of Trondheim, Norway (1995).

Ellis, N., Lim, C.J., Grace, J.R., Bi, X.T., Lim, K.S., Joyce, T., Close, R. and Zakhari, A., "Scale-Up Effect on Transition Velocity and Voidage in Turbulent Fluidized Beds", in *Proc. 6th World Cong. of Chem. Eng.* (2001).

Enwald, H. Peirano, E. and Almstedt, A.-E., "Eulerian Two-Phase Flow Theory Applied to Fluidization", Int. J. Multiphase Flow, vol. 22, Suppl., pp. 21-66 (1996).

Ergun, S., "Fluid Flow Through Packed Columns", Chem. Eng. Prog., 48(2), 89-94 (1952).

Ettehadieh, B., Gidaspow, D. and Lyczkoski, R.W., "Hydrodynamics of Fluidization in a Semicircular Bed with a Jet", AIChE J., 30, 529-536(1984).

Fan, L.-S. and Zhu, C., *Principles of Gas-Solid Flows*, Cambridge Univ. Press (1998).

Fan, L.T., Hiraoka, S. and Shin, S.H., "Analysis of Pressure Fluctuations in a Gas-Solid Fluidized Bed", AIChE J., 30(2), 346-349 (1984).

Fan, L.T., Kang, Y., Neogi, D. and Yashima, M., "Fractal Analysis of Fluidized Particle Behavior in Liquid-Solid Fluidized Beds", AIChE J., 39(3), 513-517 (1993).

Farag, H.I., Ege, P.E., Grislingas, A. and de Lasa, H.I., "Flow Patterns in a Pilot Plant-Scale Turbulent Fluidized Bed Reactor: Concurrent Application of Tracers and Fibre Optic Sensors", Can. J. Chem. Eng., 75, 851-860 (1997a).

Farag, H.I., Mejdell, T., Hjarbo, K., Ege, P., Lysberg, M., Grislingås, A. and De Lasa, H., "Fibre Optic and Capacitance Probes in Turbulent Fluidized Beds", Chem. Eng. Comm., 157, 73-107 (1997b).

Farge, M., "Wavelet Transforms and their Applications to Turbulence", Annu. Rev. Fluid Mech., 24, 395-457 (1992).

Farge, M., Kevlahan, N., Perrier, V. and Goirand, E., "Wavelets and Turbulence", Proceedings IEEE, vol. 84, no. 4, 639-669 (1996).

Ferré, J.A. and Giralt, F., "Analysis of Turbulent Signals", in *Eddy Structure Identification in Free Turbulent Shear Flows*, Ed. Bonnet, J.P. and Glauser, M.N., Kluwer Academic Publishers, Netherlands, pp. 181-194 (1993).

Foka, M., Chaouki, J., Guy, C. and Klvana, D., "Gas Phase Hydrodynamics of a Gas-Solid Turbulent Fluidized Bed Reactor", Chem. Eng. Sci., 51(5), 713-723 (1996).

Formisani, B., Girimonte, R. and Pataro, G., "The Influence of Operating Temperature on the Dense Phase Properties of Bubbling Fluidized Beds of Solids", Powder Tech., 125, 28-38 (2002).

Geldart, D. and Rhodes, M.J., "From Minimum Fluidization to Pneumatic Transport —A Critical Review of the Hydrodynamics", in *Circulating Fluidized Bed Technology*, Ed. Basu, P., Pergamon Press, pp. 21-31 (1985).

Geldart, D., Ed., *Gas Fluidization Technology*, Wiley-Interscience Pub., New York (1986).

Gera, D., Gautam, M., Tsuji, Y., Kawaguchi, T. and Tanaka, T., "Computer Simulation of Bubbles in Large-Particle Fluidized Beds", Powder Tech., 98, 38-47 (1998).

Gidaspow, D. and Huilin, L., "Collisional Viscosity of FCC Particles in a CFB", AIChE J., 42(9), 2503-2510 (1996).

Gidaspow, D. and Huilin, L., "Equation of State and Radial Distribution Functions of FCC Particles in a CFB", AIChE J., 44(2), 279-293 (1998).

Gidaspow, D., "Hydrodynamics of Fluidization and Heat Transfer: Supercomputer Modeling", App. Mech. Rev., 39, 1-22 (1986).

Gidaspow, D., *Multiphase Flow and Fluidization. Continuum and Kinetic Theory Descriptions*, Academic Press, San Diego (1994).

Gilbertson, M.A. and Yates, J.G., "The Motion of Particles Near a Bubble in a Gas-Fluidized Bed", J. Fluid. Mech., 323, 377-385 (1996).

Goldschmidt, M.J.V., Kuipers, J.A.M. and van Swaaij, W.P.M., "Hydrodynamic Modelling of Dense Gas-Fluidised Beds Using the Kinetic Theory of Granular Flow: Effect of Coefficient of Restitution on Bed Dynamics", Chem. Eng. Sci., 56, 571-578 (2001).

Grace, J.R. and Sun, G., "Fines Concentration in Voids in Fluidized Beds", Powder Tech., 62, 203-205 (1990).

Grace, J.R. and Sun, G., "Influence of Particle Size Distribution on the Performance of Fluidized Bed Reactors", Can. J. Chem. Eng., 69, 1126-1133 (1991).

Grace, J.R., "Contacting Modes and Behaviour Classification of Gas-Solid and Other Two-Phase Suspensions", Can. J. Chem. Eng., 64, 353-363 (1986).

Grace, J.R., "Agricola Aground: Characterization and Interpretation of Fluidization Phenomena", AIChE Symp. Ser., 88, no. 289, pp. 1-16 (1992).

Grace, J.R., "Some Reflections on Turbulent Fluidization and Dense Suspension Upflow", Powder Tech., 113, 242-248 (2000).

Groen, J.S., Oldeman, R.G.C., Mudde, R.F. and Van Den Akker, H.E.A., "Coherent Structures and Axial Dispersion in Bubble Column Reactors", Chem. Eng. Sci., 51(10), 2511-2520 (1996).

Hage, B. and Werther, J., "Capacitance Probe Measurements of Solids Volume Concentrations and Velocities Inside an Industrial Circulating Fluidized Bed Combustor", AIChE Symp. Ser., 93, no.317, 55-60 (1997a).

Hage, B. and Werther, J., "The Guarded Capacitance Probe – A Tool for the Measurement of Solids Flow Patterns in Laboratory and Industrial Fluidized Bed Combustors", Powder Tech., 93, 235-245 (1997b).

Hartge, E.-U., Rensner, D. and Werther, J., "Solids Concentration and Velocity Patterns in Circulating Fluidized Beds", in *Circulating Fluidized Bed Technology II*, Ed. Basu, P. and Large, J.F., pp. 165-180 (1986).

Hartman, M., Trnka, O., Svoboda, K. and Vesely, V., "Turbulent Fluidization", Chemicke Listy, 95(9), 556-562 (2001). In Czech.

Hay, J.M., Nelson, B.H., Briens, C.L. and Bergougnou, M.A., "The Calculation of the Characteristics of a Chaotic Attractor in a Gas-Solid Fluidized Bed", Chem. Eng. Sci., 50(3), 373-380 (1995).

Herbert, P.M., Gauthier, T.A., Briens, C.L. and Bergougnou, M.A., "Application of Fibre Optic Reflection Probes to the Measurement of Local Particle Velocity and Concentration in Gas-Solid Flow", Powder Tech., 80, 243-252 (1994).

Hernández, J.A. and Jiménez, J., "Bubble Formation in Dense Fluidized Beds", Phys. Fluids A, 3(5), 1457 (1991).

Hetsroni, G., "Particle-Turbulence Interaction", Int. J. Multiphase Flow, 15(5), 735-746 (1989).

Hilborn, R.C., *Chaos and Nonlinear Dynamics: An Introduction for Scientists and Engineers*, Oxford Univ. Press (1994).

Hinze, J.O., "Turbulent Fluid and Particle Interaction", Prog. in Heat Mass Transfer, 6, 433-452 (1982).

Hinze, J.O., *Turbulence. An Introduction to Its Mechanism and Theory*, McGraw-Hill Book Co., New York (1959).

Hlawatsch, F. and Boudeaux-Bartels, G.F., "Linear and Quadratic Time-Frequency Signal Representations", IEEE Signal Processing Magazine, 9(2), 21-67 (1992).

Hoffmann, A.C. and Yates, J.G., " Experimental Observations of Fluidized Beds at Elevated Pressure", Chem. Eng. Comm., 41, 133-149 (1986).

Horio, M., Chapter 2, in *Circulating Fluidized Beds*, Ed. Grace, J.R., Avidan, A.A. and Knowlton, T.M., pp. 21-85 (1997).

Horio, M., Ishii, H. and Nishimuro, M., "On the Nature of Turbulent and Fast Fluidized Beds", Powder Tech., 70, 229-236 (1992a).

Horio, M., Mori, K., Takei, Y. and Ishii, H., "Simultaneous Gas and Solid Velocity Measurements in Turbulent and Fast Fluidized Beds", in *Fluidization VII*, Ed. Potter, O.E. and Nicklin, D.J., Engineering Foundation, N.Y., pp. 757-762 (1992b).

Hrenya, C.M. and Sinclair, J.L., "Effects of Particle-Phase Turbulence in Gas-Solid Flows", AIChE J., 43(4), 853-869 (1997).

Huilin, L., Gidaspow, D. and Bouillard, J.X., "Dimension Measurements of Hydrodynamic Attractors in Circulating Fluidized Beds", Powder Tech., 90, 179-185 (1997).

Hurst, H.E., "Methods of Using Long-Term Storage in Reservoirs", Trans. ASCE, 116, 770-808 (1951).

Ihme, F., Schmidt-Traub, H. and Brauer, H., "Theoretical Studies on Mass Transfer at and Flow Past Spheres", Chemie. Ing. Tech., 44(5), 306-613 (1972).

Ishii, M., *Thermo-Fluid Dynamic Theory of Two-Phase Flow*, Eyrolles, Paris, (1975).

Issangya A.S., Grace, J.R., Bai D. and Zhu J., "Further Measurements of Flow Dynamics in a High-Density Circulating Fluidized Bed Riser", Powder Tech., 111, 104-113 (2000).

Issangya, A.S., *Flow Dynamics in High Density Circulating Fluidized Beds*, Ph.D. Dissertation, UBC, Vancouver, Canada (1998).

Jackson, R., "Locally Averaged Equations of Motion for a Mixture of Identical Spherical Particles and a Newtonian Fluid", Chem. Eng. Sci., 52, 2457-2469 (1997).

Jenkins, J.T. and Savage, S.B., "A Theory for the Rapid Flow of Identical, Smooth, Nearly Elastic, Spherical Particles", J. Fluid Mech., 130, 187-202 (1983).

Jiang, P. and Fan, L.-S., "On the Turbulent Radial Transfer of Particles in a CFB Riser", in *Circulating Fluidized Bed Technology VI*, Ed. Werther, J., pp. 83-88 (1999).

Jin, Y., Yu, Z., Wang, Z. and Cai, P., "A Criterion for Transition From Bubbling to Turbulent Fluidization", in *Fluidization V*, Ed. Φstegaard, K. and Sϕrensen, A., Engineering Foundation, N.Y., pp. 289-296 (1986).

Johnsson, F., Larsson, G. and Leckner, B., "Pressure and Flow Fluctuations in a Fluidized Bed – Interaction with the Air-Feed System", Chem. Eng. Sci., 57, 1379-1392 (2002).

Johnsson, F., Svensson, A. and Leckner, B., "Fluidization Regimes in Circulating Fluidized Bed Boilers", in *Fluidization VII*, Eds. Potter, O.E. and Nicklin, D.J., Engineering Foundation, N.Y., pp. 471-478 (1992).

Johnsson, F., Zijerveld, R.C., Schouten, J.C., van den Bleek, C.M. and Leckner, B., "Characterization of Fluidization Regimes by Time-Series Analysis of Pressure Fluctuations", Int. J. Multiphase Flow, 26, 663-715 (2000).

Johnsson, H. and Johnsson, F., "Measurements of Local Solids Volume-Fraction in Fluidized Bed Biolers", Powder Tech., 115, 13-26 (2001).

Joshi, J.B., Vitankar, V.S., Kulkarni, A.A., Dhotre, M.T. and Ekambara, K., "Coherent Flow Structures in Bubble Column Reacotrs", Chem. Eng. Sci., 57, 3157-3183 (2002).

Judd, M.R. and Goosen, R., "Effects of Particle Shape on Fluidisation Characteristics of Fine Particles in the Freely Bubbling and Turbulent Regimes", in *Fluidization VI*, Ed. Grace, J.R., Shemilt, L.W. and Bergougnou, M.A., Engineering Foundation, N.Y., pp. 41-48 (1989).

Kage, H., Agari, M., Ogura, H. and Matsuno, Y., "Frequency Analysis of Pressure Fluctuation in Fluidized Bed Plenum and its Confidence Limit for Detection of Various Modes of Fluidization", Adv. Powder Tech., Int. J. Soc. Powder Tech. Japan, 11(4), 459-475 (2000).

Karamavruç, A.I. and Clark, N.N., "Local Differential Pressure Analysis in a Slugging Bed Using Deterministic Chaos Theory", Chem. Eng. Sci., 52(3), 357-370 (1997).

Katul, G., Vidakovic, B. and Albertson, J., "Estimating Global and Local Scaling Exponents in Turbulent Flows Using Discrete Wavelet Transformations", Physics of Fluids, 13(1), 241-250 (2001).

Kehoe, P.W.K. and Davidson, J.F., "Continuously Slugging Fluidised Beds" Chemeca '70, The Institution of Chemical Engineers, Symposium Series No. 33, Butterworths, Australia, pp. 97-116 (1970).

Kevlahan, N.K.-R., Hunt, J.C.R. and Vassilicos, J.C., "A Comparison of Different Analytical Techniques for Identifying Structures in Turbulence", in *Eddy Structure Identification in Free Turbulent Shear Flows*, Ed. Bonnet, J.P. and Glauser, M.N., Kluwer Academic Publishers, Netherlands, pp. 311-324 (1993).

Kikuchi, R. and Tsutsumi, A., "Characterization of Nonlinear Dynamics in a Circulating Fluidized Bed by Rescaled Range Analysis and Short-Term Predictability Analysis", Chem. Eng. Sci., 56, 6545-6552 (2001).

King, D.F., "Estimation of Dense Bed Voidage in Fast and Slow Fluidized Beds of FCC Catalyst", in *Fluidization VI*, Ed. Grace, J.R., Shemilt, L.W. and Bergougnou, M.A., Engineering Foundation, N.Y., pp. 1-8 (1989).

King, D.F., Mitchell, F.R.G. and Harrison, D., "Dense Phase Viscosities of Fluidised Beds at Elevated Pressures", Powder Tech., 28, 55-58 (1981).

Kobayashi, N., Yamazaki, R. and Mori, S., "A Study on the Behavior of Bubbles and Solids in Bubbling Fluidized Beds", Powder Tech., 113, 327-344 (2000).

Koch, D.L. and Hill, R.J., "Inertial Effects in Suspension and Porous-Media Flows", Ann. Rev. Fluid Mech., 33, 619-647 (2001).

Koch, D.L. and Sangani, A.S., Particle Pressure and Marginal Stability Limits for a Homogenous Monodisperse Gas-Fluidized Bed: Kinetic Theory and Numerical Simulations", J. Fluid Mech., 400, 229-263 (1999).

Kono, H.O., Aksoy, E. and Wang, Y.-Z., "Transient Motion of Waves and Eddies of Aggregated Emulsion on the Wall Surface of Circulating Fluidized Beds", in *Circulating Fluidized Bed Technology VI*, Ed. Werther, J., pp. 119-123 (1999).

Krishna, R. and van Baten, J.M., "Scaling Up Bubble Column Reactors with the Aid of CFD", Trans IChemE, vol. 79, part A, 283-309 (2001).

Krohn, D.A., "Intensity Modulated Fiber Optic Sensors – Overview", Proceedings of SPIE, Int. Soc. for Optical Eng., 718, 2-11 (1987).

Kuipers, J.A.M., van Duin, K.J., van Beckum, F.P.H. and van Swaaij, W.P.M., "A Numerical Model of Gas-Fluidized Beds", Chem. Eng. Sci., 47, 1913-1924(1992).

Kulkarni, A.A., Joshi, J.B., Kumar, V.R. and Kulkarni, B.D., "Wavelet Transform of Velocity-Time for the Analysis of Turbulent Structures in a Bubble Column", Chem. Eng. Sci., 56, 5305-5315 (2001).

Kunii, D. and Levenspiel, O., *Fluidization Engineering*, Butterworth-Heinemann, Boston, 2nd Edition (1991).

Kurose, R., Misumi, R. and Komori, S., "Drag and Lift Forces Acting on a Spherical Bubble in a Linear Shear Flow", Int. J. Multiphase Flow, 27, 1247-1258 (2001).

Lancia, A., Nigro, R., Volpicelli, G. and Santoro, L., "Transition from Slugging to Turbulent Flow Regimes in Fluidized Beds Detected by Means of Capacitance Probes", Powder Tech., 56, 49-56 (1988).

Lanneau, K.P., "Gas-Solid Contacting in Fluidized Beds", Trans. Instn. Chem. Engrs., 38, 125-143 (1960).

Lee, G.S. and Kim, S.D., "Bed Expansion Characteristics and Transition Velocity in Turbulent Fluidized Beds", Powder Tech., 62, 207-215 (1990).

Lee, G.S. and Kim, S.D., "Pressure Fluctuations in Turbulent Fluidized Beds", J. of Chem. Eng. of Japan, 21, 515-521 (1988).

Lee, G.S. and Kim, S.D., "Rise Velocities of Slugs and Voids in Slugging and Turbulent Fluidized Beds", Korean J. of Chem. Eng., 6(1), pp.15-22 (1989).

Lettieri, P., Micale, G., Cammarata, L. and Colman, D., "Computational Fluid Dynamics Simulations of Gas Fluidized Beds: A Preliminary Investigation of Different Modelling Approaches", CFX Technical note (2002).

Lettieri, P., Newton, D. and Yates, J.G., "High Temperature Effects on the Dense Phase Properties of Gas Fluidized Beds", Powder Tech., 120, 34-40 (2001).

Letzel, H.M., Schouten, J.C., Krishna, R. and van den Bleek, C.M., "Characterization of Regimes and Regime Transitions in Bubble Columns by Chaos Analysis of Pressure Signals", Chem. Eng. Sci., 52(24), 4447-4459 (1997).

Leu, L.-P., Huang, J.-W. and Gua, B.-B., "Axial Pressure Distribution in Turbulent Fluidized Beds", in *Proc. 2nd Asian Conf. Fluidized-Bed and Three-Phase Reactors*, pp. 71-79 (1990).

Levenspiel, O., "G/S Reactor Models – Packed Beds, Bubbling Fluidized Beds, Turbulent Fluidized Beds and Circulating (Fast) Fluidized Beds", Powder Tech., 122, 1-9 (2002).

Lewalle, J., Delville, J. and Bonnet, J.-P., "Decomposition of Mixing Layer Turbulence into Coherent Structures and Background Fluctuations", Flow, Turbulence and Combustion, 64, 301-328 (2000).

Li, H., "Identification of Coherent Structure in Turbulent Shear Flow with Wavelet Correlation Analysis", J. of Fluids Eng., 120, 778-785 (1998).

Li, J., "Compromise and Resolution – Exploring the Multi-Scale Nature of Gas-Solid Fluidization", Powder Tech., 111, 50-59 (2000).

Li, J. and Kwauk, M., *Particle-Fluid Two-Phase Flow*, Metallurgical Ind. Press, Beijing (1994).

Li, J., Reh, L., Tung, Y. and Kwauk, M., "Comparison of Fluidization Behaviour in Different Flow Regimes", in *Proc. of 5th National Fluidization Conference*, pp. 110-113 (1990). In Chinese.

Li, J., Wen, L., Ge, W., Cui, H. and Ren, J., "Dissipative Structure in Concurrent-Up Gas-Solid Flow", Chem. Eng. Sci., 53(19), 3367-3379 (1998).

Li, J., Wen, L., Qian, G., Cui, H., Kwauk, M., Schouten, J.C. and van den Bleek, C.M., "Structure Heterogeneity, Regime Multiplicity and Nonlinear Behavior in Particle-Fluid Systems", Chem. Eng. Sci., 51(11), 2693-2698 (1996).

Li, Y., McLaughlin, J.B., Kontomaris, K. and Portela, L., "Numerical Simulation of Particle-Laden Turbulent Channel Flow", Physics of Fluids, 13(10), 2957-2967 (2001).

Libby, P.A., *Introduction to Turbulence*, Taylor and Francis, Washington (1996).

Lin, Q., Wei, F. and Jin, Y., "Transient Density Signal Analysis and Two-Phase Micro-Structure Flow in Gas-Solids Fluidization", Chem. Eng. Sci., 56, 2179-2189 (2001).

Lischer, D.J. and Louge, M.Y., "Optical Fibre Measurements of Particle Concentration in Dense Suspensions: Calibration and Simulation", Applied Optics, 31(24), 5106-5113 (1992).

Liu, J., Grace, J.R. and Bi, X.T., "Simultaneous Determination of Particle Velocity, Concentration and Flux Using a Novel Multi-Functional Optical Fibre Probe: I. Probe Development and Validation", AIChE J., in press (2003a).

Liu, J., Grace, J.R. and Bi, X.T., "Simultaneous Determination of Particle Velocity, Concentration and Flux Using a Novel Multi-Functional Optical Fibre Probe: II. Hydrodynamic Measurements in a High-Density Circulating Fluidized Bed", AIChE J., in press (2003b).

Liu, J., *Particle and Gas Dynamics of High Density Circulating Fluidized Beds*, Ph.D. Dissertation, UBC, Vancouver, Canada (2001).

Louge, M. and Opie, M., "Measurements of the Effective Dielectric Permittivity of Suspensions", Powder Tech., 62, 85-94 (1990).

Louge, M., "Experimental Techniques" in *Circulating Fluidized Beds*, Ed. Grace, J.R., Knowlton, T. and Avidan A.A., Chapter 9, Chapman and Hall, London (1996).

Louge, M.Y., Mastorakos, E. and Jenkins, J.T., "The Role of Particle Collisions in Pneumatic Transport", J. Fluid. Mech., 231, 345-359 (1991).

Lu, C., Xu, Y., Shi, M. and Fu, S., "Two-Area Model for Bubble Distribution in a Turbulent Fluidized Bed of Fine Particles", Chinese J. of Chem. Eng., 5(4), 287-295 (1997).

Lu, C., Xu, Y., Shi, M., Shen, F., Zhao, M. and Peng, J., "Study of Radial Voidage Profile in a Large-Scale Gas-Solids Turbulent Fluidized Bed", Petrochem. Eng., 25(5), 315-317 (1996).

Lu, X. and Li, H., "Wavelet Analysis of Pressure Fluctuation Signals in a Bubbling Fluidized Bed", Chem. Eng. J., 75, 113-119 (1999).

Lun, C.K.K. and Savage, S.B., "Effects of an Impact Velocity Dependent Coefficient of Restitution on Stresses Developed by Sheared Granular Materials", Acta Mechanica, 63(1-4), 15-44 (1986).

Lun, C.K.K., Savage, S.B., Jeffrey, D.J. and Chepurniy, N., "Kinetic Theories for Granular Flow: Inelastic Particles in Couette Flow and Slightly Inelastic Particles in a General Flowfield", J. Fluid Mech., 140, 223-256 (1984).

Lyczkowski, R.W., Gamwo, L.K., Dobran, F., Ai, Y.H., Chao, B.T., Chen, M.M. and Gidaspow, D., "Validation of Computed Solids Hydrodynamics and Pressure Oscillations in a Bubbling Atmospheric Fluidized Bed", Powder Tech., 76, 65-77(1993).

M'chirgui, A., Tadrist, H. and Tadrist, L., "Experimental Investigation of the Instabilities in a Fluidized Bed Origin of the Pressure Fluctuations", Phys. Fluids, 9 (3), 500-509 (1997).

Ma, D. and Ahmadi, G., "A Thermodynamical Formulation for Dispersed Multiphase Turbulent Flows-II", Int. J. Multiphase Flow, 16, 341-351 (1990).

Mainland, M.E. and Welty, J.R., "Use of Optical Probes to Characterize Bubble Behavior in Gas-Solid Fluidized-Beds", AIChE J., 41(2), 223-228 (1995).

Mallat, S., *A Wavelet Tour of Signal Processing*, Academic Press, San Diego, 2nd Ed. (2001).

Marzocchella, A. and Salatino, P., "The Dynamics of Fluidized Beds Under Pressure", AIChE Symp. Ser., 92(313), 25-30 (1996).

Massimilla, L. "Behavior of Catalytic Beds of Fine Particles at High Gas Velocities", AIChE Symp. Ser., 128(69), pp. 11-13 (1973).

Matheson, G.L., Herbst, W.A. and Holt, P.H., "Characteristics of Fluid-Solid Systems", Ind. Eng. Chem., 41, 1099-1104 (1949).

Matsuno, T., Yamaguchi, H., Oka, T., Kage, H. and Higashitani, K., "The Use of Optic Fiber Probes for the Measurement of Dilute Particle Concentrations. Calibration and Application to Gas-Fluidized Bed Carryover", Powder Tech., 36, 215-221 (1983).

Matsuura, A. and Fan, L.-S., "Distribution of Bubble Properties in a Gas-Liquid-Solid Fluidized Bed", AIChE J., 30, 894-903 (1984).

Maxwell, J.C, "On the Dynamical Theory of Gases", Phil. Trans. R. Soc. London, 157, 49-88 (1866).

Maxwell, J.C., *Electricity and Magnetism*, Vol. 1, Clarendon, Oxford (1892).

McComb, W.D., *The Physics of Fluid Turbulence*, Oxford University Press. (1990).

Mello, T.M., Diamond, P.H. and Levine, H., "Hydrodynamic Modes of a Granular Shear Flow", Phys. Fluids A, 3(9), 2067-2075 (1991).

Meneveau, C., "Analysis of Turbulence in the Orthonormal Wavelet Representation", J. Fluid. Mech., 232, 469-520 (1991).

Meredith, R.E. and Tobias, C.W., "Resistance to Potential Flow Through a Cubical Array of Spheres", J. Appl. Phys., 31(7), 1270-1273 (1960).

Meyer, Y., *Wavelets – Algorithms and Applications*, Soc. Ind. Appl. Math., Philadelphia (1993).

Mori, S. and Wen, C.Y., "Estimation of Bubble Diameter in Gaseous Fluidized Beds", AIChE J., 21(1), 109-115 (1975).

Morikawa, H., *Entrainment from Pilot Scale Turbulent Fluidized Beds with FCC Particles*, Internal Report, UBC, Vancouver, Canada (1999).

Morikawa, H., Bi, H.T., Lim, C.J. and Grace, J.R., "Entrainment from Pilot Scale Turbulent Fluidized Beds of FCC Particles", in *Fluidization X*, Ed. M. Kwauk, J. Li and W.-C. Yang, pp. 181-188 (2001).

Morooka, S., Kawazuishi, K. and Kato, Y., "Holdup and Flow Pattern of Solid Particles in Freeboard of Gas-Solid Fluidized Bed with Fine Particles", Powder Tech., 26, 75-82 (1980).

Motard, R.L. and Joseph, B., Ed., *Wavelet Applications in Chemical Engineering*, Kluwer Academic Pub., Boston (1994).

Mudde, R.F., Lee, D.J., Reese, J. and Fan, L.-S., "Role of Coherent Structures on Reynolds Stresses in a 2-D Bubble Column", AIChE J., 43(4), 913-926 (1997).

Musmarra, D., Poletto, M., Vaccaro, S. and Clift, R., "Dynamic Waves in Fluidized Beds", Powder Tech., 82, 255-268 (1995).

Nakajima, M., Harada, M., Asai, M., Yamazaki, R. and Jimbo, G., "Bubble Fraction and Voidage in an Emulsion Phase in the Transition to a Turbulent Fluidized Bed", in *Circulating Fluidized Bed III*, Ed. Basu, P., Horio, M. and Hasatani, M., Pergamon Press, Oxford, pp. 79-84 (1991).

Newton, D., Fiorentino, M. and Smith, G.B., "Comments and Experimental Data on the Transition from Bubbling to Turbulent Fluidization", in *Proc. of the 6th World Cong. of Chem. Eng.* (2001).

Nieuwland, J.J., Meijer, R. Kuipers, J.A.M. and Van Swaaij, W.P.M., "Measurements of solids concentration and axial solids velocity in gas-solid two-phase flows", Powder Tech., 87, 127-139 (1996).

Ogden, R.T., *Essential Wavelets for Statistical Applications and Data Analysis*, Birkhäuser, Boston (1997).

Pain, C.C., Mansoorzadeh, S. and de Oliveira, C.R.E., "A Study of Bubbling and Slugging Fluidised Beds Using the Two-Fluid Granular Temperature Model", Int. J. of Multiphase Flow, 27, 527-551 (2001).

Peeler, P.K., Lim, K.S. and Close, R.C., "Effect of Temperature on the Turbulent Fluidization Regime Transition", in *Circulating Fluidized Bed Technology VI*, Ed. Werther, J., pp. 125-130 (1999).

Pell, M., *Gas Fluidization*, Elsevier, Amsterdam (1990).

Peters, E.E., *Fractal Market Analysis. Applying Chaos Theory to Investment Economics*, Wiley, New York (1994).

Piepers, H.W. and Rietema, K., "Effects of Pressure and Type of Gas on Gas-Solid Fluidization Behaviour", in *Fluidization VI*, Ed. Grace, J.R., Shemilt, L.W. and Bergougnou, M.A., Engineering Foundation, N.Y., pp. 203-210 (1989).

Pita, J.A. and Sundaresan, S., "Gas-Solid Flow in Vertical Tubes", AIChE J., 37(7), 1009-1018 (1991).

Polashenski, W., Jr. and Chen, J.C., "Normal Solid Stress in Fluidized Beds", Powder Tech., 90, 13-23 (1997).

Reade, W.C. and Collins, L.R., "Effect of Preferential Concentration on Turbulent Collision Rates", Phys. Fluids, 12, 2530-2540 (2000).

Reh, L. and Li, J., "Measurement of Voidage in Fluidized Beds by Optical Probes", in *Circulating Fluidized Bed Technology III*, Ed. Basu, P., Horio, M. and Hasatani, M., Pergamon Press, Oxford, pp. 163-170 (1990).

Ren, J., Mao, Q., Li, J. and Lin, W., "Wavelet Analysis of Dynamic Behavior in Fluidized Beds", Chem. Eng. Sci., 56, 981-98 (2001).

Rensner, D. and Werther, J., "Estimation of the Effective Measuring Volume of Single-Fibre Reflection Probes for Solid Volume Concentration Measurements", Part. Part. Syst. Charact., 10, 48-55 (1993).

Rensner, K. and Werther, J., "Modeling and Application of a Fiber Optical Measuring System for Higher Concentrated Multiphase Flows", Laser Anemometry, vol. 2, ASME, 753-761 (1991).

Rhie, C.M. and Chow, W.L., "Numerical Study of the Turbulent Flow Past an Airfoil with Trailing Edge Separation", AIAA J1, 21, 1527-1532 (1983).

Rhodes, M. J. and Geldart, D., "Transition to Turbulence?", in *Fluidization V*, Ed. Φstegaard, K. and Sϕrensen, A., Engineering Foundation, N.Y., pp. 281-288 (1986).

Rhodes, M., "What is turbulent fluidization?", Powder Tech., 88, 3-14 (1996).

Richardson, J.F. and Zaki, W.N., "Sedimentation and Fluidization: Part I", Trans. Instn. Chem. Engrs., 32, 35-53 (1954).

Rioul, O. and Vetterli, M., "Wavelets and Signal Processing", IEEE SP Magazine, 8(4), 14-38 (1991).

Robinson, S.K., "Coherent Motions in the Turbulent Boundary Layer", Ann. Rev. Fluid Mech., 23, 601-639 (1991).

Ross, K.A. and Pence, D.V., "Wavelet and Fractal Analyses of Fluidized Bed Heat Transfer", HTD-vol. 351, in *Proceedings of the ASME Heat Transfer Division*, pp. 245-253 (1997).

Rowe, P.N. and MacGillivray, H.J., "The Structure of a 15cm Diameter Gas Fluidised Bed Operated at up to 1 m/s and Seen by X-Rays", in *Fluidization*, Ed. Grace, J.R. and Matsen, J.M., pp. 545-553 (1980).

Rowe, P.N., "Drag Forces in a Hydraulic Model of a Fluidised Bed – Part II", Trans. Instn. Chem. Engrs., 39, 175-180 (1961).

Samuelsberg, A. and Hjertager, B.H., "Computational Modeling of Gas/Particle Flow in a Riser", AIChE J., 24(6), 1536-1546 (1996).

Sangani, A.S., Mo, G., Tsao, H.-K. and Koch, D.L., "Simple Shear Flows of Dense Gas-Solid Suspensions at Finite Stokes Numbers", J. Fluid Mech., 313, 309-341 (1996).

Savage, S.B. and Jeffrey, D.J., "The Stress Tensor in a Granular Flow at High Shear Rates", J. Fluid Mech., 110, 255-272 (1981).

Savage, S.B., "Instability of Unbounded Uniform Granular Shear Flow", J. Fluid Mech., 241, 109-123 (1992).

Saxena, S.C. and Waghmare, B., "Investigations of Pressure Fluctuation History Records of Gas-Solid Fluidized Beds", Int. J. Energy Res., 24, 495-502 (2000).

Schlichting, H., *Boundary-Layer Theory*, McGraw-Hill, Inc., 7th Ed. (1979).

Schnitzlein, M.G. and Weinstein, H., "Flow Characterization in High-Velocity Fluidized Beds Using Pressure Fluctuations", Chem. Eng. Sci., 43(10), 2605-2614 (1988).

Schouten, J.C. and van den Bleek, C.M., "Monitoring the Quality of Fluidization Using the Short-Term Predictability of Pressure Fluctuations" AIChE J., 44(1), 48-60 (1998).

Schouten, J.C., van der Stappen, M.L.M. and van den Bleek, C.M., "Deterministic Chaos Analysis of Gas-Soilds Fluidization", in *Fluidization VII*, Ed. Potter, O.E. and Nicklin, D.J., Engineering Foundation, N.Y., pp. 103-111 (1992).

Schouten, J.C., van der Stappen, M.L.M. and van den Bleek, C.M., "Scale-up of Chaotic Fluidized Bed Hydrodynamics", Chem. Eng. Sci., 51(10), 1991-2000 (1996).

Senior, R.C. and Grace, J.R, "Integrated Particle Collision and Turbulent Diffusion Model for Dilute Gas-Solid Suspensions", Powder Tech., 96, 48-78, (1998).

Seville, J.P.K., Simons, S.J.R., Broadbent, C.J., Martin, T.W., Parker, D.J. and Beynon, T.D., "Particle Velocities in Gas-Fluidized Beds" in *Fluidization VIII*, Engineering Foundation, N.Y., pp. 685-694 (1995).

Seville, J.P.K., Willett, C.D. and Knight, P.C., "Interparticle Forces in Fluidisation: A Review", Powder Tech., 113, 261-268 (2000).

Sinclair, J.L. and Jackson, R., "Gas-Particle Flow in a Vertical Pipe with Particle-Particle Interactions", AIChE J., 35(9), 1473-1486 (1989).

Skrzycke, D.P., Nguyen, K. and Daw, C.S., "Characterization of the Fluidization Behaviour of Different Solid Types Based on Chaotic Time Series Analysis of Pressure Signals", Fluidized Bed Combustion, vol. 1, ASME, pp. 155-166 (1993).

Smolders, K. and Baeyens, J., "Gas Fluidized Beds Operating at High Velocities: a Critical Review of Occurring Regimes", Powder Tech., 119, 269-291 (2001).

Squires, K.D. and Eaton, J.K., "Measurements of Particle Dispersion Obtained from Direct Numerical Simulations of Isotropic Turbulence", J. Fluid Mech., 226, 1-35 (1991).

Sternéus, J., Johnsson, F., Leckner, B. and Palchonok, G.I., "Gas and Solids Flow in Circulating Fluidised Beds – Discussion on Turbulence", in *Circulating Fluidized Bed Technology VI*, Ed. Werther, J., pp. 89-94 (1999).

Stringer, J., "Is a Fluidized Bed a Chaotic Dynamic System?", in *International Conference on Fluidized Bed Combustion*, 1, 265-272 (1989).

Sun, B. and Gidaspow, D., "Computation of Circulating Fluidized-Bed Riser Flow for the Fluidization VIII Benchmark Test", Ind. Eng. Chem. Res., 38, 787-792 (1999).

Sun, G. and Chen, G., "Transition to Turbulent Fluidization and Its Prediction", in *Fluidization VI*, Ed. Grace, J.R., Shemilt, L.W. and Bergougnou, M.A., Engineering Foundation, N.Y., pp. 33-40 (1989).

Svoboda, K. and Hartman, M., "Influence of Temperature on Incipient Fluidization of Limestone, Lim, Coal Ash, and Corundum", Ind. Eng. Chem. Process Des. Dev., 20, 319-326 (1981).

Syamlal, M., Rogers, W. and O'Brien, T.J., "MFIX Documentation Theory Guide", Dept. of Energy, Office of Fossil Energy, Tech. Note (1993).

Tannous, K., Hemati, M. and Laguerie, C., "Identification of Flow Regime Transitions in Fluidized Beds of Large Particles by Pressure Drop Fluctuation Measurements", Brazilian J. of Chem. Eng., 13(3), 168-181 (1996).

Tasirin, S.M. and Geldart, D., "Entrainment of FCC from Fluidized Beds – A New Correlation for the Elutriation Rate Constants $K^*_{i\infty}$", Powder Tech., 95, 240-247 (1998).

Taxil, I., Guigon, P., Archimbault, F. and Gauthier, T.A., "Gas Flow Characterization in Turbulent Fluidization for FCC Catalyst", in *Fluidization* IX, Ed. Fan, L.-S. and Knowlton, T.M., Engineering Foundation, N.Y., pp.69-76 (1998).

Taxil, I., Guigon, P., Archimbault, F., Bayle, J. and Gauthier, T., "Analyse des Signaux Temporels de Pression dans un Lit Fluidisé Turbulent de FCC", Can. J. Chem. Eng., 78, 586-589 (2000).

Tayebi, D., Svendsen, H.F., Grislingås, A., Mejdell, T. and Kohannessen, K., "Dynamics of Fluidized-bed Reactors. Development and Application of a New Multi-fibre Optical Probe", Chem. Eng. Sci., 54, 2113-2122 (1999).

Townsend, A.A., *The Structure of Turbulent Shear Flow*, Cambridge University Press, Cambridge, 2nd Ed. (1976).

Toyoda, K., Okamoto, T. and Shirahama, Y., "Eduction of Vortical Structures by Pressure Measurements in Noncircular Jets" in *Eddy Structure Identification in Free Turbulent Shear Flows*, Ed. Bonnet, J.P. and Glauser, M.N., Kluwer Academic Publishers, Netherlands, pp. 125-136 (1993).

Trnka, O., Veselý, V. and Hartman, M., "Identification of the Sate of a Fluidized Bed by Pressure Fluctuations", AIChE J., 46(3), 509-514 (2000).

Tsonis, A.A., *Chaos: From Theory to Applications*, Plenum Press, New York (1992).

Tsuji, Y., Morikawa, Y. and Shiomi, H., "LDV Measurements of an Air-Solid Two-Phase Flow in a Vertical Pipe", J. Fluid Mech., 139, 417-434 (1984).

Tsukada, M., *Fluidized Bed Hydrodynamics, Heat Transfer and High Temperature Process Development*, Ph.D. Thesis, Tokyo University of Agriculture and Technology, Tokyo (1995).

Tsukada, M., Nakanishi, D. and Horio, M., "The Effect of Pressure on the Phase Transition from Bubbling to Turbulent Fluidization", Int. J. Multiphase Flow, 19(1), 27-34 (1993).

Tsuo, Y.P. and Gidaspow, D., "Computation of Flow Patterns in Circulating Fluidized Beds", AIChE J., 36, 885-896 (1990).

Tung, Y., Yang, Z., Xia, Y., Zheng, W., Yang, Y. and Kwauk, M., "Assessing Fluidizing Characteristics of Powders", in *Fluidization VI*, Ed. Grace, J.R., Schmitt, L.W. and Bergougnou, M.A., Engineering Foundation, N.Y., pp. 169-176 (1989).

Tzeng, J.-W., Chen, R.C. and Fan, L.-S., "Visualization of Flow Characteristics in a 2-D Bubble Column and Three-Phase Fluidized Bed", AIChE J., 39, 733-744, (1993).

Umekage, T. and Yuu, S., "Measurement of Drag Force Acting on Spherical Particle in Multiparticle System", Nihon Kikaigakkai Rombunshu. B-Hen. Transactions of the Japan Society of Mechanical Engineers. Series B., 65(634), 1948-1954 (1999).

Unser, M. and Blu, T., "Why Restrict Ourselves to Compactly Supported Basis Functions?", in *Proc. SPIE Conference on Mathematical Imaging: Wavelet Applications in Signal and Image Processing IX*, San Diego, vol. 4478, pp. 331-314 (2001).

van den Akker, H.E.A., "Coherent Structures in Multiphase Flows", Powder Tech., 100, 123-136 (1998).

Van den Moortel, Azario, E., Santini, R. and Tadrist, L., "Experimental Analysis of the Gas-Particle Flow in a Circulating Fluidized Bed Using a Phase Doppler Particle Analyzer", Chem. Eng. Sci., 53(10), 1883-1899 (1998).

van der Schaaf, J., *Dynamics of Gas-Solids Fluidized Beds*, Delft University Press, the Netherlands, Dissertation (2002).

van der Schaaf, J., Schouten, J.C. and van den Bleek, C.M. "Origin, Propagation and Attenuation of Pressure Waves in Gas-Solid Fluidized Beds", Powder Tech., 95, 220-233 (1998).

van Ommen, J.R., Schouten, J.C., vander Stappen, M.L.M. and van den Bleek, C.M., "Response Characteristics of Probe-Transducer Systems for Pressure Measurements in Gas-Solid Fluidized Beds: How to Prevent Pitfalls in Dynamic Pressure Measurements", Powder Tech., 106, 199-218 (1999).

van Wachem, B.G.M., Schouten, J.C., Krishna, R. and van den Bleek, C.M., "Validation of the Eulerian Simulated Dynamic Behaviour of Gas-Solid Fluidised Beds", Chem. Eng. Sci. , 54, 2141-2149 (1999).

van Wachem, B.G.M., Schouten, J.C., van den Bleek, C.M., Krishna, R. and Sinclair, J.L., "Comparative Analysis of CFD Models of Dense Gas-Solid Systems", AIChE J., 47(5), 1035-1051 (2001).

Venderbosch, R.H., *The Role of Clusters in Gas-Solids Reactors*, Ph.D. Dissertation, Twente University, the Netherlands (1998).

Verloop, J. and Heertjes, P.M., "Periodic Pressure Fluctuations in Fluidized Beds", Chem. Eng. Sci., 29, 1035-1042 (1974).

Vial, C., Poncin, P., Wild, G. and Midoux, N., "A Simple Method for Regime Identification and Flow Characterisation in Bubble Columns and Airlift Reactors", Chem. Eng. and Processing, 40, 135-151 (2001).

Wang, C., Wang, Y., Jin, Y. and Yu, Z., "Effect of Particle Mean Size on the Performance of Fluidized Beds with FCC Particles", in *Symposium of the 1st Annual Conference of Chinese Society of Particle Technology*, Beijing, pp. 333-337 (1997). In Chinese.

Wang, W., and Li, Y., "Hydrodynamic Simulation of Fluidization by Using a Modified Kinetic Theory", Ind. Eng. Chem. Res., 40, 5066-5073 (2001).

Wang, Z. and Wei, F., "Similarity of the Particles Concentration Distribution between Bubbling and Turbulent Fluidized Beds", in *Symposium of the 1st Annual Conference of Chinese Society of Particle Technology*, Beijing, pp. 396-400 (1997). In Chinese.

Weast, R.C., *Handbook of Chemistry and Physics*, CRC Press, 1st Student Ed. (1988).

Wen, C.Y. and Yu, Y.H., "Mechanics of Fluidization", Chem. Eng. Prog. Symp. Series, 62, 100-111 (1966).

Wen, F. and Evans, J., "Effect of Particle Inertia on the Instability of a Particle-Laden Flow", Computers and Fluids, 25(7), 667-676 (1996).

Weng, H. and Lau, K.-M., "Wavelets, Period Doubling, and Time-Frequency Localization with Application to Organization of Convection Over the Tropical Western Pacific", J. Atmospheric Sciences, 5(17), 2523-2541 (1994).

Werther J. and Molerus, O., "The Local Structure of Gas Fluidized Beds – I. A Statistically Based Measuring System", Int. J. of Multiphase Flow, 1, 103-122 (1973a).

Werther J. and Molerus, O., "The Local Structure of Gas Fluidized Beds – II. The Spatial Distribution of Bubbles", Int. J. of Multiphase Flow, 1, 123-138 (1973b).

Werther, J. and Wein, J., "Expansion Behavior of Gas Fluidized Beds in the Turbulent Regime", AIChE Symp. Ser., 301, 31-44 (1994).

Werther, J., "Measurement Techniques in Fluidized Beds", Powder Tech., 102, 15-36 (1999).

Whitcher, B., Guttorp, P. and Percival, D.B., "Wavelet Analysis of Covariance with Application to Atmospheric Time Series", J. Geophys. Res., 105(D11), 14,941-14,962 (2000).

White, R.B. and Zakhari, A., "Characterisation of Flow Regimes in the Base of a CFB Riser", in *Circulating Fluidized Bed Technology VI*, Ed. Werther, J., pp. 143-148 (1999).

Wiesendorf, V. and Werther, J., "Capacitance Probes for Solids Volume Concentration and Velocity Measurements in Industrial Fluidized Bed Reactors", Powder Tech., 110, 143-157 (2000).

Witt, P.J., Perry, J.H. and Schwarz, M.P., "A Numerical Model for Predicting Bubble Formation in a 3D Fluidized Bed", Applied Math. Modelling, 22, 1071-1080 (1998).

Xu, G., Nomura, K., Bai, Y., Sun, G., Nakagawa, N., Li, J. and Kato, K., "Characteristics of Pressure with Respect to Heterogeneous Flow Structure in Fluidized Beds", J. Chem. Eng. Japan, 31, 236-243 (1998).

Xu, G., Sun, G., Nomura, K., Li, J. and Kato, K., "Two Distinctive Variational Regions of Radial Particle Concentration Profiles in Circulating Fluidized Beds Risers", Powder Tech., 101, 91-100 (1999).

Yamazaki, R., Asai, M., Nakajima, M. and Jimbo, G., "Characteristics of Transition Regime in a Turbulent Fluidized Bed", in *2nd China-Japan Fluidization Conference*, Beijing, pp. 720-725 (1991).

Yamazaki, R., Ueda, N., and Jimbo, G., "Mechanism of Incipient Fluidization in Fluidized Bed at Elevated Temperature", J. Chem. Eng. Japan, 19(4), 251-257 (1986).

Yang, W.C. and Chitester, D.C., "Transition between Bubbling and Turbulent Fluidization at Elevated Pressure", AIChE Symp. Ser., 84(262), 10-21 (1988).

Yates, J.G. and Newton, D., "Fine Particle Effects in a Fluidized-Bed Reactor", Chem. Eng. Sci., 41(4), 801-806 (1986).

Yates, J.G., "Effects of Temperature and Pressure on Gas-Solid Fluidization", Chem. Eng. Sci., 51(2), 167-205 (1996).

Yerushalmi, J. and Cankurt, N.T., "Further Studies of the Regimes of Fluidization", Powder Tech., 24, 187-205 (1979).

Yudine, M., "Physical Considerations on Heavy-Particle Diffusion", in *Atmospheric Diffusion and Air Pollution*, Advances in Geophysics, vol. 6, Academic Press, New York, pp. 185-191 (1959).

Yuu, S., Nishikawa, H. and Umekage, T., "Numerical Simulation of Air and Particle Motions in Group-B Particle Turbulent Fluidized Bed", Powder Tech., 118, 32-44 (2001).

Zenz, F.A. and Othmer, D.F., *Fluidization and Fluid-Particle Systems*, Reinhold Pub. Corp., N.Y. (1960).

Zethræus, B., Adams, C. and Berge, N., "A Simple Model for Turbulent Gas Mixing in CFB Reactors", Powder Tech., 69, 101-105 (1992).

Zhang, D.Z. and Rauenzahn, R.M., "A Viscoelastic Model for Dense Granular Flows", J. Rheol., 41 (6), 1275-1298 (1997).

Zhang, D.Z. and Rauenzahn, R.M., "Stress Relaxation in Dense and Slow Granular Flows", J. Rheol., 44 (5), 1019-1041 (2000).

Zhang, D.Z. and VanderHeyden, W.B., "High-Resolution Three-Dimensional Numerical Simulation of a Circulating Fluidized Bed", Powder Tech., 116, 133-141 (2001).

Zhang, D.Z. and VanderHeyden, W.B., "The Effects of Mesoscale Structures on the Macroscopic Momentum Equations for Two-Phase Flows", Int. J. Multiphase Flow, 28, 805-822 (2002).

Zhang, H., Johnston, P.M., Zhu, J.-X., de Lasa, H.I. and Bergougnou, M.A., "A Novel Calibration Procedure for a Fibre Optic Solids Concentration Probe", Powder Tech., 100, 260-272 (1998).

Zhang, X. Qian Y., Guo, S. and Zhang, Y., "Application of the Optical Fibre Probe to the Measurement of the Bubble Characteristics in a Turbulent Fluidized Bed with FCC Particles", J. of South China Univ. of Tech. Press, 25(8), 20-24 (1997).

Zheng, Y., Wan, X., Qian, Z., Wei, F. and Jin, Y., "Numerical Simulation of the Gas-Particle Turbulent Flow in Riser Reactor Based on κ-ε-κ_p-ε_p-Θ Two Fluid Model", Chem. Eng. Sci., 56, 6813-6822 (2001).

Zhou, H., Lu, J. and Lin, L., "Turbulence Structure of the Solid Phase in Transition Region of a Circulating Fluidized Bed", Chem. Eng. Sci., 55, 839-847 (2000).

Zhou, L.-X., *Theory and Numerical Modeling of Turbulent Gas-Particle Flows and Combustion*, Science Press and CRC Press, Beijing (1994).

Zhu, J.-X., Li, G.-Z., Qin, S.-Z., Li, F.-Y., Zhang, H. and Yang, Y.-L., "Direct Measurements of Particle Velocities in Gas-Solids Suspension Flow Using a Novel Five-Fiber Optical Probe", Powder Tech., 115, 184-192 (2001).

Zijerveld, R.C., Johnsson, F., Marzocchella, A., Schouten, J.C. and van den Bleek, C.M., "Fluidization Regimes and Transitions from Fixed Bed to Dilute Transport Flow", Powder Tech., 95, 185-204 (1998).

APPENDIX A

COLUMN III: 1.56 M DIAMETER FLUIDIZATION COLUMN

The 1.56 m diameter, 15 m tall cold-model is located at CSIRO Division of Minerals in Clayton. This large-scale cold model rig, commissioned in November 1996, was designed to be able to operate in both bubbling and circulating modes. A photograph is shown in Figure A.1.

A.1 Rig modification

A.1.1 Cyclone inlet area

As shown in Figure A.2, the 1.56 m fluidization column is equipped with two 1.1 m diameter cyclones in parallel, each with an inlet area of 0.27 m x 1.1 m. One cyclone inlet was blocked to increase the cyclone inlet velocity of the gas from 2.6 m/s to 5.1 m/s for a superficial gas velocity in the column of 0.8 m/s. Though it was desirable to reduce the second cyclone inlet area in order to further increase the inlet velocity, physical constraints (position of inlet in relation to the supporting frame) made this impossible.

A.1.2 Distributor plate and pressure drop

The orifice plate contained 18 bubble caps of 152 mm diameter arranged in an equilateral triangular configuration with a 310 mm pitch (see Figures A.3 and A.4). The air inlet diameter was reduced with a PVC socket of 64 mm, shown in Figure A.5, to obtain a desirable open area ratio of 3%. Also of note in Figures A.3 and A.5 is the lack of an active bubble cap at the centre of the plate.

A.1.3 Solids storage

The lack of storage capacity for solids became one of the challenges during operation. One possible option was to utilize the return leg capacity as the storage vessel. It was possible to blow the bulk of the solids over to the return leg when the return leg was not being aerated. This provided some control over solids handling, e.g. when necessitated by a weld failure of the traversing probe arm or by probe calibrations. However, there was a risk of losing a considerable fraction of the fines after repeated storage of solids in the return leg.

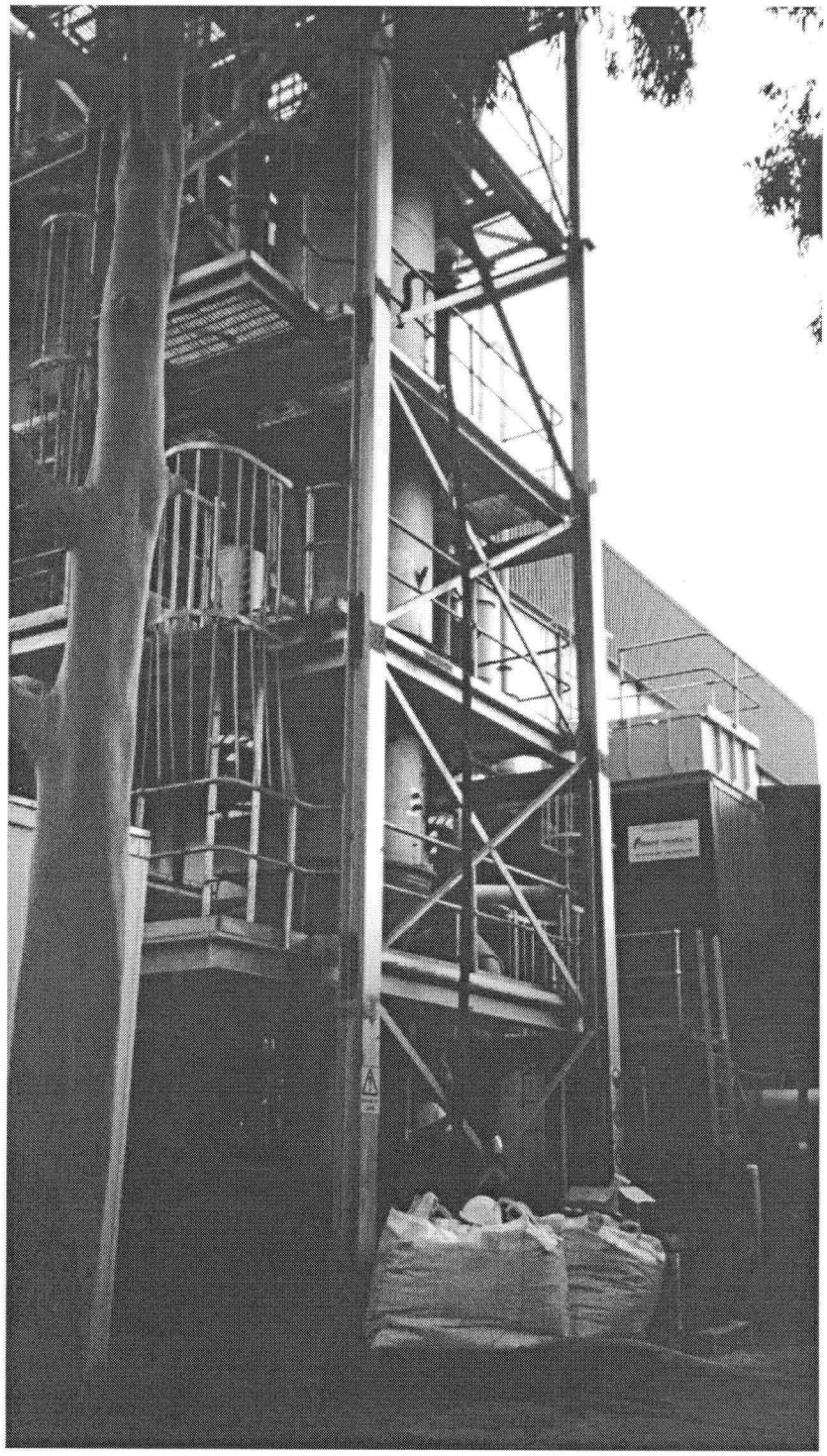

Figure A.1 Photograph of the 1.56 m fluidization column standing beside heavy tech building at CSIRO Minerals, Clayton.

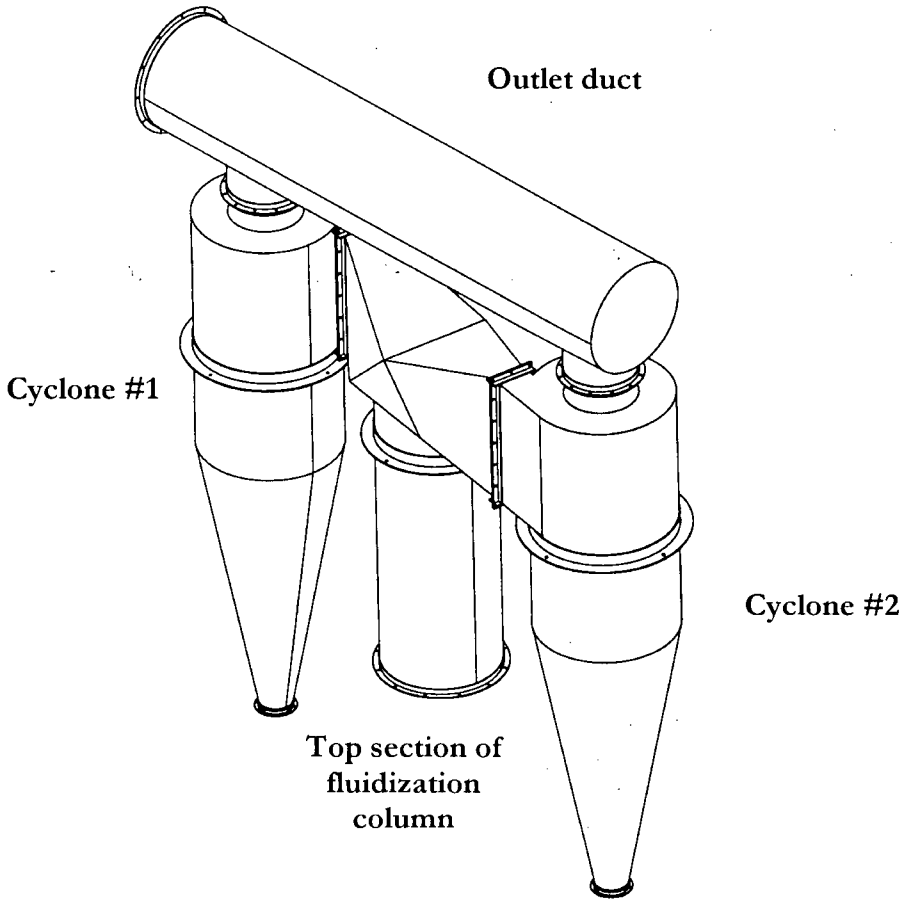

Figure A.2 Isometric view of cyclones and top of 1.56 m fluidization column.

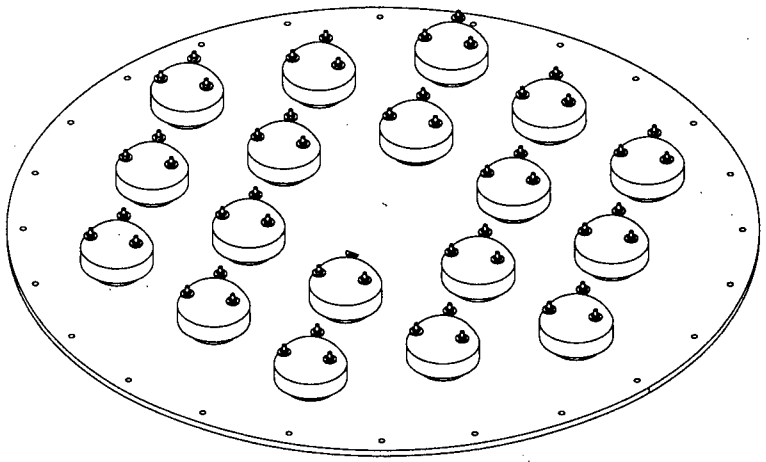

Figure A.3 Schematic diagram showing bubble caps on distributor of 1.56 m diameter fluidization column.

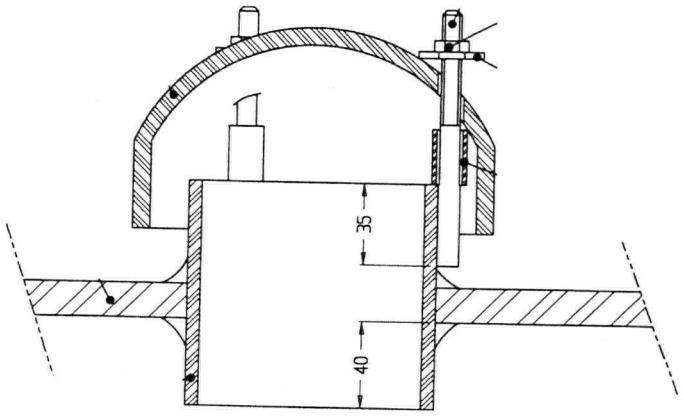

Figure A.4 Schematic of bubble cap (in mm) as originally installed.

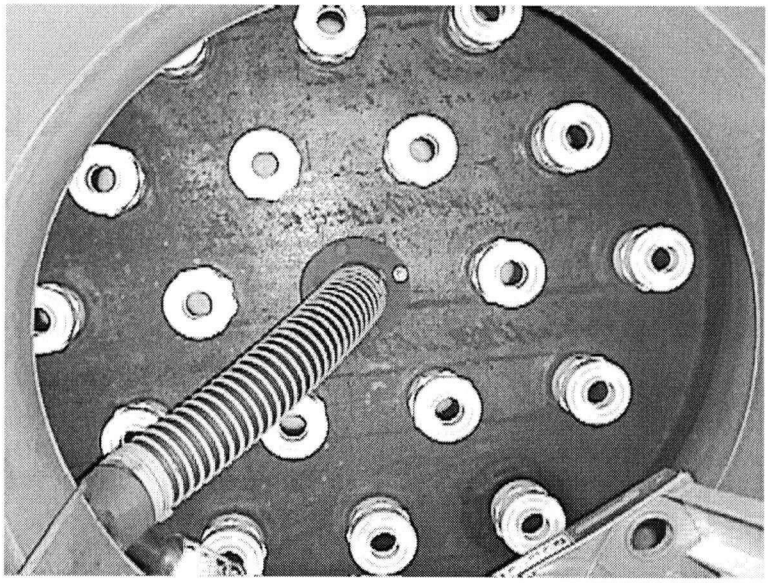

Figure A.5 Photograph taken upward from the plenum chamber of the 64 mm sockets installed to reduce the open area of air inlet and the central bubble cap removed from service.

A.2 Traversing arm design and construction

The probe arm sockets, shown in Figure A.6, allowed the traversing probe arms to be pushed in or pulled out of the rig to allow the radial position in the bed to be set and maintained. A photograph in Figure A.7, taken from the distributor plate, depicts traversing probe arm #2 positioned at the centre of the column.

A.3 Commissioning the rig

Running the unit in the turbulent fluidization flow regime required changes to the bubble cap inlet area to achieve a desirable grid pressure drop, and in the cyclone inlet area as described in Section A.1.1. Once the modifications were complete, the blower capacity was tested in the empty column. Since the downstream bag filter was open to atmosphere, leak tests prior to delivery of solids were very limited. FCC particles were injected into the column from a pressurized tanker through a 102 mm Camlock fitting into an opening about 2.2 m above the distributor. A small flow of gas was supplied through the distributor to minimize solids falling into the chamber. This procedure went smoothly. Approximately 3.8 tonnes of FCC were added in this manner.

Preliminary runs included those to test for leakage from the unit. Leakage from the bag filter was significant when operated without back pressure purges. Even with new gaskets, all hatches, including the cyclone inlet flange at the top, required a thick coating of silicone sealant to prevent solids leakage. During one of the numerous shut-downs where gas was turned off abruptly, most of the solids (approx. 3 tonnes) drained through the distributor plate into the plenum chamber below.

The primary reason for losing solids through the distributor plate was attributed to the large spacing between the bottom of bubble caps and the distributor plate floor. A sudden shut-off of gas created back pressure causing solids to flow into the plenum chamber through the large gaps. In order to rely on the angle of repose of FCC, it was necessary to shorten the gap by taking the spacers out (Figure A.4) and adding 5 mm thick acrylic spacers on the distributor plate floor to lift the bubble caps 5 mm off the floor. In addition, a shut-down procedure had to be established to ensure that the gas flow decreased gradually allowing the bed closest to the distributor to de-fluidize first.

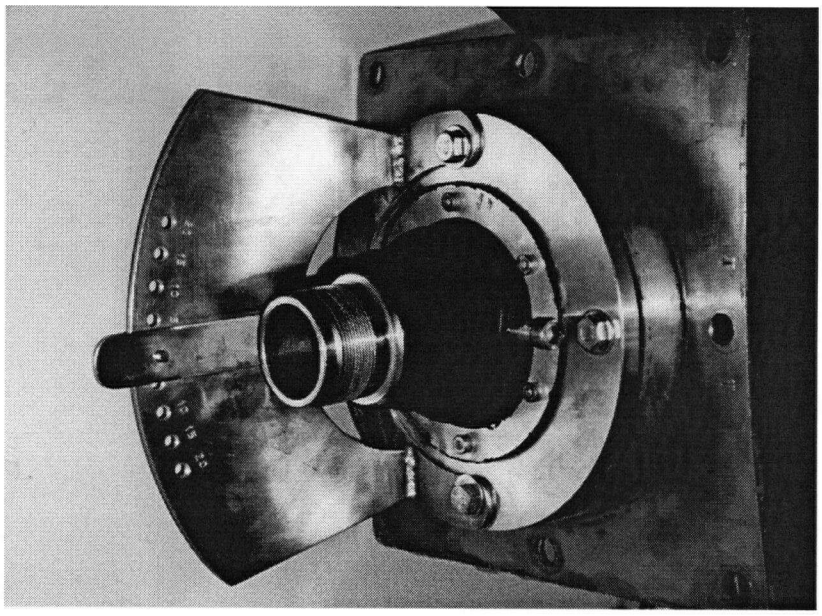

Figure A.6 Photograph of a probe arm socket depicting the interlocking angle mechanism.

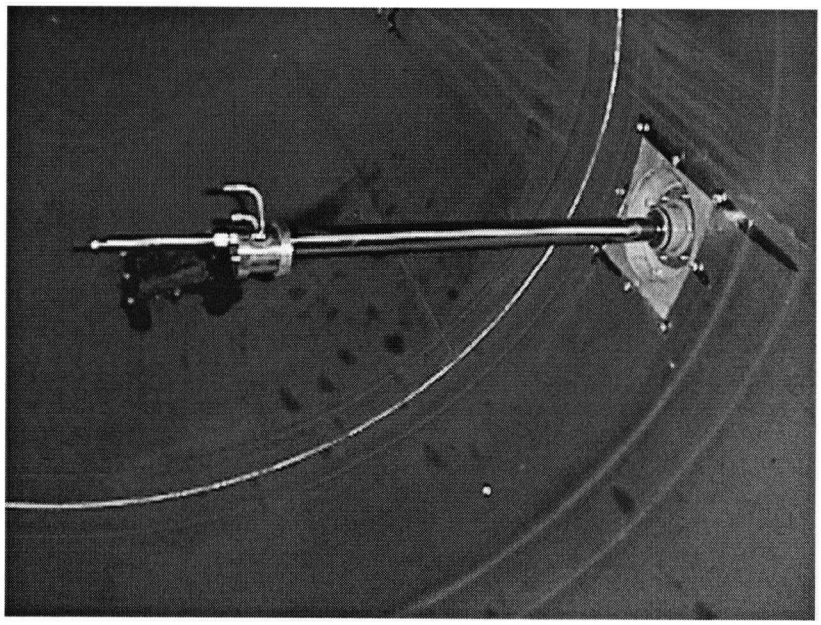

Figure A.7 Photograph of a traversing probe arm #2 positioned at the centre of an empty 1.56 m diameter column.

Implementation of these points was straightforward, but first the FCC catalyst had to be recovered from the plenum chamber. One of the challenges in handling these solids was the lack of storage, which required the injection of the solids into the rig simultaneously. Once enough solids had been pneumatically conveyed out of the region close to the manhole, the plate was removed to manually remove solids one bucket at a time. Only a week later were all solids re-stored and the system again ready for start-up.

The first run after receiving the second batch of solids came to a quick halt due to a weld failure on the first traversing probe arm casing. The probe was located in the centre at the time. With the pressure during start-up, the dense bed exerted such a force on the probe that the weld on the casing securing the probe became loose and started to discharge solids. The gas was turned off and the socket plate was tack welded to contain the solids (close to 7 tonnes) in the column. Following the reinforcement, it was determined that a pivot point in the socket was insufficient to secure the probe in position due to the increased force being exerted on the probe with additional solids. A support structure was built from scaffolds, as depicted in Figure A.8, to secure the probe. Three C clamps were used to secure the second probe arm in place. It was observed that at gas velocities close to U_c, the fluctuation in bed level was such that even with the clamps the probe exhibited violent movement (video clip available).

A.4 Pressure measurements

The responses of the two independent pressure logging systems are compared in Figure A.9. It is seen that the two pressure measurement systems gave profiles within acceptable error considering the differences in sampling frequencies (1 Hz for steady-state vs. 100 Hz for dynamic measurements), transducer response times and transducer volumes.

A.5 Summary of operating conditions

Several operating conditions were pursued in four different fluidization columns. Table A.1 provides a summary of all the experimental runs conducted in this study.

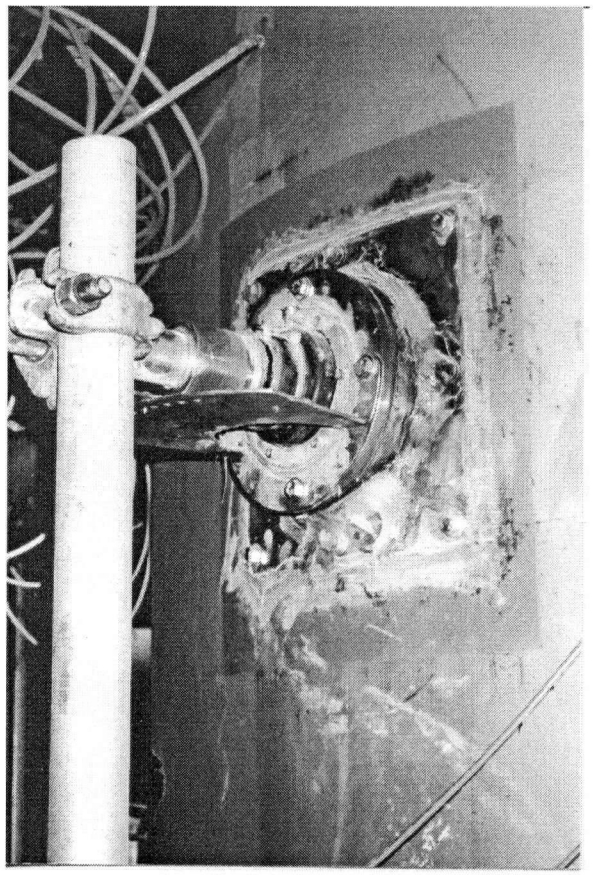

Figure A.8 Photograph of the scaffold supporting frame and a massive amount of silicone sealant after a welding failure.

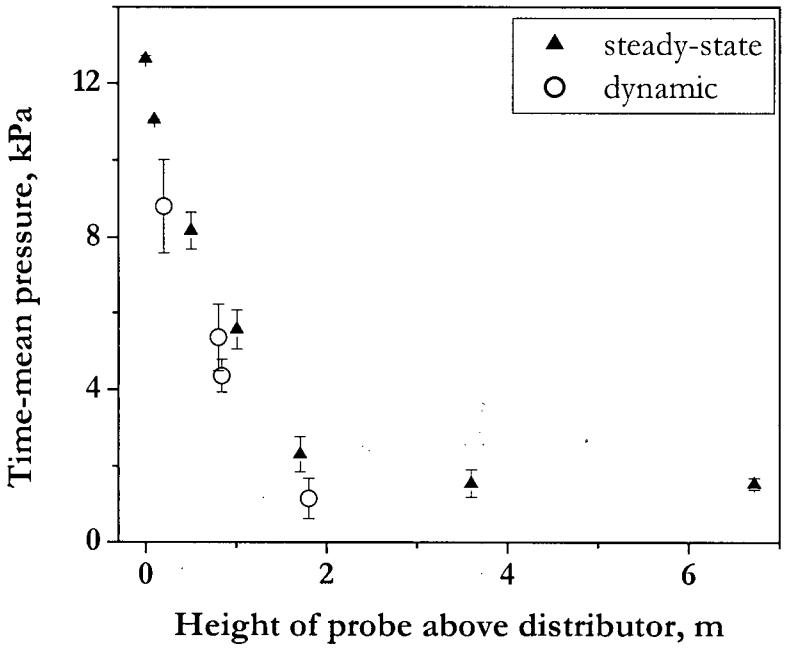

Figure A.9 Comparison of pressure profile from two data logging systems. Error bars depict maximum error of 10,000 sample size. D=1.56 m/s, U=0.43 m/s, H_0=1.2 m, FCC II.

Table A.1 Experimental conditions.

0.29 m diameter column FCC I: air	
H_0, m	**U, m/s**
0.4	0.12~0.59
0.51	0.18~0.81
0.60	0.3~1.2
0.70	0.28~1.15
0.8	0.15~1.12
1.0	0.013~1.1
1.1	0.27~1.09
1.2	0.3~1.0
1.5	0.2~1.05

0.29 m diameter column Catalyst C/Catalyst Cr: air	
H_0, m	**U, m/s**
0.6	0.05~0.71
1.0	0.2~0.96
1.5	0.16~0.89

0.11 m diameter column Catalyst C: N_2 H_0=0.7 m		
T, °C	**P, MPa**	**U, m/s**
20, 160, 240	0.1, 0.2, 0.3, 0.4	0.1~0.5

0.61 m diameter column FCC III/FCC IV: air		
Bed	**H_0, m**	**U, m/s**
Shallow	1.1	0.48~0.82
Deep	1.8	0.23~0.93
Deep	2.0	0.39~0.92
Deep	1.8~2.0	0.18~1.56

1.56 m diameter column FCC II: air		
Bed	**H_0, m**	**U, m/s**
Deep	2.0~2.4	0.15~0.74
Shallow	0.9~1.3	0.11~0.51

283

APPENDIX B

VELOCITY MEASUREMENT DATA ANALYSES

In order to pursue the analysis in an unbiased manner, pre- and post- processing of data was carried out according to the algorithms. Cross-correlation was performed on the raw data as well as on data that had been pre-processed with binary coding and cut-off methods. Elimination criteria were imposed to extract acceptable adequately-correlated data sets, prior to assigning the correlated results to void-associated and dense-phase-associated particle and void velocities. The peak detection method was also applied to compare with the results from the cross-correlation method, as outlined below.

B.1 Cross-correlation

Cross-correlation of signals was pursued according to the block diagram in Figure B.1. If the direction and structure of the flow are known and constant, cross-correlation of the signals from the two receiving fibers using

$$\Phi_{I_A I_B}(\tau) = \lim_{T\to\infty} \frac{1}{T}\int_0^T I_A(t) I_B(t+\tau)dt \tag{B.1}$$

allows deduction of the time lag, τ_{AB}, by which identical signals are separated from. From the cross-correlation coefficient function, defined by

$$\varrho_{I_A I_B} = \frac{\Phi_{I_A I_B}(\tau) - \overline{I_A(t) I_B(t)}}{\sigma_{I_A}\sigma_{I_B}} \tag{B.2}$$

τ_{AB} is determined from the maximum cross-correlation coefficient as a function of the time shift.

Three different data pre-processing methods were compared prior to performing the cross-correlation involving: (a) raw data (i.e., no pre-processing); (b) binary coding; and (c) a cut-off method. In order to distinguish signals corresponding to the dilute phase, i.e., voids, from those originating from the dense phase, a binary coding (1 if $\varepsilon_s \leq \varepsilon_{s,\,threshold}$, 0 if $\varepsilon_s > \varepsilon_{s,\,threshold}$) is used prior to performing the cross-correlation of the signals, as illustrated in Figure B.2 (b). The choice of threshold voidage, the voidage value which distinguishes the two phases, is very critical. The effect of the threshold voidage on the velocity measurement is considered in the following section.

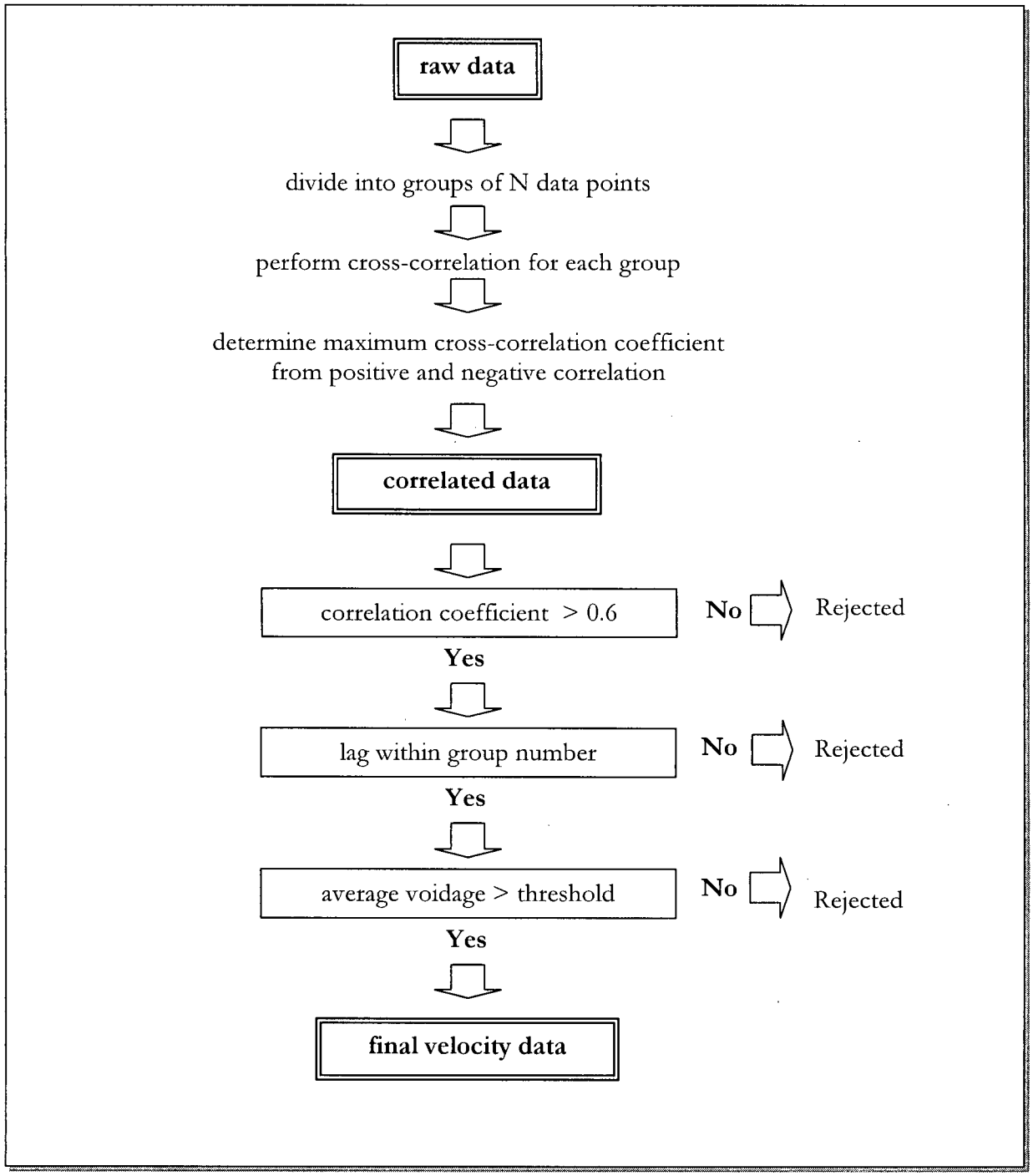

Figure B.1 Logic flow sheet for data cross-correlation and elimination.

For the current analysis, the threshold voidage is obtained from the minimum probability point between the two peaks (corresponding to the dense and dilute phases) in the probability distribution function (Bi and Su, 2001: Figure 1b). Further analysis using the binary coding method is reported in Section B.6. For the cut-off method, Figure B.2 (c), the same threshold value is used as in the binary coding method to eliminate signals originating from the dense phase..

Cross-correlation of the signals for calculating the particle velocities was first performed on a preset number of data points, the default number being 4096 points, regarded as one group. Thus, for a typical sampling frequency of 29,378 Hz, the cross-correlation coefficient was calculated for successive 139 ms bursts of data resulting in 975 groups for the overall sampling duration of 135.9 s. Elimination criteria were employed to systematically remove poorly correlated data, as well as any data with calculated (apparent) velocities differing by more than 5 standard deviations from the mean. On average, 20-40% of the groups of data were rejected through this process. The effect of group number, i.e., of the number of points for cross-correlation, N, on the velocity distribution is examined in Figure B.3. From Figure B.3, it is concluded that the difference in the results obtained without any pre-processing and by using the cut-off method is minimal. Hence it is justified to use the raw data for cross-correlation. In summary, particle velocities are calculated from cross-correlating a preset number of data points from the raw data. The assignment of the resultant particle velocity being associated to voids or the dense-phase, for the sake of distinction, is carried out through a threshold value imposed on the average voidage for each data group following the cross-correlation procedure.

B.2 Group number

In order to further investigate the effect of group number on the resulting velocity, data from the UBC column at U=0.42 m/s are next used for the analysis. The group number is varied between 100 and 10,000 points, with the resulting average velocity and voidage determined after performing the cross-correlation and elimination processes. Intuitively, in order to capture variations in particle velocity, one must strive for a smaller group number. This requires increased computational time. However, decreasing the group number generally increases the relative fraction of data eliminated, as shown in Figure B.4, implying that there are fewer representative velocity points. On the other hand, for the sample data examined above, the crossing time is calculated to be 0.029 s in this case, which corresponds to 387 points for a sampling frequency of 13,357 Hz. From Figure B.5, the sensitivity of the group number to the resulting average void-associated particle velocity and solid fraction is

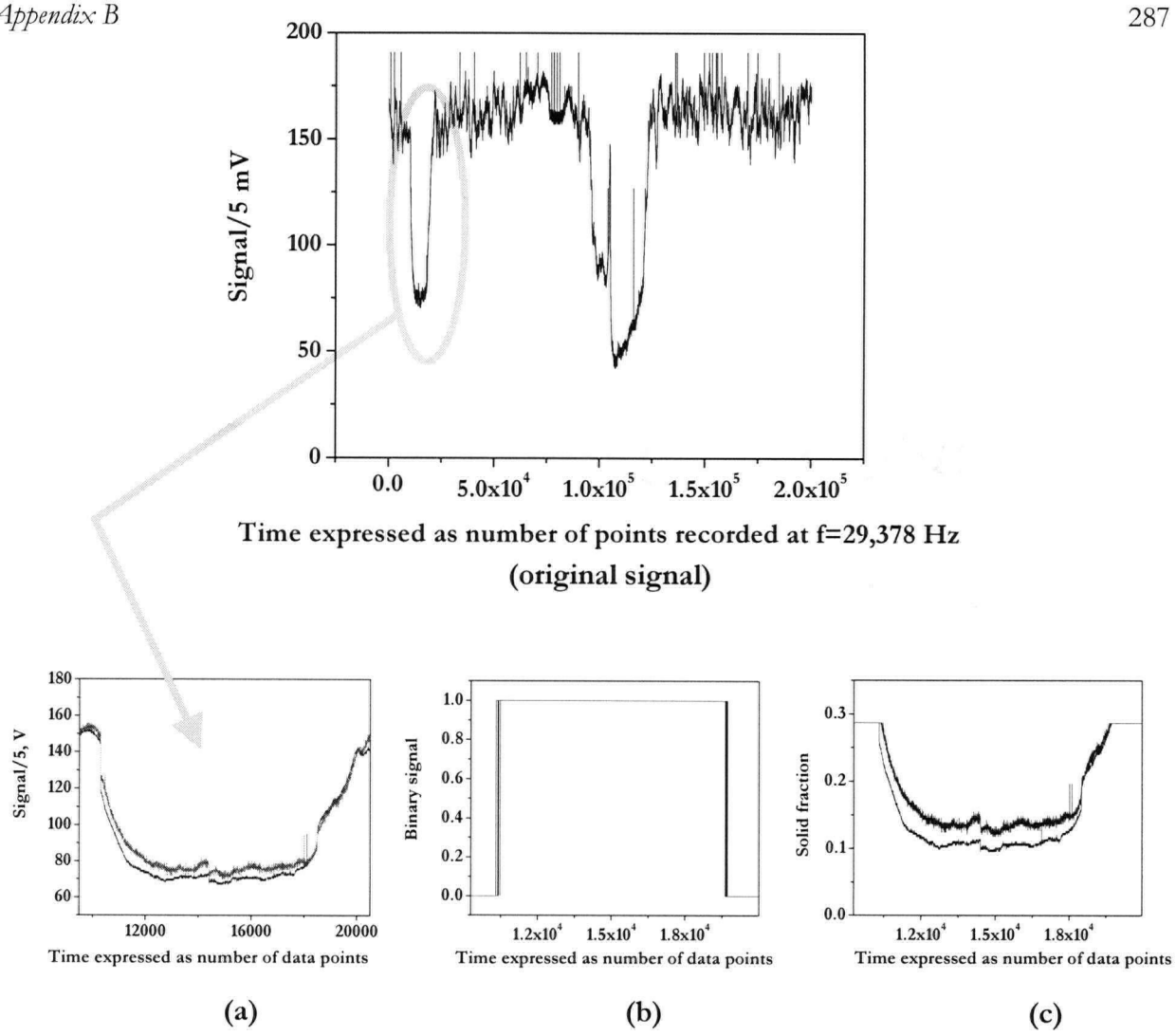

Figure B.2 (Original) Typical raw signal; (a) One void isolated from Figure 5.6; (b) Binary coding; (c) Cut-off method. D=0.61m, U=0.57 m/s, r/R=0.17, z=0.80 m, f=29,378 Hz.

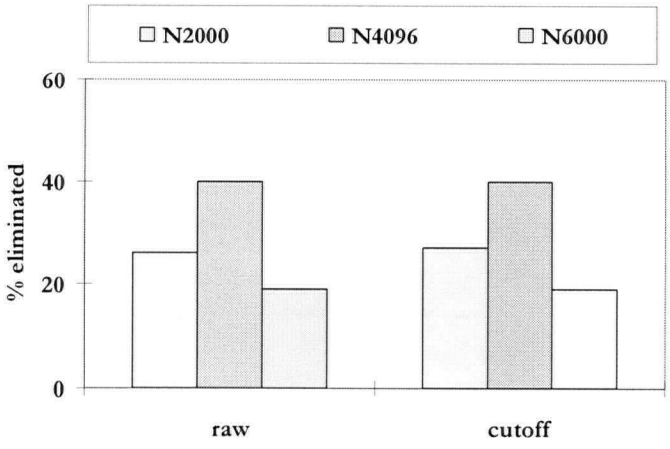

Figure B.3 Comparison of data processing method with respect to fraction of data groups eliminated. Data from Figures 5.6 (a) and (c).

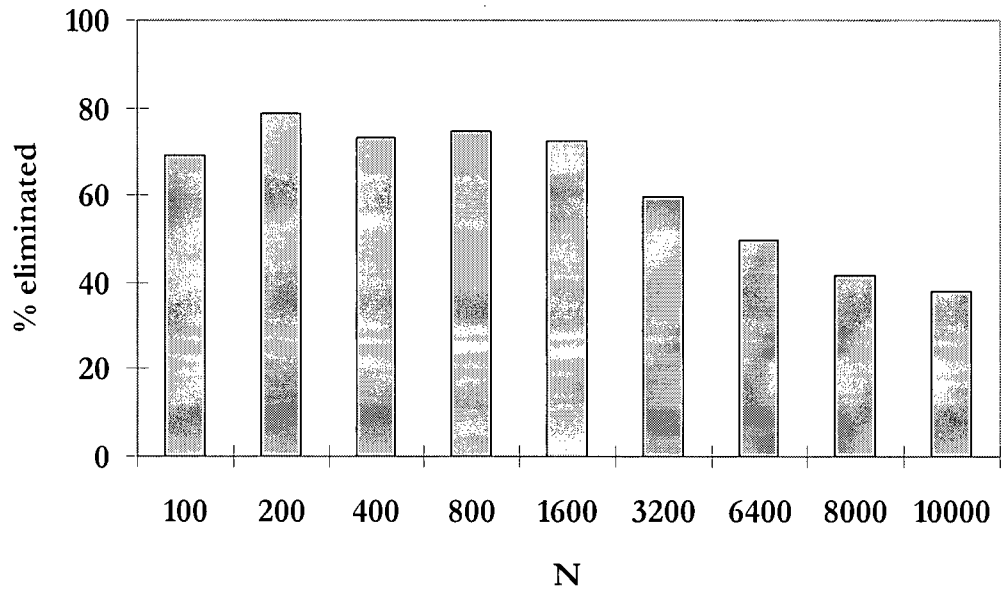

Figure B.4 Effect of group number on percentage of data eliminated for void-associated particle velocities. Threshold voidage=0.62, D=0.29 m, U=0.42 m/s, r/R=0.55, z=0.78 m, FCC I.

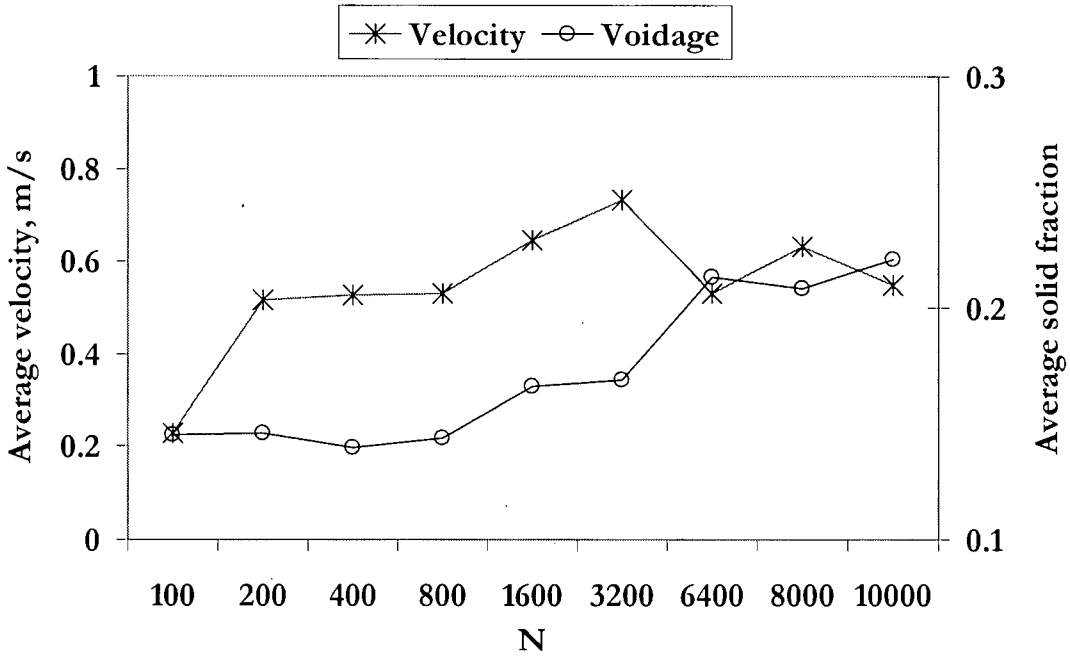

Figure B.5 Effect of group number on average velocity and solid fraction of void-associated particles. D=0.29 m, U=0.42 m/s, r/R=0.55, z=0.78 m, FCC I.

depicted. The group number must represent a short burst relative to the average time between crossings of the discrimination level. An increase of N beyond this average crossing time results in the inclusion of data not accurately represented by the average solid fraction. Since the crossing frequency is in turn affected by the void dynamics which is influenced by the superficial gas velocity, it is recommended that the crossing frequency be examined for each set of data before setting the group number for cross-correlation.

B.3 Elimination criteria

Careful consideration has been given to the elimination criteria. Firstly, the cross-correlation coefficient is required to be higher than 0.6. Secondly, the time lag is set to be higher than 1.1 time increments (inverse of sampling frequency), and lower than the maximum lag time (e.g. 0.029 s for f=13,357 Hz and N=387) for a given sampling frequency and group number. Lastly, the average voidage of each group is compared with the threshold voidage value to distinguish points resulting from a shift from the dilute phase to the dense phase. By setting the threshold value as the elimination criteria after cross-correlation, the threshold value is less significant with respect to the calculated velocity distribution.

B.4 Peak detection

The cross-correlation method of deducing the particle velocity distribution allows a large number of data to be processed. For comparison, peak detection of the signals was attempted using the software package Origin® 6.1. Signals from two fibers are plotted followed by examination by the peak-pick function. Origin® uses the moving rectangle search method where the peak is defined as the difference in height between the local maximum and minimum data points inside the rectangle, while the data values at both ends of the rectangle must be equal or larger than the rectangle height. The rectangle height and width are expressed as the percentage of the total amplitude and number of points, respectively, in the data range. Thus they are affected by the total extent of the set of data. It is only after the peaks are detected that the detected peak coordinates can be subjected to elimination due to inconsistent detection. By manually considering each peak and ensuring that the peaks are detected for both signals as a pair, one can calculate the time lag between pairs of peaks, thus obtaining velocities of particles passing the probe tip. One of the reasons why this cannot be done systematically by writing a program to perform peak-picking is the complexity of the erratic void profile, as exemplified in Figure B.2.

Figure B.6 compares void-associated particle velocity distributions obtained though cross-correlation and those detected through the peak picking method. It is suspected that the difference in the number of peaks under investigation, i.e., 201 groups for the cross-correlation method and 76 peaks from the peak detection, may account for the discrepancy in the cumulative velocities obtained from the same data set. The peak detection method is sensitive to the fluctuation of signals, as well as to the height and width of the moving rectangle.

At U=0.42 m/s, the fluctuation of particles associated with voids may exhibit difficult-to-isolate peaks, compared to the fluidizing conditions at higher gas velocities. Thus, this inconsistency is examined further by considering the data obtained at U=0.69 m/s.

Using the analysis method described above, the Origin® software detected 417 peaks, of which 193 corresponded to voidages greater than the threshold value of 0.62. On the other hand, the cross-correlation method resulted in 287 points above the threshold. The cumulative distributions of velocity presented in Figure B.7 show a better correspondence between the two methods. The normalized probability distribution of the results based on the positive and negative particle velocities, depicted in Figure B.8, reveals reasonable agreement between the two methods for positive displacement. There is a lack of detection of negative velocities for high voidages using the peak detection method. This difference should be investigated in the future to confirm if voids moving upwards or downwards can influence particle velocities in both the upwards and downwards directions.

One of the disadvantages (Zhu et al., 2001) of the cross-correlation function in determining the particle velocities is the preferential detection of the velocity of particle clusters over particles travelling individually. This is due to the tendency of large peaks in the signals to affect the value of $\varrho_{I_A I_B}$, the cross-correlation coefficient function. It is clear that this disadvantage cannot be overcome by the peak-detection method.

B.5 Dense-phase-associated particle velocity

By setting the elimination criteria to eliminate particle velocities associated with voids, a dense-phase-associated particle velocity can be deduced from the data cross-correlation.

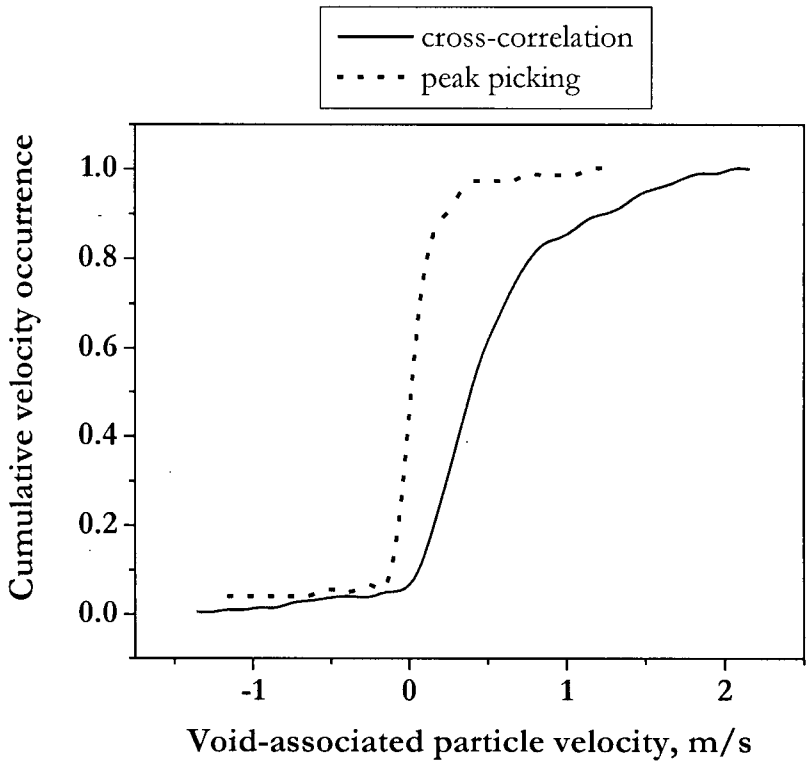

Figure B.6 Comparison of void-associated particle velocity distribution between cross-correlation and peak-picking methods. D=0.29 m, U=0.42 m/s, z=0.78 m, r/R=0.55, f=13,357 Hz, FCC I.

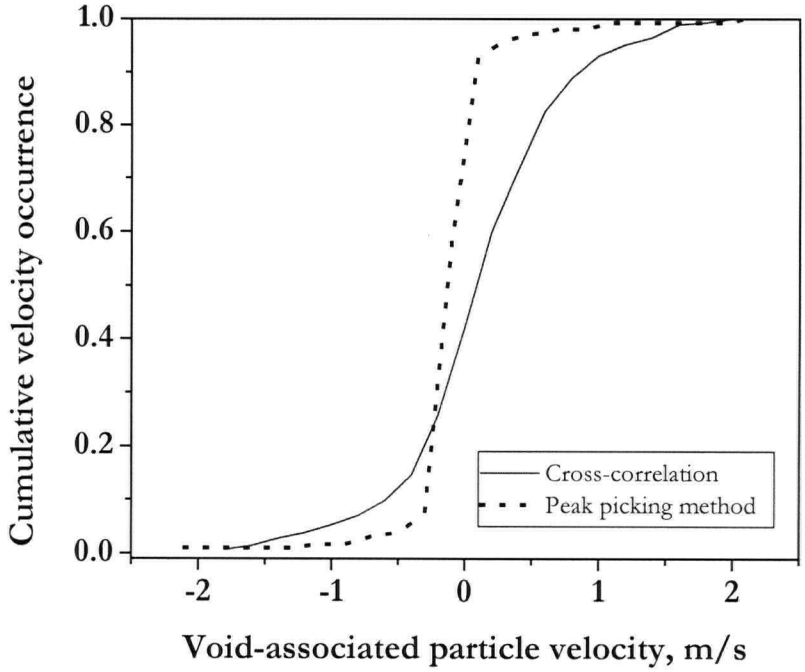

Figure B.7 Comparison of void-associated particle velocity distribution between cross-correlation and peak-picking methods. U=0.69 m/s, D=0.29 m, z=0.78 m, r/R=0.55, f=12,059 Hz, FCC I.

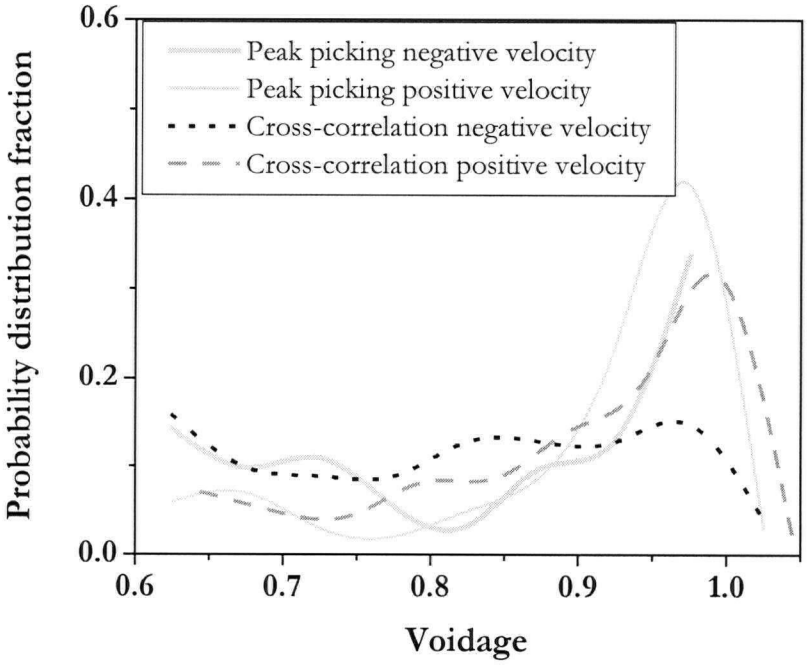

Figure B.8 Comparison of the positive and negative void-associated particle velocity distribution between cross-correlation and peak-picking methods. U=0.69 m/s, D=0.29 m, z=0.78 m, r/R=0.55, f=12,059 Hz, FCC I.

B.6 Binary coding

As noted above in Section B.1, the effect of the threshold value is most prominent when the binary coding method is employed. Examining Figure B.2 (b), the possibility of obtaining void velocities from the optical velocity probe is explored. In this section, the effect of the threshold value determined through six different methods on the resulting void velocity calculated via binary coding is explored in detail. Examined previously by Bi and Su (2001) and displayed in Figure B.9, Method (a) simply divides the two phases according to whether the local voidage exceeds the mid-value between the maximum and minimum voidage signal values. The outliers, i.e., data which fall below ε_{mf}=0.45 (for FCC) or above ε=1.0 after conversion according to the calibration values, are removed before setting the maximum and minimum voidage values. Since, as discussed above, the signal has a linear relationship with voidage for the velocity probe with a cover, the volume fraction of each phase corresponds to the area underneath the probability distribution function curve. Method (b), employed by Bayle et al. (2001), sets the threshold value at the line indicated by the arrow shown in Figure B.9 (b), i.e., at a voidage of $2\varepsilon_{peak}-\varepsilon_{mf}$. This method ensures that the threshold value lies between the maximum peak of a pdf plot for the dense phase and the dilute phase. For Method (c), the threshold value was set at a point corresponding to 0.95 times the difference between the maximum and the minimum voidage signal, as proposed by Mainland and Welty (1995) for a light-penetration type optical fiber probe. This method is, however, unsuitable for a reflective type optical fiber probe in a turbulent fluidized bed as the dense phase voidage corresponding to the maximum peak of a pdf plot, shifts toward higher voidage, and thus represents no physical meaning to the threshold value as depicted in Figure B.9 (c). The fourth method, shown in Figure B.9 (d), uses the maximum peak of the pdf plot to demonstrate the transition between the two phases. Method (e) is the minimum point cut method, proposed by Bi (1994), which employs the minimum point in the smoothed pdf plot rather than the two end points as the dividing value. Although this method was initially used to determine the threshold values in Section B.1, it becomes rather ambiguous when the dilute phase exhibits a flat pdf curve, especially for measurements near the wall. Moreover, it was difficult to mathematically express the minimum point when a smooth probability distribution was not obtained. The last method shown schematically in Figure B.9 (f) is the value which corresponds to 0.95 times the difference between the two peaks representative of dense and dilute phase in a pdf plot. Once again, this method can involve large error when either peak is indistinct. The first four methods are incorporated into the algorithm, shown in the logic flow chart in Figure B.10, and pursued to calculate the distribution of void velocity for comparison.

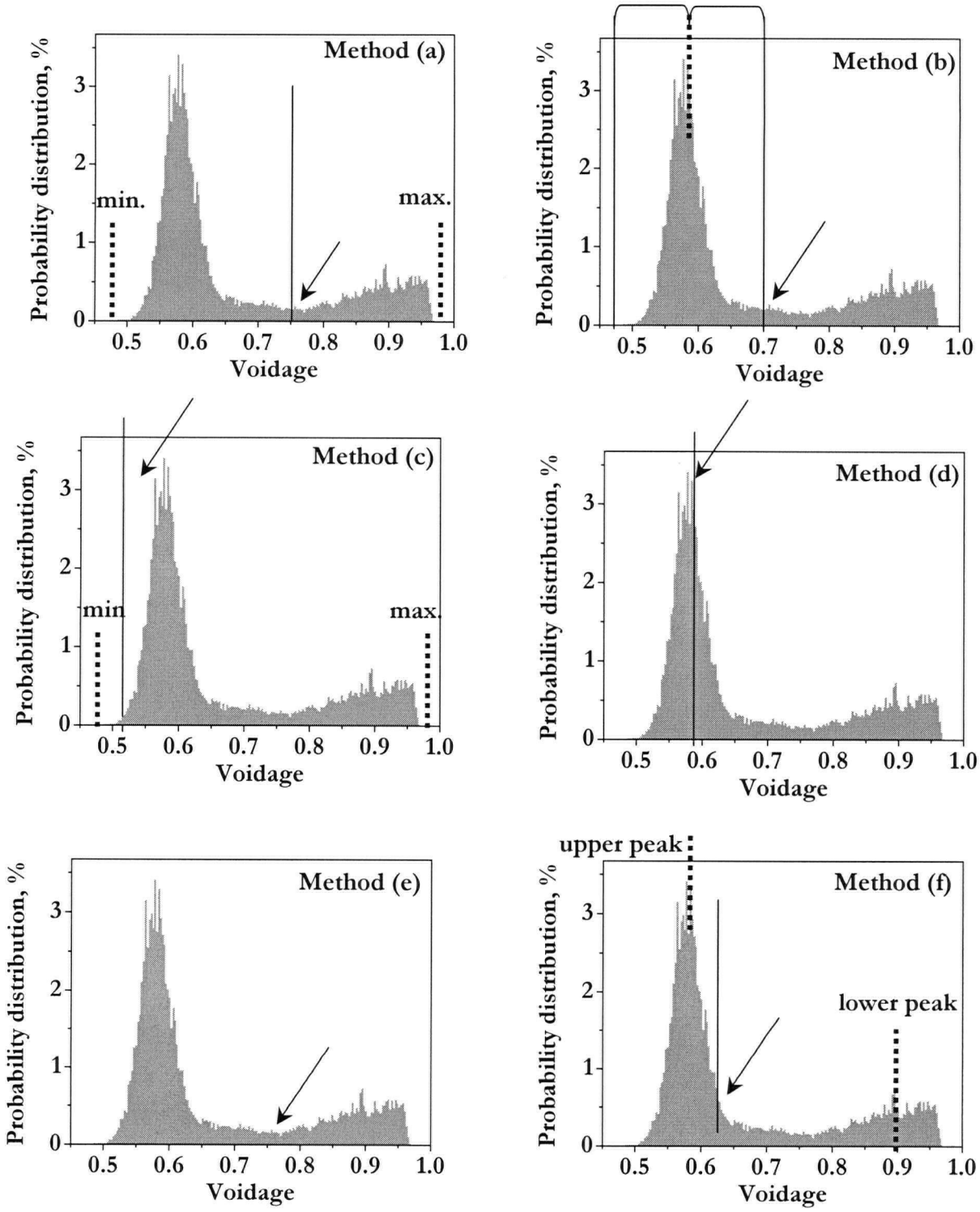

Figure B.9 Probability distribution function of local voidage measured by optical velocity probe and determination of threshold value corresponding to boundary between dilute and dense phases. U=0.69 m/s, D=0.29 m, z=0.78 m, r/R=0.55, f=12,059 Hz, FCC I.

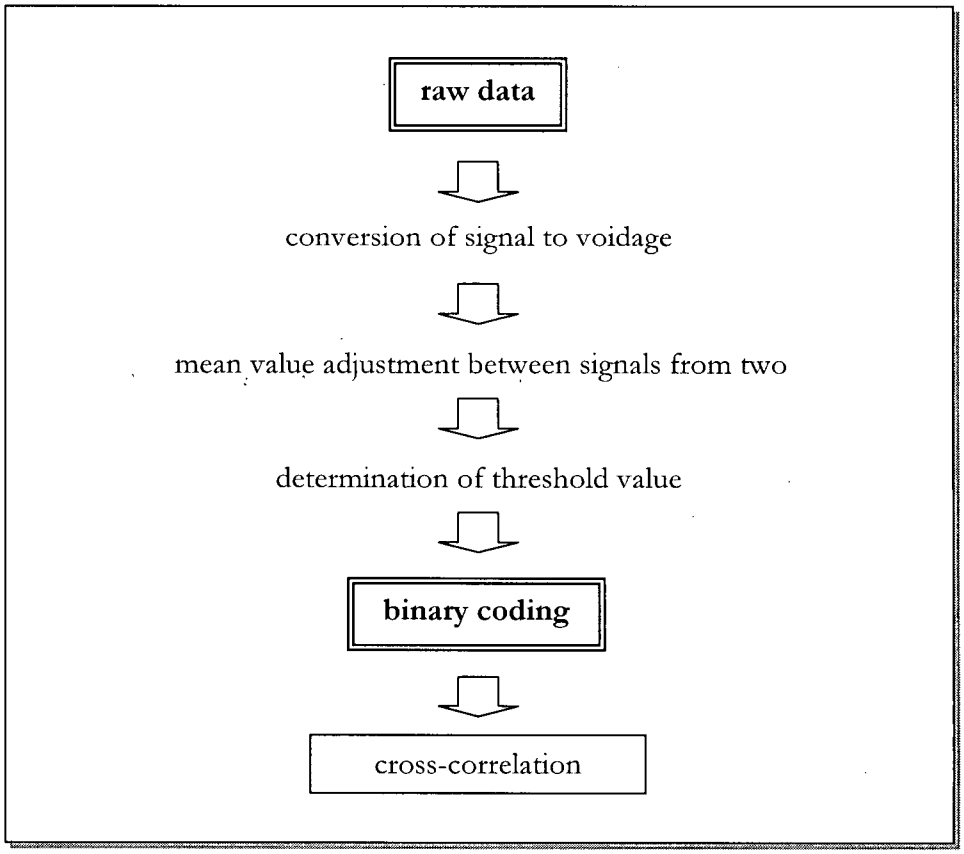

Figure B.10 Logic flow sheet for binary coding signals.

Since the binary coding method compares the time lag at threshold voidage, it can be concluded that the void velocity is higher for voids of higher voidage. This is consistent with physical insight of the voidage profile within a void, as shown in Figure B.11, where the slope of voidage vs. time plays a significant role in the lag time. Ideally, each void, if identifiable, should be isolated prior to cross-correlating the signal from the complete passage of the void.

The first four methods depicted in Figure B.9, resulted in the threshold values as summarized in Table B.1 for the data set for U=0.69 m/s, D=0.61 m, z=0.80 m and r/R=0.09 sampled at 30,147 Hz. Partial extraction of the data of 600,000 points representing 19.9 s duration was executed prior to binary coding for different threshold values. The resultant coded set of signals (four sets for four threshold values) was cross-correlated for a group number of 200. The only method, which deduced a velocity profile from binary coding, was Method (d), as depicted in Figure B.12, with most correlated data discarded from the variance of the signals being zero.

The void velocity does not seem to represent what is physically plausible in a bed of FCC particles fluidized at ambient temperature and pressure at U=0.69 m/s. From observing this section of data, it is confirmed that the considerable noise generated by one of the fibers contributed to the binary coding from which to perform the cross-correlation. Another attempt using a higher group number of 4096 was pursued before concluding that the binary coding method cannot deduce void velocities with accuracy. Much lower velocities were calculated using the same data as above, which led to the conclusion that for the optical velocity probe and its fiber size of 0.26 mm diameter fibers, the physical scale capable of capturing the dynamics is at the particle size level, and not at the macroscopic void level of order 10^{-2} m. As the optical velocity probe was developed to measure individual particles in the size range of an FCC, forcing a cross-correlation function on a binary coded signal may produce an apparent velocity profile, which is not reflective of the physical scale.

By isolating one of the voids and performing cross-correlation on the raw signals for the whole contact duration, i.e., N=30,000, the lag was $1 > 0.98$ and the void velocity was calculated to be -0.04 m/s, indicating poor correlation of signals. Thus, the velocity of voids cannot be obtained from optical fiber velocity probe signals by simply increasing the group number to represent larger scale voidage fluctuations. It is speculated that further pre-conditioning of signals may be necessary to calculate such velocities.

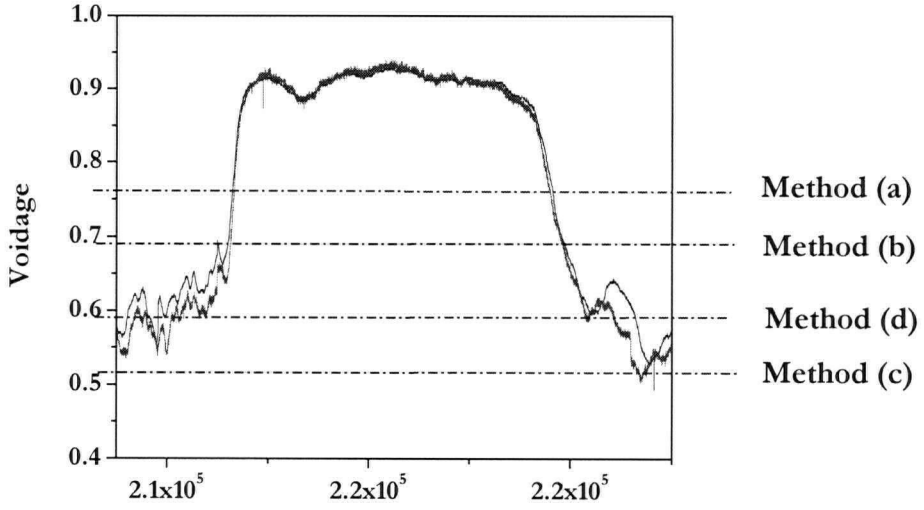

Figure B.11 Voidage signal from two fibers. Broken lines denote the threshold values from Methods (a), (b), (c), and (d). U=0.69 m/s, D=0.29 m, z=0.78 m, r/R=0.55, f=12,059 Hz, FCC I.

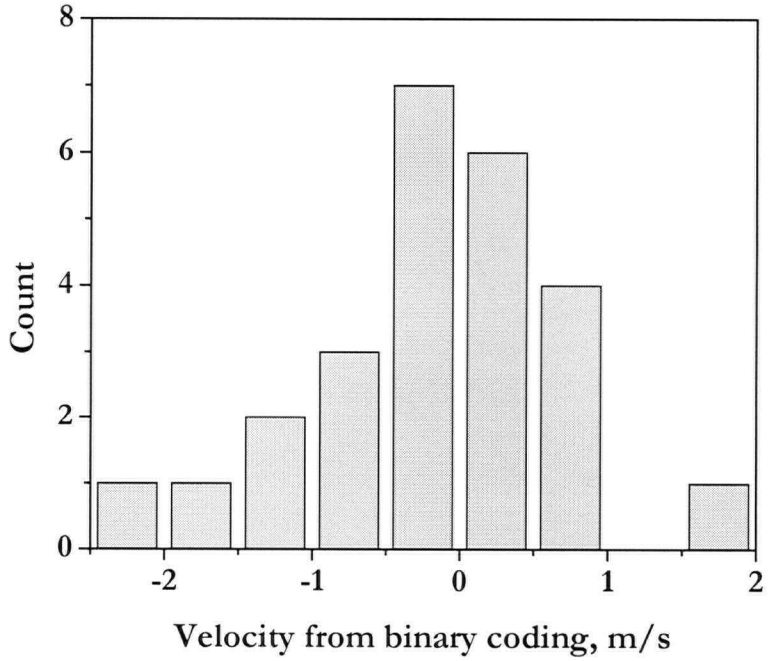

Figure B.12 Velocity distribution applying Method (d) binary coding. U=0.69 m/s, D=0.61 m, z=0.80 m, r/R=0.09, f=30,147 Hz, FCC IV.

Table B.1 Effect of threshold determination methods on threshold voidage values. U=0.69 m/s, D=0.61 m, z=0.80 m, r/R=0.09, f=30,147 Hz.

Method	Threshold voidage value
Method (a)	0.724
Method (b)	0.595
Method (c)	0.486
Method (d)	0.524

The analysis method by which to deduce the void dynamics from the optical velocity probe may not be completely exhausted; however, due to the difference in physical measurement scale, it is not pursued further at this point.

B.7 Optical fiber voidage probes

Contrary to the optical velocity probe, the optical voidage probes described in Chapter 4 are designed to measure swarms of FCC particles. As a result, and as also depicted in Figure 5.3, void passage can be accurately monitored without excessive voidage fluctuation due to particle velocity fluctuation for the case of the optical velocity probe.

A small piece of curved Plexiglas plate with 10 vertical holes spaced 0.01 m apart was mounted on the side of the 0.29 m diameter column, 0.77 m above the distributor plate. This allowed two identical optical voidage probes to be inserted anywhere between 0.01 to 0.09 m apart. The distances were such that there was no overlapping measuring region of the two probes. Thus the physical distance represented the distance on which to base the velocity calculation. Measurements were recorded for 30 s at 1000 Hz using LABTECH® data acquisition software. Signals were converted to voidage prior to being cross-correlated using the MATLAB® algorithm noted above.

Prior to calculating the void velocities, a cut-off method described in Section B.1 was imposed to eliminate any voidage fluctuation below the threshold value. In obtaining an accurate representation of the void velocities, one can characterize the voidage fluctuation in terms of binary, dense and dilute modes. Since a direct measurement of the gas velocity is extremely difficult to obtain in the case of a dense gas-solid fluidized bed, the only measurable velocity related to the gas phase is that

of voids, expressed in terms of crossing the discrimination level. The probability distribution function of voidage from data measured at z=0.78, r/R=0.70, D=0.29 m is examined in Figure B.13 to decide on the possible threshold values. Based on the analysis methods discussed in Section B.6, four threshold values are listed in Table B.2 and shown graphically in Figure B.14. Taking the crossing frequency at the maximum number of crossings, i.e., Method (d), does not truly represent the isolated voids, as demonstrated in Figure B.14. In Figure B.15, the void velocity distribution is compared for the threshold voidages of 0.527, 0.565 and 0.704 as a result of cross-correlating the signals at a group number reciprocal of the average crossing frequency for each threshold value. The cut-off threshold set by Method (d) inevitably includes voidage fluctuations considered to be in the dense phase, as shown in Figure 5.18, thus producing a peak of negative void velocities which is not found in any other threshold determination method. The other three threshold values indicate similar pdf distributions. Therefore, Method (a) is chosen to determine the threshold voidage at which to perform the cut-off in order to ensure that voidage signals relating to the dense phase are completely eliminated.

Table B.2 Effect of threshold determination methods on voidage value and crossing frequency. D=0.29 m, U=0.69 m/s, r/R=0.70, z=0.78 m, FCC I.

Threshold determination method	Threshold voidage	Average crossing cycle time, s	f_c, Hz
Method (a)	0.704	0.294	3.4
Method (b)	0.527	0.398	2.5
Method (d)	0.475	0.055	18
Method (e)	0.565	1.12	0.89

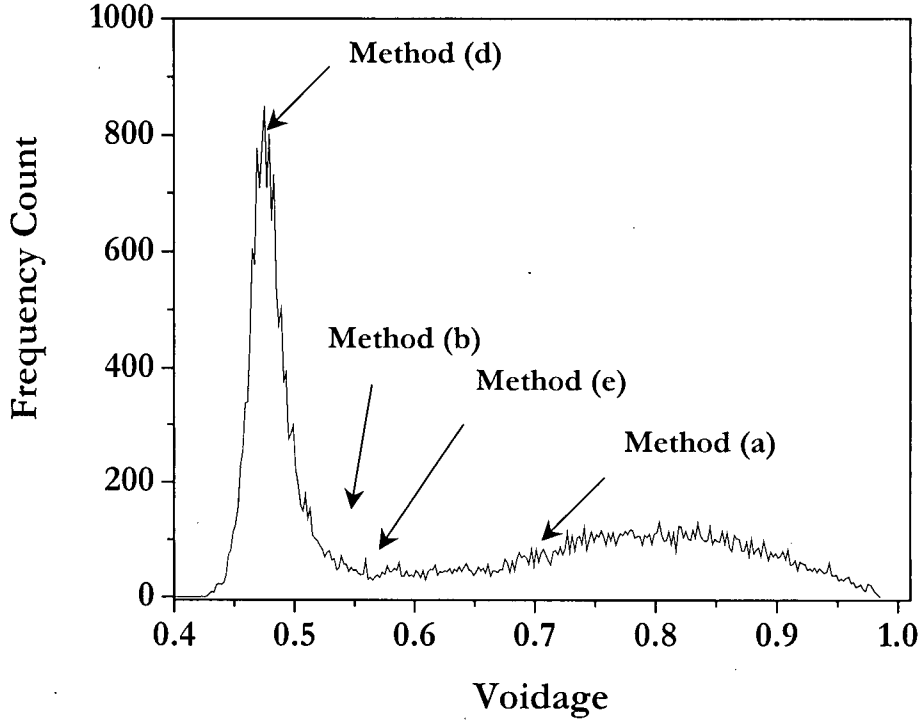

Figure B.13 Probability distribution of voidage indicating threshold values from Methods (a), (b), (d), and (e). D=0.29 m, U=0.69 m/s, r/R=0.70, z=0.78 m, FCC I.

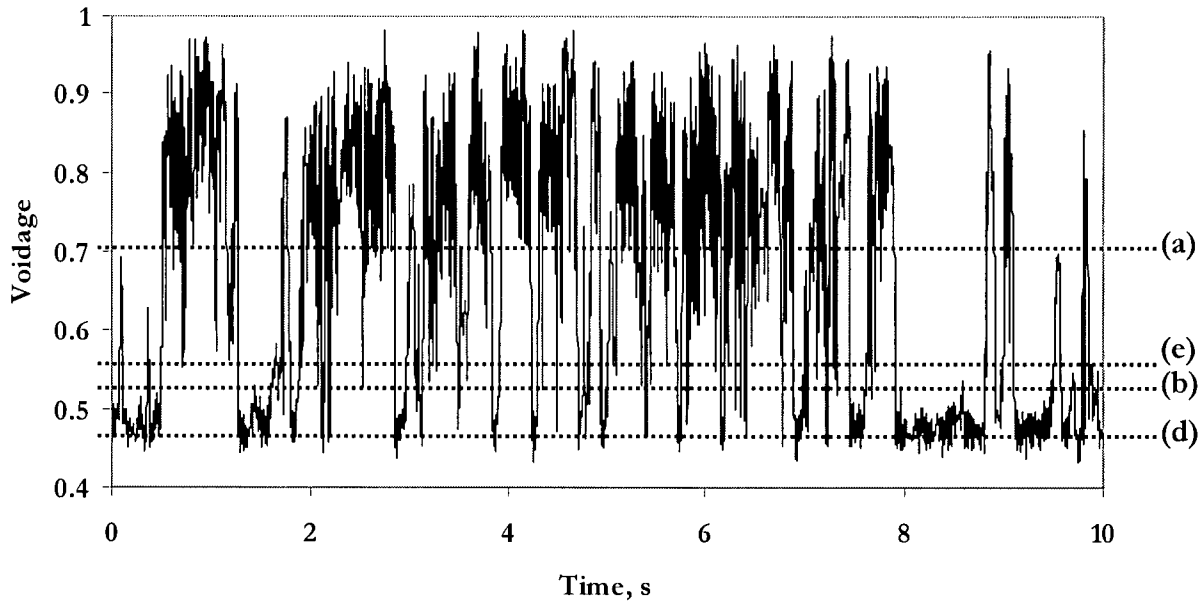

Figure B.14 Voidage fluctuation measured by optical voidage probe. D=0.29 m, U=0.69 m/s, r/R=0.70, z=0.78 m, FCC I.

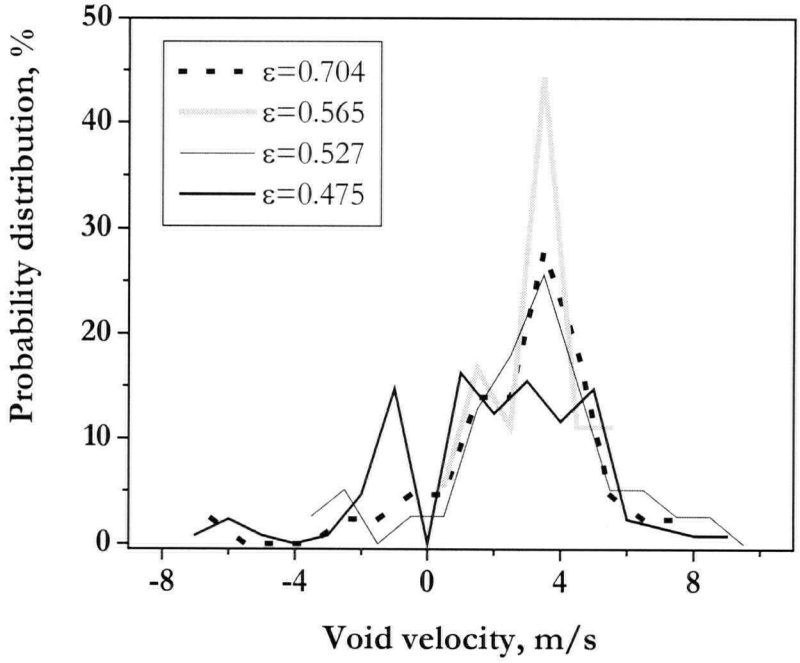

Figure B.15 Probability distribution of void velocity and its effect of threshold voidage expressed as crossing frequency. D=0.29 m, U=0.69 m/s, z=0.78 m, r/R=0.70, Δz=0.01 m, FCC I.

When there is a well defined, isolated void, the time lag from two signals can reflect the velocity at which a void is travelling. With the aid of the criteria of Matsuura and Fan (1984) we require

- signal for the upstream element is used as a trigger signal
- $t_1 < t_2$ and $t_3 < t_4$
- $0.9 < \dfrac{\tau_1}{0.5(\tau_1 + \tau_2)} < 1.1$

These conditions are shown graphically in Figure B.16. When these criteria are fulfilled, it is then possible to estimate the void velocity. The criteria require that all voids travel upward, and a clear distinction between the dense and dilute phases is provided. However, many voids detected in the gas-solid turbulent flow regime travel both upwards and downwards and without a clear distinction between the two phases, as shown in Figure B.17 taken from the same set of data as in Figure B.16. The erratic movement of voids contributes to some of the advantages in operating in this flow regime from a reactor standpoint, but they pose challenges in measurement and in defining the parameters for reactor models. Perhaps, these challenges originate from the desire to interpret the flow dynamics from a two-phase (dilute and dense phase) binary point of view. By expressing the parameters such as voidage and velocity as continuous functions, the hydrodynamics may be closer to the physics, but may impose difficulties in modelling at a macroscopic level.

Once again, the justification of the group number used for the cross-correlation must be mentioned. Figure B.18 is a typical plot of void velocity shown against voidage fluctuation vs. time. By performing the cut-off method prior to cross-correlating the signals, only signals above the threshold voidage are considered. Moreover, the x-axis error bar corresponds to the equivalent length of time a group number represents. Void velocities not represented for peaks above the threshold value of 0.704 imply a poor cross-correlation. These were eliminated by imposing the elimination criteria reported in Section B.3. The figure also illustrates the adequacy of the imposed crossing frequency of 3.4 Hz, i.e., group number of 294, determined by setting the threshold using Method (a), which captures most of the passing voids. Group numbers of 20, 100 and 300 were examined to see the effect on the resulting void velocity distribution, shown in Figure B.19. A group number of 20 did not produce any results after the elimination criteria were applied. This is most likely due to not having enough data points to distinguish the void as a peak, thus resulting in extremely poor correlation. As the void velocity distributions for group numbers of 100 and 300 are in good agreement; it was decided to use N=300 in the interest of analysis time.

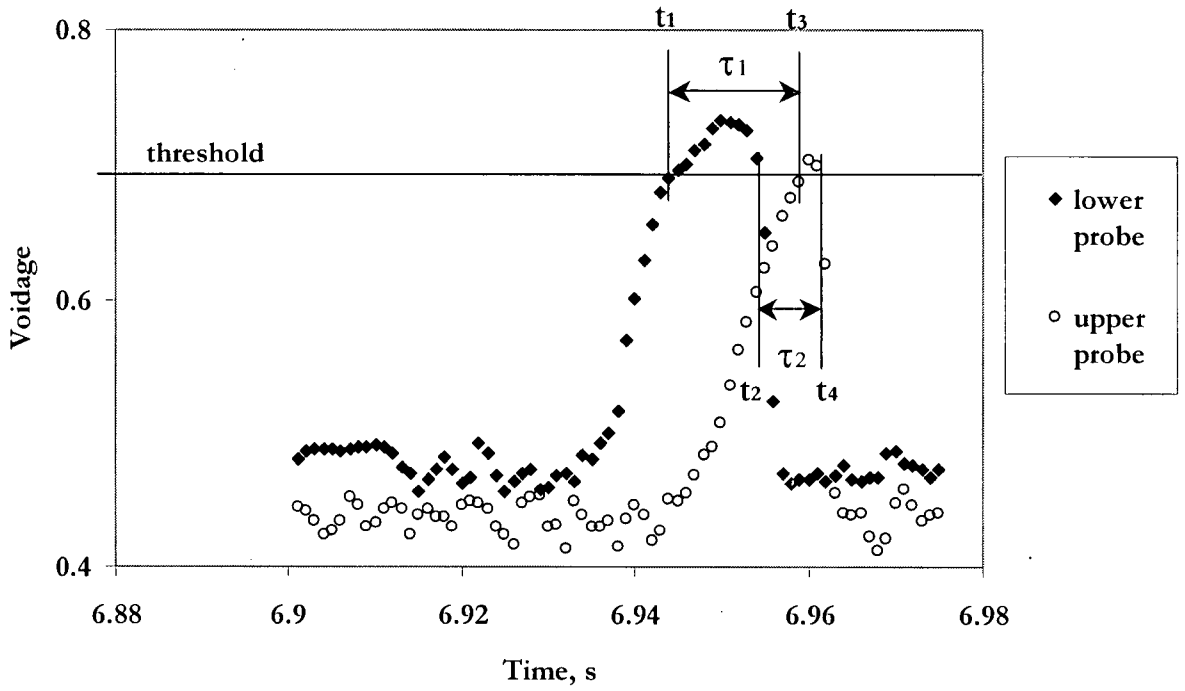

Figure B.16 Voidage signals depicting void velocity evaluation method of Matsuura and Fan (1984). D=0.29 m, U=0.90 m/s, r/R=0.70, z=0.78 m, H_0=1.5 m, FCC I.

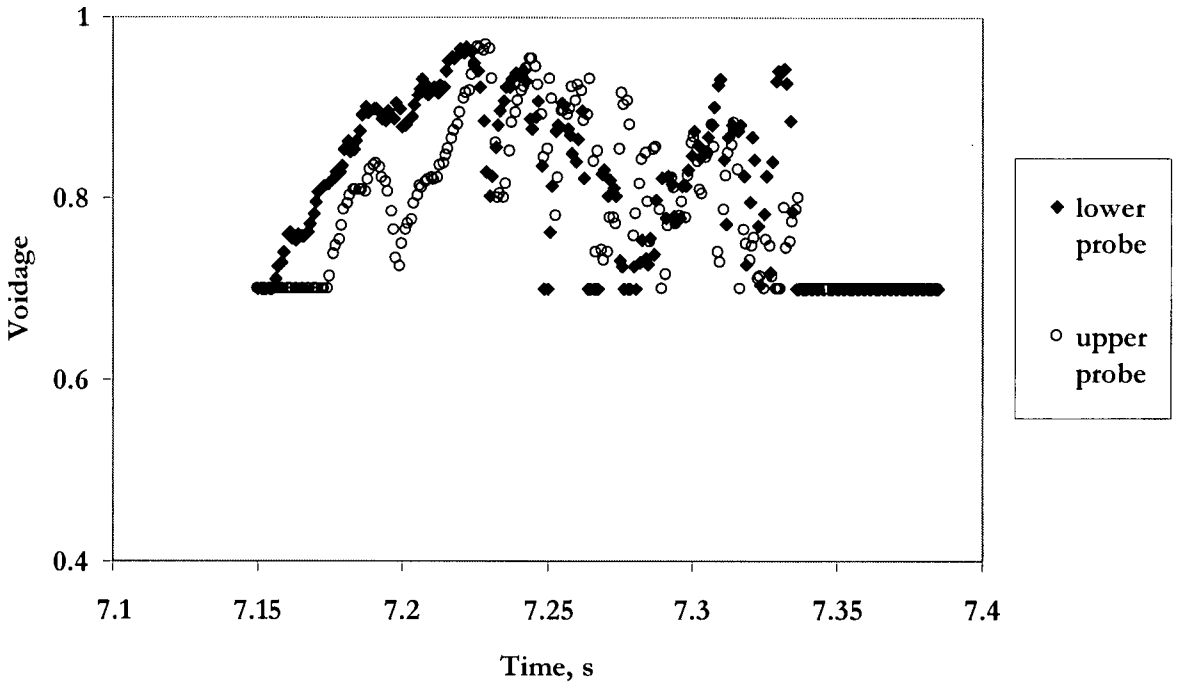

Figure B.17 Voidage signals processed by cut-off method exemplifying the erratic movement of voids. D=0.29 m, U=0.90 m/s, r/R=0.70, z=0.78 m, H_0=1.5 m, FCC I.

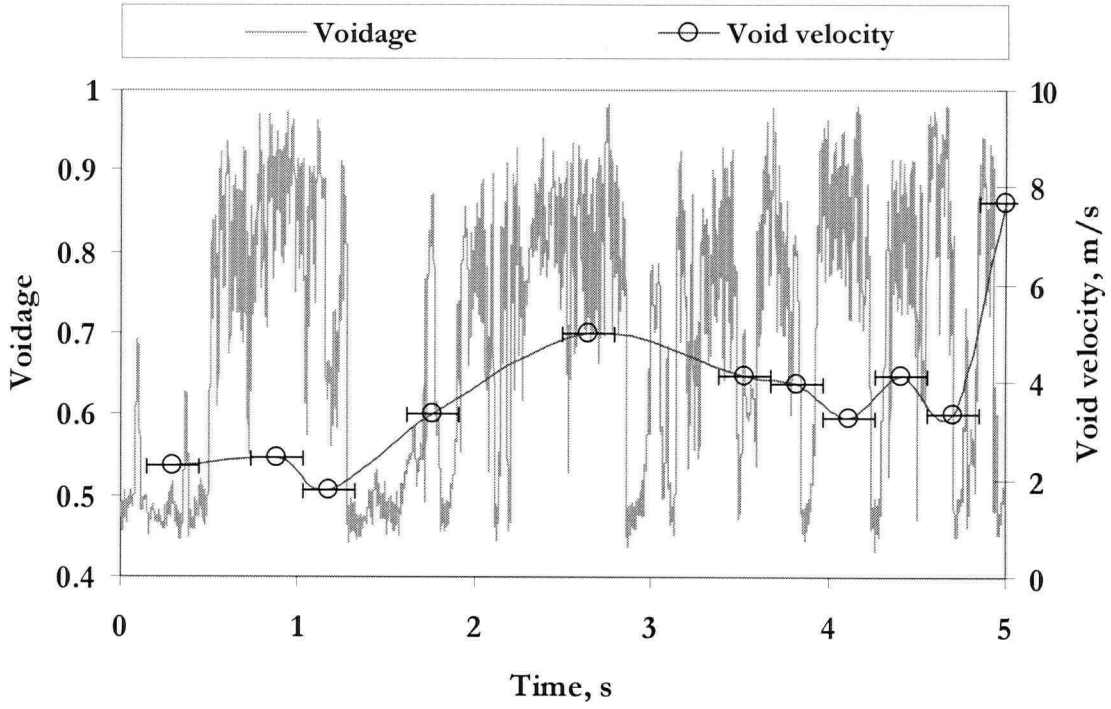

Figure B.18 Void velocity with voidage fluctuation. X error bars representing periods of signal considered for cross-correlation. Threshold voidage value=0.704 from Method (a), D=0.29 m, H_0=1.5 m, U=0.69 m/s, r/R=0.70, z=0.78 m, FCC I.

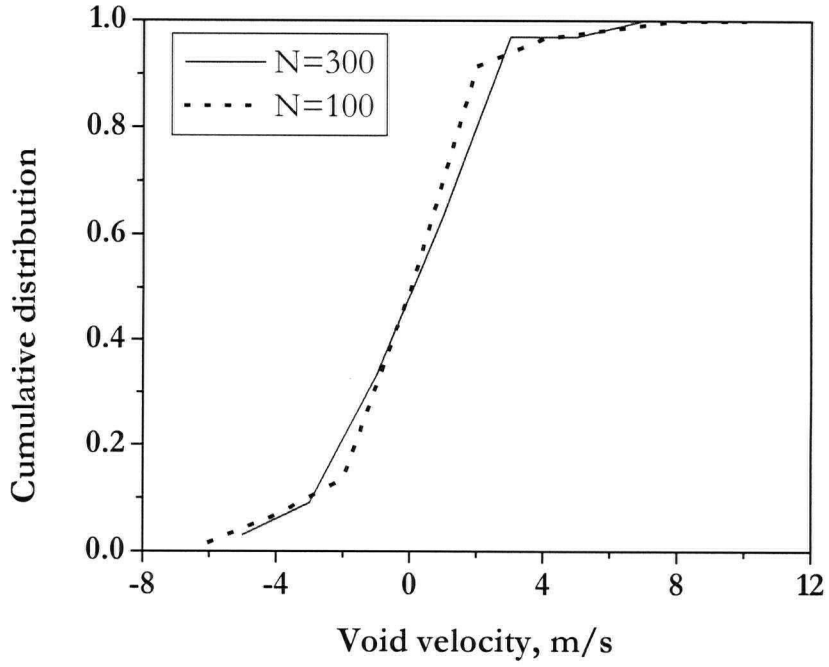

Figure B.19 Effect of group number on cumulative void velocity distribution. D=0.29 m, U=0.90 m, r/R=0.70, z=0.78 m, H_0=1.5 m, FCC I.

Ultimately, the chord length of each void could be calculated to apply the group number according to each void in order to calculate the void velocity more precisely.

B.8 Conclusions with respect to data analysis method

This section has highlighted the measurement techniques and data analysis procedures, such as the cross-correlation and the elimination processes, which allow particle and void velocities to be acquired in gas-solid fluidized beds of 0.29 and 0.61 m diameter, operated in the bubbling and turbulent flow regimes of fluidization.

From the optical fiber velocity probe acquiring data through a high-speed acquisition board, simultaneous measurement of particle velocity and solids concentration was achieved, enabling local instantaneous flow dynamics to be investigated. Particle velocities were obtained by cross-correlation of raw signals at a group number, in most cases, of 300. Particle velocities were obtained across the full voidage range for the measurements from the 0.61 m diameter column, while those from the 0.29 m diameter column were restricted to dense-phase associated particle velocities owing to the lower sampling frequencies, i.e., 13 kHz as opposed to 29 kHz for the larger column.

An attempt was made to apply binary coding to convert the data from the optical velocity probe to deduce the void velocities. This did not succeed as the results indicated very low void velocities, which were not physically plausible. It was concluded that the derived values did not reflect the physical scale of interest.

Using a pair of optical fiber voidage probes spaced a certain distance apart, the void movement was obtained in the smaller fluidized bed column. The cut-off method was applied prior to cross-correlating signals, enabling elimination of the effect of the dense phase fluctuation towards the void velocity calculation. The group number was set at 300, equivalent to 300 ms bursts, in order to capture small voids, i.e., short contact time to the probes. The cross-correlation method is considered to be desirable compared to the peak detection method for void velocity calculation owing to the physical scale of the measurement. In other words, one peak at a given voidage cannot accurately represent the velocity at which a void, which is itself of transient character and whose dimension is of order 10^{-1} m, may be travelling.

APPENDIX C

FOURIER AND WAVELET TRANSFORMATIONS

C.1 Fourier transform

The Fast Fourier Transform, FFT, transforms time domain functions into frequency domain representations. A function, f, belongs to the square-integrable function space $L^2[a,b]$ if

$$\int_a^b f^2(x)dx < \infty \tag{C.1}$$

This translates to expressing any function $f \in L^2[-\pi,\pi]$ as an infinite sum of dilated cosine and sine functions. In practice, this is approximated by a finite sum as:

$$f(x) = \frac{1}{2}a_0 + \sum_{j=1}^{J}\left(a_j \cos(jx) + b_j \sin(jx)\right) \tag{C.2}$$

The coefficients, a and b, are calculated by the inner product of the function f and the basis functions for each x,

$$a_j = \frac{1}{\pi}\int_{-\pi}^{\pi} f(x)\cos(jx)dx,\ j=0, 1, 2, \ldots. \tag{C.3}$$

$$b_j = \frac{1}{\pi}\int_{-\pi}^{\pi} f(x)\sin(jx)dx\ ,\ n=1, 2, \ldots. \tag{C.4}$$

The calculated coefficients, a_j and b_j, indicate the frequency content of the function f at the level of resolution j (Ogden, 1997). The Fast Fourier Transform reduces the time required to perform a Fourier analysis by expressing the coefficients (Chatfield, 1996) as:

$$a_j + ib_j = \frac{2\left(\sum f(x)\exp(2\pi ijx/N)\right)}{N} \tag{C.5}$$

for f(x) and N observations. In order to avoid the necessity to perform N^2 multiplications, a windowing method is applied for Discrete Fourier Transform of N samples. Origin ® software 6.1 was used to perform the FFT where the discrete data were obtained by a window function w[n]. The FFT of the sampled data is:

$$V[k] = \sum_{n=0}^{N-1} w[n]x[n]\exp(-i2\pi F_k n) \tag{C.6}$$

where x[n] is a finite-length, N samples of data; $F_k = k/N$; and n is a discrete frequency. The spectrum resolution was enhanced by choosing the Welch window:

$$w[n]=\frac{1}{2}\left[1-\cos\left(\frac{2\pi n}{N-1}\right)\right] \tag{C.7}$$

In order to reflect the amplitude in the original data, amplitude normalization was performed on the resultant FFT.

Note that the Fourier basis is an orthogonal basis, i.e., two functions, e.g. f and g with $f \perp g$, if

$$\langle f,g\rangle=0 \tag{C.8}$$

C.2 Wavelet analysis

C.2.1 Introduction to wavelet transformation

In wavelet analysis, dilating or contracting the chosen analyzing wavelet before convolving it with the signal accomplishes scale decomposition. The procedure is similar to Fourier transformation where inner products of x(t) with functions are obtained. The major difference is depicted in Figure C.1 where comparative transformation waves are plotted. In Fourier analysis concerned with approximating a function by a sum of sine and cosine functions, transformation is performed by a smooth and infinite length function, as exemplified in Figure C.1(a) by the sine wave. The behaviour of this function makes it suitable for transforming stationary signals to estimate the hidden periodicities in data.

On the other hand, transformation functions used in wavelet analysis, such as Morlet and Mexican hat wavelets plotted in Figures C.1 (b) and (c), respectively, pose distinct characteristics compared to those applied in Fourier transform. First, the irregularity of the shape of the functions contribute to the suitability in analyzing signals with discontinuities or sharp changes. Secondly, the compactly supported nature of the function permits temporal localization of the analysis. These features make wavelet analysis a potential tool for analyzing non-stationary and transient signals of imbedded short time events, or non-periodic cycles.

As wavelet analysis is being established among analysts from different disciplines, analogies between wavelet analysis and windowed Fourier transform are often drawn (e.g. Daubechies, 1992; Rioul and Vetterli, 1991; Farge, 1992; Weng and Lau, 1994; Hlawatsch and Boudreaux-Bartels, 1992).

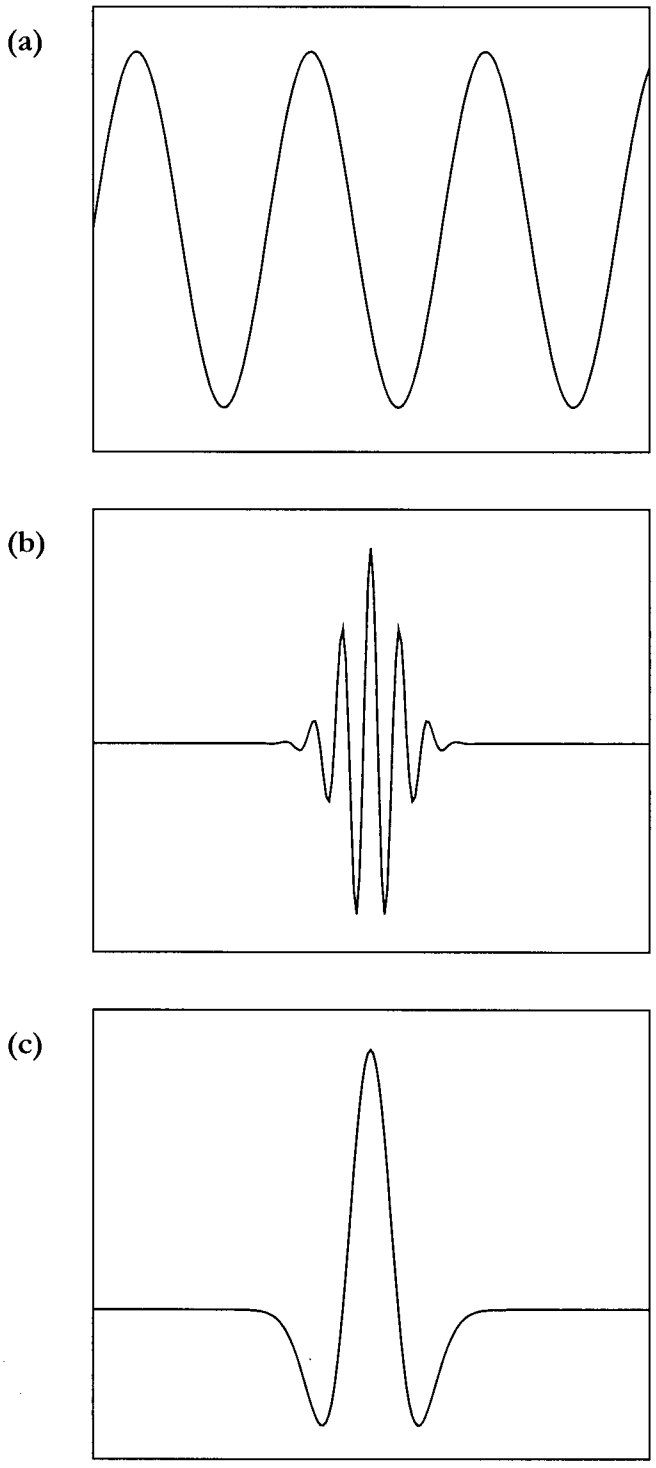

Figure C.1 Typical shapes of (a) sine wave; (b) real part of Morlet wavelet; and (c) Mexican hat wavelet.

The windowed Fourier transform is capable of adjusting the width of windows with which to perform the transformation. However, as discussed below, it cannot "zoom in" on a particular space in time. Figure C.2 represents the phase space associated with different transforms. If the object is to filter signals everywhere in time space, the Fourier transform is clearly the best choice (Figure C.2 (a)), offering perfect frequency resolution with no time information. For the windowed Fourier transform, the size of the window is kept constant while oscillation is increased for higher frequencies (Figure C.2(b)). When resolving time-frequency signal representations, one is limited by Heisenberg's uncertainty principle: the momentum and position of a moving particle cannot be known simultaneously. This implies that the exact frequency cannot be resolved for the time instant, i.e.,

$$\text{Time} - \text{Bandwidth product} = \Delta t\, \Delta\omega \geq \frac{1}{4\pi} \tag{C.9}$$

The dilation of a function in wavelet transform (Figure C.2 (c)), achieves the best possible compromise considering this limitation (Farge, 1992).

C.2.2 Comparison of wavelet transform to windowed Fourier transform

From the plot of transforming functions, e.g. Figure C.1 (a) and (b), the localizability of the wavelet transform can be seen. Here, a short comparison between Fourier and wavelet transform is presented. For further mathematical derivations, readers are directed to such references as Daubechies (1992), Ogden (1997), Mallat (2001), and Meyer (1993).

Following the derivations by Ogden (1997) and taking an example of the Gabor windowed Fourier transform, the windowing function is expressed as:

$$g_\alpha(t) = \frac{1}{\sqrt{2\alpha}} \exp\left(\frac{-t^2}{4\alpha}\right) \tag{C.10}$$

The resulting transform is defined to be:

$$G_b^\alpha f(\omega) = \int_{-\infty}^{\infty} f(t)\, g_\alpha(t-b) \exp(-i\omega t)\, dt \tag{C.11}$$

indicating the localization of the signal f about the point t = b. The simultaneous localization of the time and frequency can be demonstrated by taking the Fourier transform of Equation C.10. The windowed width of this function in the time domain is $2\sqrt{\alpha}$ and in the frequency domain is $1/\sqrt{\alpha}$.

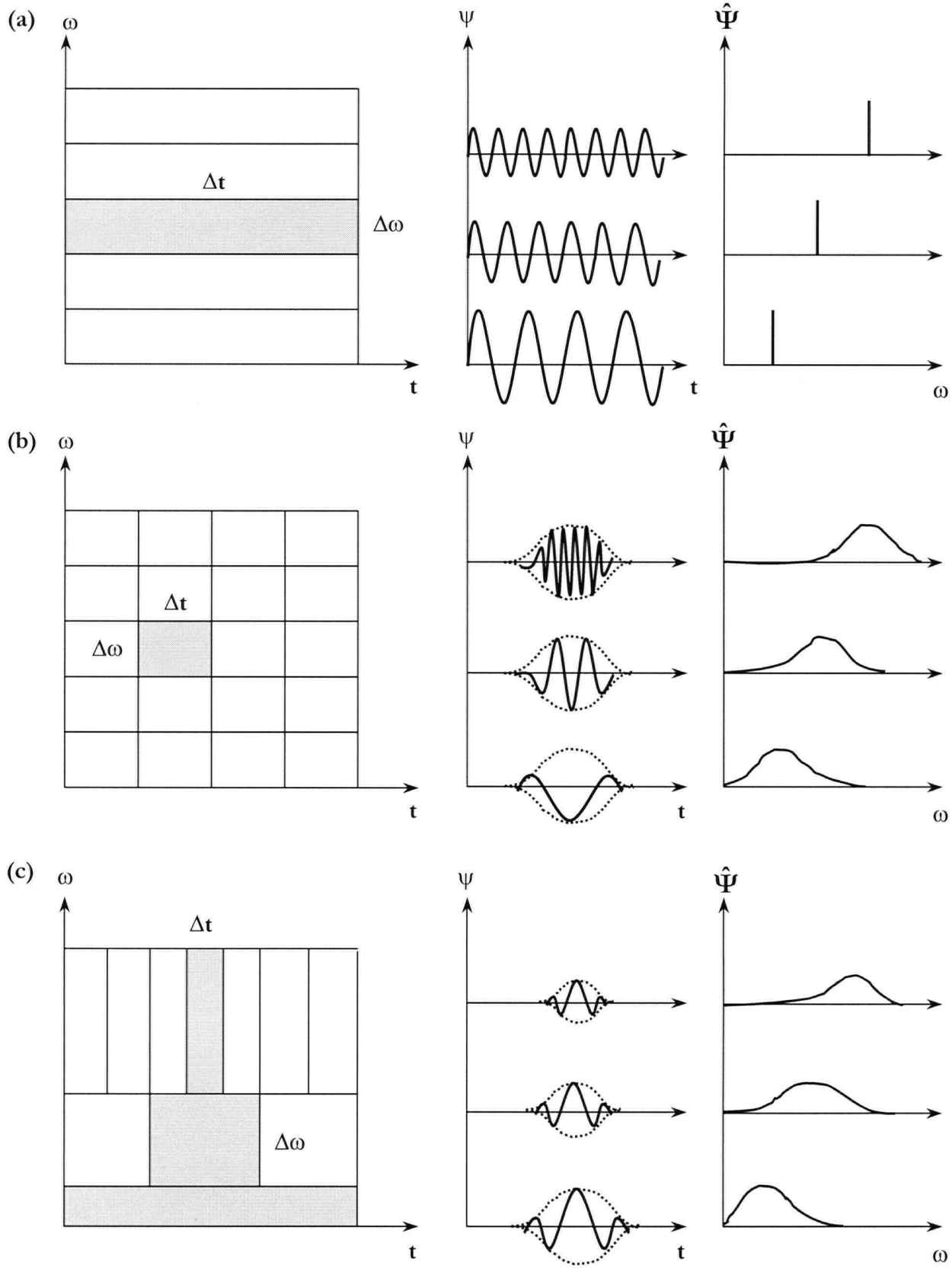

Figure C.2 Phase space associated with different transforms: (a) Fourier transform, (b) windowed Fourier transform, and (c) wavelet transform. (Adapted from Farge, 1992)

This implies that the relative widths and heights of the windows can be adjusted by altering α, while the "area" of the window remains 2.

On the other hand, the mother wavelet generates a family of translated and dilated wavelets. Indexed by j and k, with $j, k \in Z$,

$$\psi_{j,k} = 2^{j/2}\psi(s^j x - k) \tag{C.12}$$

The resulting set of functions is orthonormal. Moreover, any function $f \in L^2(\Re)$ can be approximated by a finite linear combination of the $\psi_{j,k}$. The corresponding wavelet coefficient is

$$d_{j,k} = \left\langle f, \psi_{j,k} \right\rangle = \int_{-\infty}^{\infty} f(x)\psi_{j,k}(x)dx \tag{C.13}$$

Taking the continuous form of Equation C.12 where the indexes are varied continuously, a continuous wavelet is expressed as:

$$\psi_{a,b}(x) = \frac{1}{\sqrt{a}}\psi\left(\frac{x-b}{a}\right) \tag{C.14}$$

for $a > 0$, $b \in \Re$. The resulting window function gives the time and frequency windows as:

$$\left(b + at^* - a\Delta_\psi, b + at^* + a\Delta_\psi\right) \tag{C.15}$$

$$\left(\frac{\omega^* - \Delta_{\hat{\psi}}}{a}, \frac{\omega^* + \Delta_{\hat{\psi}}}{a}\right) \tag{C.16}$$

respectively. The significance of this is that as "a" is decreased, the time window becomes narrower while the frequency window becomes wider, and vice versa. This is shown in Figure C.2.

The implication of the localization capability can be significant depending on to the objectives of the analysis. If the singularities are experimental errors, the effect is imbedded into the FT coefficients making them difficult to filter out (Farge, 1992). On the other hand, if the singularities reflect transient fluctuations, WT is capable of localizing the coefficient to provide spatial resolution. Moreover, by reconstructing the wavelet coefficients, one can obtain a signal with the singularities removed if the singularities are undesired.

In turbulent fluidized beds, voids tend to be transient and erratic (Kehoe and Davidson, 1970). By decomposing local voidage signals from optical fiber probes with WT, time localized information

regarding the spectral contribution of the signal, fractal characteristics, or non-linear interaction between phases may be revealed.

C.2.3 Different types of wavelet transform

As summarized by Daubechies (1992), continuous and discrete wavelet transformations exist, with discrete WT further divided into redundant discrete systems and orthonormally based wavelets. The proper choice of transform, and of the wavelet, depends on the information to be extracted from the signal. Some of the differences and advantages of continuous and discrete transformations are reported here without detailed mathematical explanations.

C.2.3.1 Continuous wavelet transform

The continuous wavelet transformation, CWT, can be written:

$$CWT_x^{\psi}(j,k)=\Psi_x^{\psi}(j,k)=\frac{1}{\sqrt{|j|}}\int x(i)\psi^*\left(\frac{i-k}{j}\right)di \qquad (C.17)$$

where Ψ is a specific mother wavelet; ψ^* is the complex conjugate of a daughter wavelet; j represents the dilation scale; and k is the translation coefficient. The resultant wavelet coefficients reflect how close the signal is to a particular basis function. The transformation

$$E(x)=\int|x(i)|^2=\iint|CWT(j,k)|^2\frac{dj\,dk}{j^2} \qquad (C.18)$$

results in conservation of energy, and there is no loss of information (Rioul and Vetterli, 1991; Farge, 1992). Thus, the scalogram, e.g. Figure C.5, represents a distribution of the energy of the signal in the time-scale plane, expressed in power per frequency unit. For signal analysis, Farge (1992) recommends CWT, which is suited for local differentiability of a function detecting and characterizing possible singularities.

C.2.3.2 Discrete wavelet transform

In the case of the discrete wavelet transform, the dilation scale, j, and the translation coefficient, k, take only discrete values. Filters of different cut-off frequencies are used to analyze the signal at different scales. The wavelet function can be expressed as:

$$\psi_j(k)=2^{-j/2}\psi_0\left(\frac{k}{2^j}\right) \qquad (C.19)$$

The discrete wavelet coefficients for the wavelet transform is

$$w_j(k)=\sum_{i=1}^{N}\psi_j\left(k-2^j i\right)x(i) \qquad (C.20)$$

where the number of wavelet coefficients is N/2 for j=1, N/4 for j=2, and so on until it is 1 for j=M (=$\log_2$N).

C.2.4 Details and approximations

Through the wavelet transform, a signal is linearly decomposed into different scales related to frequency. As this is the essence of multiresolution analysis, some explanations are given here. Localization of signal analysis is possible due to the compact support of a wavelet transform. The compact support is the property that $\psi(x)=0$ for all $x \notin A$, which results in limiting the integration range. However, not all wavelet bases are compactly supported, and the restrictiveness has been questioned (Unser and Blu, 2001).

Following the derivations by Daubechies (1992) and Ogden (1997), an arbitrary $L^2(\Re)$ function f is approximated by a function with compact support as $J_1 \rightarrow \infty$, i.e.,

$$\int_{-2^{J_1}}^{2^{J_1}} f^2(x)dx \rightarrow \int_{-\infty}^{\infty} f^2(x)dx \tag{C.21}$$

for $\{f: -2^{J_1} \le f < 2^{J_1}\}$. Next this approximation is further approximated by letting $f_k^{J_0}$ as the piecewise constant value of f^{J_0} over $\{x: k2^{-J_0} \le x < (k+1)2^{-J_0}\}$ which is twice as large as the original. Then,

$$f^{J_0}(x) = f_k^{J_0} \quad \text{for} \quad k \times 2^{-J_0} \le x < (k+1)2^{-J_0} \tag{C.22}$$

Then the function f^{J_0} can be written as the sum of two functions:

$$f^{J_0} = f^{J_0-1} + g^{J_0-1} \tag{C.23}$$

where

$$f_k^{J_0-1} = \frac{1}{2}\left(f_{2k}^{J_0} + f_{2k+1}^{J_0}\right) \tag{C.24}$$

with g^{J_0-1} defined as the detail function and written as:

$$g_{2k}^{J_0-1} = f_{2k}^{J_0} - f_k^{J_0-1} = f_{2k}^{J_0} - \frac{1}{2}\left(f_{2k}^{J_0} + f_{2k+1}^{J_0}\right) \tag{C.24}$$

and

$$g_{2k+1}^{J_0-1} = f_{2k+1}^{J_0} - f_k^{J_0-1} = \frac{1}{2}\left(f_{2k+1}^{J_0} - f_{2k}^{J_0}\right) = -g_{2k}^{J_0-1} \tag{C.25}$$

A decomposition using the Haar wavelet is shown in Figure C.3 (Daubechies, 1992). This graphically illustrates the above decomposition. By splitting the approximate function f^{J_0-1} according to Equation (C.23), the original function f^{J_0} can be decomposed into larger intervals.

$$\begin{aligned} f^{J_0} &= f^{J_0-1} + g^{J_0-1} \\ &= f^{J_0-2} + g^{J_0-2} + g^{J_0-1} \\ &= f^{J_0-3} + g^{J_0-3} + g^{J_0-2} + g^{J_0-1} \end{aligned} \tag{C.26}$$

Also note that each Haar wavelet complies with

$$\int_{-\infty}^{\infty} \psi_{j,k}(x)dx = 0 \tag{C.27}$$

for all $j,k \in Z$, which is the basis for an orthogonal function. As shown in Figure C.6, two wavelets with the same dilation index j but differing k can never have overlapping support, i.e., $[k2^{-j},(k+1)2^{-j})$. Thus, the wavelet functions are said to be orthogonal (Ogden, 1997).

As shown in Figure C.4, decomposition of signals using discrete wavelet transform results in splitting the signal into approximation and detail coefficients, corresponding to the low and high frequency corrections, labelled a1 and d1, respectively.

In the next step, a1 is split into the next approximation and detail coefficients, and so on. As a result, for the given example, a signal is decomposed into seven levels where the wavelet coefficients are as shown in Figure C.5.

C.2.5 Thresholding

Donoho (1993) describes the techniques in nonparametric regression where thresholding is applied to assess the estimates of coefficients in empirical wavelet expansions of unknown functions. Those details exceeding a certain threshold are discarded in the process. Further information on the nonparametric regression using wavelet estimators is provided by Antoniadis and Gijbels (2002).

The procedure outlined in Donoho (1993) for recovery of f(t) is as follows:

1) Perform the pre-conditioned, interval-adapted, pyramid wavelet filtering of Cohen et al. (1993), yielding noisy wavelet coefficients $w_{j,k}$, $j = j_0, \ldots, J$, $k = 0, \ldots, 2^j-1$.
2) Apply the soft-threshold non-linearity to the noisy empirical wavelet coefficients, with threshold $t = \frac{\sqrt{2\log(n)}\sigma}{\sqrt{n}}$, yielding estimates $\hat{\alpha}_{j,k}$ where $n = 2^{J+1}$ data.

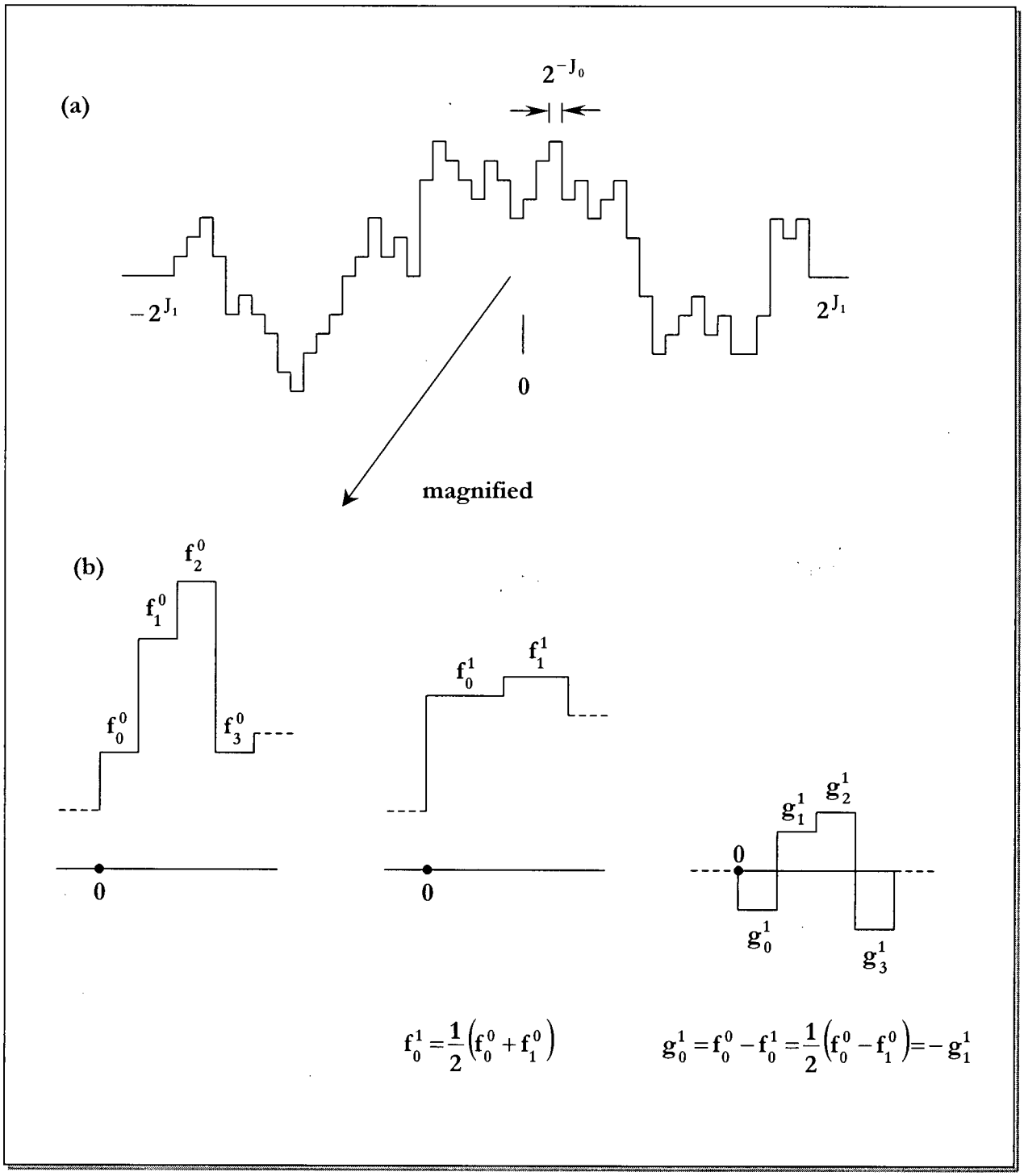

Figure C.3 (a) Function f with support $[-2^{J_1}, 2^{J_1})$ piecewise constant on $[k2^{-J_0}, (k+1)2^{-J_0})$. (b) Magnification of a portion of f. On every pair of intervals, f is replaced by its average ($\rightarrow f^1$); the difference between f and f^1 is g^1, a linear combination of Haar wavelets. (Adapted from Daubechies, 1992)

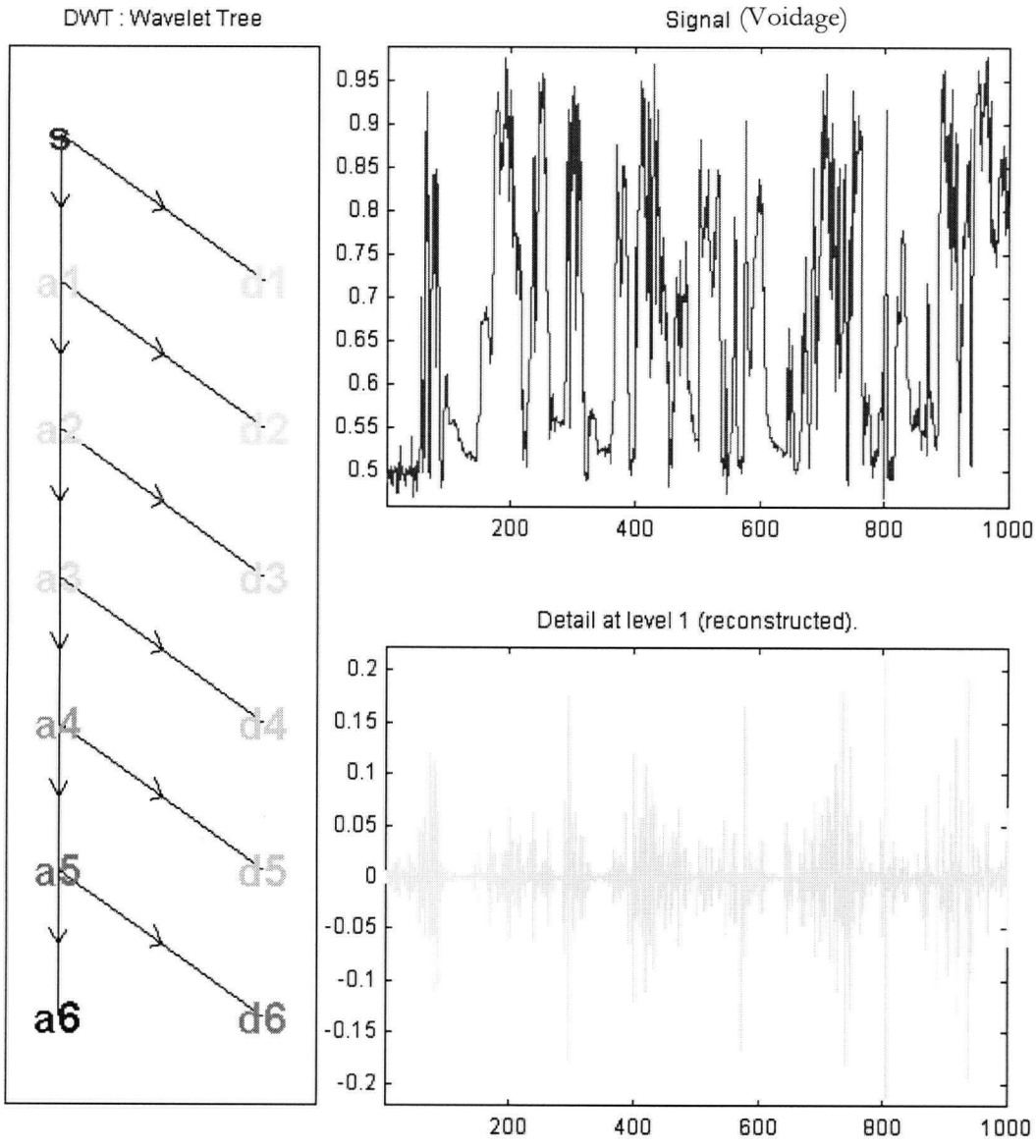

Figure C.4 Discrete wavelet decomposition and wavelet tree using Haar wavelets of voidage fluctuation from optical probe. D=0.29 m, U=0.90 m/s, r/R=0.0, H_0=1.1 m, z=0.78 m, FCC I.

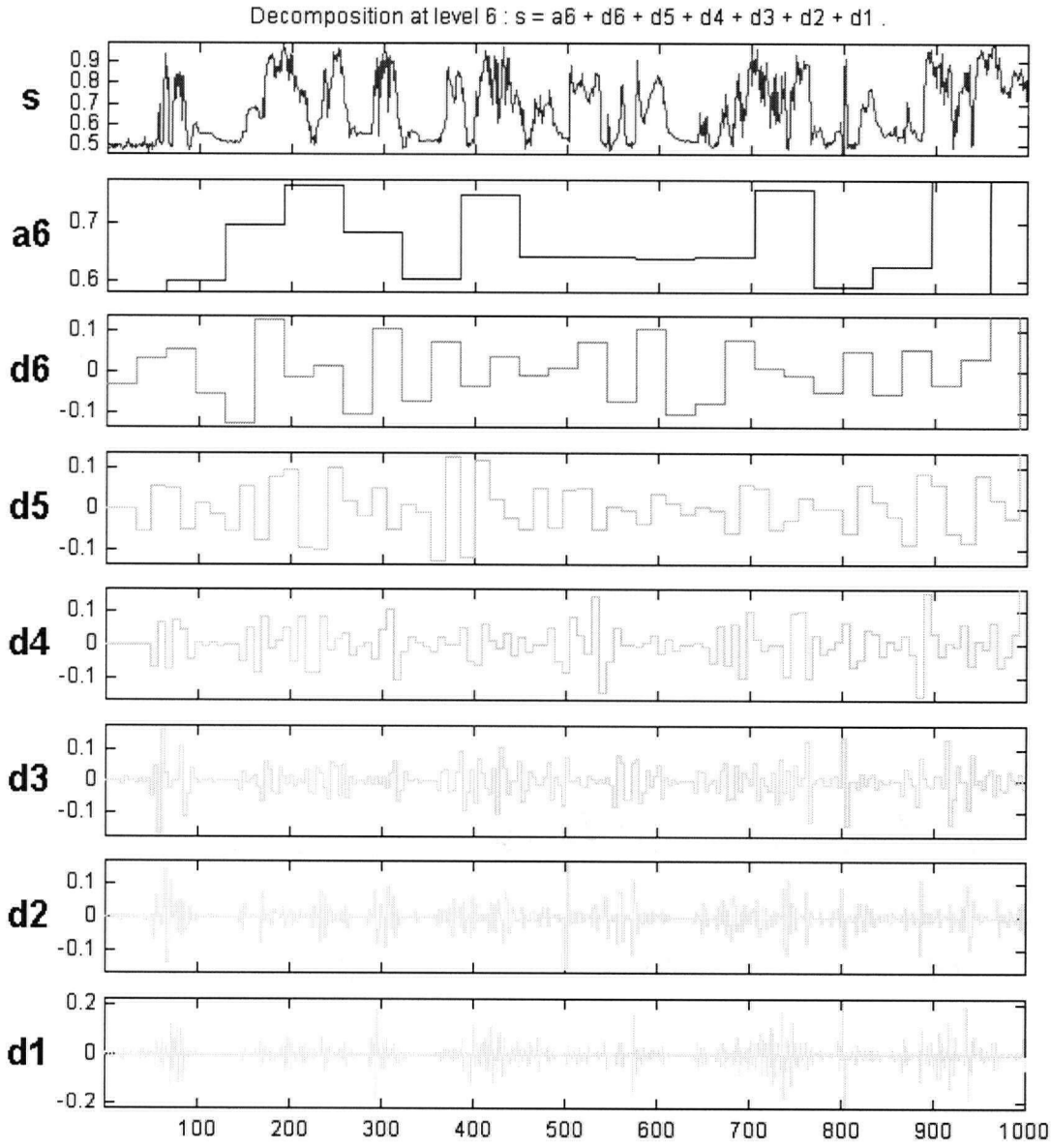

Figure C.5 Discrete wavelet decomposition of voidage fluctuation from optical probe using Haar wavelet. D=0.29 m, U=0.90 m/s, r/R=0.0, H_0=1.1 m, z=0.78 m.

3) Set all wavelet coefficients $\hat{\alpha}_{j,k}=0$ for $j > J$ and invert the wavelet transform, producing the estimate of $\hat{f}(t)$, $t\in[0,1]$.

The resulting reconstructed signal features suppress the noise considerably while retaining the sharpness of the signal. This is the main advantage in applying nonlinear wavelet transform to voidage data for void velocity calculations. Moreover, the traditional linear methods of smoothing would have broadened the sharp transitional features of the voidage fluctuation making it unsuitable for cross-correlation.

The threshold estimator of the true coefficients is expressed as:

$$\hat{\alpha}_{j,k}=\frac{\sigma}{\sqrt{n}}\delta_{\lambda}\left(\frac{\sqrt{n}\,w_{j,k}^{(n)}}{\sigma}\right) \tag{C.28}$$

where the soft thresholding function is defined as:

$$\delta_{\lambda}^{S}(x)=\begin{cases}x-\lambda, & \text{if } |x|>\lambda,\\ 0, & \text{if } |x|\le\lambda,\\ x+\lambda, & \text{if } |x|<-\lambda,\end{cases} \tag{C.29}$$

which "shrinks" coefficients beyond the threshold value toward zero by an amount equal to the threshold, λ. For further details on the thresholding method, see Donoho et al. (1995).

APPENDIX D

HYDRODYNAMIC AND CFD MODELLING

D.1 Introduction

Two-phase flows are encountered in many industrial applications, such as the energy sector, paper and food manufacturing, medical applications, and environmental phenomena. The complexity of multiphase flow has contributed to the limited understanding of the flow compared with "mutual cross-fertilization between theory and experiment" as in the developmental understanding of the single phase flow (Schlichting, 1979). The fundamental problem encountered in modelling hydrodynamics of fluidized bed is the motion of the two phases of which the interface is unknown and transient, and the interaction is understood only for a limited range of conditions (Gilbertson and Yates, 1996). The first intuition in resolving the two-phase mixture is to treat each phase by standard continuum mechanics with boundary and jump conditions to solve the governing equations at the interfaces (Ishii, 1975). However, it is quickly realized that the mathematical difficulties of the non-linearity of the equations and in defining the interpenetrating and moving phase boundaries make numerical solutions very difficult. Several approaches have been used to predict two-phase flows, such as the Eulerian continuum approach, Lagrangian trajectory approach, and kinetic theory of granular flow. It is the intent of this Appendix to present a possible theoretical approach to model the dense phase gas-solid fluidized bed operated in the turbulent fluidization flow regime. First, primary forces acting on a fluidized particle are examined leading to the effect of particles on a fully developed gas stream. Next, the effect of turbulence on two-phase flow is considered, including a review of the current status of models.

D.2 Primary forces acting on a fluidized particle

When a particle is subjected to an upflow of gas, the forces acting on the particle are in equilibrium, i.e.,

$$\Sigma F = \frac{1}{6}\pi d_p^3 \varrho_p g - \frac{1}{6}\pi d_p^3 \varrho_g g - \frac{1}{8}\pi d_p^2 C_D \varrho_g U^2 + \frac{1}{8}\pi d_p^3 \varrho_p \frac{du_s}{dt} = 0 \qquad (D.1)$$

The terms from left to right are: gravitational, buoyancy, drag and accelerational forces. At steady-state, the particle terminal velocity can be obtained from the above equation as:

$$U_t = \sqrt{\frac{4}{3}\frac{d_p g(\varrho_p - \varrho_f)}{C_D \varrho_f}} \tag{D.2}$$

The properties of a particle in a continuous gas phase can be expressed as the ratio of the inertia over viscous forces, i.e., the Reynolds number

$$Re_p = \frac{U \varrho_g d_p}{\mu} \tag{D.3}$$

The drag coefficient, C_D is a function of Reynolds number and particle shape. A summary of parameters used in this study is presented in Table D.1 where the Archimedes number describing the integrated effect of material properties of both fluid and particles is

$$Ar = \frac{d_p^3 g \varrho_g (\varrho_p - \varrho_g)}{\mu^2} \tag{D.4}$$

Table D.1 Summary of fluid and particle characteristic parameters based on typical FCC used in those parts of this work carried out at UBC.

Parameter	Value
$\overline{d_p}$	75 μm
ϱ_p	1560 kg/m^3
Re_p (U=0.2~1.2 m/s)	1~5.8
Re_D (U=0.2~1.2 m/s) assuming single phase	3.80×10^3 ~ 2.28×10^4
Ar	24.5
m_s (for ε=0.45 and 0.99)	1680 and 14, respectively

D.3 Forces acting on solids in gas-solid multiphase flows

When a collection of solid particles is fluidized, the solid phase exhibits a resistance to flow. This internal friction results from interparticle forces between adjacent particles. In determining the dominant forces in gas-solid fluidized beds, both dynamic interparticle forces arising from the relative movement of particles in the force field, and static interparticle forces, such as electrostatic, van der Waals, and capillary forces must be included. The interparticle forces are a function of the interaction between the gas and solid phases. They are also functions of the voidage, ε, representing

a volumetric concentration of the fluid phase, and the particle mass loading, m_s, defined as the ratio of the mass of the particles to the mass of the gas in the computational domain.

D.3.1 Drag Forces

The drag force on a single sphere in a fluid has been well studied and empirically correlated, e.g. Clift et al. (1978) and Bird et al. (2002), for a wide range of particle Reynolds numbers. With the increasing availability of computational power, numerous studies have been reported in which the equations of continuity and motion of particles in unsteady flow fields have been solved. Kurose et al. (2001) reported on the three-dimensional numerical simulation of a solid particle for $0.5 \le \mathrm{Re}_p \le 200$, and confirmed that the drag coefficient is well represented by:

$$C_D = \frac{24}{\mathrm{Re}'_p}\left(1 + 0.15\,\mathrm{Re}'^{\,0.687}_p\right) \tag{D.5}$$

However, when a single particle moves in a dispersed two-phase mixture, the resistance experienced by the particle is affected by the presence of other particles in the fluid phase. Wen and Yu (1966) empirically included this effect on the drag coefficient as:

$$C_D = \varepsilon^{-4.7} C_{Ds} \tag{D.6}$$

where C_{Ds} is the drag coefficient of a single sphere in an infinite expanse of fluid. Although the full range of flow was covered, i.e., laminar, intermediate and turbulent regions, their experiments were performed solely in a particulate fluidized bed of liquid and solids. The drag force represents the interphase momentum transfer between gas and solid phases, and is one of the dominant forces in the gas-phase momentum balance (Hrenya and Sinclair, 1997). Numerous correlations have been reported in the literature, as summarized in Table D.2.

Table D.2 Drag coefficients.

Investigators	Coefficients related to drag force
Wen and Yu (1966)	$\beta = \frac{3}{4} C_D \frac{(1-\varepsilon_s)\varepsilon_s \varrho_g \lvert \upsilon_g - \upsilon_s \rvert}{d_p} (1-\varepsilon_s)^{-2.65}$
Ma and Ahmadi (1990)	$\beta = \frac{18\mu_g}{d_p^2} \frac{\varepsilon_s}{\left(1 - \frac{\varepsilon_s}{\varepsilon_{s,max}}\right)^{2.5\varepsilon_{s,max}}} \left(1 + 0.1\,\mathrm{Re}^{0.75}\right)$
Syamlal et al. (1993)	$\beta = \frac{3}{4} C_D \frac{\varepsilon_s (1-\varepsilon_s) \varrho_g}{V_r^2 d_p} \lvert \upsilon_g - \upsilon_s \rvert$

Gidaspow (1994) applying the Ergun (1952) equation for higher volume fractions	$\beta = 150\frac{\varepsilon_s^2\mu_s}{\varepsilon_g d_p^2} + 1.75\frac{\varepsilon_s \varrho_g \lvert \upsilon_g - \upsilon_s \rvert}{d_p}$ for $\varepsilon_s > 0.2$ $\beta = \frac{3}{4}C_D\frac{\varepsilon_g(1-\varepsilon_g)\varrho_g\lvert \upsilon_g - \upsilon_s \rvert}{d_p}\varepsilon_g^{-2.65}$ for $\varepsilon_s \le 0.2$
Rowe (1961)	$C_D = \frac{24}{(1-\varepsilon_s)Re'_p}\left[1 + 0.15\left((1-\varepsilon_s)Re_p\right)^{0.687}\right]$ for $(1-\varepsilon_s)Re'_p < 1000$ $C_D = 0.44$ for $\varepsilon_g Re'_p \ge 1000$
Li and Kwauk (1994)	dense phase: $C_{D_c} = \left(\frac{24}{Re_c} + \frac{3.6}{Re_c^{0.313}}\right)\varepsilon_c^{-4.7}$ where $Re_c = \frac{\left(U_c - \frac{U_{dc}\varepsilon_c}{1-\varepsilon_c}\right)d_p\varrho_g}{\mu}$ dilute phase: $C_{D_f} = \left(\frac{24}{Re_f} + \frac{3.6}{Re_f^{0.313}}\right)\varepsilon_f^{-4.7}$ where $Re_f = \frac{\left(U_f - \frac{U_{df}\varepsilon_f}{1-\varepsilon_f}\right)d_p\varrho_g}{\mu}$ inter-phase: $C_{D_i} = \left(\frac{24}{Re_i} + \frac{3.6}{Re_i^{0.313}}\right)(1-f)^{-4.7}$ where $Re_i = \frac{\left(U_f - \frac{U_{dc}\varepsilon_f}{1-\varepsilon_c}\right)(1-f)\varrho_g}{\mu}$
Ihme et al. (1972)	$C_D = \frac{24}{Re'_p} + 5.48\,Re'^{-0.573}_p + 0.36$ for viscous flow regime

D.3.2 Particle inertia

Particle inertia plays an important role at the microscale, and enhances the collision rate due to large fluctuations in the particle concentration (Koch and Hill, 2001). Inertia has been linked in characterizing the stability of fluidized beds (Koch and Sangani, 1999) and of a particle-laden flow (Wen and Evans, 1996), owing to the non-linear nature of the governing equations. Inertial terms

are often neglected for Re << 1. However, in recent years, inertial suspensions, i.e., particle suspensions in which inertia significantly affects the particle length scale, have gained more attention in light of increased computational power in carrying out direct numerical simulations (e.g. Squires and Eaton, 1991; Reade and Collins, 2000). Koch and Hill (2001) noted that the complexity in the flow patterns originating from inertial instabilities of the homogeneous state of fluidization hinders the understanding of hydrodynamics, and contributes to challenges in scale-up. In investigating the mechanisms of particle radial transfer in a CFB riser, Jiang and Fan (1999) analyzed their experimental data from the perspective of eddy-particle interactions and particle collisions. The current level of understanding of inertial suspension was reviewed by Koch and Hill (2001).

For gas-solid suspensions with large ρ_p/ρ_f ratio, the inertia of the particles becomes significant for $St \geq O(1)$, while the inertia of the gas is negligible, i.e., $Re << 1$. In this situation, linear and quasi-steady equations of motion can be obtained for the gas phase (Koch and Hill, 2001). Simulation of 54 particles revealed that for zero Stokes number, the particles follow the streamlines of the mean flow (Sangani et al., 1996). As the Stokes number is increased, the particle inertia is sufficient that particle velocity diverges from the mean fluid velocity, and particle-particle collisions become significant. Thus, the analogy to the kinetic theory of gases can be applied with a large variance in the instantaneous particle velocity. However, there are deviations from the molecular dynamics, with energy being dissipated by inelastic collisions in a suspension of macroscopic particles. Further developments in the kinetic theory for dense gas-solid suspensions is summarized in Section D.4.3.

D.3.3 Electrostatic forces

Electrostatic charges in gas-solid fluidized beds are primarily generated by an imbalance in the molecular structure of relatively non-conductive materials due to friction between gas, particles and reactor walls. Static electricity is discharged when the potential gradient is accumulated and breaks down the insulator. Such static charges in a fluidized bed can result in agglomeration, reduction in the flux of elutriated particles (Briens et. al, 1992), increased pressure drops, decreased bed expansion, channelling, and even explosions.

The higher superficial gas velocities in the turbulent fluidization flow regime compared to the bubbling regime causes significantly more particle-particle and particle-wall interactions, thus leading to increased electrostatic forces. While electrostatic charges are normally not considered in hydrodynamic modelling, there is evidence that their effects should not be ignored.

D.3.4 Other forces

- Saffman force: This is the lift force due to fluid shear.
- Magnus effect: The Magnus effect describes lift force due to particle bodily rotation.
- Basset term: This is the force associated with the previous movements of the particle and accounting for the effect of the deviation in flow pattern from steady state conditions. The term expresses the acceleration of one phase relative to the other as a result of momentum being diffused through the boundary layer. However, it can be considered negligible for $\rho_g/\rho_s < 0.002$ and $d_p > 1\mu m$ (Enwald et al., 1996).
- Added mass effect: This effect results from acceleration of fluid surrounding particles. The accelerating phase must overcome the inertia of the mass that lies in its path. This effect can be neglected for high particle-to-gas density ratios.
- Coulomb force: The attraction or repulsion of particles as a result of their electrical charges constitutes the Coulomb force.
- van der Waals forces: These are intermolecular dipole/dipole, dipole/non-polar, and non-polar/non-polar forces. While intermolecular van der Waals forces decay as a^{-7}, where a is the molecular separation, the interparticle van der Waals force between spherical particles decays as a^{-2} (Seville et al., 2000).
- Capillary forces: This force arises from the sum of surface tension forces and the pressure deficit in the liquid bridge between particles. It occurs when there is liquid present in the system, and is affected by the properties of liquid such as its surface tension and viscosity (Seville et al., 2000).

D.4 Hydrodynamic modelling

Modelling has been the focus for many researchers in fluidized bed reactor applications. Process modelling requires knowledge of kinetics (chemical reaction, mass and heat transfer), and hydrodynamics (flow, dispersion, and contacting, including momentum transfer), and the coupling of these components (Levenspiel, 2002). Traditionally, scale-up has been done by beginning with a small test rig, followed by strategic increases of reactor size. However, this procedure is expensive and uncertain, while fluidized bed modelling is challenging owing to the complexity of the two-phase flow.

For gas-solid fluidization, numerous simulation studies have been conducted with flow regime specific models. Though industrial fluidized beds are often operated in the turbulent fluidization

flow regime, modelling of this flow regime has received little attention. Abba (2001) provided a promising tool on modelling across the gas-solid flow regimes. The model uses probabilistic averaging of hydrodynamic and dispersion variables through interpolation between three regime-specific models with the probabilities based on the uncertainty in the flow regime transitions.

Mechanistic modelling of two-phase flow based on the conservation laws of mass, momentum and energy through computational fluid dynamics is another method. It is gaining attention with the advent of increased computational capabilities in attempts to capture the essential flow physics. Two distinct approaches have been adopted: a discrete method based on molecular dynamics; and a continuous approach based on continuum mechanics regarding two phases as inter-penetrating continua. These two approaches have been compared by Gera et al. (1998).

D.4.1 Discrete particle model

In the Lagrangian model of two-phase flow, the Newtonian equations of motion for each individual particle are solved with inclusion of the effects of particle collisions and forces acting on the particle phase by the gas. Particle-particle collisions are modelled by one of two approaches: the hard sphere approach and the soft sphere approach. The hard sphere approach treats particle interaction based on binary collisions, and employs collision laws that account for energy dissipation due to non-ideal particle interactions by means of empirical coefficients of restitution and friction. Moreover, collisions are processed one at a time (Gera et al., 1998). On the other hand, the soft shell approach can estimate the forces of interaction between multiple particle-particle or particle-wall contacts (Kobayashi et al., 2000). It employs an empirical spring stiffness, dissipation constant, and friction coefficient. The distinct element method (DEM) is one of the trajectory models, which can calculate the particle velocity and the corresponding particle trajectory to examine the interactions such as those due to multi-body collisions. Trajectory models are applied to multiphase flows for dilute systems where a continuum model for the particle is not appropriate. Though models based on DEM allow the effect of various particle properties on the motion of fluid to be studied, it is normally limited to no more than $\sim 10^7$ particles, as a result of computational limitations. For small particles, such as typical catalyst particles that have diameters of ~75 μm, it then becomes difficult to simulate any meaningful reactor volume.

D.4.2 Continuum model

In the continuum modelling scheme, collections of particles are modelled using continuous medium mechanics. The solid particles in such two-fluid models are generally considered to be identical having a representative diameter and density. The continuum approximation is applicable for volumes that are sufficiently small in comparison with the scale of the macroscopic changes of the flow, but large enough to contain a significant number of particles to allow characteristic phenomena such as density and velocity to be treated as continuous variables (Drew and Passman, 1999). The general idea in formulating the two-fluid model is to treat each phase as an interpenetrating continuum and therefore to construct integral balances of continuity, momentum and energy for both phases, with appropriate boundary conditions and jump conditions for phase interfaces. Since the resultant continuum approximation for the solid phase has no equation of state, and lacks some variables such as viscosity and normal stress (Pain et al., 2001), certain averaging techniques and assumptions must be made to obtain a momentum balance for the solids phase.

As reviewed extensively by van Wachem et al. (2001), the difference in the governing equations originates in how the resultant forces due to interaction with the fluid are treated on the surfaces of the particles. The continuity equation is expressed as:

$$\frac{\partial}{\partial t}\left(\varepsilon_i \varrho_i\right) + \nabla \cdot \left(\varepsilon_i \varrho_i \upsilon_i\right) = m_i' = 0 \tag{D.7}$$

for each phase.

The momentum equations of Jackson (1997) include the solid volume fraction multiplied by the gradient of the total gas-phase stress tensor; and both stresses are treated equally with respect to the gas volume fraction and the gradient operators:

$$\varrho_g \varepsilon_g \left(\frac{\partial \upsilon_g}{\partial t} + \upsilon_g \cdot \nabla \upsilon_g \right) = \varepsilon_g \nabla \cdot \overline{\overline{\tau}}_g - \varepsilon_g \nabla P - \beta\left(\upsilon_g - \upsilon_s\right) + \varepsilon_g \varrho_g g \tag{D.8}$$

$$\varrho_s \varepsilon_s \left(\frac{\partial \upsilon_s}{\partial t} + \upsilon_s \cdot \nabla \upsilon_s \right) = \varepsilon_s \nabla \cdot \overline{\overline{\tau}}_g - \varepsilon_s \nabla P + \nabla \cdot \overline{\overline{\tau}}_s + \beta\left(\upsilon_g - \upsilon_s\right) + \varepsilon_s \varrho_s g \tag{D.9}$$

The momentum equations of Ishii (1975) applied to gas-solid flow (Enwald et al., 1996) only include the solid volume-fraction multiplied by the gradient of the pressure; in the gas-phase momentum balance, the pressure carries the gas volume fraction outside the gradient operator; and the shear stress carries that gas volume fraction inside the gradient operator.

$$\varrho_g \varepsilon_g \left(\frac{\partial \upsilon_g}{\partial t} + \upsilon_g \cdot \nabla \upsilon_g \right) = \nabla \cdot \varepsilon_g \overline{\overline{\tau}}_g - \varepsilon_g \nabla P - \beta \left(\upsilon_g - \upsilon_s \right) + \varepsilon_g \varrho_g g \tag{D.10}$$

$$\varrho_s \varepsilon_s \left(\frac{\partial \upsilon_s}{\partial t} + \upsilon_s \cdot \nabla \upsilon_s \right) = -\varepsilon_s \nabla P + \nabla \cdot \overline{\overline{\tau}}_s + \beta \left(\upsilon_g - \upsilon_s \right) + \varepsilon_s \varrho_s g \tag{D.11}$$

These differences may be significant when the gas-phase shear stress plays an important role (van Wachem et al. 2001). The stress tensor for the solid phase can be expressed (Wang and Li, 2001) as:

$$\overline{\overline{\tau}}_s = \left[-P_s - \varepsilon_s \left(\lambda_s - \frac{2}{3} \mu_s \right) (\nabla \cdot \upsilon_s) \right] I + \varepsilon_s \mu_s \left[(\nabla \upsilon_s) + (\nabla \upsilon_s)^T \right] \tag{D.12}$$

Averaging theorems are applied to construct a continuum for each phase in order for the Eulerian description of single-phase flows to be extended to the multiphase flow. Although the transport coefficients of the gas phase may be reasonably represented by those for a single-phase flow with certain modifications, the transport coefficients of the solid phases must account for gas-particle interactions and particle-particle collisions. The absence of the stress term of the particle phase in the particulate momentum equation has led to different models adopting different enclosing methods such as empirical formulas (Gidaspow, 1986; Tsuo and Gidaspow, 1990; Sun and Gidaspow, 1999), closure of a particulate turbulent equation (Zhou, 1994), or a kinetic theory model (Sinclair and Jackson, 1989; Gidaspow, 1994; Hrenya and Sinclair, 1997; Cheng et al, 1999) where the motion of a single particle is used to describe turbulent motion of particles.

D.4.3 Kinetic theory of granular flow

Recently, the kinetic theory of gases has been extended to model the motion of a dense collection of nearly elastic spherical particles. Granular flow draws on an analogy to the kinetic energy of gases. The particle temperature, Θ, is a parameter related to the total kinetic energy of translation resulting from particle velocity fluctuations. The particle temperature equation can be expressed in terms of production of fluctuations by shear, dissipation by kinetic and collisional heat flow, dissipation due to inelastic collisions, production due to fluid turbulence or due to collisions with molecules, and dissipation due to interaction with the fluid (Gidaspow, 1994).

The kinetic theory of gases is based on the assumption that gaseous particles (atom/molecules) behave like point centres of mass, which most of the time exert no force on one another. The macroscopic characteristics of a gas are due to the independent motion of the molecules, since gas molecules exert forces on each other only during the brief instants when they collide. Thus, temperature is a parameter related to the average kinetic energy of molecules in the form:

$$\text{translational kinetic energy of a mole of gas} = N_0 \frac{\overline{mc^2}}{2} = \frac{3}{2}RT \tag{D.13}$$

The distribution of the speed of molecules is expressed as a Maxwell-Boltzmann distribution function (Maxwell, 1866):

$$\frac{\Delta N}{N} = 4\pi\left(\frac{m}{2\pi kT}\right)^{3/2} \exp\left(\frac{-mc^2}{2kT}\right) c^2 \Delta c \tag{D.14}$$

which exhibits a normal distribution.

For dense gas-solid suspensions, an analogy can be utilized where collisions among particles are the sole mechanism for the transport of mass, momentum, and energy. A granular temperature, Θ, is defined to represent the specific kinetic energy of the velocity fluctuations or the translational fluctuation energy resulting from the particle velocity fluctuations. In granular flow it is assumed that particle velocity fluctuations about the mean result in collisions between particles being swept along together by the mean flow. Detailed derivations of the model have been presented by Jenkins and Savage (1983) and Lun et al. (1984).

By assuming that the probability of observing a particular magnitude of one velocity component is independent of the other velocity components, three-dimensional space equipartition of energy is expressed as:

$$\Theta = \frac{1}{3}\left\langle c^2 \right\rangle \tag{D.15}$$

Important differences between a kinetic theory for a classical dense gas and for a granular material (Jenkins and Savage, 1983) are:

1) Inhomogeneity of the mean flow is necessary to force collisions and to derive the velocity fluctuations.
2) Collisions between particles of a granular material involve loss of energy. (Compare this to the kinetic theory of gases, where the collisions are assumed to be elastic.)

The Maxwellian velocity distribution for a single particle is expressed as:

$$f(\upsilon_1, r_1) = n\left(\frac{1}{2\pi\Theta}\right)^{3/2} \exp\left[-\frac{(\upsilon - U_p)^2}{2\Theta}\right] \tag{D.16}$$

As assumed by Savage and Jeffrey (1981), the distribution function is expressed as the product of a normalized pair-distribution function and the single particle velocity distribution function for each particle such that:

$$f^{(2)}(c_1, r_1, c_2, r_2) = g(r_1, r_2) f^{(1)}(c_1, r_1) f^{(1)}(c_2, r_2) \tag{D.17}$$

where $g(r_1,r_2)$ is the configurational pair-correlation function defined by:

$$g(r_1, r_2) = \frac{n^{(2)}(r_1, r_2)}{n^2} \rightarrow 1 \text{ for } |r_1 - r_2| >> d_p \tag{D.18}$$

since the joint probability of finding particles at r_1 and r_2 is simply the product of the individual probabilities. For a pair of particles subjected to a mean shear flow, the radial distribution function becomes distorted into an ellipsoidal distribution and exhibits anisotropy (Fan and Zhu, 1998). Restricting the expression to situations where U_{21} is small relative to $\Theta^{1/2}$, the configurational pair-correlation function becomes (Jenkins and Savage, 1983):

$$g(r_1, r_2) = g_0 \left[1 - \frac{k \cdot U_{21}}{\sqrt{\pi \Theta}} \right] \tag{D.19}$$

where k is the collisional vector.

The resulting pair-distribution function at collisions becomes:

$$f^{(2)}(c_1, r_1, c_2, r_2) = g_0 \frac{n_1 n_2}{8\pi^3 (\Theta_1 \Theta_2)^{3/2}} \left[1 - \frac{k \cdot U_{21}}{\sqrt{\pi \Theta}} \right] \exp\left(- \left[\frac{(\upsilon_1 - U_1)^2}{2\Theta_1} + \frac{(\upsilon_2 - U_2)^2}{2\Theta_2} \right] \right) \tag{D.20}$$

A Taylor series expansion is performed in order to evaluate the collisional flux of fluctuation energy, the collisional stress tensor and the rate of energy dissipation. These values, based on constitutive relations, are substituted into the hydrodynamic equations of conservation of mass, momentum and energy.

In order to close the equations for the particle phase, an energy balance is required for the granular temperature, Θ. The conservation of the solid fluctuating energy is expressed by:

$$\frac{3}{2} \left[\frac{\partial}{\partial t} (\rho_s \varepsilon_s \Theta_s) + \nabla \cdot (\rho_s \varepsilon_s \upsilon_s \Theta_s) \right] = \overline{\overline{\tau}}_s : \nabla \upsilon_s + \nabla \cdot (k \nabla \Theta_s) - \gamma_s \tag{D.21}$$

In a particle-laden turbulent channel flow, Li et al. (2001) reported an increase in particle loading by up to a factor of 2. The energy balance for the gas phase then became less significant, while the decrease in particle loading resulted from the accumulation of particles near the wall due to coherent eddies. For the range of particle loading studied, varying the restitution coefficient between 0.9 and 1 did not significantly alter the results.

The granular theory assumes that particle-particle collisions are binary and instantaneous. The validity of these assumptions is questionable in suspensions with large particle volume fractions where the gravitational and cohesive forces lead to extended interparticle contact and reduced effect of particle inertia (Zhang and Rauenzahn, 1997; Koch and Hill, 2001).

D.4.4 Restitution coefficient, e

The coefficient of restitution quantifies the elasticity of particle collisions between the value of 1, for fully elastic collisions, and 0 for fully inelastic collisions. It was utilized by Jenkins and Savage (1983) to account for the loss of energy due to collision of particles, which is not considered in classical kinetic theory. The energy dissipated as a result of collisions of granular inelastic particles has been calculated to obtain the ratio of the velocity fluctuations to the mean flow as a function of the coefficient of restitution (Lun et al., 1984). A decrease in the coefficient of restitution results in less elastic collisions generating more fluctuating kinetic energy (Goldschmidt et al., 2001). The effective restitution coefficient taking frictional losses into account has been defined as:

$$e_{cff} = e - \frac{\pi}{2}\mu_{cf} \tag{D.22}$$

for a small coefficient of friction, $\mu_{cf} < 0.15$. The influence of the coefficient of restitution on the hydrodynamics of dense gas-fluidized beds has been studied by Goldschmidt et al. (2001), where the best qualitative agreement between experimental and simulation results was obtained for e_{eff}=0.9.

Hrenya and Sinclair (1997) reported that the inelasticity of particle-particle collisions may be the cause of particle accumulation near the wall in CFB risers. They concluded that the unrealistic sensitivity to the coefficient of restitution was due to the inadequacy of the assumption that the particle interactions are binary and instantaneous. In dense two-phase flows, the particle interaction time may be much larger than the particle mean free flight time. Thus, the assumption that a pair of particles completes its interaction before interacting with another particle may be invalid as the solids concentration increases (Zhang and Rauenzahn, 2000).

Zhang and Rauenzahn (1997) numerically solved for the restitution coefficient in a binary collision of particles lubricated by viscous resin where solid-solid contacts between the coated particles were unimportant. With the force transmitted through resin and the soft-shell approach, they obtained

$$e = \exp\left(-\frac{T_c}{2T_r}\right)\left[\cos(\omega T_c) + \frac{T_n}{\sqrt{8T_r^2 - T_n^2}}\sin(\omega T_c)\right] \tag{D.23}$$

where T_c is the time required for the distance between the particles to return to r_0; T_n is the time scale associated with the natural frequency of the spring-mass system; and T_r is the relaxation time. This suggests that the coefficient of restitution is independent of the relative incoming velocity of the particles. Moreover, in a dense system when particles are in contact with other particles, the shear stress was found to depend only on the viscous-dominated forces between the particles.

Using a charge coupled device (CCD) camera, Gidaspow and Huilin (1998) estimated the velocity variances of the strands in a riser, and computed the granular temperature, from which the particle-plastic wall restitution coefficient was estimated to be e_w=0.96 for FCC in a circulating fluidized bed riser.

D.4.5 Radial distribution function, g_0

The configurational pair-correlation function in structural studies of the liquid state describes fluctuations in density around a given atom and determines the thermodynamic properties. Thus, the radial distribution function, g_0, describes the ratio of the local number density at a distance r from the central particle to the bulk number density (Gidaspow and Huilin, 1998).

$$\Delta N = 2\pi \bar{r}\frac{N}{AREA}g(\bar{r})\Delta r \tag{D.24}$$

where N is the number of particles in the observed area. Thus,

$$\text{local density of particles} = \left(\frac{N}{AREA}\right)g(r) \tag{D.25}$$

where $r = \sqrt{(x_i - x_j)^2 + (y_i - y_j)^2}$ to prevent any two particles occupying the same location, for $r \le d$, $g(r) = 0$. As $r \to \infty$, hence $g(r) \to 1.0$,

$$\text{local density} = \text{local density} \times g(r) \tag{D.26}$$

The simplest intermolecular potential energy function to determine the thermodynamic properties is the hard-sphere model (Savage and Jeffrey, 1981). A semi-empirical equation of state proposed by Carnahan and Starling (1969) is for mixtures of hard-sphere fluids. Table D.3 summarizes radial distribution functions reported in the literature.

Table D.3 Radial distribution functions.

Investigators	Radial distribution function
Carnahan and Starling (1969)	$g_0 = \frac{1}{1-\varepsilon_s} + \frac{3\varepsilon_s}{2(1-\varepsilon_s)^2} + \frac{\varepsilon_s^2}{2(1-\varepsilon_s)^3}$
Lun and Savage (1986)	$g_0 = \left(1 - \frac{\varepsilon_s}{\varepsilon_{s,max}}\right)^{-2.5\varepsilon_{s,max}}$
Sinclair and Jackson (1989)	$g_0 = \left[1 - \left(\frac{\varepsilon_s}{\varepsilon_{s,max}}\right)^{1/3}\right]^{-1}$
Gidaspow (1994)	$g_0 = \frac{3}{5}\left[1 - \left(\frac{\varepsilon_s}{\varepsilon_{s,max}}\right)^{1/3}\right]^{-1}$
Gera et al. (1998)	$g_0 = \frac{1}{1-\varepsilon_s} + \frac{3\varepsilon_s}{2(1-\varepsilon_s)^2}$

D.4.6 Solids pressure, P_a

Solids pressure is the force per unit area exerted by the change in the total momentum transport of the motion of particles and their interactions. Originally, Anderson and Jackson (1969) introduced this concept in modelling the stability of a homogeneous fluidized bed. The solid phase elastic modulus, $G(\varepsilon_g)$, can be considered as a thermodynamic property of solids expressed as:

$$-\nabla P_s = G(\varepsilon_g)\nabla \varepsilon_g \tag{D.27}$$

Expressions for $G(\varepsilon_g)$ are listed in Table D.4.

Table D.4 Solid phase elastic modulus.

Investigators	Solid phase elastic modulus
Ettehadieh et al. (1984)	$G(\varepsilon_g) = 10^{-8.76\varepsilon_g + 5.43}$
Bouillard et al. (1989)	$G_1(\varepsilon_g) = \exp(-600(\varepsilon_g - 0.376))$ $G_2(\varepsilon_g) = \exp(-500(\varepsilon_g - 0.422))$ $G_3(\varepsilon_g) = \exp(-20(\varepsilon_g - 0.62))$
Kuipers et al. (1992)	$G(\varepsilon_g) = \exp(-100(\varepsilon_g - 0.45))$

Lyczkowski et al. (1993)	$G(\varepsilon_g) = \exp(-600(\varepsilon_g - 0.39))$
Benyahia et al. (1997)	$G(\varepsilon_g) = 10^{-8.5\varepsilon_g + 5.43}$

The strong dependency on empiricism in the solid pressure and voidage relationship has been criticized (Kobayashi et al., 2000).

Numerous recent attempts have been made to determine the particle pressure from the magnitude of the particle velocity fluctuations obtained by applying the kinetic theory of granular flow (Lun et al., 1984).

$$P_s = \varrho_s \varepsilon_s \Theta + 2 g_0 \varrho_s \varepsilon_s^2 \Theta (1+e) \tag{D.28}$$

where the first term on the right side represents the kinetic contribution (momentum transferred through the system by particles moving across imaginary shear layers in the flow); the second term the momentum transferred by direct collisions. Three primary mechanisms for the generation of the bulk stresses were introduced as dry friction, transport of momentum by particle translation, and momentum transport due to particle interactions (Savage and Jeffrey, 1981). The latter study focused on moderately high solids concentrations and shear rates where most particle interactions are collisions occurring over very short time intervals and dry frictional rubbing contacts are relatively infrequent. Taking the possibility of contact time of long duration and frictional collisions into account, Wang and Li (2001) incorporated the three transport mechanisms into the solid pressure term as:

$$P_s = \varepsilon_s \varrho_s \Theta + 2\varepsilon_s^2 \varrho_s (1+e) g_0 \Theta + \varepsilon_{s,max} \varrho_s \exp[-100.6(\varepsilon_{s,max} - \varepsilon_s) - 0.894] \tag{D.29}$$

with the frictional particle pressure obtained from the empirical expression of Campbell and Wang (1991).

Gera et al. (1998) compared the two-fluid model to the discrete element method, setting particle pressure as:

$$P_s = 2\varepsilon_s^2 \varrho_s (1+e) g_0 \Theta \text{ for non-frictional regime (when } \varepsilon > \varepsilon_0) \tag{D.30}$$

$$P_s = (1-\varepsilon) 10^{24} (\varepsilon - \varepsilon_0)^{10} \text{ for frictional regime (when } \varepsilon \le \varepsilon_0) \tag{D.31}$$

where ε_0 is the compaction gas phase volume fraction (to prevent voidage from displaying unrealistically low values). They reported the sensitivity of the solid pressure parameter to simulate

the bubbling characteristics of fluidized beds using two-fluid model. On the other hand, the variation in the empirical input of spring stiffness or frictional coefficient in DEM did not significantly alter the bubble characteristics.

Experimentally, pressure transducers have been employed to measure the solid phase normal stress over long sampling times (Campbell and Wang, 1990 and 1991; Polashenski and Chen, 1997). From the measured solid phase normal stress, the solid shear viscosity was calculated with the help of the kinetic theory. The viscosity was found to be underestimated compared to previously reported experimental values. Further work is required to obtain the constitutive relations of kinetic theory and to test its adequacy to capture the total stress generated by the particle phase (Polashenski and Chen, 1997).

D.4.7 Particle shear viscosity, μ_s

The particle shear viscosity refers to the tangential forces exerted by the particle phase resulting from interparticle collisions. Since a solid-phase is not a physically continuous fluid, this is not a real physical property. However, similar to the solid pressure term of the previous section, a solid-phase viscosity can be derived from kinetic theory considerations, including kinetic and collisional terms. Boemer et al. (1995) noted that at high particle concentrations, the particle viscosity is several orders of magnitude larger than the gas viscosity. Gidaspow and Huilin (1996) reported the collisional viscosity of FCC particles from particle velocity distributions through the dense-phase kinetic theory. The granular temperature increased sharply as the collision frequency increased up to particle concentrations of 0.1, beyond which Θ was observed to decrease as the mean free path of the particles decreased with increasing particle concentration. The large-scale oscillations of particles from a numerical simulation (Arastoopour, 2001) agreed well with the experimental data of Gidaspow and Huilin (1996). Some expressions used for solid shear viscosity based on kinetic theory are listed in Table D.5.

Table D.5 Particle shear viscosity expressions in the literature.

Investigators	Particle shear viscosity
Lun et al. (1984)	$\mu_s = \frac{4}{5}\varepsilon_s^2 \varrho_s d_p g_0 (1+e)\sqrt{\frac{\Theta}{\pi}} + \frac{1}{15}\sqrt{\Theta\pi}\frac{\varrho_s d_p g_0 (1+e)\left(\frac{3}{2}e-\frac{1}{2}\right)\varepsilon_s^2}{\left(\frac{3}{2}-\frac{1}{2}e\right)}$ $+\frac{1}{6}\sqrt{\Theta\pi}\frac{\varrho_s d_p \varepsilon_s\left(\frac{3}{4}e+\frac{1}{4}\right)}{\left(\frac{3}{2}-\frac{e}{2}\right)} + \frac{10}{96}\sqrt{\Theta\pi}\frac{\varrho_s d_p}{(1+e)\left(\frac{3}{2}-\frac{1}{2}e\right)g_0}$
Balzer and Simonin (1993)	$\mu_s = \frac{4}{5}\varepsilon_s^2 \varrho_s d_p g_0 (1+e)\sqrt{\frac{\Theta}{\pi}} + \frac{\Theta(\varrho_s\varepsilon_s)^2}{2\beta + \varrho_s\varepsilon_s^2\frac{(1+e)(3-e)}{5}\frac{6}{d_p}\sqrt{\frac{16\Theta}{\pi}}}$
Syamlal et al. (1993)	$\mu_s = \frac{4}{5}\varepsilon_s^2 \varrho_s d_p g_0 (1+e)\sqrt{\frac{\Theta}{\pi}} + \frac{1}{15}\sqrt{\Theta\pi}\varrho_s d_p g_0 \frac{(1+e)\left(\frac{3}{2}e-\frac{1}{2}\right)}{\left(\frac{3}{2}-\frac{e}{2}\right)}\varepsilon_s^2$ $+\frac{1}{12}\frac{\varepsilon_c d_p \varrho_s \sqrt{\Theta\pi}}{\left(\frac{3}{2}-\frac{e}{2}\right)}$
Gidaspow (1994)	$\mu_s = \frac{4}{5}\varepsilon_s^2 \varrho_s d_p g_0 (1+e)\sqrt{\frac{\Theta}{\pi}} + \frac{1}{15}\sqrt{\Theta\pi}\varrho_s d_p g_0 (1+e)\varepsilon_s^2$ $+\frac{1}{6}\sqrt{\Theta\pi}\varrho_s d_p \varepsilon_s + \frac{10}{96}\sqrt{\Theta\pi}\frac{\varrho_s d_p}{(1+e)g_0}$
Hrenya and Sinclair (1997)	$\mu_s = \frac{4}{5}\varepsilon_s^2 \varrho_s g_0 (1+e)\sqrt{\frac{\Theta}{\pi}} + \frac{1}{15}\sqrt{\Theta\pi}\frac{\varrho_s d_p g_0 (1+e)\left(\frac{3}{2}e-\frac{1}{2}\right)\varepsilon_s^2}{\left(\frac{3}{2}-\frac{e}{2}\right)}$ $+\frac{1}{6}\sqrt{\Theta\pi}\frac{\varrho_s d_p \varepsilon_s\left(\frac{1}{2}\left(1+\frac{\lambda_{mfp}}{R}\right)+\frac{3}{4}e-\frac{1}{4}\right)}{\left(\frac{3}{2}-\frac{1}{2}e\right)\left(1+\frac{\lambda_{mfp}}{R}\right)}$ $+\frac{10}{96}\sqrt{\Theta\pi}\frac{\varrho_s d_p}{(1+e)\left(\frac{3}{2}-\frac{1}{2}e\right)g_0\left(1+\frac{\lambda_{mfp}}{R}\right)}$

Pain et al. (2001)	$\mu_s = \frac{4}{5}\varrho_s\varepsilon_s d_p g_0(1+e)\sqrt{\frac{\Theta}{\pi}}$

D.4.8 Solids phase (bulk) viscosity: λ_s

The solids phase bulk viscosity (Lun et al., 1984; Samuelsberg and Hjertager, 1996) depicts the resistance of the particle suspension to compression:

$$\lambda_s = \frac{4}{3}\varepsilon_s^2\varrho_s d_s g_0(1+e)\sqrt{\frac{\Theta}{\pi}} \qquad \text{(D.32)}$$

D.5 Turbulence in two-phase flow

In reviewing the development of turbulence models in gas solid flow, Samuelsberg and Hjertager (1996) noted that earlier models considered the conservation of mass and momentum equations using an Eulerian approach and extensions of single phase flow expressions, such as the well-known κ-ε model to predict the effect of turbulence on the dispersed phase. However, the flow was treated as inviscid, and particle-particle interactions in the solid phase were neglected, making the model unsuitable for bubbling beds, circulating fluidized bed risers, and pneumatic transport. Based on the kinetic theories of nonuniform dense gases derived mathematically in the 1920s by Chapman and Enskog (Chapman and Cowling, 1970), Jenkins and Savage (1983) derived and solved the conservation equation for the granular temperature, as described in Section D.4.3. In the following section, the treatment of turbulence in each phase is presented prior to reviewing the models representing turbulent two-phase flow.

D.5.1 Gas phase turbulence

The gas phase turbulence is characterized by the scale-changing process-cascading energy scheme producing smaller eddies for self-sustaining turbulence. This is indicated by a power-law fall-off at high frequencies in the power spectra (frequencies between 4 and 10 Hz for fluidization of silica sand at U=2.2 m/s, Sterneus et al., 1999). Micro-scale fluctuations enhance contacting and mixing, and are generated in the gas phase and by interaction between gas and particles. On the other hand, the macro-scale motion is responsible for the convective transport of gas from one point to another. The overall dispersion coefficient can be obtained by superposition of a small-scale and a large-scale dispersion coefficient. Dominant forces in the gas-phase momentum balance are the pressure drop and the drag force, while the contribution of diffusion becomes negligible. The description of gas-phase turbulence is therefore relatively unimportant for dense-phase flows.

D.5.2 Particle phase turbulence

The basis for particle phase turbulence is the observation that the solid phase exhibits a "turbulent-like" behaviour: The large transient fluctuations in the suspension density give rise to time-dependent "Reynolds-like" stresses in the solid phase. The origin of turbulence in two-phase flow has been linked to instabilities, such as the formation of bubbles and slugs in fluidized beds, traced to the particle phase inertia. The particle motion can be partitioned into the fluctuating velocity associated with the organized motion of collections of particles and the fluctuations at the level of individual particles. These fluctuations account for the generation and dissipation of turbulent kinetic energy in both phases, and exchange of this energy between the phases (Dasgupta et al., 1994). Based on the analogy between the random particle motion arising from particle collisions and the thermal motion of molecules in a gas, the pressure and viscosity of the solid phase depend on the intensity of the particle velocity fluctuations (Hrenya and Sinclair, 1997). Using a particle dynamic analyzer, Zhou et al. (2000) identified anisotropic turbulence at all scales in a CFB riser. The particle turbulent intensity was shown to decrease as the probe traversed towards the column axis. The magnitude of the fluctuating particle motion in turbulent flow is influenced by the intensity of turbulence, particle inertia, and the crossing trajectory effect (Yudine, 1959). In a dilute suspension as in a CFB, the presence of particles is considered to provide an additional parallel pathway in dissipating turbulent energy cascaded from large energetic eddies in the gas phase (Senior and Grace, 1998).

D.6 Turbulent two-phase flow models applied to fluidized beds

Sinclair and Jackson (1989) and Pita and Sundaresan (1991) applied the laminar gas/laminar particle model, and reported on the unrealistic degree of sensitivity to the inelasticity of particle-particle collisions. By ignoring gas turbulence, the model did not distinguish regimes in which collisions dominated the interactions of particles with turbulent eddies.

Louge et al. (1991) applied the turbulent gas/laminar particle model to investigate the role of particle collisions in pneumatic transport of large and heavy particles. Since the ratio of particle relaxation time to a typical large-eddy turbulent timescale is large (Hinze, 1972), it was assumed that the gas-phase turbulence influences the mean velocity of the particles, but not their random motion. At higher particle loadings, the model predictions did not compare well with the experimental data of Tsuji et al. (1984) as the expressions used for the mixing length and wall functions were based on a single-phase gas turbulence model (Bolio et al., 1995).

Dasgupta et al. (1994) examined the origin of turbulence and accounted not only for the inertial instability in the gas phase, but also for the particle phase inertia. The physical model is the turbulent gas/turbulent particle model allowing the generation and dissipation of turbulent kinetic energy in both phases and exchange of this energy between the phases. In a dense suspension, the turbulent fluctuations in particle velocity originate from particles being constrained to shear near the walls, through the collective inertia and the effective viscosity developing from collisions between particles.

Another turbulent gas/turbulent particle model was suggested by Zheng et al. (2001) in their κ-ε-κ_p-ε_p-Θ two-fluid model. They incorporated particle turbulence terms analogous to those for the gas. Comparison between the κ-ε-κ_p-ε_p-Θ model with two different dissipation of energy terms, and the κ-ε-Θ model revealed that the κ-ε-κ_p-ε_p-Θ model with inclusion of the dissipation of turbulent energy caused by the turbulent interactions between gas and particle phases gave closer agreement with experimental values. The transfer and dissipation of turbulent energy between the two phases were shown to affect the particle pseudo-temperatures and particle turbulent kinetic energy distribution, thus affecting the particle velocities and solid volume fraction distributions. Numerous studies, e.g. Hernández and Jiménez (1991), Mello et al. (1991) and Savage (1992), have shown the instabilities of a system originating from the collective motion of the particle phase, even when the inertial terms in the gas phase are neglected. This indicates that it is important to include the turbulent kinetic energy terms of the particle phase in simulation models.

D.7 Modelling turbulent fluidized beds

A two-fluid model was applied to simulate a gas-solid turbulent fluidized bed by Zhang and VanderHeyden (2001, 2002). Recognizing the differences in contributions of the added mass and drag reduction effects to different scales, they proposed a two-average approach to distinguish the microscale at a particle level from the mesoscale structures, i.e., bubbles, clusters and streamers. The closure quantities were examined against experimental data of van den Moortel et al. (1998). The excess gas superficial velocities of 0.5-2.0 m/s for Group A powders indicated that the bed was operated in the turbulent fluidization flow regime. The distinction between the interfacial forces for mesoscale structures and the particle length scale enabled different dominant forces to be examined at different levels in the bed. The added-mass effect of the mesoscale structures became a dominant force, arguably because the density associated with the mesoscale added-mass is related to the

mixture density, instead of the gas phase. A new relative velocity reduction coefficient was introduced to account for the reduction in averaged drag between the two phases due to the smaller relative velocity than indicated by the macroscopic relative velocity in the dense phase region. Their two-dimensional contour plot of particle volume fraction indicated a realistic profile. However, the entrained particles were fed from the bottom of the bed, which may have altered the flow at the bottom.

In a technical note by Lettieri et al. (2002), Geldart Group B particles were fluidized to study the transition from bubbling to slugging and turbulent fluidization using a two-fluid model. In order to observe the transition at U=0.35 m/s, the system pressure was raised to 10 bar, resulting in a considerable increase in bed expansion accompanied by greater homogeneity. However, only the first 4 seconds of the simulation were reported without statistically steady-state operation being achieved.

A Eulerian/Lagrangian model was used to simulate a Geldart Group B particle turbulent fluidized bed by Yuu et al. (2001). Close to 486,000 particles were simulated in a three-dimensional bed. The particle turbulent intensity was predicted to increase near the wall, and they were able to simulate the existence of global circulation of particles. In the high particle concentration region, two phenomena were observed: voids causing an increase in particle inertia resulting in destabilization of the flow and enhancing the turbulence; and particles increasing the drag force interaction terms causing a reduction in particle turbulence, depending on the conditions.

D.8 Simulation using CFX

An attempt was made in this project to carry out numerical simulations based on the governing equations discussed above (Equations D.7, D.10 and D.11) using a commercial software package, CFX 4.4 from AEA Technology, Harwell, UK. This version utilizes the kinetic theory of granular flow for closure of the solid stress terms. Among the available CFD software packages, CFX has shown some success in simulating fluidized beds (Witt, et al., 1998; Arastoopour, 2001; Zheng et al., 2001; van Wachem et al., 2001; Krishna and van Baten, 2001; Calis et al., 2001). The objective was to investigate the feasibility of using such a commercial code as a tool to simulate turbulent fluidized beds for further study and scale-up. Due to time constraints, it was not possible to complete satisfactory simulations of a turbulent fluidized bed of FCC particles. However, the steep learning

curve in manoeuvring the software and obtaining converged solutions, particularly in multiphase flow, may have some merit in subsequent simulations using CFX.

D.8.1 Computer speed and capacity

The system requirement for running CFX on a Windows based operating system is the Intel-based workstation with minimum RAM of 256 MB. Secondary hard drive of 120 GB capacity was installed later to accommodate the large output files, e.g. several 100 kB to 1 MB.

D.8.2 Computational techniques

CFX employs the Rhie-Chow (Rhie and Chow, 1983) algorithm for discretization. The governing equations presented in Section D.4 are partial differential equations, which are highly nonlinear and coupled. Thus it is not possible to obtain analytical solutions. The numerical method involves the finite-volume approach with values such as velocity, pressure and temperature defined at the centre of the control volumes. Velocity-pressure corrections were formulated using SIMPLEC (modified version of Semi-Implicit Method for Pressure Linked equations) algorithms. Fully implicit backward differencing was used to discretize time-dependent terms. An algebraic multi-grid linear solver method was adopted for velocity, pressure and volume fraction terms.

D.8.3 Geometry and grid generation

The simulated geometry was created using CFX-BUILD to create a two-dimensional slice of the turbulent fluidized bed of 0.29 m diameter and 4.5 m height. Since CFX adopts a multi-block structure to construct the geometry of the domain, it was necessary to build the geometry with four solids (blocks) as indicated in Figure D.1 in order to accommodate the second inlet representing the particle return area. The overall structure was set as [x y z]=[4.5 m, 0.286 m, 0.01 m]. The 0.01 m depth dimension is more than 100 particle dimensions, sufficient to prevent bridging effects.

Structured grids consisting of grid lines, which do not cross within a cell, and only cross once with a neighbouring cell, were used for discrete representation of the geometric domain. Mesh seeds for solids (blocks) 1 through 3, i.e., three blocks indicated in Figure D.1, were set to be uniform at 9, 24 and 107 seeds in x-direction, with 40 seeds in the y-direction. Solid (block) 4 was meshed with a one-way-bias-mesh seed of 175. Mesh quality was checked using CFX-SOLVER. Key details are listed in Table D.6.

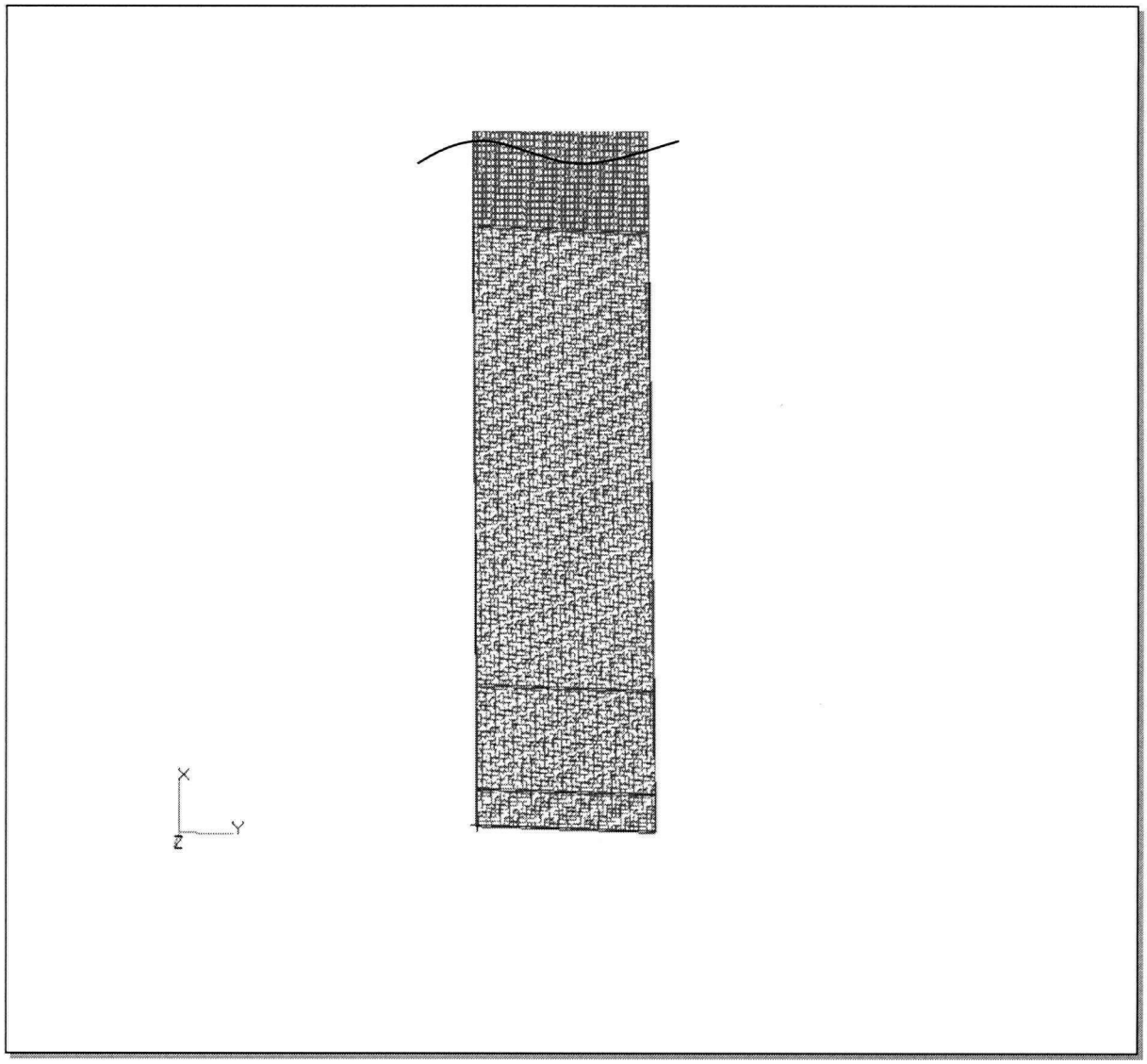

Figure D.1 Modelling geometry for 2D simulation of a turbulent fluidized bed. Green rectangle depicts three solids, i.e., areas, that are set as 3D patch to set static bed height of FCC. The 2D patch highlighted with pink shows the secondary inlet patch to feed solids back in to the column. Top of the column geometry is not shown.

Table D.6 Grid quality for Aug02-geo02.

	MAX VALUE	MIN VALUE
ORTHOG. DEVIATION	3.44E-04	0.00E+00
GRID EXPANSION	1.53E+00	1.00E+00
CELL VOLUME	2.36E-06	4.85E-07
SKEW RATIO	1.00E+00	1.00E+00
TWIST ANGLE	3.44E-04	0.00E+00
TAPER RATIO	1.00E+00	1.00E+00

D.8.4 Boundary and conditions

Boundary conditions were specified through CFX-BUILD. The inlet was set as a Dirichlet inlet of a gas phase. Normal velocity was set at 0.5 m/s with volume fraction of gas at 1.0. The outlet was set as a pressure boundary where both solids and gas were allowed to escape. The absolute outlet pressure was set at 101.3 kPa. The vertical walls normal to the z-direction were set as symmetry planes, and normal to the y-direction were vertical walls with a bed of FCC particles is introduced into the calculation domain through a USER-3D patch, which was set in CFX-BUILD. The static bed height was set at 1 m, equivalent to the three blocks depicted in Figure D.1. The condition of the initial bed was written in USRINT in User Fortran code. USRINT was called at the initial step in the simulation, and toggled off for the subsequent runs restarted from the initialized bed output file. no slip conditions for both phases.

D.8.5 Command file

The governing equations of continuity and momentum were set as Equations D.7, and D.10 and D.11, respectively. The inter-phase non-drag force terms such as virtual mass, lift, wall lubrication and turbulent dispersion forces were not included. The flow, set by writing the command file through CFX-Environment, is two-phase, transient, and turbulent. All operating variables and physical properties and parameters were set in the command file. The time step was varied between 1.0E-04 and 5.0E-4. Under-relaxation factors were set to overcome the instability resulting from non-linearity of the transport equation, thus improving the convergence rates. For the U and V velocities, and κ and ε values, the under-relaxation factors were set at 0.4 based on a recommendation by the technical support staff at CFX. Another method to improve the

convergence rate was to set false time step factors, with the time increment chosen arbitrarily to achieve the best convergence rate. For U and V velocities and volume fractions, the value was set at 1.0E-03.

The algebraic multi-grid method was used to solve the discretized equations for the U and V velocities, pressure, and volume fraction. By choosing the algebraic multi-grid option, the equations are solved on a series of coarsening meshes, chosen algebraically rather than geometrically. This is applied to the linearized difference equations for each control volume in the flow where a simultaneous linear equation solver uses an iterative solution method. Double precision was set for all variables. Setting the numerical precision of the solution procedure led to improved convergence at the cost of increased requirements for memory and CPU time.

D.8.6 User Fortran

Certain User Fortran codes were modified and called upon during the simulation. The following codes were called from the command file: USRINT, USRCVG, USRTRN, USRBCS.

D.8.6.1 USRINT

As described in Section D.9.4, this routine is used to set the initial condition of the particle bed, and overwrites the default initial conditions. An inlet voidage of 1.0 was set with a voidage of 0.45 set for the initial bed condition.

D.8.6.2 USRCVG

This subroutine is called at the end of each iteration to set the convergence criterion, or to modify solution parameters.

D.8.6.3 USRTRN

This routine is called after the initial guess and at the end of each iteration. It was used to calculate the mass flow rate at the pressure boundary at the exit to record the solids entrainment from the bed, and to monitor the total inventory of solid in the system.

D.8.6.4 USRBCS

This routine can be called to specify boundary conditions that change with time or number of iterations. It was used to re-introduce the solids entrained and monitored through pressure boundary and UNRTRN, respectively.

D.8.6.5 CVIS

This subroutine was called to update the solid viscosity term in the kinetic theory of granular flow.

D.8.7 Parameters

As a first attempt, the most promising set of equations for fast convergence and accurate physical results listed by van Wachem et al. (1999) was adopted in this simulation. The drag coefficient was automatically set for different flow regimes:

$$C_D = \frac{24}{Re'} \qquad 0 \le Re \le 0.2 \qquad (D.33)$$

$$C_D = \frac{24}{Re'}\left(1+0.15Re'^{\,0.687}\right) \qquad 0 \le Re \le 500 \text{ to } 1000 \qquad (D.34)$$

$$C_D = 0.44 \qquad 500 \text{ to } 1000 \le Re \le 1 \text{ to } 2\times10^5 \qquad (D.35)$$

For high particle concentrations, the Gidaspow modification was applied in the form of a multiplicative factor on the drag of $(1-\varepsilon_s)^{-1.65}$. The resulting interaction coefficient expressions used in the simulations are:

$$\beta = 150\frac{\varepsilon_s^2\mu_g}{\varepsilon_g d_p^2} + 1.75\frac{\varepsilon_s\varrho_g\left|\upsilon_g-\upsilon_s\right|}{d_p} \qquad \text{for } \varepsilon_s > 0.2 \qquad (D.36)$$

$$\beta = \frac{3}{4}C_D\frac{\varepsilon_g\varrho_g\left|\upsilon_g-\upsilon_s\right|}{d_p}(1-\varepsilon_s)^{-1.65} \qquad \text{for } \varepsilon_s \le 0.2 \qquad (D.37)$$

A discontinuity exists at the solids volume fraction of 0.2.

The solid pressure, and the bulk and shear viscosities were expressed by the granular temperature as:

$$P_s = \varrho_s\varepsilon_s\Theta\left(1+2(1+e)g_0\varepsilon_s\right) \qquad (D.38)$$

$$\lambda_s = \frac{4}{3}\varepsilon_s\varrho_s d_p g_0(1+e)\left(\frac{\Theta}{\pi}\right)^{0.5} \qquad (D.39)$$

$$\mu_s = \frac{10\sqrt{\pi}\,\varrho_s d_p\sqrt{\Theta}}{96(1+e)g_0\varepsilon_s}\left(1+\frac{4}{5}(1+e)g_0\varepsilon_s\right)^2 + \frac{4}{5}\varepsilon_s\varrho_s d_p g_0(1+e)\sqrt{\frac{\Theta}{\pi}} \qquad (D.40)$$

The radial distribution function was given by:

$$g_0 = 0.6\left(1-\left(\frac{\varepsilon_s}{\varepsilon_{s,max}}\right)^{1/3}\right)^{-1} \qquad (D.41)$$

as suggested by Gidaspow (1994).

D.8.8 Convergence

In order to monitor the convergence, the mass source residual was set as a convergence criterion. Figure D.2 depicts a typical gas mass residual, which is the sum of the absolute values of the residuals in each cell for the mass equation (Equation D.7), with iteration. This provides a good guide to convergence.

In order to improve the convergence, some of the strategies are to request a more accurate solution of the inner iterations; or to select a better outer iteration strategy; or to employ a greater under-relaxation; or a combination of these techniques (CFX-4 SOLVER manual). In our simulation, maximum outer iteration and time steps were adjusted to seek better conversion. In addition, it was necessary to incorporate under-relaxation of the equations, and false time step factors to accelerate each equation independently. The technical support staff at CFX through private communications recommended the values set in the simulation through the command file. Further variations of these parameters is required to optimize convergence rates.

D.8.9 Typical result

Figure D.3 is a voidage profile of a typical result from a 2D CFD simulation using CFX. At time 0.0 s, the bed has been fluidized at U=3.5E-03 m/s, a superficial gas velocity close to minimum fluidization velocity. When the superficial velocity was impulsively increased to 0.5 m/s, the bed expansion increased monotonically with time up to 4.0 s. Qualitative assessment of the voidage profile indicates elongated voids with a diffuse dense phase. However, the simulation indicated much too much particle entrainment. Experimental runs indicate an entrainment rate of ~0.1 $kg/m^2/s$, which translates to emptying out a 1.0 m static bed of FCC particles in order of a few hours, as opposed to a few minutes with the simulation. This discrepancy cannot only be due to the simulation being two-dimensional, although the effect of wall boundary conditions on the simulation must be studied. However, the interparticle and particle-fluid interaction terms must be carefully investigated for more accurate simulation. Convergence for the simulation with a restitution coefficient of 0.99 could not be achieved within the time frame of this study. Typical CPU time for the simulation was 51.1 hours for 5 s of real-time simulation.

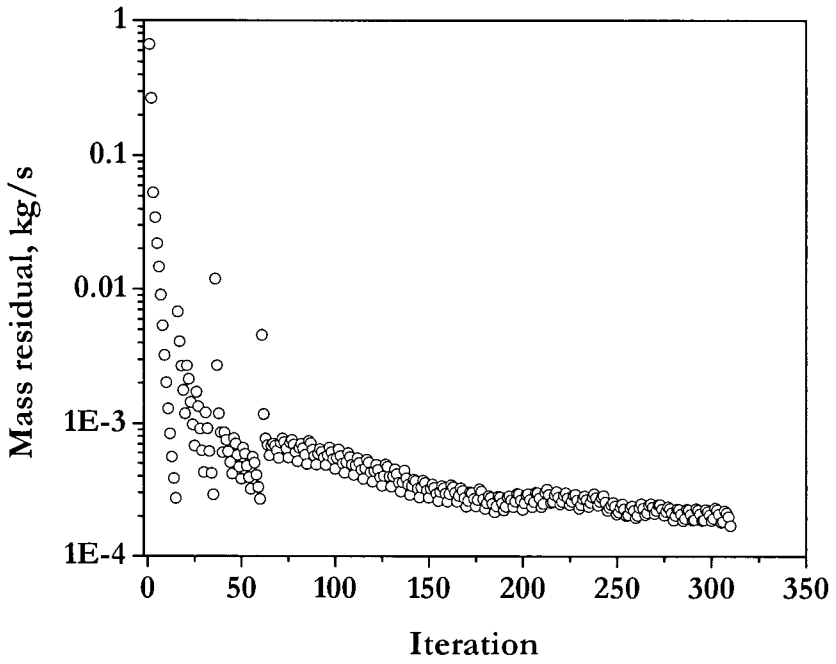

Figure D.2 Mass residual of gas phase with iteration. Run # Oct022-m01.

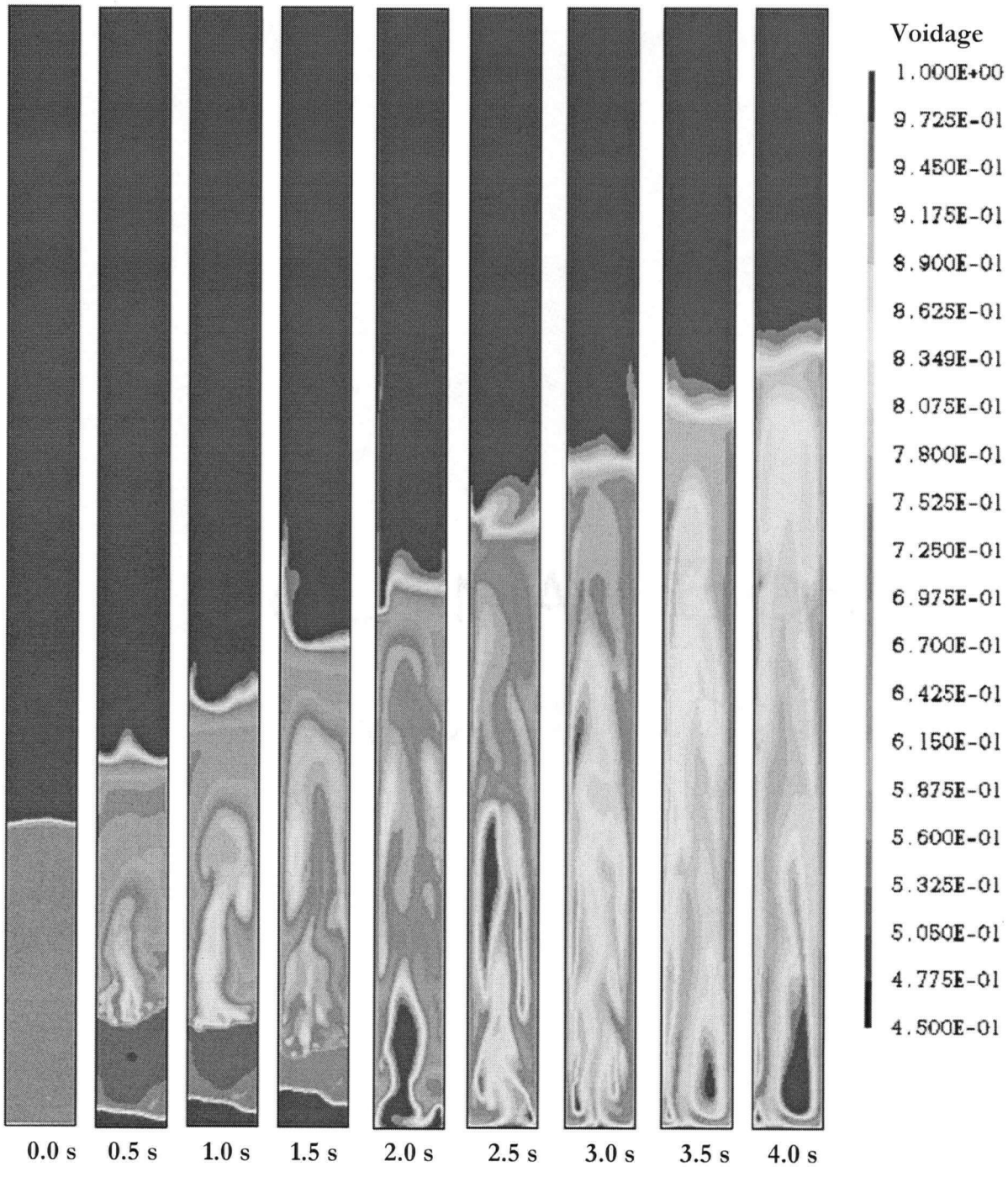

Figure D.3 Simulated voidage profile of 2D fluidized bed operated at atmospheric pressure, U=0.5 m/s. Initial bed height 1.0 m. Coefficient of restitution 0.9. Run # Aug02-m01,m02,m04.

D.8.10 Future studies

The simulation of a turbulent fluidized bed using CFX presented here is far from complete. Numerous subsequent studies are required to develop a set of codes to accurately predict the hydrodynamics for scale-up purposes. Parametric analyses on the drag coefficient, restitution coefficient, and solid stress terms are required to ensure proper coupling of interaction terms. Moreover, particle turbulence should be included. Though 2D and 3D simulations have been reported to give qualitatively similar results (Lettieri et al., 2002), this must be confirmed with experimental values from 2D and 3D beds.

D.9 Conclusions

In this appendix, the forces contributing to the hydrodynamics and the parameters involved in hydrodynamic modelling of fluidized beds have been reviewed in order to provide an understanding of some of the physics governing gas-solid flows. A challenge resides in having very few experimental studies contributing to the understanding of the turbulent flow of fluid-particle mixtures.

The fluid and particle mechanics prevailing in fluidized beds are considered to enable realistic formulation of the processes occurring in complex flows. Given the increase in computational capabilities (memory and speed), CFD has become a powerful tool for modelling hydrodynamics based on governing equations. The kinetic theory approach provides a promising means of closure. However, the inability to measure solid pressure constitutes a major obstacle in using continuity and momentum equations for interpenetrating continua between phases (Mathur and Saxena, 1989).

A commercial computational fluid dynamic software package, CFX, was used to simulate the flow of a gas-solid turbulent fluidized bed. Due to time constraints, it was impossible to complete this part of the study. However, certain techniques in obtaining converging solutions were adopted and are listed here for future study purposes. While CFD is now a standard tool for single-phase flows, it is still at the development stage for dense multiphase systems, such as fluidized beds. Further work is required to make CFD suitable for fluidized bed reactor modelling and scale-up.

Further studies

- Interparticle forces become increasingly significant in dense two-phase flow. Incorporation of not only the collisional effect through kinetic theory of granular flow, but also frictional and kinetic forces may be necessary to account for the particle stress in two-fluid models, such as those incorporated in Wang and Li (2001). Another approach in dealing with the frictional force is to lump the effects into the coefficient of restitution. However, in light of the over-sensitivity to the coefficient of restitution on hydrodynamic simulation (Pita and Sundaresan, 1991; Hrenya and Sinclair, 1997; Gera et al., 1998), careful investigation is required to establish the particle-particle interaction principles.
- Careful experiments using Geldart D particles, or numerical simulations through DEM may provide further understanding of the particle-particle interactions and their relation to the coefficient of restitution. Although the soft-sphere method uses the dashpot, spring and friction slider factors, these empirical inputs have relatively little influence on the simulated hydrodynamics (Gera et al., 1998). Thus, DEM simulation coupled with experimentation on interparticle phenomena may advance the understanding.
- In terms of particle-fluid interactions, the adequacy of the drag coefficient based on group effects must be investigated for dense two-phase suspensions. The drag force in multi-particle system is affected by voidage and particle Reynolds number (Umekage and Yuu, 1999). Numerical simulation of drag and lift forces on a spherical bubble in comparison to a solid particle has shown the difference in the lift between a bubble and a solid particle attributed to pressure and viscous contributions (Kurose et al., 2001). Further study along this line is required.
- Two-fluid models using the kinetic theory require solving for the granular temperature, which is a function of the dissipation of fluctuation energy. A more careful derivation of the quadratic equation, or a full partial differential equation for the granular temperature may be required for application of the kinetic theory to systems that may be sensitive to the restitution coefficient. Gidaspow and Huilin (1998) have reported on the granular temperature deduced from the experimental two-dimensional particle velocity fluctuations in a CFB riser. More such experimental work is greatly needed.